



Hydraulics of dams & river structures

Farhad Yazdandoost

Jalal Attari

**Also available as a printed book
see title verso for ISBN details**

HYDRAULICS OF DAMS AND RIVER STRUCTURES

PROCEEDINGS OF THE INTERNATIONAL CONFERENCE ON
HYDRAULICS OF DAMS AND RIVER STRUCTURES, 26–28 APRIL
2004, TEHRAN, IRAN

Hydraulics of Dams and River Structures

Edited by

Dr. Farhad Yazdandoost

*K.N.Toosi University of Technology, Tehran,
Iran*

Dr. Jalal Attari

*Power and Water University of Technology,
Tehran, Iran*



A.A.BALKEMA PUBLISHERS Leiden/London/New
York/Philadelphia/Singapore

Copyright © 2004 Taylor & Francis Group plc, London, UK

All rights reserved. No part of this publication or the information contained herein may be reproduced, stored in a retrieval system, or transmitted in any form or by any means, electronic, mechanical, by photocopying, recording or otherwise, without written prior permission from the publisher.

Although all care is taken to ensure the integrity and quality of this publication and the information herein, no responsibility is assumed by the publishers nor the author for any damage to property or persons as a result of operation or use of this publication and/or the information contained herein.

Published by: A.A.Balkema Publishers, a member of Taylor & Francis Group plc
<http://www.balkema.nl/> and <http://www.tandf.co.uk/>

This edition published in the Taylor & Francis e-Library, 2005.

“To purchase your own copy of this or any of Taylor & Francis
or Routledge’s collection of thousands of eBooks please go to
<http://www.ebookstore.tandf.co.uk/>.”

ISBN 0-203-02409-5 Master e-book ISBN

ISBN Volume: 90 5809 632 7 (Print Edition)
ISBN CD-ROM: 90 5809 673 4 (Print Edition)

Table of contents

Hydraulics of Dams and River Structures—Yazdandoost & Attari (eds)

© 2004 Taylor & Francis Group, London, ISBN 90 5809 632 7

Preface	x
 <i>Part 1: Hydraulic Structures</i>	 1
 <i>1. Air-water flow</i>	 2
Air-water flows in water engineering and hydraulic structures. Basic processes and metrology <i>H.Chanson</i>	3
De-aeration of a diversion tunnel of a large-scale hydroelectric scheme <i>H.Sigg, U.Keller, P.U.Volkart & H.-E.Minor</i>	22
Free-surface aeration in dam break waves: an experimental study <i>H.Chanson</i>	34
New model investigations on two-phase chute flow <i>K.Kramer, W.H.Hager & H.-E.Minor</i>	45
Evaluation of incipient-aeration point on spillways <i>A.Najafi & M.Yasi</i>	57
 <i>2. Intakes and outlets</i>	 68
Air entrainment at Guri Dam intake operating at low heads <i>G.Montilla, A.Marcano & C.Castro</i>	69
3-D CFD modeling-investigation of potential vortex formation at the intakes of Caruachi Powerhouse <i>A.Marcano, L.Rojas-Solórzano, M.Reyes & J.Marín</i>	79
Numerical unsteady flow model simulation during the sluice closure of Caruachi Dam <i>A.Marcano, C.Castro, I.Mendes & E.Martinez</i>	93
Yacyretá Dam: spillways modification to reduce total dissolved gases concentrations downstream of the dam	104

<i>J.D.Bacchiega & C.A.Fattor</i>	
Hydromatrix [®] : a new way to generate hydropower	118
<i>H.Drobir & V.Keinberger</i>	
3. Hydrodynamic forces	127
Impulse waves from laboratory scale to mega-tsunamis	128
<i>W.H.Hager, H.M.Fritz & A.Zweifel</i>	
Extreme wave transients in reservoirs, their characteristics and interaction with dams	149
<i>T.L.Gvelesiani, A.Huber, Ch.Koutitas & G.T.Matcharadze</i>	
Dynamic pressure fluctuations at real-life plunge pool bottoms	158
<i>E.F.R.Bollaert, P.A.Manso & A.J.Schleiss</i>	
A new procedure to evaluate dynamic uplift of concrete linings or rock blocks in plunge pools	169
<i>E.F.R.Bollaert</i>	
Instantaneous pressure field on a submerged jump stilling basin	181
<i>R.A.Lopardo, C.A.Fattor, M.C.Lopardo & J.M.Casado</i>	
Aspects of vibrations and fatigue of materials related to coherent structures of macroturbulent flows	189
<i>R.A.Lopardo, C.A.Fattor, J.M.Casado & M.C.Lopardo</i>	
Scale effect on pressure fluctuations over sills in stilling basins	199
<i>D.Berzi, E.Larcan, S.Mambretti & E.Orsi</i>	
Analysis of the air rubber dam using “ANSYS”	212
<i>H.Musavi-Jahromi, A.H.Navabi & A.M.Horr</i>	
4. Energy dissipators	221
Plunge pool scour in prototype and laboratory	222
<i>S.Pagliara, W.H.Hager & H.-E.Minor</i>	
Experimental investigations on high-velocity jet characteristics and its influence on plunge pool rock scour	233
<i>P.A.Manso, E.F.R.Bollaert & A.J.Schleiss</i>	
Effect of sill arrangement on maximum scour depth DS of abruptly enlarged stilling basins	245
<i>A.M.Negm</i>	
Energy dissipation and hydrodynamic forces of aerated flow over macro-roughness linings for overtopped embankment dams	256
<i>S.André, J.Matos, J.-L.Boillat & A.J.Schleiss</i>	
Experimental study of energy loss at drops	267
<i>H.Musavi-Jahromi, F.Salmasi & M.Bina</i>	
Dam safety: the use of guidance documents for the training of Inspecting Engineers	277

5. Reservoir sedimentation	285
Impacts of Sanmenxia Dam and management strategies <i>B.S.Wu & Z.Y.Wang</i>	286
New approach in determining useful life of reservoirs <i>J.S.Yeoh, J.H.Loveless & A.M.Siyam</i>	307
The use of labyrinth weir in a reservoir flushing system <i>J.H.Loveless & J.S.Yeoh</i>	318
Numerical and physical modelling concerning the removal of sediment deposits from reservoirs <i>H.Scheuerlein, M.Tritthart & F.Nuñez Gonzalez</i>	328
Application of fine sediment behavior to sedimentation management in Miwa Dam, Japan <i>M.Umeda, M.Okano & G.Yokomori</i>	342
Management of reservoir sedimentation due to turbidity currents by technical measures <i>C.D.Oehy & A.J.Schleiss</i>	354
6. Stepped spillways	365
Energy dissipation along stepped spillways <i>G.Valentin, P.U.Volkart & H.-E.Minor</i>	366
Velocity and pressure field in skimming flow in stepped spillways <i>A.Amador, M.Sánchez Juny, J.Dolz, F.Sánchez-Tembleque & J.Puertas</i>	375
Stepped spillways for embankment dams. Review, progress and development in overflow hydraulics <i>H.Chanson & C.A.Gonzalez</i>	384
Part 2: River Structures	395
7. Scouring and sedimentation around structures	396
Recent views on the origin of river meandering and braiding <i>M.S.Yalin</i>	397
Time-dependent local scour at piled bridge foundations <i>G.Oliveto, A.Rossi & W.H.Hager</i>	407
Time evolution of scour at comparatively long abutments <i>C.M.S.Fael & A.H.Cardoso</i>	416

Local scour downstream of grade control structures <i>C.Adduce, M.La Rocca & P.Mele</i>	428
Scouring profile at channel junction <i>S.M.Borghei, A.Nazari & A.R.Daemi</i>	438
8. <i>Numerical approaches in hydrodynamics of river flow</i>	445
An improved implicit solution for the two dimensional shallow water equations using unstructured grids <i>S.Komaie & W.Bechteler</i>	446
A fully mesh-less Lagrangian numerical method for prediction of free water surface <i>L.Farhadi & B.Ataie-Ashtiani</i>	461
Numerical study of flood routing in compound channels <i>S.A.Ayyoubzadeh & A.Zahiri</i>	471
A finite volume method for solving SWE in rivers on complex topographies <i>D.Farshi & H.-E.Minor</i>	481
Application of a Boussinesq-type equation to flow over trapezoidal profile weirs <i>Y.T.Zerihun & J.D.Fenton</i>	491
Hydrodynamics of three-dimensional density currents <i>B.Firoozabadi</i>	502
9. <i>River response to hydraulic structures</i>	510
Experimental analysis on the hydraulic efficiency of mudflow breakers <i>A.Armanini, C.Dalri, F.Della Putta, M.Larcher, L.Rampanelli & M.Righetti</i>	511
Sub-critical flow in open channel junction <i>A.Behrangi, S.M.Borghei & A.R.Daemi</i>	522
Boundary shear stress distribution in a V-shaped channel <i>M.Mohammadi & D.W.Knight</i>	534
10. <i>Hydroinformatic applications</i>	547
Cardiff Bay barrage and managing the impounded water quality <i>R.A.Falconer & B.Lin</i>	548
River flow forecasting using artificial neural networks <i>M.Zakermoshfegh, M.Ghodsian & Gh.A.Montazer</i>	563
Evaluation of the application of neural networks on real-time river flood prediction <i>M.T.Dastorani</i>	571

Prediction of salinity intrusion in Arvand River <i>B.Sherkati-Azin, A.Etemad-Shahidi & E.Jabbari</i>	585
Author index	595

Preface

Hydraulics of Dams and River Structures—Yazdandoost & Attari (eds)

© 2004 Taylor & Francis Group, London, ISBN 90 5809 632 7

This volume contains papers selected for presentation at the International Conference on Hydraulics of Dams and River Structures in Tehran, Iran on 26–28th April 2004. Hydraulic structures and river works are essential for the development of countries. This is more significant in the millennium development goals owing to scarcity of water for the ever-increasing population of the world. The objective of this conference is to bring together researchers and practitioners to exchange views and experiences on hydraulics of structures associated with rivers and dams. It is further hoped and anticipated that this would lead to a state of the art of the current practice to improve design of hydraulic structures especially in developing countries. Not overlooking the ever growing need for more enhanced and profound non-structural approaches in water resources management issues, it is deliberated that through such a conference the wealth of knowledge and experience in the field would be shared and the structural aspect of water resources management is given its deserved share in sustainable development of infra-structure. In this respect it is hoped that series of specialised conferences of this nature will continue to be held in future.

This conference has been jointly organised by the Iranian Hydraulic Association, International Association of Hydraulic Engineering and Research and the Iranian National Water Research Institute.

The papers are grouped into ten chapters covering the full spectrum of interest in the field. Chapter 1 highlights the importance of air-water flow interaction. In Chapter 2 we raise the important topic of intakes and outlets. A good number of papers were received on the topic of hydrodynamic forces which are presented in Chapter 3. Chapter 4 includes papers on energy dissipators. Of increasing importance is the issue of reservoir sedimentation, which is covered in Chapter 5. Chapter 6 focuses on stepped spillways. We then move to river oriented papers. Chapter 7 highlights research work done on scouring and sedimentation around structures, whereas Chapter 8 is dedicated to the area of numerical approaches in hydrodynamics of river flow. River response to hydraulic structures is dealt with in Chapter 9 and the volume is concluded with Chapter 10, where the important topic of hydroinformatic applications is attended to.

It is hoped that the papers presented will serve both the research and professional communities dealing with the issue. Prudent implementations of ideas and techniques presented here should lead to more sustainable and cost-effective solutions.

We most kindly thank the authors for providing papers of high quality and the members of the International and Local Scientific Committees for their assistance in assessment of selected papers. Joint efforts and collaboration of two specialised committees of the IAHR, namely the Fluvial Hydraulics Committee and the Hydraulic Structures Committee has greatly enhanced the essence of participation in this activity

and is hereby sincerely appreciated. The support and contributions provided by the local sponsors and the supporters has been instrumental in organising the conference. Finally we wish to thank our colleagues at WRI, the conference secretariat, whose hard work and enthusiasm made this volume a valuable compilation of research achievements.

Farhad

Yazdandoost

Jalal Attar

Part 1:
Hydraulic structures`

1.

Air-water flow

Air-water flows in water engineering and hydraulic structures. Basic processes and metrology

H.Chanson

Dept. of Civil Eng., The University of Queensland, Brisbane, Australia

Hydraulics of Dams and River Structures—Yazdandoost & Attari (eds)

© 2004 Taylor & Francis Group, London, ISBN 90 5809 632 7

ABSTRACT: Hydraulic researchers had been leading air-water flow studies until the mid-1950s. Since progresses have been dominated by multiphase flow experts despite the relevance of “white water” phenomena to hydraulic engineering. In this lecture the writer reviews the basic mechanisms of air entrainment: singular aeration and interfacial entrainment. The relevant instrumentation and data processing technique are detailed. Later recent progresses in unsteady flow measurements and in seawater are discussed.

1 INTRODUCTION

In Nature, air-water flows are commonly encountered at waterfalls, in mountain torrents and at wave breaking. “White waters” are also observed in aesthetical fountains and in hydraulic structures (e.g. PLUMPTRE 1993, CHANSON 1997) (Fig. 1). One of the first scientific accounts was made by LEONARDO DA VINCI (AD 1452–1519). He described numerous flow situations and he commented the entrainment of air at waterfalls, plunging jet flows, drop structures, running waters, breaking waves, calling the air-water mixture foam (*schiuma*) and white waters (*bianchezza*). He was intrigued by air entrainment when waters plunge into a receiving pool of water: “Where the water issues forth from the said pool (...) falling or descending through the air, this water acquires weight and impetus; and then piercing the water where it strikes, it tears it apart and dives down



Figure 1. Air entrainment at Chinchilla weir (Australia)—Note self-aeration down chute and in hydraulic jump (foreground)—The beige colour of water is caused by three-phase mixing (air, water & sediment).

in fury (...) accompanied by the air which has been submerged with it"; "If (...) air is submerged with impetus it comes back out of the water"; "Air can never of itself remain beneath the water but always wishes to be above" (McCURDY 1956, Vol. 2). LEONARDO DA VINCI recognised with discernment that air entrainment at plunging jet is related to the momentum ("impetus") of impinging flow. Recent studies highlighted indeed that the impact velocity of the plunging jet is a dominant parameter (WOOD 1991, CHANSON 1997).

Air-water flows have been studied recently compared to classical fluid mechanics. Although some researchers observed free-surface aeration and discussed possible effects (e.g. STEWART 1913), the first successful experimental investigations were conducted during the mid-20th century (CHANSON 1997, HAGER and KRAMER 2003). That is, EHRENBERGER (1926) in Austria, and STRAUB and ANDERSON (1958) in North-America. The latter data set is still widely used by engineers and researchers: e.g., it was cited 24 times between 1985 and June 2001 in Science Citation Index Expanded™. Another important work was the series of experiments performed on the Aviemore dam spillway in New Zealand (KELLER 1972, CAIN 1978) under the supervision of I.R.WOOD. Laboratory and prototype experimental investigations showed the complexity of the free-surface aeration process. Ian R.WOOD further developed the basic principles of modern self-aerated flow calculations. In particular, the uniform equilibrium

air-water flow properties (WOOD 1983), the air content and mean velocity distributions (CAIN and WOOD 1981, WOOD 1984) and the gradually-varied air-water flow properties (WOOD 1985).

These significant findings are not complete and the contribution of hydraulic engineers to gas-liquid flow research has been relatively modest for the last 40 years. Fundamental research has been dominated by chemical, mechanical and nuclear engineers. For example, the intrusive phase-detection needle probe design was developed by Professor S.G.BANKOFF (NEAL and BANKOFF 1963); phase detection optical fibre probes were developed in the late 1960s (JONES and DELHAYE 1976) despite dubious claims! For the period 1985–2003, hydraulic and civil engineering researchers contributed less than 3% of all publications in International Journal of Multiphase Flow. In 2004, hydraulic professionals and researchers lack advanced multiphase flow expertise. In the following paragraphs, the basic mechanisms of air entrainment are discussed and new advances in air-water flows are presented.

2 FREE-SURFACE AERATION IN TURBULENT FLOWS: BASIC MECHANISMS

2.1 Basic definitions

Air entrainment, or free-surface aeration, is defined as the entrainment/entrapment of undissolved air bubbles and air pockets that are carried away within the flowing fluid. The resulting *air-water mixture* consists of both air packets within water and water droplets surrounded by air. It includes also spray, foam and complex air-water structures. In *turbulent flows*, there are two basic types of air entrainment process. The entrainment of air packets can be localised or continuous along the air-water interface (Fig. 2). Examples of *local aeration* include air entrainment by plunging jet and at hydraulic jump (Fig. 1). Air bubbles are entrained locally at the intersection of the impinging jet with the surrounding waters (Fig. 2 Top). The intersecting perimeter is a singularity in terms of both air entrainment and momentum exchange, and air is entrapped at the discontinuity between the high-velocity jet flow and the receiving pool of water. *Interfacial aeration* (or continuous aeration) is defined as the air entrainment process along an air-water interface, usually parallel to the flow direction: e.g., in chute flows (Fig. 1 Left, Fig. 2 Middle). An *intermediate case* is a high-velocity water jets discharging into air. The nozzle is a singularity, characterised by a high rate of aeration, followed by some interfacial aeration downstream at the jet free-surfaces (Fig. 2 Bottom).

2.2 Local (singular) aeration mechanism: air entrapment at plunging jets

With local (singular) aeration, air entrainment results from some discontinuity at the impingement perimeter: e.g., plunging water jets, hydraulic jump flows. One basic example is the vertical plunging jet (Fig. 2 Top). At plunge point, air may be entrapped when the impacting flow conditions exceeding a critical threshold (McKEOGH 1978, ERVINE et al. 1980, CUMMINGS and CHANSON 1999). McKEOGH (1978) showed

onset velocity increases with decreasing jet turbulence. For vertical water jets, the dimensionless onset velocity may be correlated by:

$$\frac{V_e * \mu_w}{\sigma} = 0.0109 * (1 + 3.375 * \exp(-80 * Tu)) \quad (1)$$

where V_e is the onset velocity, μ_w is the liquid dynamic viscosity, σ is the surface tension and Tu is the ratio of the standard deviation of the jet velocity fluctuations about the mean to the jet impact velocity (CUMMINGS and CHANSON 1999).

For jet impact velocities slightly larger than the onset velocity, air is entrained in the form of *individual bubbles and packets*. The entrained air may have the form of “kidney-shaped” bubbles which may break up into two “daughter” bubbles, “S-shape” packets, or elongated “finger” that may break-up to form several small bubbles by a tip-streaming mechanism, depending upon the initial size of the entrained air packet. The air entrainment rate is very small, hardly measurable with phase detection intrusive probes. At higher impact velocities, the amount of entrained air becomes significant and the air diffusion layer is clearly marked by the *white plume* generated by the entrained bubbles. Air entrainment is an unsteady, rapidly-varied process. An *air cavity is set into motion* between the impinging jet and the surrounding fluid and it is stretched by turbulent shear (Fig. 3). The air cavity behaves as a ventilated air sheet and air pockets are entrained by discontinuous gusts at the lower tip of the elongated air cavity. Initial aeration of the impinging jet free-surface may further enhance the process (VAN DE SANDE and SMITH 1973, BRATTBERG and CHANSON 1998).

In the very-near flow field (i.e. $(x-x_1)/d_1 < 5$), the flow is dominated by air entrapment and the interactions between gas and liquid entrainment (Fig. 3). Dominant flow features include an *induction trumpet* generated by the liquid entrainment and the *elongated air cavity* at jet impingement (thickness δ_{al}). Experimental observations showed that the air entrapment/entrainment process is very dynamic and it interacts substantially with the transfer of momentum across the mixing layer. There is a distinct discontinuity between the impinging jet flow and the induction trumpet as sketched in Figure 3 which shows an instantaneous “snapshot” of the entrapment region. Experimental data indicated a

velocity discontinuity across the elongated air cavity: $V_i \propto (V_1 - V_e)^{0.15}$, where V_1 is the jet impact velocity and V_i is the liquid entrainment velocity in the induction trumpet (CHANSON 2002). It is believed that air entrainment takes place predominantly in the elongated cavity by a Couette flow motion (Fig. 3 Right). For two-dimensional plunging jets, the air entrainment rate q_{air} may be estimated as:

$$q_{air} = \int_{d_1}^{d_1 + \delta_{al}} V_{air} * dy \approx \frac{V_1 + V_i}{2} * \delta_{al} \quad (2)$$

Downstream of the entrapment region (i.e. $(x-x_1)/d_1 > 5$), the distributions of void fractions exhibit smooth, derivative profiles which follow closely simple analytical solutions of the advective

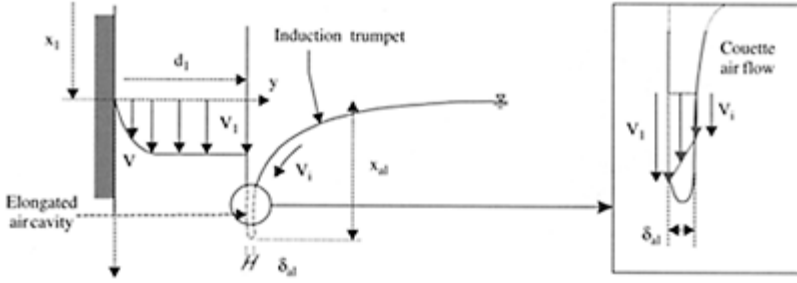


Figure 3. Detail of the air entrainment region and the very-near flow field.

diffusion equation for air bubbles (CHANSON 1997). For two-dimensional vertical jets, it yields:

$$C = \frac{Q_{air}}{Q_w} * \frac{1}{\sqrt{4 * \pi * D^{\#} * \frac{x-x_1}{Y_{Cmax}}}} * \left(\exp \left(-\frac{\left(\frac{y}{Y_{Cmax}} - 1 \right)^2}{4 * D^{\#} * \frac{x-x_1}{Y_{Cmax}}} \right) + \exp \left(-\frac{\left(\frac{y}{Y_{Cmax}} + 1 \right)^2}{4 * D^{\#} * \frac{x-x_1}{Y_{Cmax}}} \right) \right) \quad (3)$$

where $D^{\#}$ is a dimensionless air bubble diffusivity and $Y_{Cmax}=y(C=C_{max})$. CUMMINGS and CHANSON (1997) and BRATTBERG and CHANSON (1998) presented successful comparisons between Equation (3) and experimental data. With circular plunging jets, the analytical solution of the diffusion equation becomes:

$$C = \frac{Q_{air}}{Q_w} * \frac{1}{4 * D^{\#} * \frac{x-x_1}{Y_{Cmax}}} * \exp \left(-\frac{1}{4 * D^{\#} * \frac{x-x_1}{Y_{Cmax}}} * \left(\frac{r}{Y_{Cmax}} \right)^2 + 1 \right) * I_0 \left(\frac{1}{2 * D^{\#} * \frac{x-x_1}{Y_{Cmax}}} * \frac{r}{Y_{Cmax}} \right) \quad (4)$$

where I_0 is the modified Bessel function of the first kind of order zero. CHANSON and MANASSEH (2003) and CHANSON et al. (2002) showed successful comparisons between Equation (4) and experimental data.

2.3 Interfacial aeration process: self-aeration down a steep chute

Examples of interfacial aeration include spillway flows and “white waters” down a mountain stream (Fig. 1, 2 Middle and 4). On smooth and stepped (skimming flow) chutes, the upstream flow is non-aerated but free-surface instabilities are observed. Such wave instabilities were mentioned by ANWAR (1994), CHANSON (1997) and MATOS et al. (1999) for example. The location of inception of free-surface aeration is clearly defined however (Fig. 4). Downstream the flow becomes rapidly aerated. Self aeration may induce significant flow bulking, air-water mass transfer drag reduction while it may prevent cavitation damage (FALVEY 1980, 1990, WOOD 1983, CHANSON 1994).

KEULEGAN and PATTERSON (1940) analysed wave instability and implied that air bubbles may be entrained by a breaking wave mechanism at the free surface. Photographs by CAIN (1978) at Aviemore dam spillway showed that air is entrained by the action of a multitude of irregular vortices



Figure 4. Skimming flow down Trigomil stepped spillway (Mexico): $Q_w=1,017 \text{ m}^3/\text{s}$, chute width: 75 m (Courtesy of Drs Sanchez-Bribiesca and Gonzales-Villareal).

acting next to the free-surface. Basically air bubble entrainment is caused by turbulence fluctuations acting next to the air-water free surface. Through the “free-surface”, air is continuously trapped and released. Air bubbles may be entrained when the turbulent kinetic energy is large enough to overcome both surface tension and gravity effects. The turbulent velocity be greater than the surface tension pressure and the bubble rise velocity component for the bubbles to be carried away:

$$v' > \text{Maximum} \left(\sqrt{\frac{8 * \sigma}{\rho_w * d_{ab}}}; u_r * \cos \theta \right) \quad (5)$$

where v' is an instantaneous turbulent velocity normal to the flow direction, σ is the surface tension, ρ_w is the water density, d_{ab} is the diameter of the entrained bubble, u_r is the bubble rise velocity and θ is the channel slope (ERVINE and FALVEY 1987, CHANSON 1993). Equation (5) predicts the occurrence of air bubble entrainment for $v' > 0.1$ to 0.3 m/s . The condition is nearly always achieved in prototype chute flows because of the strong turbulence generated by boundary friction. Interfacial aeration involves both the entrainment of air bubbles and the formation of water droplets. The air-water mixture flow consists of water surrounding air bubbles ($C < 30\%$), air surrounding

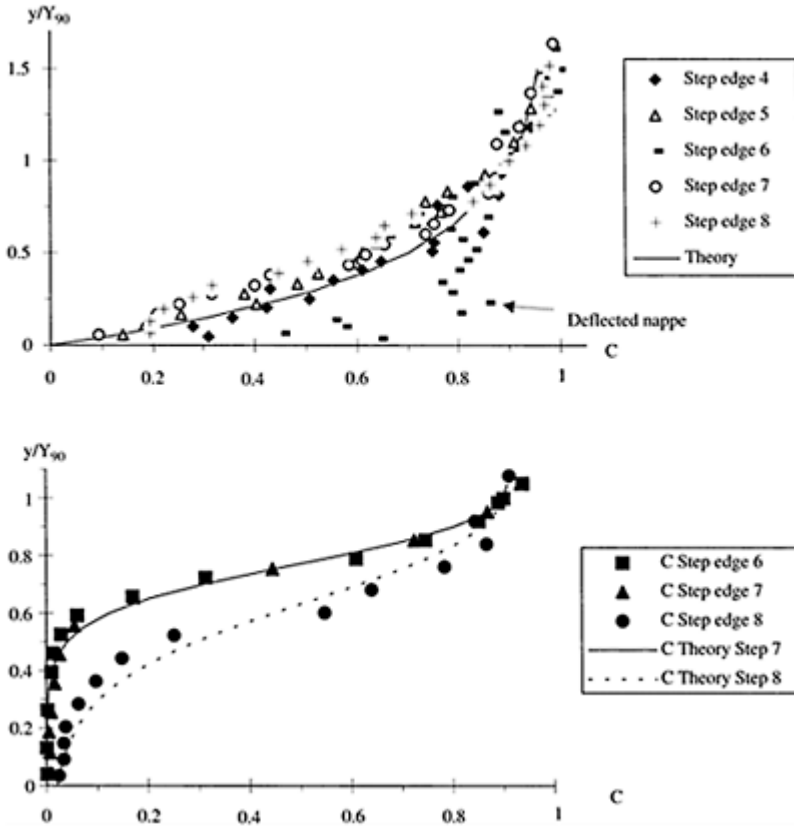


Figure 5. Dimensionless distributions of void fraction in stepped chute flow ($\theta=21.8^\circ$, step height: 0.1 m, chute width: 1 m). Top: Transition flow, $q=0.058 \text{ m}^2/\text{s}$ (data measured at outer step edges)—Comparison with Equation (6). Bottom: Skimming flow: $q=0.182 \text{ m}^2/\text{s}$ (data measured at outer step edges)—Comparison with Equation (7).

water droplets ($C>70\%$) and an intermediate flow structure for $0.3<C<0.7$ (Fig. 2 Middle). (REIN (1998) and CHANSON (1999) discussed specifically the spray region (i.e. $C>95\%$)). Note that waves and wavelets propagate downstream along the free-surface. A phase detection probe, fixed in space, will record a fluctuating signal corresponding to both air-water structures and wave passages, adding complexity of the interpretation of the signal (TOOMBES 2002).

Downstream of the inception point of free-surface aeration, air and water are fully mixed, forming a homogeneous two-phase flow (CHANSON 1995, 1997). The advective diffusion of air bubbles may be described by simple analytical models. In transition flows down a stepped chute, the distributions of void fraction follow closely:

$$C = K' * \left(1 - \exp\left(-\lambda * \frac{y}{Y_{90}}\right) \right) \quad \text{Transition flows} \quad (6)$$

where y is distance measured normal to the pseudo-invert, Y_{90} is the characteristic distance where $C=90\%$, K' and λ are dimensionless function of the mean air content only. Equation (6) compared favourably with experimental data (CHANSON and TOOMBES 2002) (Fig. 5 Top).

In skimming flows and smooth-chute flows, the air concentration profiles have a S-shape that may be modelled by:

$$C = 1 - \tanh^2 \left(K' - \frac{y}{2D_0} + \frac{\left(\frac{y}{Y_{90}} - \frac{1}{3}\right)^3}{3 * D_0} \right) \quad \text{Skimming \& smooth-chute flows} \quad (7)$$

where K' is an integration constant and D_0 is a function of the mean void fraction only. In Figure 5 (Bottom), laboratory data are compared successfully with Equation (7). Although Figure 5 highlights different shapes of void fraction distribution between transition and skimming flows, Equations (6) and (7) derive from the same basic equation assuming different diffusivity profiles (CHANSON and TOOMBES 2002)

3 BASIC METROLOGY IN HYDRAULIC ENGINEERING

In hydraulic engineering, classical measurement devices (e.g. Pitot tube, LDV) are affected by entrained bubbles and might lead to inaccurate readings. When the void fraction C exceeds 5 to 10%, and is less than 90 to 95%, the most robust instrumentation is the intrusive phase detection probes: optical fibre probe and conductivity/resistivity probe (JONES and DELHAYE 1976, BACHALO 1994, CHANSON 1997,2002). The intrusive probe is designed to pierce bubbles and droplets (Fig. 6A). For example, the probe design shown in Figure 6A was designed with a small frontal area of the first tip and with a displaced second tip (offset $<0.2*\Delta x$) to avoid wake disturbance from the leading tip. Tests showed the absence of wake disturbance during all the experiments (CHANSON 1995). A typical probe signal output is shown in Figure 6B. Although the signal is theoretically rectangular, the probe response is not exactly square because of the finite size of the tip, the wetting/drying time of the interface covering the tip and the response time of the probe and electronics (e.g. CUMMINGS 1996).

3.1 Data processing

The basic probe outputs are the void fraction, bubble count rate and bubble chord time distributions with both single-tip and double-tip probe designs. The void fraction C is the proportion of time that the probe tip is in the air. The bubble count rate F is the number of

bubbles impacting the probe tip. The bubble chord times provide information on the air-water flow structure. For one-dimensional flows, chord sizes distributions may be derived (e.g. CHANSON et al. 2002).

A dual-tip probe design (Fig. 6A) provides additionally the air-water velocity, specific interface area, chord length size distributions and turbulence level. The velocity measurement is based upon the successive detection of air-water interfaces by two tips. In turbulent air-water flows, the successive detection of all bubbles by each tip is highly improbable and it is common to use a cross-correlation technique (e.g. CROWE et al. 1998). The time-averaged air-water velocity equals:

$$V = \frac{\Delta x}{T} \quad (8)$$

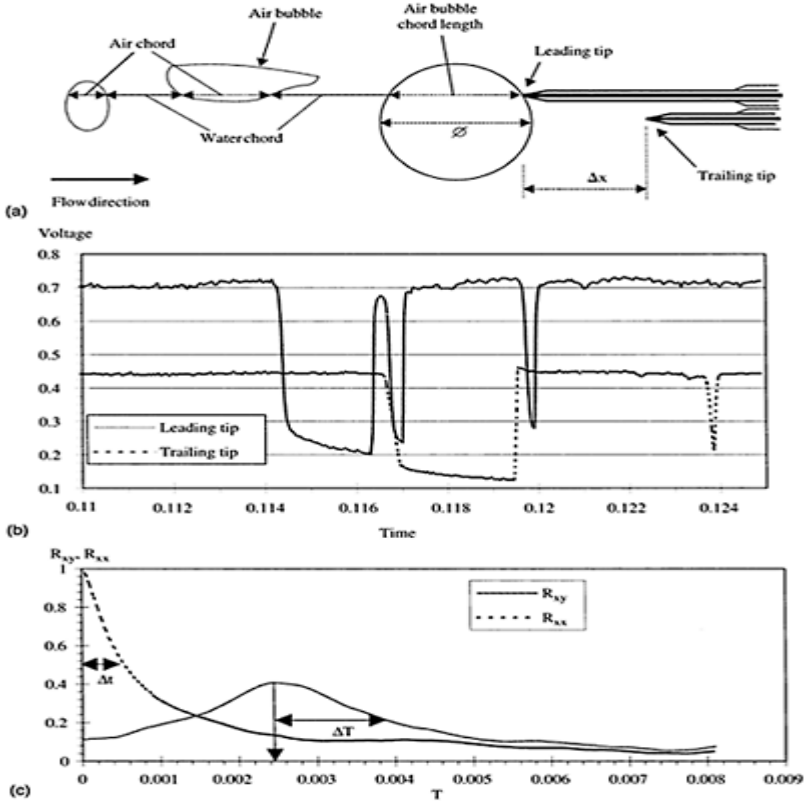


Figure 6. Local air-water flow measurements in skimming flow down a stepped chute (16° slope, $h=0.10$ m, $d_c/h=1.5$) with a double-tip conductivity probe (scan rate: 40 kHz per tip, $\varnothing=0.025$ mm, $\Delta x=8$ mm)—

$C=0.09$, $V=3.05$ m/s, $F=121$ bubbles per second, $y=39$ mm, step 8. (a) Sketch of bubble impact on phase-detection probe tips (dual-tip probe design); (b) Voltage outputs from a double-tip conductivity probe; (c) Normalised auto-correlation and cross-correlation functions.

where Δx is the distance between tips and T is the time for which the cross-correlation function R_{xy} is maximum (Fig. 6C). The shape of the cross-correlation function provides further information on the velocity fluctuations (CHANSON and TOOMBES 2002). The turbulent intensity may be derived from the broadening of the cross-correlation function compared to the auto-correlation function:

$$Tu = \frac{u'}{V} = 0.851 * \frac{\sqrt{\Delta T^2 - \Delta t^2}}{T} \quad (9)$$

where ΔT as a time scale satisfying: $R_{xy}(T+\Delta T)=0.5 R_{xy}(T)$, R_{xy} is the normalised cross-correlation function, and Δt is the characteristic time for which the normalised autocorrelation function R_{xx} equals 0.5 (Fig. 6C). The autocorrelation function R_{xx} provides some information on the air-water flow structure. A dimensionless integral length scale is:

$$I_L = 0.851 * \frac{\Delta t}{T} \quad (10)$$

A time series analysis gives information on the frequency distribution of the signal which is related to the air & water (or water & air) length scale distribution of the flow. Chord sizes may be calculated from the raw probe signal outputs. The results provide a complete characterisation of the streamwise distribution of air and water chords, including the existence of bubble/droplet clusters (e.g. CHANSON and TOOMBES 2002). The measurement of air-water interface area is a function of void fraction, velocity, and bubble sizes. The specific air-water interface area a is defined as the air-water interface area per unit volume of air and water. For any bubble shape, bubble size distribution and chord length distribution, it may be derived from continuity:

$$a = \frac{4 * F}{V} \quad (11)$$

where Equation (11) is valid in bubbly flows ($C < 0.3$). In high air content regions, the flow structure is more complex and the specific interface area a becomes simply proportional to the number of air-water interfaces per unit length of flow ($a \propto 2 * F/V$).

4 NEW DEVELOPMENTS IN AIR-WATER FLOW APPLICATIONS

While air-water flow measurements have been successfully conducted in models and prototypes, current techniques are limited to steady freshwater flows. In unsteady flows, the processing technique must be modified. Early experiments in seawater suggested that biochemicals, surfactants and living organisms interact with the flow turbulence and may affect drastically the air entrainment processes. Both issues are briefly discussed below.

4.1 Unsteady flow measurements

Air-water flow measurements in unsteady flows are difficult, although prototype observations of sudden spillway releases and flash floods highlighted strong aeration of the leading edge of the wave associated with chaotic flow motion and energy dissipation (Fig. 7). Figure 7A presents a flood wave advancing down the Brushes Clough dam stepped spillway. Figure 7B shows a laboratory experiment of dam break wave propagation down a stepped waterway.

In unsteady air-water flows, the measurement processing technique must be adapted (STUTZ and REBOUD 2000, CHANSON 2003), in recent experiments, local void fractions were calculated over a short time interval $\tau = \Delta X / C_s$ where C_s is the measured surge front celerity and ΔX is the control volume streamwise length. Measurements were conducted in a stepped chute at several locations X' measured from the vertical step face. Figure 8 shows dimensionless distributions of void fractions at $X' = 1.0\text{m}$ for several times $(t - t_s)$, where t_s is the time of passage of wave front. The legend indicates the control volume streamwise length ΔX and the dimensionless time $(t - t_s) * \sqrt{g/d_0}$, where d_0 is a measure of the initial flow rate $Q(t=0+)$:

$$d_0 = \frac{9}{4} * \sqrt[3]{\frac{Q(t=0+)^2}{g * W^2}} \quad (12)$$

and W is the channel width. For an ideal dam break, d_0 would be equivalent to the initial water depth behind the dam. The data are compared with corresponding steady flow data. The distributions of void fractions demonstrated a very strong aeration of the leading edge for $(t - t_s) * \sqrt{g/d_0} < 1.1$ to 1.3. In Figure 8, the data for $(t - t_s) * \sqrt{g/d_0} = 0.25, 0.25, 0.455, 0.66$ and 2.11 yielded depth-averaged void fractions $C_{\text{mean}} = 0.47, 0.54, 0.40$ and 0.25 respectively. In steady flow, the mean air content was $C_{\text{mean}} = 0.20$.

At the front of the wave, the void fraction distributions had roughly a linear shape:

$$C = 0.90 * \frac{y}{Y_{90}} (t - t_s) * \sqrt{g/d_0} < 1.2 \quad (13)$$

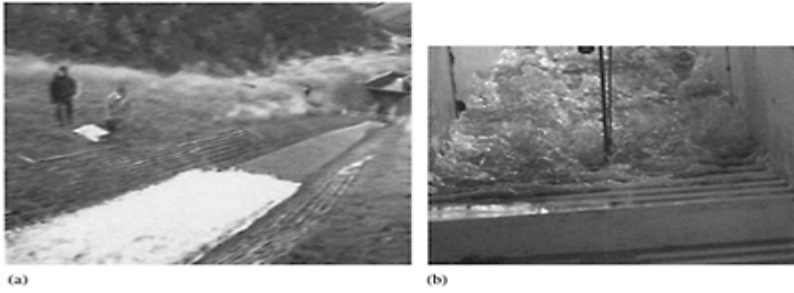


Figure 7. Advancing flood waves down stepped chutes (leading edge of dam break waves); (a) Flood wave propagating down Brushes Clough dam spillway during field tests in 1994 (Courtesy of Dr R.BAKER)— $Q(t=0+) \sim 0.5 \text{ m}^3/\text{s}$, 18.4° slope, $h=0.19 \text{ m}$; (b) Looking upstream at an advancing wave on step 16 with an array of conductivity probes in foreground— $Q(t=0+)=0.055 \text{ m}^3/\text{s}$, $d_o=0.241 \text{ m}$, 3.4° slope, $h=0.07 \text{ m}$ ($W=0.5 \text{ m}$).

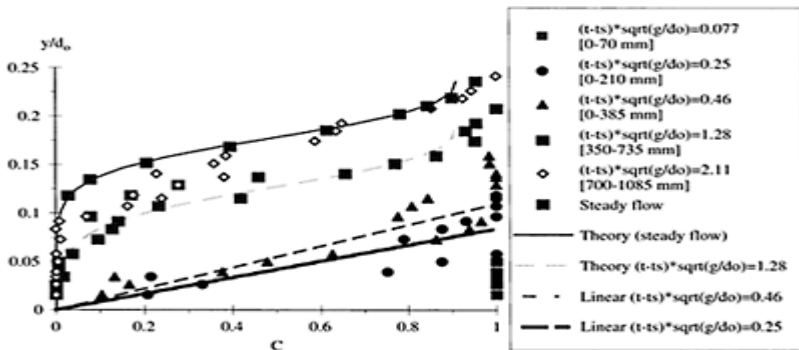


Figure 8. Dimensionless void fraction distributions behind the wave front leading edge ($Q(t=0+)=0.075 \text{ m}^3/\text{s}$, $d_o=0.300 \text{ m}$, $h=0.07 \text{ m}$, $l=1.2 \text{ m}$, Step 10, $C_s=2.61 \text{ m/s}$, $X'=1.0 \text{ m}$)—

Comparison with steady flow data, and Equations (13) and (7).

where Y_{90} is the location where $C=90\%$. Equation (13) is a limiting case of the analytical solution of air bubble diffusion equation for steady transition flows down stepped chute (Eq. (6)). For larger times ($t-t_s$), the distribution of air concentration may be described by a advective diffusion model (Eq. (7)). Equations (13) and (7) are plotted for steady and unsteady flow conditions in Figure 8. For all experiments, a major change in void fraction

distribution shape took place for $(t-t_s) * \sqrt{g/d_0} \sim 1.1$ to 1.5 . Possible explanations may include non hydrostatic pressure distributions at the leading wave front, some change in air-water flow structure associated with a change in rheological fluid properties, a change in gas-liquid flow regime, with a plug/slug flow regime in front a homogenous bubbly flow region behind, and some alteration in shear stress distributions and boundary friction.

Further air-water velocity measurements were conducted in the wave front. At the leading edge, instantaneous velocity measurements suggested a boundary layer region with a potential region above. The data showed however unusually large velocities at the leading edge, although the velocity distribution tended rapidly toward a quasi-steady flow pattern. At the leading edge, boundary layer velocity data were compared successfully with an analytical solution of the Navier-Stokes equations (first Stokes problem):

$$\frac{V}{U} = \text{erf}\left(\frac{y}{2 * \sqrt{\nu_T * (t - t_s)}}\right) \quad (14)$$

where U is the fre-stream velocity, ν_T is the kinematic viscosity, and y is the distance normal to the invert. Despite some scatter, the results suggested a turbulent boundary layer flow. The data yielded a ratio of air bubble diffusivity to eddy viscosity of about unity, implying very strong interactions between momentum transfer and air bubble diffusion processes.

4.2 Air entrainment in seawater

While most studies of air entrainment were conducted with freshwater, a small number of basic studies in seawater suggested that air entrainment may be an entirely different process, although the physical fluid properties are close (Table 1). Some studies considered the size of bubbles produced by a frit, showing that bubble coalescence was drastically reduced in saltwater compared to freshwater experiments (e.g. SCOTT 1975, WALKDEN 1999). Similar trends were recorded during wave flumes and tilting bucket experiments (BOWYER 1992, HAINES and JOHNSON 1995), although most works used visual observations implying very-low void fraction flow conditions.

An experimental study of developing flow region of plunging jets was conducted systematically with freshwater, seawater and salty freshwater (CHANSON et al. 2002). The results indicated lesser air entrainment in seawater than in freshwater, all inflow parameters being identical. It was hypothesised that surfactants, biological and chemical elements harden the induction trumpet and diminish air entrapment at impingement in

seawater. Typical bubble sizes were millimetric in seawater with mean chords of about 3–6 mm. Seawater bubbly flows contained comparatively a greater number of fine bubbles than freshwater plunging jets for identical inflow conditions. These fine bubbles (less than 0.5 mm) have a slower rise velocity and they give a visual, misleading appearance to the air-water flow suggesting inaccurately that very fine bubbles are predominantly entrained in seawater plunging jets (Fig. 9).

Table 1. Measured physical properties of water solutions (after CHANSON et al. 2002).

Property	Tap water	Seawater	Salty tap water (3.45% solution)	Remarks
(1)	(2)	(3)	(4)	(5)
Density (kg/m^3)	998.2	1,024		1,024 At 20° Celsius
Dynamic viscosity (Pa.s)	1.015 E-3	1.22 E-3		1.18 E-3 At 20° Celsius
Kinematic viscosity (m^2/s)	0.925 E-6	0.97 E-6		0.962 E-6 At room temperature (about 22°C)
Surface tension (N/m)	0.073	0.076		0.075 At room temperature (22°C)
Conductivity ($\mu\text{S}/\text{cm}$)	87.7	49,000		53,600 At 25° Celsius
pH	6.83	8.1		6.94 At room temperature (22°C)

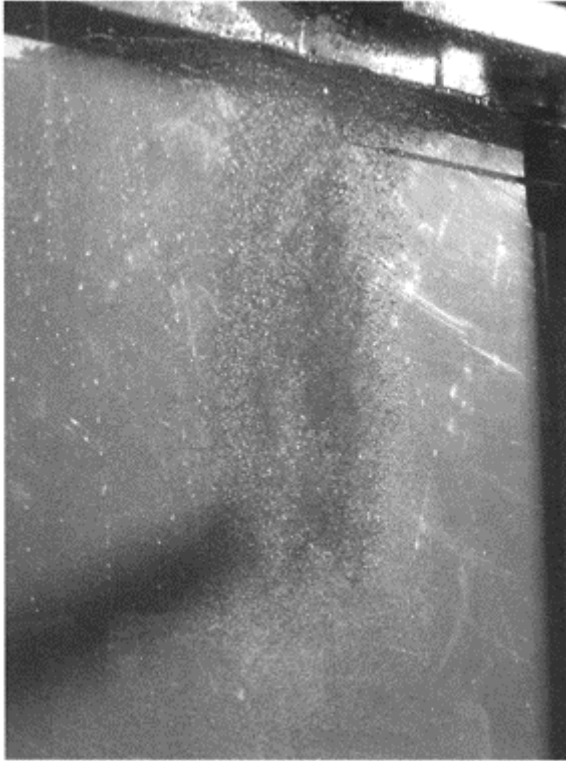


Figure 9. Air bubble entrainment at circular plunging jet in seawater
 $d_n=0.0125$ mm, $x_1=0.050$ m, $V_1=2.46$ m/s

Air entrainment at plunging jets differed between saltwater and seawater with less air and smaller bubbles entrained in seawater. The results implied that classical dimensional analysis is incomplete unless physical, chemical and biological properties other than density, viscosity and surface tension are taken into account. Overall the study demonstrated that air entrainment in the Sea is a complicated process which cannot be modelled accurately in small-size wave flumes nor with fresh water experiments. It was hypothesised that organic matter might also play a role in inhibiting bubble entrainment in seawater while living organisms may interact with the flow turbulence.

5 SUMMARY AND CONCLUSION

There are two basic mechanisms of air entrainment: local/singular entrapment and interfacial aeration. In hydraulic structures, both phenomena are observed, and “white

waters” may induce some flow bulking and drag reduction, and they may contribute to air-water mass transfer and prevention of cavitation damage. These issues must be properly understood by professionals and taken into account in modern design of hydraulic structures.

In hydraulic engineering, the void fraction (or air concentration) ranges typically from zero (clear-water) to 100% (pure air), and the prototype flows are highly turbulent. For such flow conditions, it is acknowledged that the most robust instrumentation is the intrusive phase-detection probe. The basic probe outputs include the void fraction, bubble count rate, time-averaged velocity and turbulence intensity. Further outputs include bubble and droplet chord size distributions, the streamwise distributions of bubbles and the air-water flow structure.

The same type of instrumentation maybe used in unsteady air-water flows and in seawater. In the latter case, preliminary results suggested that a different air-water flow structure in seawater.

ACKNOWLEDGMENTS

The writer thanks his past and present students Dr P.D.CUMMINGS, Carlos GONZALEZ, Chung-hwee “Jerry” LIM, Chye-guan SIM, Chee-chong TAN, York-wee TAN, Dr L.TOOMBES for their help and assistance.

REFERENCES

- ANWAR, H.O. (1994). “Self-Aerated Flows on Chutes and Spillways—Discussion.” *Jl of Hyd. Engrg.*, ASCE, Vol. 120, No. 6, pp. 778–779.
- BACHALO, W.D. (1994). “Experimental methods in Multiphase Flows.” *Intl Jl of Multiphase Flow*, Vol. 20, Suppl., pp. 261–295.
- BOWYER, P.A. (1992). “The Rise of Bubbles in a Glass Tube and the Spectrum of Bubbles Produced by a Splash.” *Jl of Marine Res.*, Vol. 50, pp. 521–543.
- BRATTBERG, T., and CHANSON, H. (1998). “Air Entrainment and Air Bubble Dispersion at Two-Dimensional Plunging Water Jets.” *Chemical Engineering Science*, Vol. 53, No. 24, Dec., pp. 4113–4127. Errata: 1999, Vol. 54, No. 12, p. 1925.
- CAIN, P. (1978). “Measurements within Self-Aerated Flow on a Large Spillway.” *Ph.D. Thesis*, Ref. 78–18, Dept. of Civil Engrg., Univ. of Canterbury, Christchurch, New Zealand.
- CAIN, P., and WOOD, I.R. (1981). “Measurements of Self-aerated Flow on a Spill way.” *Jl. Hyd. Div.*, ASCE, 107, HY11, pp. 1425–1444.
- CHANSON, H. (1993). “Self-Aerated Flows on Chutes and Spillways.” *Jl of Hyd. Engrg.*, ASCE, Vol. 119 No. 2, pp. 220–243. Discussion: Vol. 120, No. 6, pp. 778–782.
- CHANSON, H. (1994) “Drag Reduction in Open Channel Flow by Aeration and Suspended Load.” *Jl of Hyd. Res.*, IAHR, Vol. 32, No. 1, pp. 87–101
- CHANSON, H. (1995). “Air Bubble Entrainment in Free-surface Turbulent Flows. Experimental Investigations.” *Report CH46/95*, Dept. of Civil Engineering, University of Queensland, Australia, June, 368 pages.
- CHANSON, H. (1997). “*Air Bubble Entrainment in Free-Surface Turbulent Shear Flows*” Academic Press, London, UK, 401 pages.
- CHANSON, H. (1999). “Turbulent Open-Channel Flows: Drop-Generation and Self-Aeration. Discussion.” *Jl of Hyd. Engrg.*, ASCE, Vol. 125, No. 6, pp. 668–670.

- CHANSON, H. (2002). "Very Strong Free-Surface Aeration in Turbulent Flows: Entrainment Mechanisms and Air-water Flow Structure at the "Pseudo" Free-Surface", in *"Interaction of Strong Turbulence with Free Surfaces"*, World Scientific, Advances in Coastal and Ocean Engineering Series, Vol. 8, Singapore, M.BROCCHINI and D.H.PEREGRINE Ed., Vol. 8, pp. 65–98.
- CHANSON, H. (2003). "Sudden Flood Release down a Stepped Cascade. Unsteady Air-water Flow Measurements. Applications to Wave Run-up, Flash Flood and Dam Break Wave." *Report CH51/03*, Dept of Civil Eng., Univ. of Queensland, Brisbane, Australia, 142 pages.
- CHANSON, H., and MANASSEH, R. (2003). "Air Entrainment at a Circular Plunging Jet. Physical and Acoustic Characteristics." *Jl of Fluids Eng.*, Trans. ASME, Vol., July.
- CHANSON, H., and TOOMBES, L. (2002). "Air-water Flows down Stepped chutes: Turbulence and Flow Structure Observations." *Intl Jl of Multiphase Flow*, Vol. 27, No. 11, pp. 1737–1761.
- CHANSON, H., AOKI, S., and HOQUE, A. (2002). "Scaling Bubble Entrainment and Dispersion in Vertical Circular Plunging Jet Flows: Freshwater versus Seawater." *Proc. 5th Intl Conf. on Hydrodynamics ICHD 2002*, Tainan, Taiwan, H.H.HWUNG, J.F.LEE & K.S.HWANG Editors, pp. 431–436.
- CROWE, C., SOMMERFIELD, M., and TSUJI, Y. (1998). *"Multiphase Flows with Droplets and Particles."* CRC Press, Boca Raton, USA, 471 pages.
- CUMMINGS, P.D. (1996). "Aeration due to Breaking Waves." *PhD thesis*, Dept. of Civil Engrg., University of Queensland, Australia.
- CUMMINGS, P.D., and CHANSON, H. (1997). "Air Entrainment in the Developing Flow Region of Plunging Jets. Part 2: Experimental." *Jl of Fluids Eng.*, Trans. ASME, Vol. 119, No. 3, pp. 603–608.
- CUMMINGS, P.D., and CHANSON, H. (1999). "An Experimental Study of Individual Air Bubble Entrainment at a Planar Plunging Jet." *Chem. Eng. Research and Design*, Trans. IChemE, Part A, Vol. 77, No. A2, pp. 159–164.
- ERVINE, D.A., and FALVEY, H.T. (1987). "Behaviour of Turbulent Water Jets in the Atmosphere and in Plunge Pools." *Proc. Instn Civ. Engrs., London*, Part 2, Mar. 1987, 83, pp. 295–314. Discussion: Part 2, Mar.–June 1988, 85, pp. 359–363.
- ERVINE, D.A., McKEOGH, E.J., and ELSAWY, E.M. (1980). "Effect of Turbulence Intensity on the rate of Air Entrainment by Plunging Water Jets." *Proc. Instn Civ. Engrs.*, Part 2, June, pp. 425–445.
- FALVEY, H.T. (1980). "Air-water Flow in Hydraulic Structures." *USBR Engrg. Monograph*, No. 41, Denver, Colorado, USA.
- FALVEY, H.T. (1990). "Cavitation in Chutes and Spillways." *USBR Engrg. Monograph*, No. 42, Denver, Colorado, USA, 160 pages.
- HAGER, W.H., and KRAMER, K. (2003). "Historical Development of Free-Surface Chute Aeration." *Proc. 30th IAHR Biennial Congress*, Thessaloniki, Greece, J.GANOULIS and P.PRINOS Ed., Vol. E, pp. 389–396.
- HAINES, M.A., and JOHNSON, B.D. (1995). "Injected Bubble Populations in Seawater and Fresh water Measured by a Photographic Method." *Jl of Geophysical Res.*, No. 100, No. C4, pp. 7057–7068.
- JONES, O.C., and DELHAYE, J.M. (1976). "Transient and Statistical Measurement Techniques for two-Phase Flows: a Critical Review." *Intl Jl of Multiphase Flow*, Vol. 3, pp. 89–116.
- KELLER, R.J. (1972). "Field Measurement of Self-Aerated High Speed Open Channel Flow." *Ph.D. thesis*, Dept. of Civil Eng., Univ. of Canterbury, New Zealand.
- KEULEGAN, G.H., and PATTERSON, G.W. (1940). "A Criterion for Instability of Flow in Steep Channels." *Trans. Am. Geophysical Union*, Pt II, Vol. 21, July 1940, pp. 594–596.
- MCCURDY, E. (1956). "The Notebooks of LEONARDO DA VINCI." *Jonathan Cape*, London, UK, 6th edition, 2 volumes.
- McKEOGH, E.J. (1978). "A Study of Air Entrainment using Plunging Water Jets." *Ph.D. thesis*, Queen's University of Belfast, UK, 374 pages.

- MATOS, J., SÁNCHEZ, M., QUINTELA, A., and DOLZ, J. (1999). "Characteristic Depth and Pressure Profiles in Skimming Flow over Stepped Spillways." *Proc. 28th IAHR Congress*, Graz, Austria, Session B14, 6 pages
- NEAL, L.S., and BANKOFF, S.G. (1963). "A High Resolution Resistivity Probe for Determination of Local Void Properties in Gas-Liquid Flows." *Am. Inst. Chem. Jl*, Vol. 9, pp. 49–54.
- PLUMPTRE, G. (1993). "*The Water Garden*" *Thames and Hudson*, London, UK.
- REIN, M. (1998). "Turbulent Open-Channel Flows: Drop-Generation and Self-Aeration." *Jl of Hyd. Engrg.*, ASCE, Vol. 124, No. 1, pp. 98–102. Discussion: Vol. 125, No. 6, pp. 668–670.
- SCOTT, J.C. (1975). "The preparation of Water for Surface Clean Fluid Mechanics." *Jl of Fluid Mech.*, Vol. 69 part 2, pp. 339–351.
- STEWART, W.G. (1913). "The Determination of the N in Kutter's Formula for Various Canals, Flumes and Chutes on the Boise Project and Vicinity." *Report on 2nd Annual Conf. on Operating Men*, USBR, Boise, Idaho, USA, Jan., pp. 8–23.
- STRAUB, L.G., and ANDERSON, A.G. (1958). "Experiments on Self-Aerated Flow in Open Channels." *Jl of Hyd. Div.*, Proc. ASCE, Vol. 84, No. HY7, paper 1890, pp. 1890–1 to 1890–35.
- STUTZ, B., and REBOUD, J.L. (2000). "Measurements within Unsteady Cavitation." *Experiments in Fluids*, Vol. 29, pp. 545–552.
- TOOMBES, L. (2002). "Experimental Study of air-water Flow Properties on Low-Gradient Stepped Cascades." *Ph.D. thesis*, Dept of Civil Engineering, The University of Queensland.
- VAN DE SANDE, E., and SMITH, J.M. (1973). "Surface Entrainment of Air by High Velocity Water Jets." *Chem. Eng. Science*, Vol. 28, pp. 1161–1168.
- WALKDEN, M.J.A. (1999). "Model Wave Impulse Loads on Caisson Breakwaters: Aeration, Scale and Structural Response." *Ph.D. thesis*, University of Plymouth, UK, 250 pages.
- WOOD, I.R. (1983). "Uniform Region of Self-Aerated Flow." *Jl Hyd. Eng.*, ASCE, Vol. 109, No. 3, pp. 447–461.
- WOOD, I.R. (1984). "Air Entrainment in High Speed Flows." *Proc. Intl. Symp. on Scale Effects in Modelling Hydraulic Structures*, IAHR, Esslingen, Germany, H.KOBUS editor, paper 4.1.
- WOOD, I.R. (1985). "Air Water Flows." *Proc. 21st IAHR Congress*, Melbourne, Australia, Keynote address, pp. 18–29.
- WOOD, I.R. (1991). "*Air Entrainment in Free-Surface Flows*" *IAHR Hydraulic Structures Design Manual No. 4*, Hydraulic Design Considerations, Balkema Publ., Rotterdam, The Netherlands, 149 pages.

De-aeration of a diversion tunnel of a large-scale hydroelectric scheme

Hansjürg Sigg, Urs Keller, Peter U. Volkart & Hans-Erwin Minor
*Laboratory of Hydraulics, Hydrology and Glaciology (VAW), Swiss
Federal Institute of Technology (ETH), Switzerland*

Hydraulics of Dams and River Structures—Yazdandoost & Attari (eds)

© 2004 Taylor & Francis Group, London, ISBN 90 5809 632 7

ABSTRACT: Due to the influence of a varying water level in the main reservoir, the Jökulsá Tunnel as diversion tunnel from a secondary intake is subjected to a transition from free-surface to pressurized flow. As to avoid damage in the main conduit as well as of the hydraulic equipment, the air entrained into and transported downstream by the pressurized flow has to be removed before the junction of the two tunnel branches. A novel concept of de-aeration, basically consisting of vertical drill holes distributed along the Jökulsá Tunnel, was developed and technical feasibility ascertained by means of two physical hydraulic models. A concise description of the concept itself as well as of the modeling procedures is given.

1 OVERVIEW OF THE PROJECT

The Jökulsá Tunnel is part of the Kárahnjúkar Hydroelectric Scheme which is under construction in Eastern Iceland. With this development, Landsvirkjun (The National Power Company, Iceland) as the owner of the works harnesses the two glacial rivers Jökulsá á Dal and Jökulsá í Fljótsdal. The power station will have an installed capacity of 630 MW, a flow rate of 126 m³/s and a powergenerating capacity of 4450 GWh/year.

Damming river Jökulsá á Dal at Mt. Fremri Kárahnjúkur creates the Háslón reservoir. An approximately 40 km long headrace tunnel conveys the water from here to the underground powerhouse. A secondary reservoir, Ufsarlón, is created by damming river Jökulsá í Fljótsdal. Ufsarlón is connected to the main headrace tunnel via the more than 13 km long Jökulsá Tunnel. An overview of the project site is given in Figure 1.

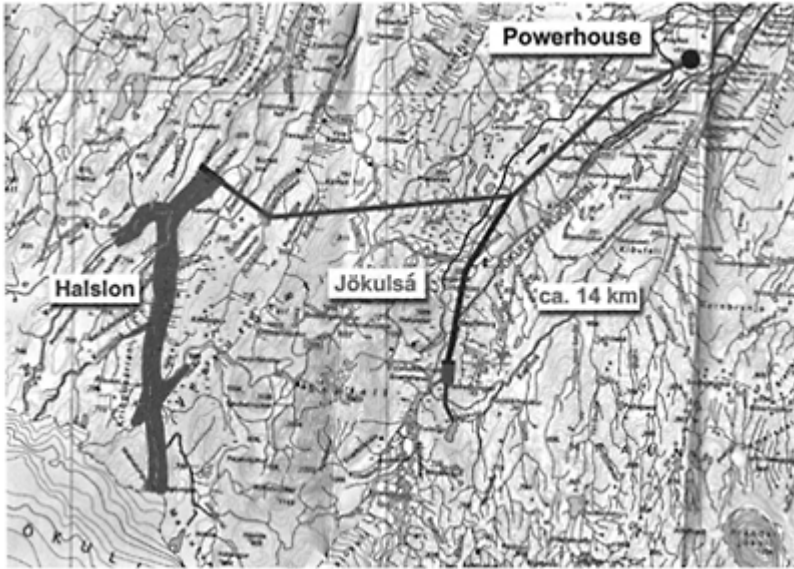


Figure 1. Overview of the project area with the main headrace tunnel originating from Háslón Reservoir and the Jökulsá Tunnel as secondary diversion tunnel.

The Jökulsá Tunnel, excavated by tunnel-boring-machine, will have an ID of 6.5 m with a circular shape. Its slope is 1.3% for the first approx. 14 km. The remaining part until the junction with the main headrace tunnel is then significantly steeper.

The flow regime in the Jökulsá Tunnel is strongly influenced by the water level in the Háslón Reservoir that can vary within 75 m. Additionally, the discharges in the Jökulsá Tunnel will vary within a wide range with a maximum design discharge QWD of 100 m³/s. This variation induces a transition from free surface to pressurized flow in the conduit, which can take place almost over the whole only slightly inclined reach of the tunnel. The imminent hydraulic jump will entrain air into the pressurized part from where it has to be removed before entering the main headrace tunnel. Preferably this is to be done within the slightly inclined stretch in the Jökulsá Tunnel.

2 THEORETICAL BACKGROUND

2.1 *Involved hydrodynamic processes*

The presented concept implies air entrainment into the pressurized reach of the Jökulsá Tunnel through a hydraulic jump. Along the pressurized reach two-phase flow patterns with air moving either upstream or downstream are to be expected. Finally, as the air has

to be removed from the pressurized flow, air-water mixture flow in a shaft or drill hole has to be governed as to ascertain system efficiency and safety.

2.2 Air entrainment through a hydraulic jump

The determining factors for this process are the approach flow depth h_1 and the clear water discharge Q_w . Accordingly, Kalinske & Robertson (1943) proposed Equation 1 to estimate the volumetric amount of air Q_A entrained into the flow and the air demand β respectively:

$$\beta = \frac{Q_A}{Q_w} = 0.0066 \cdot (Fr_1 - 1)^{1.4} \quad (1)$$

Derived from model tests in a 0.1494m ID pipe Equation 1 seems to estimate β rather well also under prototype conditions. Falvey (1980) presents Equation 1 as a regression through prototype data from different dams.

It has to be mentioned, that Kalinske & Robertson (1943) explicitly did not consider whether air is conveyed further downstream or whether it is expelled again through the hydraulic jump into the aerated reach of the conduit. This might compromise direct comparison with prototype data, where it is not clear, if the distinction between air entrainment alone and air entrainment and air transport was possible.

2.3 Air transport along the closed conduit

Air transport along a closed conduit is common above all in process engineering. Possible flow patterns in horizontal or only slightly inclined conduits are given in Figure 2.

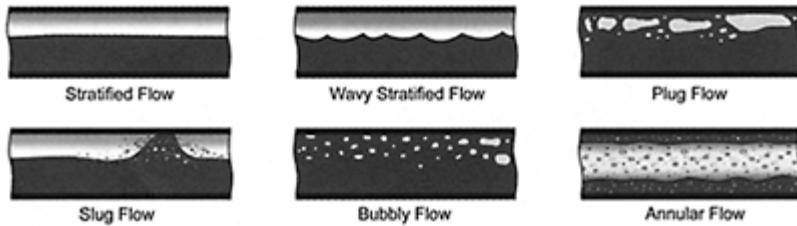


Figure 2. Possible two-phase flow patterns in horizontal or only slightly inclined closed conduits.

So-called flow pattern maps as presented in Figure 3 are commonly used as predictive means. Depending on the superficial velocities of the liquid phase (u_{SL}) and the gas phase (u_{SG}) the prevailing flow pattern can be deduced.

Calculation of the superficial velocities in a circular conduit can be done according to Equation 2 and Equation 3 for the liquid and the gas phase respectively.

$$u_{SL} = \frac{Q_W}{\pi r^2} \quad (2)$$

$$u_{SG} = \frac{Q_A}{\pi r^2} \quad (3)$$

where r is the radius of the conduit.

It has to be mentioned, that the common flow pattern maps are considering pipe diameters of typically 0.02 to 0.09 m. Although normalized with the cross-section of the conduit, direct applicability to any larger diameter is not given. Bertola (2002) e.g. mentions stratification effects growing with diameter (0.08 m) which affect not only the properties of the prevailing flow pattern but also the run of the boundaries between the different patterns. Similar observations were made by Keller, Volkart & Minor (2003) for a pipe diameter of 0.292 m. Therefore, solely direct application of these flow pattern maps and deduced flow properties did not seem favorable in the context of the Jökulsá Tunnel.

Another means to describe and predict the prevailing flow pattern is provided by Falvey (1980). Figure 4 is derived from various prototype and model investigations and represents areas of different flow patterns and the direction of bubble movement depending on both, a dimensionless flowrate (analogous to the Froude Number) and the slope of the conduit. While shortcomings in terms of the size of the conduit are ruled out in this case (as also prototype data is integrated), the diagram is only trustworthy at steeper slopes and higher dimensionless flowrates as those encountered at the Jökulsá Tunnel.

2.4 Air-water mixture flow at de-aeration points

At the de-aeration points, the air has to be removed from the flow and conveyed to the free atmosphere. For removing the air from the flow and its collection only few design suggestions from hydraulic engineering applications and models exist, e.g. Hahn (1985). Conveying the air then to the free atmosphere involves structures such as shafts or drill holes which are usually vertical or close to vertical due to economic and geo-technical reasons.

For such vertical structures in which an air-water mixture prevails, considerations similar to those for horizontal conduits are common. Again, they originate mostly from process engineering and are derived from rather small pipe diameters (0.02 m to 0.09 m). Nevertheless, valuable conclusions for the present case can be drawn namely from the very common Taylor-Bubbles in stagnant liquid.

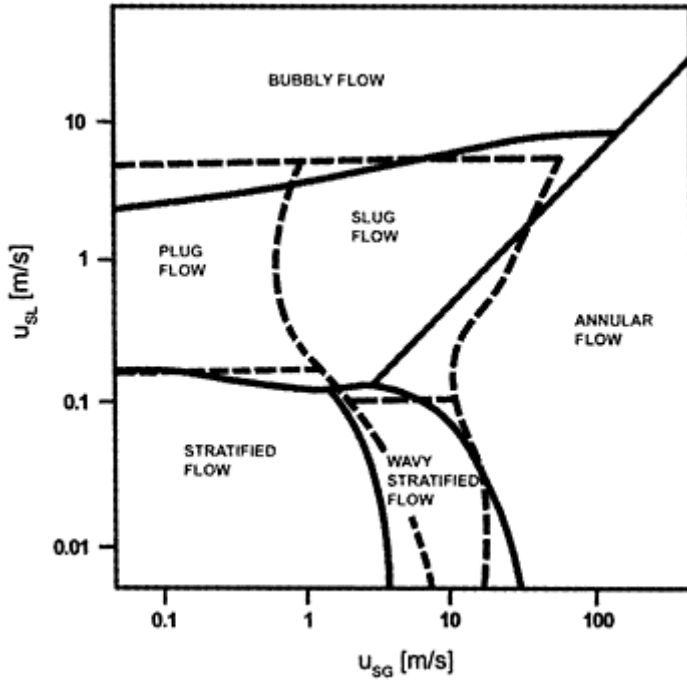


Figure 3. Flow pattern map for horizontal conduits according to the experiments by Mandhane, Gregory & Aziz (1974) (continuous line) and according to the calculations by Taitel & Dukler (1976) (dashed line).

Such Taylor-Bubbles or similar flow patterns are to be expected in rather small vertical conduits such as vertical drill holes. Flow patterns, such as bubbly flow prevail as the diameter of the vertical conduit is enlarged to the size of a veritable shaft, assuming the volumetric amount of air remaining the same.

Concluding all theoretical considerations, hydraulic model assessment of the problems posed still remained inevitable. Nevertheless, valuable information allowing for more profound interpretation of model results could be gathered.

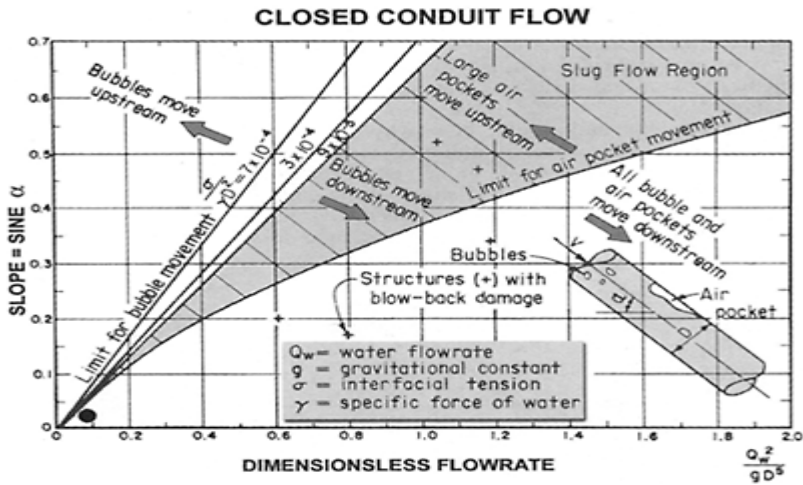


Figure 4. Air-flow patterns in a closed conduit with a circular cross-section according to Falvey (1980). The location for the design discharge of $100 \text{ m}^3/\text{s}$ in the Jökulsá Tunnel is marked with a black dot.

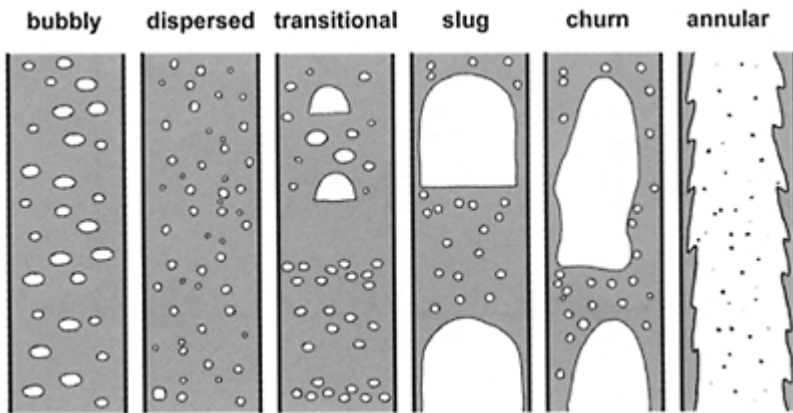


Figure 5. Flow patterns as they may occur in a vertical conduit. Taylor-Bubble-like bubbles are depicted in the slug flow pattern.

3 EXPERIMENTAL CONCEPT AND SET-UP

Due to the complexity of the investigations, a phased procedure appeared being favorable, as the outcome of each phase could, in the negative case, induce its discontinuation. The following two phases were scheduled:

- Phase 1 aiming at assessing the general technical feasibility of the concept had first to investigate the availability of any possible reference or past experience, providing the frame of theoretical background as presented above. Subsequently, first physical model tests had to qualitatively judge the feasibility of de-aeration concepts.
- Phase 2 was aiming at defining design criteria for the overall concept as well as for the de-aeration structures themselves. Detailed physical model tests at a significantly larger scale than the preliminary tests were to be carried out as to achieve the necessary quality of results.

In phase 1 the experimental set-up basically consisted of an approx. 34 m long Perspex tube with an ID of 0.292 m and a slope of 1.3%. The scaling factor accordingly was set to $\lambda_1=22.26$.

The de-aeration device was kept very simple according to the preliminary character of the investigations. It consisted of a vertical Perspex tube of an ID of 0.098 m (model scale) and an inset allowing for changes of the de-aeration orifice just above the tunnel soffit. Concluding the results of phase 1, the boundary conditions for phase 2 could be set. These included the feasibility of a concept with de-aeration points distributed more or less equidistantly along the Jökulsá Tunnel (interval ca. 1000 resulting in 13 m maximum local pressure head at the first fully pressurized de-aeration device).

The set-up of the larger model of phase 2 basically also consisted of a Perspex tube. With the ID being 0.484m a significantly larger scaling factor $\lambda_2=13.43$ resulted. The model covered a length of approx. 115m upstream and 33m downstream of a single point of de-aeration (prototype values). Instead of a simple shaft-like de-aeration tube, a more complex Perspex structure was mounted on the tube to allow for the modeling of a de-aeration chamber, where air may accumulate before being expelled to the free atmosphere. Due to economic reasons, Landsvirkjun preferred drill holes to be investigated as means of air evacuation from the tunnel instead of shafts. Therefore, tubes with ID of 0.3 m, 0.4 m and 0.5 m (prototype dimensions) were investigated. An overview of the model set-up of phase 2 is given in Figure 6.

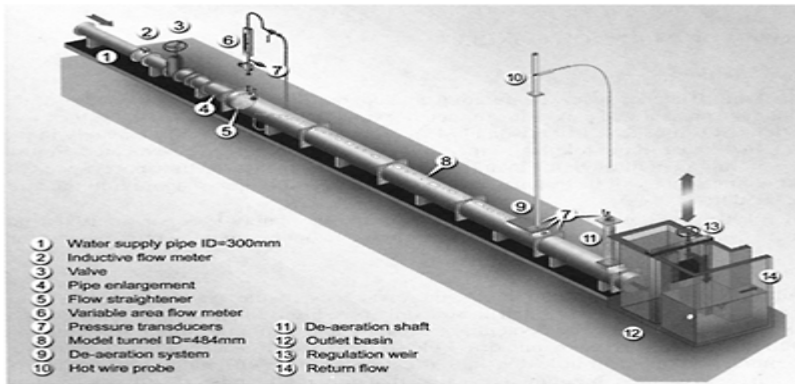


Figure 6. Schematic overview of the second model erected at VAW.

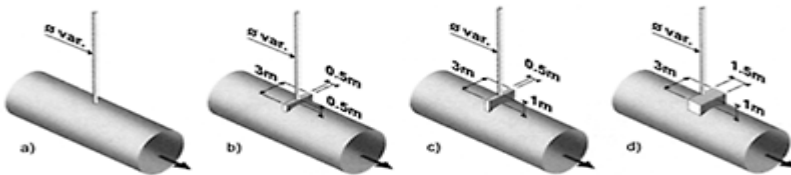


Figure 7. Four basic designs for the de-aeration structure, ranging from a drill hole alone and two options with a de-aeration slot to a simple de-aeration chamber connecting the tunnel with the drill hole.

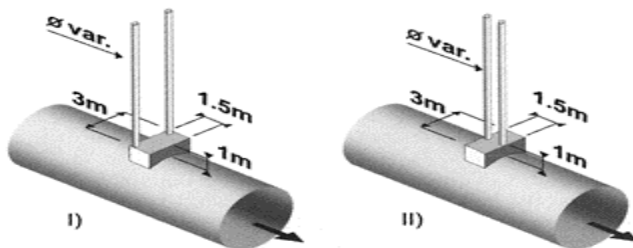


Figure 8. Alternative options with the de-aeration chamber according to Figure 7 (d) and two drill holes either

perpendicular to (I) or along the tunnel axis.

Four different basic designs for the de-aeration structure as presented in Figure 7 were investigated. Additionally, basing on design (d) from Figure 7, different numbers and layouts of drill-holes were assessed as depicted in Figure 8.

4 PROPOSED DE-AERATION CONCEPT

4.1 *General findings*

Judgement of the efficiency of any de-aeration concept requires profound knowledge of the volume flux Q_A along the pressurized part of the tunnel. Maximally, Q_A could reach the values according to the estimations of Kalinske & Robertson (1943), provided the air transport capacity in the conduit is sufficient. In the case of the Jökulsá Tunnel, smaller values Q_A are to be expected. Figure 9 shows both, the air entrainment through the hydraulic jump and the measured transport capacity Q_{AT} . The differential volume flux will be evacuated through the hydraulic jump again into the atmospheric part of the conduit.

At $QWD=100 \text{ m}^3/\text{s}$, β in the pressurized reach is approximately 1‰. For safety reasons this air flux has to be evacuated from the water flow through one operating de-aeration device only.

4.2 *Efficiency of a single de-aeration point*

With the introduction of a de-aeration slot the efficiency of the system increases significantly compared to the case with a 0.3 m ID drill-hole only (see Figure 10). Longitudinal enlargement of the slot additionally improves the de-aeration capacity and with one simple de-aeration chamber connected to the terrain surface by one drill hole (ID=0.3 m) it reaches already values >99%.

Sinking more than one drill-hole does not affect de-aeration efficiency substantially. Observations at designs as presented in Figure 8 revealed, that only if aligned perfectly perpendicular to the tunnel axis, there is a certain balance in impingement of two drill holes. Otherwise the drill hole upstream always discharges the bulk volume flux of air.

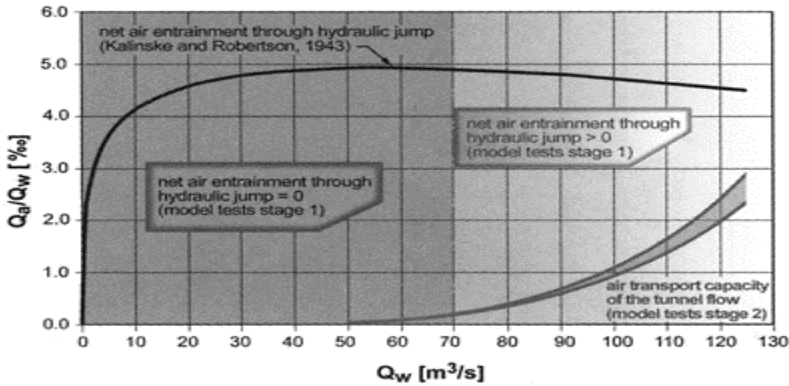


Figure 9. Air entrainment through a hydraulic jump according to Kalinske & Robertson (1943), the actually measured air transport capacity in the model tests.

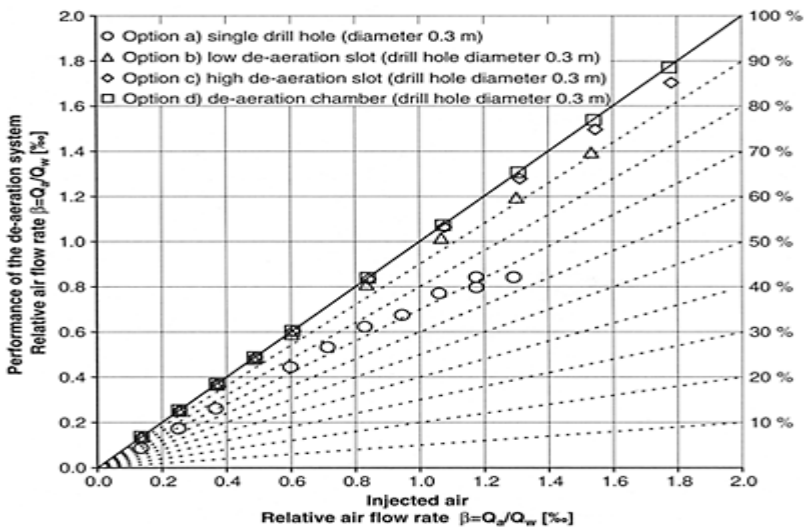


Figure 10. Influence of the different layouts of the de-aeration device on the system efficiency.

Excessive pressure head at the operating de-aeration point has to be avoided, as de-aeration efficiency decreases. This also prevents intervals between the de-aeration devices from being significantly longer than 1000 m.

4.3 Air-water two-phase flow patterns within the drill holes

The dominant flow pattern in the model can be categorized as slug flow, but in the prototype a flow pattern closer to transitional flow may be expected.

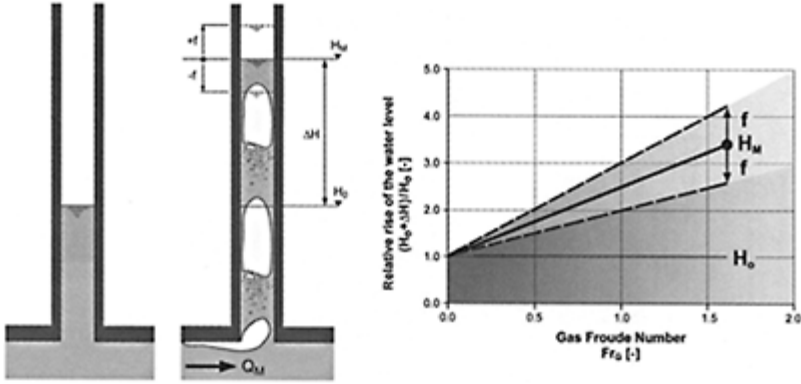


Figure 11. Definition sketch (left) and measured values (right) for swell and fluctuations of the water level in a de-aeration drill hole. H_0 is the water level in the drill hole without air evacuation (measured from the tunnel soffit). ΔH is the additional rise of water level, H_M the mean water level and f the fluctuation around this mean, all observed during air evacuation. Q_M is the air-water mixture discharge.

Due to the upward airflow in the drill hole, the water level in the drill hole is rising when evacuating air (see Figure 11). Air expulsions cause swell and high fluctuations of the water level. These phenomena do not have to be expected to be as powerful in the prototype as observed in the model because of the more tranquil flow pattern in the prototype.

The swell and the fluctuations decrease by enlarging the ID of the drill hole as the related gas Froude number Fr_G decreases under otherwise unchanged conditions. The ID of 0.3 m marks a minimum below which flow patterns are not predictable or on the safe, less fierce, side respectively.

5 CONCLUSIONS AND OUTLOOK

The feasibility of the investigated de-aeration concept for the Jökulsá Tunnel could be confirmed and detailed design criteria provided. A satisfactory efficiency of de-aeration (>99%) is obtained with a simple de-aeration chamber connected to the terrain surface by one drill hole of 0.3 m ID.

When evacuating air, swell and fluctuations of the water level may be encountered. Both can be reduced by enlarging the ID of the drill holes. Finally, although the results are very positive in term of air evacuation, a significant enlargement of the diameter of the last evacuator downstream is recommended for safety reasons.

REFERENCES

- Bertola, V. 2002. Slug velocity in horizontal gas-liquid flow. *Experiments in Fluids* **32**, 722–727.
- Falvey, H.T. 1980. Air-water flow in hydraulic structures. *Engineering Monograph No. 41*. Bureau of Reclamation, Denver, Colorado.
- Hahn, U. 1985. Lufteintrag, Lufttransport und Entmischungsvorgang nach einem Wechselsprung in flachgeneigten, geschlossenen Rechteckgerinnen (in German). *Bericht Nr. 52*. Oskar v. Miller-Institut, Oberrach.
- Kalinske, A.A. & Robertson, J.M. 1943. Closed Conduit Flow. *Transactions ASCE* **108**, 1435–1447.
- Keller, U., Volkart, P.U. & Minor, H.-E. 2003. Tail water influenced transition from free surface to pressurized flow in bottom outlet tailrace tunnels. *Proc. 30th IAHR Congress*, Thessaloniki, accepted.
- Mandhane, J.M., Gregory, G.A. & Aziz, K. 1974. A flow pattern map for gas-liquid flow in horizontal pipes. *Int. J. Multiphase Flow* **1**, 537–553.
- Taitel, Y. & Dukler, A.E. 1976. A model for predicting flow regime transition in horizontal and near horizontal gas-liquid flow. *AIChE J.* **22**, 47–55.

Free-surface aeration in dam break waves: an experimental study

H.Chanson

Dept. of Civil Eng., The University of Queensland, Brisbane, Australia

Hydraulics of Dams and River Structures—Yazdandoost & Attari (eds)

© 2004 Taylor & Francis Group, London, ISBN 90 5809 632 7

ABSTRACT: New air-water flow experiments were conducted in the leading edge of dam break waves. The data highlighted the chaotic nature of the surge and provided new insights in the distributions of void fraction, velocity and air/water chord sizes. The results demonstrated a highly aerated surge front with a developing turbulent boundary layer. At the leading edge, observed mean air contents exceeded 40 to 50%, implying that sediment motion would be predominantly bed-load.

1 INTRODUCTION

Flood waves resulting from dam breaks have been responsible for numerous losses of life (Fig. 1). Related cases include flood waves resulting from gate malfunction or failure of an upstream reservoir, flash floods and debris flows. Other forms of sudden flood waves include natural lake breach, glacier lake outburst floods (GLOF) and flooding of valleys during armed conflicts (Fig. 1A). Despite few earlier studies (DRESSLER 1954, ESCANDE et al. 1961), current knowledge of dam break wave surging down rough sloping waterways is still rudimentary while the aerated nature of the advancing front, evidenced by photographs and witnesses, remains un-quantified. During a debris flow flash flood, local witnesses reported that “*the surge front advanced rather slowly down-valley as a huge ‘black’ mass of water full of debris. The surge emitted a loud noise ‘like many helicopters’ and a foul mud-smell. The valley bottom was wreathed in misty clouds of water vapour; the river banks were trembling; houses were shaking*” (GALAY 1987, p. 2.36).

During the present study, flash flood surges were generated in a large stepped chute. This investigation provides new information on the rate of energy dissipation and wave front propagation. Unsteady two-phase flow measurements were conducted in the surge front to gain new insights into the air-water flow and its possible impact on debris and sediment motion.

2 EXPERIMENTAL SETUP

New experiments were performed in the 25 m long 0.5 m wide flume ($S_o \approx 0.065$, $\theta = 3.4^\circ$) previously used by CHANSON (2003) (Table 1). A precise discharge was delivered by a pump controlled

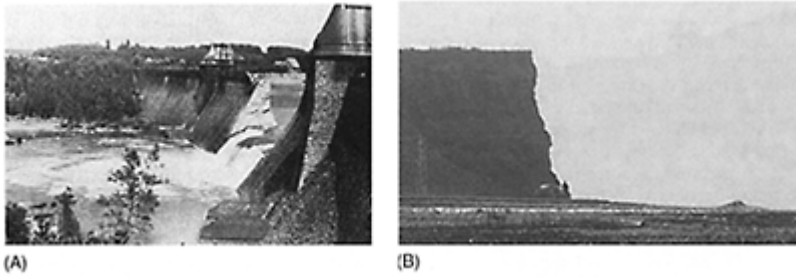


Figure 1. Photographs of dam break.
(A) Möhne dam break (17 May 1943)
(B) Zeyzoun dam break (4 June 2002).

Table 1. Summary of unsteady dam break wave flow experiments.

Experiment	θ (deg.)	h (m)	$Q(t=0+)$ (m^3/s)	Steady flow regime	Remarks
(1)	(2)	(3)	(4)	(5)	(6)
Brushes Clough dam	18.4	0.19	0.5	Skimming	Inclined downward steps, trapezoidal channel (2 m bottom width).
CHANSON (2003)					
Series 1	3.4	0.143	0.019 to 0.075	Nappe NA3	10 horizontal steps ($l=2.4$ m). $W=0.5$ m. Nozzle depth: $d_n=0.030$ m.
Series 2	3.4	0.0715	0.040 to 0.075	Trans./Skim.	18 horizontal steps ($l=1.2$ m). $W=0.5$ m. Nozzle depth: $d_n=0.030$ m.
Present study	3.4	0.0715	0.050 0.060 0.065 0.070	Skimming	18 horizontal steps ($l=1.2$ m). $W=0.5$ m. Nozzl depth: $d_n=0.030$ m. Air-water flow measurements on Step 16.

Notes: $Q(t=0+)$: initial discharge; d_n : approach flow depth; h: Step height; l: step length.

with an adjustable frequency AC motor drive TaianT-Verter K1/N1 (Pulse Width Modulated design), enabling an accurate discharge adjustment in a closed-circuit system. The flow was fed through a smooth convergent nozzle. The nozzle exit was 30 mm high and 0.5 m wide. The stepped invert configuration consisted of a 2.4 m long horizontal invert followed by 18 identical steps ($h=0.0715$ m, $l=1.2$ m).

2.1 Instrumentation

The flow rates in steady flow conditions were measured with a Dall™ tube flowmeter, calibrated on site with a sharp-crested weir. The accuracy on the discharge measurement was about 2%. The surging flow was studied with digital still- and video-cameras using high-shutter speed (1/1,000 to 1/10,000 sec.).

Air-water flow properties were measured with two systems. Air concentrations and bubble count rates were recorded with a series of single-tip conductivity probes (needle probe design). Each probe consisted of a sharpened rod (platinum wire $\varnothing = 0.35$ mm) which was insulated except for its tip and set into a metal supporting tube (stainless steel surgical needle $\varnothing = 1.42$ mm) acting as the second electrode. The second apparatus was a double-tip conductivity probe. The inner electrode was a platinum wire (99.9% purity, $\varnothing = 0.15$ mm) and the outer electrode was a stainless steel surgical needle ($\varnothing_{\text{int}} = 0.5$ mm, $\varnothing_{\text{ext}} = 0.8$ mm). Each tip was identical and the distance between sensor was $\Delta x_{\text{tip}} = 8.9$ mm. The probe was designed with a small frontal area of the first tip (i.e. 0.5 mm^2) and with a displaced second tip (offset: 1.4 mm). The design prevents wake disturbance from the leading tip and tests showed the absence of wake during all experiments (CHANSON 1995). With both systems of probes, the probe sensors were aligned in the flow direction and excited by an air bubble detector developed at the University of Queensland (UQ82.518) with a response time of less than 10 μs and calibrated with a square wave generator. The probe output signals were scanned at 10 kHz per channel for six seconds.

Data acquisition was triggered manually immediately prior to the flow arrival. Visual observations showed that the wave front was roughly two-dimensional. All measurements were taken on the centreline of step 16 at several distances x' from the step vertical face (Fig. 2). At each location x' , a single-tip conductivity probe (i.e. reference probe) was set on the invert, acting as a time reference, while the other probes were set at different elevations. Each experiment was repeated until sufficient data were obtained for each vertical profile. The displacement of the probes in the direction normal to the invert was controlled by a fine adjustment travelling mechanism. The error in the probe position was less than 0.2 mm and 2 mm in the vertical and horizontal directions respectively.

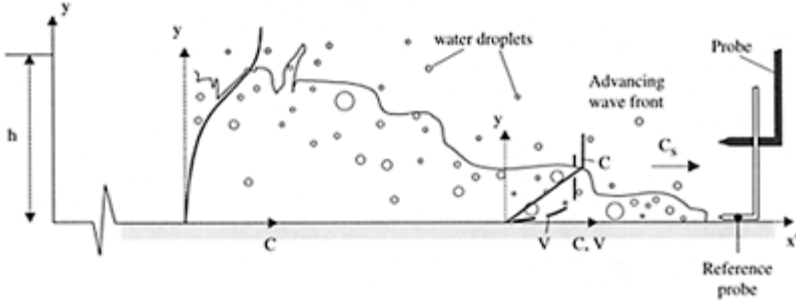


Figure 2. Definition sketch.

2.2 Data processing

Steps were painted with red and white stripes spaced 50 mm apart. Video-taped movies were analysed frame-by-frame. The error on the time was less than 1/250 s and the error on the longitudinal position of the wave front was ± 1 cm.

The conductivity probe signal outputs were processed using a single threshold technique. The threshold was set at about 50% of the air-water voltage range. Unsteady void fractions C and bubble count rates F were calculated during a short time interval τ such as $\tau = \Delta x / C_s$ where C_s is the surge front celerity measured with the video-cameras and Δx is the control volume streamwise length. Preliminary tests indicated that $\Delta x \geq 70$ mm to contain a minimum of 5 to 20 bubbles (CHANSON 2003). The selection was consistent with the processing technique of STUTZ and REBOUD (2000). The bubble count rate was calculated as: $F = N_{ab} / \tau$ where N_{ab} is the number of bubbles detected during the time interval τ . Bubble and water chord sizes were deduced from measured chord times where the bubble chord time t_{ch} is defined as the time spent by the bubble on the probe tip.

Velocity data were calculated from individual droplet events impacting successively the two probe sensors. The velocity was deduced from the time lag for air-to-water interface detections between leading and trailing tips respectively. For each meaningful event, the interfacial velocity was calculated as: $V = \Delta x_{tip} / \delta t$ where Δx_{tip} is the distance between probe sensors and δt is the interface traveling time between probe sensors.

2.3 Boundary flow conditions

Prior to the start of each experiment, the recirculation pipe system and convergent intake were emptied. The channel was initially dry. The pump was rapidly started. The electronic controller had a 5 sec. ramp. The pump reached its nominal power (i.e. discharge) at least 10 sec. prior to the water entering the channel. The flow rate $Q(t=0+)$ was maintained constant until at least 10 sec. after the wave front reached the downstream end of the flume (Table 1).

Previously, steady flow experiments were conducted in the same channel with smooth and stepped invert configurations (CHANSON and TOOMBES 2002). These steady air-water flow results provided the limiting conditions of the present study of unsteady flows.

3 BASIC RESULTS

3.1 Wave front propagation

For all experiments, visual observations showed that the wave front propagated basically as a succession of free-falling nappe, nappe impact and horizontal runoff. For comparison, the flow regime observations in steady flows are summarised in Table 1 (column 5). The surging flow exhibited a nappe flow behaviour for all discharges and geometries (Table 1). The wave front was chaotic and highly aerated, in particular for the largest flow rates, with strong spray, splashing and wavelets. Water packets were commonly projected to heights greater than 3 to 4 step heights, while some droplets reached heights of more than 8 to 10 step heights. Visually the experiments in the large-size flume had a similar appearance to the surging flow observed at Brushes Clough dam spillway (Table 1).

The propagation of the wave leading edge was recorded for a range of unsteady flow conditions (Table 1). Although experimental observations suggested an almost linear relationship between wave front location and time, wave front celerity data showed that the flow was accelerated in the first 4 to 6 steps. Further downstream, a gradual decay in celerity was observed. The data were compared successfully with HUNT's (1982) theory for dam break wave down sloping chutes assuming an equivalent Darcy-Weisbach friction factor $f=0.05$, irrespective of the discharge and step height. This flow resistance value is close to air-water flow measurement results in steady flow conditions yielding $f \sim 0.047$ (CHANSON and TOOMBES 2002).

In the following sections, air-water flow properties, in the horizontal runoff flow region predominantly, are detailed.

3.2 Void fraction distributions

Typical distributions of void fractions in the horizontal runoff are presented in Figure 3 at a location x' . Each void fraction data set was recorded at a time t measured from the first water detection by the reference probe, and time values are reported in figure caption. In Figure 3, y is the distance normal to the invert (Fig. 1), d_0 is a measure of the initial discharge $Q(t=0+)$:

$$d_0 = \frac{9}{4} * \sqrt[3]{\frac{Q(t=0+)^2}{g * W^2}} \quad (1)$$

and W is the chute width. At the front of the wave, the void fraction distributions had a roughly linear shape:

$$C = 0.9 * \frac{y}{Y_{90}} \quad 0.1 < t * \sqrt{g/d_0} < 1.3 \quad (2)$$

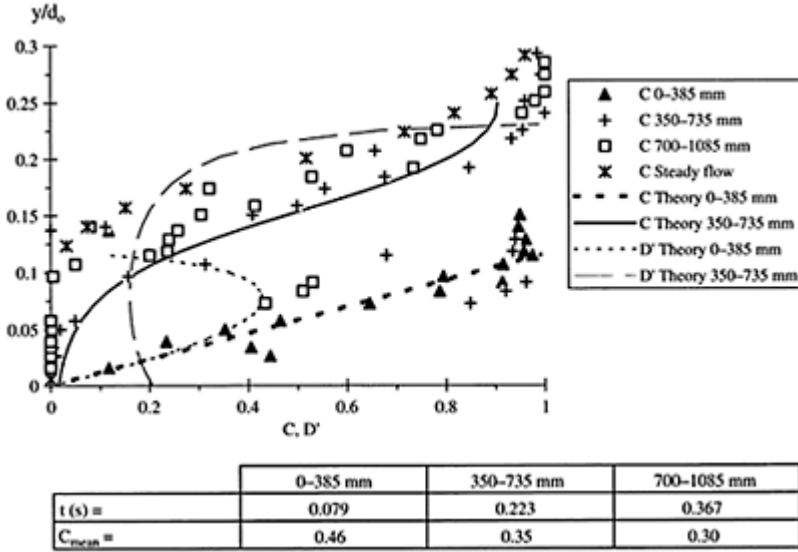


Figure 3. Dimensionless distributions of instantaneous void fractions C and air bubble diffusivity D' —Comparison with Equations (2) and (3) ($Q(t=0+)=0.075 \text{ m}^3/\text{s}$, step 16, $x'=0.8 \text{ m}$, $\Delta x=385 \text{ mm}$).

where Y_{90} is the height where $C=0.90$. For larger times t , the distributions of air concentration were best described by the diffusion model:

$$C = 1 - \tanh^2 \left(K' - \frac{y}{2 * D_0} + \frac{\left(\frac{y}{Y_{90}} - \frac{1}{3} \right)^3}{3 * D_0} \right) \quad t * \sqrt{g/d_0} > 1.3 \quad (3)$$

where K' and D_0 are functions of the mean air content only (CHANSON 2003). Equations (2) and (3) are plotted for unsteady and steady flow conditions in Figure 3. The analytical models compare favourably with the data.

Equations (2) and (3) are analytical solutions of the advective diffusion of air bubbles assuming respectively the following distributions of dimensionless turbulent diffusivity of air bubbles:

$$D' = \frac{C * \sqrt{1-C}}{0.9} \quad 0.1 < t * \sqrt{g/d_0} < 1.3 \quad (4)$$

$$D' = \frac{D_0}{1 - 2 * \left(\frac{y}{Y_{90}} - \frac{1}{3} \right)^2} \quad t * \sqrt{g/d_0} > 1.3 \quad (5)$$

where $D' = D_t / ((u_r)_{Hyd} * \cos\theta * Y_{90})$, D_t is the turbulent diffusivity, $(u_r)_{Hyd}$ is the rise velocity in hydrostatic pressure gradient. Equations (4) and (5) are plotted in Figure 3 in thin dashed lines. The shape of Equation (4) is similar to the sediment diffusivity distribution developed by ROUSE (1937) which yields to the Rouse distribution of suspended matter.

3.3 Discussion

The data demonstrated consistently strong aeration of the surge front, especially within the first 0.3 to 0.7m behind the leading edge. The result has direct implications in terms of sediment processes at the front of flash floods and swash zone runup on beaches. The large amount of “white waters” reduces buoyancy and increases the relative density of sediment particles. For example, the relative density s of quartz particles increases from 2.65 to 5.3 when the mean void fraction C_{mean} increases from 0 to 50%. The present findings imply that heavy sediment particles are more likely to be subjected to bed-load motion rather than suspension in flash flood surges.

The data highlighted further a major change in void fraction distribution shape for $t * \sqrt{g/d_0} \sim 1.2$ to 1.5. Possible explanations might include (a) a non-hydrostatic pressure field in the leading front of the wave, (b) some change in air-water flow structure between the leading edge and the main flow associated with a change in rheological fluid properties, (c) a gas-liquid flow regime change with some plug/slug flow at the leading edge and a homogenous bubbly flow region behind, and (d) a change in boundary friction between the leading edge and the main flow behind. All these mechanisms would be consistent with high-shutter speed movies of leading edge highlighting very dynamic spray and splashing processes.

4 VELOCITY DISTRIBUTIONS

Figure 4 presents interfacial velocity distributions in the horizontal runoff region. In Figure 4A, each data point represents the velocity of the first air-to-water interface detected at each location y . (The data were measured for $t < 0.12$ s.) Figure 4B shows the mean velocity for an entire recording (i.e. for less than 6 sec.) at each location y . Each data point is the median velocity (or the average velocity if less than ten successful detections occurred). The number of successful interface detections is also shown for each location as well as the ratio of velocity standard deviation to mean velocity. For large interface counts, this ratio equals the turbulence intensity Tu . For small successive interface events (< 10), the results are not statistically meaningful. Indeed Figure 4B highlights high levels

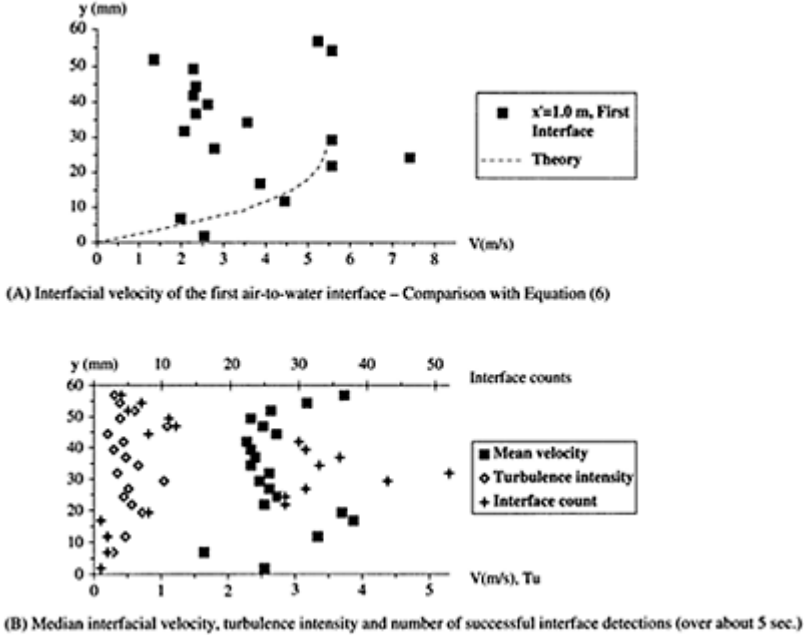


Figure 4. Velocity distributions at the surge leading edge ($Q(t=0+)=0.065 \text{ m}^3/\text{s}$, step 16, $x'=1.0 \text{ m}$).

of turbulence in the surging flow, with Tu ranging from 0.2 to 1.1 with a mean value of about 50% in Figure 4B.

In the horizontal runoff flow and at the surge leading edge, the data highlighted an unsteady boundary layer next to the invert with a potential flow region above (Fig. 4A). The finding is consistent with earlier laboratory experiments by MANO (1994) who studied unsteady wave runup using bubble tracer and high speed video. In Figure 4A, present data are compared with an analytical solution of the Navier-Stokes equations (first Stokes problem):

$$\frac{V}{U} = \text{erf}\left(\frac{y}{2 * \sqrt{\nu_T * t}}\right) \quad (6)$$

where U is a free-stream velocity, t is the time, ν_T is the momentum exchange coefficient (or “eddy viscosity”) and erf is the Gaussian error function defined as:

$$\text{erf}(u) = \frac{2}{\sqrt{\pi}} * \int_0^u \exp(-t^2) * dt \quad (7)$$

Equation (6) is shown in Figure 4. The values of U and ν_T were determined from the best fit of the data. For the data shown in Figure 4A, $\nu_T=1$ to $2.3 \text{ E-3 m}^2/\text{s}$. Despite crude approximations leading to Equation (6), experimental results implied a turbulent

boundary layer. For comparison, in laboratory wave runup and small debris flows, the boundary layer is believed to be laminar (MANO 1994, HUNT 1994), while the boundary layer is turbulent in prototype dam break flows and large debris flows (HUNT 1984, 1994).

Based upon void fraction and velocity measurements, the air bubble diffusivity D_t and eddy viscosity ν_T which satisfy Equations (2) and (6) respectively yield a ratio D_t/ν_T of about unity. The ratio D_t/ν_T compares the effects of the difference in diffusion of a discrete particle and small coherent fluid structure, as well as the effect of entrained air on the turbulence field. The result ($D_t/\nu_T \propto 1$) seems to suggest strong interactions between the air bubble diffusion and momentum exchange processes.

5 AIR-WATER FLOW STRUCTURE

Air and water chord size measurements demonstrated a broad range of bubble and droplet sizes from less than 0.5 mm to more than 50mm. The median air chord sizes were typically between 1 and 10 mm, and the distributions were skewed with a preponderance of smaller bubbles compared to the mean. Time variations in air-water flow structure were conducted at several cross-sections in the horizontal runoff flow (i.e. $x \geq 0.4$ m). At the wave leading edge ($t < 0.1$ s), air and water chord sizes were comparable with median sizes of about 3–6 mm. This might suggest that individual bubble entrainment was associated with the ejection of water droplet of similar size. For larger times t , the order of magnitude of median air chord sizes remained basically constant and independent of time. But water chord sizes tended to increase with time, especially for $y/Y_{90} < 0.7$.

Such a different behaviour might be related to fundamental differences between air bubbles and water droplets. Water droplets have a momentum response time about 46,000 times larger than that of an air bubble of identical diameter (e.g. CROWE et al. 1998). As the bubble response time is significantly smaller than the characteristic time of the flow, bubble trapping in large-scale turbulent structures is a dominant mechanism in the bubbly flow region. Bubbles may remain trapped for very long times, the bubbly flow structure has some memory of its past, and it is affected by its previous structure. In the spray region, drop formation results from surface distortion, tip-streaming of ligaments and interactions between eddies and free-surface. Once ejected, the droplet response time is nearly two orders of magnitude larger the air flow response time. Most droplets have a short life and the spray region has little memory of its past. The spray structure may then change very rapidly in response to changes in flow conditions, while the bubbly flow region is deeply affected by its earlier structure.

6 SUMMARY AND CONCLUSIO

New dam break wave experiments were conducted systematically down a 25 m long flat waterway with a stepped invert. Visual observations highlighted the chaotic nature of the advancing flow associated with strong aeration of the leading edge. Unsteady air-water flow measurements were performed in the wave front using a series of conductivity probes. The results demonstrated quantitatively strong aeration of the leading edge and

the presence of a turbulent boundary layer next to the invert. The results suggest predominantly bed-load sediment motion near the leading edge, because the sediment relative density is inversely proportional to the air and water fluid density.

Measurements of air and water chord sizes highlighted a wide range of bubble and droplet sizes. Time-variations of air-water flow structure were observed. At the leading edge entrained bubbles and ejected droplets had similar sizes. Behind, however, the median water chord sizes increased with time, although the bubble sizes did not change. Overall the results emphasised the complicated nature of the dam break wave flow and its leading edge.

ACKNOWLEDGMENTS

The writer thanks his students Chung-hwee "Jerry" LIM, York-wee TAN, Chye-guan SIM, and Chee-chong TAN for their help and assistance.

REFERENCES

- CHANSON, H. (1995). "Air Bubble Entrainment in Free-surface Turbulent Flows. Experimental Investigations." *Report CH46/95*, Dept. of Civil Engineering, University of Queensland, Australia, June, 368 pages.
- CHANSON, H. (2003). "Sudden Flood Release down a Stepped Cascade. Unsteady Air-Water Flow Measurements. Applications to Wave Run-up, Flash Flood and Dam Break Wave." *Report CH51/03*, Dept. of Civil Eng., Univ. of Queensland, Brisbane, Australia, 142 pages.
- CHANSON, H., and TOOMBES, L. (2002). "Energy Dissipation and Air Entrainment in a Stepped Storm Waterway: an Experimental Study." *Jl of Irrigation and Drainage Engrg.*, ASCE, Vol. 128, No. 5, pp. 305–315.
- CROWE, C, SOMMERFIELD, M., and TSUJI, Y. (1998). "Multiphase Flows with Drop lets and Particles." *CRC Press*, Boca Raton, USA, 471 pages.
- DRESSLER, R. (1954). "Comparison of Theories and Experiments for the Hydraulic Dam-Break Wave." *Proc. Intl Assoc. of Scientific Hydrology Assemblée Générale*, Rome, Italy, Vol. 3, No. 38 pp. 319–328.
- ESCANDE, L., NOUGARO, J., CASTEX, L., and BARTHET, H. (1961). "Influence de Quelques Paramètres suru ne Onde de Crue Subite à l'Aval d'un Barrage." *Jl La Houille Blanche*, No. 5, pp.565–575.
- GALAY, V (1987). "Erosion and Sedimentation in the Nepal Himalaya. An Assessment of River Processes." *CIDA, ICIMOD, IDRC & Kefford Press*, Singapor
- HUNT, B. (1982). "Asymptotic Solution for Dam-Break Problems." *Jl of Hyd. Div.*, ASCE, Vol. 108, No.HY1, pp. 115–126.
- HUNT, B. (1984). "Perturbation Solution for Dam Break Floods." *Jl of Hyd. Engrg.*, ASCE, Vol. 110, No. 8 pp. 1058–1071.
- HUNT, B. (1994). "Newtonian Fluid Mechanics Treatment of Debris Flows and Avalanches." *Jl of Hyd. Engrg.*, ASCE, Vol. 120, No. 12, pp. 1350–1363.
- MANO, A. (1994). "Boundary Layer Developed near Surging Front." *Coastal Engineering in Japan*, Vol. 37, No. 1, pp. 23–3

- ROUSE, H. (1937). "Modern Conceptions of the Mechanics of Turbulence." *Transactions*, ASCE, Vol. 102, pp. 463–543.
- STUTZ, B., and REBOUD, J.L. (2000). "Measurements within Unsteady Cavitation." *Experiments in Fluids*, Vol. 29, pp. 545–552.

New model investigations on two-phase chute flow

K.Kramer, W.H.Hager & H.-E.Minor

*Laboratory of Hydraulics, Hydrology and Glaciology (VAW), Swiss
Federal Institute of Technology, Zurich, Switzerland*

Hydraulics of Dams and River Structures—Yazdandoost & Attari (eds)

© 2004 Taylor & Francis Group, London, ISBN 90 5809 632 7

ABSTRACT: For protection of spillway chutes and bottom outlets against cavitation damage, air is normally added by chute aerators in regions where the cavitation number falls below a critical value. Until today, the detrainment process downstream of an aerator has not been thoroughly investigated. This paper presents new model investigations of a hydraulic chute model focusing on the streamwise development of the air detrainment process. Results enable to predict the reduction of mean air concentration, depending on the air inflow, the inflow Froude number and the chute slope. It is also proven that the minimum air concentration on a chute is a function of the streamwise Froude number only.

1 INTRODUCTION

1.1 Problem outline

A key problem of high-velocity chute flows is the potential of cavitation damage at chute bottoms. Cavitation may cause major damage to chutes, spillway tunnels or bottom outlets. The risk of cavitation damage is related to the cavitation number

$$\sigma = \frac{p_o - p_v}{\rho(v^2/2)} \quad (1)$$

where σ =cavitation number, p_o =local pressure, p_v =vapour pressure of water, ρ =density of water, v =approach flow velocity.

The reduction of cavitation damage by air addition was introduced by Peterka (1953). Several other investigations concerning the minimum air concentration required to avoid cavitation damage were conducted over the last 50 years. Even if the proposals ranges

between 1–2% (Rasmussen 1956) and 5–8% (Peterka 1953), all scientists agree that a small amount of air close to the chute bottom reduces the risk of cavitation damage significantly. In supercritical open chute flow, air is either entrained at the free surface or added at the chute bottom with chute aerators. According to Falvey (1990), spillways should be provided with aerators if the cavitation number falls below a minimum required value of the order of $\sigma_{crit} \leq 0.2$. Practical design guidelines are given by Falvey (1990), Wood (1991) and Vischer and Hager (1998).

The current design methods for aerator spacing are weak because the detrainment process, i.e. the behaviour of the air flow downstream of the aerator, is not fully understood. Air detrainment of high-speed flows occurs mainly on relatively flat spillways, for which the surface air entrainment is small. If aerators are located too closely, excessive air flow is provided resulting in uneconomically high chute side walls and in supersaturation. If aerator spacing is too large, however, flow conditions with cavitation damage may occur, as previously outlined. Accordingly, information on air detrainment is necessary to design a chute (Kramer et al. 2002).

Air concentration measurements in the vicinity of chute aerators were provided by Volkart and Chervet (1983). The region of uniform self-aerated chute flows was particularly investigated by Wood (1983) thereby accounting for the data of Straub and Anderson (1958). The data set was extensively used to establish the current design criteria. Gangadharaiah et al. (1970) provided additional measurements similarly to those of Straub and Anderson, yet the streamwise development

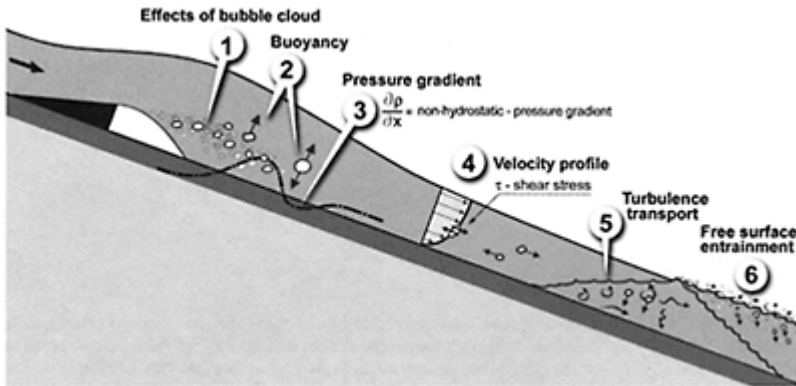


Figure 1. Forces acting on bubbles downstream of chute aerator.

of the air content between the aerator and the uniform flow region has not been investigated. This project intends to add model data with particular interest to the average air concentration and its minimum value, depending on hydraulic boundary conditions.

1.2 Motion of a single bubble in turbulent flow

The transport process of a single bubble in turbulent flow is the basis for air detrainment on chutes. According to Falvey & Irvine (1988), it is influenced by four main forces, namely: (1) Inertial, (2) Drag, (3) Buoyancy, and (4) Turbulent eddy transport forces. Rutschmann et al. (1986) found a dependence of the non-hydrostatic pressure gradient on the bubble rise velocity whereas Kobus (1991) mentioned an influence of bubble clouds on the single bubble transport process. The bubble transport direction depends on the algebraic sign of the pressure gradient. Figure 1 shows air bubbles downstream of an aerator subjected to these influences.

2 EXPERIMENTS

The experiments were conducted in a prismatic rectangular chute $b=0.5$ m wide, $l=14$ m long with a variable bottom slope ranging from 0% to 50%. The following inflow conditions were adjusted: (1) Water discharge Q_w up to 250 l/s, (2) Inflow depth $0.04 \leq h_o \leq 0.12$ m, and (3) Inflow Froude number $F_o = Q_w / (gh_o^3 b^2)^{0.5}$ between $3 \leq F_o \leq 12$. Two different set-ups for air addition to the water flow were employed, namely: (1) Pre-aerated discharge, where the air was added to the supply pipe to obtain a well-defined upstream cross section, and (2) Chute aerator as used for prototypes. The air-water ratio $\beta = Q_a / Q_w$ was varied between $15\% \leq \beta \leq 30\%$. No air $\beta=0$ was added for certain experiments, where the influence of free surface aeration alone was investigated. All results in this paper are based on pre-aerated measurements. The chute bottom was PVC made with an estimated equivalent sand roughness $k_s=0.01$ mm.

Air bubbles in a hydraulic model are known to be relatively larger than in prototypes. According to Wood (1991), the Froude similarity law can be adopted, provided: (1) Model scale is large enough to suppress viscous effects, (2) Turbulent intensity in the model has adequate kinetic energy to overcome the surface tension and bubble uplift forces. All measurements in the present project were conducted for fully turbulent flow. Inflow Reynolds numbers were between $5.8 \cdot 10^5 \leq R_o \leq 2.6 \cdot 10^6$ and inflow Weber numbers between $100 \leq W_o \leq 200$. Accordingly, scale effects are irrelevant in this project.

The following quantities were measured with a fiber-optical probe: (1) Local air concentration C , (2) Characteristic mixture flow velocity v_m , and (3) Bubble diameter d_b . The data collection and acquisition was automated to handle the large data sets. Further description of the hydraulic model and the measuring technique give Kramer et al. (2002).

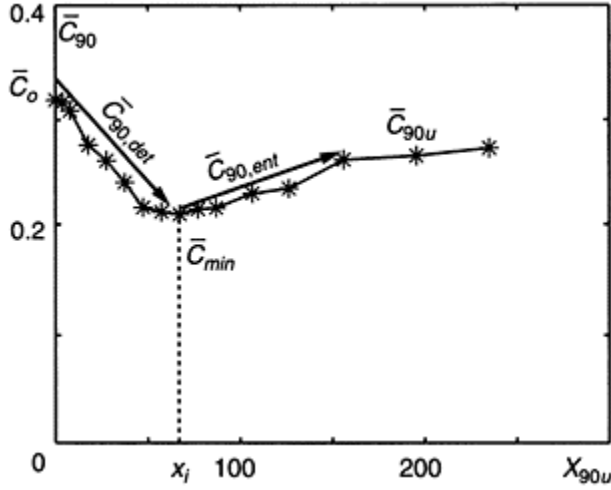


Figure 2. Typical average air concentration \bar{C}_{90} as a function of non-dimensional distance X_{90u}

3 STREAMWISE DEVELOPMENT OF AVERAGE AIR CONCENTRATION

3.1 Typical air concentration development

Observations were made to analyze the effect of hydraulic parameters by varying single parameters. Figure 2 shows, as an example, the average air concentration

$$\bar{C}_{90} = \frac{1}{h_{90}} \int_0^{h_{90}} C(z) dz \quad (2)$$

as a function of non-dimensional location $X_{90u}=x/h_{90u}$, where z is the coordinate perpendicular to the chute bottom, h_{90} is the mixture flow depth with $C=90\%$ and h_{90u} is the mixture flow depth measured at the end of the channel not necessarily equal to the uniform mixture flow depth. The streamwise average air concentration \bar{C}_{90} decreases, starting from the inflow air concentration \bar{C}_o , to a minimum \bar{C}_{min} . The average inflow air concentration is a function $\bar{C}_o=(\beta, F_o)$, and is additionally influenced from the jetbox arrangement. The minimum concentration is a function $\bar{C}_{min}=f(F(x))$, where $F(x)$ is the streamwise Froude number. The point of air inception was demonstrated to collapse with the point of minimum air concentration. The point of inception $x=x_i$ is located where the local flow depth $h=h(x)$ is equal to the thickness of turbulent boundary layer $\delta=\delta(x)$ (Vischer & Hager 1998).

In the region downstream of \bar{C}_{min} air is entrained from the free surface resulting in an increasing air concentration \bar{C}_{90} up to a uniform average air concentration $\bar{C}_{90u} = f(S_o)$ depending on the bottom slope only. This typical curve was observed for all measurements in the present project. Earlier statements referring to inflow and uniform flow conditions only, proposed a direct relation between the inflow and the uniform region. This paper analyses the hydraulic influences to this typical curve $\bar{C}_{90}(X_{90u})$ which can be divided in five parts, namely: (1) Inflow air concentration \bar{C}_o , (2) Air detrainment $\bar{C}_{90,det}$, (3) Minimum air concentration \bar{C}_{min} , (4) Air entrainment $\bar{C}_{90,ent}$, and (5) Uniform air concentration \bar{C}_{90u} . Where air detrainment $\bar{C}_{90,det}$ and air entrainment $\bar{C}_{90,ent}$ functions describe the streamwise development of average air concentration along the chute. The classical air detrainment $\Delta\bar{C}$ per chute meter can be calculated by subtraction of average air concentration for two distinctive locations using equation (3).

3.2 Effect of Froude number

The effect of the Froude number is analysed using average air concentration curves \bar{C}_{90} for varying chute slopes, constant inflow depth and constant inflow air concentration. Figure 3 shows the

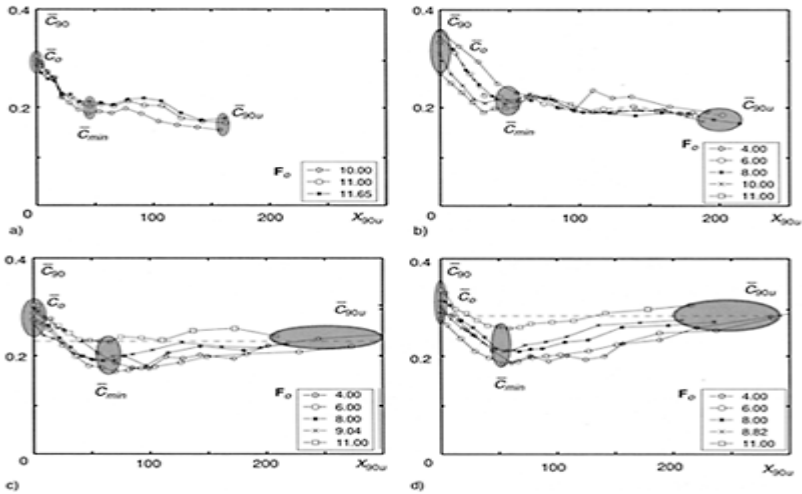


Figure 3. Mean air concentration \bar{C}_{90} as a function of non-dimensional distance X_{90u} for various slopes for (a) $S_o = 0.0\%$, (b) $S_o = 10\%$, (c) $S_o = 30\%$, (d) $S_o = 50\%$.

streamwise average air concentration curves \bar{C}_{90} as a function of non-dimensional location X_{90u} for the four bottom slopes $S_o=0\%$, 10%, 30% and 50%. All curves decrease first, starting from the inflow air concentration \bar{C}_o to a minimum \bar{C}_{min} , as previously outlined. The average minimum air concentration \bar{C}_{min} for steeper slopes $S_o=30\%$ and 50% is better defined than for $S_o=0\%$ and 10%. On flat chutes, the minimum air concentration is defined at the break between the steep detrainment curves and the downstream flow region where the air concentration curves slightly decrease to the uniform mean air concentration \bar{C}_{90u} .

3.3 Air detrainment

Figure 4 shows the same data as in Figure 3, shifted in the x-direction on the generalized air detrainment curve (3), providing that the inflow air concentration \bar{C}_o is known. Its best fit is

$$\bar{C}_{90,det} = aX_{90u} + c \quad (3)$$

where $a=f(S_o)<0$ and $c=0.4$ is a constant. The parameter

$$X_{shift} = \frac{(\bar{C}_o - 0.4)}{a} \quad (4)$$

which shifts each curve on (3) depends on the inflow air concentration. The parameter a varies between $-0.003 \leq a \leq -0.0017$ for the four chute slopes investigated.

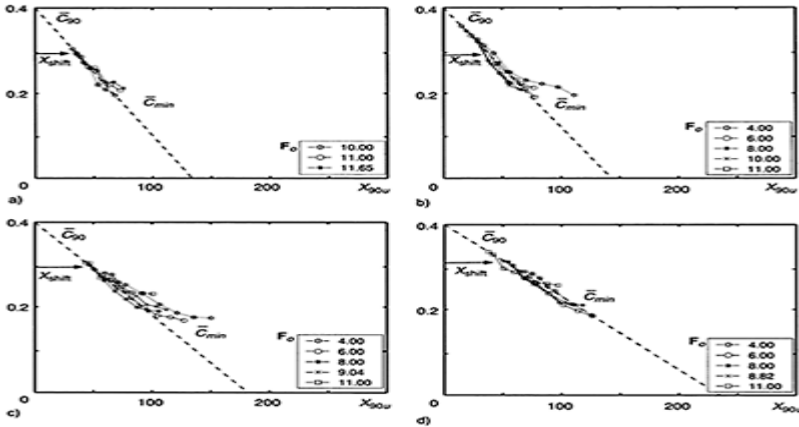


Figure 4. Mean air detrainment $\bar{C}_{90,det}$ as a function of non-dimensional distance X_{90u} for various chute slopes S_o (as in Figure 2), (---) (3), (a)

$a=-0.003$, (b) $a=-0.0028$, (c)
 $a=-0.0022$, (d) $a=-0.0017$.

3.4 Minimum air concentration

The minimum air concentration \bar{C}_{min} is an important parameter for chute protection, even if only average numbers are considered. It was found to be a function of bottom slope, mixture flow depth and streamwise Froude number. The Froude number development depends directly on the flow depth and thus on the bottom slope as $\bar{C}_{min} = f(F(x))$. It was found that the overall flow development is more important than local details.

The arithmetic average of the inflow Froude number and the Froude number at the inception point $F_{o-min} = (F_o + F(\bar{C}_{min}))/2$ was considered to result in

$$\bar{C}_{min} = 0.015F_{o-min}. \quad (5)$$

For inflow Froude numbers $F_o \geq 6$ and bottom slopes $S_o \geq 10\%$ the correlation is $R^2=0.89$ (Figure 5). For small bottom slopes no free surface air entrainment occurs and the air concentration falls finally to zero. For Froude numbers $F_{o-min} \geq 10$, the average minimum air concentration did never fall below $\bar{C}_{min} = 0.17$.

3.5 Effect of bottom slope

According to Figure 4 the average air detrainment is not a function of the inflow Froude number only but of chute slope as well. Equation (3) involves the parameter a as a function of the sine of

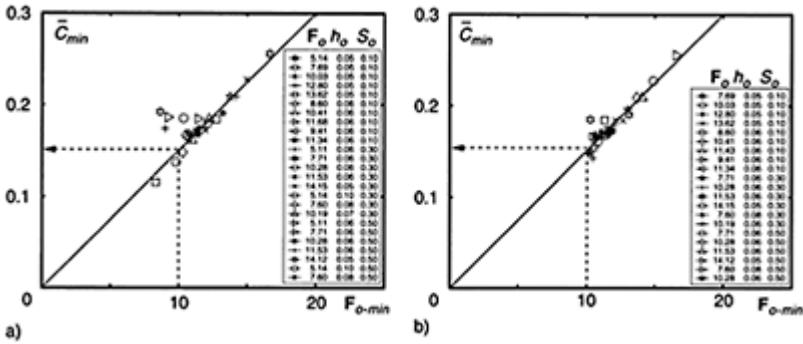


Figure 5. Minimum air concentration \bar{C}_{min} against streamwise Froude number F_{o-min} for $S_o \geq 10\%$, (---) (5), (a) all

data, correlation $R^2=0.59$, (b) data
 $F_o \geq 6$, correlation $R^2=0.89$.

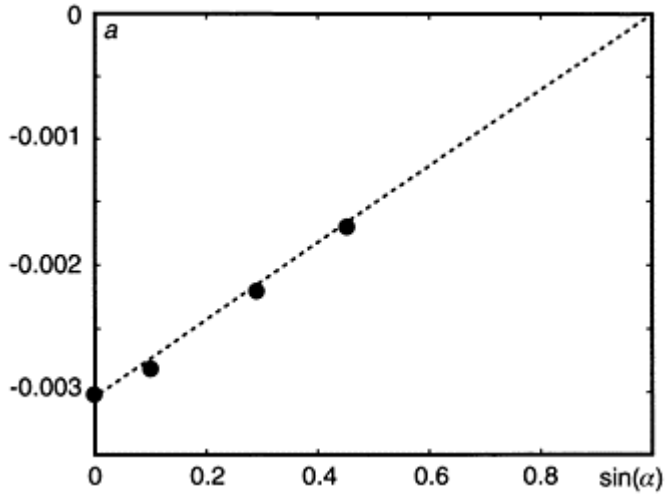


Figure 6. Parameter a from equation (3) as a function of chute angle $\sin(\alpha)$, $R^2=0.98$, (---) (6).

the chute angle $\sin \alpha = 0.003(\sin(\alpha) - 1)$. Figure 6 shows this parameter as a function of chute slope with the best fit

$$a=0.003(\sin(\alpha)-1).$$

(6)

This equation allows calculating the reduction of the average air concentration in the region between a given inflow air concentration and the minimum air concentration \bar{C}_{min} .

3.6 Air entrainment

Ehrenberger (1926) established that air is entrained in high-speed chute flows by free surface aeration. This is an important feature for aerator spacing because no additional aerator is normally needed beyond the inception point. The streamwise behaviour of the average air concentration downstream of the point of inception was considered by e.g.

Hager (1991) stating that the uniform air concentration \bar{C}_{90u} depends on the chute slope only, based on Straub and Anderson's (1958) classical data set. The streamwise development of average air concentration for chute flows was investigated by Kramer et al. (2003), focusing the region downstream of the point of inception. The present paper expands these basic observations.

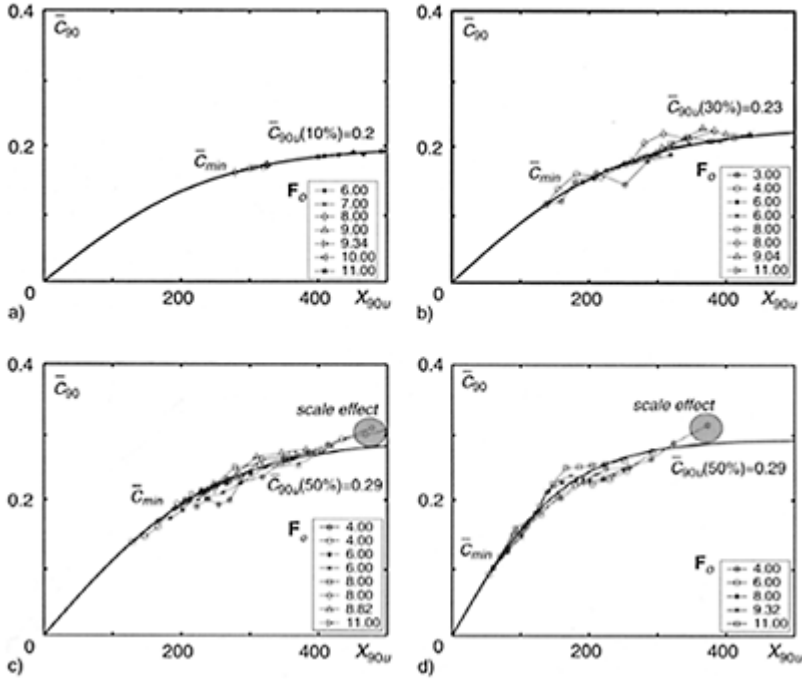


Figure 7. Mean air entrainment $\bar{C}_{90,ent}$ as a function of non-dimensional distance X_{90u} for various chute slopes, (---) (7), (a) $S_o=10\%$, (b) $S_o=30\%$, (c) $S_o=50\%$, (d) $S_o=50\%$, non-aerated flow.

The air entrainment was analysed as the detrainment previously, by replacing the inflow air concentration by the minimum air concentration at the point of inception. The best analytic fit was found to be the hyperbolic tangent function

$$\bar{C}_{90,ent} = \bar{C}_{90u} \tanh(bX_{90u}) \quad (7)$$

with $b=0.004$ for pre-aerated, and $b=0.006$ for non-aerated flows. Figures 7a-c show the air entrainment downstream of the point of minimum air concentration for various chute slopes. For the horizontal chute $S_o=0$ no air entrainment at all was observed. The measurements were shifted on the function approximated by equation (7). The general form of this equation with $b=0.004$ depends on the uniform air concentration \bar{C}_{90u} only. Two outliers are notable in Figure 7c and one in Figure 7d relating to the data sets with the smallest discharges. Both data sets appear to deviate from the general trend at their ends, because of a sudden increase of \bar{C}_{90} . It is presumed that scale effects and minute

shock waves have affected these data without an influence on the general trend. These three data points are specially marked in Figures 7c and d, respectively. Figure 8a shows the air entrainment $\bar{C}_{90,ent}$ as a function of X_{90u} for the four investigated chute slopes S_o , based on Figure 7. The influence of the bottom slope on the uniform air concentration is obvious, with higher uniform air concentration for steeper slopes.

Figure 8b compares \bar{C}_{90u} from the present project with proposals from Hager (1991) and Chanson (1997) applying Straub and Anderson's (1958) data. The large deviations between the two data sets can be traced back to the effect of surface roughness. Whereas Straub and Anderson used an artificially roughened surface resulting in more air entrained, the present project was based on a smooth boundary surface. This effect needs additional attention in the future.

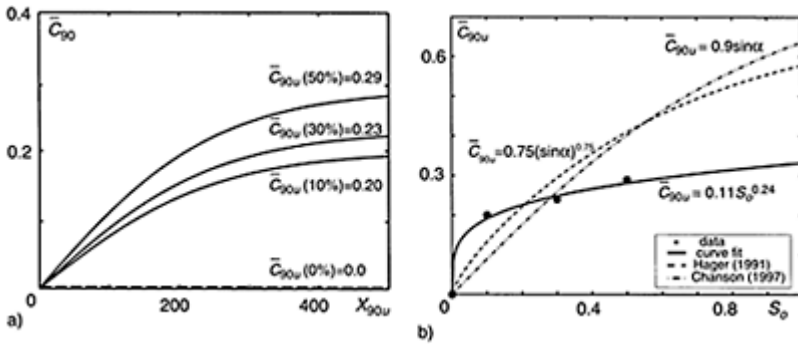


Figure 8. (a) Streamwise development of average air entrainment $\bar{C}_{90,ent}$ for all chute slopes S_o , (---) (7), (b) average uniform air concentration \bar{C}_{90} against chute slope.

4 CONCLUSIONS

This paper intends to add new model investigations for two-phase chute flow. Streamwise data of local air concentration, local mixture velocity and bubble size were taken in a hydraulic model. It focused on the development of the average air concentration \bar{C}_{90} .

Three important effects apply for the average air concentration \bar{C}_{90} , namely:

- (1) The air detrainment curve depends on the inflow air concentration \bar{C}_o and the bottom slope S_o ,

- (2) The minimum air concentration \bar{C}_{min} depends on a combination of the inflow Froude number F_o and the local Froude number at the point of inception $F(\bar{C}_{min})$, and
- (3) The air entrainment follows a tangent hyperbolic function up to uniform average air concentration \bar{C}_{90u} .

It can therefore be concluded that the amount of air supplied is not significant, but the transport capacity of the turbulent water flow is the determining factor. If the transport capacity is low, the air will detrain independent of the bottom slope. For very turbulent flow relating to high Froude numbers, the air will not fall below a minimum value, however.

ACKNOWLEDGEMENT

This project was supported by the Swiss National Science Foundation (Project No. 2100–057081. 99/1) and the Swiss Committee on Dams.

REFERENCES

- Chanson, H. 1997. *Air bubble entrainment in free-surface turbulent shear flows*. San Diego: Academic Press.
- Ehrenberger, R. 1926. Wasserbewegung in steilen Rinnen (Schusstennen) mit besonderer Berücksichtigung der Selbstbelüftung. *Zeitschrift des Österreichischen Ingenieur- und Architekten-Vereins*: 78(15/16): 155–1 78(17/18): 175–179(in German).
- Falvey, H.T., & Irvine, D.A. 1988. Aeration in jets and high velocity flows. *Proc. Model-Prototype Correlation of Hydraulic Structures*, Colorado, Colorado Springs, 25–55.
- Falvey, H.T. 1990. Cavitation in chutes and spillways. *Engineering Monograph No. 42*. Bureau of Reclamation, Denver, Colorado.
- Gangadharaiah, T., Lakshmana Rao, N.S., & Seetharamiah, K. 1970. Inception and entrainment in self-aerated flows. *Journal of the Hydraulics Division, ASCE* **96**(HY7): 1549–1565.
- Hager, W.H. 1991. Uniform aerated chute flow. *Journal of Hydraulic Engineering* **117**(4): 528–533.
- Kobus, H. 1991. Introduction to air-water flows. In I.R.Wood (ed.) *Air entrainment in free-surface flows*: 1–28, Rotterdam: Balkema.
- Kramer, K., Hager, W.H., & Minor, H.-E. 2002. Air detrainment in high-speed chute flows. *Proc. Hydraulic Measurement & Experimental Methods*, Estes Park, Colorado, CD-Rom.
- Kramer, K., Hager, W.H., & Minor, H.-E. 2003. Development of mean air concentration on chute flow. *Proc. 30th IAHR Congress*, Thessaloniki, Theme D: 687–694.
- Peterka, A.J. 1953. The effect of entrained air on cavitation pitting. *Proc. 5th IAHR -ASCE Joint Conference*, Minnesota, Minneapolis, 507–518.
- Rasmussen, R.E.H. 1956. Some experiments on cavitation erosion in water mixed with air. *Proc. 1st Int. Symposium on Cavitation in Hydrodynamics*, London **20**:1–25.
- Rutschmann, P., Volkart, P., & Wood, I.R. 1986. Air entrainment at spillway aerators. *Proc. 9th Australasian Fluid Mechanics Conference*, Auckland, 350–353.
- Straub, L.G., & Anderson, A.G. 1958. Experiments on self-aerated flow in open channels. *Journal of the Hydraulics Division, ASCE* **84**(HY7) Paper 1890:1–50
- Vischer, D.L., & Hager, W.H. 1998. *Dam hydraulics*. Chichester: John Wiley & Sons.

- Volkart, P., & Chervet, A. (1983). Air slots for flow aeration. *VAW Mitteilung* 66. ETH, Zürich.
- Wood, I.R. 1983. Uniform region of self-aerated flow. *Journal of Hydraulic Engineering* **109**(3): 441–461.
- Wood, I.R. 1991. *Air entrainment in free-surface flows*. Rotterdam: Balkema.

Evaluation of incipient-aeration point on spillways

A.Najafi

Postgraduate Student, Irrigation Structures, Urmia University, Iran

M.Yasi

Assistant Professor, Urmia University, Iran

Hydraulics of Dams and River Structures—Yazdandoost & Attari (eds)

© 2004 Taylor & Francis Group, London, ISBN 90 5809 632 7

ABSTRACT: Determination of the inception point for self-aeration is of great importance in the design of dam spillways. Several semi-empirical methods have been presented to calculate the location of this critical point. This paper examines the order of prediction errors and the degree of reliability from the application of current methods in compare with available experimental data on the incipient-aeration point, both in model and prototype. The results indicate that the relationships of Wood, et al. (1983), Keller & Rastogi (1977), and Ferrando & Rico (2002) are accurate enough for preliminary design purposes. An average underestimation of 1% should be considered with an order range of error between –44% and +58%. Computational procedure is illustrated by several examples of dam spillways in Iran, on the anticipated location of the critical point and its possible deviation from the average predicted value.

1 INTRODUCTION

Open-channel flow on chutes and spillways is characterised by turbulent, supercritical and non-uniform flow, from which acceleration and boundary layer development occur simultaneously over a considerable length of the steep slope (Keller & Rastogi, 1975). The process of air entrainment begins where the outer limit of the boundary layer meets the flow surface (Fig. 1). Turbulence generated by the bed shear and vertical component of velocity causes the development of waves and surface eddies resulting in natural self-aeration, and a white appearance of water flow is observed (Falvey, 1980).

The first consideration in the design of chutes and spillways is the location of the critical point, that is, the incipient point downstream from the spillway crest where aeration first begins (Fig. 1). This is important, particularly in the study of possible occurrence of cavitation along the non-aerated flow region, and for the computation of flow profile with its attendant bulking free surface downstream (Keller & Rastogi, 1975,

1977). The location of the incipient point downstream from the spillway crest (X_c) depends largely on the turbulent characteristics of the flow over the spillway, thereby is a function of spillway type (free overflow/gated), upstream slope face of the crest, crest shape, chute slope and configuration, surface-bed roughness, and unit discharge (Keller et al. 1974, Chanson 1996).

In the literature, several empirical, semi-empirical and theoretical methods have been presented to evaluate the location of the incipient point. The most common methods are those developed by Bauer (1954), Keller & Rastogi (1977), Wood, et al. (1983), Hager & Blaser (1998), and Ferrando & Rico (2002), as presented in Table 1.

The aim of the present study is not to examine the basic theoretical formulation and assumptions made by different researches. The main target is to bring hydraulic engineers with a state of the art of the current methods for the evaluation of the critical point in preliminary design of large spillways. This technical paper compares the calculated values of X_c from different methods in Table 1 with those measured in available physical studies, both in model and in prototype. The order of prediction error and discrepancies resulted from the application of each of these methods are presented. The most simple and accurate way is proposed for the preliminary determination of

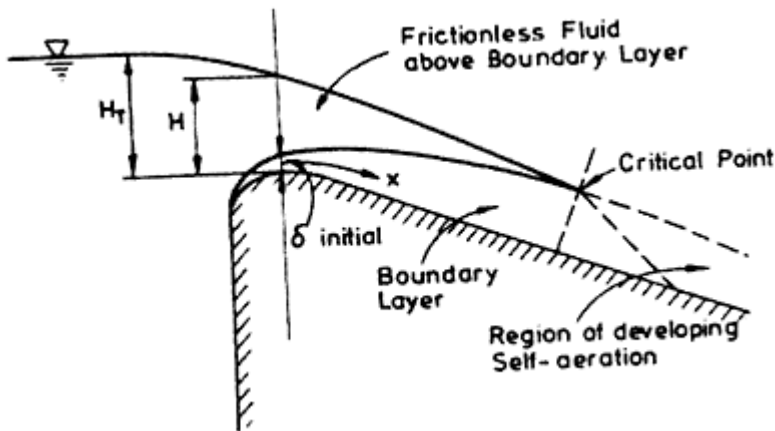


Figure 1. General feature of flow over a spillway.

Table 1. Calculation methods for the location of incipient point from the spillway crest (X_c).

Reference	X_c	Remarks
Bauer(1954)	$\frac{\delta}{X_c} = 0.0254 \left(\frac{X_c}{k_s} \right)^{-0.135}$	Empirical formula based on model data; X_c is calculated by trial and error
Keller & Rastogi (1977)	Design charts and tables presented	Based on K- ϵ turbulent model; model and prototype data; WES spillway shape: explicit solution

		for specific chute slopes
Wood, Ackers & Loveless(1983)	$\frac{X_c}{k_s} = 13.6(\sin \theta)^{0.0796} F_*^{0.713}$	Semi-empirical formula; for any chute slopes
	$F_* = \frac{q}{(g s k_s^3)^{0.5}}$	
	$s = \sin \theta$	
Hager & Blaser (1998)	$\frac{X_c}{N_c} = 16(\sin \theta)^{-0.6} \left(\frac{k_s}{N_c} \right)^{-0.08}$	Theoretical solution of boundary layer development in conjunction with the Bauer (1954) relationship
	$N_c = \left(\frac{q^2}{g} \right)^{\frac{1}{3}}$	
Ferrando & Rico (2002)	$X_c = \left(\frac{q}{0.05642 k_s^{0.056} (\sin \theta)^{0.34}} \right)^F$	Modified and extended method of Cain and Wood (1981); for any chute slopes.
	$F = (1.46443 k_s^{0.0054} (\sin \theta)^{0.0027})^{-1}$	

δ =Boundary layer thickness to be equal to flow depth; k_s =Roughness height; θ =Chute angle;
 q =Unit discharge.

the location of critical point. Typical examples illustrate the degree of confidence in computational results for several dam spillways in Iran.

2 EXPERIMENTAL DATA

In the literature, available experimental data on the location of inception point on spillways (X_c) are limited. Table 2 summarizes the general characteristics of the input data from worldwide model and prototype studies, which adequately covers a large range of physical and hydraulic conditions.

Table 2. General characteristics of available experimental data on spillways.

Data	Reference	Dam spillway	k_s (mm)	Chute slope (degree)	Type of spillway	Range of unit discharge (m ² /sec)	Number of measuring data on X_c
Model and prototype*	Keller & Rastogi (1977)	Group A	1.5	10	WES (Standard Ogee)	1.34–74.99	6
		Group B	1.5	50		1.34–74.99	6
Prototype	Hickox (1945)	Norris (USA)	1.5	55	Ogee	1.12–8.40	7
	Hickox (1945)	Douglas (USA)	1.5	50	Ogee	1.65–4.11	6

Michels & Lovely (1953)	Glen maggiee (Australia)	1.5	59	Ogee (Over flow)	0.3–8.87	4
Michels & Lovely (1953)	Werribee (Australia)	1.5	60	Ogee	0.14–0.2	2
Keller (1972)	Aviomore (NZ)	1.524	45	Ogee (Gated)	2.44–6.65	2
Cain (1978)	Aviomore (NZ)	1.524	45	Ogee (Gated)	2.23–3.16	2
Ning & Wang(1993)	Bikou (China)	1.5	18.5	Ogee	16.07–18.20	3

* Distinction between model and prototype data not reported.

Table 3. Comparison between actual and calculated values of X_c , using Group A data.

q (m ² /sec)	$X_{c(act)}$ (m)	Bauer(1954)		Keller & Rastogi (1977)		Wood, et al. (1983)		Hager & Blaser (1998)		Ferrando & Rico (2002)	
		$X_{c(cal)}$ (m)	E%	$X_{c(cal)}$ (m)	E%	$X_{c(cal)}$ (m)	E%	$X_{c(cal)}$ (m)	E%	$X_{c(cal)}$ (m)	E%
1.34	18	24	33	18	0	19	6	42	133	19	6
6.71	55	78	42	59	7	60	9	133	142	59	7
6.98	59	80	36	61	3	61	3	137	132	61	3
15.03	103	139	35	107	4	106	3	238	131	105	2
34.85	182	257	41	193	6	193	6	436	140	191	5
74.99	314	426	36	335	7	334	6	757	141	329	5
Range of errors %		33–42		0–7		3–9		131–142		2–7	
Ave. Errors %		37		5		6		137		5	

X_c =The location of critical point; $X_{c(act)}$ =Actual value of X_c ; $X_{c(cal)}$ =Calculated value of X_c .

Depending on the various chute slopes and unit discharges, a number of 38 measuring tests on the X_c is included in the input data, in Table 2. Typical details of such data are presented in Tables 3 and 4

3 COMPUTATIONAL PROCEDURE

Predicted values of X_c have been calculated for each of the 38 sets from the 9 groups of data provided in Table 2, using the five methods presented in Table 1. Typical computational results are presented in Tables 3 and 4 for two groups of the input data.

Table 4. Comparison between actual and calculated values of X_c , Norris Dam Spillway.

q (m ² /sec)	$X_{c(act)}$ (m)	Bauer(1954)		Keller & Rastogi (1977)		Wood, et al. (1983)		Hager & Blaser (1998)		Ferrando & Rico(2002)	
		$X_{c(cal)}$ (m)	E%	$X_{c(cal)}$ (m)	E%	$X_{c(cal)}$ (m)	E%	$X_{c(cal)}$ (m)	E%	$X_{c(cal)}$ (m)	E%
1.12	14	12	-14	9	-34	11	-22	14	5	9	-35
1.17	16	12	-21	9	-42	11	-29	15	-5	9	-41
3.56	35	28	-20	23	-34	25	-28	33	-4	20	-41
3.60	36	28	-23	38	5	25	-31	33	-8	20	-44
6.64	47	44	-6	69	47	39	-17	52	12	31	-33
8.02	51	49	-4	64	26	44	-13	60	18	36	-29
8.40	50	51	3	66	31	46	-9	62	23	37	-26
Range of errors %		(-23) -(3)		(-42) -(47)		(-31)- (-9)		(-8) -(23)		(-44)- (-26)	
Ave. errors %		-13		0		-21		6		-36	

X_c =The location of critical point; $X_{c(act)}$ =Actual value of X_c ; $X_{c(cal)}$ =Calculated value of X_c .

The percentage of the prediction error (E%) from the application of each of the five methods was calculated by the following relationship.

$$E\% = \left(\frac{X_{c(cal)} - X_{c(act)}}{X_{c(act)}} \right) \times 100 \quad (1)$$

where $X_{c(act)}$ =actual value of X_c ; and $X_{c(cal)}$ =Calculated value of X_c . Positive value of E% in Equation 1 illustrates an overestimation by the predictive method, while the resulted negative value denotes underestimation.

Tables 3 and 4 also present the range and the average of errors resulted from the application of each method for any of the two groups of the data sets. Table 5 summarizes the overall order of errors (both range and average) in the prediction of X_c by the five different methods, using all 38 sets of the 9 groups of data.

Furthermore, normal distribution was assumed for the 38 predictive values of errors (E%) in each method, and corresponding standard deviations (S.D.) were calculated. Deviation from the mean value was examined in two probability levels of 68% (\pm S.D.) and 95% (\pm 2S.D.). The results are presented in Table 6. Figure 2 also indicates the mean and the range of predictive errors with 68% probability of occurrence.

4 RESULTS AND DISCUSSION

The results presented in Table 5 indicate that most of the predictive methods (except that from Wood, et al. 1983) tend to overestimate the X_c by some degrees. Out of 38 sets of data, the methods of Bauer (1954), Keller & Rastogi (1977), Hager & Blaser (1998), and Ferrando & Rico (2002) overestimate the X_c in 66%, 60%, 89% and 55% cases, respectively.

Tables 5 and 6 indicate that the results from the method of Hager & Blaser (1998) seem to be out of order when compares with the corresponding results from the other methods. This method overestimates the X_c largely, with an average error of +53% and with a wide and unbalanced range of errors between -29% and +142%. The method of Bauer (1954) is also rated to be inaccurate, resulting in an overestimation by an average of +16% in a range of -7% to +77%.

Table 6 and Figure 2 indicate that the order of errors from the application of three methods of Keller & Rastogi (1977), Wood, et al. (1983), and Ferrando & Rico (2002) are well consistent, and more accurate than the two other methods. The average estimation error is rated to be -2%, +1%,

Table 5. Predictive error of X_c by different methods in Table 1, using data from Table 2.

Source of Data	Predictive error (%): Range (Mean)				
	Bauer (1954)	Keller & Rastogi (1977)	Wood, et al. (1983)	Hager & Blaser (1998)	Ferrando & Rico (2002)
Group A	33-42 (37)	0-7 (5)	3-9 (6)	131-142 (137)	2-7 (5)
Group B	12-23 (18)	(0)-(8) (2)	0 (0)	38-44 (41)	0-6 (3)
Norris Dam	(-25)-(-2) (-13)	(-44)-(-47) (-6)	(-39)-(-10) (-22)	(-6)-(-24) (5)	(-44)-(-26) (-37)
Dauglas Dam	(-8)-(-45) (6)	(0)-(59) (18)	(-20)-(-36) (-4)	12-82 (30)	(-32)-(-9) (-22)
Glenmaggie Dam	(-7)-(-77) (10)	(-30)-(0) (-12)	(-43)-(-57) (-3)	(-29)-(-107) (26)	(-43)-(-60) (-2)
Werribee Dam	5-8 (7)	(-37)-(-31) (-34)	0-1 (1)	33-50 (42)	6-8 (7)
Aviomore Dam	31-48 (40)	9-13 (11)	14-35 (25)	63-91 (77)	17-39 (28)

Aviomore Dam	13–17 (15)	(–1)–(9) (4)	(–1)–(0) (0)	40–4 (41)	0–3 (2)
Bikou Dam	22–30 (26)	(–7)–(1) (–4)	(–2)–(3) (–1)	79–90 (86)	(–2)–3 (–1)
Overall Error	(–7)–(77) (16)	(–44)–(59) (–2)	(–43)–(57) (1)	(–29)–(142) (53)	(–44)–(60) (–2)
Overestimation Cases (%)	66%	60%	47%	89%	55%

Table 6. Statistical representation of predictive errors in X_c by different methods.

Error (%)	Predictive methods				
	Bauer (1954)	Keller & Rastogi (1977)	Wood, et al. (1983)	Hager & Blaser (1998)	Ferrando & Rico (2002)
Mean Value (E)	+16	–2	+1	+53	–2
Standard Deviation (S.D.)	23	21	19	48	23
Probability of 68% ($E \pm S.D.$)	(–7, +39)	(–23, +19)	(–18, +20)	(5, +111)	(–25, +21)
Probability of 95% ($E \pm 2S.D.$)	(–30, +62)	(–44, +40)	(–37, +58)	(–43, +149)	(–48, +44)
Absolute Range	(–7, +77)	(–44, +59)	(–43, +57)	(–29, +142)	(–44, +60)

and –2%, respectively. The corresponding standard deviations are in close agreement, with the order of 21%, 19% and 23%, respectively. The absolute range of errors in these three methods are almost consistent with 95% probability level of estimation.

No specific judgment is being considered for the choice of the best predictive method among the three methods of Keller & Rastogi (1977), Wood, et al. (1983), and Ferrando & Rico (2002). The application of each of these three methods seems to be accurate enough for preliminary prediction of X_c , taking into account for corresponding average and range of estimation errors, as presented in Table 6.

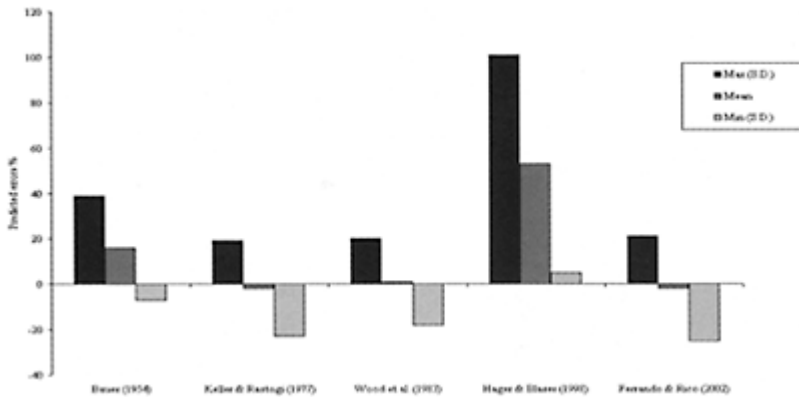


Figure 2. Prediction error of X_c by different methods (average, and range of $\pm S.D.$).

5 APPLICATION

There is a lack of physical data on the location of critical point for dam spillways in Iran. Nevertheless, the results from this study have been utilised to illustrate a more reliable methodology for the prediction of X_c . Table 7 presents the required physical information of five previously designed and/or constructed spillways in Iran. The value of X_c has been calculated by each of the three recommended methods (Keller & Rastogi 1977; Wood, et al. 1983; and Ferrando & Rico 2002), using 3 different flow conditions. Under each method, the X_c was first calculated using the original relationship in Table 1. Then, the overall error limit of the applied method was used from Table 6 to calculate the possible deviation from the predicted X_c . Finally, the original X_c was adjusted using the average estimation error of the method in Table 6. As a final decision, mean value of the adjusted X_c from the three methods was calculated for each spillway, and possible limit of the prediction was considered, as presented in Table 7.

For example, for the case of the Bookan (old) spillway, and under flow level of $q=10 \text{ m}^2/\text{s}$, it is considered that the air entrainment would be occurred on the spillway chute at a distance of 51 m from the crest (in average), which could be deviated in practice in a range between 29 m to 83 m. Figure 3 demonstrates the possible occurrence of the critical point over the Bookan (old) spillway under three different flow conditions.

6 CONCLUSION

It is of great importance to evaluate accurately the critical point where air entrainment begins on a dam spillway. Among the several predictive methods, the relationships of Wood, et al. (1983), Keller & Rastogi (1977), and Ferrando & Rico (2002) are more consistent and accurate for the prediction of the location of critical point (X_c). As

presented in Table 6, the average estimation error of each of these three methods is rated to be +1%, -2%, and -2%, respectively. The corresponding standard deviations are in the order of 19%, 21% and 23%, respectively.

The average value of the predicted X_c from these 3 methods is recommended for the preliminary design of spillways. An average underestimation of 1% should be considered, with an order range of error between -44% and +58% (corresponding to 95% confidence limit). Computational procedure for the evaluation of X_c is illustrated by several examples, as presented in Table 7.

It is noted that the effects of surface roughness (k_s), chute slope (θ), and flow level (q) are directly included in these predictive methods. The location of critical point is to be moved further downstream in the case of a smoother spillway, with a milder chute slope, and under higher flow conditions. The results confirm with the accepted properties of the turbulent-boundary layer

Table 7. Prediction of X_c by different methods for selected dams spillways, in Iran.

Dam	Type of spillway	q (m^2/sec)	Keller & Rastogi(1977)	Wood, et al. (1983)	Ferrando & Rico (2002)	Predicted $X_c(m)$	Occurrence of critical point on spillways
			$X_c(m)$	$X_c(m)$	$X_c(m)$		
Bookan (old)	Ogee	10	51*	51*	52*	51 ⁺	Yes
$k_s=1.5mm$	(Free overfall)	15	29-81**	29-80**	29-83**	29-83 ⁺⁺	No
$P=50m$			50***	52***	51***		
$\theta=56$			71*	68*	70*	69 ⁺	
$L=60$		20	40-113**	39-107**	39-112**	39-113 ⁺⁺	No
			70***	69***	69***		
			82*	84*	86*	83 ⁺	
			46-130**	48-132**	48-138**	46-138 ⁺⁺	
			80***	85***	84***		
Bookan (new)	Ogee	10	55*	52*	53*	53 ⁺	Yes
$k_s=1.5mm$	(Gated)	15	37-87**	30-82**	30-85**	30-87 ⁺⁺	No
$P=50m$			54***	53***	52***		
$\theta=53$			73*	69*	71*	71 ⁺	
$L=63m$		20	41-116**	39-108**	40-114**	39-116 ⁺⁺	No
			72***	70***	70***		
			85*	85*	87*	86 ⁺	

			48–135**	48–133**	49–139**	48–139 ⁺⁺	
			83***	86***	85***		
Karron (3)	(Gated)	10	71*	59*	60*	63 ⁺	Yes
$k_s=1.5\text{mm}$	Ogee		40–113**	34–93**	34–96**	34–113 ⁺⁺	
$P=200\text{m}$			70***	60***	59***		
$\theta^\circ=30$		15	90*	79*	80*	82 ⁺	Yes
$L=400\text{m}$			50–143**	45–124**	45–128**	45–143 ⁺⁺	
			88***	80***	78***		
		20	114*	97*	98*	102 ⁺	Yes
			64–181**	55–152**	55–157**	55–181 ⁺⁺	
			112***	98***	96***		
Raeis	Ogee	10	50*	50*	51*	50 ⁺	Yes
Ali	(Gated)		28–80**	29–79**	29–82**	29–82 ⁺⁺	
Delvari			49***	51***	50***		
$k_s=1.5\text{mm}$		15	66*	67*	68*	67 ⁺	Yes
$P=117\text{m}$			37–105**	38–105*	38–109**	38–109 ⁺⁺	
$\theta^\circ=67$			65***	68***	67***		
$L=155\text{m}$		20	79*	82*	84*	81 ⁺	Yes
			44–126**	47–129**	47–134**	47–134 ⁺⁺	
			77***	83***	82***		
Shafa	Ogee	10	55*	52*	53*	53 ⁺	Yes
Rood	(Free over fall)		37–87**	30–82**	30–85**	30–87	
$k_s=1.5\text{mm}$			54***	53***	52***		
$P=124\text{m}$		15	73*	69*	71*	71 ⁺	Yes
$\theta^\circ=53$			41–116**	39–08**	40–114**	39–116 ⁺⁺	
$L=127\text{m}$			72***	70***	70***		
		20	85*	85*	87*	85 ⁺	Yes
			48–135**	48–133**	49–139**	48–139 ⁺⁺	
			83***	86**	85***		

k_s =Roughness height; θ =Chute angle; β =Spillway height; L =Spillway length.

*Direct calculation; **Predicted range of X_c based on the overall error limit; ***Adjusted X_c based on the mean errors; +Mean value of predicted X_c ; ++Limit of possible value of X_c .

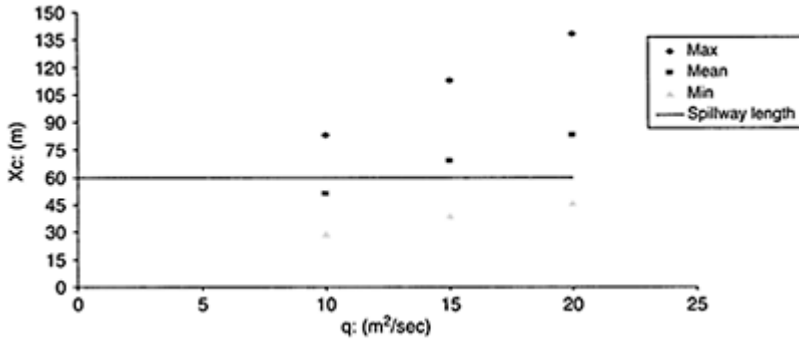


Figure 3. Predictive values of X_c versus unit discharge (q) for Bookan (old) Dam Spillway, Iran.

development on spillways. Uncertainties and existing deviations in the prediction of X_c need to be further tested by physical studies, both in model and prototype, for the effects of spillway type, crest shape and geometry of the chute, in a particular dam spillway.

REFERENCES

- Cain, P. & Wood, I.R. 1981. Measurements of self-aerated flow on a spillway. *Journal of Hydraulic Division, ASCE*, 107(HY11): 1425–1444.
- Chanson, H. 1996. *Air bubble entrainment in free-surface turbulent shear flows*. London Academic Press.
- Falvey, H.T. 1980. *Air water flow in hydraulic structures*. Water Resources Technical Publication, Engineering monograph No. 41, U.S. Dept. of Interior, U.S. Printing Office, Denver, Colorado.
- Ferrando, A.M. & Rico, J.R. 2002. On the incipient aerated flow in chutes and spillways. *Journal of Hydraulic Researches*, 40 (1): 95–97.
- Hager, W. & Blaser, F. 1998. Draw down curve and incipient aeration for chute flow. *Canadian Journal of Civil Engineering*, No.25:467–473.
- Keller, R.J., Lai, K.K. & Wood, I.R. 1974. Developing region in self-aerating flows. *Journal of Hydraulic Division, ASCE*, 100 (HY4): 553–568.
- Keller, R.J. & Rastogi, A.K. 1975. Prediction of flow development on spillways. *Journal of Hydraulic Division, ASCE*, 101 (HY9): 1171–1184.
- Keller, R.J. & Rastogi, A.K. 1977. Design charts for predicting critical point on spillways. *Journal of Hydraulic Division, ASCE*, 103 (HY12): 1417–1429.
- Wood, I.R., Ackers, P. & Loveless, J. 1983. General method for the critical point on spillways. *Journal of Hydraulic Division, ASCE*, 109 (HY2): 305–307.

2.

Intakes and outlets

Air entrainment at Guri Dam intake operating at low heads

G.Montilla, A.Marcano & C.Castro

*C.V.G.EDELCA, Hydraulics Department, Basic Engineering Division,
Macagua, Edo. Bolívar, Venezuela*

Hydraulics of Dams and River Structures—Yazdandoost & Attari (eds)

© 2004 Taylor & Francis Group, London, ISBN 90 5809 632 7

ABSTRACT: Experimental investigations of air entrainment inside the intakes of Guri Dam Second Powerhouse operating below critical submergence reservoir level, were carried out on a non-distorted 1:30 scale Froudian Physical Model. Scale effects were considered taking into consideration the—state of art—experience on physical modeling practice of submerged intakes. Prototype observations were done and compared with model results to achieve similarity between the two physical systems. Visual observations and measurements were taken inside the intake and, in the reservoir approach region to assess the behavior of the flow phenomenon under study. Turbine flow operation conditions where vortex formation occur were identified and curves for-free air entrainment flow-inside the intakes, were developed below elevation 240, design critical submergence operation of the project which adds in operating safely the 630 MW units.

1 INTRODUCTION

Guri (10000MW) Project is located on the Caroni river Basin at southeastern Venezuela and is presently generating 52000 GWH/year firm energy, which accounts for the 50% of the total national electricity demand. Guri Dam houses 20 Francis generators, including ten 725 MW units, which can discharge between 300 and 600 m³/s, for a net design head of 142 m, at normal pool elevation of 270. Design of the intakes, carried out in the 60ths (Fig. 1.a) contemplates two 9.6 width 23 m height streamlined rectangular water passages, provided with 3 gate slots connected to the atmosphere to allow placing of maintenance stop-logs and, service and emergency intake gates. The intake structure is connected to a 10.5 m diameter penstock by means of a convergent hydrodynamic curve of 29 m radius. Intake roof and invert intake elevations are set to EI 236, 5.9 and 217 m, respectively. During the last 3 years, very low inflow to Guri reservoir combined with required over-exploitation of the dam planned firm energy led to unusual pool levels, and there is some possibility than in 2004 dry season, units may operate below critical design

pool elevation, EI 240. This situation created some warning on EDELCA operators due to the potential occurrence of air being taken by the intakes with undesirable performance on the turbine operation. Air entrainment prediction inside intakes is complex due to many factors involved, due to its unstable nature and, to its relation with flow parameters, intake geometry and, approach conditions of a particular project. To predict the Guri intakes operation at very low heads and particularly to evaluate the air entrainment potential, a non-distorted 1:30 Scale Physical Model was built (Figs. 1.a and 1.b) in transparent plexiglass, consisting on one full geometry intake, provided with the trashrack (Fig. 1.c) and, the 3 slots to place the stop-log, service and emergency gates. Guri reservoir was reproduced in the model by a constant elevation tank sufficiently large to allow symmetric laboratory approach conditions. The investigations were divided into two parts: the first part aimed to describing the phenomenon of air bubbles and air dragged mechanism inside the intake and, the second part documents the tendency of vortex formation in the reservoir.

2 MODEL SIMILARY

2.1 *Dimensional analysis*

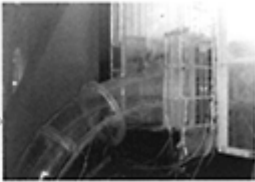
For engineering purposes, vortex formation, and air entrainment and drag into the intake depends on fluid properties, flow characteristics, approach and, intake geometry. To allow for the phenomenon investigation and report of results of any flow system to be independent of the unit system, it is convenient to use classical dimensional analysis, in terms of the important non-dimensional parameters.

The functional expression (1) showing the non-dimensional parameters describing the phenomenon under study is (Fig. 1.a):

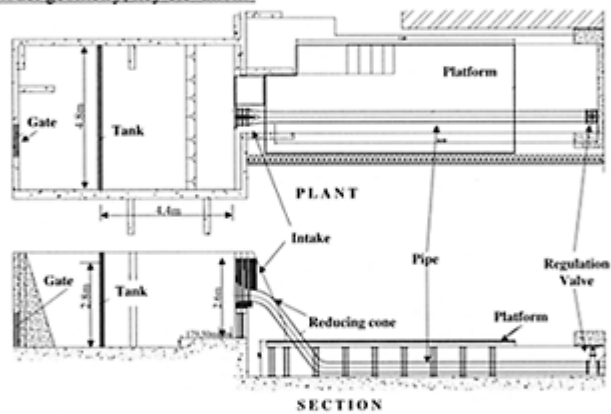
$$f\left(\frac{h}{D}, \frac{V \cdot D}{\nu}, V \cdot \sqrt{\frac{\rho \cdot D}{\sigma}}, \frac{V}{\sqrt{g \cdot D}}, \frac{\Gamma}{D \cdot V}\right) = f(S, Re, We, Fr, N\tau) = 0 \quad (1)$$

where S=Submergence; Re=Reynolds Number; We=Weber Number; Fr=Froude Number; N τ =Circulation Number; D=Penstock Diameter; V=Flow Velocity; Γ =Flow circulation; σ =Flow Surface Tension; ν =Kinematic Fluid Viscosity; g=Acceleration Due to Gravity.

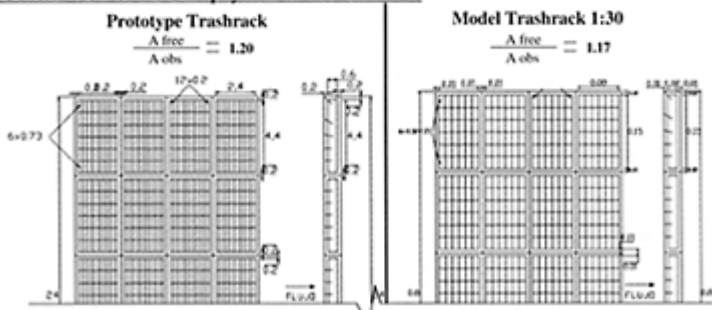
Functional equation (1) suggested that being the two systems similar geometrically wise and with similar approach flow patterns, results from the model system will depend on gravitational, viscous, circulation and, surface tension forces.



a) Intake model geometry, key elevations



b) General view of the Guri physical model scale 1:30



c) Trashrack arrangement-prototype and model

Figure 1. Physical Model of Guri intake Scale 1:30.

2.2 Geometry comparison

In the Scale 1:30 physical model, every geometric detail of the prototype was reproduced, in order to keep similarity of the solid conveyance boundaries to guarantee adequate visual observations and its extrapolation to prototype performance. However, trashrack prototype dimensions of the elements thickness were not practical to be reproduced in the model and a criteria of the obstructed area of the prototype trashrack was adopted resulting in a distortion factor ($\Delta=2$), or in a factor of free area for the intake flow of 55% and, 54% for prototype and model, respectively which was considered satisfactory for model reproduction in that respect (Fig. 1.c).

The expression (2) shows the distortion relationship used to maintain reciprocity of the trashracks flow areas between model and prototype:

$$\frac{A_m}{A_p} = X_r \cdot L_r = \Delta \cdot L_r^2 \quad (2)$$

where A_m =Model Area; A_p =Prototype Area; X_r =Horizontal Scale; L_r =Vertical Scale; Δ =Distortion.

2.3 Viscous and surface tension effects

Physical modeling of vortex formation and air dragged into intakes has been controversial through decades and up to present there is not a standard methodology to approach this phenomenon that include consideration of viscous, gravity, surface tension and flow turbulence, as the most important ones. To reproduce all these forces simultaneously in the model as they are present in the prototype will result in satisfying equation (1) for both physical systems which is conflictive (Ettema, 2000).

In laboratory practice, criteria for similarity of centrifugal forces are used and the remaining forces acting on the phenomenon are accounted for by approximated methods that may not reflect rigorously the flow behavior. As a result of this approximation “scale effects”—term that normally justifies deviations from model to prototype performance—are brought about, and practical expertise suggest reducing them as it is possible either by building a model as large as economically feasible in a given laboratory installations and/or, by operating the model with flow conditions resembling more like prototype behavior. In this particular case the phenomenon is directly linked to the gravitational force, this criterion suggests using Froude similarity. However, viscous, surface tension, and turbulence level of the flow are considered as scale effects. Model scale is then selected so working conditions of the model flow are acceptable, and model flow conditions are controlled to reduce remaining scale effects. Vortex originates by fluid rotation and whether they appear and their intensity will be related to the rotational streamlines patterns that occurred in the intake neighborhood. For this reason many investigations on model vortex formation have demonstrated that scale effects are negligible when Reynolds (Re) and Weber Numbers (We) are sufficiently high. Daggett & Keulegan (1974), demonstrated that viscous effects are negligible when $Re > 3.2 \cdot 10^4$ being in Guri Physical Model Scale 1:30, $Re = 4.4 \cdot 10^5$ and $Re = 2.2 \cdot 10^5$ for flows of 600

and $300 \text{ m}^3/\text{s}$, respectively, the latter suggest that viscous effects are suppressed if the model is operated by using the Froude law.

With regard to surface tension, Jain (1978), who used fluids of different surface tension demonstrated that vortex and air entrainment in model studies are not affected for $We > 11.0$, this condition is satisfied by the Guri 1:30 Physical Model which was operated at $43.0 < We < 86.0$.

2.4 Exaggeration of model discharge

A technique used by some authors to account for scale effects is to increase the operating discharge during the model tests. Model discharges are increased and so is flow velocity, then model operation in terms of hydraulic total roughness are plotted against Re until the first becomes independent of Re (Semenkov, 2003). However, a difficulty arises when applying this technique since model flow patterns and the Circulation Number change as a result of the increasing discharge. For this reason different authors based on previous investigations, Denny & Young (1957), consider this method conservative and should be used with reserve. In Guri 1:30 Scale Model discharge was increased to exaggerate the flow patterns thus enhancing flow conditions for the vortex to be formed in the reservoir, up to $2.3Q$, being Q the project discharge.

3 MODEL TEST CONDITIONS

Tests were executed in two stages: first group of tests were done inside the intake and, a second stage tests were done in the reservoir region. First group of tests included examination of air bubble formation and vortex development mechanisms inside the intake. Second group of tests include reservoir vortex formation in the free reservoir elevation and, their interaction with the trashrack. Project conditions of the tests were as follows: (1) Guri reservoir levels 240.0, 237.0, 235.0 and 232.0 m, (2) Model flows between 300 and $1400 \text{ m}^3/\text{s}$ which include normal and exaggerated Q , (3) With trashracks, and without stop-logs or gates placed on the slots.

4 TESTS RESULTS

4.1 Velocity distributions

Figure 2 shows a sample of the model flow velocity distribution along the left intake bay, as measured upstream of the intake for reservoir $El=240.0 \text{ m}$. This distribution is rather uniform when the intake is completely submerged, ($El > 236.7 \text{ m}$). However, when the intake is not submerged, a series of stationary waves on the free surface appear as the flow upper streamlines hit the intake upper boundary, these waves may contribute to inhibit vortex formation on the free surface. When the intake is submerged ($El=240.0 \text{ m}$ and, with exaggerated discharge $Q > 1000 \text{ m}^3/\text{s}$) local velocity

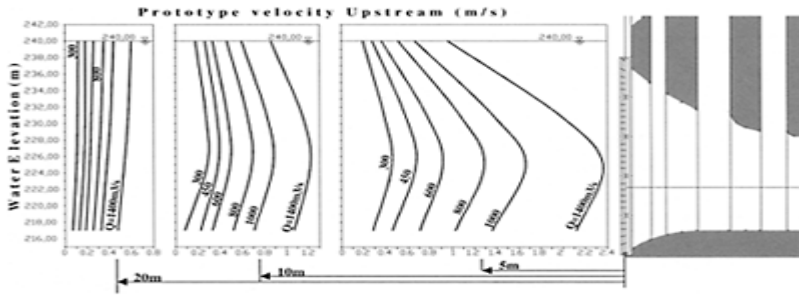


Figure 2. Velocity distribution upstream of intake.

pulsations with deviations-up to the 10%-at the point of the maximum velocities—(Fig. 2) were recorded, this behavior suggests a trend for vortex formation due to higher velocity concentrations near the intakes.

4.2 Vortex formation and air dragged

Figure 3 shows, for El=240.0 m, that the average type of vortex (Knauss, 1987) for $Q < 600 \text{ m}^3/\text{s}$ ($Fr < 0.7$) is less than 2. Moreover, the maximum frequency of occurrence of vortex formation is 32% (5 minutes observation time), which is estimated to be a low frequency of vortex presence and, it may not represent a hazard to the turbine. However, when Q is exaggerated, $Q=1.7Q$, vortex of the Types 3, 4 and 5 start to show on the free surface, $Fr > 1.1$. In the prototype (April 2003, for Guri reservoir elevation of 244.56 m.), it was observed vortex formation, Types 1 and 2 ($h/D=2.1$, Figs. 4–8). This limited 2003 and 1985 prototype data and its comparison with similar model tests

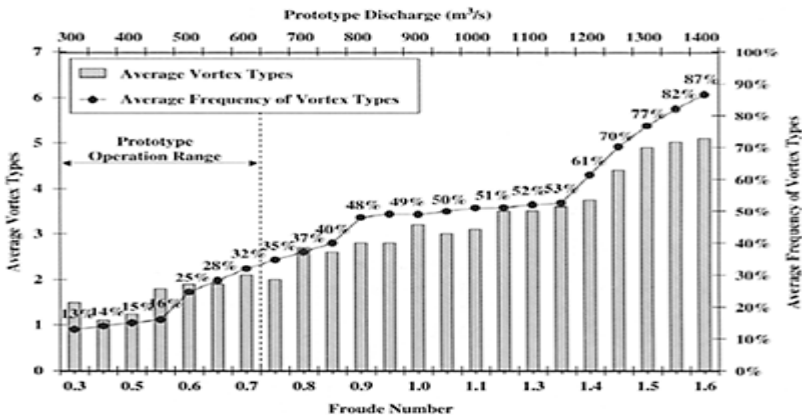


Figure 3. Occurrence and frequency of types of vortex, El 240.0.

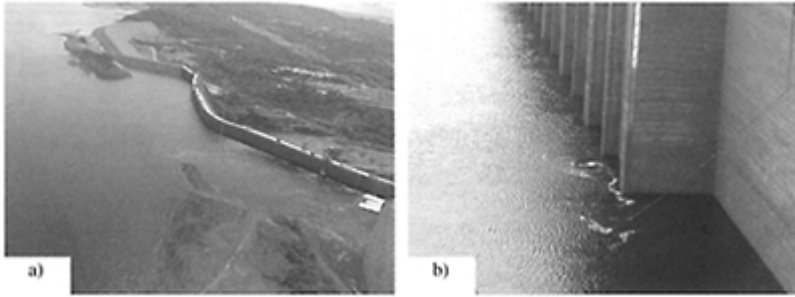


Figure 4. Vortex formation, Type 2 in the prototype, April 2003.

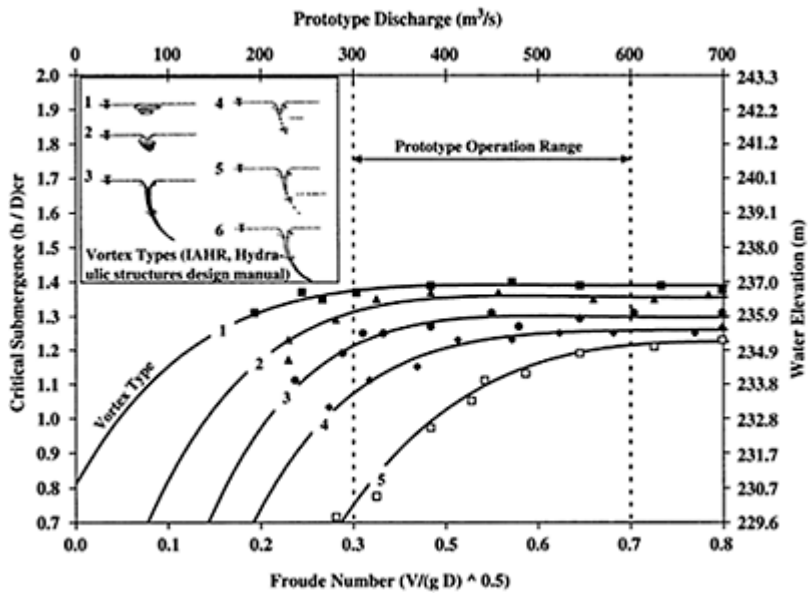


Figure 5. Vortex formation in the slots.

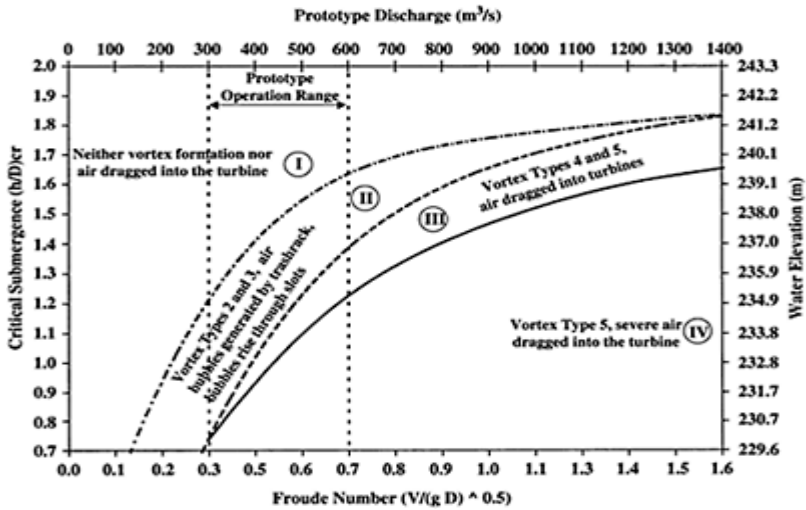


Figure 6. Occurrence of vortex at slots, air bubble formation and drag to the turbine.

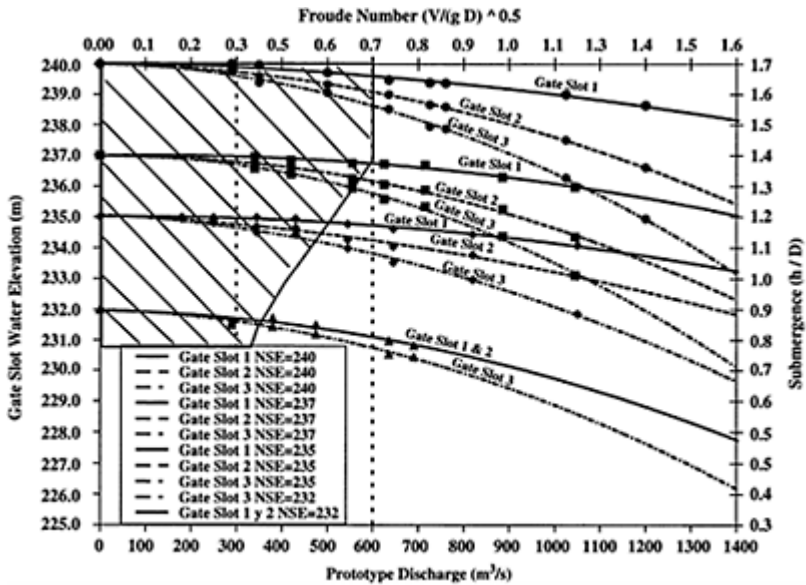


Figure 7. Operation range of the turbines, water levels at the slots and reservoir elevations.

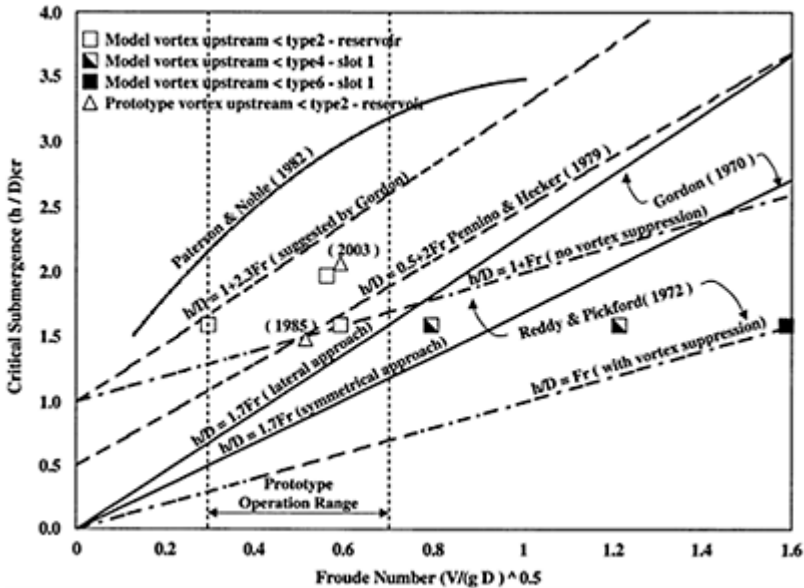


Figure 8. Occurrence of vortex formation—Guri model and prototype.

(Fig. 8) permits verifying that the model is capable of reproducing the prototype behavior even without need to exaggerate the model Q , meaning that the model fulfills flow pattern similarity in this respect. Inside the intake, tests indicate that vortex are not formed by lack of submergence but for flow separation from the slots for $h/D < 1.4$ (Fig. 5). The vortex intensity becomes important for $h/D < 1.25$ when vortex Type 4 and 5 appear. These vortices are capable of generating air bubbles that are dragged downstream by the flow (Fig. 6).

The dashed region (Fig. 7) shows the operation range of the turbine to avoid air bubble formation below critical submergence elevation (El 240 m). Some points of the model and prototype observations from Guri Intakes reported herein are plotted together with curves advanced by other authors (Fig. 8). This data include conditions of normal Q (Vortex Type 1 and 2) and exaggerated Q , which include vortex Types 3, 4, and 5 (Knauss, 1987).

5 CONCLUSIONS

In this investigation viscous and surface tension effects were considered, the test results together with the prototype limited data permits concluding that the Model Scale 1:30 is sufficiently large to allow for scale effects due to the relatively low Re and We Numbers to be higher than minimum values reported in the literature, thus these effects can be reported as negligible. Boundary geometry along with slots and sheared flows resulting from flow interaction with these features are well represented and its correct model

reproduction resulted of prime importance in vortex generation, air bubbles formation and air drag from the slots to lower reaches of the penstock and eventually to the unit. Free area for the flow passing the trashrack was respected by the model construction, with a criteria that looks acceptable for correct full scale reproduction.

The technique of increasing the flow discharge proved useful in enhancing the vortex formation potential of the flow and its interaction with the boundaries, vortex intensity and frequency, air bubbles formation and eventual drag into the penstock are promoted as Q is increased.

Velocities profiles were developed in the model and identification of flow local velocities deviations up to 10% were recorded. These pulsations were unsteady and its occurrence are closed associated to vortex formation.

Based on this investigation, an operation range for the turbines is proposed. However, the amount of air dragged at the slots as seen in the model (Vortex Types 4 and 5), bubble size and air volume associated, has to be further investigated since marginal volumes of air entrained at atmospheric pressure, may not be necessarily detrimental for turbine operation.

REFERENCES

- Ettema, R. 2000, "Hydraulic Modeling: Concepts and Practice", Sponsored by Environmental and Water Resources Institute of the American Society of Civil Engineers.
- Semenkov, V. 2003, "Report About Hydraulic Department".
- Gordon, J.L. 1970, "Vortices at Intakes", Water Power.
- Knauss, J. 1987, "Swirling Flow Problems at Intakes", Hydraulic Structures Design Manual, IAHR 4.
- Daggett, L.L. & Keulegan, G.H. 1974, "Similitude in free-surface vortex formations", ASCE, Journal of Hydraulic Engineering, 100, HY11.
- Jain, A.K., Ranga Raju, K.G. & Garde, R.J. 1978, "Vortex Formation at Vertical pipe Intakes", ASCE, Journal of Hydraulic Engineering, 104, HY10.
- Denny, D.E & Young, G.H.J. 1957, "The Prevention of Vortices and Swirling at Intakes", IAHR Congress Lissabon, Paper C1

3-D CFD modeling-investigation of potential vortex formation at the intakes of Caruachi Powerhouse

A.Marcano

*C.V.G.EDELCA Dept. of Hydraulics, San Felix, Estado Bolívar,
Venezuela*

L.Rojas-Solórzano

*Associate Professor, Dept. of Energy Conversion, Universidad Simón
Bolívar, Venezuela*

M.Reyes

*Associate Professor, Dept. of Thermodynamics, Universidad Simón
Bolívar, Venezuela*

J.Marín

*Graduate Student, Dept. of Mechanical Engineering, Universidad Simón
Bolívar, Venezuela*

Hydraulics of Dams and River Structures—Yazdandoost & Attari (eds)

© 2004 Taylor & Francis Group, London, ISBN 90 5809 632 7

ABSTRACT: In this paper, the 3-D CFD simulation of the free-surface flow approaching the intakes of Caruachi Powerhouse is presented. The aim of the investigation is to determine whether or not vortex structures are likely to appear from the water surface through the intakes, as the result of the presence of cofferdams placed few meters upstream of the intakes. The presence of cofferdams was a note of concern with regard to the effects they might have on the turbine intakes once the hydroelectric central starts operating. In all the considered conditions, results did not show neither strong surface vortices in the proximities of the Powerhouse intakes, nor air entrainment-entrapment towards the intakes, which reflects the safe operation of the turbines in the presence of the cofferdams. The latter added in decision taking on leaving the cofferdams submerged instead of removing them, which resulted in cost savings for the project.

1 CARUACHI PROJECT AND CARONI RIVER DIVERSION

The Caruachi project located on the Caroni River at Southeastern Venezuela will add 2.196 MW up to the national electricity market. The power plant, equipped with 12 Kaplan units and a 30.000 m³/s capacity Spillway, is located 59 Km downstream of Guri Dam and 25 Km upstream of Macagua Dam, and conforms together with Tocoma Dam, the Lower Caroni Hydroelectric Development. During the first stage of construction of Caruachi Project, a 3 Km-long cofferdam, named Cofferdam "A" and Cofferdam "B", hereafter, made of rock fill and concrete, respectively were built few meters upstream the turbine intakes to allow construction of the main structures in the dry (i.e., Spillway, Powerhouse, intakes, gravity dams, etc.). The river was diverted from its natural path, within a channel 350 meters width, in its left bank, to allow a maximum flowrate of 13.000 m³/s, regulated at Guri reservoir while Caruachi Project construction was ongoing. During the second stage of construction, the river was diverted through 18, 5.5×9 m bottom sluices left in the Spillway lower body, to allow the left embankment dam to be erected. Following the sluice closure on December, 2002 the reservoir was filled and, two generating units have been commissioned since April 2003. Construction schedule contemplates commercial operation of the last unit in early 2006.

Normally, cofferdams are built as temporary structures and they should be removed at least partially, after they fulfilled their purpose of keeping construction areas in the dry. However, removing cofferdams built on large rivers is complex and might result uneconomical. For this reason, due consideration should be given to either removing or leaving them submerged, provided hydraulic flow behavior is acceptable i.e., avoiding additional energy losses and/or malfunctioning of the operating units because of undesirable swirling flow at intakes, vortex formation, and flow separation. At Caruachi Project the presence of Cofferdams "A" and "B" was a note of concern regarding to the effects they might have on the turbine intakes once the hydroelectric central starts operation. In this paper, results of a 3 Dimensional CFD numerical model that was set up to investigate potential vortex formation at the intakes of Caruachi units, due to the presence of the Cofferdams "A" and "B", are presented.

2 CFD ANALYSIS OF THE PROBLEM

The detailed calculation of the fluid motion within a complex geometry is a very difficult task from the analytical point of view, since the simultaneous solution of momentum, continuity and sometimes energy governing equations is required under boundary and initial conditions which many times are as complex as the geometry itself. During the last years it has been demonstrated that many complex problems may be satisfactorily solved through finite difference, finite element, finite control volume and other discretization techniques.

CFD is a computational technique for the numerical solution of the time and spatially discrete fluid mechanics governing equations. In this work, CFX4.3TM is used as the base open CFD code, which is designed and validated for computing the flow field by using the finite control volume technique.

2.1 Numerical issues

The numerical method works by dividing the physical region into a large number of control volumes (AEA Technology, 1997). The set of differential governing equations are written as algebraic equations within each of those control volumes, after applying finite differences to relate the pressure, velocity and other variables (e.g., volumetric fraction) with values in neighbor volumes. The solution to the problem consists in the solution of a non-linear system of algebraic equations.

The control volume method divides the domain into a large number of control volumes with a central node and, in general, each control volume is connected to neighboring control volumes.

All the terms in the governing equations, except the convective term, are spatially discretized using second order central differences. A hybrid scheme is used to discretize the convective term. The non-linear nature of the governing equations leads to an iterative solution procedure of the system of equations. The pressure term is dealt as a source term in the momentum equation and the SIMPLEC (Patankar, 1983) algorithm is used to couple the mass and momentum equations. This semi-implicit algorithm solves the continuity equation through a pressure correction term for the velocity components. Further details are presented in the next sections.

2.2 Free surface air-water modeling

To model the air-water segregated flow, the mass conservation of each phase is solved as one of the set of governing equations, while the momentum equation (i.e., Navier-Stokes equation, since the fluids are Newtonian) for each phase are added up to get rid of the interphase momentum transfer. There is a closure equation for the volume fraction, which states that both phases volume fraction must add up to one at every fluid location.

Despite of the Navier-Stokes and continuity equations are the governing equations, even for turbulent regime, the size of the required mesh and time stepping would make it prohibitive to solve the smallest turbulence time- and length-scales in today's computers. Therefore, the turbulence is modeled using the Reynolds Averaged Navier-Stokes (RANS) and mass equations and the two-equation model based on the turbulent viscosity and the turbulent kinetic energy " k " and turbulent dissipation " ϵ ", named the k - ϵ model with wall functions (AEA Technology, 1997). The k - ϵ model has proven effectiveness in solving industrial problems.

The multiphase model considers the possibility of air-water mixture, at a larger scale than molecular, while still at smaller scale than what being solved for. That is, each phase is treated as an inter-penetrating continuum, which implies that each phase may be present in every control volume and, the phase volume fraction is equal to the fraction of volume occupied. Therefore, the problem is solved in an Eulerian-Eulerian frame of reference for the two phases, even though the intrinsic volumetric forces (e.g., gravity) will determine, through mass conservation, the solely existence, co-existence or non-existence of a single phase.

Both phases are considered to be incompressible and isothermal.

Therefore, the governing equations are presented, indicating with the sub-index each phase, as follows:

Mass Conservation:

$$\nabla \cdot (r_\alpha \rho_\alpha U_\alpha) = 0 \quad (1)$$

Linear Momentum:

$$\frac{\partial}{\partial t}(\rho U) + \nabla \cdot (\rho U \otimes U - \mu(\nabla U + (\nabla U)^T)) = (B - \nabla p) \quad (2)$$

In eqn. (2), the left-hand-side terms represent the transport of convective and diffusive momentum.

The right-hand-side term represents the body and pressure forces. Furthermore, in this equation:

$$U_\alpha = U_\beta = U \quad (3)$$

$$P_\alpha = P_\beta = P \quad (4)$$

$$\rho = \sum_{\alpha=1}^2 r_\alpha \rho_\alpha \quad (5)$$

$$\mu = \sum_{\alpha=1}^{Np} r_\alpha \mu_\alpha \quad (6)$$

And the algebraic restriction for the addition of all volume fractions at each control volume:

$$\sum_{\alpha=1}^2 r_\alpha = 1 \quad (7)$$

The multiphase model here proposed has proven to give a good approximation (i.e., CRS4 Technical Report 99/20, 1999) when the gravity force trends to stratify the phases as in free surface flows. In this case, the volume fractions are equal to 1 or 0 everywhere, except at the interphase, which makes it reasonable to have a unique velocity field for both phases.

2.3 Interphase refinement algorithm

During the simulation convergence iterative process, the water and air, initially mixed, tend to segregate due to their differences in density, creating homogeneous volume fraction fields for each phase, equal to 0 or to 1, such that it suddenly changes at the two-fluid interphase. To avoid a blurry interphase caused by numerical diffusion of the volumetric fraction equations (mass conservation for each phase), a refinement algorithm is used. This surface contouring algorithm requires a local fine mesh and therefore a proficient user-analyst.

In detail, the algorithm adjusts the volumetric fraction of the fluids at the interphase for each iteration. The interphase is defined as the surface in which volume fraction for both fluids, r_1 and r_2 , are equal to 0.5 each. First, the program identifies the control volumes at the interphase, by checking whether or not $r_1=0.5$ for certain control volume changes sign with respect to its neighbors. Then, the program identifies the fluid on the wrong side of the interphase and translates it to the right side, ensuring the volume conservation. During this procedure, all the interphase volumes are fixed.

2.4 Turbulent model

The two-equation model used in these simulations is the standard k - ϵ with wall functions for dampening the turbulent viscosity near the walls. The equations of the model are:

Transport of Turbulent Kinetic Energy k :

$$\nabla \cdot \left(r_\alpha \left(\rho_\alpha U_\alpha k_\alpha - \left(\mu + \frac{\mu_{T\alpha}}{\sigma_k} \right) \nabla k_\alpha \right) \right) = r_\alpha S_{k\alpha} \quad (8)$$

Transport of the Dissipation Rate of Turbulent Kinetic Energy ϵ :

$$\nabla \cdot \left(r_\alpha \left(\rho_\alpha U_\alpha \epsilon_\alpha - \left(\mu + \frac{\mu_{T\alpha}}{\sigma_\epsilon} \right) \nabla \epsilon_\alpha \right) \right) = r_\alpha S_{\epsilon\alpha} \quad (9)$$

where the respective source terms are given by:

$$S_{k\alpha} = P_\alpha + G_\alpha - \rho_\alpha \epsilon_\alpha \quad (10)$$

$$S_{\epsilon\alpha} = \frac{\epsilon_\alpha}{k_\alpha} (C_{1\epsilon} (P_\alpha + C_{3\epsilon} \max(G_\alpha, 0)) - C_{2\epsilon} \rho_\alpha \epsilon_\alpha) \quad (11)$$

P and G are the production of k , by shear and body forces, respectively (AEA Technology, 1997).

The turbulent viscosity is calculated through the Prandtl-Kolmogorov relationship:

$$\mu_{T\alpha} = C_\mu \rho_\alpha \frac{k_\alpha^2}{\epsilon_\alpha} \quad (12)$$

and the empirical coefficients (taken for free turbulence cases) given by: $C_\mu=0.09$; $C_1=1.44$; $C_2=1.92$; $C_3=0.0$; $C_k=0.4187$; $\sigma_k=0.7179$; $\sigma_\epsilon=1.6$.

3 DISCRETIZATION OF THE GOVERNING EQUATIONS

The differential expressions of the several terms in the governing equations are integrated within each control volume, and the discrete treatment of the derivatives is performed by using finite differences, otherwise known as the finite volume method, with all variables defined at the center of the control volumes in the domain. The resulting discrete set of

equations reflects the connection of the volume center and its neighbor volume centers. All equations, except by the mass conservation have a similar general layout:

$$\frac{\partial(\rho\phi)}{\partial t} + \nabla \cdot (\rho U \phi) - \nabla \cdot (\Gamma \nabla \phi) = S \quad (13)$$

Where, Γ is the effective diffusivity (laminar+turbulent) for the transport of the intensive property given by (velocity or specific energy, for instance, for the momentum and energy equations, respectively). When eqn. (13) is integrated within the control volume, it leads to:

$$\int \frac{\partial(\rho\phi)}{\partial t} dV + \int \rho \phi U \cdot n dA - \int \Gamma \nabla \phi \cdot n dA = \int S dV \quad (14)$$

All terms, in all equations are discretized using second order central differences, but the advective term and its coefficients which are determined using the Rie-Chow algorithm (see AEA Technology, 1997). In particular, the advective term is treated using the Hybrid (Upwind/Central differences) method, named HDS, which is robust and accurate.

4 NUMERICAL SIMULATIONS

After developing a preliminary 2-D and 3-D model to adjust the appropriate mesh refinement, boundary and initial conditions in an economical time-frame, the final 3-D model considers the most important details of the civil structures, since they are a very important part in the study. The final mesh was chosen when the difference in global mass error, between coarser and finer meshes, lied under 1%, always paying major attention to cofferdams and free level mesh quality.

Details of the actual structure are shown in Figs 1 and 2. The main dam is integrated to the Powerhouse and the dam is 55 m height and 360 m long. There are 12 Kaplan turbo-generator units mounted onto a structure 60 m long. The Spillway is 178.16 m long and overflow section is at 70.55 m.a.s.l. The CFRD left Dam is 900 m long and 50 m height, while the left embankment dam is 4.200 m long and 45 m height, both connected to the main concrete dam structure.

Once the project is finished, normal pool elevation will be 91.25 m.a.s.l. After studying photographs, bathymetric surveys drawings of the river bed and the actual prototype site, a final 3-D model geometry was developed resulting in a mesh with over 380.000 elements (Figs 3–5).

The computational equipment used for the simulations (both 2-D and 3-D) was an Intel Pentium IV PC/1.7 GHz CPU clock speed/400 MHz bus speed/512 MB Ram/64 MB SDRam video memory, with the following characteristic convergence performance:

- (a) 2-D introductory case: 4–6 hours per case
- (b) 3-D case: Preliminary/12–15 hours per case; Final/24–36 hours per case

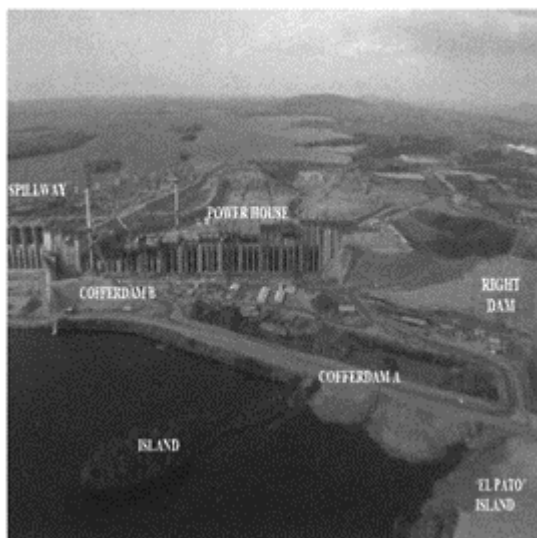


Figure 1. Aerial photograph of Caruachi Powerhouse and Civil Works.



Figure 2. Aerial photograph of Caruachi Dam (Abutment details).

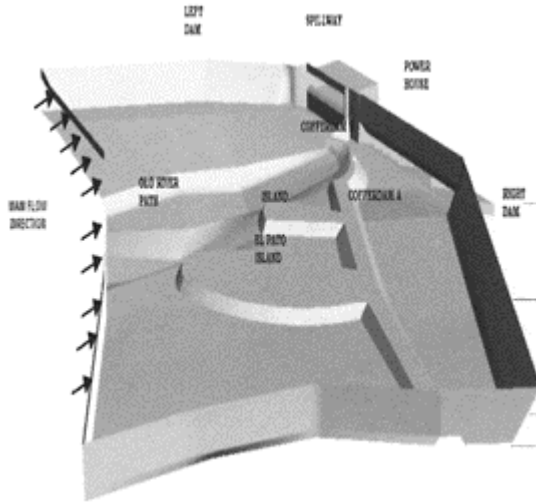


Figure 3. 3-D Geometric model.

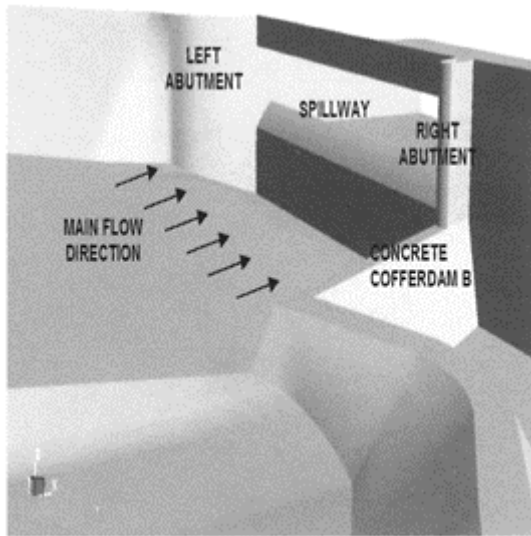


Figure 4. Abutment details in 3-D model.

5 BOUNDARY AND INITIAL CONDITIONS

The simulations consider the river upstream level under different Spillway and Powerhouse operating conditions. The level of the river is preset via a hydrostatic

pressure gradient at the entrance, while an amount of water flow is withdrawn through the machines and the Spillway via a uniform velocity profile. The roof of the geometry was declared open to the free flow of air (Fig. 6). The initial condition corresponds to a homogeneous mixture of water-air at rest within the whole domain, and then perturbed by the boundary conditions at $t=0+$.

6 SIMULATED CASES

During the simulations, six flow conditions/cases were explored: (I) Maximum infrequent riverlevel (92.40 m.a.s.l), flow of $5000 \text{ m}^3/\text{s}$ through all Powerhouse units, flow of $25000 \text{ m}^3/\text{s}$ through the Spillway; (II) Maximum infrequent river-level (92.40 m.a.s.l), flow of $5000 \text{ m}^3/\text{s}$ through all Powerhouse units, flow of $25000 \text{ m}^3/\text{s}$ through the Spillway, but no cofferdams present, for comparison purposes with the most critical condition resulted from the cofferdamexisting simulation; (III) Minimum infrequent river-level (88.55 m.a.s.l), flow of $550 \text{ m}^3/\text{s}$ only through Unit 12, flow of $4450 \text{ m}^3/\text{s}$ through the Spillway; (IV) Minimum infrequent river-level (88.55 m.a.s.l), flow of $550 \text{ m}^3/\text{s}$ only through Unit 9, flow of $4450 \text{ m}^3/\text{s}$ through the spillway; (V) Maximum normal river-level (91.25 m.a.s.l), flow of $5000 \text{ m}^3/\text{s}$ through all Powerhouse units, no flow through the Spillway; (VI) Maximum normal river-level (90.25 m.a.s.l), flow of $5000 \text{ m}^3/\text{s}$ through all Powerhouse units, no flow through the Spillway. For space limitations in this paper, only cases I and II will be discussed (see more in Rojas-Solórzano, et al., 2002). Further details of the computational field space are shown in Fig. 7.

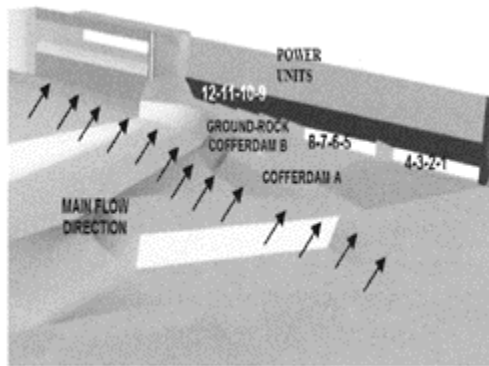


Figure 5. Powerhouse detail in 3-D model.

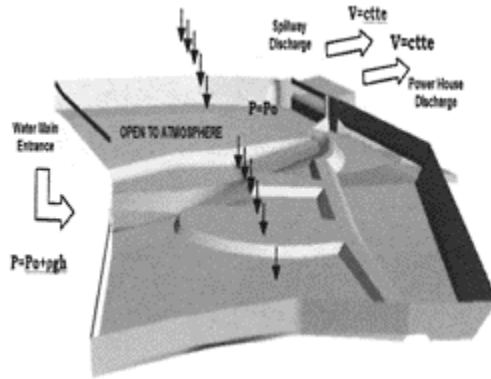


Figure 6. Boundary conditions.

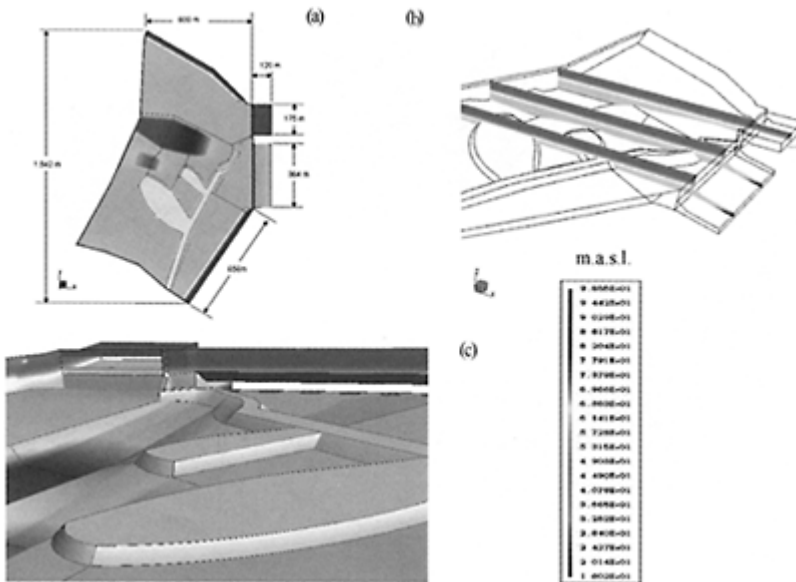


Figure 7. Surface details with levels of the computational model with cofferdams (a) Upper view with approximate dimensions, (b) Side view, (c) Perspective view of Powerhouse and Spillway.

7 EFFECTS CAUSED BY COFFERDAMS “A” AND “B”

Figures 8–10 depict a comparison between conditions with and without Cofferdams “A” and “B”, named cases I and II, respectively. Both cases are shown for the maximum infrequent river level of 92.4 m.a.s.l. and flowrate of $5000\text{m}^3/\text{s}$ through the entire Powerhouse and $25.000\text{ m}^3/\text{s}$ through the Spillway. Fig. 11 refers to case III, for lower level and different conditions.

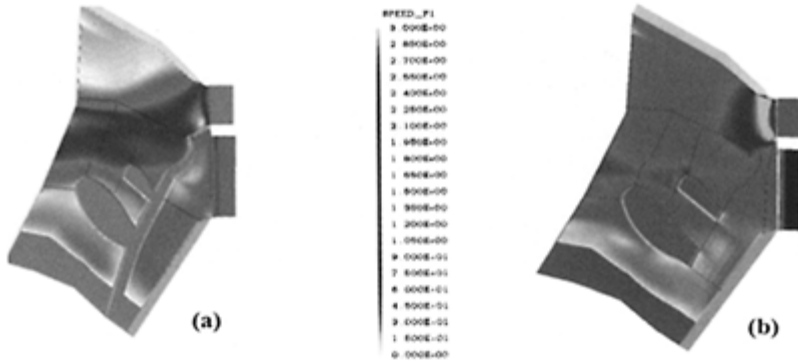


Figure 8. Velocity field (speed) contour plot at 53 m.a.s.l.: (a) Case I, (b) Case II.

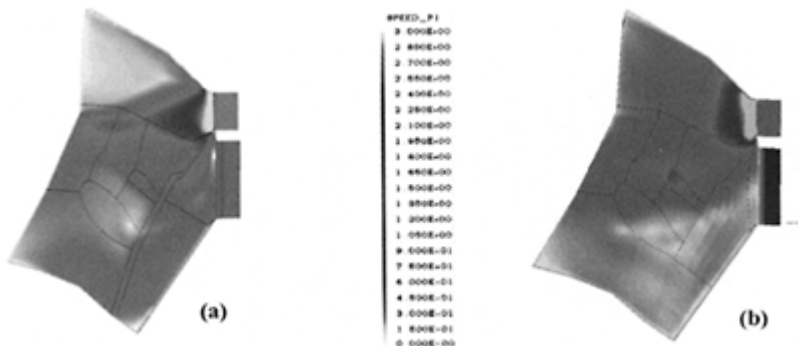


Figure 9. Velocity field (speed) contour plot at 89.4 m.a.s.l.: (a) Case I, (b) Case II.

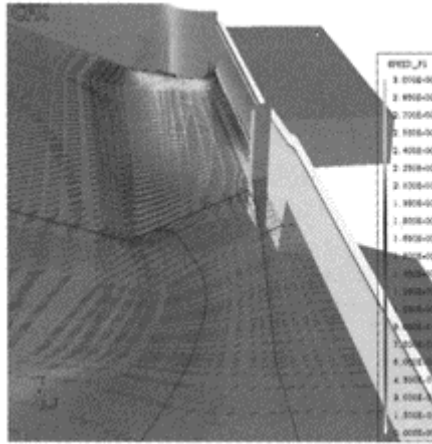


Figure 10. Case II (with cofferdams):
velocity field and speed at 54 m.a.s.l.

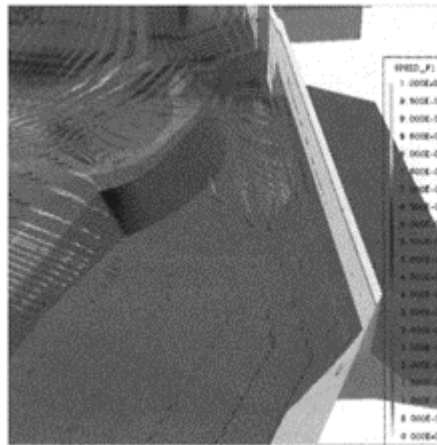


Figure 11. Caso III (with cofferdams):
velocity field and speed at 88.55
m.a.s.l. (free surface).

Fig. 8 shows a velocity contour plot at 40 meters under the free surface (i.e., 7 meters under the cofferdam top for case I). It is clearly depicted that the presence of the cofferdams does not affect appreciably the uniform distribution of flow approaching the Powerhouse and Spillway. Nevertheless, the cofferdam (case II) favors the re-orientation of a large volume of waterflow through the original river path by the left side of the islands. Figure 9, at 3 meters under the free surface, shows no noticeable differences between cases I and II, at the dam vicinity. However it is appreciated the uneven flow

contribution coming from the left side and right side. The cofferdam slows down the waterflow coming along the left dam, while impulses the waterflow running along the right dam, either in the forward or backward direction.

Fig. 10 shows the well-behaved flow field above the cofferdam at 54 m.a.s.l. It is appreciated the larger velocities at the Spillway entrance, and a uniform velocity approaching the Powerhouse intakes, with no signs of vortex formation.

Fig. 11 depicts the velocity field at the free surface, nearby the Powerhouse for case III (i.e., 88.55 m.a.s.l. river level, with Unit 12 in stand-alone operation and 4450 m³/s through the Spillway). This was the only case in which vortices (2 of them), though weak, were observed. At lower depths (not shown in this paper), no signs of vortices were observed, indicating that these vortices responded to the natural superficial flow re-orientation of the large volume of water impacting the dam.

8 CONCLUDING REMARKS

This paper presents the numerical simulation of the flow approaching the Caruachi Dam when Cofferdams “A” and “B” are present. Results lead to the following conclusions:

No surface vortices with air entrainment were observed in the vicinity of the Powerhouse when the cofferdams “A” and “B” were present. Far under the free surface, it is observed how the cofferdams favor the waterflow through the original river path, while near the free surface favor the re-accommodation of the waterflow with a larger presence along the right dam, but without major effects on the proximity to the Powerhouse intakes. Therefore, for the supposed flow conditions, air entrainment towards the power units is discarded, i.e., cofferdams “A” and “B” are not likely to affect significantly the operation of power units, under the conditions here considered.

REFERENCES

- AEA Technology Engineering Software, Inc., CFX-4.3, “Solver Manual”, 1997.
- Casey M. and Wintergerste, T. 2000, “Special Interest Group on Quality and Trust in Industrial CFD: Best Practice Guidelines”, European Research Community on Flow, Turbulence and Combustion (ERCOFTAC), Version 1.0, January 2000.
- Consulta Internet: <http://www.aeat.com/>.
- Consulta Internet: <http://www.cfdtech.com/>.
- CRS4 Technical Report 99/20, “Simulation of the Free Surface Flow inside a Rotating Cylinder”, <http://www.crs4.it/~cfdea/LMfreesurf/rotcyl.html>, 1999.
- Hubred G., Mason A., Parks S. and Petty Ch., “Dispersed Phase Separations: Can CFD Help?.” ETCE 2000/OMAE2000 Conference. New Orleans, LA. Feb. 2000.
- Patankar, S. and Spalding, D., “A Calculation Procedure for Heat, Mass and Momentum Transfer in Three Dimensional Parabolic Flows”, Int. Journal of Heat and Mass Transfer, 15 pp, 1787, 1972.
- Patankar, S., “Numerical Heat Transfer and Fluid Flow”, Ed. Hemisphere, New York (1983).
- Rhie, C. and Chow, W., “Numerical Study of the Turbulent Flow Past an Airfoil with Trailing Edge Separation”, AIAA J1,21 pp, 1527–1532, 1983.

- Rojas-Solórzano, L., Reyes, M., Oberto, L. y López D., “Simulación Numérica del Efecto de las Ataguías A y B sobre las Condiciones de Entrada a la Casa de Máquinas de la Represa Caruachi, Reporte CEMFAFUNINDES/EDELCA, Contrato GPOF-1249.2/01, 2001–2002.
- Streeter V. y Wylie B., “Mecánica de Fluidos”. Sexta Edición. 1979.
- Van Doormal, J. and Raithby, G., “Enhancements of the SIMPLE Method for Predicting Incompressible Fluid Flows”, Numerical Heat Transfer, 7 pp, 147–163, 1984.
- White, F.M., “Viscous Fluid Flow”, 1989.

Numerical unsteady flow model simulation during the sluice closure of Caruachi Dam

A.Marcano, C.Castro, I.Mendez & E.Martinez
*C.V.G. EDELCA, Hydraulics Department, Basic Engineering Division,
Macagua, Edo. Bolívar, Venezuela*

Hydraulics of Dams and River Structures—Yazdandoost & Attari (eds)

© 2004 Taylor & Francis Group, London, ISBN 90 5809 632 7

ABSTRACT: Caruachi Hydroelectric Project conforms together with Guri, Tocoma and, Macagua the Lower Caroni Hydroelectric Development. Second Stage of River Diversion at Caruachi included diverting the Caroni River through 18, 5.5×9m sluices in the spillway lower body that after being closed by gates permitted the reservoir filling. In order to define the precise timing for closure of the sluices and to program the reservoir filling, an Unsteady Flow One-dimensional Numerical model was set up based on the model FEQ. The mathematical model was validated under unsteady state conditions using field observations. This paper describes the different criteria used to program the sluice closure and reservoir filling, according to the requirements to ensure dam safety and stability during the filling, the criteria to meet the system energy supply, the numerical model set up, its calibration and operation during the sluice closure maneuvers and filling of the reservoir and, the model-prototype conformity obtained during these processes.

1 INTRODUCTION

Caruachi dam presently under construction is located at the Southeastern region of Venezuela. This—run of the river—2196 MW is one of the cascade hydropower plants of the Lower Caroni Development and construction schedule required 2 stages of River Diversion. The First Stage included river diversion by means of 350 m width natural channel that was created by a cofferdam. The cofferdam permitted building on the dry, the two-body spillway, the powerhouse and, the right CFRD dam. The Second Stage required river diversion through 18, 5.5×9m sluices located in the lower body of the spillway structure which allowed building the left embankment dam. Finally, the sluices closure and reservoir filling permit tests and commissioning of the generating units.

Sluices closure and reservoir filling processes involve rigorous hydraulic study due to the need of coordinating flow balance to simultaneously fill Caruachi reservoir and, maintain a suitable discharge and headwater variations in Macagua 2968 MW, located only 22 km downstream, and provided with a small reservoir. Regulating discharge is done at Guri Dam (9715MW), located 59km upstream of Caruachi Project that predetermines the hydroenergetic characteristics of the Lower Caroni Cascade System, responsible of generating a total of the 70% of the national energy consumption. Since sluice closure and reservoir filling of Caruachi is a time dependent problem, a numerical unsteady model of all Lower Caroni River was built based on all premises required by the system taken in account: energy requirements, hydraulics, geotechnical, structural, construction and environmental restraints. This paper shows the construction of the mathematical model and the model-prototype correlation of discharge and water levels during the sluice closure and reservoir filling of Caruachi Project as part of the Lower Caroni River System.

2 THE LOWER CARONI RIVER SYSTEM

The Caroni River from Guri to its junction with the Orinoco River, comprises a stretch of 110 km (Figure 1). The river runs on a solid gneiss granitic rocky bed, no sediment load is present except some localized loose sand in form of bars that get suspended occasionally, product of mining activities that still remains at some natural river reaches. River morphology is varied and includes very irregular cross sections, wide but shallow and narrow but deep channel reaches, some cross sections are kilometers wide. The following structures are built thus representing hydraulic controls that are included in the numerical model architecture: at Guri regulating Dam, two powerhouses are continuously operating with a variable flow pattern flowing through Necuima Canyon and enters a natural river expansion until Tocoma Dam (2160 MW) where First Diversion cofferdams located 59 km downstream of Guri Dam, receives Guri outflow, and its reservoir level was raised as the process of closing the 18 sluices was done. Macagua Project consisting of three powerhouses operate as—run off the river—powerplants with constant reservoir elevation, 54.50. Manning “n” roughness coefficients for the different river reaches changes from stretch to stretch as obtained from previous investigations. Discharge characteristics of Guri two Powerhouses are specified in the model by hourly prototype information. Rating curves from Tocoma cofferdams are prescribed from physical hydraulic model results. At Caruachi, headwater elevations are specified together with the number of sluices in operation and, spillway overflow information at the final stage of sluice closure. Outflow hydrographs at Caruachi site are routed through Macagua reservoir under prescribed turbine flows at the Macagua three powerhouses with limitation of the fixed reservoir at EI 54.50 approximately. Water levels at the confluence Orinoco-Caroni River allow knowing water depth variation at Macagua downstream reach nearby to the Metropolitan area Puerto Ordaz-San Felix (Figure 2).

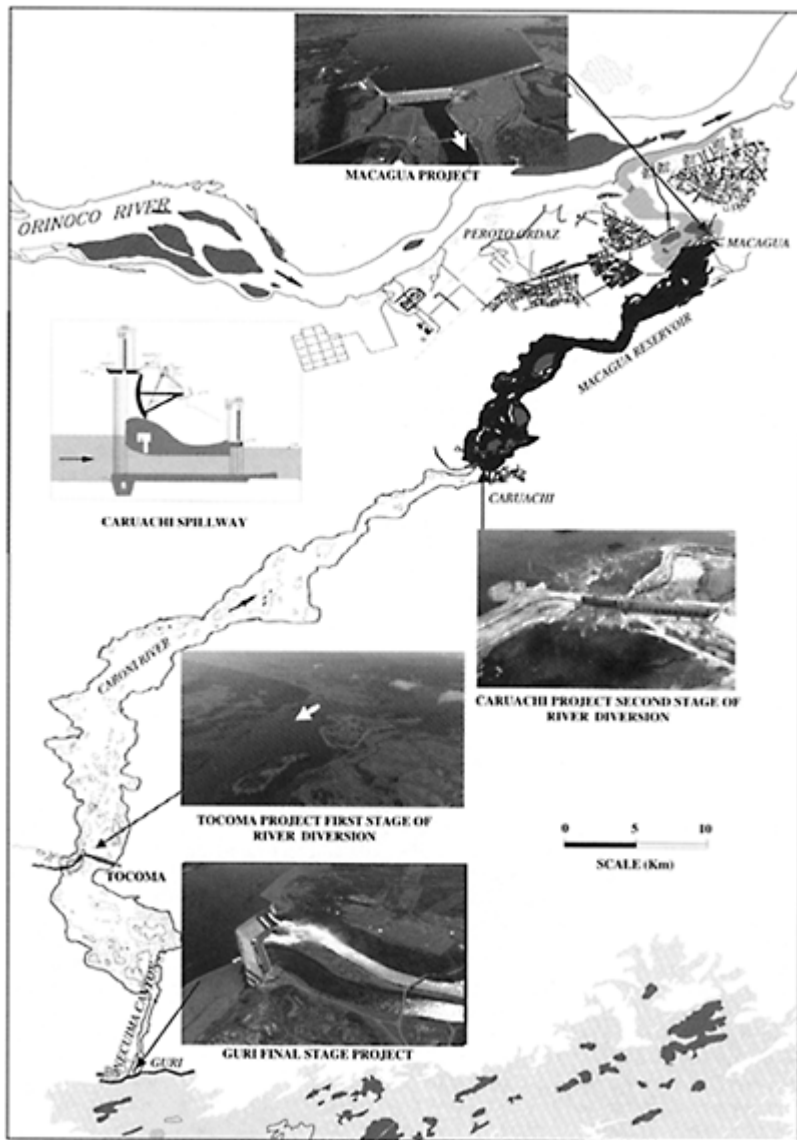


Figure 1. Lower Caroni River System—December 2002.

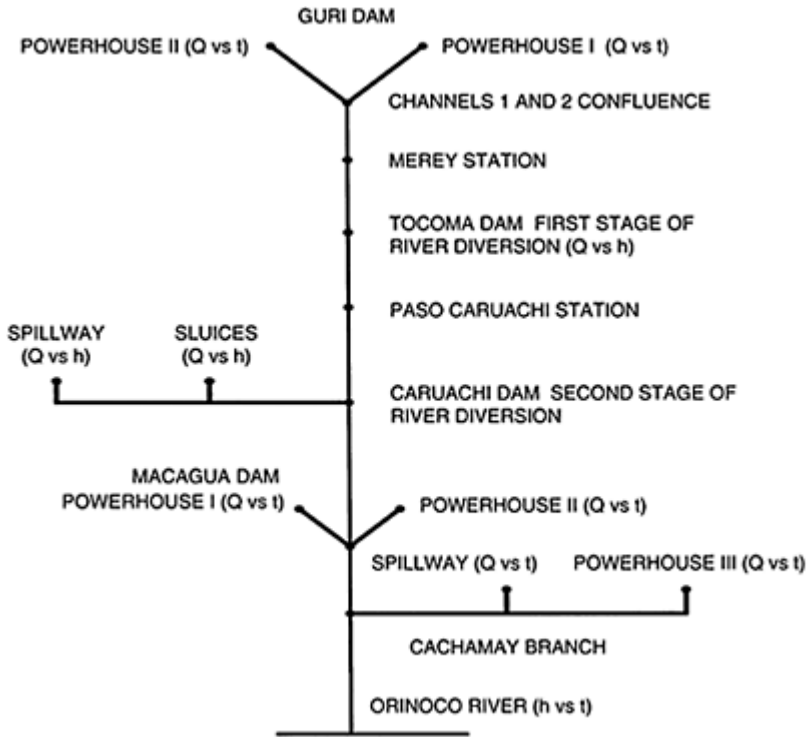


Figure 2. FEQ numerical model-schematization for Lower Caroni River System—December 2002.

are built, 18 km downstream of Guri Dam. Caruachi Second Stage of River Diversion

3 FREE SURFACE UNSTEADY FLOW NUMERICAL MODEL-FEQ FOR LOWER CARONI RIVER SYSTEM

The Full Equations (FEQ) model for the simulation of one-dimensional unsteady flow was used in order to know water level and discharge variation throughout control structures at Tocoma, Caruachi

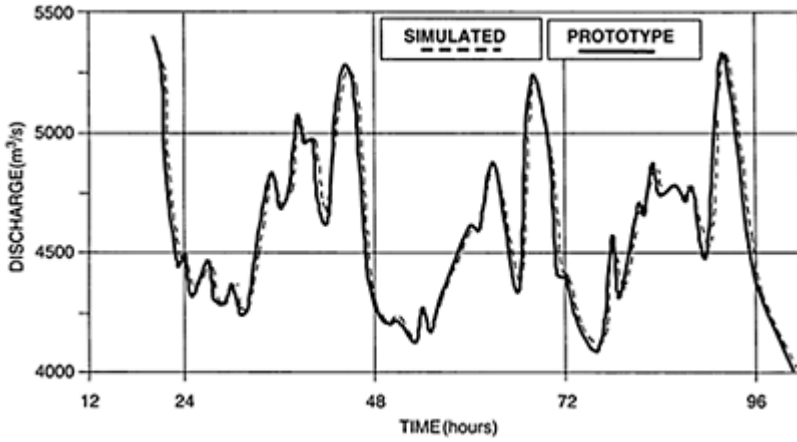


Figure 3. Numerical model calibration at Merey gauge station under unsteady flow conditions.

and Macagua dams. The equation of conservation of mass

$$\left(\frac{\partial Q}{\partial x} \right) + \left(\frac{\partial A}{\partial t} \right) = 0 \quad (1)$$

and conservation of momentum

$$\left(\frac{\partial y}{\partial x} \right) + \frac{V}{g} \left(\frac{\partial V}{\partial x} \right) + \frac{1}{g} \left(\frac{\partial V}{\partial t} \right) = S_o - S_f \quad (2)$$

are used by FEQ to calculate the flow-depth versus time along the reach from Guri Dam to Caroni-Orinoco river confluence, where Q =discharge throughout control volume, x =volume control length, A =area of volume cross section, t =time, y =water depth, V =average velocity at cross section, S_o =channel slope and S_f =energy gradient. The estimation of hydraulic variables in the stream system results from known initial and boundary conditions with an implicit-difference approximation such as Preissman method.

4 MODEL CALIBRATION AND VALIDATION

The adjustment of FEQ model parameters, such as Manning's n , contraction and expansion coefficients, requires knowledge of the hydraulic system in order to simulate observed river behavior. The model calibration aims to reproduce observed data for steady and unsteady flow conditions. In the case of steady state flow, the HEC-2 program, which is widely known for gradually varied flow calculations, was used to simulate rating curves along the river based on 179 cross sections and 49 gage stations of

water discharge and stage, along the 110 km river length. Runs performed for a range of discharge permitted obtaining Manning's n values to match prototype known water elevations. To run initial conditions in FEQ program, Manning's " n " values from HEC-2 fed the input data of FEQ, thus the comparison of water profiles from Guri to Orinoco River evidenced similar results in both models. In the case of unsteady flow, the FEQ model calibration is derived from Guri power house discharges by means of two hydrograph measured at Merey and Paso Caruachi stations which have permanent limnigraphs. Figure 3 shown measured and simulated hydrograph in Merey station where the FEQ reproduces the prototype hydrograph. Paso Caruachi station provides hydrographs to verify the model calibration (Figure 4). Even though additional adjustments may be necessary to reproduce the river behavior, the FEQ results matches the hydrograph trend. However,

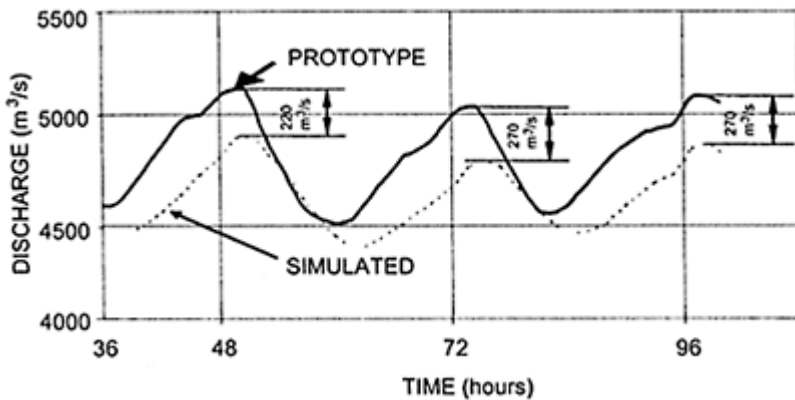


Figure 4. FEQ calibration at Paso Caruachi station under unsteady flow conditions.

they are different in discharge and time. The flood wave simulated arrived 1.48 hours later than the measured one. This effect is attributed to the volume of off-channel storage in the prototype which is not correctly simulated by FEQ. On the other hand, computed discharges were different. Nevertheless, discharges differences are within 5% of total discharge which, from practical engineering judgment results acceptable, taken in account accuracy of water levels and discharge data.

5 OPERATION OF THE MODEL FOR THE SLUICE CLOSURE-STRATEGY FOR SOLUTION

Calculations are based on energetic, hydraulics, geotechnical and construction criteria that can be summarized as follows:

- (1) Maintain Macagua and Guri Projects energy generation offer to fulfill the national electrical system demand. In addition, Macagua reservoir drawdown should not be less than 52 m.a.s.l, to avoid turbine malfunction.
- (2) Control reservoir rate rising to permit monitoring the performance of the permanent structures such as concrete structures, earth dam and rock fill dam. The reservoir rate raising should not increase more than 0.5 m/day. Additional criteria included allowing time for reservoir shore forest handling and, fauna rescue on the reservoir islands.
- (3) Guarantee Caruachi construction schedule including tests on the first generator.
- (4) Avoid prolonged high flow velocities in the last sluices to close due to high risk of cavitation potential for expected maximum velocity in the order of 22 m/s.

FEQ model allows the evaluation of several alternatives in order to get an optimum sluice closure program and reservoir filling under the following methodology:

- (1) Given the energy system demand during the sluices closure which needed to be supplied by the Guri-Macagua powerplants.
- (2) Compute the flood wave characteristics from Guri powerhouses to Caruachi dam including the effect created by the sluice closure maneuvers and obtain Macagua energy generation, by FEQ numerical model, maintaining the different adopted criteria.
- (3) Compare Macagua resulting generation patterns with required patterns at Macagua. This procedure was repeated until energy supply in the system and criteria adopted are satisfied.

6 SLUICE CLOSURE PLANNING

A preliminary unsteady state FEQ numerical model was set up and different scenarios of closure and their implications on the river system downstream of Caruachi were evaluated using a flat hydrograph of constant $Q=5000 \text{ m}^3/\text{s}$ outflowing Guri Dam. Results showed that no special provisions were needed when closing the first 13 sluices with regards to downstream implications. However, FEQ model simulations results showed that for every one of the final 5 sluices to be closed, a instantaneous reduction of 20% ($1000 \text{ m}^3/\text{s}$, in average) of the Caroni River total flow into Macagua reservoir, thus creating a significant effect on the powerplants normal output generation pattern (Table 1). Case 4 was considered adequate and it contemplates the closure of sluices N° 14 to 17 one every 2 days and, sluice N° 18 two hours after sluice N° 17, for a total time of 6 days, 2 hours. During actual closure according to Case 4, there will be a 1 m drawdown of the Macagua reservoir and a minimum temporary inflow of be $3500 \text{ m}^3/\text{s}$, the system will normalize in 2 days and 18 hours after the closure of the sluice N° 18. The latter was satisfactory for Macagua Powerplants generation. Improvement of the FEQ Model by using real hourly hydrograph at Guri dam and taking provisions of the real conditions of required generation at Macagua powerplants, permitted obtaining the final scheme of closure (Figure 5). This scheme fulfilled all the criteria required by the project as mentioned above.

Table 1. Regulation at Macagua during closure of the 5 last sluices unsteady flow simulation.

		Results				
		Caruachi		Macagua		
Case	Closure duration Sluices: 14 AL 18 (d-days, h-hours)	Maximum inflow in Caruachi (m ³ /s)	Minimum outflow (m ³ /s)	Minimum inflow regulated (m ³ /s)	Duration of the regulation (d-days, h-hours)	Minimum HW during the regulation (m.a.s.l.)
1	10 h(a)	5000	300	2000	3d	52.65
2	5d(b)	5000	2465	3100	3d 51h	53.99
3	10d(c)	5000	3315	3850	4d	53.95
4	6d 2h(d)	5000	2480	3500	2d 18h	53.50

Notes: (a) Closure last 5 sluices each every 2 hours.
 (b) Closure last 5 sluices each every 1 day.
 (c) Closure last 5 sluices each every 2 days.
 (d) closure sluices 14 to 17 each every 2 days and sluice 18 two hours after closure of sluice.

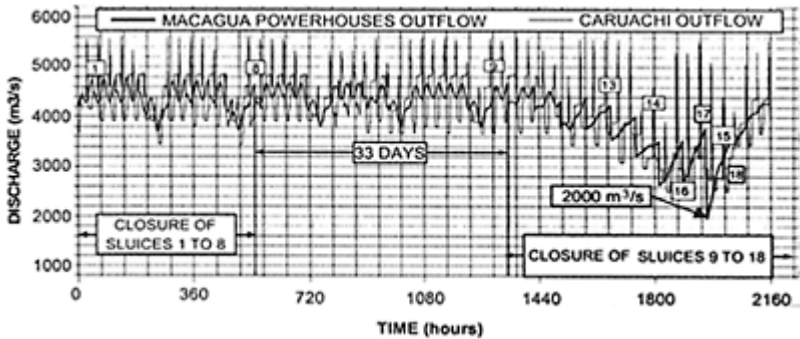


Figure 5. Outflow variation at Caruachi and Macagua during closure of 18 sluices.

7 PLANNING THE FILLING OF CARUACHI RESERVOIR

Raising of Caruachi reservoir starts with the closure of the 18 sluices, from EI 58.5 to EI 78.8, and proceeds with a spillway operation to complete normal pool elevation, EI 91.25 by storing an additional 2200 millions m³ and maintaining the Macagua reservoir and

powerplants under normal operating conditions, releasing an average flow of $4000\text{m}^3/\text{s}$ from Caruachi impounding reservoir to supply Macagua Project. A scheme of reservoir filling was planned based on results from a numerical unsteady flow model allowing raising the reservoir at a rate of 0.20 m/day , which resulted in a total filling time of approximately 58 days.

8 NUMERICAL MODEL-PROTOTYPE CONFORMITY

Closure of Sluices N° 1 to N° 8-Prototype-Numerical Model Correlation: With respect to reservoir elevation at Caruachi, and using a full unsteady state model, water levels computed resulted 0.3 m higher than prototype, this discrepancy arises as a result of a hydraulic control created by the submerged prototype cofferdam that imposed higher headwater levels in the field system, and this difference was not contemplated by the numerical model. Macagua average reservoir headwater prediction results very close to field measurements (Figure 6) with differences of the order of 0.20 m .

Closure of Sluices N° 9 to N° 18-Prototype-Numerical Model Correlation: Comparison of computed and measured prototype values of reservoir levels at Caruachi following closure of Sluices N° 9 to 13, there exists a maximum difference of 0.3 m whereas for the last 5 sluices, sluices 14 to 18, this discrepancy disappears as a result of the hydraulic control been suppressed by cofferdam being fully submerged by the flow (Figure 7).

Filling of Caruachi Reservoir-Prototype-Numerical Model Correlation: Figure 8 shown that prototype filling time was 62 days after the sluice closure operations ended with the closure of sluice 18. The planning filling time of 58 days almost predict the real filling time at prototype. Both curves present an average slope of 0.20 m/day that satisfy the reservoir rate raising criteria, ensure water supply to Macagua dam and, deadline scheduled test of the Caruachi first generator.

9 CONCLUSIONS

The FEQ model of the Lower Caroni River System predicted successfully the time sequence for the sluices closure and program for the reservoir filling according to the requirements to ensure dam safety and stability during the filling and the criteria to meet the system energy supply. The model-prototype conformity obtained during the process demonstrated the effectiveness of one

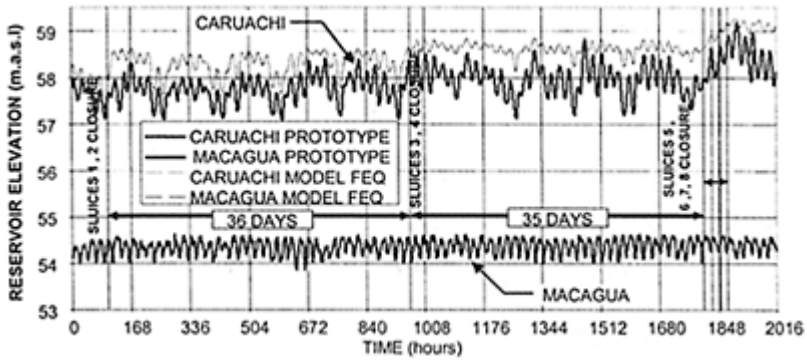


Figure 6. Caruachi and Macagua reservoir elevations—Numerical Model-Prototype correlation during closure of sluices 1 to 8.

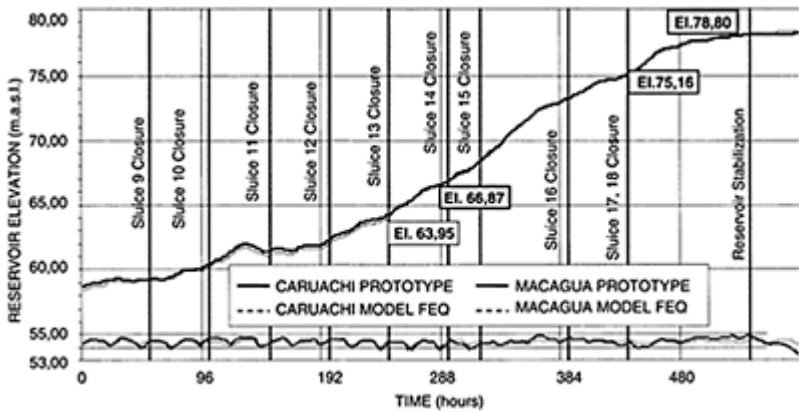


Figure 7. Caruachi and Macagua reservoir elevations—Numerical Model-Prototype correlation during closure of sluices 9 to 18.

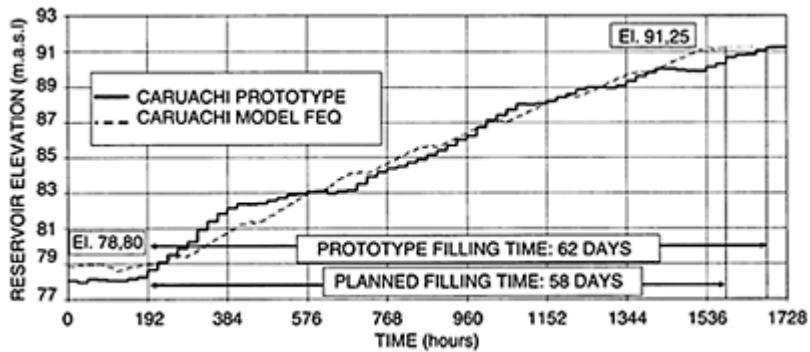


Figure 8. Caruachi prototype/planned elevations during filling of the reservoir.

dimensional unsteady flow model that allows solving the complexities involved in the processes of the sluices closure and reservoir filling of Caruachi Dam, as part of the Lower Caroni hydrosystem. During the processes of sluice closure and reservoir filling it was found vital the cooperation of a multidisciplinary group consisting of hydraulicians, geotechnicians, structural, mechanical, powerplants operators, energy delivery planners and, environmental engineers of EDELCA.

REFERENCES

- Marcano, A. (2001). Caruachi Project on the Caroní River-“Key Hydraulic Issues related to Second Stage of River Diversion”. XXIX IAHR Congress, Beijing. Special Seminar SS-2.
- Martínez, E., Antonini, M., Pérez, P., Marcano, A. & Castro, C. (2001). Evaluación Multidisciplinaria del impacto de las maniobras de cierre de los ductos de desvío. V Jornadas de EDELCA, Venezuela.

Yacyretá Dam: spillways modification to reduce total dissolved gases concentrations downstream of the dam

J.D.Bacchiega & C.A.Fattor

*Hydraulic Structures Division, Hydraulics Laboratory, National
Institute of Water, Buenos Aires, Argentina*

Hydraulics of Dams and River Structures—Yazdandoost & Attari (eds)

© 2004 Taylor & Francis Group, London, ISBN 90 5809 632 7

ABSTRACT: The integral project of spillways and energy dissipators has to ensure the pass of the design flood without endangering the stability of the dam. In low ogee spillways, a hydraulic jump stilling basin allows normally the restitution of the flow to the river with a low residual energy that must be compatible with the characteristics of the riverbed. Air-entrainment devices to reduce cavitation risks are often included as an additional safety element. The location of these hydraulic structures in shallow waters with very rich fishes population can present an excellent performance from the hydraulic viewpoint but hazardous for the normal development of those fishes. This situation was reached in Yacyretá dam, where the excessive amount of air into the flow was responsible of the massive fishes mortality as a consequence of having exceeded the standard values of total dissolved gases (TDG). In the present article, the variables considered for the refurbishment of the spillways are presented, having taken as design condition the reduction of air-entrainment in the spillway and the energy dissipator.

1 INTRODUCTION

The hydraulic project of spillways and energy dissipators is strongly related to the safety criteria of the dam. On one hand, the design of the spillway must guarantee the pass of the discharge design with admissible reservoir elevations, without putting under risk the stability of the dam. On the other hand, the energy dissipator must ensure the discharge of the flow to the river with low residual energy, compatible with the geomorphologic conditions of the riverbed, avoiding in that way significant local and general scour.

Besides that, it is very extended the construction of air-entrainment devices in order to ensure the integrity of the hydraulic structures against cavitation effects.

The location of this type of structures in shallow water rivers with rich fishes communities, where the functioning conditions previously mentioned can be perfectly accomplished, can result hazardous for the fishes preservation. This situation was reached in Yacyretá dam where, because of an operation of the spillway in August 1994, the excessive amount of air into the flow was responsible of the massive fishes mortality as a consequence of having exceeded the standard values of total dissolved gases (TDG). For this reason, corrective measures were analysed in order to avoid the repetition of a similar event, which is certainly complex from the environmental point of view.

2 DESCRIPTION OF THE DAM AND ITS STRUCTURES

Yacyretá hydroelectric development is located on Paraná river, in the boundary of Argentina and Paraguay, close to the Argentinean village of Ituzaingó (Fig. 1).

Paraná river has a mean discharge of $11700 \text{ m}^3/\text{s}$ at the location of the dam, with water depths less than 4 m-high. The dam is 67 km long (including lateral closures), and includes the hydroelectric power plant of 2700 MW of installed capacity, navigation lock and two spillways.

VBP spillway is located on Principal branch, with a capacity of $55000 \text{ m}^3/\text{s}$, while VBAC spillway is located on Aña-Cuá branch and its capacity is $40000 \text{ m}^3/\text{s}$; consequently, the total discharge capacity is $95000 \text{ m}^3/\text{s}$. VBP has 18 spans of 15 m wide each one, with sector gates, and a 342m wide and 100m long hydraulic jump energy dissipator; the lowest elevation of the stilling basin is 15m below the riverbed elevation (Fig. 2). On the other hand, VBAC has 16 spans (15m wide), with sector gates, and an energy dissipator similar to VBP spillway.

Air-entrainment devices, designed to reduce cavitation risks, have been projected in both spillways.

During August 1994, an operation of VBP spillway was responsible of massive fishes mortality downstream of the dam. In that occasion, VBP was managed according to the operation rules, this is following a uniform opening of the gates and a hydraulic head given by $H/H_d=0.61$ on the crest, where H_d is the design head.

Studies carried out by U.N.N.E. (1994) determined that fishes were affected for the bubble disease, as it happened downstream of some dams located on Snake and Columbia rivers (U.S.A). This disease appears due to the very high TDG concentrations, so that values close to 105–110% can affect the life of the bottom fishes; these fishes cannot compensate this effect with a deeper submergence because of the low water depths in this part of the river. This diagnosis was confirmed by means of TDG levels measurements. These records showed TDG concentrations so high as 150% immediately downstream of the stilling basin, with values of 125% at 70 km from the dam.

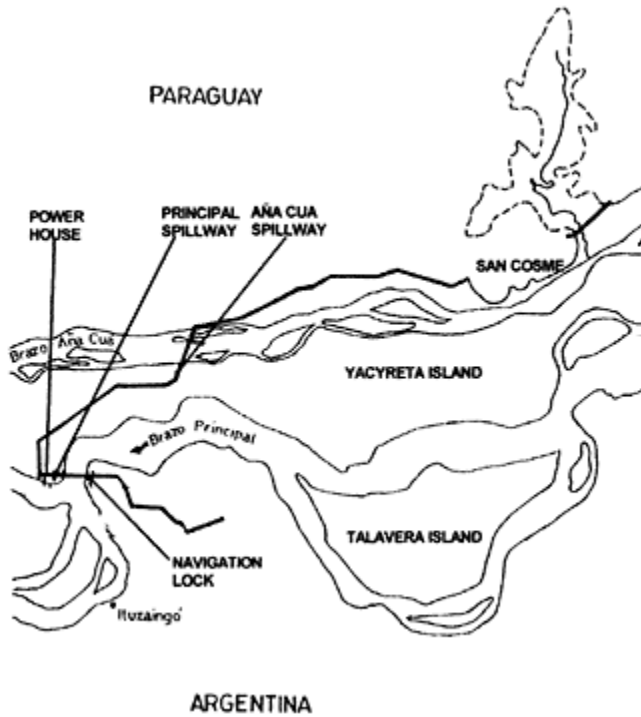


Figure 1. General layout.

Transitory actions were adopted while definitive corrective measures started to be analysed. The spillway operation was modified, discharging the same flow by four gates completely opened. Air-entrainment was reduced, but circulation currents could eventually enter riverbed granular material to the stilling basin, increasing the risk of damages.

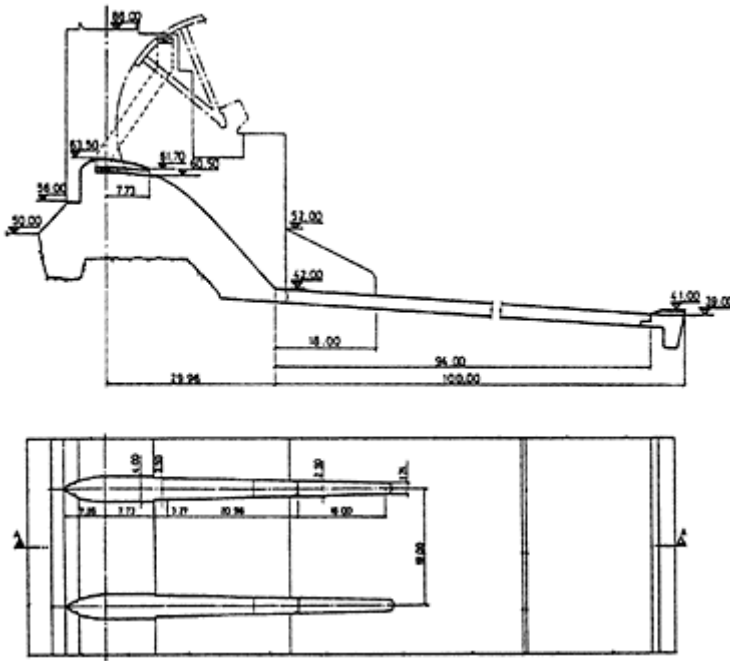


Figure 2. Principal spillway (VBP).

3 GLOBAL ANALYSIS—BACKGROUNDS EVALUATION

4

CONCEPTUAL STATEMENT OF ALTERNATIVES

After the fishes mortality downstream of VBP, some alternatives were evaluated to reduce high TDG levels, being able to analyse structural and non-structural measures. The former could imply the construction of some structures that would permit a wide operation of the spillways without exceeding critical TDG levels; the latter action is mainly related to operative restrictions of the spillway and complementary measures to keep acceptable environmental conditions.

These measures must be able the operation of the spillway with admissible TDG levels. Between the antecedents, it was possible to find standard values defined by U.S.EPA (1986), which establishes 110% as maximum TDG concentration. Another standard values are given by Fidler & Miller (1997), who determine maximum TDG concentrations as high as 110% for water depths deeper than 1 m, and between 103% and 110% for water depths less than 1 m.

Consequently, the analysis of structural measures to reduce TDG concentrations downstream of the dam were developed on the basis of standard values and experiences

gained from the spillways modification of dams located on Snake and Columbia rivers (John Day, Bonneville, Ice Harbor, etc.), with references from Ebel (1979) and U.S.Army Corps of Engineers (1984).

The alternatives are basically defined for an horizontal ramp, whose location and dimensions are adjusted to reduce the water jet submergence in the hydraulic jump, getting TDG levels substantially lower compared to the original situation and compatible with the standards.

Under these conditions, four alternatives of ramps were tested. Table 1 shows the characteristics of the alternatives, being ΔH the distance from the crest to the horizontal ramp.

5 EXPERIMENTAL METHODOLOGY

Two physical models were built to analyse the hydrodynamic behaviour of the alternatives presented above.

First, a 1:50 length scale two-dimensional physical model was implemented to evaluate the alternatives by considering the flow pattern (submergence and stability of the jet, air bubbles

Table 1. Definition of ramp alternatives tested in the physical model.

Alternative	ΔH (m)	Elevation (m)	Length (m)	Height (m)
I	4.50	59.00	3.50	2.73
II	6.50	57.00	3.50	3.17
III	7.50	56.00	3.50	3.36
IV	6.50	57.00	4.00	3.67

in water, circulation currents, etc.), the velocities field along the stilling basin (to evaluate the sense and intensity of the bottom velocities and the residual energy) and the pressures field in the structures involved for the flow. This model, which represents a central span and two half spans, does not permit the representation of TDG levels. Instead of this, comparative measurements of amount and distribution of air reached for each alternative were carried out. This analysis and the previous one allowed selecting the best alternative. Under these conditions, the measurements concerning the velocities and pressures fields permitted to estimate the new scheme from the energy dissipation viewpoint, as well as to consider the eventual risk of cavitation for a structure where the air-entrainment devices were removed.

The second model is a 1:115 length scale three-dimensional physical model that reproduces VBP, the power plant, the navigation lock and a part of the dam, as well as a sector of the reservoir and the river downstream of the dam, being this last one represented with granular material. The goal of this model is to evaluate the hydrodynamic functioning of the ramp selected in the two-dimensional model when actual boundary conditions (with three-dimensional characteristics) are included. In this

way, it is possible to analyse the general flow pattern (stability of the submerged jet, interaction of the jet between adjacent spans, incidence of the power plant, etc.), the distribution of velocities and the local scour downstream of the spillway, and the eventual incorporation of river bed granular material into the stilling basin.

Two reservoir elevations were considered for the studies in the models, resulting from $H/H_d=0.61$ and $H/H_d=1$ on the spillway crest, being the last one the corresponding to the maximum normal reservoir elevation. The tail water was adjusted according to the flow discharge through all the structures, and gate openings from 1 m to total opening were analysed.

6 ANALYSIS OF RESULTS

6.1 *Original project: flow pattern*

The hydraulic behaviour observed in the original spillway is characterised for the presence of a hydraulic jump inside the stilling basin, being able to see that the submergence of the hydraulic jump depends on the discharge and the tail water elevation. The uniform opening of the gates allows seeing big horizontal-axis vortexes with strong circulation currents. This flow pattern ensures the self-cleaning of the energy dissipator, which is very important for this kind of structure. It can be seen, for the design flow discharge, that the residual energy downstream of the stilling basin is absolutely compatible with the dam safety and the stability of riverbanks.

As regards the air-entrainment device, Figure 3 shows that the jet flowing on the aerator produces a cavity with sub atmospheric pressure, making possible the entrainment of air that reaches the bottom of the stilling basin.

Besides, the interaction of the jet with the front of the hydraulic jump produces the superficial entrainment of air into the jump, but air bubbles do not reach the bottom of the stilling basin.

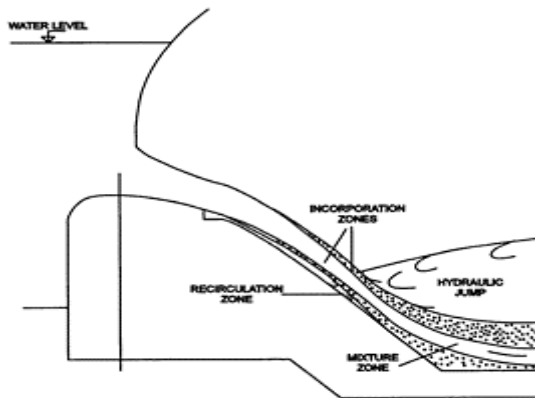


Figure 3. Original project: flow pattern.

6.2 Modified project: flow pattern

The location of the ramp on the spillway profile produces a considerable change in the flow pattern. A high velocity superficial flow is observed for low discharges, producing a circulation zone with inversion of the velocity profile and generating very low air-entrainment close to the stilling basin bottom. However, this velocity inversion implies some risks due to an eventual incorporation of riverbed granular material in the stilling basin. It was detected, even for the highest discharges, a displacement of the hydraulic jump towards downstream as well as a circulation at the toe of the spillway that stays there for all the range of flow discharges.

The tests carried out by INA (1995) showed that the ramp defined in Alternative IV, whose length is $l=0.216.H_d$ and its distance respect to the spillway crest is $t=0.351.H_d$, presents the most satisfactory results. With this alternative, for $H/H_d=1$ and $Q/Q_{\max}<0.35$, a circulation involving a velocity profile inversion can be observed. The intensity of the turbulence in that circulation zone as well as its length depends on Q/Q_{\max} and the submergence S .

On the other hand, for $H/H_d=1$ and $Q/Q_{\max}>0.35$, circulation zone at the toe of the spillway still remains and the hydraulic jump is displaced downstream. Figure 4 allows seeing the characteristic flow pattern for $Q/Q_{\max}=1$. Figure 5 shows two velocity profiles measured at $x/L_s=0.54$, being L_s the stilling basin length, for $H/H_d=1$, and $Q/Q_{\max}=0.12$ and $Q/Q_{\max}=1$.

The flow pattern and its circulation zone are related to the self-cleaning of the energy dissipator. In this case, any material reaching the toe of the stilling basin will be always circulating if the spillways are under operation, which can present risk of erosion due to abrasion. On the other hand,

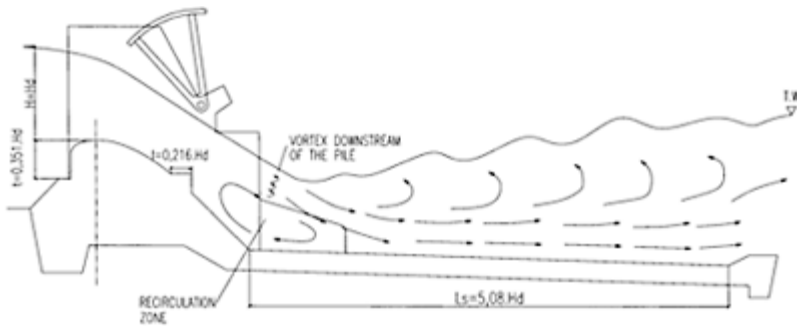


Figure 4. Flow pattern, $Q/Q_{\max}=1$ and $H/H_d=1$.

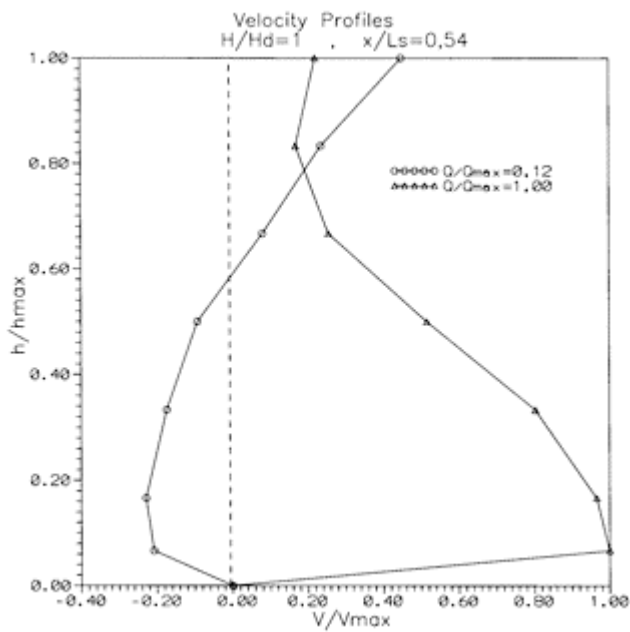


Figure 5. Velocity profiles.

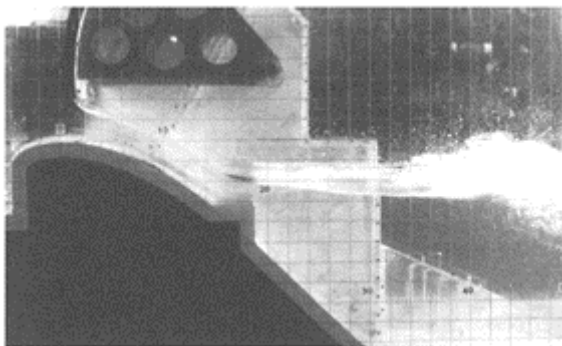


Figure 6. Two-dimensional model.

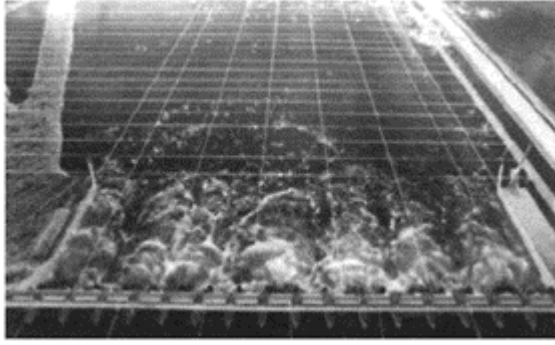


Figure 7. Three-dimensional model.

the efficiency of the energy dissipator is less than the original condition because of the displacement of the hydraulic jump, throwing the results presented in 6.4. Figures 6 & 7 present the general flow pattern observed in the two physical models for the deflector selected.

6.3 Hydrodynamic conditions

As regards the hydrodynamic actions, the modification of the spillway profile induces a change respect to the original design. These changes can be analysed by means of some parameters that represent the intensity of turbulence as C'_p and $C_{0.1}$, being these coefficients defined as follow:

$$C'_p = \frac{\sqrt{(p'_i/\gamma)^2}}{U^2/2g} \quad (1)$$

$$C_{0.1} = \frac{(\bar{p} + p'_{0.1})/\gamma}{U^2/2g} \quad (2)$$

where C'_p =coefficient of fluctuating pressures; $C_{0.1}$ =coefficient of pressures related to a probability of occurrence of 0.1%; p'_i =term of fluctuating pressure; \bar{p} =mean pressure; γ =specific weight of water; U =mean velocity of the flow at the inlet of the jump; g =gravity acceleration.

Bacchiega & Fattor (1999) examined the variation of $C'_p = f(x/L_s) = f(x/L_s)$ for $H/H_d=1$, considering $Q/Q_{\max}=0.35$ y $Q/Q_{\max}=1$. For the situation defined for $H/H_d=1$ and $Q/Q_{\max}=0.35$, it is possible to characterize different tendencies along the structure. In this way, for $0 < x/L_s < 0.11$, where x is measured from the spillway crest, C'_p and $C_{0.1}$ are higher in the original profile than the modified spillway because of the direct action of the hydraulic jump. For $0.11 < x/L_s < 0.85$, which involves a great fraction of the total

length of the stilling basin, C'_p is higher for the original design but $C_{0.1}$ is upper for the spillway including the deflector.

On the other hand, for $H/H_d=1$ and $Q/Q_{\max}=1$, the variation of $C'_p = f(x/L_s)$ presents some differences between the two spillways (Fig. 8). Even though the last part of the spillway profile is submitted to similar hydrodynamic conditions, C'_p results substantially superior for the modified spillway in $0 < x/L_s < 0.20$, reaching a maximum value of 0.088 for $x/L_s=0.11$. For $x/L_s > 0.20$ the highest values of C'_p are related to the original design, with exception of a singular maximum detected at $x/L_s=0.47$. The evaluation of $C_{0.1}$ (Fig. 9) shows higher values for the original spillway in the last section of the spillway and inside the energy dissipator in the range $0 < x/L_s < 0.17$, with a peak value of 1.04 for $x/L_s=0.08$; downstream, the magnitudes of $C_{0.1}$ are superior for the modified spillway except for a singular peak observed at $x/L_s=0.47$.

6.4 Scour downstream of the stilling basin—riverbed material incorporation in the dissipator

Another relevant aspect to be analysed in relation to the global functioning of the modified spillway, with a $0.216.H_d$ -long ramp located at $t=0.351.H_d$ below the spillway crest, is the erosion

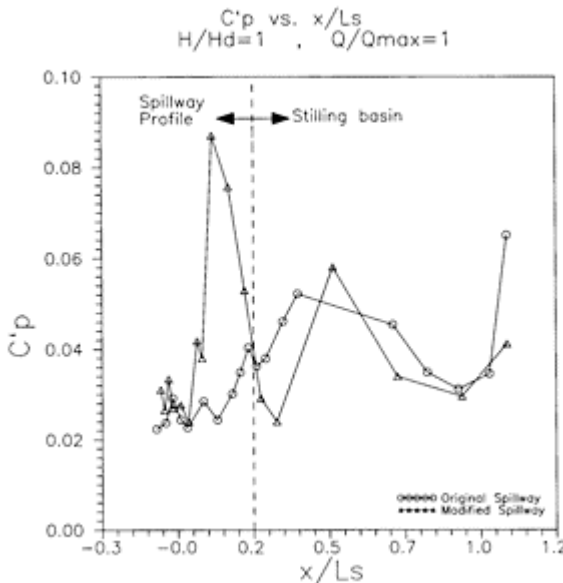


Figure 8. Analysis of the coefficient C'_p

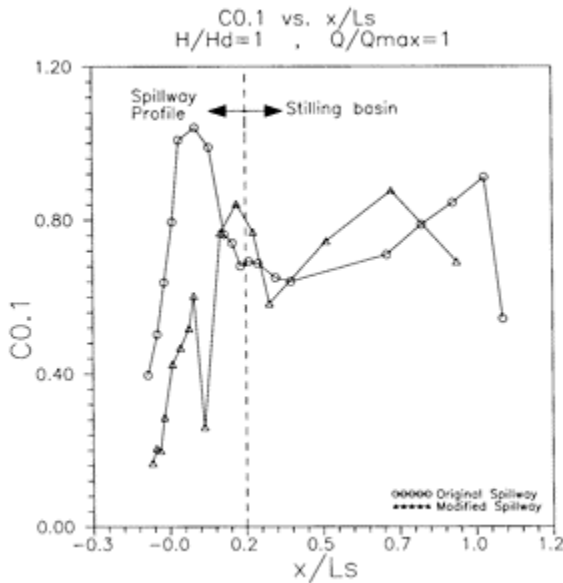


Figure 9. Analysis of the coefficient $C_{0.1}$.

downstream of the stilling basin. Tests carried out by INA (1995) showed an increase of the local erosion with the modified spillway, putting into evidence a decay in the energy dissipation performance in comparison to the original design.

Additionally, the new flow pattern and hydrodynamic conditions observed as a consequence of the inclusion of the ramp in the spillway profile are responsible, for some conditions of operation, of the entrance of riverbed granular material into the stilling basin. These consequences are not reached in the original design under the same operation conditions. As a result, the stilling basin losses one of the main characteristics of the original energy dissipator, which is its self-cleaning property.

7 CURRENT SITUATION

The massive fishes mortality of August 1994 impelled the studies of measures on both spillways to reduce TDG concentrations. VBP tests were carried out at INA facilities in Ezeiza (Argentina), while VBAC studies were developed in Asuncion (Paraguay). After completing the studies, and taking into account the degree of advance of VBAC construction, this spillway was finally completed with the construction of the deflectors on each span. VBAC spillway is currently under operation with discharges that must be higher, for ecological reasons, than $1500 \text{ m}^3/\text{s}$. Figure 10 allows observing the general behaviour for an operation with $28000 \text{ m}^3/\text{s}$, being able to see the superficial jet deflector for the horizontal ramp.

Regarding VBP, its operation was not so extended after the incident of the fishes mortality because the hydroelectric power plant, which includes 20 Kaplan turbines, was gradually put into service since September 1994. Spillway modification started some years later, being able to observe a stage of the construction in Figure 11.

Finally, it must be said that because of the prompt changes in the operation of the spillways and the structural measure finally completed, new fishes mortality events were not observed after August 1994.

8 CONCLUSIONS

VBAC and VBP original projects ensured an optimum behaviour from the hydrodynamic viewpoint. However, fishes mortality downstream of VBP in August 1994 impelled to evaluate the modification of the spillways to reduce TDG concentrations, which was the reason of that incident.



Figure 10. Operation of the VBAC
 $Q=28.000 \text{ m}^3/\text{s}$.



Figure11. VBP: construction of the deflectors.

VBP modification studies were carried out in two physical models, being able to elect the best option of deflector defined for a $0.216.H_d$ -long horizontal ramp located $0.351.H_d$ below the spillway crest.

The deflector avoids the deep submergence of the jet, decreasing the presence of air bubbles close to the stilling basin bottom and reducing TDG levels in the prototype. However, there are some negative aspects like the absence of air-entrainment devices, the displacement of the hydraulic jump downstream of the stilling basin (for high discharges), a decay in the energy dissipation performance and the loss of the self-cleaning with the modified spillway.

Finally, it must be remarked that this kind of solution allows reducing the risk of a serious event of fishes mortality, being convenient to make exhaustive inspections of the integrity of the stilling basin and, if it were necessary, to proceed with its maintenance.

REFERENCES

- Bacchiega, J.D. & Fattor, C.A. 1999. Environmental Considerations in the Design of Spillways: Analysis of Hydrodynamic Behaviour. *XXVII IAHR Congress*, Graz, Austria, August 22–27 1999.
- Ebel, W.J. 1979. Effect of the atmospheric gas supersaturation on survival of fish and evaluation of proposed solutions. National Marine Fisheries Service, Northwest and Alaska Fisheries Center, Coastal Zone and Estuarine Studies Division. Seattle, Washington, July, 1979.
- Fidler, L.E. & Miller, S.B. 1997. British Columbia Water Quality Criteria for Dissolved Gas Supersaturation Technical Report. Aspen Applied Sciences Ltd., Cranbrook, British Columbia.
- INA. 1995. Studies of the modification of Principal branch spillway. *LHA-144-01-95, Internal Report*, Ezeiz Argentina, December, 1995.

- U.N.N.E. 1994. Technical report on fishes mortality in Paraná river. Universidad Nacional del Nordeste, Facultad de Ciencias Veterinarias, Instituto de Ictiología. Corrientes, Argentina, August, 1994.
- U.S.A.C.E. 1984. Research summary: Spillway deflectors to reduce buildup of nitrogen saturation. United States Army Corps of Engineers, North Pacific Division, Hydraulic Laboratory.
- U.S.EPA. 1986. United States Environmental Protection Agency. Quality Criteria for Water. EPA-440/ 5-86-001.

HYDROMATRIX[®]: a new way to generate hydropower

H.Drobir

*Institute of Hydromulic Engineering, Vienna University of Technology,
Austria*

V.Kienberger

VA TECH HYDRO GmbH & Co, Linz, Austria

Hydraulics of Dams and River Structures—Yazdandoost & Attari (eds)

© 2004 Taylor & Francis Group, London, ISBN 90 5809 632 7

ABSTRACT: HYDROMATRIX[®] technology is a new concept in hydraulic energy generation. This technology, which was developed by VA TECH HYDRO in Linz, Austria, and the experimental investigations were carried out at the hydraulic laboratory of the Institute of Hydraulic Engineering of the Vienna University of Technology in Austria. The practical application of the HYDROMATRIX[®] technology is the HYDROMATRIX[®] module. The HYDROMATRIX[®] module is a compact arrangement of several bulb turbines installed on a steel structure. The steel structure contains not only the turbines with draft tubes and draft tube gates on the downstream side. There are trash racks in the front of the turbines and rooms for electric equipment and control systems. Only a cable is required to deliver the electric current from the module to the consumer.

1 INTRODUCTION

HYDROMATRIX[®] technology is a most economic turbine-generator-solution for satisfying lowhead hydropower applications in existing weirs or dams using water passage structures such as sluices, outlets and channels. The HYDROMATRIX[®] module is a compact arrangement of several bulb turbines including trash racks, draft tubes, rooms for hydropower units, electric switchgear and control systems. Spillway flaps can be installed on the top of the module structure for storage regulation.

What are the main conditions and application criteria for using a HYDROMATRIX[®] module? The structure of the civil constructions must be available and suitable for

HYDROMATRIX® application. In many cases only a minor civil construction is necessary. HYDROMATRIX® modules are installed as mentioned above in existing power plant structures for regulating dams of run-off-river projects, in sluices of ship locks, in intake towers and in irrigation dams. In case of flood it is possible to remove the module, if water passage is needed for flood discharge. The module is removed by hoisting devices and can also be raised out of the water for repair works or revision.

2 APPLICATION OF HYDROMATRIX® TECHNOLOGY

In order to achieve technically and economically feasible applications, the following criteria should be met. At the moment the most economic solution is provided by a plant discharge of approximately $100 \text{ m}^3/\text{s}$. The available head is from 3 m up to 30 m and a sufficient submergence of the draft tubes by the tail water level is to be ensured. The electric output per unit is between 200 kW and 700 kW. The turbines are unregulated propeller turbines with the standard diameters of bulb turbine and generator ranging from 0.8 m up to 1.33 m and an unit discharge range from $4 \text{ m}^3/\text{s}$ up to $10 \text{ m}^3/\text{s}$ (VA Tech Hydro, 2001).

As a minimum 2 turbines should be mounted on a module. The minimum head should not be less than 2.5 m. But at the hydraulic laboratory of the Institute of Hydraulic Engineering of the Vienna

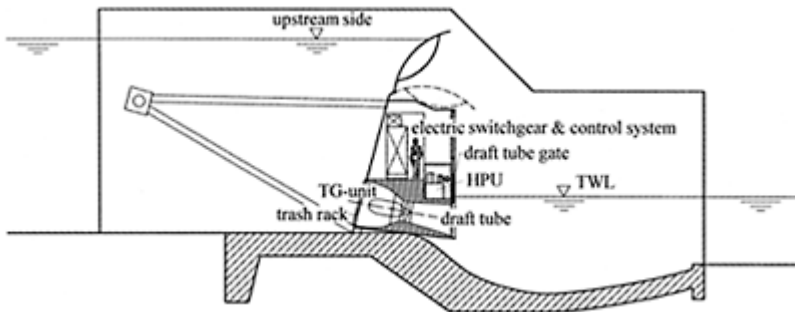


Figure 1. HYDROMATRIX® module integrated in the body of a tensile strained radial gate.

University of Technology we are working on developing a module for smaller turbine discharge and smaller head without submergence at the tail-water side. This new type of HYDROMATRIX® module could be especially applied to the weir overflow of irrigation systems.

By using HYDROMATRIX® technology run-off-river power stations without powerhouses are possible. All what you need is a weir. The spillways of the weir are blocked off by radial gates with flaps on it. The bulb turbines, the draft tubes and the draft tube gates are integrated into the body of the radial gate. The intakes to the bulb

turbines are openings in the skin plate of the radial gate. The waterways to the turbines are watertight pipes. The trash racks at the intakes are plane with the skin plate's upstream surface. If the discharge increases and oversteps the maximum flow of the turbines, first the flaps are lowered. In case of further increase of the inflow the radial gates have to be raised from operating position. Radial gates and flaps are moved by hydraulic hoisting devices.

Existing intake structures of water reservoirs for drinking water or other purposes, large lock and dam navigational structures are also ideal opportunities for the use of the HYDROMATRIX® technology. In locks for ship transfer the turbine-generator units can even be specifically designed to run in both directions if such is required to satisfy lock operations.

The efficiency of a conventional bulb turbine is about 95%. With the generator efficiency of 98% the total efficiency of the turbine-generator system is 93%. The efficiency of the HYDROMATRIX® turbine is approximately 90% and the HYDROMATRIX® generator that goes with it has an efficiency of 95%. Therefore the total efficiency of the system is near 86% and only 7% smaller than a conventional turbine-generator solution (VA Tech Hydro, 2001).

3 ADVANTAGES OF HYDROMATRIX® TECHNOLOGY

A lot of advantages make HYDROMATRIX® technology an attractive solution. The generated energy is clean and environmental friendly according to the Kyoto-protocol. Compared with conventional power plants, HYDROMATRIX® technology has less environmental impact. The customer can use existing intake structures without new civil constructions. In this case there are no geological risks and there is no additional land use.

Projects that cannot be developed in a feasible way by using conventional turbine-generator designs may now be developed profitably by means of the HYDROMATRIX® approach. The HYDROMATRIX® design utilizes a factory assembled grid of small propeller turbine-generator units. It combines the advantages of proven technology and low cost installation. HYDROMATRIX® systems are standardized modular concepts with high availability. Construction and start-up schedules can be shortened and will take only 1 to 1.5 years. For flood conditions and for repair or maintenance work HYDROMATRIX® modules are easy removable.

By using HYDROMATRIX® solution for run-off river power stations, no power house is required. With this concept the construction costs are markedly reduced. HYDROMATRIX® technology enables customers to tap the unused hydropower potential of intake towers, ship lock sluices, navigation and irrigation dams by using existing civil structures to develop a valuable renewable energy resource.

4 ELECTROMECHANICAL EQUIPMENT OF A HYDROMATRIX® MODULE

A turbine-generator unit consists of a stay ring with fixed stay vanes, a fixed blade propeller type runner of aluminum-bronze and an induction type generator directly connected to the turbine runner. The stator forms a watertight steel fabricated housing and is mounted to the stay ring. Two bearings situated within the bulb support the generator rotor, shaft and runner rotating assembly. The shaft seal is of the mechanical face seal type and is located within the generating housing.

Each module consists of a stiff, steel fabricated structure, which supports the turbine-generator units. Rubber seals are provided at the bottom of the module as well as along the module sides to prevent or minimize bypass leakage. The module also includes steel fabricated draft tubes with integrated control gates on the downstream side. The draft tube shape and length are optimized to achieve high turbine efficiency. Depending on the site conditions trash racks, bulkheads or roller gates can be incorporated into the module steel structure. In case of radial gates, where the HYDROMATRIX® modules are integrated into the radial gate's body, the tightness of the gate is given by the gate's sealing.

The electrical equipment is a standardized container type switchgear station, which includes the generator switchgear, the control and protection system as well as the reactive power compensation. For larger module sizes this electric switchgear is placed inside the module.

Few auxiliary systems are necessary for operating a HYDROMATRIX® plant. Where the capacity of an existing crane is insufficient for lifting the modules, a new crane has to be supplied and installed. HYDROMATRIX® modules integrated with any sorts of gates are moved by hydraulic hoisting devices.

Depending on the pollution of the water, a trash rack-cleaning machine can be supplied as part of the system as well. In order to ensure an independent power supply for the auxiliaries an emergency generator can also be provided (VA Tech Hydro, 2001)

Concerning the impact by feeding into an existing electricity network there are only good experiences at the projects realized until now.

5 EXPERIMENTAL INVESTIGATIONS ON A HYDROMATRIX® MODULE

The investigation presented here deals with a HYDROMATRIX®-application in the radial gate bays of an existing dam. In the USA a lot of dams have been built for purpose of ship navigation and flood control in the thirties of the last century. In the early thirties settlement in the surroundings of the dam was sparse and therefore there was no or less need of electricity.

Now the population density has increased, so that power production has been taken into account. Instead of the construction of a powerhouse, 5 HYDROMATRIX® power modules are planned to be installed in the existing 11 radial gate bays which are used for

flood control at the investigated project. When the HYDROMATRIX® power modules are generating electricity the radial gates are opened.

This concept reduces the civil costs markedly. Normally the spillways or gate bays are sealed up by closed radial gates. The modules are put in the gate bays by no bay's discharge. In case of an emergency the radial gate can be blocked at a partial position. The HYDROMATRIX® power modules now act as emergency stop logs. The modules have to be lowered into flood discharged bays. Downpull forces act, but the module structure is so complex, that it is not possible to calculate these acting forces caused by the underflow.

The experimental investigations were carried out at the hydraulic laboratory of the Institute of Hydraulic Engineering of the Vienna University of Technology. The total capacity of the 5 HYDROMATRIX® power modules will be about 85 MW; the average yearly production will be 353 GWh. The following pages of this paper will be mainly concerned with these investigations (Prenner, 2003).

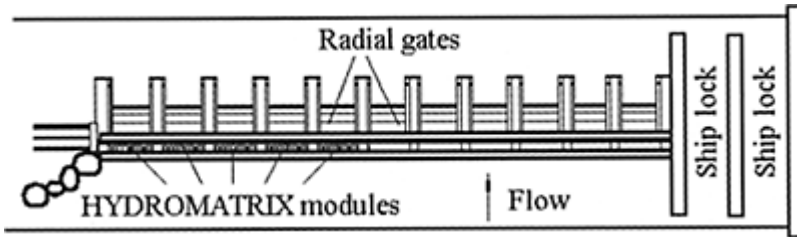


Figure 2. General layout of a dam for ship navigation and flood control. Installation of HYDROMATRIX® modules in the stop log slots of radial gate bays.

6 INTERACTION OF UNDERFLOW AND DOWNPULL FORCES

There are some scientific studies and corresponding publications on downpull forces acting by underflow. The downpull forces depend on the geometry of gate-bottom and gate-lip as well as on the downstream water level. Based on the scientific work of Naudascher (Naudascher, 1991) and of model tests by Drobir and Markovic (Drobir, 2001; Markovic, 2003) the downpull acting on a high head pressure gate can be calculated on the basis of experimentally ascertained downpull coefficients, which were determined for relative gate opening at various gate geometries. However, these studies cannot be used to estimate the quantitative influences of hydrodynamic forces on the given complex structure.

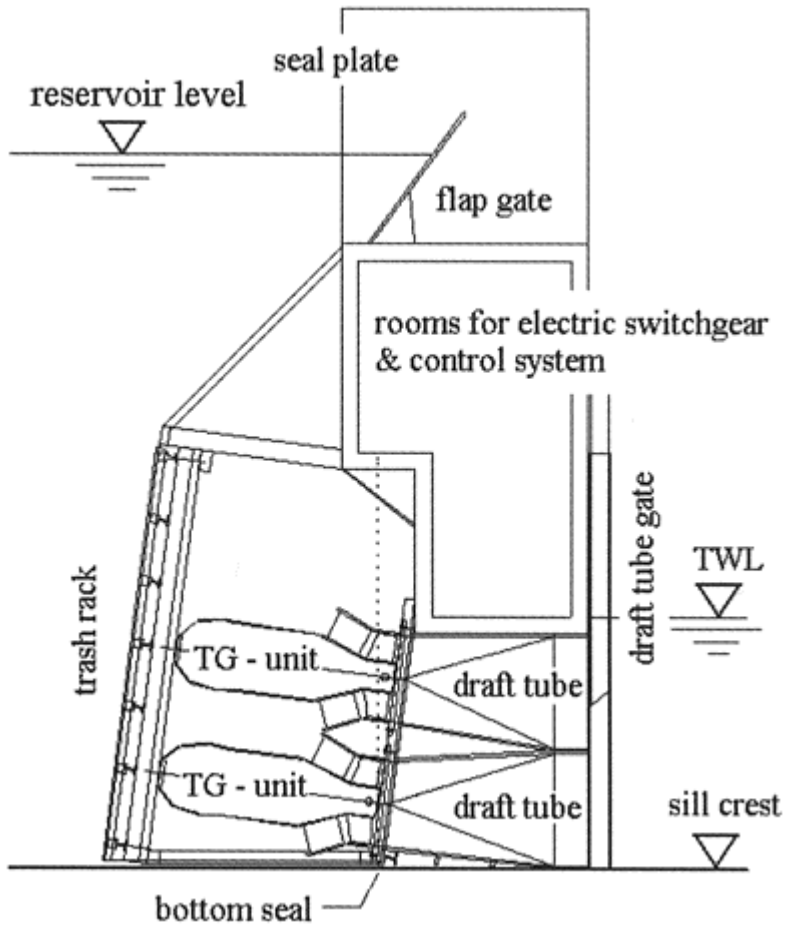


Figure 3. Cross section of the module box in the stop log slots of radial gate bays.

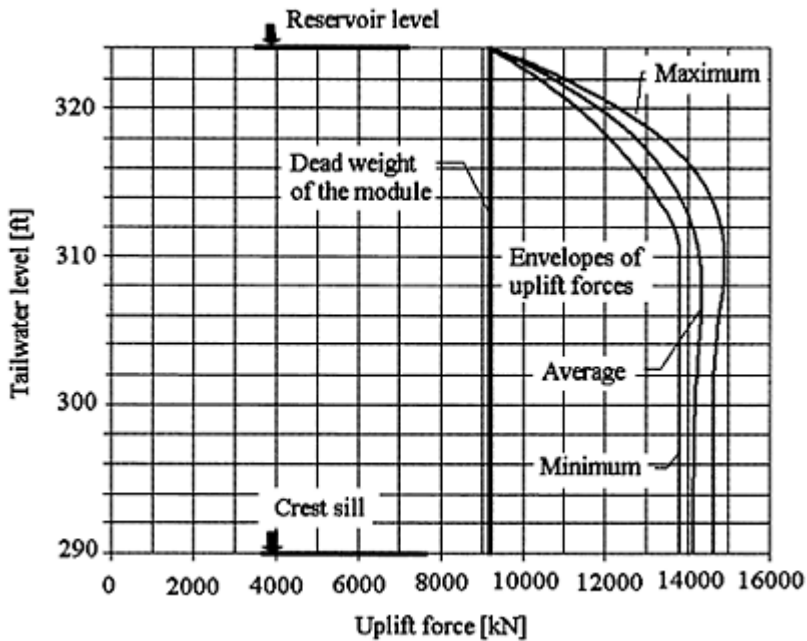


Figure 4. Maximum, average and minimum envelopes of lifting forces in correlation to lowering position of the module and to the downstream level.

The pressure distribution at the bottom surface, which occurs during jet separation at the bottom edge of a gate leaf by underflow conditions, is affected by so-called “viscosity effects”. Generally viscosity completely determines the beginning, the intensity and the structure of the turbulence. Naudascher (Naudascher, 1991) found out, that up to a certain critical Reynold’s number of underflow, the pressure distribution obtained from model tests is similar to the prototype. This critical Reynold’s number is $Re_c = 1.3 \cdot 10^5$. In the context of our investigations these requirements were fulfilled within the range of maximum occurring lifting forces and also under most other underflow conditions.

The experiments have revealed three main types of underflow conditions depending on tailwater level.

6.1 Phase I of underflow

If the tailwater-level is low, the discharge occurs as a free jet. This free jet in the downstream direction does not touch the bottom seal which is at the upstream end of the draft tube. The flow around all construction elements upstream of the sealing face (trash rack, generators, etc.) causes an increase in the hydrodynamic uplift forces acting on the module. The jet emerges into tailwater and the discharge depends on the opening of the module at a maximum.

6.2 Phase II of underflow

The tailwater-level is so high that the bottom jet touches the end of the draft tube. As a result of the flow-deflection at the draft tube downstream of the bottom seal, additional negative pressure forces—and thereby greater downpull forces—are generated. Energy dissipation with intensive waves formation acting immediately downstream of the draft tube leads to massive buoyancy fluctuations on the module and activate maximum downpull forces. According to the opening of the module the downpull is at a maximum level.

6.3 Phase III of underflow

The module is fully submerged by the tailwater. The lifting forces are reduced by the action of full buoyancy forces. According to the opening of the module the discharge decreases to a greater extent.

7 EXPERIMENTS

A sectional Plexiglas-model of the HYDROMATRIX[®] power module, developed for the ship navigation and flood control dam, was set up in a 44 cm wide flume at the hydraulic laboratory of the Institute of Hydraulic Engineering of Vienna University of Technology. This sectional model embodies 3 turbine-axes in with. The tests were carried out according to the Froude's law of similarity using a model scale of 1:12.5 (Kobus, 1978).

A so-called “emergency case”—due to functional problems the radial gate could not be moved from the opening position—was simulated. The downpull forces acting on the module in different opening positions were measured according to different underflow conditions. These downpull forces had strong dynamic properties caused by an extensive formation of waves by submerged surface roller. The dynamic forces resulted vibrations, but the natural frequency of the module was quite different from the frequencies of the acting dynamic forces.

7.1 Test results

In underflow phase I a relatively constant downpull occurred in a range of maximum magnitude of little more than one half of the dead weight of the HYDROMATRIX[®] power module. Maximum downpull forces act in phase II, if the jet hits the downstream edge of the draft tube.

8 CONCLUSION

This paper is mainly concerned with the application of HYDROMATRIX[®] technology. HYDROMATRIX[®] technology is a most economic turbine-generator-solution for low-head hydropower applications in existing dams or weirs. The practical application of HYDROMATRIX[®] technology is the HYDROMATRIX[®] power module. HYDROMATRIX[®] module is a new concept of hydropower utilization. The module is a

compact arrangement of unregulated propeller turbines with pertinent facilities. If a HYDROMATRIX[®] power module is installed in weir structures, it has to ensure the energy generation as well as the function of a gate or an emergency stop log. For this purpose hydraulic model tests were carried out to determine the lifting forces of a HYDROMATRIX[®] power module during flood flow. In correlation to the tailwater-level different underflow conditions (phases) could be observed. These flow types basically influenced the size of the lifting forces.

REFERENCES

- Drobir, H. 2002. Hydromatrix—A new way to generate hydropower. *Annuaire de l'univerite d'architecture, de genie civil et de geodesie—Sofia. Proceedings*: 1–9.
- Drobir, H., Kienberger, V & Seyerl, J. 2001. Downpull on tunnel-type high-head leaf gates. XXIX IAHR Congress Proceedings, Theme D, Vol. II: 473–478.
- Kobus, H. 1978. Wasserbauliches Versuchswesen. *Mitteilungsheft Nr.4. Deutscher Verband für Wasserwirtschaft*.
- Markovic, J., Prenner, R. & Drobir, H. 2003. Reduction of downpull for forces on high head gates. XXX IAHR Congress Proceedings, Theme D: 535–542.
- Naudascher, E. 1991. Hydrodynamic Forces. 3. IAHR Hydraulic Structures Design Manual. Rotterdam: Balkema.
- Prenner, R., Yücel, L. & Kienberger, V 2003. A new concept in hydropower- HYDROMATRIX[®]-technology: Drag forces on a advanced HYDROMATRIX[®]-module. XXIX IAHR Congress Proceedings, Theme D, Vol. II: 743–750.
- Prenner, R. & Drobir, H. 2002. Downpull tests on a HYDROMATRIX[®] module Report of the Institute of Hydraulic Engineering, Vienna University of Technology.
- VA Tech Hydro. 2001. HYDROMATRIX[®] product information
- VA Tech Hydro. 2001. Water. Power. Hydromatrix. <http://www.hydromatrix.com/>.

3.

Hydrodynamic forces

Impulse waves from laboratory scale to mega-tsunamis

Willi H.Hager, Hermann M.Fritz* & Andreas Zweifel

VAW, ETH-Zentrum, Zurich, Switzerland

*Presently Georgia Institute of Technology, Savannah, USA

Hydraulics of Dams and River Structures—Yazdandoost & Attari (eds)

© 2004 Taylor & Francis Group, London, ISBN 90 5809 632 7

ABSTRACT: Impulse waves are counted to the most dangerous natural hazards, because of the large masses of slide material involved, the huge waves triggered on large water bodies and their tremendous devastation potential. A spectacular and destructive impulse wave in relation to hydropower installations occurred on October 9, 1963 in North-eastern Italy. Since this incident, dam safety has become a global issue and all major dams have to be assessed against such phenomena.

VAW has conducted a variety of experimental research relating to impulse waves, mainly to account for the large risk that is involved with these natural hazards in relation with reservoirs to produce hydropower in Alpine countries. Within the past six years, two PhD theses were completed of which the primary purpose was to investigate these devastating waves, thereby using modern instrumentation and advanced computer systems for data analysis and evaluation. The following is a summary of results that may be of interest to hydraulic engineers both working with scale models and with numerical methods.

1 INTRODUCTION

Impulse waves are among the largest waves that occur on earth, with recorded wave heights up to several hundreds of meters, as compared to maximum waves due to wind or earth quakes of typically 10m. Impulse waves are thus also referred to as *mega tsunamis*.

Impulse waves may produce devastating natural disasters when impacting large water bodies such as man-made reservoirs, lakes or fjords provided nearby infrastructure or villages are involved. The most important historical event occurred on October 1963 at the Vajont dam in Northern Italy, thereby generating a huge impulse wave that overtopped the arch dam and rushing down to the Longarone village. Within seconds, almost the complete settlement was flooded leaving back some 2500 fatalities. The slide volume was $V_s=240 \times 10^6 \text{ m}^3$, had a density of roughly $\rho_s=2.6 \text{ t/m}^3$, the slide angle was $\alpha=40^\circ$, the reservoir volume was $V_w=115 \times 10^6 \text{ m}^3$, its maximum depth amounted to

$h_{max}=240$ m and the maximum wave run-up height at the opposite reservoir shore was $R_{max}=270$ m. Figure 1 shows an imaginary impulse wave on Vajont reservoir which destructed the village after the flood wave had passed. This incident marked the real initiation for the presently well established *dam safety regulations* applied worldwide, because it demonstrated at once that dams have to withstand such catastrophes to exclude dam overtopping in the future. Figure 2 shows photographs in the aftermath of the tragedy. One may see the slide area and the arch dam, as also the run-up reach on the right reservoir side. Other impressive photographs are available by Weber (1964) and Kiersch (1964).

Impulse waves received research attention after World War II mainly in the USA, such as by Johnson and Bermel (1949). These experiments involved steel disks that were dropped into shallow water and represented a simulation of the nuclear bombs released on the Bikini atoll. Wiegel (1955) used triangular wedges and rectangular bodies to model slides in water bodies. Yet, his experiments were conducted below the water surface and thus may not be realistic to compare rigid body with granular slides. Prins (1958) also dropped rigid bodies onto a water surface and looked mainly at the wave propagation process. No description of wave generation accompanied this research. Nakamura et al. (1969) again employed rigid bodies to simulate the generation and run-up of tsunamis on shores. Kamphuis and Bowering (1970) conducted an experimental study in which a weighted tray

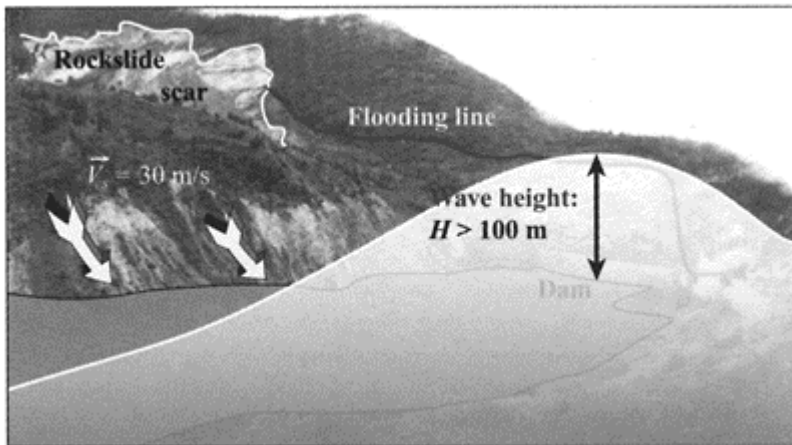


Figure 1. Sketch of impulse wave as generated on Vajont reservoir in 1963 (Zweifel 2003).

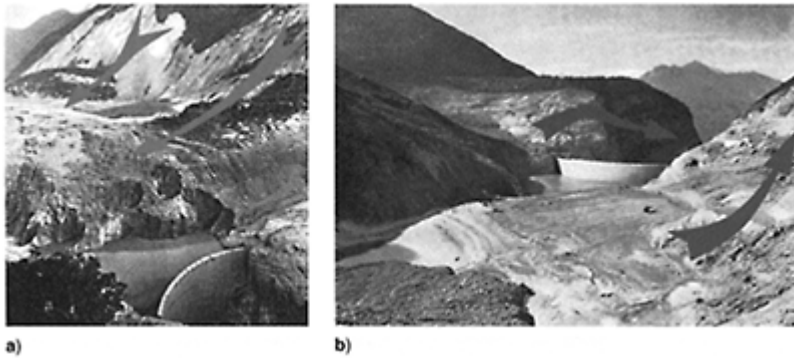


Figure 2. Vajont disaster (a) slide area on the left reservoir side, (b) run-up area on opposite side.

was emplaced by a roller ramp into a flume 45 m long. This study demonstrated the effect of slide Froude number on the maximum wave height. A significant paper was presented by Wiegel et al. (1970) relating to the linear wave theory and a comparison with model observations. Some effects of the usually non-linear tsunamis were obtained but the major characteristics of waves generated again by vertically falling bodies were in disagreement with observations. A major conclusion of this study was that Froude similitude may be applied to such phenomena, provided attention is paid for scale effects.

A computational approach towards impulse waves was presented by Noda (1971). His approach is limited mainly by the complex wave generation mechanism and the highly non-linear wave equations. Raney and Butler (1976) presented a simplified numerical model to predict wave propagation over a reservoir and conducted model tests for the Libby Dam, USA. They clearly stated that impulse waves cannot be exclusively modelled numerically (at that time) and that model observations in this research domain are essential. Pugh and Harris (1982) studied a particular dam site and determined the prominent features of impulse waves with a hydraulic model. Their results are site specific as most others and may not readily be used for general statements. The photos shown by Bertacchi et al. (1988) in the aftermath of the *Val Pola* rockslide in Valtellina, Italy, may give an impression of the forces that result from such natural disasters. In this case, a water body formed because of the slide deposits across the valleys, which would have broken if no bypass tunnel had been erected for its drainage. Harbitz et al. (1993) presented a mathematical model based on the shallow water equations to simulate impulse waves in Norway's fjords. Their problems were as with previous modellers because impulse waves are essentially in the transition regime between the shallow and the deep-water waves, for which the pressure distribution is non-hydrostatic, i.e. in disagreement with the basic shallow water wave assumption. Recently, Mader and Gittings (2002) reproduced the main flow features of the Lituya Bay case study (Fritz et al. 2001) with a full Navier-Stokes Automatic Mesh Refinement AMR Eulerian compressible hydrodynamic code.

This review demonstrates a relatively small research activity in this field. The main reasons are: (1) Impulse waves produced by granular slides involve a complex three-phase flow; (2) Numerical modellers need to know the wave generation process to initiate wave generation; (3) Instrumentation needed to investigate such flows is complicated and costly; and (4) Most funding is directed to case studies such that practically no generalised results are available. VAW was involved in the understanding and the physical modelling of impulse waves since decades. The present international design guidelines are partly based on these research projects. Since the early 1970s, various research projects were conducted, such as by Huber (1980) to detail the difference between solid block and granular slides. Sander (1990) then investigated propagation features of impulse waves in a two-dimensional channel. The run-up characteristics of impulse waves on adjacent water body shores were investigated by Müller (1995) thereby pointing to the effect of small energy dissipation during the run-up process because those waves hardly break. These works were summarized by Vischer and Hager (1998).

The most recent works on impulse waves were conducted by Fritz (2002) and Zweifel (2003). Fritz designed a novel experimental stand including a *pneumatic landslide generator*, in which masses of up to 108 kg of various shapes were accelerated to result in slide impact velocities of almost 10 m/s (Fritz and Moser 2003c). The slide shape prior to impact onto the water body was scanned with two *laser distance sensors* to investigate the slide profile. The pneumatic slide generator allowed a release of well-controlled slides and thus gives well-defined initial conditions for wave generation. The exact wave profiles along with the temporal development of the slide profiles in the wave channel are thus available. A pulsed laser light sheet served as a basis for *Particle Image Velocimetry* (PIV) observations to study the initiation and generation of impulse waves. Over three seconds some 150 images could be stored in the computer to detract velocity profiles at various incidents of slide impact onto the water body. Typical results obtained by Fritz (2002) are summarized below. The propagation of impulse waves over the test channel was then recorded with capacitance wave gages along the 8 m long tailwater reach.

Whereas Fritz (2002) and Fritz et al. (2003, 2004) contributed mainly to the understanding of impulse wave generation due to granular slides, Zweifel (2002) and Zweifel et al. (2003) investigated both the propagation characteristics of impulse waves, and the effect of slide density on the main wave features. Two additional items have so far not received attention, namely the effects of impact slide angles and the slide sediment non-uniformity. These are subjects to deal with in the future.

2 DESCRIPTION OF EXPERIMENTS

The advance of experimental instrumentation has had a significant impact on the solution of extremely fast flow phenomena. Both Fritz and Zweifel profited from recent developments to investigate the three-phase flow features of impulse waves, namely a solid granular slide into a fluid body that entrains air at higher slide velocities. The results contributed to the understanding of impulse wave generation and propagation.

Figure 3 shows the experimental setup in a rectangular channel 11 m long, 0.50 m wide and 1 m high. The propagation of waves along the channel was recorded with capacitance wave gages of 1 mm water depth reading accuracy, provided observations

were with blackwater. As discussed below, impulse waves may entrain air at the wave front due to turbulence. The accuracy of these gages could be poorer under those conditions, and the wave profiles were analyzed in detail to remove errors from this feature. The channel where the impulse waves were generated was covered because of spray that might damage the instrumentation. A detailed description of the test stand and the instrumentation used is available (Fritz 2002).

The slides were generated with granulate to simulate conditions as occur with glacier or rock falls. Up until today, most research was conducted with rigid bodies. The experiments are then simpler because the release and the impact onto the water body may be easily controlled. It was decided to use granular slides to retain the main features of real-world slides resulting in complications with the methods adopted and in increased cost for the instrumentation.

Figure 4(a) shows the slide granulate used for the present research. It consists of Barium-Sulphate coated with plastics. Preliminary experiments revealed that usual gravel had a large drawback because of scratching the windows of the test channel. The finally selected material had a typical

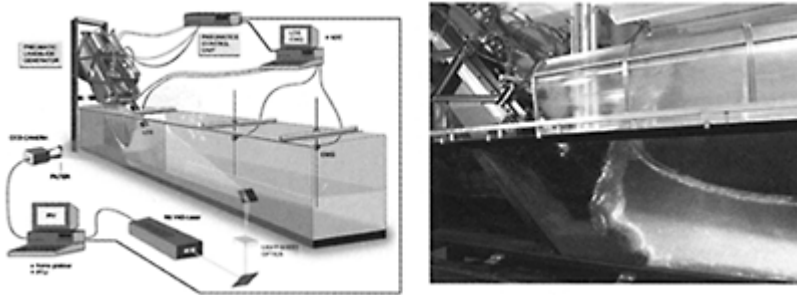


Figure 3. Experimental set-up including pneumatic landslide generator, laser distance sensors, capacitance wave gauges and digital particle image velocimetry.

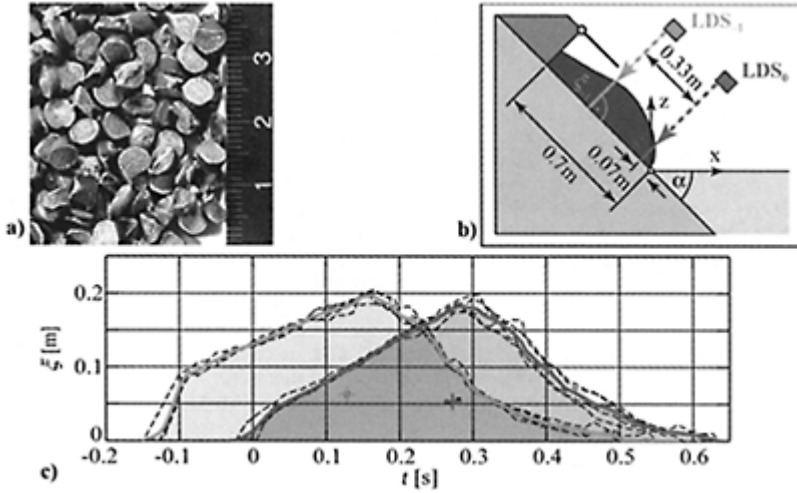


Figure 4. Slide granulate and granular slide profiles prior to impact on water body.

diameter of $d_s=4$ mm, a grain density $\rho_g=2.64$ t/m³, a porosity of 39%, an internal friction angle of 43° and a dynamic bed friction angle of 24° (Fritz 2002). Figure 4(b) shows the two scanning sensors for the definition of the slide profile at impact onto the water body, whereas Figure 4(c) relates to the two slide profiles mentioned.

The experimental installation allowed producing impulse waves for a variety of experimental conditions. Figure 5 is a definition sketch. At the impact moment, the slide (subscript s) may be defined with its maximum height s , its volume V_s , its density ρ_s and its length. The latter effect is relatively small given that various slide shapes led to identical results, except when the slide velocity is extremely small and the momentum added by the slide may have an effect on the water wave. Slide masses $m_s=\rho_s V_s$ of 27, 54 and 108 kg were considered, slide densities were 0.95, 1.65, 2.20 and 2.65 t/m³, slide heights as released from the pneumatic slide generator were between 0.05 and 0.20 m, and at impact usually some 80%, slide lengths were varied between 0.50 and 2.3 m, the impact velocities of the gravitational slide center were from 2 to some 9 m/s, and still water depths ranged from $h=0.15$ to 0.675 m. As mentioned, the slide angle $\alpha=45^\circ$ was kept constant. The main parameters investigated were the absolute wave maximum a_M , the development of maximum amplitude along the channel $a(x)$ where the coordinate system $(x; z)$ had its origin at the intersection of the water level with the slide ramp. Further, the wave celerity c was investigated along with the wave length L .

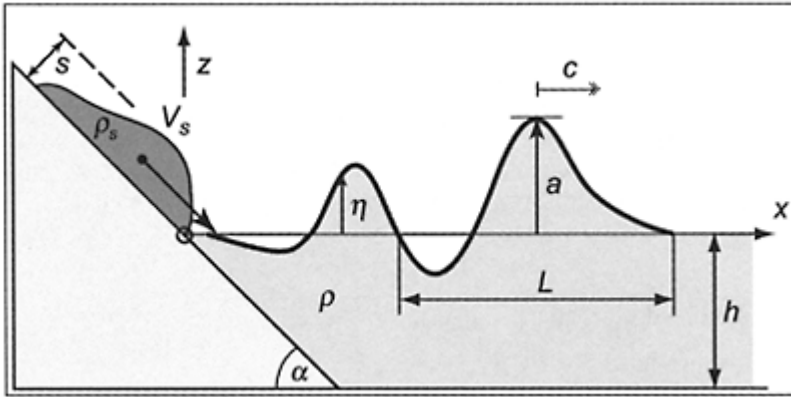


Figure 5. Definition sketch for plane impulse waves.

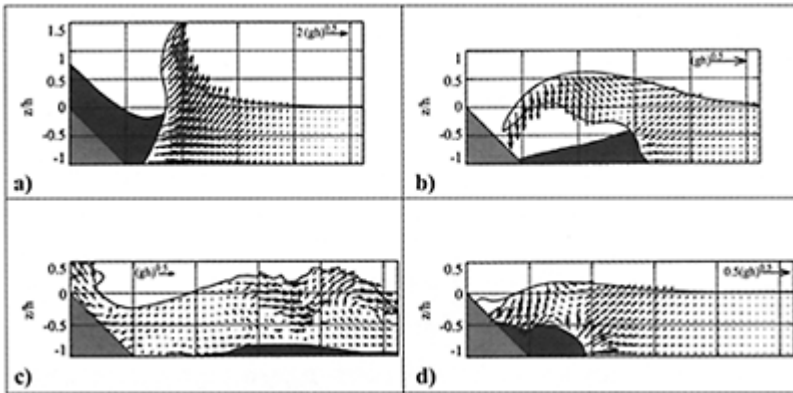


Figure 6. Principal impulse wave types according to Fritz (2002).

3 MAIN FLOW PHENOMENA

The generation of impulse waves is closely associated with the so-called slide Froude number $F = v_s / (gh)^{1/2}$, where v_s is slide impact velocity, g is gravitational acceleration, and h is still water height, with subscript s denoting slide parameters (Fig. 5). The following first part refers to slides of density $\rho_s = 2.65 \text{ t/m}^3$, for which the effect of relative density is dropped, therefore. Depending on F , Fritz (2002) introduced four different wave generation types, namely (Fig. 6):

- (1) *Outward collapsing impact crater* involving a large pressure interface between the slide front and the water resulting in an almost vertical piling up of the wave origin;

- (2) *Backward collapsing impact crater* in which the slide material glides below the water and generates a reversed flow over the slide separated with an immense air cavity;
- (3) *Dissipative transient bore* similar to a typical diameter of $d_s=4$ mm, a step-like propagation of a hydraulic surge; and
- (4) *Unseparated flow*, in which the slide material glides gently below the water body, lifts the latter and pushes the water in the downstream direction.

These wave types were identified in the order of reduced slide Froude numbers, i.e. (1) occurs for extremely large F typically of the order of 5, whereas (4) results for small F of the order of 1 to 2. The Vajont case has an impact velocity of 30 m/s, a water depth of 200 m, such that $F=1.1$, resulting in a solitary wave that propagated over the dam crest with a celerity of $c=[g(a+h)]^{1/2}=55$ m/s, where $a=100$ m is the wave amplitude.

According to Fritz (2002) flow separation and the impact crater types may be predicted by accounting for the slide Froude number F and relative slide thickness $S=s/h$. Flow separation was defined by the occurrence of a water body detachment on the back of the slide. For separated flows, an air cavity is located between the upward water body and the downward slide material. The Froude number separating (subscript S) these two flow types is defined as

$$F_s=[(5/3)+(1/2)S] \quad (1)$$

The two types can thus be described as

- A. Unseparated flow provided $F < F_s$
- B. Separated flow provided $F > F_s$

Another general classification of impulse waves as introduced by Fritz relates to impact phenomena with, and without an impact crater (subscript C). With

$$F_c=[4-(5/2)S] \quad (2)$$

the two types may be specified by

- C. Backward collapsing crater wave type $F < F_c$
- D. Outward collapsing crater wave type $F > F_c$

Figure 7 shows these four types and illustrates the various types with typical impact photos. The research project of Zweifel (2003) related to the propagation features of impulse waves in the same two-dimensional channel as a test case for future numerical modelling. The maximum (subscript M) relative wave height $A_M=a_M/h$ close to the slide impact region depends significantly on the slide densimetric Froude number F_s , and slightly on the relative slide thickness $S=s/h$. Large waves result for high impact velocity, relatively small still water depth and high slide density, therefore. Further, the wave propagation characteristics were studied using more than 200 detailed wave experiments with four different relative slide densities, and different slide geometries varying from short-high to long-low shapes. All wave profiles defined a unique wave decay with the relative

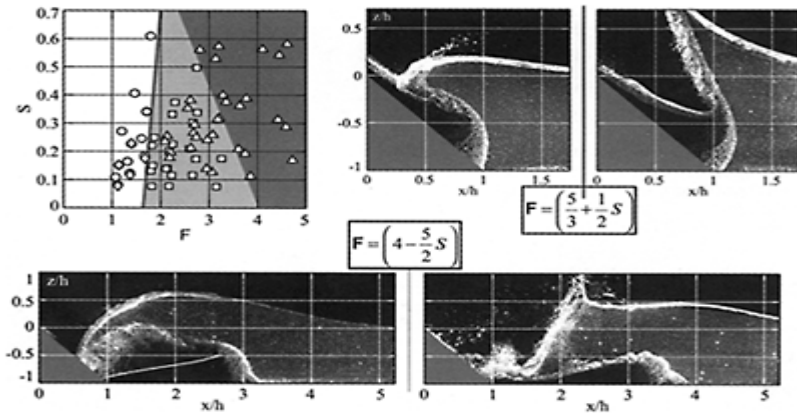


Figure 7. Flow separation and impact crater types (Fritz 2002).

amplitude A as a function of the slide densimetric Froude number and the relative location $X=x/h$. Accordingly, the two researches allow insight in the most prominent features of impulse waves under two main restrictions:

- (1) All results apply only for a *slide angle* of $\alpha=45^\circ$, which may be considered typical in applications, yet is a major restriction, and
- (2) Results were generated with uniform granular material. Applications involve sediment mixtures, and it is yet unclear whether a median sediment size may be used for appropriate description of granulometry.

4 RESULTS

4.1 Unseparated flow type

Figure 8 relates to the main features of the flow field for unseparated flow, as previously defined. It is seen that the impact of the slide front creates a wave crest in the water body, whereas the slide end gives a wave trough. Once the entire slide has entered the water body, a secondary wave is generated whose height is smaller in most cases, however. The water displacement is similar as the slide volume. The air detrainment at the end of slide flow into the water indicates the presence of water flow through the granular slide body, given that the pore volume is filled with water, resulting in large air pockets that rise from the back of the slide. In unseparated flow the amount of air induced into the water body by the slide detrainment increases proportionally with the slide volume. The air detrainment reduces relatively fast with time, such that the second wave was formed mainly by the run-up along the inclined ramp in the wake of the slide and subsequent run-down (Fig. 6c).

The vector fields involving the streamwise and transverse velocity components are also shown in Figure 8. Additional plots of the streamlines by Fritz reveal the formation

of a full saddle point in the back of the slide. The location of the saddle point indicates the location of instantaneous zero velocity points. The largest absolute water particle velocities in the wave field were measured always below the wave crests, yet this was only a small portion of the shallow water wave propagation velocity. The vertical particle velocities were zero along vertical lines through the wave crests, and they were a maximum at the location of the largest slope of the water surface. The in-plane

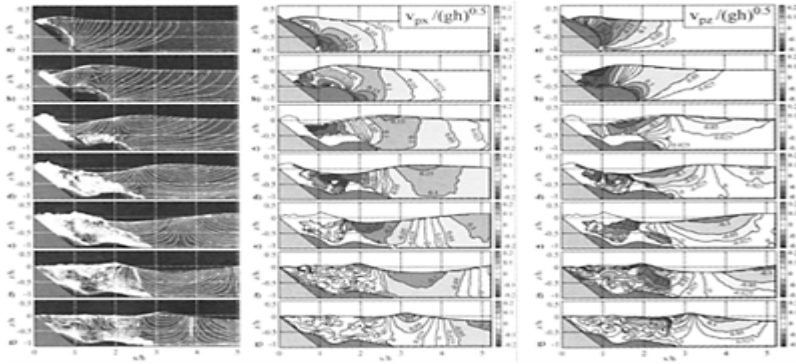


Figure 8. Prominent features of unseparated flow field for $F=1.7$, $V=0.39$, $S=0.19$, $h=0.30$ m (Fritz 2002).

divergence of the flow field was roughly zero in the entire blackwater flow area. Accordingly, the fundamental assumption of a two-dimensional model is confirmed. No out-of-plane motion was observed except in the massive phase mixing and the dissipation area in the wake of the slide.

The water flow in the wave generation area and the flow below the outward propagating impulse waves were irrotational. Vorticity was observed on the slide surface due to the shear and in the mixing zone above the landslide deposit due to dissipative turbulence. The PIV data confirmed the assumption of irrotationality made by the wave theories according to the Laplace equation. A stream function thus determines the velocity vector field. The first wave crest and wave trough have significantly different characteristics than the second wave. The leading wave is of intermediate water depth wave close to the shallow water wave regime whereas the trailing waves closer to the deep water wave regime. The second wave exhibits the classical Stokesian wave profile, as defined by Wiegel (1964) or Le Méhauté (1976).

4.2 Outward collapsing crater flow type

Figure 9 shows a typical example of the outward collapsing impact crater regime with a Froude number of $F=3.2$. The water flow around the penetrating landslide separated on the slide shoulder; the water was initially expelled upwards and outward by the entry of the slide front thus forming a water crater. This crater exposed the ramp and the back of

the slide to the atmosphere, with a water volume exceeding the slide volume significantly. When the growth of the crater is terminated outward bulk motion of water was still present as a residuum. The collapse occurred after the water crater had reached its maximum size and the water rushed inwardly due to gravity. The outward collapsing crater resulted in a main positive leading wave and a negative surge. The inrush of water tended to fill the crater from downstream. The backward motion was initiated at the bottom of the crater wall where the pressure is a maximum. The leading wave crest was issued by the crater rim and propagated outward during the crater collapse. The run-up of the surge on the inclined ramp and the subsequent run-down formed a secondary wave system.

The velocity vector fields and the streamline plots reveal the formation of a half saddle in the water uplift zone above the deposition ridge. This half saddle separates the outward from the inward flow. The largest velocities were measured locally around the slide front during slide penetration into the water body, and in the splash. The water particle velocity below the wave crests was only a

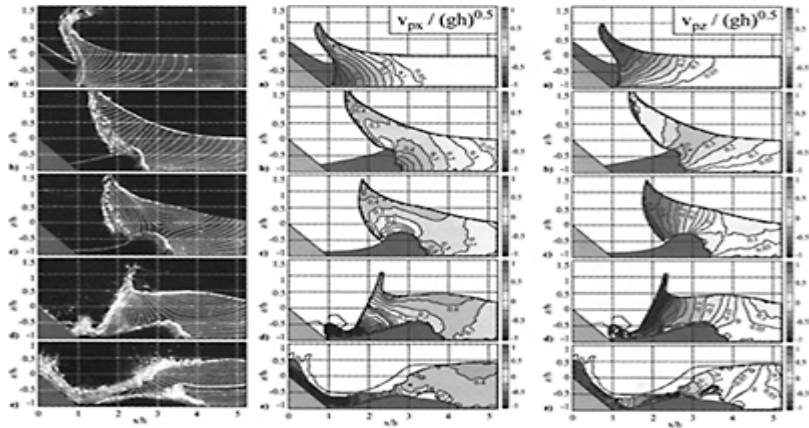


Figure 9. Outward collapsing crater flow field for $F=3.2$, $V=0.79$, $S=0.31$ and $h=0.30$ m (Fritz 2002).

fraction of the shallow water wave velocity, yet was larger than for the previous case due to increased wave height. The largest negative values of the horizontal velocity components were observed in the inward rush and run-up along the inclined ramp during the collapse of the impact crater. The negative vertical velocity maxima were observed at the beginning of the crater collapse along the crater walls.

The kinetic energy of the landslide imparted on the water body was only partially converted into the potential energy of the uplift, whereas a significant part prevailed as kinetic energy in the form of the velocity field imposed onto the water body. The in-plane divergence was roughly zero again in the blackwater region, confirming the existence of a velocity potential. Large divergence was observed during the cavity collapse and the inward rush. Slide granulate was sheared off during the penetration of the slide. It then

detached from the crater wall and fell through the water during cavity collapse. Noteworthy are the large negative divergence values along the slide front during slide penetration, which indicate the presence of a low velocity water flow through the granulate during slide detrainment. The features of irrotationality and vorticity generation during slide impact were similar as for the unseparated flow regime.

4.3 Bore formation regime

Figure 10 refers to the trailing bore formation as observed for the largest slide Froude numbers. This caused an outward collapsing impact crater analogously to Figure 9. The sequence begins with the first wave trough after the leading wave crest has left. The local reduction in water level is transmitted outward as a wave trough. The inward motion along the channel bottom collides with the run-down forming a surge. This surge propagates outward on the top of the backward flow as a transient bore, a key feature being the dissipation process during its early phase. While the collapse of the crater is not dissipative a considerable amount of the energy imparted to the fluid is lost as a result of turbulent mixing at the impact site from the rebound of the inward flow. The energy dissipation in a transient bore was computed numerically with the momentum and the Bernoulli equations. In contrast to the trivial solutions of a hydraulic jump the full forms including the unsteady terms were considered. The energy dissipated remained constant at roughly 40% of the total energy supply by the landslide, independent of the lip shape. The bore propagated roughly at the shallow water wave celerity, as discussed below. As the bore propagates and decays, it is transformed into a non-breaking bore and finally into a non-linear wave. Once the underlying incoming flow reaches subcritical conditions or the bore height becomes smaller than 60% of the

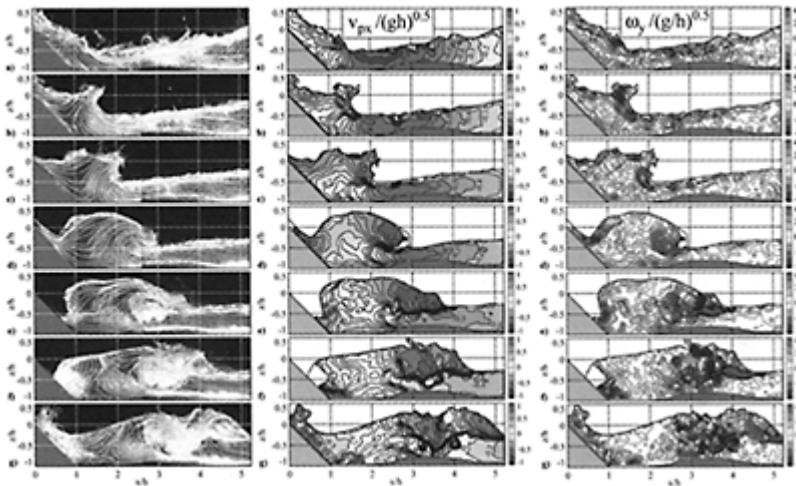


Figure 10. Features of typical trailing bore formation for $F=4.7$, $V=0.39$, $S=0.17$, $h=0.30$ m (Fritz 2002).

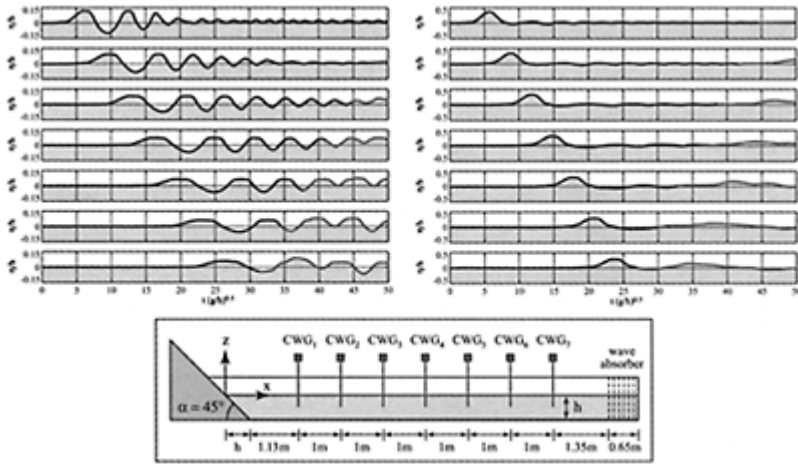


Figure 11. Wave gage recordings for Non-linear oscillatory wave (left) and Solitary-like wave (right); Definition of wave gage location (bottom).

incoming flow depth, the dissipative bore no longer exists (Le Méhauté 1976). Then, it transforms into a transitory non-dissipative undular bore.

The internal flow features of the trailing bore regime were again detected with PIV analysis. A half-saddle along the ramp marked the collision between the rush-down and the inward rush resulting in a spike at the free surface. The half-saddle propagated outward with the bore. The largest velocities were measured locally along the ramp and in the breaking bore. The horizontal water particle velocity in the bore exceeded even the shallow water wave velocity based on the still water depth. The vertical velocity in the bore was smaller than the horizontal components. The in-plane divergence field was significantly noisier than for the previous flow types due to massive phase mixing and air entrainment during bore formation. In contrast to the previous flow types, the positive vorticity values were much larger due to the wave breaking process, such that the assumption of irrotational flow does not hold for the bore regime.

4.4 Wave propagation

The wave propagation features were recorded with seven capacitance wave gages, as previously mentioned. Due to the relatively short wave channel, only the near-field of impulse wave propagation was investigated. Except for some special experiments, the still water depth was kept at a minimum of $h=0.30$ m to inhibit scale effects mainly due to viscosity. Impulse waves may generate four different wave types, namely (1) Non-linear oscillatory waves, (2) Non-linear transition waves, (3) Solitary-like waves and (4) Dissipative transient bores (Fig. 11).

Figure 12 relates to cases (1) and (3) and defines the location of the wave gages within the wave channel. The waves observed in the present research may be classified into four domains, as shown in Figure 12. The classification involves again the slide Froude number $F = v_s / (gh)^{1/2}$ and the relative slide thickness $S = s/h$. Depending on the wave types (1) to (4), one may observe from Figure 12 and with $F(i) = (l_i - 8S)$ where $l_i = 4, 6.6, 8.2$ for wave transitions $i = 1, 2, 3$

$$\text{Type(1)} \quad F < F_{(1)} \quad (3)$$

$$\text{Type (2)} \quad F_{(1)} < F < F_{(2)} \quad (4)$$

$$\text{Type (3)} \quad F_{(2)} < F < F_{(3)} \quad (5)$$

$$\text{Type(4)} \quad F > F_{(3)} \quad (6)$$

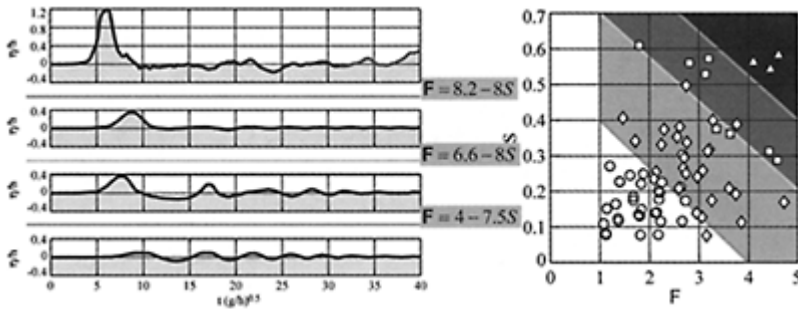


Figure 12. Wave type classification based on wave profiles (left) and diagram showing wave types plotted in a diagram slide Froude number versus relative slide thickness (right).

Type (1) thus results for relatively slow and thin slides; type (2) to (4) waves were produced by slides with a continuously larger slide Froude number F or a larger slide thickness S . Details on wave breaking characteristics are given by Fritz (2002).

4.5 Maximum wave crest amplitude

The maximum amplitude a_C of a wave crest (subscript C) observed during impulse wave generation and propagation is of interest. The data of Fritz result in ($R^2 = 0.93$)

$$a_C/h = (1/4)F^{1.4}S^{0.8} \quad (7)$$

or approximately proportional to $(F^2 S)^{3/4}$ demonstrating the dominant effect of the slide Froude number, and a smaller effect of the relative slide thickness. Note that the relative slide volume $V=V_s/(bh^2)$ had no effect on the maximum crest amplitude indicating that the slide front has the main influence on the wave propagation mechanism and thus the maximum wave amplitude.

4.6 Wave celerity

The wave propagation velocities of individual wave crests and troughs were determined from gage to gage. A definition plot is given in Figure 13. For each run six wave celerities were determined over a range of $3 < X < 25$, where $X=x/h$ is the relative streamwise coordinate with the origin as defined in Figure 5.

The celerity of the leading (subscript 1) wave crest c_{c1} may be compared with the theoretical approximation for a solitary wave

$$c_{c1}/(gh)^{1/2}=1+(a_{c1}/2h) \quad (8)$$

Note that (8) is a first order approximation of the wave celerity $c_{c1}=[g(a_{c1}+h)]^{1/2}$ as proposed by Russell and Boussinesq in the 19th century. Figure 13 compares the experimental data with (8) from where a reasonable agreement is noted for the first wave crest, whereas the second wave crest propagates some 20% slower than predicted with (8). A similar result was also found for the first and second wave troughs, which lags accordingly the solitary wave celerity. Fritz (2002) considered also the wave length evolution, the wave length prediction, the wave non-linearity, the leading wave crest volume, and the impact energy conversion.

4.7 Energy conversion

The kinetic impact slide energy is $E_s = (1/2)m_s v_s^2$ for which v_s is the centroid velocity upon impact on the water body. This amount of energy is converted by the impact process and results in a reduced

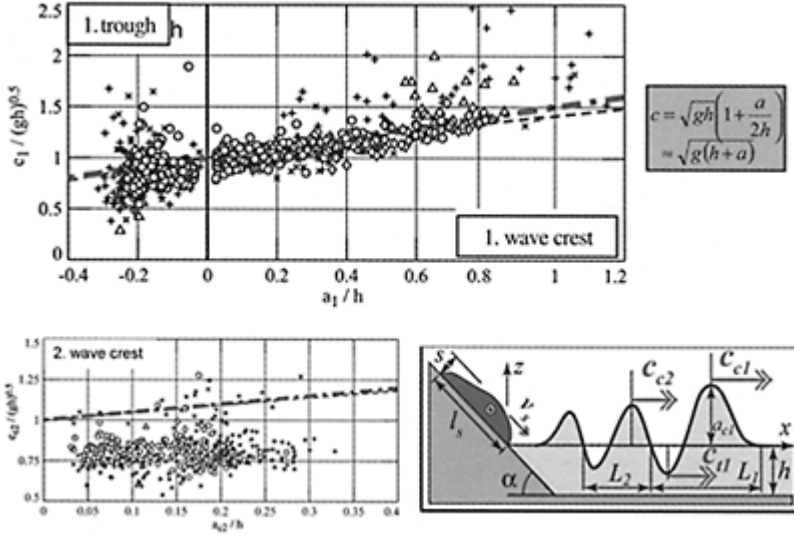


Figure 13. Wave celerity of first and second waves, and definition sketch for celerity observation.

energy content in the downstream wave train, due to energy dissipation during the mass transfer. Both the kinetic and the dynamic energies of the wave train were numerically determined based on the wave gage records. Two procedures were considered: (1) Integration encompassed only the first wave crest to result in E_{c1} over the length L_1 of the first wave; and (2) The total wave train energy E_{wt} comprising the entire energy from the initial rise to the end of the wave train. Figure 14 shows the main results as

$$E_{c1}/E_s = 0.10F^{0.8}V^{-0.3} \quad (9)$$

$$E_{wt}/E_s = (1/8)F^{0.5}V^{-1} \quad (10)$$

In Eq. (9), the relative slide thickness has a dominant effect, whereas this role is taken over by the relative slide volume in (10). Between 2 and 30% of the slide energy are transferred to the first wave crest, whereas some 5 to 40% may be transferred to the total wave train.

4.8 Applicability of classical wave theories

All measured impulse waves were non-linear. However, there exists no general non-linear wave theory as compared to those for the shallow water or the deep water linear waves. The Stokes theory of finite amplitude deep water waves, the cnoidal and the solitary waves theories are the main frame works available for non-linear waves. The range of validity of the Stokes, and the cnoidal wave theories may be defined depending

on an Ursell number $U=aL^2/h^3=26$, as shown in Figure 15. The cnoidal wave theory may be applicable for most impulse waves as occur in nature, and it applied in particular to the leading wave characteristics, as was also demonstrated with the expression for the wave celerity. However, for $U<26$, i.e. for long and short waves, the Stokes wave theory applies to impulse waves. Often, this limitation refers to the trailing wave portion from the second wave crest backwards. A major result of this research thus demonstrates that the shallow water wave equations are a poor selection for impulse waves.

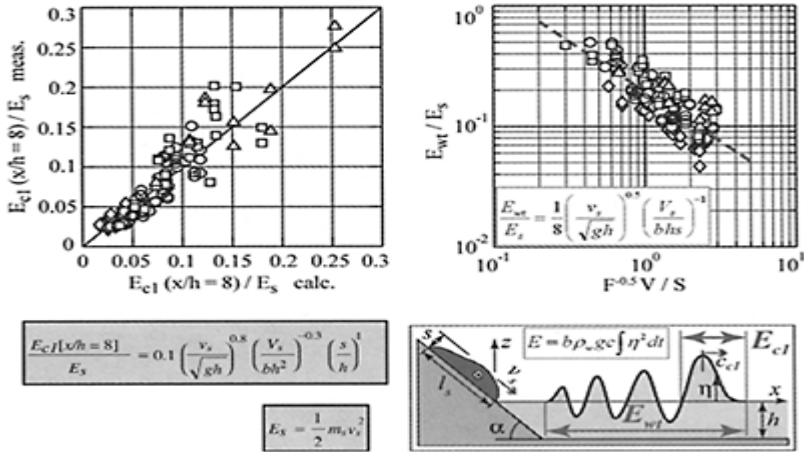


Figure 14. Slide to wave energy conversion, including relative energy content of first wave crest and of total wave train; Definition sketch.

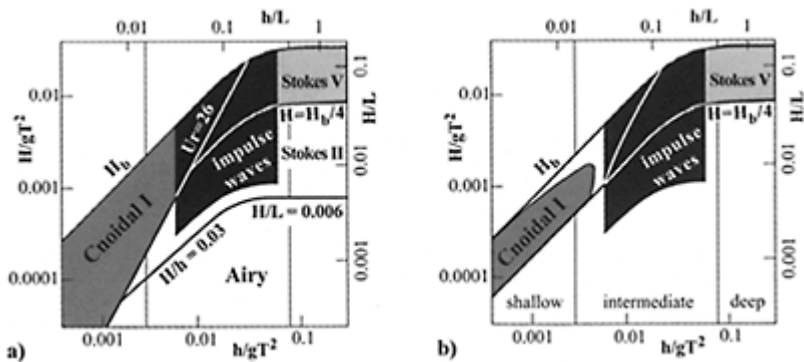


Figure 15. Comparison of impulse waves with non-linear wave theories

according to (a) Le Méhauté (1976)
and (b) Dean(1970).

4.9 Effect of slide angle

The previous results were detracted from observations with a slide angle of $\alpha=45^\circ$. The *mechanism* of wave generation may be subject to significant variation for other slide angles. From the numerical point of view, it is important to know whether all relevant angles produce almost irrotational flows, as those for 45° . Slide deposits in the water body will be more elongated for small slide angles, whereas a more compact slide deposition is expected for almost vertical slides. The air entrainment will also be relatively small for small angles, and is expected to increase with the slide angle.

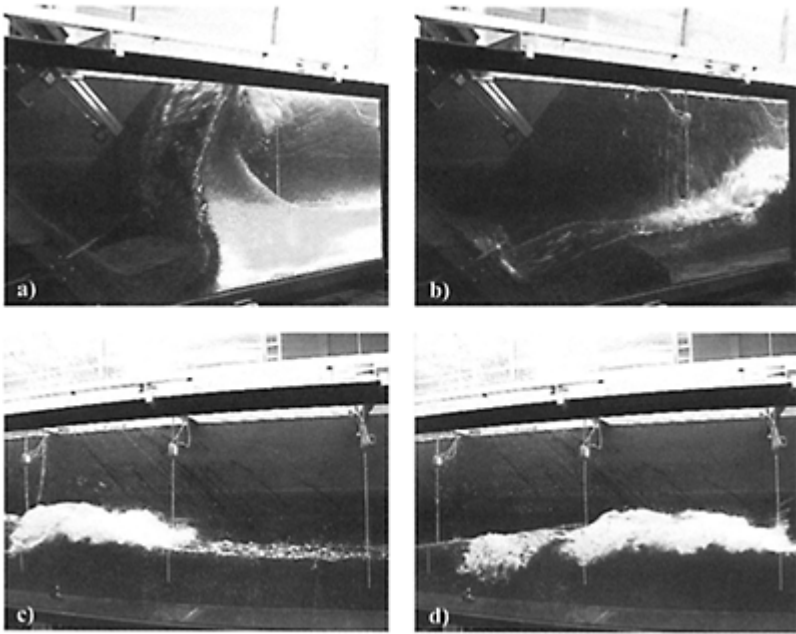


Figure 16. Spray development (top) and air entrainment in wave front (bottom) for impulse waves with a large slide Froude number (Zweifel 2003).

However, there is no quantitative information available today, such that these deficiencies must be subject of detailed future research. It will also be interesting to see whether the present capacitance wave gages may be still used under extremely large air entrainment. This aspect posed sometimes difficulties in the data analysis, because only

the fluid portion of a wave crest region could be properly recorded, whereas the top air-water layer needed some special treatment.

To apply the momentum flux equation for impulse waves shortly prior and after slide impact on the water body, the *boundary pressure distribution* along the sloping ramp and the horizontal portion of the impact reach must be known. So far, no pressure observations were collected and the fundamental equations of fluid flow may not be applied. In order to add knowledge, pressure observations with a novel device must be collected in the future. Then, both the complete velocity and boundary pressure fields are known. Figure 16 shows some interesting observations relating to the wave front characteristics shortly after slide impact and during the propagation of the leading impulse wave.

Provided the governing mechanisms of impulse wave generation and near-field propagation are understood in terms of the basic hydraulic parameters, the following problems can be solved:

1. Definition of *boundary conditions* to be applied shortly after the generation of the impulse wave, such that no detailed numerical modelling of the impact phase would be needed, including both the boundary pressure and velocity fields.
2. Knowledge of the *prominent impulse wave features* relating to the impact slide geometry, the subaqueous slide deposition geometry and the type of impulse to be expected, in terms again of the slide Froude number, relative slide thickness, density ratio between solid and fluid phases, and slide angle and granulometry.
3. Determination of the most salient characteristics of near-field impulse wave propagation to calibrate numerical codes, by accounting for both the hydraulic parameters and the reservoir geometry. These results are significant in order that computational results are realistic.

5 CONCLUSIONS

This review on the generation and propagation of impulse waves gives a summary on recently conducted research at VAW, ETH Zurich, Switzerland. It was stated that significant results may be obtained when profiting from the latest accomplishments relative to advanced instrumentation, combined with a detailed analysis of the complex experimental results. These relate at present to particular cases in terms of impact slope and slide material but may be generalized within a short time when additional research will be completed. The present data may be of value for numerical modellers to circumvent the complex impulse wave generation process that is governed by a three-phase flow in the standard case. Detailed research results may be obtained from sources specified below.

ACKNOWLEDGEMENT

The authors would like to acknowledge the support of the Swiss National Science Foundation for the projects 2100-050586.97 and 2000-061541.

REFERENCES

- Bertacchi, P., Fanelli, M., Maione, U. (1988). An overall approach to the emergence hydraulic problems from the natural dam and lake formed by the Val Pola rockslide. *16 ICOLD Congress* San Francisco C32:1439–1456.
- Dean, R. (1970). Relative validities of water wave theories. *Journal of Waterways, Harbors and Coastal Division ASCE* 96(WW1): 105–119.
- Harbitz, C.B., Pedersen, G., Gjevik, B. (1993). Numerical simulations of large water waves due to landslides. *J. Hydraulic Engineering* 119(12):1325–1339.
- Johnson, J.W., Bermel, K.J. (1949). Impulsive waves in shallow water as generated by falling weights. *Trans. American Geophysical Union* 30(2):223–230.
- Kamphuis, J.W., Bowering, R.J. (1970). Impulse waves generated by landslides. *Proc. 12th Coastal Engineering Conference ASCE* 1:575–588.
- Kiersch, G.A. (1964). Vaiont reservoir disaster. *Civil Engineering* 34(3):32–39; 34(7):70; 35(3):63; 35(9):74.
- Le Méhauté, B. (1916). *An introduction to hydrodynamics and water waves*. Springer:New York.
- Mader, C.L., Gittings, M.L. (2002). Modeling the 1958 Lituya Bay mega-tsunami II. *Science of Tsunami Hazards* 20(5):241–250.
- Nakamura, M., Shiraishi, H., Sasaki, Y. (1969). Hydraulic characteristics of tsunami acting on dikes. *13 IAHR Congress* Kyoto C6:1–15.
- Noda, E.K. (1971). Water waves generated by a local surface disturbance. *J. Geophysical Research* 76(30): 7389–7400.
- Prins, J.E. (1958). Characteristics of waves generated by a local disturbance. *Trans. American Geophysical Union* 39(5):865–874.
- Pugh, C.A., Harris, D.W. (1982). Prediction of landslide-generated water waves. *14 ICOLD Congress* Rio de Janeiro Q54(R20):283–315.
- Raney, D.C., Butler, H.L. (1976). Landslide generated water wave model. *J. Hydraulics Division ASCE* 102(9): 1269–1282.
- Weber, E. (1964). Die Katastrophe von Vaiont in Oberitalien. *Wasser- und Energiewirtschaft* 56(2/3):61–69.
- Wiegel, R.L. (1955). Laboratory studies of gravity waves generated by the movement of a submerged body. *Trans. American Geophysical Union* 36(5):759–774.
- Wiegel, R.L. (1964). *Oceanographical engineering*. Prentice-Hall: Englewood Cliffs, N.J.
- Wiegel, R.L., Noda, E.K., Kuba, E.M., Gee, D.M., Tornberg, G.F. (1970). Water waves generated by landslides in reservoirs. *Journal of the Waterways and Harbours Division ASCE* 96(2):307–333 ; 97(2):417–423; 98(1):72–74.
- VAW contributions
- Fritz, H.M., Hager, W.H., Minor, H.-E. (2001). Lituya Bay case: Rockslide impact and wave run-up. *Science of Tsunami Hazards* 19(1):3–22.
- Fritz, H.M. (2002). Initial phase of landslide generated impulse waves. *Mitteilung* 178. Versuchsanstalt für Wasserbau, Hydrologie und Glaziologie VAW, ETH:Zürich.
- Fritz, H.M., Hager, W.H., Minor, H.-E. (2003a). Landslide generated impulse waves 1: Instantaneous flow fields. *Experiments in Fluids*, to be published.
- Fritz, H.M., Hager, W.H., Minor, H.-E. (2003b). Landslide generated impulse waves 2: Hydrodynamic craters. *Experiments in Fluids*, to be published.
- Fritz, H.M., Moser, P. (2003c). Pneumatic landslide generator. *Intl Journal Fluid Power* 4(1):49–57.
- Fritz, H.M., Hager, W.H., Minor, H.-E. (2004a). Near field characteristics of landslide generated impulse waves 1: Wave profiles, amplitudes and celerity. *Journal of Waterway, Port, Coastal and Ocean Engineering*, submitted for publication.

- Fritz, H.M., Hager, W.H., Minor, H.-E. (2004b). Near field characteristics of landslide generated impulse waves. *Journal of Waterway, Port, Coastal and Ocean Engineering*, submitted for publication.
- Huber, A. (1980). Schwallwellen in Seen als Folge von Felsstürzen. *Mitteilung* 47. Versuchsanstalt für Wasserbau, Hydrologie und Glaziologie VAW, ETH:Zürich (in German).
- Müller, D. (1995). Auflaufen und Überschwappen von Impulswellen an Talsperren. *Mitteilung* 137. Versuch-sanstalt für Wasserbau, Hydrologie und Glaziologie, ETH:Zürich (in German).
- Sander, J. (1990). Weakly nonlinear shallow water waves generated by a moving boundary. *Mitteilung* 105. Versuchsanstalt für Wasserbau, Hydrologie und Glaziologie, VAW, ETH:Zürich.
- Vischer, D.L., Hager, W.H. (1998). *Dam hydraulics*. John Wiley & Sons:Chichester.
- Zweifel, A. (2002). Einfluss der Rutschmassendichte auf Impulswellen. *Mitteilung* 174:91–100. Versuchsanstalt für Wasserbau, Hydrologie und Glaziologie VAW, ETH: Zürich (in German).
- Zweifel, A., Hager, W.H., Minor, H.-E. (2003). Impulse waves: Effects of slide density. *30th IAHR Congress Thessaloniki A*: 417–424

Extreme wave transients in reservoirs, their characteristics and interaction with dams

T.L.Gvelesiani

Georgian Technical University, Tbilisi, Georgia

A.Huber

Consulting Engineer, Zurich, Switzerland

Ch.Koutitas

Aristotle University Thessaloniki, Greece

G.T.Matcharadze

Georgian Technical University, Tbilisi, Georgia

Hydraulics of Dams and River Structures—Yazdandoost & Attari (eds)

© 2004 Taylor & Francis Group, London, ISBN 90 5809 632 7

ABSTRACT: In the paper waves in natural and artificial reservoirs caused by landslides are considered. These waves can endanger human lives as well as the ecological stability of adjacent areas.

The issue is considered in the framework of investigation of a two dimensional (2D) case of the wave generation in narrow water basins. Based on the theoretical and experimental data analysis, main parameters predominantly affecting wave process in reservoir are revealed as well as wave decreasing character while it is propagating along the reservoir and wave run-up effects on dams.

Based on the analysis of computational data, a simplified “engineering” formula is obtained to ensure short-range forecasting of wave maximal amplitudes (run-up heights) on the upstream face of vertical walls (concrete dams, lakeside protective walls, steep bank slopes, etc.).

Comparison shows that the theoretical and experimental results practically are fully consistent with each other.

1 INTRODUCTION

Generation of large waves in natural and artificial reservoirs (lakes, bays, fiords, reservoirs of HPPs, irrigative basins etc.) may often be caused by rapid landslide masses effects. These extreme landslide-generated waves can be called landslidegenic or impulse waves. The water depths of these basins are comparable to the wave lengths and bear similarity with long period waves such as tsunami (Huber 1996), (Mamradze et al. 1991).

History knows many cases of generation of such waves in different reservoirs. Their overtopping of dams and transformation along up- and downstreams, may cause tremendous fatalities and property damage (Mamradze et al. 1991). Extreme cases may be caused also as a result of dam erosion and subsequent dam break flood waves in the lower valley.

Basically these waves are investigated on the basis of mathematical modeling using the small amplitude waves (SAW) and shallow water (SW) approximate theories, as well as on physical models of real reservoirs or lakes fragments.

Based on the first theory two- and three-dimensional (2D, 3D) boundary value problems were solved analytically and numerically (for prismatic and nonprismatic basins respectively) to describe potential (not rotational) motion of linear waves in relatively deep reservoirs e.g. (Gvelesiani et al. 1999b), (Mamradze et al. 1991). The same theory was used in researching seismogenic waves a dam overtopping process (Gvelesiani et al. 1992a). According to SW theory 1D and 2D (in plan) depth-averaged (water particles vertical acceleration is neglected) non-linear equations were solved numerically e.g. (Koutitas 1977), (Koutitas & Papadopoulos 1996). This theory is typically applied to relatively shallow water basins (open channels, shallow basins etc.).

In a number of cases preliminary estimates of landslidegenic waves may be adequate for practice when the knowledge of the order of magnitude is sufficient, such as for the initial stage of design of hydro-projects and feasibility studies. Furthermore, this approach is appropriate in cases of acute hazards when time is not available for scale model studies or computations. Such estimate technique has to be based on the proper empirical and theoretical (computational) data analysis and simple relationships to be developed.

2 LANDSLIDE CHARACTERISTICS

Rapid assessment of the waves amplitudes in reservoir restricted by modeling the wave process with a 2D approach will be the main issue considered below.

The empirical and computational results have shown (Huber 1996), (Mamradze et al. 1991) that the height of the maximal landslidegenic waves is a function of:

1. Slide volume W_0 being plunged into the water;
2. Duration t_0 (or velocity V_L) of the landslide diving process;
3. Geometrical characteristics of the reservoir (e.g. the water depth h and the reservoir length l for the plane 2D case of a rectangular shaped reservoir).

The first and third parameters were usually determined in advance. The process of a landslide duration in water (t_0) based on the theoretical research carried out by T.Gvelesiani (Mamradze et al. 1991) is effected by the following parameters:

$$t_0 = f[\alpha, W(x), h, \rho_s/\rho_0, s_0, f_c, K_H, L_{mid}], \quad (1)$$

where α —slope angle at the impact side; $W(x)$ —slide volume diving in water (there x is a distance along the slope counted off the water level); h —reservoir water depth near the impact site; ρ_s/ρ_0 —relative slide density (ρ_s and ρ_0 —the slide and water density); s_0 —initial distance from the frontal point of the landslide (until it begins to move) to the water level; f_c and K_H —Coulomb friction and head resistance coefficients; L_{mid} —midsection (or a characteristic height) of the landslide body.

In accordance with the computational data analysis (Mamradze et al. 1991), when h and s_0 are fixed values, the main effect on t_0 value has the first above-mentioned three parameters; thus approximately we have

$$t_0 = f[\alpha, W(x), \rho_s/\rho_0] \quad (2)$$

3 2D WAVE PROBLEM SOLUTION

The plane (2D) hydrodynamic problem relating to the landslidegenic wave generation in a narrow reservoir has been solved analytically (Mamradze et al. 1991) based on the SAW theory and the following assumptions:

- the reservoir has a rectangular shape (in longitudinal cross section);
- its depth and length (distance between landslide site and a dam) equal to h and l respectively (Fig. 1)
- the mass of the liquid, whose volume amounts to the volume of the landslide body, is flowing into the reservoir at the landslide site ($x=0$) during the time interval $0 \leq t \leq t_0$;
- the inflow velocity is the function of $V(z, t) = V_f(t)F(z)$ and the inflow height may vary within the following ranges $0 < h_0/h \leq 1.0$.

The above mentioned problem solution obtained by T.Gvelesiani (Mamradze et al. 1991) expressed as a wave amplitude may be written as follows:

$$\eta(x, t) = -\frac{V}{l} \int_0^t \int_0^{-h_0} f(\tau)F(\xi) d\tau d\xi - \frac{2V}{l} \sum_{n=1}^{\infty} \frac{\cos a_n x}{ch a_n h} \int_0^t \int_0^{-h_0} f(\tau)F(\xi) \cos \gamma_n(t - \tau) ch a_n(h + \xi) d\tau d\xi, \quad (3)$$

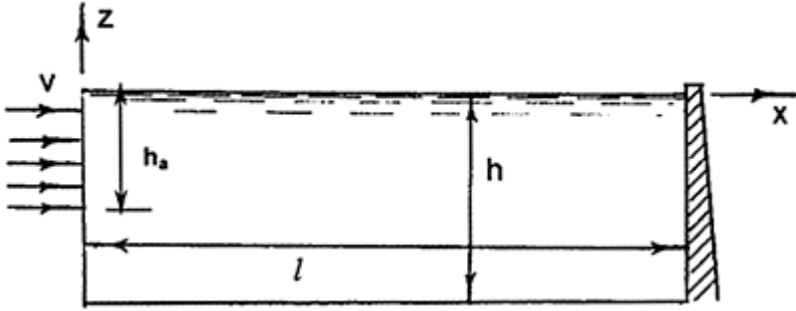


Figure 1. The design scheme for the case of 2D wave generation.

where

$$a_n = \frac{n\pi}{l}, \quad n = 1, 2, \dots; \quad \gamma_n = \sqrt{a_n g t h a_n h}$$

This expression can describe computationally the full unsteady plane wave process in narrow reservoir caused by landslide mass inflow considering wave dispersion, reflection and waves superposition phenomena.

The computational results based on (3) have shown that the approximation $f(t)=1$ when $0 \leq t \leq t_0$, $f(t)=0$ when $t < 0$, $t > t_0$ and $h_0=h$ is practically acceptable. In this case the specific volume W is determined as follows:

$$W = \frac{W_0}{b_1} = Dh = V t_0 h, \quad (4)$$

where W landslide volume distributed uniformly above:

- (a) width of the landslide $b_1=b$ (in 2D case);
- (b) width of the reservoir $b_1=B$ (when the 3D wave process is considered in a 2D approximation) and D =average width of the landslide plunged in the water.

After using undimensional parameters:

$$V^* = \frac{V}{\sqrt{gh}}; \quad t^* = \frac{t}{h}; \quad x^* = \frac{x}{h}; \quad \eta^* = \frac{\eta}{h}; \quad t_0^* = t_0 \sqrt{\frac{g}{h}}; \quad t^* = t \sqrt{\frac{g}{h}} \quad (5)$$

$$W^* = \frac{W}{h^2}; \quad D^* = \frac{D}{h}$$

Equation (4) can be written thus

$$W^* = D^* = V^* t_0^*, \quad (6)$$

as for equation (3) it may be expressed by the following function

$$\eta^* = V^* f(t_0^*, l^*, x^*, t^*), \quad (7)$$

$$\frac{\eta^*}{V^* t_0^*} = \frac{\eta^*}{D^*} = \frac{1}{t_0^*} f(t_0^*, l^*, x^*, t^*)$$

Considering that $W^* = D^*$, equation (7) may be written as follows

$$\eta^* = \frac{W^*}{t_0^*} f(t_0^*, l^*, x^*, t^*) \quad (8)$$

This expression shows, that the computations through equation (3), allow to construct the waves profiles or function $\eta = f(x)$ for certain t_i^* moments (Fig. 2a,b) and to describe wave oscillations (as a function of t) for certain x^* points.

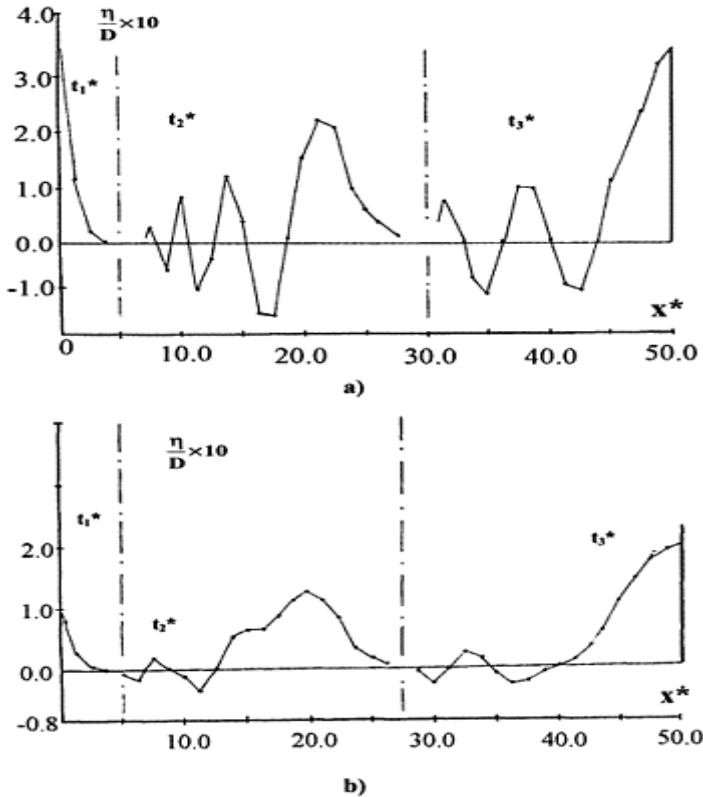


Figure 2. The waves profiles in the reservoir ($l^* = 5.0$), (a) the relative landslide duration $t_0^* = 2.5$; (b) $t_0^* = 10$.

4 THEORETICAL AND EXPERIMENTAL RESULTS AND THEIR SUBSTANTIATION

It is essential to note that expressions (8) and (2) substantiate theoretically the correct structure of the empirical formula obtained by A. Huber (Huber & Hager 1997) in the following form:

$$H = 0.88 \sin \alpha \left(\frac{\rho_s}{\rho_0} \right)^{\frac{1}{4}} (W)^{\frac{1}{4}} \left(\frac{1}{x^*} \right)^{\frac{1}{4}}, \quad (9)$$

where H —wave height.

The wave profiles constructed for relative time moments (Fig. 2a,b) show that in general, $\eta = KH$, where K is the coefficient which is varied in the limits $0 < K \leq 1.0$ ($K \approx 1$ near the landslide

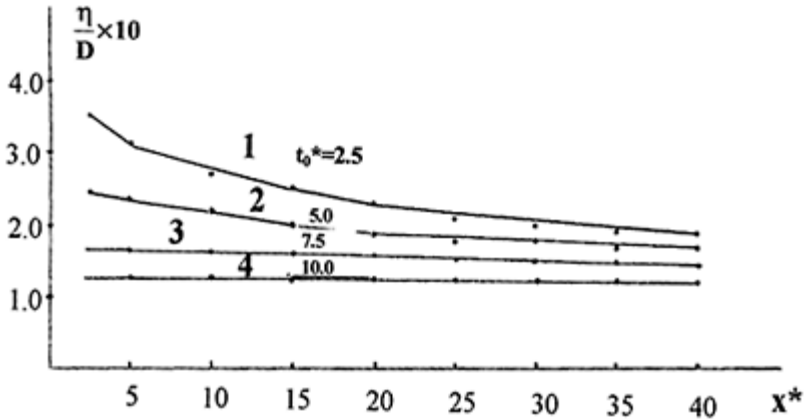


Figure 3. The relative first wave amplitude decreasing as the relative distance x^* of wave propagation increases.

site and at the dam site). These profiles correspond with the case when $l^* = 50$, $t_0^* = 2.5$ (Fig. 2a) and $t_0^* = 10$ (Fig. 2b).

In relatively fast landslide processes ($t_0^* = 2.5$), the first wave has maximal amplitude near the landslide site ($x=0$) and at the vertical dam site ($x=l^*$) as a result of reflection; at the middle part of the reservoir the amplitudes are significantly lower. In the case of relatively slow landslides ($t_0^* = 10.0$), the wave amplitudes are about two times less than at the dam site, their lengths are increasing and shapes growing flatter as compared with the first case (Fig. 2a,b).

Figure 3 illustrates the extent of the relative first wave amplitude decreasing as the relative distance x^* of wave propagation increases. The relative landslide process duration t_0^* varies (t_0^* 2.5; 5.0; 7.5; 10.0).

The computation tests result analysis using equation (3) allowed to obtain (T.Gvelesiani) special graphs as well as the simplified “engineering” formula for quick (short-term) forecasting of the maximal amplitude (water level raising, run-up height) of the first landslidegenic wave on the upstream face of vertical walls (concrete waterside protective walls, dams, steep bank slopes, etc.). The formula applied under following condition: $10 \leq l \leq 50$; $2.5 \leq t_0^* \leq 7.5$ is expressed in a form of

$$\frac{\eta_{\max}}{D} = (0.70 - 0.008l^*) - (0.05 - 0.001l^*)t_0^*. \quad (10)$$

It is necessary to note that the above-mentioned theoretical method may be applicable for the cases of forecasting 2D linear waves when the extent of “disturbance” (landslide impact) is relatively small and consequently the following conditions: $D^* \leq 1.0$ and $t_0^* \leq 2.5$ are fulfilled (Mamradze et al. 1991).

4.1 Analysis of computational examples

Example 1

Input Data: slide volume is $W_0=80,000 \text{ m}^3$; slide width is $b=100 \text{ m}$; reservoir width is $B=b=100 \text{ m}$; impact slide slope is $\alpha=45^\circ$; water depth is $h=30 \text{ m}$; landslide relative density is $\rho_s/\rho_0=2.7$; the relative wave propagation distances from the impact site ($x^*=0$) are $x^*=x/h=5; 10; 15; 20; 25; 30; 35$.

For the case $x^*=5$, the wave height from empirical formula (9) is

$$H = H_{\text{emp}} = 0.88 \cdot \sin 45^\circ (2.7)^{1/4} \left(\frac{80,000}{100} \right)^{1/2} \left(\frac{1}{5} \right)^{1/4} = 22.3 \cdot 0.66 = 14.9 \text{ m}.$$

Table 1. The first wave maximal amplitudes obtained empirically and theoretically.

x^*	5	10	15	20	25	30	35	40
$\left(\frac{1}{x^*} \right)^{1/4}$	0.67	0.56	0.51	0.47	0.45	0.43	0.41	0.40
H_{emp}	14.9	12.5	1.4	10.5	10.0	9.6	9.1	8.9
$\eta_{\text{emp}}=0.6H_{\text{emp}}$	8.9	7.5	6.8	6.3	6.0	5.8	5.5	5.3
$\frac{\eta_{\text{theor}}}{D} 10$ (Fig.3)	3.1	2.7	2.5	2.3	2.1	2.0	1.9	1.85
η_{theor}	8.2	7.2	6.7	6.1	5.6	5.3	5.1	4.9

The length of the slope underwater is $S=h/\sin \alpha=30/0.7=42.9$ m. The average duration of the landslide motion in the water is $t_0=S/V_L$ where V_L —landslide average velocity, which is determined theoretically (Mamradze et al. 1991) $V_L=8.5$ m/sec. The landslide duration is thus $t_0=42.9/8.5=5.0$ sec. and

$$t_0^* = t_0 \sqrt{g/h} = 5.0 \cdot 0.49 \approx 2.5.$$

Figure 2a shows, that $h=0.6H$. Therefore the wave amplitude in accordance with equation (9) is equal to $\eta=0.6 \cdot 14.9=8.9$ m or $\mu=\eta_{\text{emp}}=8.9$ m

Theoretical results are obtained based on the graphs on Figure 3 (when $t_0^* = 2.5$).

$$\frac{\eta}{D} = 3.1,$$

where $D=W/h=800/30=26.6$ m. Thus $\eta=3.1(26.6/10)=8.2$ m or $\eta=\eta_{\text{theor}}=8.2$ m.

Analogous calculation results for indicated different x^* values are summarized in Table 1. Comparison of the theoretical and empirical results (η_{emp} and η_{theor}) shows practically very good coincidence.

Example 2

Input data: The landslide characteristics on the lake bank slope are the same as in the example 1. Lake width is $B=200$ m; lake depth is $h=30$ m; distance from the landslide site to the lakeside protective wall (design lake length) is $l=300$ m and thus the relative length is $l^*=10$. It is required to estimate the maximal amplitude (run up height) of the wave η_{max} on the protective wall.

Considering that the waves in this 3D case propagate from the site the landslide to both in the direction of the concrete wall and to the opposite side of the lake, and then the “design” landslide volume \bar{W}_0 should be taken approximately equal to

$$\bar{W}_0 = \frac{W_0}{2} = \frac{80,000}{2} = 40,000 \text{ m}^3.$$

In the case of 2D approximation of the wave process the specific volume W is $W = \bar{W}_0/B = 40,000/200=200 \text{ m}^2$ and therefore $D=W/h=200/30=6.7$ m. Thus from equation (10):

$$\eta_{\text{max}}=6.7[(0.70-0.008 \cdot 10)-(0.05-0.001 \cdot 10)2.5]=3.5 \text{ m}.$$

More accurate wave maximal amplitudes (run-up heights) forecasting technique need to be developed based on both computational analysis through the 3D wave problem solution (Mamradze et al. 1991) and proper empirical results (Huber & Hager 1997).

5 CONCLUSIONS

The landslidegenic (impulse) 2D wave determination technique in narrow longitudinal water basins (reservoirs, lakes, etc.) is substantiated by empirical and theoretical research. The technique may be applied for the forecast of the linear wave whole unsteady process

and the waves main parameters such as: maximal amplitudes, wave profiles, run-up heights on waterside walls, dams, etc. when a landslide impact is characterized by the following criteria: $D^* \leq 1.0$; $t_0^* \leq 2.5$ (where D^* —relative width of landslide submerged in the water; t_0^* —relative duration of the landslide process at the underwater slope).

REFERENCES

- Gvelesiani, T.L. et al. 1992a. Computer-aided design of dam crest overflow by high waves (Analytical solution). A.30. International symposium on Dams and Extreme Floods. (ICOLD). Granada, Spain: 268–276.
- Gvelesiani, T.L. et al. 1999. Mathematical model of nonstational hydrodynamic process caused by mobile mud flow on the bottom of reservoir. Bulletin of the Georgian Academy of Sciences. Vol. 159, N3:457–459
- Huber, A. 1996. Quantifying impulse wave effects in reservoirs. Commission Internationale Des Grands Barrages. Dix-neuvieme Congres des Grands Barrages Florence. Italy: 563–581.
- Huber, F. & Hager, W.H. 1997. Forecasting impulse waves in reservoirs.
- Koutitas, C.G. 1997. Finite element approach to waves due to landslides. J. Hydraul. Div. Proc. ASCE. Vol. 109, Hy9:
- Koutitas, C. & Papadopoulos, G. 1996. Numerical simulation of the aseismically induced tsunami of 7 Febr. 1963 in the Western Corinthos Bay. Proc. Tsunami Symp. Paris.
- Mamradze, G.P. Gvelesiani, T.L. & Jinjikhashvili, G.I. 1991. Forecasting of waves in reservoirs under seismic actions. Moscow: Energoatomizdat.

Dynamic pressure fluctuations at real-life plunge pool bottoms

E.F.R.Bollaert, P.A.Manso & A.J.Schleiss

Laboratory of Hydraulic Constructions of the Swiss Federal Institute of Technology Lausanne (EPFL), Switzerland

Hydraulics of Dams and River Structures—Yazdandoost & Attari (eds)

© 2004 Taylor & Francis Group, London, ISBN 90 5809 632 7

ABSTRACT: Scour of rock downstream of dam spillways may be generated by jet impact. Generally, jets impact into a plunge pool downstream and diffuse through the pool. This results in a turbulent shear layer, which generates significant pressure fluctuations that might enter underlying rock joints. Recent research performed at the Laboratory of Hydraulic Constructions in Lausanne revealed that these pressure fluctuations may be amplified inside rock joints and are directly responsible for progressive break-up of the rock. Hence, appropriate assessment of these pressure fluctuations is crucial for a physically correct scour evaluation. At present, a respective amount of data is available on pressure fluctuations measured on laboratory models and for perfectly flat pool bottoms. However, real-life plunge pools are characterized by a much more complicated bottom profile, which changes during scour formation. Therefore, a research project focuses on measurements of pressure fluctuations at appropriately shaped, laboratory scaled pool bottoms. The profiles to be tested have been derived from observed model and/or prototype cases. The obtained results are described in a companion paper.

1 INTRODUCTION

Scour of rock downstream of dam spillways is generated by high velocity jet impact. Generally, the falling jet impacts into a plunge pool downstream of the dam and diffuses through the water depth of the pool. This results in a highly turbulent and aerated shear layer at the water-rock interface. This shear layer is constituted of turbulent eddies, which generate significant dynamic pressure fluctuations that might enter underlying rock joints. Recent experimental and numerical research performed at the Laboratory of Hydraulic Constructions revealed that these pool bottom pressure fluctuations may be

amplified inside underlying rock joints and are directly responsible for progressive break-up of the rock.

Hence, appropriate assessment of these pressure fluctuations is crucial for a physically correct scour evaluation. At present, a respective amount of data is available on dynamic pressure fluctuations measured on laboratory models and for perfectly flat pool bottoms. However, real-life plunge pools are characterized by a much more complicated bottom profile. The simplest observable shape of a real-life bottom profile is not flat but rather triangular or elliptical.

Therefore, a research project has been elaborated focusing on measurements of dynamic pressure fluctuations at appropriately shaped, laboratory scaled pool bottoms. The bottom profiles to be tested have been derived from an extensive literature review of observed model and/or prototype cases. The obtained results will be systematically analyzed and compared with similar results but for flat pool bottoms. The first results are described in a companion paper by Manso et al. (2004).

This approach will allow assessing the influence of the plunge pool bottom geometry on the process of progressive break-up of fractured rock.

2 EXPERIMENTAL FACILITY

2.1 General

The experimental set-up (Fig. 1) consists of two main parts (Bollaert, 2002): a) a 3 m diameter cylindrical basin in steel reinforced plastic, simulating the plunge pool, and b) a 1 mm thin steel

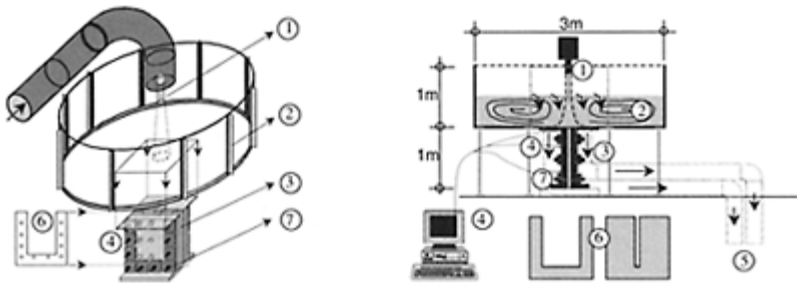


Figure 1. Perspective view and side view of the experimental facility: (1) cylindrical jet outlet, (2) reinforced plastic cylindrical basin, (3) pre-stressed two-plate steel structure, (4) Pressure sensors, (5) restitution system, (6) thin steel sheeting pre-stressed between steel structure

(defining the form of artificial 1D-2D joints), (7) pre-stressed steel bars.

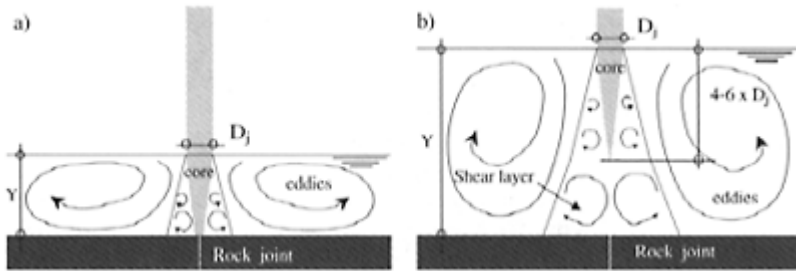


Figure 2. Plunging jets: (a) jet core impact (for $Y/D_j < 4-6$); (b) developed jet impact (for $Y/D_j > 4-6$).

sheeting, modeling the rock joint. This steel sheeting is pre-stressed between two 100mm thick steel plates with a weight of 1 ton each. The jet outlet has a cylindrical or convergent shape, for a nozzle diameter of 0.057 m or 0.072 m. The installation produces mean jet velocities of maximum 35m/s. A series of maximum 8 flush-mounted micro pressure sensors (pressure range 0.287 bar, 3 mm diameter diaphragm) simultaneously record dynamic pressure fluctuations at the plunge pool bottom and inside the rock joint, for data acquisition rates of 1–20 kHz. The water depth in the plunge pool can be varied from 0 to 0.9 m. This is sufficient to create a high-velocity diffusing turbulent shear layer that impacts the underlying rock joint.

The turbulence intensities at the jet outlet have been measured between 3 and 6%. The observed jets are compact because of their small fall heights (max. 0.50m) and a small degree of break-up (max. 0.35).

2.2 Turbulence conditions in pool

The impact of a jet into a pool is governed by jet diffusion through a medium at rest. Momentum exchange with the pool creates a progressively growing shear layer, characterized by an increase of the jet's total cross section and a convergence of the core of the jet (Fig. 2). Dynamic pressures acting at the water-rock interface can be generated by core jet impact, occurring for small plunge pool depths, or by impact of a fully developed macroturbulent shear layer, occurring for ratios of pool depth to jet thickness Y/D_j higher than 4 to 6. The exact Y/D_j ratio dividing these two regimes depends on jet outlet conditions and low-frequency jet stability. For the present study, a value of Y/D_j between 5 and 6 has been deduced from the tests.

3 DYNAMIC PRESSURES AT FLAT POOL BOTTOMS

3.1 Mean and fluctuating dynamic pressures

The mean and root-mean-square dynamic pressure values are defined at the jet's centerline (subscript a). The mean pressure measurements are presented in Figure 3a for core and developed jet

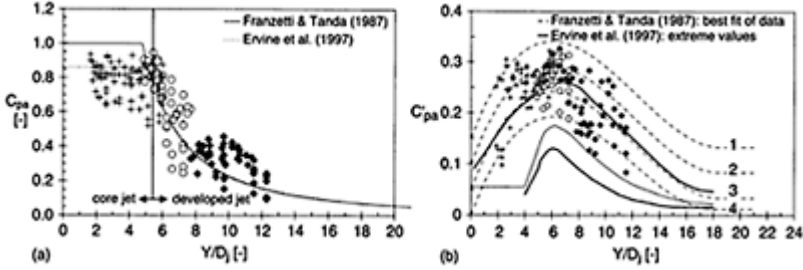


Figure 3. (a) Non-dimensional mean dynamic pressure coefficient C_{pa} as a function of Y/D_j ; (b) Non-dimensional fluctuating dynamic pressure coefficient C'_{pa} as a function of Y/D_j .

impact conditions. The mean dynamic pressure coefficient C_{pa} , defined as the mean dynamic head divided by the kinetic energy of the impacting jet

$$C_{pa} = \frac{(p^{\text{mean}}/\gamma)}{(V^2/2g)} \quad (1)$$

shows similar tendencies with the best fits of available literature data on circular impinging jets (Franzetti & Tanda, 1987; Irvine et al., 1997). However considerable scatter can be observed for all jet impact conditions. The scatter is due to variability in the aeration rate and jet turbulence. Irvine et al. (1997) defined C_{pa} as a function of Y/D_j and of the air concentration α_i , at the impact point in the pool:

$$C_{pa} = 38.4 \cdot (1 - \alpha_i) \cdot \left(\frac{D_j}{Y}\right)^2 \quad \text{for } Y/D_j > 4-6 \quad (2)$$

$$C_{pa} = 0.85 \quad \text{for } Y/D_j < 4-6$$

The air concentration at impact α_i is defined as a function of the volumetric air-to-water ratio β :

$$\alpha_i = \frac{\beta}{1 + \beta} \quad (3)$$

A summary of expressions for β can be found in Bollaert (2002). As shown in equation (3), the mean dynamic pressure decreases with increasing air content in the plunge pool. This, however, does not take into account the jet turbulence. Jet turbulence can have a significant influence on the mean pressure value. In the present facility, the higher mean values of C_{pa} were obtained at very high air concentrations with a jet having a low turbulence level.

The root-mean-square pressure coefficient C'_{pa} of the fluctuating part of the dynamic pressures is presented in Figure 3b and is defined as the root-mean-square value of the fluctuating dynamic head (RMS) divided by the kinetic energy of the impacting jet

$$C'_{pa} = \frac{(RMS/\gamma)}{(V^2/2g)} \quad (4)$$

The general form of the relationship between the root-mean-square values and the Y/D_j ratio is in good agreement with previous findings and with the theory of two-dimensional diffusion of a jet through a medium at rest. Initially, turbulence increases with increasing plunge pool depth until a certain maximum value is obtained. Then it decreases again with further increasing plunge pool depth due to increasing diffusion effects.

The data are significantly higher than previously reported values (Ervine et al. (1997) and Franzetti & Tanda (1987)). The mean increase of C'_{pa} is on the order of 0.05 to 0.10. This is not surprising when one considers that the facility generates near-prototype spectral characteristics.

Table 1. Polynomial coefficients and regression coefficient for different turbulence intensities.

Tu [%]	a_1	a_2	a_3	a_4	Type of jet
<1	0.000220	-0.0079	0.0716	0	Compact
1-3	0.000215	-0.0079	0.0716	0.050	Intermediate
3-5	0.000215	-0.0079	0.0716	0.100	Undulating
>5	0.000215	-0.0079	0.0716	0.150	Very undulating

As pointed out before, the higher frequency part of the spectral content of an impacting jet is much closer to reality than on small-scale models. The root-mean-square values are obtained by integration of the spectral curves over the frequency range of interest and, thus significantly higher values are obtained.

For core jets, large scatter is obtained, with values ranging between 0.10 and 0.35. The lower values correspond to ideal core jet impact conditions, i.e. without any jet instabilities. For these impact conditions and for small jet fall lengths, the turbulence of the jet at the pool bottom becomes very close to the initial jet turbulence intensity Tu .

The latter was estimated at the present facility at 0.04 to 0.05. Similar results were obtained by Franzetti & Tanda (1987), who apparently only considered perfect core jet impact conditions.

No ideal core jet impact is observed on the present facility. Apparently, even a small water depth is able to destabilize the core of the impacting jet such that its fluctuations at impact are substantially higher than the initial turbulence intensity Tu . Similar results have been obtained by most of previous research and are obviously not that unusual. For example, Ervine et al. (1997) seem to have encountered the same effects. Their values for core jet impact lie between 0.03 and 0.22, which indicates the results might have been influenced by core instabilities. This phenomenon has, to the authors' knowledge, never been investigated.

For developed jet impact, maximum values of C'_{pa} of up to 0.30–0.35 are obtained, for Y/D_j ratio between 5 and 8. Although diffusion effects become predominant at higher ratios, resulting in a quasi-linear decay of the root-mean-square values, substantial high values (0.25) may still persist at Y/D_j ratios of up to 10–11.

The measured data points have been approximated by a third order polynomial regression (equation (7)). This polynomial form has been obtained through curve fitting the upper limit of the data as given by Ervine et al. (Figure 3b). The regression coefficient for this curve fitting was equal to 0.99 and yielded the following relationship:

$$C'_{pa} = a_1 \cdot \left(\frac{Y}{D_j}\right)^3 + a_2 \cdot \left(\frac{Y}{D_j}\right)^2 + a_3 \cdot \left(\frac{Y}{D_j}\right) + a_4 \quad (5)$$

The coefficients a_1 to a_4 are summarized in Table 1 and define four similar-shaped curves but with different offsets. These curves agree with the measured data and can be used up to a Y/D_j ratio of 18–20. For higher ratios, the value that corresponds to a ratio of 18–20 are proposed. The offset depends on the initial turbulence intensity Tu of the jet.

The curve with the highest root-mean-square values is valid for jets with an undulating character or jets with a Tu that is higher than 5%. The curve with the lowest values is applicable to a turbulence intensity that is lower than or equal to 1%. In between, two other curves have been defined. They are appropriate for intermediate turbulence levels.

The key issue is that the low-frequency pressure fluctuations have been directly related to the turbulence intensity, Tu . This was defined as the root-mean-square value of the longitudinal velocity. In fact, the turbulence intensity comprises a whole range of frequencies each of which will influence the pressure fluctuation. Nevertheless, it is believed that the turbulence intensity defined by Tu can be used as the significant parameter.

Based on the experimental results, it is recommended to relate the choice of C_{pa} to the choice of C'_{pa} in the following manner: the higher the selected curve of root-mean-square values, the lower the choice for the mean pressure value. This is logical when considering that turbulent jets generate high root-mean-square values, but low mean pressures.

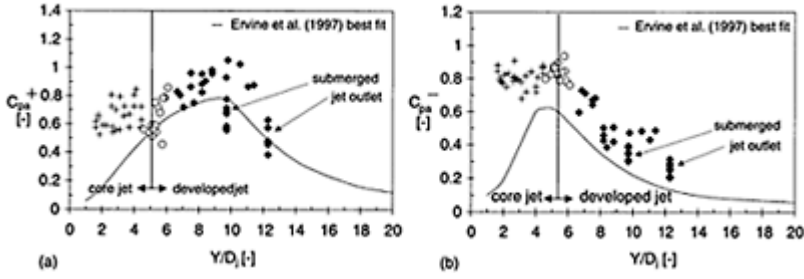


Figure 4. (a) Non-dimensional positive extreme dynamic pressure value C_{pa}^+ as a function of the ratio Y/D_j ; (b) Non-dimensional negative extreme dynamic pressure value C_{pa}^- as a function of the ratio Y/D_j

3.2 Extreme dynamic pressures

The extreme positive and negative pressure coefficients C_{pa}^+ and C_{pa}^- are presented in Figure 4. They are defined as the net positive and negative fluctuation from the mean dynamic pressure value divided by the kinetic energy of the jet:

$$C_{pa}^+ = \frac{(p^{\max} - p^{\text{mean}}/\gamma)}{(V^2/2g)} \quad (6)$$

$$C_{pa}^- = \frac{(p^{\text{mean}} - p^{\min}/\gamma)}{(V^2/2g)} \quad (7)$$

The trend of data is in good agreement with available literature data, while the absolute values are far more extreme. For positive extremes, the measured C_{pa}^+ values are higher by a value of 0.10–0.50. For negative extremes, the differences in C_{pa}^- values range from 0.10 to 0.30. Extreme values obtained at submerged jet outlet conditions are in better agreement with previously published data although the negative extremes are larger.

It is believed that the larger extreme values are again the result of the use of near-prototype jet velocities. Another reason could be the high air entrainment because extreme values that were obtained under submerged jet conditions (without any air) are in good agreement with previous data.

3.3 Spectral energy of dynamic pressures

The spectral content of the pressures under the jet's centreline S_{xx} is analyzed in the frequency and the Strouhal domain. $S_{xx}(f)$ is defined as a decomposition with frequency

of the variance σ^2 of the pressure fluctuations. It is presented in non-dimensional form by dividing it by this variance. The spectral content defines the cyclic character of the pressures and indicates how the energy of the jet is distributed over different frequencies. The Strouhal number $S_{h,p}$ is defined as follows:

$$S_{h,p} = \frac{f \cdot Y}{V_j} \quad (8)$$

in which f stands for the frequency (in [Hz]) and V_j for the mean jet velocity at impact in the plunge pool (in [m/s]). The eddies of the shear layer are governed by Y and V_j . Hence, dynamic pressures at the pool bottom that directly result from these eddies should also depend on these parameters. Moreover, the non-dimensional spectral contents in the Strouhal domain should be similar for different jet velocities. Dynamic pressures measured outside of the shear layer do not follow this law. They depend on Y but the governing velocity field is completely different. Figure 5 shows the non-dimensional power spectral density corresponding to a 72 mm jet diameter. The results are presented for core jets and developed jets and for the frequency and Strouhal domains. Figure 5a

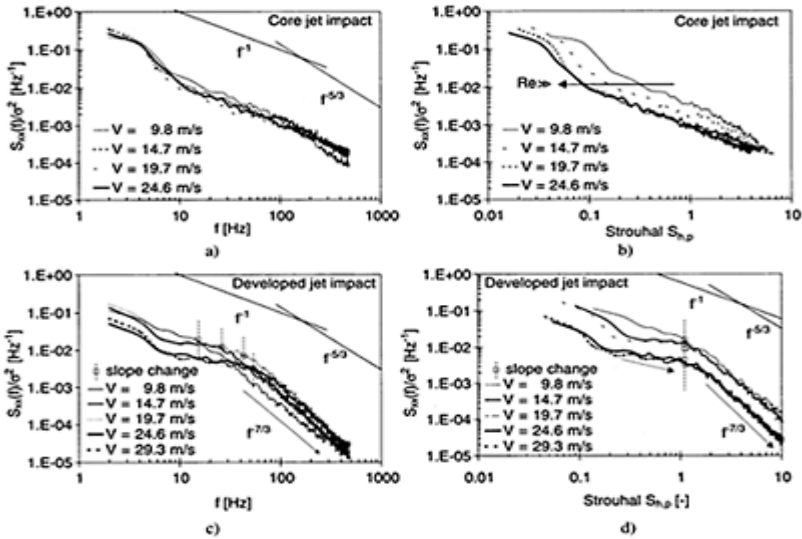


Figure 5. Non-dimensional power spectral density of dynamic pressures at the plunge pool bottom: (a) core jet in the frequency domain; (b) core jet in the Strouhal domain; (c) developed jet in the frequency domain; (d) developed jet in the Strouhal domain.

shows that the spectral curves for core jet impact are characterized by a linear decay with a slope of -1 , even at high frequencies (beyond 100 Hz). Moreover, it can be seen by Figures 5a & 5b that core jet impact does not collapse to a single curve in the non-dimensional domain. The spectral curves collapse to a single curve in the frequency domain because the surrounding turbulent shear layer and related eddy sizes do not affect the core of the jet. On the other hand, developed jet impact produces more spectral energy at low and intermediate frequencies as shown in Figures 5c and 5d. The spectral curves decay at a quasi-linear $-7/3$ slope, corresponding to values available in literature (Bearman, 1972; Huot et al, 1986).

4 REAL-LIFE POOL BOTTOM CONFIGURATIONS

The aim of the research project is to measure pressure fluctuations inside more realistic plunge pool and rock joint geometries. Previous tests were performed for a cylindrical plunge pool with a perfectly flat bottom. This, however, only happens in the beginning of the erosion process; with progressing scour of the rock mass, the form of the pool bottom transforms into a highly irregular shape (Kobus et al., 1979; Rajaratnam, 1981). This shape is thereby influenced by the joint sets and the relative strength of the rock mass. Some possible shapes are presented in Figure 6.

The first shape is conical (Fig. 6a), with slope angles close to the natural angle of repose of the fractured rock material. This shape corresponds to the ones generally observed on granular bottoms and is representative for highly fractured rock or rock with a very low erosion resistance. The corresponding sketch presents the possible parameters of such a pool bottom, i.e. the height and the width of the steps, as well as the angle of the average slope of the pool walls.

The second shape (Fig. 6b) is typical for rock with a high degree of fracturing in the horizontal direction and a high erosion resistance. This automatically results in deep scour holes with slope

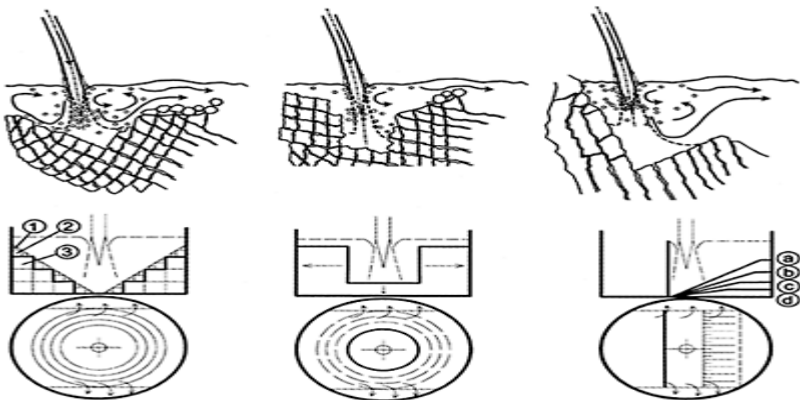


Figure 6. Three different shapes of the plunge pool bottom, as a function of

the joint set patterns and the degree of fracturing of the rock mass: a) conical shape with varied roughness (1, 2, 3), b) cylindrical shape with varied diameter, c) skewed V-shape with varied slope (a, b, c, d).

angles that are much steeper than the natural angle of repose of the material. Such a particular (cylindrical) shape might have a profound influence on the diffusion and recirculation pattern of the jet in the pool.

The last shape is asymmetrical and considers a rock mass that is highly jointed in one particular direction. This conducts to a skewed V-shape as presented (Fig. 6c). The corresponding sketch indicates how the experimental facility accounts for this shape. As the angle of impact of the impacting jet is fixed, the rock mass has been rotated to match with the jet and to respect the relative angles between the jet and the slope of the walls.

The recirculating eddies of the turbulent two-phase shear layer of the impacting jet are influenced by the shape of the pool bottom. As such, the spatial distribution of the pressure fluctuations at the pool bottom should be quantified for different bottom configurations. In addition, the statistical characteristics of the hydrodynamic flow should be assessed for the corresponding integral scales of turbulence and persistence time of maximum pressures. This should allow to define to which extend the turbulent fluctuations of the jet change during the scouring process and the ability of the corresponding vorticity to up-lift potential rock blocks.

5 CONCLUSIONS

The present article presents the results of near-prototype scaled measurements of dynamic pressure fluctuations at flat plunge pool bottoms. Statistical characteristics of the dynamic pressures are analyzed in both the time and the frequency domain, and a comparison with available scaled literature data is made.

Furthermore, the basis for new dynamic pressure investigations are outlined, focusing on the assessment of the mutual influence of the plunge pool bottom geometry and the development of dynamic pressure fluctuations. This aspect is of direct relevance to scour hole formation and is discussed in a companion paper by Manso et al. (2004).

REFERENCES

- Bearman, P.W. 1972. An investigation of the forces on flat plates normal to a turbulent flow. *Journal of Fluid. Mechanics* (46) 177–198.
- Bollaert, E. 2002. Transient water pressures in joints and formation of rock scour due to high-velocity jet impact. *Communication 13 Laboratory of Hydraulic Constructions*. EPFL, Switzerland.

- Bollaert, E., Falvey, H.T. & Schleiss, A. 2002. Assessment of turbulent jet impingement in plunge pools: the particular characteristics of a near-prototype physical model study. *Proceedings of Riverflow 2002*. Louvain-la-Neuve. Belgique.
- Ervine, D.A., Falvey, H.R. & Withers, W. 1997. Pressure fluctuations on plunge pool floors. *Journal of Hydraulic Research*, IAHR. (35) 2.
- Franzetti, S. & Tanda, M.G. 1987. Analysis of turbulent pressure fluctuation caused by a circular impinging jet. *International Symposium on New Technology in Model Testing in Hydraulic Research*. India: 85–91.
- Manso, P.A., Bollaert, E.F.R, Schleiss, A.J., 2004. Experimental investigations on jet behaviour in plunge pool rock scour. International Conference on Hydraulics of Dams and River Structures, Teheran, Iran.
- Kobus, H., Leister, P. & Westrich, B. 1979. Flow field and scouring effects of steady and pulsating jets impinging on a moveable bed. *Journal of Hydraulic Research*. (17) 3:175–192.
- Rajaratnam, N. 1981. Erosion by plane water jets. *Journal of Hydraulic Research*. (19) 4:339–358.
- Huot, J.P., Rey, C. & Arbey, H. 1986. Experimental analysis of the pressure field induced on a square cylinder by a turbulent flow. *Journal of Fluid Mechanics*. (162):283–298.

A new procedure to evaluate dynamic uplift of concrete linings or rock blocks in plunge pools

E.F.R.Bollaert

AquaVision Engineering Inc., FluvialTech Group, Lausanne, Switzerland

Hydraulics of Dams and River Structures—Yazdandoost & Attari (eds)

© 2004 Taylor & Francis Group, London, ISBN 90 5809 632 7

ABSTRACT: A new procedure to evaluate dynamic uplift of concrete slabs or rock blocks in plunge pools is presented. The procedure is based on near-prototype scaled measurements of transient pressure fluctuations over and under the slabs or blocks, and on appropriate assessment of the 2D pressure field at impact in the plunge pool. The pressures that occur at the surface of a slab or block (plunge pool bottom) are assessed by means of appropriate dynamic pressure coefficients. The pressures underneath the slabs or blocks are governed by transient pressure waves. Their assessment can be performed by two methods: (1) by investigating surface pressures that enter the joints and applying a maximum possible impulsion on the slab/block (taken from near-prototype scaled tests), and (2) by direct numerical modeling of the temporary and spatially distributed transient pressure field, based on known dynamic pressures that enter the joints. By relating the transient underpressures to the corresponding surface pressures, and by establishing appropriate correlations over the slab or block surface, extreme net uplift pressures can be deduced, defining so whether uplift will occur or not.

1 INTRODUCTION

Dynamic uplift of concrete slabs that form the protection lining of stilling basins and plunge pools is a well known phenomenon. Also, sudden ejection of rock blocks at plunge pool bottoms contributes to scour formation. The slabs or blocks are ejected by a sudden net pressure difference between the surface and the underside. This pressure difference may become much larger than the submerged weight of the slab/block and eventual anchorage forces.

The net uplift pressure is determined first of all by the spatially distributed and time-dependent 2D pressure field at the surface of the slab/block. For small rock blocks, spatial correlation of pressures is of less importance. For concrete slabs, which can be much larger than the spatial persistence of the pressure fluctuations, instantaneous spatial correlations at the slab surface are necessary in order to correctly assess the two-dimensional character of the impacting turbulent flow field. This can be obtained by means of appropriate physical model tests.

Second, as a function of these surface pressures, a pressure builds up underneath the slab/block by propagation of pressure waves through the joints and eventually through the drainage system. This underpressure field is time-dependent and may be of highly transient character. Its assessment can be performed by two methods: (1) by investigating the surface pressures and by applying a maximum possible impulsion on the slab/block (available from near-prototype scaled model tests), and (2) by direct numerical modeling of the temporary and spatially distributed transient pressures, based on known pressures that enter the joints.

The present paper presents a new method to evaluate uplift of concrete slabs or rock blocks by simultaneous quantification of the 2D surface pressure field and the underpressure field due to transient pressure wave propagation through the joints. By relating the transient underpressures to the corresponding surface pressures, and by establishing appropriate correlations over the slab or block surface, extreme net uplift pressures can be deduced.

The resistance of the slabs/blocks is expressed by their submerged weight, by shear and interlocking forces along joints, and by tensile steel forces in case of anchored slabs.

2 PHILOSOPHY OF TRANSIENT UNDERPRESSURES

The assumption of a pressure that acts underneath a slab/block is based on pressure pulses that travel through the joints as waves with a certain celerity. The character of the underpressures depends on the assumptions that are made on the wave celerity. Two approaches exist:

1. For high wave celerities, i.e. $O(10^2-10^3)$ m/s, the pressures travel quasi instantaneously through the joints and net uplift pressures are expressed by equating the difference between a surface pressure field (which travels at the much lower velocities of the turbulent eddies) and an instantaneous underpressure field. Transient effects are neglected and the underpressures are determined as an average of the pulse values at the joint entrances. Because temporal and spatial wave characteristics are neglected in the analysis, this is called the *dynamic pressures approach* (see Figure 1b; Bellin & Fiorotto, 1995).
2. Secondly, based on near-prototype tests of high-velocity jet impact on artificial joints, (Bollaert, 2003a), the air-water flow mixture in the joints generates much lower wave celerities, i.e. $O(10^1-10^2)$ m/s. Hence, for slab/block lengths of $O(10^1)$ m, the pressure wave needs some time to be installed underneath. Also, considering the joint as resonator volume and the impacting flow as exciter, transient oscillations and resonance effects may occur. An increase of the joint length and/or a decrease of the wave celerity decrease the fundamental resonance frequency. For resonance

frequencies that approach the main spectral frequencies of the impacting flow, an interaction may lead to pressure amplification. Thus, underpressures are determined by the pulses at the joint entrances AND by the transient characteristics of the medium. This method is called the *transient pressures approach* (see Figure 1c; Bollaert, 2002).

For real-life cases, both approaches can be applied and compared, providing beneficial (dynamic) and conservative (transient) engineering assumptions. The transient pressures approach needs a quantification of the possible amplification of pressure pulses inside the joints.

This can be performed in two different ways: (1) based on a maximum possible impulsion, function of the surface pressures (Bollaert, 2002); and (2) based on a direct numerical simulation of transient two-phase underpressures as a function of a surface pressure field that has to be defined at the joints (for example taken from physical model tests).

Finally, the existence of a net uplift pressure on a slab causes the slab to move. For anchored slabs, not only the slab weight but also the steel stresses will prevent the slab from moving. This results in a dynamic equilibrium that is very similar to a spring-mass system and that can be expressed by Newton's law (see next paragraph). For such a dynamic system, the *persistence time* of the net pressure difference might be of importance. This underlines the need for a fully transient approach.

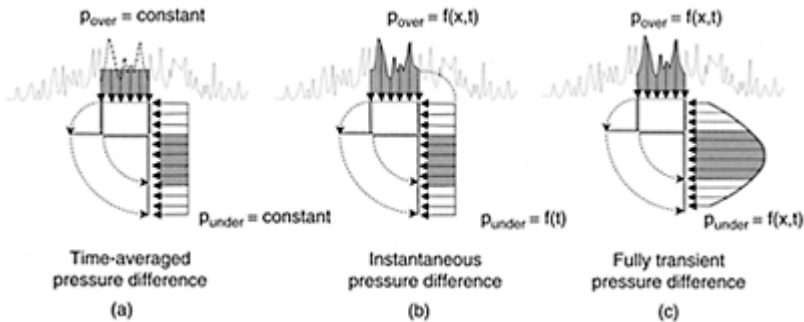


Figure 1. Dynamic pressure patterns on a concrete slab: (a) time-averaged pressure difference, (b) dynamic pressure difference, (c) fully transient pressure difference.

3 TWO-DIMENSIONAL SURFACE PRESSURE FIELD

3.1 General

The flow conditions at the slabs/blocks are determined by the impacting turbulent flow. The parameters of interest are the mean and the fluctuating dynamic pressures at the water-concrete/rock interface, as well as their spatial extent. The pressure field can be described statistically by means of *dynamic pressure coefficients*. These coefficients represent the pressures in a non-dimensional manner by dividing them by the incoming kinetic energy of the flow:

$$C_p = (p_{\text{mean}} - Y)/(V_j^2/2g) \quad \text{mean dynamic pressure}$$

$$C'_p = (\sigma)/(V_j^2/2g) \quad \text{fluctuating dynamic pressure}$$

$$C_p^+ = (p_{\text{max}} - p_{\text{mean}} + Y)/(V_j^2/2g) \quad \text{maximum positive deviation from the mean dynamic pressure}$$

$$C_p^{\text{max}} = (p_{\text{max}})/(V_j^2/2g) \quad \text{maximum dynamic pressure}$$

in which Y stands for the water depth in the stilling basin, σ for the root-mean-square (hereafter: RMS) value of the pressure fluctuations, p_x for the measured relative pressure

in [m] and $V_j^2/2g$ is the incoming kinetic energy head of the flow. For jet impact, pressure coefficients are well described by available model and near-prototype scaled experiments (Ervine et al., 1997; Bollaert, 2002). For a hydraulic jump, the statistical characteristics of the pressures are also well known (Toso & Bowers, 1988; Fiorotto & Rinaldo, 1992).

For a hydraulic jump, the dynamic pressure field is merely homogeneous in the lateral direction, because of the one-dimensional hydraulic jump inflow characteristics. For jet impact, the dynamic pressure field is two-dimensional and explained in detail hereafter.

3.2 Dynamic pressure coefficients for jet impact

The pressure coefficients for jet impact have to be determined at every location of the 2D pool floor. The used mathematical expressions distinguish between points that are situated directly under the jet's centerline and points that are situated radially outwards. Most expressions propose an equation for the centerline coefficients and apply an exponential decay radially outwards.

The mean pressure coefficient at the centerline C_{pa} is defined by Y/D_j , the velocity at impact V_j and the air concentration at impact α_i . For small pool depths (core jets) its value is close to the unity. For larger pool depths (developed jets), this value quickly

decreases, and finally becomes insignificant at Y/D_j ratios superior to 10–12. The C_{pa} coefficient is defined as:

$$C_{pa} = 38.4 \cdot (1 - \alpha_i)^{1.345} \cdot \left(\frac{D_j}{Y}\right)^2 \quad \text{for } Y/D_j > 4-6 \text{ (developed jets)}$$

$$C_{pa} = 0.85 \quad \text{for } Y/D_j < 4-6 \text{ (core jets)}$$

The root-mean-square coefficient C'_p , depends on the Y/D_j ratio and the initial turbulence intensity of the jet Tu . Based on near-prototype experiments (Bollaert, 2002), a polynomial regression of third order has been defined and yields the following relationship (Bollaert, 2002):

$$C'_p = a_1 \cdot \left(\frac{Y}{D_j}\right)^3 + a_2 \cdot \left(\frac{Y}{D_j}\right)^2 + a_3 \cdot \left(\frac{Y}{D_j}\right) + a_4$$

The first and the fourth coefficients have been modified in the way indicated at Table 1. This results in four similar-shaped curves but with a different offset. These curves were found to agree with the measured data and can be used up to a Y/D_j ratio of 18–20. For higher ratios, a low value of 0.05 is proposed. The curve with the highest values is for diffusing jets or jets with Tu higher than 5%. The curve with the lowest values is applicable to compact jets, which are smooth-like, with a Tu that is lower than or equal to 1%. In between, two other curves have been defined.

The dynamic pressure coefficients for the maximum positive deviations from the mean use relationships that are based on model data by Ervine et al. (1997). Then, based on near-prototype scaled data by Bollaert (2002), an offset in the coefficients of around 0.20 (towards more extreme values) is applied to the best-fit curve as found by Ervine et al. (1997). The use of prototype velocities results in more extreme pressures, because turbulent energy is more correctly represented than on a model scale, especially at higher frequencies (Bollaert et al., 2002).

Furthermore, it is believed that the most extreme pressure pulses correspond to high frequencies and thus occur on very small surfaces (very small integral scales). For most applications, high frequencies have very small integral scales and probably do not affect the two-dimensionally averaged maximum pressure values that are used to compute slab uplift. Applying high-frequency extremes everywhere over a slab surface is physically incorrect and would result in estimated uplift pressures that are much too high. The maximum dynamic pressure value C_{p}^{\max} is obtained by superposing the maximum positive deviation to the mean value.

The radial persistence of the mean dynamic pressures values is described by an exponential decay. Details can be found in Bollaert (2002). For practical purposes, the following expressions are convenient (Bollaert et al., 2002) (C_{pr} stands for the radial pressure coefficient):

$$\frac{C_{pr}}{C_{pa}} = e^{-3 \cdot \left(\frac{r}{r_{\max}}\right)^2} \quad \text{for core jets} \quad \text{and} \quad \frac{C_{pr}}{C_{pa}} = e^{-6 \cdot \left(\frac{r}{r_{\max}}\right)^2} \quad \text{for developed jets}$$

The radial distribution of the fluctuating dynamic pressure coefficient C'_{pa} can be compared to the corresponding value under the jet's centreline. For practice, the following expressions are proposed (Bollaert et al, 2002):

$$\frac{C'_{pr}}{C'_{pa}} = e^{-3 \cdot \left(\frac{r}{r_{\max}}\right)^2} \quad \text{for developed jets and all } r \text{ values}$$

$$\frac{C'_{pr}}{C'_{pa}} = e^{-3 \cdot \left(\frac{r}{r_{\max}} - 0.5\right)^2} \quad \text{for core jets and } r > 0.5 \cdot r_{\max}$$

$$\frac{C'_{pr}}{C'_{pa}} = 1 \quad \text{for core jets and } r < 0.5 \cdot r_{\max}$$

Table 1. Polynomial coefficients and regression coefficient for different turbulence intensities.

Tu [%]	a1	a2	a3	a4	Type of jet
<1	0.000220	-0.0079	0.0716	0	Compact
1-3	0.000215	-0.0079	0.0716	0.050	Intermediate
3-5	0.000215	-0.0079	0.0716	0.100	Undulating
>5	0.000215	-0.0079	0.0716	0.150	Very undulating

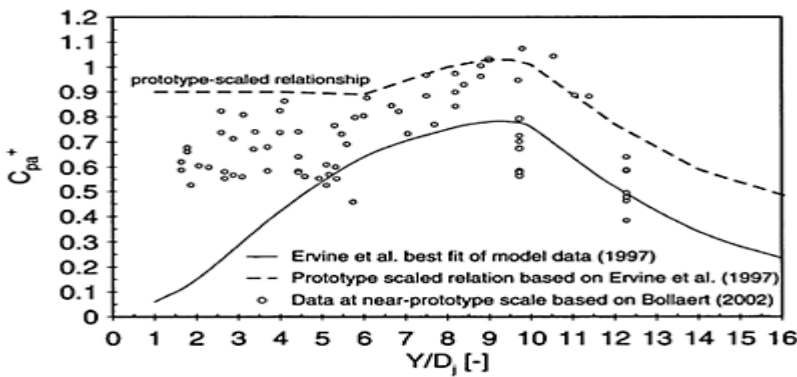


Figure 2. Extreme dynamic pressure coefficient C_{pa}^+ . Data based on Bollaert et al. (2002).

For maximum dynamic pressure coefficients, the following expressions are proposed for core jets and for developed jets with $Y/D_j < 8$:

$$\frac{C_{pr}^+}{C_{pa}^+} = e^{-0.5 \cdot \left(\frac{r}{r_{max}} - 0.5\right)^2} \quad 0.5 \cdot r_{max} < r < 3.5 \cdot r_{max}$$

For highly developed jets with a Y/D_j value >8 , the radial persistency of the maximum pressure fluctuations decreases and the following equation is proposed:

$$\frac{C_{pr}^+}{C_{pa}^+} = e^{-0.75 \cdot \left(\frac{r}{r_{max}} - 0.25\right)^2} \quad 0.5 \cdot r_{max} < r < 3.0 \cdot r_{max}$$

4 TRANSIENT UNDERPRESSURE FIELD

4.1 Maximum possible impulsion

The first way of computation uses a maximum possible dynamic impulsion on a slab/block, which is defined as a function of the Y/D_j ratio based on near-prototype instantaneous measurements of over-and underpressures (Bollaert, 2002):

$$C_I = 0.0035 \left(\frac{Y}{D_j}\right)^2 - 0.119 \left(\frac{Y}{D_j}\right) + 1.22$$

C_I is defined as the product of a net uplift pressure C_{up} times a persistence time T_{up} and has to be multiplied by $V^2 L/gc$ to obtain the net maximum impulsion I_{max} [ms] on a slab/block.

4.2 Numerical computation of transient underpressures

Second, the transient underpressures can be computed based on the transient flow equations applied to a homogeneous two-phase fluid and using surface pressure records at the joint entrances as input to the model, as presented below:

The numerical modeling results in the total force under the slab expressed as:

$$F_u = \sum_i p_{ui} \cdot A_{ui}$$

in which A_{ui} stands for the area of application of p_{ui} . The uplift force is simply computed as the arithmetic average of the underpressures times the total slab area. The influence of transient pressures is then expressed by means of a transient amplification factor Γ defined as the ratio of the average underpressure to the average of the maximum surface pressures p_{sj} :

$$\Gamma = \frac{(\sum_i p_{ui}/i)}{(\sum_j p_{sj}/j)}$$

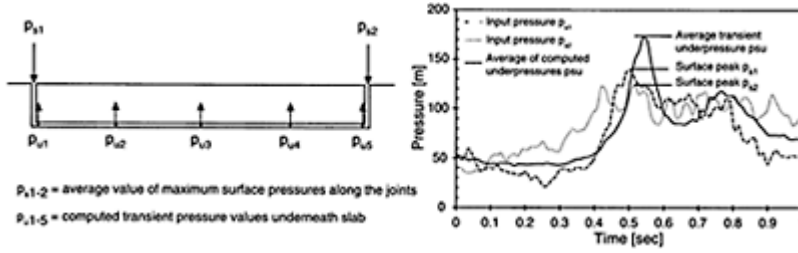


Figure 3. Methodology and results of numerical computations of transient underpressures.

The amplification factor only accounts for the underpressures and not for the surface pressure field. It defines the maximum amplification that the underpressures may exhibit due to transient wave effects in the joint. Hence, for a transient slab uplift computation, the dynamic underpressures without transients are multiplied by this amplification factor to obtain fully transient values. Based on Bollaert (2002) and (2003b), appropriate factors are 1.2 to 1.4.

5 DYNAMIC SLAB/BLOCK UPLIFT

5.1 General equations

Dynamic uplift of slabs/blocks can be mathematically expressed by the differential equation valid for a spring-mass system with a forced vibration by means of an external forcing function. Damping effects may be neglected at first order. The equation expresses a balance of stabilizing and destabilizing forces as a function of time (Fiorotto & Salandin, 2000):

$$F_{stab}(t) = F_{destab}(t)$$

The stabilizing forces consist of the weight m (or submerged weight) and eventually the stresses induced in the steel anchors. The weight is defined by the density ρ_c and the height h_s . The dynamic stiffness of the anchors is determined by the elastic modulus, the sectional area A_{st} and the length of the anchors L_{st} . The equilibrium is written per unit of slab surface as follows (equation only valid for positive displacements of $z(t)$):

$$\rho_c \cdot h_s \cdot z''(t) + \frac{E_{st} \cdot A_{st}}{L_{st}} \cdot z(t) = p(t)$$

in which $p(t)$ stands for the net uplift pressure on the slab. Solving this equation as a function of time expresses the uplift of the slab governed by the inertia of its mass and the stiffness of the anchors. During slab uplift, the underpressure is assumed constant. Also, the elastic properties of the water and the underlying rock are neglected. The

standard solution of this 2nd order linear differential equation with constant coefficients is written as follows:

$$z(t) = \frac{[C_2]}{[C_1]} - \left[\frac{[C_2]}{[C_1]} \cdot \cos(\sqrt{C_1} \cdot t) \right]$$

The solution consists of the sum of two periodic motions with a different frequency but the same amplitude. The first motion on the right hand side is constant (zero frequency) and the second motion on the right hand side is cosinusoidal with a frequency ω and a period T . In other words, the function $z(t)$ reaches its maximum value at time:

$$t = \frac{\pi}{\sqrt{C_1}}$$

The corresponding maximum possible steel stress is written:

$$\sigma_{st,max} = \frac{z_{max}}{L_{st}} \cdot E_{st} = 2 \cdot \frac{p(t)}{A_{st}} = 2 \cdot \sigma_{st,static}$$

It can be seen that the dynamic equilibrium results in maximum steel stresses $\sigma_{st,max}$ that are *twice as high* as the static maximum steel stress $\sigma_{st,static}$. This maximum dynamic steel stress can only be reached provided that the persistence time of the net uplift pressure equals or exceeds the time period T needed to build up the cosinusoidal motion of the slab.

Hence, the persistence time of the net uplift pressure pulse is essential. Very short pulses will not be able to develop the cosinusoidal motion of the slab and, thus, the static steel stresses are valid. Pulses of longer duration allow this motion and dynamic steel stresses to fully develop. The persistence time necessary for pressure pulses to reach the static (t_{static}) and dynamic (t_{dyn}) stresses can be computed based on available information on the steel and slab characteristics. An estimate of the persistence time T_{res} of a pressure pulse is made by expressing the resonance frequency of the joint as a function of the wave celerity c and the joint length L_j . For typical slab lengths of 10–20m and celerities of 100–500 m/s, the following values are computed:

$$f_{res} = \frac{c}{2 \cdot L_j} = 2.5 - 25[\text{Hz}]$$

$$T_{res} = \frac{1}{f_{res}} = 0.04 - 0.4[\text{s}]$$

Hence, based on general macro-turbulent flow assumptions, with frequencies that are well below 25 Hz (Toso & Bowers, 1988), it is considered in the following that surface pressure fluctuations have a persistency that significantly exceeds the above computed values.

5.2 One-dimensional (1D) or two-dimensional (2D) approach

Depending on the ratio of the integral scale of the pressure fluctuations (spatial persistency of pulses) to the slab/block dimensions, a 1D or 2D approach has to be chosen for appropriate computation of the net uplift pressures. The 1D approach is plausible when the slab/block dimensions are on the same order of magnitude as the integral scale. The integral scale generally is on the order of half to one times the incoming characteristic flow height, i.e. the diameter of an impacting jet or the initial flow depth for a hydraulic jump. Hence, for (relatively small) rock blocks, spatial correlation of pressures is generally not so important.

For concrete slabs, with side lengths much larger than the integral scale, instantaneous spatial correlations between several locations at the slab surface are strictly speaking necessary in order to correctly assess the two-dimensional character of the impacting turbulent flow field. This can be performed by means of physical model testing, but is time- and cost consuming and does not provide information on the 2D transient underpressure field, which is hard to simulate.

Therefore, a simplified approach is presented here. The approach considers that the total surface pressure (force) is accurately represented by the average value of the time-averaged surface pressures. Then, the following steps are applied, based on Figure 4:

1. A certain number of positive pressure spots are transferred via the joints underneath the slab and generate underpressures. The number of spots and the area over which they act underneath the slab is unknown. Also, their amplitude is not exactly known.
2. The amplitude of these spots can be represented by the average value of the maximum surface pressures along the joints. This assumption is plausible based on the significant two-dimensional diffusion that will occur when a localised pulse enters a wide joint (Bollaert, 2002). The average may be determined in both X and Y directions, based on the corresponding sets of opposite joints, resulting so in a *pseudo-2D* approach
3. The area of application of this pulse under the slab is considered 1D, i.e. corresponding to a *strip* with a length equal to the slab length and a width to be defined, but minimum one times the integral scale of the surface pressures. The 1D strip width that results in the exact 2D underpressure can be determined based on 2D laboratory measurements of net uplift forces on slabs available in literature.
4. For hydraulic jumps, direct force measurements on 2D slabs are available (Bellin & Fiorotto, 1995). Assuming that these net uplift pressures have been measured for a time-averaged surface pressure field, the exact 2D underpressure field can be deduced.
5. The 1D strip width provides the relationship between a 1D and a 2D approach, based on 2D model tests for hydraulic jumps, and is considered applicable to jet impact also.
6. The computed underpressure is multiplied by the transient multiplication factor Γ .

6 CONCLUSIONS

The present article presents a new procedure to compute failure of concrete slabs of stilling basins due to net uplift pressures. The procedure accounts for the 2D pressure field over the slab and considers that pressure pulses are transferred via the joints under the slabs. There, transient wave effects may amplify the uplift pressures. The transient underpressures are defined based on the 1D two-phase transient flow equations and their area of application under the slab is determined by means of available net uplift forces on 2D slabs under hydraulic jump impact.

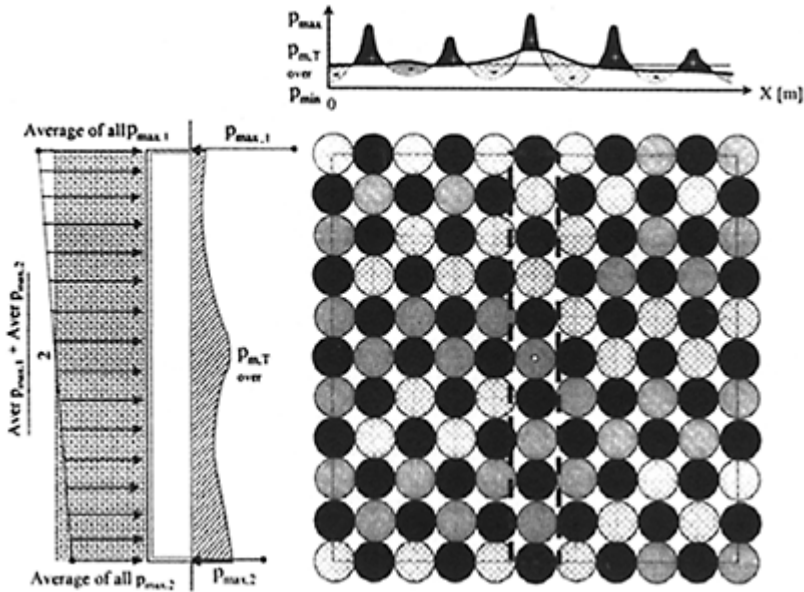


Figure 4. Sketch of spatial pressure distribution for a small integral scale of pressure fluctuations (pm=instantaneous spatial average pressure values). Positive spots are in black, negative in gray.

REFERENCES

- Bollaert, E. 2002. Transient water pressures in joints and formation of rock scour due to high-velocity jet impact. *Communication 13 Laboratory of Hydraulic Constructions*. EPFL, Switzerland.

- Bollaert, E. 2003a. The influence of joint aeration on dynamic uplift of concrete slabs of plunge pool linings. *XXXth IAHR Congress*. Thessaloniki. Greece.
- Bollaert, E. 2003b. Numerical modeling of hydrodynamic forces on Folsom Dam stilling basin. *USArmy Corps of Engineers, Sacramen to District*, Report Aqua Vision Engineering Inc.
- Bollaert, E., Falvey, H.T. & Schleiss, A. 2002. Assessment of turbulent jet impingement in plunge pools: the particular characteristics of a near-prototype physical model study. *Proceedings of Riverflow 2002*. Louvain-la-Neuve. Belgique.
- Ervine, D.A., Falvey, H.R. & Withers, W. 1997. Pressure fluctuations on plunge pool floors. *Journal of Hydraulic Research*, IAHR. (35) 2.
- Bellin, A. & Fiorotto, V. 1995. Direct dynamic force measurement on slabs in spillway stilling basins. *Journal of Hydmulic Engineering*, ASCE. (121) 10:686–693.
- Fiorotto, V. & Rinaldo, A. 1992. Fluctuating uplift and lining design in spillway stilling basins. *Journal of Hydraulic Engineering*, ASCE. (118) 4.
- Toso, J. & Bowers, E.C. 1988. Extreme pressures in hydraulic jump stilling basin. *Journal of Hydraulic Engineering*, ASCE (114) 8:829–843.

Instantaneous pressure field on a submerged jump stilling basin

R.A.Lopardo, C.A.Fattor, M.C.Lopardo & J.M.Casado
*National Water Institute (INA) Casilla Correo, Ezeiza, Buenos Aires,
Argentina*

Hydraulics of Dams and River Structures—Yazdandoost & Attari (eds)

© 2004 Taylor & Francis Group, London, ISBN 90 5809 632 7

ABSTRACT: The mean flow and the fluctuating motion are necessary to get a proper physical knowledge of the submerged jump. The mean flow analysis allows the determination of the general pattern of the flow, such as the submerged jump length and the mean pressures field. An empirical equation for the estimation of the length of submerged jump is proposed.

On the other hand, for the fluctuating motion interpretation, the experimental research on the associated turbulence was made. For this purpose, the authors developed an extensive laboratory research for the instantaneous pressures field determination, taking into account different flow boundary conditions. Because of the random nature of the process, the experimental study of the instantaneous pressure field was based on the knowledge of several statistical parameters of amplitudes and frequencies as functions of the Froude number and the submergence factor.

1 INTRODUCTION

The submerged jump is a turbulent flow generated on a horizontal floor downstream a sluice gate. It can be considered as an intermediate state between two well-known hydraulic phenomena with different physical characteristics: the free hydraulic jump and the turbulent jet diffusion in a semiinfinite media.

Even though the macroscopic hydraulic design of stilling basins, based on mean pressure and velocity values, were the subject of numerous research in the past, some of these known aspects are verified in this paper with the author's data.

Well-known "design criteria" covering the macroscopic analysis for conventional structures can be found in manuals for hydraulic engineers, whose results have been obtained from laboratory experiments and prototype data. In spite of this, the problems

and destruction of stilling basins have not been avoided. The internal flow of hydraulic jump is essentially an unsteady flow subjected to macroturbulent random fluctuations and it is not sufficiently known. Macroturbulence is associated with vortex motion of large size and low frequencies. The random nature of these fluctuating actions requires the stochastic approach to reach results for practical applications.

Hydraulic jump energy dissipation is always related to severe pressure fluctuations acting on the floor and walls of stilling basins. Fluctuating actions may be responsible for important damages in hydraulic structures caused by the lifting of whole slabs, structural vibrations, fatigue of materials and intermittent cavitation due to instantaneous depressions.

Due to the random nature of the process, the power spectra density function and the probability distribution function are the most suitable ways of presenting a quantitative description. By means of the spectral and the probabilistic analysis the following statistical parameters required for design purposes are presented: rms amplitude, amplitudes with 0.1% of probability (for cavitation tendency analysis), the skewness of the probability density function, peak frequencies (for vibration analysis) and zero-crossing frequency (for estimation of fatigue of materials). These parameters, being currently considered for submerged hydraulic jump, were previously analysed for free hydraulic jumps (Lopardo, 1988).

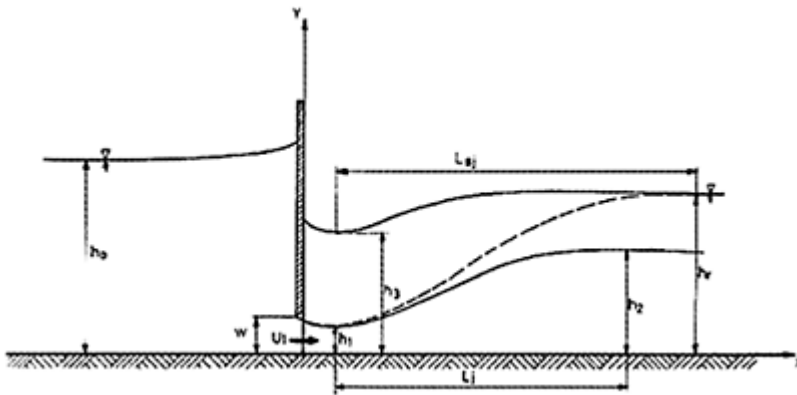


Figure 1. Submerged hydraulic jump.
Definition sketch.

2 LENGTH OF SUBMERGED JUMP

Even when numerous researchers made the macroscopic analysis of the free hydraulic jump, the literature on submerged jump is certainly scarce. By means of the application of the momentum and mass conservation principles (Govinda Rao & Rajaratnam, 1963) the depth relationship h_3/h_1 can be characterized as a function of two non dimensional parameters: the incident Froude Number $F_1 = U_1/\sqrt{gh_1}$ and the "submergence

coefficient" $S=(h_r-h_2)/h_2$, where h_r is the tailwater depth (Fig. 1) and h_2 is the subsequent depth for the free hydraulic jump with the same incident Froude Number.

The macroscopic analysis allows obtaining the equation (1), which has an interesting experimental verification, (Sauma Haddad et al., 1992):

$$h_3/h_1 = \{(1 + S)^2 \sigma^2 - 2F_1^2[1 - (\sigma(1 + S))^{-1}]\}^{1/2} \quad (1)$$

where σ is the relationship h_2/h_1 for the free hydraulic jump, given by Bélanger by the equation(2):

$$h_2/h_1 = \sigma = 0.5[(1 + 8F_1^2) - 1]^{0.5} \quad (2)$$

The most controversial macroscopic variable for submerged jump stilling basins is the length of the submerged jump " L_r ", which depends on the criteria to select the inflow and the downstream end sections of the jump. A tentative empirical formulation (Rajaratnam, 1967) is given by the equation (3):

$$L_r/h_2=6.1+4.9S \quad (3)$$

but the jump length is not defined and it is not valid for the boundary condition $S=0$ (free jump).

Macroscopically, it is possible to consider the submerged jump length as the distance between the "vena contracta" section downstream the sluice gate and the section where the free surface can be considered as horizontal. This definition, which cannot cover the whole macroturbulent phenomena, can be adopted as a good first approximation, compatible with the mean flow resolution. As it was experimentally demonstrated (Sauma Haddad, 1992) the upstream section can be located at 1.5 times the sluice gate opening ($x=1.5 w$).

Experimental results allow to show the non dimensional parameter $L_r/(h_r-h_3)$ as a function of the submergence coefficient S (Fig. 2). The choice of the new non-dimensional parameter takes into account the low dependence with the incident Froude Number F_1 .

By applying a regression analysis, the empirical equation (4) can be suggested:

$$L_r/(h_r-h_3)=6+41.2S \quad (4)$$

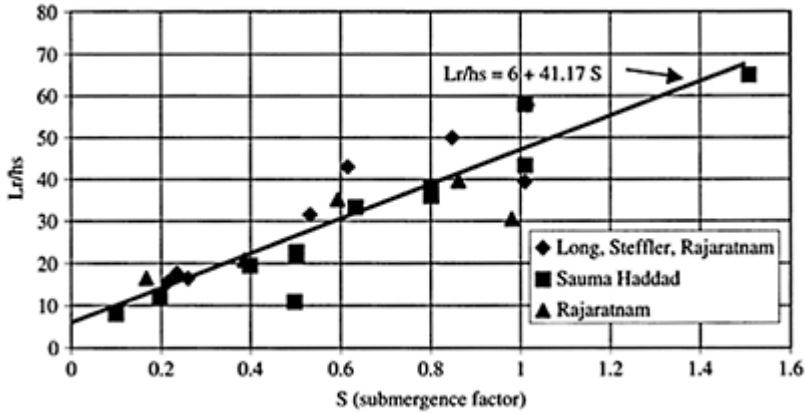


Figure 2. Length of the submerged hydraulic jump.

with a correlation coefficient $R=0.93$. The experimental data included in Figure 2 cover the range of incident Froude numbers $3 < F_1 < 8$ and submergence coefficients between $S=0.1$ and $S=1.5$. With the same results the equation (3) has $R=0.48$.

3 MEAN AMPLITUDES OF PRESSURE FLUCTUATIONS

Following previous experimental conclusions (Lopardo, 1988), experimental tests were accomplished for incident Reynolds number R_1 up to 100,000 and sluice gate openings larger than 3 cm, for incident Froude numbers between $F_1=3$ and $F_1=6$ and submergence factors $0.1 < S < 1.1$.

The mean quadratic pressure fluctuation values can be represented by the “coefficient” of pressure amplitude of fluctuation, defined as

$$C'_p = \frac{\sqrt{p'^2}}{\rho \frac{U_1^2}{2}} \quad (5)$$

where the quadratic mean value of the signal is used to characterize the rms. amplitude of pressure fluctuation.

With the support of a data bank created in the Water National Institute of Argentina (Sauma Haddad, 1992) and new experimental verifications it is possible to analyse the instantaneous pressure fluctuations field for submerged jumps.

Then, it is necessary to include the submergence factor “S”, previously defined. The experimental research covers the range $0.1 < S < 1.1$ for four different incident Froude numbers between $F_1=3$ and $F_1=6$.

As it was previously presented for free jumps on horizontal stilling basins (Lopardo, 1985), Figure 3 shows the C'_p value for submerged jumps with $3 < F_1 < 6$ for $S=0.3$. The

obtained data demonstrates that C'_p values rise for decreasing incident Froude numbers in the upstream zone ($x/h_1 < 10$). On the other hand, C'_p values increase for increasing Froude numbers in the downstream region of the stilling basin ($x/h_1 > 30$).

To take a look on the influence of the submergence factor, Figure 4 shows diverse C'_p data as a function of x/h_1 , for seven different S values, including $S=0$ (free jump condition) for a given incident Froude number $F_1=3$. For $x/h_1 > 12$ the general data distribution allows to get a coherent conclusion: the submergence factor increases the intensity of mean pressure fluctuations on the stilling basin's floor. The free jump C'_p value is a half or lower than the same value for the biggest S factor considered in the experiments ($S=1.1$). Although is more difficult to obtain general

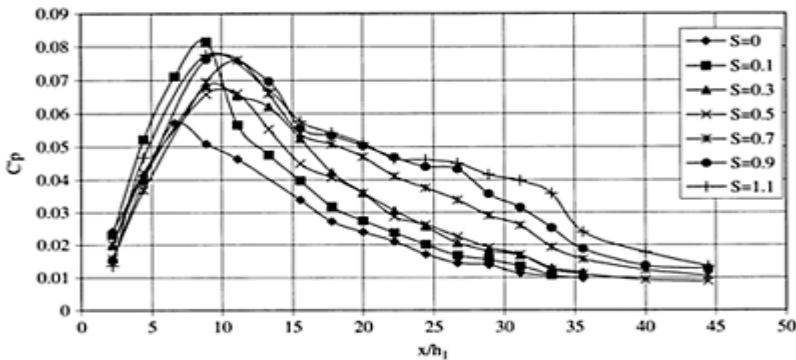


Figure 3. C'_p values as a function of x/h_1 for $F_1=3$ and diverse submergence factors.

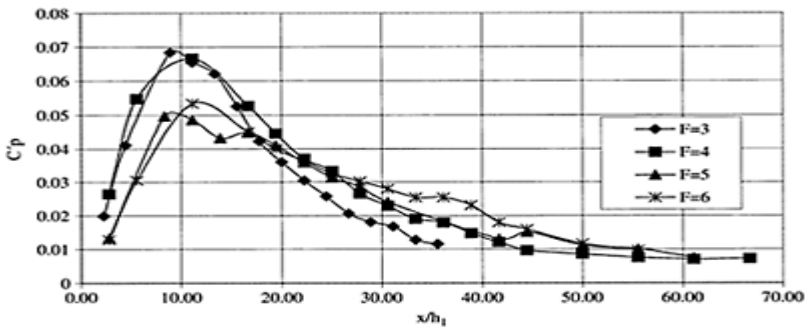


Figure 4. C'_p values as a function of x/h_1 for $S=0.3$ and diverse incident Froude Numbers.

conclusions for the upstream region, the submerged jump seems always to have more turbulence intensity than the free jump.

Experimental data from other authors (Long et al., 1990) demonstrates that submerged jump has a three-dimensional velocity field, with two vertical vortexes downstream of the gate. This aspect certainly contributes on the increase of macroturbulence intensity.

4 PEAK AMPLITUDES OF PRESSURE FLUCTUATIONS

It is also relevant to the subject the knowledge of the peak value of the semi-amplitude with a 0.1% probability of being exceeded by more negative values $C'_{p(-)}$

This parameter, which is defined by equation (6), is important for assessing the effect of the uplift of bottom slabs and especially the tendency to cavitation by pressure pulses:

$$C'_{p(-)} = \frac{p'_{0.1}}{\rho \frac{U^2}{2}} \quad (6)$$

For free hydraulic jump stilling basins, there is information about the C'_{p} and $C'_{p(-)}$ values for several incident Froude numbers, derived from laboratory experimental research (Lopardo, 1985).

Due to turbulence is a random phenomenon, the maximum and minimum values on a record of instantaneous pressures lack statistical validity, depending on the length of the record. For the present study, those values that have a probability of being exceeded only by 0.1% in both directions (positive and negative) will be considered as positive and negative “extreme” values. Thus, the value having 99.9% probability of being exceeded by more negative values will be designated as $C'_{p(+)}$, while the value having 0.1% probability of being exceeded by more negative values will be designated as $C'_{p(-)}$.

Thus, we have the equations 7 and 8:

$$\eta(+) = \frac{C'_{p(+)}}{C'_p} \quad (7)$$

$$\eta(-) = \frac{C'_{p(-)}}{C'_p} \quad (8)$$

As it is obvious, a difference between the extreme positive and negative values of the amplitude probability density function implies that Gauss's equation fails to interpret it correctly. The statistical distribution always shows a certain skewness, which is defined as equation 9:

$$S_w = \frac{\int_{-\infty}^{+\infty} p'^3 P(p') dp'}{\sqrt{p'^2}} \quad (9)$$

where $P(p')$ is the probability function of variable p' , which is the instantaneous fluctuation of pressure. The skewness of the amplitude probability density function is a statistical parameter that characterizes certain interesting aspects of the random signals.

It should be borne in mind that the transition from positive to negative S_w values seems to imply the possibility of a separation of the boundary layer from the bottom, which has been discussed elsewhere (Lopardo et al., 1999).

Figure 5 and Figure 6 are presented as an example. They show the variation of the statistical parameters $\eta(+)$, $\eta(-)$ and S_w as functions of x/L_r for a given submergence coefficient ($S=0.5$). The data dispersion is bigger than the free jump experimental information, particularly for the skewness values. However, it is possible to suggest the following empirical lineal functions (10):

$$\begin{aligned} \eta(+)&=3.86-0.46(x/L_r), & \eta(-)&=-2.63-1.14(x/L_r) & \text{and} \\ S_w&=0.41-0.48(x/L_r) \end{aligned} \quad (10)$$

These experimental results are similar to the free jump data, but with a slope of the lineal relationship always lower for the submerged jump. This conclusion shows a "more Gaussian" behaviour for pressure fluctuations in submerged jumps than free jumps.

When the degree of submergence increases the slope of the lineal relationship $C'_{p(+)} / C'_p$ decreases with the distance. For a submergence coefficient $S>1$, that relationship can be considered as a constant for different x/L_r values.

For technical purposes, it can be estimated that for submergence coefficients $S>1$, at any x/L_r point and incident Froude Number $3<F_1<6$, the relationship between the maximum positive deflection ($P'_{99.9\%}$) and the rms value is in the order of 4 and the relationship between the maximum negative deflection ($P'_{01\%}$) and the rms value is around -3.

Experimental data allows to observe how decreases the slope of the lineal function $S_w=f(x/L_r)$ for increasing values of the submergence coefficient S . Finally, for $S>1$, the line has not negative slope. The approximation curve must be just considered as an example, without the intention to reach a complete interpretation of this complex process.

5 CONCLUSIONS

Some experimental results are presented for the submerged hydraulic jump. From the macroscopic point of view, the proposal of an empirical equation to estimate the length of the jump is suggested.

For the fluctuating motion interpretation, the experimental research developed allows to calculate C'_p the value for different incident Froude numbers and several submergence coefficients.

As the rms pressure fluctuation value is not enough for cavitation tendency analysis or slab lift actions calculation, the relationship between the maximum deflections in both sides, positive and negative, are estimated.

These results demonstrate that increasing the submergence coefficient, the slope of the lineal law which connects the relationship $C'_{p(+)} / C'_p$ with the distance x/L_r decreases. This law is a constant for submergence coefficients $S > 1$.

This result is clearly confirmed with the experimental representation of the skewness factor of the probability density function of pressure amplitudes, for different incident Froude numbers and several submergence coefficients.

REFERENCES

- Govinda Rao, N.S. & Rajaratnam, N. 1963. The submerged hydraulic jump. *Journal of Hydraulic Division, ASCE, Vol.89*: pp. 139–162.
- Long, D. et al. 1990. LDA study of submerged hydraulic jump. *Journal of Hydraulic Research, Vol. 28, No 4*: pp. 437–460.
- Lopardo, R.A. 1985. Metodología de estimación de presiones instantáneas en cuencos amortiguadores (*Methodology for estimation of instantaneous pressures in stilling basins*). *Anales de la Universidad de Chile, V Series, No 8*. Santiagode Chile: Chile: pp.437–455.
- Lopardo, R.A. 1988. Stilling basin pressure fluctuations. *International Symposium on Model-Prototype Correlation of Hydraulic Structures*. Colorado Springs: USA: pp.56–73.
- Lopardo, R.A. et al. 1999. Physical modelling and design estimation of instantaneous pressures in stilling basins. *Proceedings of the XXVIII IAHR Congress*. Graz: Austria, CD-ROM version.
- Rajaratnam, N. 1967. Hydraulic jumps. *Advances in Hydrosience, Academic Press, Vol 4*. New York: USA: pp. 197–280.
- Sauma Haddad, J.C. 1992. Resalto sumergido (*Submerged jump*). *Report INCYTH LHA-116-02-92, INA*. Ezeiza, Argentina.
- Sauma Haddad, J.C. et al. 1992. Contribución al estudio macroscópico del resalto sumergido (*Contribution to the macroscopic study of the submerged jump*). *XV Latin American Congress, IAHR*. Cartagena: Colombia. Vol. 1, pp. 73–82.

Aspects of vibrations and fatigue of materials related to coherent structures of macroturbulent flows

R.A.Lopardo, C.A.Fattor, J.M.Casado & M.C.Lopardo
*National Institute of Water Casilla Correo, Ezeiza, Buenos Aires,
Argentina*

Hydraulics of Dams and River Structures—Yazdandoost & Attari (eds)

© 2004 Taylor & Francis Group, London, ISBN 90 5809 632 7

ABSTRACT: Macroturbulent flows in stilling basins can be analysed by their coherent structures, being necessary to determine length and time scales to get a comprehensive understanding of the phenomena involved. The peak frequencies of the main vortexes transported for the mean flow can be evaluated if the main parameters of the coherent structures are determined, making possible the determination of the Strouhal number as well as its comparison with the natural frequency of the structures submerged in the macroturbulent flow and, in this way, estimating potential problems of resonance.

On the other hand, the effect of the fatigue in an eventual loss of resistance of the steel bars embedded in the concrete can be experimentally determined by means of the zero-crossing frequency. In this way, the number of times of the steel bars passing from traction to compression and vice versa can be estimated.

The experimental data involving vibrations aspects are limited, in this article, to a free hydraulic jump downstream of a vertical gate with incident Froude number $F_1=3$, and a rectangular slab of width b and non-dimensional length $a/h_1=3$, where a is the length of the slab and h_1 is the water depth at the inlet to the jump. As regards the analysis of fatigue, results for $3 < F_1 < 6$ are presented, also considering a free hydraulic jump downstream of a vertical gate.

1 INTRODUCTION

Energy dissipation in stilling basins produces dynamic loads on the bottom slabs. Some characteristics of the coherent structures of the macroturbulent flow can be analysed from the calculation of the fluctuating loads on slabs of a free hydraulic jump stilling basin. The analysis of the autocorrelation function of the random loads at different locations along the bottom of the hydraulic jump allows estimating an approximate magnitude of the scale of times of the turbulence, as well as obtaining information regarding the main period of the fundamental vortexes. This last information can also be obtained from power spectra analysis of individual records of pressure fluctuations along the bottom of the hydraulic jump.

The first purpose of this article is to analyse the characteristics of the coefficient of autocorrelation of fluctuating loads for different sizes of slabs, given through a/h_1 , where “ a ” is the length of the slab and “ h_1 ” is the initial depth of the jump (Fig. 1). In this way, the relationship a/h_1 not only constitute a parameter of the dimensions of the slab but also an important reference of the size of the macroturbulent structures of the hydraulic jump compared to the slab length.

Due to the fact that turbulent flow represents an alternating load on hydraulic structures, the second aim of this work is to present a methodology to estimate the reduction of the resistance of the metallic elements due to fatigue effects.

2 STRUCTURAL VIBRATIONS

The stochastic approach of pressure fluctuations by means of laboratory experimental data allows the estimation of the peak Strouhal number of the process S_p , which is expressed by equation 1:

$$S_p = \frac{f_p \cdot h_1}{U_1} \quad (1)$$

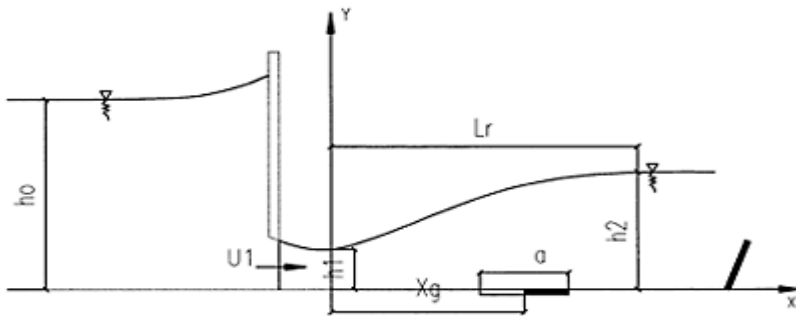


Figure 1. General sketch.

where f_p =peak frequency; h_1 =initial depth of the jump; and U_1 =initial velocity of the jump.

This result is important for vibration analysis. The peak frequency, which is necessary to calculate S_p , can be easily obtained from the power spectra of an individual record. It has been demonstrated (Lopardo & Henning, 1986) that S_p decreases gradually with the distance x/h_1 and it is not seriously affected by the incident Froude number F_1 , being F_1 defined by equation 2:

$$F_1 = \frac{U_1}{\sqrt{g \cdot h_1}} \quad (2)$$

where g =gravity acceleration.

Another aspect related to the variation of S_p is that at one half of the jump length, the Strouhal number falls sharply and remains practically constant towards downstream.

The stochastic approach of S_p obtained from laboratory basic research for free hydraulic jump on a horizontal bottom cannot be extrapolated to different shapes and flow configurations. The submergence factor has relative importance, but geometric boundary configuration is relevant.

Another methodology to obtain S_p is to proceed to the spatial integration of the pressures field acting upon a series of pressure transducers that define, by this way, a slab of length a , repeating this process for different lengths of slabs. Because the whole length of the hydraulic jump can be involved in this analysis, the variation of the autocorrelation coefficient of fluctuating forces as a function of x/h_1 (location of the slab) can be evaluated for each condition of a/h_1 . The autocorrelation is a function that brings information only depending on the difference of time τ , which is expressed in equation 3:

$$\tau = t' - t \quad (3)$$

The coefficient of autocorrelation can be defined by equation 4 as follows:

$$A(\tau) = \frac{\overline{p(t) \cdot p(t')}}{\bar{p}^2} \quad (4)$$

where $p(t)$ =instantaneous pressure at time t ; $p(t')$ =instantaneous pressure at time t' ; \bar{p} =mean pressure. The coefficient of autocorrelation is 1 for $\tau=0$ and less than 1 for τ different from zero.

In the present case, the analysis is developed on the forces of fluctuating origin acting on a rectangular slab, obtained from the integration of pressure fluctuations. Consequently, the autocorrelation coefficient of forces can be defined by equation 5:

$$A_f(\tau) = \frac{\overline{f(t) \cdot f(t')}}{\bar{f}^2} \quad (5)$$

where $f(t)$ =instantaneous force at time t ; $f(t')$ =instantaneous force at time t' ; and \bar{f} =mean force.

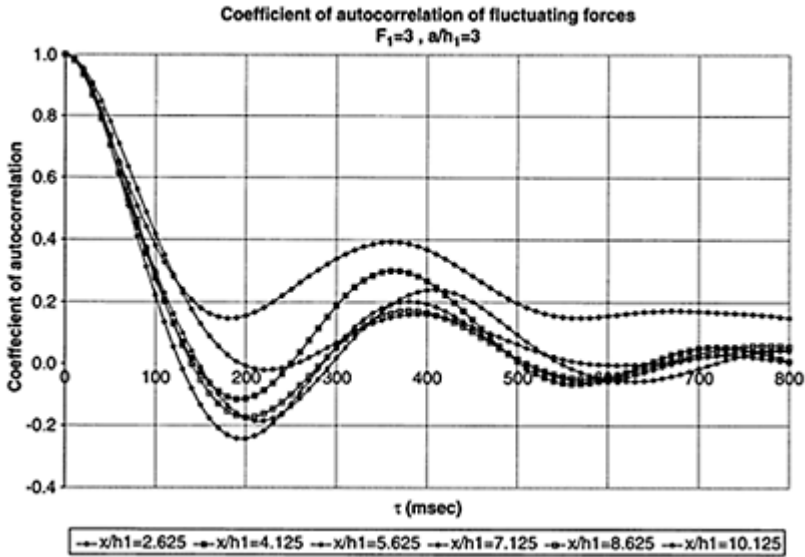


Figure 2. Variation of the coefficient of autocorrelation of fluctuating forces.

This analysis, developed by Lopardo et al. (1998), allows getting as a result a series of curves, which are similar to those presented in Figure 2, where it is feasible to see the variation of the autocorrelation coefficient $Af(\tau)$ for $F_1=3$ and $a/h_1=3$. These curves show a tendency to decrease, having a minimum and a second relative maximum before reaching the final decay, which tends to the statistic independence $Af(\tau)=0$ for τ increasing to infinitum.

For values x/h_1 less than the slab length ($x/h_1 < 3$) the first minimum value is higher than zero, which means that the macroturbulent structure is not completely developed in this area. When x/h_1 increases, the curves of autocorrelation $Af(\tau)$ show that the first minimum crosses the zero, reaching the lowest value (negative) around $x/h_1=7$, and increasing after that.

As regards the variation of the values of $Af(\tau)$ it can be observed that for $x/h_1 < 11.5$ the curves of autocorrelation present a first minimum close to $\tau=200$ msec and a relative maximum peak for $350 \text{ msec} < \tau < 400$ msec. For values of $x/h_1 > 11.5$ (Fig. 3) the curves show a continuous decay. This singular aspect allows concluding that the spatial scale of the macroturbulent structures is significant compared to the size of the slab, which is similar to say that the spatial integration of the fluctuating pressures on a slab of non-dimensional length a/h_1 involves similar phenomena.

A change of the macroturbulent structure of the flow is detected for slab locations so that $x/h_1 > 11.5$. That location, for $F_1=3$, is equivalent to consider $x/L_r=0.70$, where L_r is the length of the hydraulic jump. It is interesting to remark that similar conclusions were reached some years ago by means of measurements of fluctuating pressures in the bottom of hydraulic jumps downstream of sluice gates (Lopardo & Henning, 1986).

The curve of $Af(\tau)$ obtained by the spatial integration of the pressures field has a second maximum, between 350 msec and 400 msec, for $x/L_r < 0.70$. Then, it is reasonable to estimate that the peak frequency of the macrovortexes induced by the flow will be between 2.5 Hz and 3 Hz with independence of x/h_1 if $x/L_r < 0.70$. Strouhal numbers can be calculated with these frequencies, being able to verify the results by means of individual fluctuating pressures measurements along the bottom of the hydraulic jump.

Comparing the autocorrelation of forces with the power spectra in one point, it can be concluded that in the region where the autocorrelation curves are not monotonously decreasing ($x/h_1 > 11.5$) the peak frequency of an individual power spectra practically agrees with the value $1/\tau$ of the second maximum.

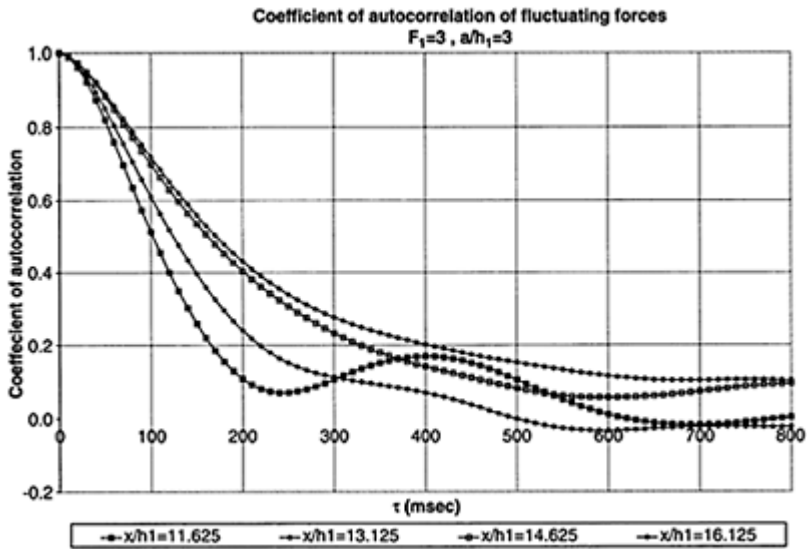


Figure 3. Variation of the coefficient of autocorrelation of fluctuating forces.

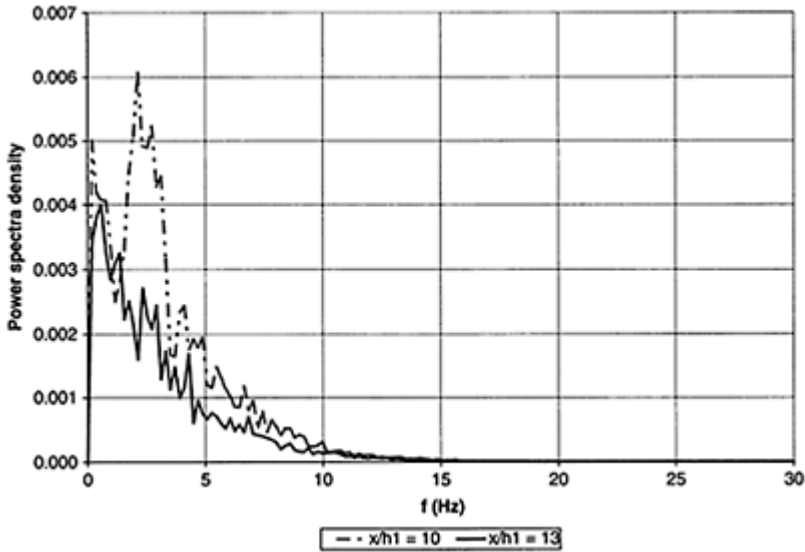


Figure 4. Power spectra analysis.

On the other hand, the peak frequency of an individual power spectra is closer to zero for $x/h_1 > 11.5$, with a power spectra whose shape is also monotonously decreasing. This fact shows the classic distribution of energy well-known as “energy fall”.

Peak frequencies of the macroturbulent structures of the flow can be properly characterized by means of Strouhal number, directly obtained from individual power spectra. Figure 4 illustrates a situation where the gravity centre of the slab is located at $x/h_1 = 11.6$; the pressure gauge located at $x/h_1 = 10$ has a peak frequency of 2.5 Hz and the power spectra of the point located at $x/h_1 = 13$ has a lower peak frequency, with a monotonously decreasing power spectra.

As regards the variation of S_p , obtained of the autocorrelation function of fluctuating forces, respect to x/L_r , there is a scarce influence of the location along the hydraulic jump if $x/L_r < 0.7$. Besides that, it is remarkable the proximity with the values obtained from the power spectra of isolated points.

Finally, the integration of the coefficient of autocorrelation presented in Figure 3 for those cases where $Af(\tau) \rightarrow 0$ when $\tau \cong 800$ allows obtaining an average value $T = 0.59$ sec that can be estimated as a sort of “time scale of the macroturbulent flow”. If the mean lengths inside the hydraulic jump could be represented by the average value of the initial and the subsequent depth of the hydraulic jump (H) and the celerity of the pressures wave is expressed for equation 6, the celerity would result $c/U_1 = 0.67$.

$$c = 2 \cdot \pi \cdot \frac{H}{T} \quad (6)$$

It is interesting to remark that, according to experiences carried out by Lopardo et al. (1984), the celerity in the upstream region of the hydraulic jump established downstream of a chute spillway (with different inlet conditions to the situation developed in this

article) is $c/U_1=0.55$, having obtained the celerity c from the functions of spatial correlation.

3 FATIGUE ESTIMATION

The theory of the resistance of materials shows that the resistance of steel decreases significantly under an oscillating load. This is the case of the anchors of the slabs in conventional stilling basins.

The integration at any time of fluctuating pressures acting on a generic surface, results in a random force and moment, variable with time, that induce successive alternating loads on the anchors. The numerous studies related to fatigue aspects, show that the levels of stress of the steel depends exclusively on the number of times N that the anchors work. Then, the main unknown in this situation is the factor N , and its knowledge allows solving the problem with some of the several functions that relate the reduction of resistance by fatigue with N , found in the literature. The variable N depends on two independent events: a) the hydrodynamic characteristic of the macroturbulent flow and b) the effective operation of the stilling basin under the design discharge (obtained by hydrologic analysis).

The study of the first topic must be done considering the crossing frequency corresponding to the level of solicitation able to produce traction in the anchors of the slabs. This frequency represents the number of times per second that the macroturbulent action produces traction efforts on the anchors. This frequency multiplied by the operating time of the spillway gives the needed parameter N .

As a first approach, the field of pressure fluctuations beneath free and submerged hydraulic jump can be assumed as an ergodic, stationary and Gaussian stochastic process of zero average value. With these hypotheses, experimentally confirmed, the theory of random waves is valid.

The integration at any time of fluctuating pressure p' acting on a generic surface, results in a random force and moment, variable with time, that induce successive alternating loads on the anchors. The Strouhal number S_c can be defined by equation 7:

$$S_c = \frac{h_1}{T_c \cdot U_1} \quad (7)$$

where T_c is the mean period between up-crossings by a certain value of the pressure fluctuation. According to an article of Lopardo & Sauma Haddad (1993), S_c can be expressed for equation 8:

$$S_c = S_0 \cdot \exp \left[\frac{-(p'_c)^2}{2 \cdot m_0} \right] \quad (8)$$

This dimensionless expression shows that the Strouhal number S_c , which includes the unknown frequency, is a function of the zero crossing Strouhal number S_0 (conformed with f_0 , which

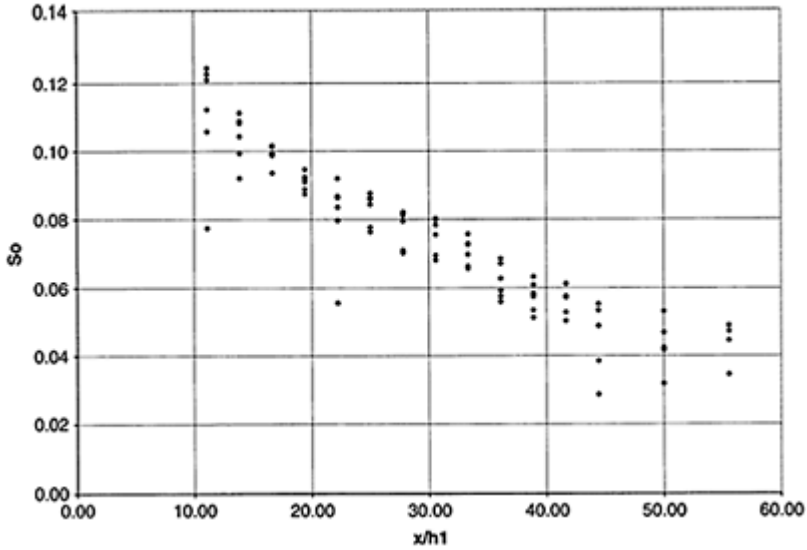


Figure 5. Adjustment between experimental data and equation $16-F_1=6$.

is obtained from the power spectra laboratory data), the variance of the record of the pressure fluctuation m_0 and the critical pressure fluctuation p'_c that is able to put in traction the anchorage.

The hydrodynamic characteristics (incident Froude number, submergence degree, spatial distribution of slabs) are known. With these parameters p'_c can be estimated through a static analysis of the slabs. The coefficient of pressure fluctuations C'_p gives the variance m_0 . In this way the problem was reduced to evaluate S_0 , which is defined by equation 9:

$$S_0 = \frac{f_0 \cdot h_1}{U_1} \quad (9)$$

By means of dimensionless analysis, S_0 can be written as in equation 10:

$$S_0 = \Gamma\left(\frac{x}{h_1, F_1, s}\right) \quad (10)$$

where s is the submergence factor defined by equation 11:

$$s = \frac{h_r - h_2}{h_2} \quad (11)$$

According to the experimental results S_0 is apparently independent of the submergence s , depends on F_1 and decreases linearly with x/h_1 . The experiments were carried out for hydraulic conditions given by $3 < F_1 < 6$ and $0 < S < 1.10$. The statistical analysis of the experimental data resulted in the empirical equations 12 to 15 (R being the correlation coefficient):

$$S_0 = 0.23 - 0.0037 \cdot (x/h_1); R^2 = 0.81, \text{ valid for } F_1 = 3 \quad (12)$$

$$S_0 = 0.17 - 0.0023 \cdot (x/h_1); R^2 = 0.91, \text{ valid for } F_1 \quad (13)$$

$$S_0 = 0.13 - 0.0016 \cdot (x/h_1); R^2 = 0.79, \text{ valid for } F_1 \quad (14)$$

$$S_0 = 0.12 - 0.0016 \cdot (x/h_1); R^2 = 0.93, \text{ valid for } F_1 \quad (15)$$

On the other hand, equation 16 brings an empirical general expression of S_0 as a function of F_1 and x/h_1

$$S_0 = \frac{0.66}{F_1} - 0.014 \cdot F_1^{-1.28} \cdot \frac{x}{h_1} \quad (16)$$

In order to see the adjustment of the last expression, Figure 5 shows the experimental model test results and the empirical equation for slabs below an horizontal stable hydraulic jump stilling basin without spillway piers or other appurtenances for $F_1 = 6$.

4 CONCLUSIONS

The function autocorrelation of fluctuating pressures allows an approximate determination of the scale of time and the peak frequency of the fundamental vortexes transported by the flow. Strouhal numbers are highly similar to those obtained from power spectra analysis of individual records of pressure fluctuations.

The slabs of the bottom of a hydraulic jump stilling basin downstream a vertical sluice gate receive loads whose frequency is almost constant for x/h_1 less than a critical value, and without changes with the distance to $x/L_r < 0.70$. For $x/L_r > 0.70$, the function autocorrelation show a monotonously decreasing tendency. The results presented show a close agreement with previous studies involving aspects of space-time correlation of pressure fluctuations and peak frequencies for different inlet conditions to the hydraulic jump (Lopardo & Henning, 1986). The knowledge of the coefficient of autocorrelation allows calculating an integral time scale, which results 0.59 sec. for the condition analysed in this article. Some estimations based on these considerations bring as a result that the celerity of the pressure wave is $c/U_1 = 0.67$, which is higher than the values calculated for hydraulic jumps downstream of chute spillways.

A methodology to estimate the fatigue aspects on structures submerged in macroturbulent flows was developed. The problem was solved with the aid of the zero crossing Strouhal number. The paper gives empirical dimensionless relations to evaluate this parameter in the submerged hydraulic jump. This methodology can be applied to

study other hydraulic structures with the aid of the physical modeling, in order to establish specific relations for S_0 in each case.

REFERENCES

- Lopardo, R.A. et al. 1984. Correlación de presiones instantáneas inducidas por un resalto hidráulico libre estable, *XI Congreso Latinoamericano de Hidráulica IAHR*, Buenos Aires, 1984, Vol. I, pág. 23–34.
- Lopardo, R.A. et al. 1998. Una aproximación a la frecuencia dominante de estructuras coherentes en flujos macroturbulentos. *XVIII Congreso Latinoamericano de Hidráulica*, Oaxaca, Mexico, Octubre 1998.
- Lopardo, R.A. & Henning, R.E. 1986. Efectos de las condiciones de ingreso al resalto sobre el campo de presiones instantáneas, *XII Congreso Latinoamericano de Hidráulica*, Sao Paulo, Brasil, 1986, Vol. 1, pp. 116–127.
- Lopardo, R.A. & Sauma Haddad, J.C. 1993. Estimation of fatigue aspects on structures submerged in macroturbulent flows, *Advances on Hydro-Science and Engineering*, Washington D.C., U.S.A., 1993, Vol. 1, Part A, pp.1006–1012.

Scale effect on pressure fluctuations over sills in stilling basins

D.Berzi, E.Larcan, S.Mambretti & E.Orsi
Politecnico di Milano, Dept. I.I.A.R., Milan, Italy

Hydraulics of Dams and River Structures—Yazdandoost & Attari (eds)

© 2004 Taylor & Francis Group, London, ISBN 90 5809 632 7

ABSTRACT: This paper concerns the analysis of some aspects of the pressure fluctuations over the upstream face of a sill in a stilling basin. The hydrodynamic forces acting on the sill have to be known, in order to properly design such a structure; so not only the value of the average pressures, but also a quantitative characterization of the distribution of the pressure fluctuations, due to the intense turbulence of the flow, seems very important. Moreover an investigation on the non-dimensional numbers that rule the phenomenon of pressure fluctuations is necessary for a correct modeling of this type of fluid-structure interactions.

1 INTRODUCTION

When a supercritical flow collides with a sill in a stilling basin, a great amount of turbulence is generated and a lot of energy is dissipated. Therefore, great forces, characterized by instantaneous values even much higher than their time-averaged value, work on the structure. A design performed without taking into account these fluctuations can be dangerous. Not only because it is important to define the static force which the structure has to resist at, but also for the possibility of hydro elastic phenomena.

Several works deal with the time-averaged pressures on the upstream face of the sill (Karki 1976, Ohtsu et al. 1991, Guadagnini et al. 1994,1998). The fluctuating component of the pressures is, instead, less studied (Bowers & Tsai 1969, Akbari et al. 1982, Chen & Luo 1984). In order to analyse this phenomenon, one can use two different approaches: investigating the statistical characteristics of the probability distribution of the pressure, in the time domain; obtaining some information about the flow field from the spectrums, in the frequency domain (Berzi & Larcan 2003). Here, the former is used and, in particular, the aim of this work is determining the RMS value of the fluctuating pressures on the basis of some relevant parameters of the flow. The RMS value is important because, for example, it is related to the maximum force acting on the slab beneath the hydraulic jump (Fiorotto & Rinaldo 1992); moreover, one can evaluate the force on the structure, in order to design properly the stilling basin, adding a multiplier of the RMS

value to the time-averaged one. The data of three series of experimental runs, performed at laboratory and real scale, are employed and allow a better comprehension of the scale effects and the role of the non-dimensional parameters. This provides also useful information about the similarity to apply for experimental studies regarding analogue phenomena.

2 THEORETICAL FRAME

A supercritical flow colliding with a sill can originate: a) a free or forced hydraulic jump (Rajaratnam 1964); b) a jet with a central vein and side-zones where the flow is moving backwards; c) a continuous free surface flow over the sill with negligible air entrapment. The presence of one of these three different flow conditions, as described by many authors (Karki 1976, Ohtsu et al. 1991, Guadagnini et al. 1994, 1998), depends on two non-dimensional parameters that represent the influence of the obstacle geometry and the kinematics of the current: s/h_1 e Fr_1 . s/h_1 is the ratio between the height of the sill s and the flow depth h_1 at the first undisturbed section upstream the sill, where the pressure distribution can be considered hydrostatic; $Fr_1 = V_1(gh_1)^{-0.5}$ is the Froude number of the flow in this section, with V_1 average velocity and g gravitational acceleration. A Cartesian plane (Fr_1 , s/h_1) can be used for defining the different flow conditions. The more complete analysis seems to be performed by Guadagnini et al. (1994,1998): three flow regions called α , β and γ are defined and the analytical expressions of the curves, representing the transition from one region to another, are indicated. Figure 1 shows a scheme of the flow field in a condition: Q is the flow-rate and X_s the distance between the sill and the first undisturbed section upstream of the sill. It can be noticed the roller of the hydraulic jump (zone II) localized over the sill and the triangular region (zone IV) at the bottom of the sill originated from the separation of the main flow (zone III), because of the adverse pressure gradient due to the obstacle. A stagnation point (Ohtsu et al. 1991) is present where the main flow attaches to the sill. This characteristic flow field can explain the peculiar S-shape of the pressure distribution along the vertical axe of the upstream sill surface, with a maximum at the stagnation point.

A dimensional analysis about the time-averaged pressures (Cigada et al. 1996) shows that, in addition to the non-dimensional position y/s (y is the distance from the channel bottom), they depend only on the parameters s/h_1 and Fr_1 . Two series of experiments allowed to confirm this analysis and provide a mathematical expression of this relation (Borsani et al. 1998, 2000).

A dimensional analysis can also be performed upon the local RMS values σ of the pressures. In a non-dimensional format:

$$F\left(\frac{\sigma}{0.5\rho V_1^2}, \frac{y}{s}, \frac{s}{h_1}, Fr_1, Re_1\right) = 0 \quad (1)$$

represents the relation that has to be determined. Here, ρ is the fluid density and $Re_1 = V_1 h_1 \nu^{-1}$ is the Reynolds number of the flow relative to the first undisturbed section upstream of the sill, with ν kinematical viscosity of the fluid. Equation (1) becomes:

$$\varphi \left(\frac{\sigma^*}{0.5\rho V_1^2}, \frac{\sigma}{\sigma^*}, \frac{y}{s}, \frac{s}{h_1}, Fr_1, Re_1 \right) = 0 \quad (2)$$

where:

$$\sigma^* = \frac{1}{s} \int_0^s \sigma(y) \cdot dy \quad (3)$$

represents the space-averaged RMS value of the pressures along the vertical axe of the upstream sill surface. If one assumes that σ/σ^* depends only on the non-dimensional position y/s , Equation (2) becomes:

$$\varphi_1 \left(\frac{\sigma^*}{0.5\rho V_1^2}, \frac{s}{h_1}, Fr_1, Re_1 \right) \varphi_2 \left(\frac{\sigma}{\sigma^*}, \frac{y}{s} \right) = 0 \quad (4)$$

Experimental data are required in order to provide an expression for the functions φ_1 and φ_2 . The influence of the Reynolds number on the RMS value σ^* is definitely not negligible, unlike on the time-averaged pressures. As shown by Lopardo & Henning (1985), indeed, the non-dimensional ratio between the pressure RMS value σ^* and the kinetic height $0.5\rho V_1^2$ is an index of the fraction of the energy of the flow dissipated for turbulence. So, the Reynolds number, a measure of the turbulence of the flow, has to be considered in the evaluation of the effective value of the pressures.

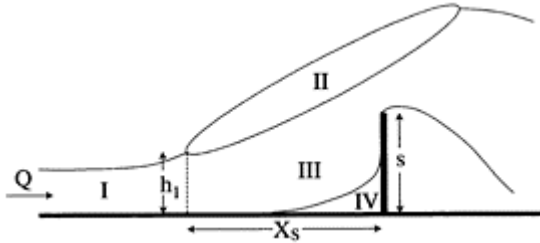


Figure 1. Example of flow condition in region α .

3 EXPERIMENTAL RUNS

Three series of experiments with different geometrical scales have been performed. Hereafter the descriptions of the experimental set-ups and the tables with the characteristics of the tests performed are shown. Figure 2 points out the general scheme of the experimental set-up. The tests performed in laboratory are called 'Laboratory 1' and '2'; those runs carried on at real scale are called 'Field'.

3.1 Laboratory 1

It is composed of a rectangular 6 m long flume with slope $i=0$ and width $B=0.4$ m; a transverse sill with same width, height $s=0.075$ m and thickness 0.02 m is present. Pressure records refer to 9 points localized along the vertical axe of the upstream sill surface; they have been performed through dynamic transducers linked to an electronic equipment for data acquisition.

Every acquisition has been carried out in 9 minutes; with the aid of some preliminary tests, it was possible to see that statistical moments, up to fourth order, are stable with this duration. The sampling frequency adopted is 128 Hz, since a first analysis of the fluctuating components allows us to say that the range of the significant frequencies of the signal is 0–20 Hz. The frequency response of the acquisition system, as indicated in Cigada et al. (1996), has no influence on collected data. The characteristics of the Laboratory 1 tests are listed in table 1 (Borsani et al. 1998).

3.2 Field

Tests have been performed at the desilting channel of the Sernio traverse in Valtellina (Italy); it is 20 m long with a width $B=5.01$ m; in this case the sill was of adjustable height ($s=0.5, 0.6$ and 0.7 m). Pressure acquisition system is similar to that used in the laboratory; the number of the transducers changes with the height of the sill: 8 when $s=0.7$ m, 7 when $s=0.6$ m and

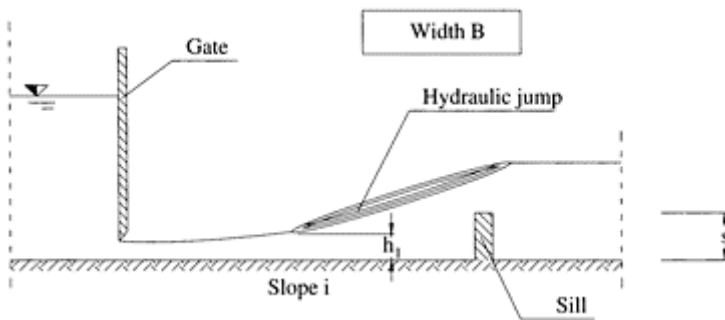


Figure 2. General scheme of the experimental set-up.

Table 1. Laboratory 1 tests.

s (m)	Test	Q (m ³ /s)	h_1 (m)	Fr_1	S/h_1	Re_1	p^*/γ (cm H ₂ O)	σ^*/γ (cm H ₂ O)	Flow region
0.075	M-A	0.034	0.025	6.99	3.06	83547	25.0	4.9	β
	M-B	0.029	0.025	5.94	3.02	72212	18.0	3.1	$\alpha-\beta$
	M-C	0.034	0.022	8.10	3.35	84560	25.4	4.8	β
	M-D	0.036	0.013	8.91	3.44	90502	27.6	5.4	β

M-E	0.024	0.022	5.12	3.07	53399	14.9	1.7	α
M-F	0.018	0.014	8.96	5.43	45234	13.9	2.3	$\alpha-\beta$
M-G	0.016	0.014	8.10	5.47	40426	12.1	1.8	α
M-H	0.014	0.014	7.02	5.40	35820	10.1	1.3	α
M-I	0.017	0.017	6.11	4.34	43256	11.8	1.3	α
M-L	0.020	0.017	7.09	4.36	49805	14.6	2.3	α
M-M	0.022	0.017	8.13	4.44	55620	16.9	3.1	β
M-N	0.025	0.017	8.99	4.41	62027	19.8	3.8	β

6 when $s=0.5$ m. The lowest transducer is at 0.025 m from the bottom, the others are equidistant. In this case every test has been performed in 1 hour with a sampling frequency of 100 Hz. The characteristics of the Field tests are listed in table 2 (Borsani et al. 2001, Berzi & Larcán 2003).

3.3 Laboratory 2

The flume used is the same described at the Section 3.1, but the height s of the sill is equal to 0.12 m. There are 12 transducers linked to 12 equidistant points along the vertical axe of the upstream sill surface. The sampling frequency is 300 Hz, while every test has been performed in 25 minutes. The sampling time necessary for the stability at least of the first and second statistical moment is clearly a function of the Reynolds number; obviously it increases, when the turbulence increases. The characteristics of the Laboratory 2 tests are listed in table 3.

Table 2. Real scale tests.

s (m)	Test	Q (m ³ /s)	h_1 (m)	Fr_1	s/h_1	Re_1	P^*/γ (cm H ₂ O)	σ^*/γ (cm H ₂ O)	Flow region
0.70	P-A	4.36	0.11	7.63	6.36	872000	126.2	21.9	α
	P-B	6.47	0.15	7.11	4.67	1294000	149.3	30.0	α
	P-C	8.52	0.18	7.13	3.89	1703000	161.9	31.9	$\alpha-\beta$
	P-D	16.80	0.32	5.93	2.19	3360000	292.2	68.9	β
	P-E	14.85	0.28	6.40	2.50	2970800	286.0	68.8	β
	P-F	12.75	0.25	6.51	2.80	2550000	253.4	63.1	β
	P-G	10.53	0.22	6.52	3.18	2106000	203.0	48.5	β
0.60	P-H	16.85	0.33	5.68	1.82	2537200	302.5	65.7	$\beta-\gamma$
	P-I	12.69	0.25	6.48	2.40	1700000	275.6	64.5	β
	P-L	8.50	0.18	7.11	3.33	880800	179.7	40.8	β

0.50	P-O	4.40	0.13	6.00	4.62	874000	122.7	24.0	α
	P-P	4.37	0.13	5.95	3.85	1723000	151.8	32.8	α
	P-Q	16.68	0.33	5.62	1.52	1606000	306.8	60.6	γ - β
	P-R	12.67	0.26	6.10	1.92	872000	334.0	62.6	β - γ
	P-S	8.62	0.18	7.20	2.78	1294000	222.9	47.6	β
	P-Z	8.03	0.18	6.72	2.78	1703000	211.5	42.9	β

Table 3. Laboratory 2 tests.

s (m)	Test	Q (m ³ /s)	h_1 (m)	Fr_1	s/h_1	Re_1	P^*/γ (cm H ₂ O)	σ^*/γ (cm H ₂ O)	Flow region
0.12	C1	0.059	0.034	7.72	3.53	530258	41.7	11.3	β
	C2	0.069	0.034	8.93	3.53	613822	50.2	16.3	β
	C3	0.075	0.034	9.69	3.53	665913	59.2	21.1	β
	C4	0.080	0.034	10.31	3.53	708476	65.0	24.1	β
	C5	0.085	0.033	11.42	3.64	753082	71.9	27.4	β
	C6	0.053	0.034	6.86	3.53	471325	36.3	8.0	β
	C7	0.057	0.034	7.32	3.53	502914	38.7	9.5	β
	D1	0.063	0.034	8.16	3.53	561001	36.9	12.5	β
	D2	0.066	0.034	8.54	3.53	586610	41.0	14.9	β
	D3	0.072	0.030	11.15	4.00	644347	47.6	19.4	β
	D4	0.077	0.033	10.35	3.64	682372	53.1	21.9	β
	D5	0.082	0.033	11.10	3.64	731663	59.7	25.2	β
	D6	0.074	0.033	9.94	3.64	655633	49.8	28.4	β
	D7	0.087	0.033	11.69	3.64	770839	66.8	28.4	β
	E2	0.055	0.041	5.34	2.93	473852	23.7	3.2	α
s (m)	Test	Q (m ³ /s)	h_1 (m)	Fr_1	s/h_1	Re_1	P^*/γ (cm H ₂ O)	σ^*/γ (cm H ₂ O)	Flow region
0.12	E3	0.061	0.040	6.20	3.00	532604	31.8	8.5	β
	E4	0.064	0.039	6.72	3.08	557805	35.1	10.8	β
	E5	0.070	0.039	7.33	3.08	608502	37.0	12.4	β
	E6	0.074	0.039	7.76	3.08	643572	40.2	14.8	β
	E7	0.079	0.039	8.28	3.08	686691	46.1	18.0	β
	F1	0.062	0.040	6.30	3.00	540906	31.8	8.5	β

F2	0.071	0.039	7.45	3.08	618214	38.2	13.2 β
F3	0.076	0.039	8.01	3.08	664461	43.4	16.4 β
F4	0.082	0.039	8.59	3.08	712397	50.3	20.2 β
F5	0.085	0.039	8.87	3.08	736013	54.4	22.4 β
F6	0.087	0.039	9.10	3.08	754791	56.7	23.9 β
F7	0.091	0.039	9.51	3.08	789178	61.4	26.5 β
F8	0.088	0.039	9.26	3.08	767985	58.8	24.8 β
F9	0.093	0.039	9.73	3.08	806787	62.2	26.8 β
G1	0.104	0.039	10.88	3.08	902317	63.7	27.0 β
H1	0.066	0.040	6.70	3.00	575081	29.9	6.2 β
H2	0.078	0.040	7.85	3.00	674121	39.9	12.3 β
H3	0.080	0.040	8.05	3.00	690916	42.0	13.9 β
H4	0.088	0.039	9.28	3.08	770069	54.8	20.1 β
H5	0.084	0.039	8.85	3.08	733817	48.8	17.2 β
H6	0.091	0.039	9.59	3.08	795760	57.5	21.9 β
H7	0.074	0.039	7.80	3.08	646754	37.1	10.4 β
H8	0.065	0.040	6.53	3.00	560721	27.4	4.9 β
H9	0.099	0.040	9.99	3.00	857525	58.2	22.1 β
I2	0.102	0.039	10.74	3.08	890857	77.0	32.0 β
I3	0.107	0.045	9.09	2.67	915400	80.2	33.5 β
I4	0.070	0.046	5.73	2.61	594190	32.1	8.2 β
I5	0.082	0.046	6.68	2.61	693079	43.8	15.6 β
I6	0.086	0.045	7.29	2.67	734813	50.3	19.1 β
I7	0.072	0.046	5.86	2.61	607879	33.2	9.3 β
I8	0.093	0.045	7.90	2.67	795808	59.2	23.8 β
L2	0.083	0.046	6.83	2.61	708460	38.7	10.6 β
L3	0.088	0.046	7.18	2.61	744896	45.2	10.6 β
L4	0.094	0.045	7.99	2.67	804699	48.0	15.4 β
L5	0.108	0.045	9.14	2.67	920877	70.6	24.9 β
L6	0.104	0.045	8.84	2.67	890900	65.7	22.9 β
L7	0.101	0.045	8.59	2.67	865308	62.3	21.6 β
L8	0.099	0.045	8.38	2.67	843892	59.0	20.3 β

L9	0.093	0.045	7.83	2.67	788529	50.6	16.7	β
L10	0.096	0.042	9.01	2.86	827145	54.6	18.5	β
M1	0.080	0.052	5.45	2.31	665616	36.4	9.1	β
M2	0.085	0.052	5.82	2.31	710866	42.1	12.1	β
M3	0.112	0.051	7.84	2.35	934174	75.0	26.6	β
M4	0.077	0.052	5.23	2.31	639148	33.2	7.6	β
M5	0.090	0.051	6.30	2.35	750643	47.8	15.3	β
M6	0.117	0.051	8.19	2.35	975283	83.9	30.0	β
M7	0.113	0.051	7.95	2.35	946598	78.6	28.0	β
N1	0.083	0.058	4.80	2.07	677316	31.6	4.8	α
N2	0.085	0.058	4.90	2.07	691604	33.9	6.6	β
N3	0.087	0.058	5.05	2.07	713096	37.2	8.5	β
N4	0.091	0.058	5.24	2.07	739256	40.6	10.4	β
N5	0.080	0.059	4.53	2.03	653411	30.5	4.2	α/β

4 ANALYSIS OF EXPERIMENTAL DATA

Figure 3 shows in the cartesian plane $(Fr_1, s/h_1)$ the three flow regions (Guadagnini et al. 1994, 1998) and the experimental runs performed. It can be noticed that every test refers to α or β condition; an experimental investigation regarding the γ region will be carried on in a future.

Experimental results are used in order to provide an expression for the functions φ_1 and φ_2 indicated at Section 2.

Figure 4 shows the experimental values of σ/σ^* as a function of the non-dimensional position y/s relative to the tests performed in laboratory. It can be noticed the S-shape typical also of the timeaveraged pressures, consequent to the flow field due to the fluid structure interaction. Measurement errors and influence of other non-dimensional parameters cause a certain scattering of experimental data. Anyhow, it can be accepted the hypothesis that σ/σ^* depends only on y/s ; the relation can be

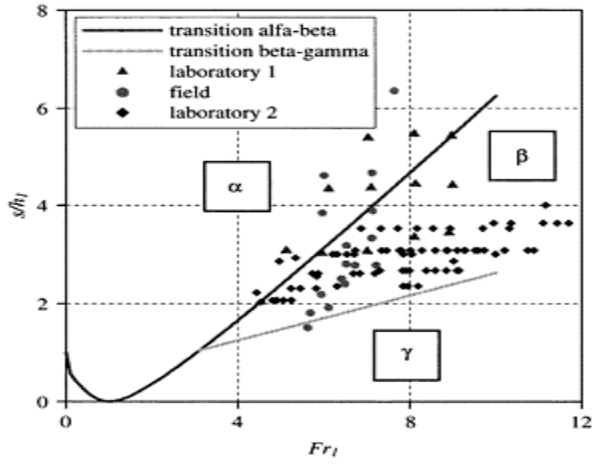


Figure 3. Flow regions and tests performed.

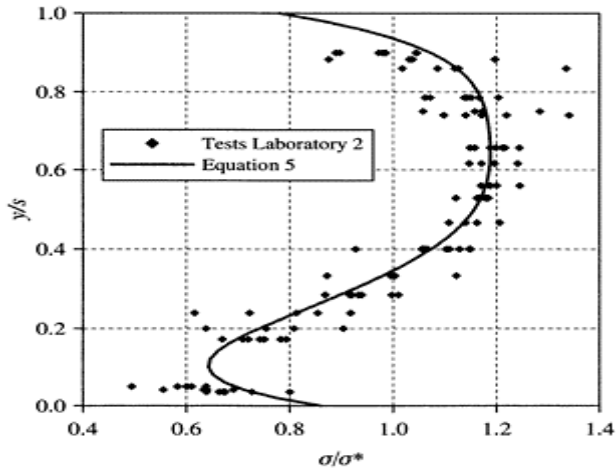


Figure 4. Agreement between experimental data of σ/σ^* function of y/s and Equation 5.

expressed as a fifth order polynomial:

$$\frac{\sigma}{\sigma^*} = \sum_{k=0}^5 a_k \left(\frac{y}{s}\right)^k \quad (5)$$

A regression over the experimental data provide these values for the coefficients in Equation (5): $a_0=0.1$; $a_1=-6.66$; $a_2=42.86$; $a_3=92.04$; $a_4=85.02$; $a_5=-9.65$. Figure 4 shows also the curve of Equation (5).

Concerning function ϕ_1 Figure 5 proves that the Reynolds number Re_1 affects the RMS value of pressures; non-dimensional a values (ratio of σ to $0.5\rho V_1^2$ relative to tests characterised by similar values of Froude number Fr_1 (7.11 and 7.09) and s/h_1 (4.67 and 4.36), but different Reynolds numbers (the Field test Re_1 is more than one order of magnitude greater than the Laboratory test Re_1 , respectively 1294000 and 49805) are shown.

As stated by many authors (Cigada et al. 1996, Borsani et al. 1998), only Fr_1 and s/h_1 have an influence on the non-dimensional value of p^* :

$$p^* = \frac{1}{s} \int_0^s \bar{p}(y) \cdot dy \quad (6)$$

where \bar{p} represents the time-averaged local pressure.

One can suppose that the a value is affected by Fr_1 and s/h_1 because these parameters have an influence on the non-dimensional p^* ; therefore, the parameter σ^*/p^* , ratio of energy dissipated by turbulence to energy absorbed from the structure, could depend only on the Reynolds number. Equation (4) becomes, then:

$$\eta\left(\frac{\sigma^*}{p^*}, Re_1\right) \phi\left(\frac{p^*}{0.5\rho V_1^2}, Fr_1, \frac{s}{h_1}\right) \varphi_2\left(\frac{\sigma}{\sigma^*}, \frac{y}{s}\right) = 0 \quad (7)$$

Function ϕ is provided from Borsani et al. (2000). The function η can be obtained in a graphic format (Fig. 6), because it is not possible to derive now an analytical expression.

It can be noticed that, for low Reynolds number, σ^*/p^* increases more than proportionally with Re_1 ; then, there is an intermediate region ($10^6 < Re_1 < 2 \cdot 10^6$) where no experimental result is

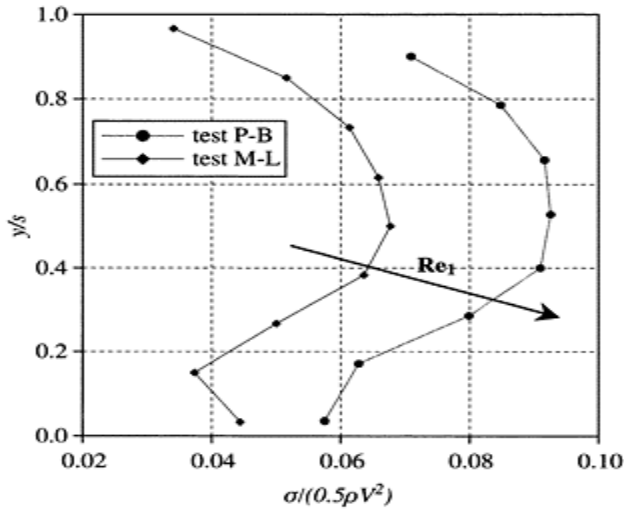


Figure 5. Influence of Re_1 on the non-dimensional RMS value σ .

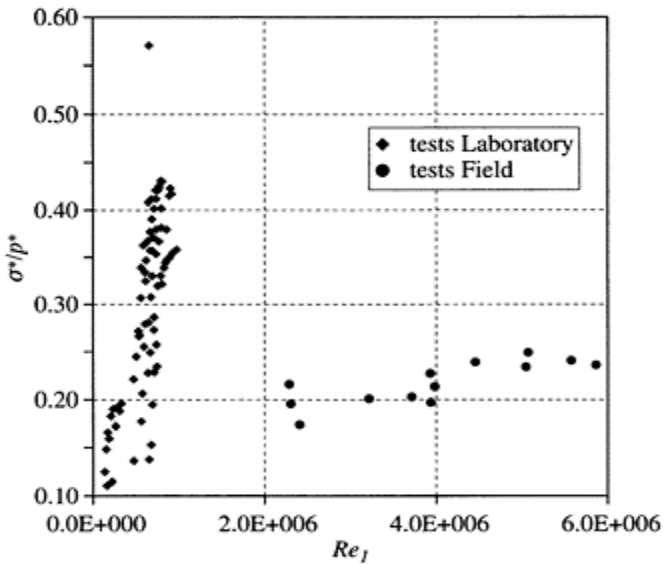


Figure 6. Relation between σ^*/p^* and Re_1 .

available, is present; finally, at high Reynolds number σ^*/p^* values are smaller and increase less than proportionally with Re_1 , reaching an almost constant value. It seems that this behaviour is similar to the relation between the Drag coefficient and the

Reynolds number for a sphere in a flow (Munson et al. 1998). Probably, a critical value of the Reynolds number, localized in the Re_1 range not yet investigated, exists; when it is reached the characteristics of the pressure fluctuations changes abruptly, due perhaps to the characteristics of the boundary layer over the sill surface.

5 CONCLUSIONS

This paper focuses on the pressure fluctuations over the upstream surface of a sill transversal to a supercritical flow. In particular the influence of some non-dimensional parameters on the RMS value of pressures is analyzed, because it play an important role in designing immersed structures. It is shown that the Froude similarity allows a correct modelling concerning the time-averaged pressures, while also the Reynolds number is essential regarding the RMS value σ . The ratio between the spaceaveraged RMS value σ^* of the pressures and the space-time averaged pressure p^* depends only on Re_1 . So, the scale effect (Narayanan 1984), relative to the different non-dimensional parameters, can be determined, concerning the geometrically simple case of a supercritical flow-sill interaction; regarding more complex structures, anyhow, this research provides useful information about the physics of the phenomenon, in order to properly perform experiments. The relation between σ^*/p^* and Re_1 is graphically provided, but experimental results, in the range $10^6 < Re_1 < 2 \cdot 10^6$ and $Re_1 > 6 \cdot 10^6$, are missing. A further analysis, regarding experiments with these values of Reynolds number, shall be performed in a future; moreover, an experimental study about the effects of more complex obstacle geometry on the flow field characteristics appears to be necessary.

REFERENCES

- Akbari, M.E., Mittal, M.K. & Pande, P.K. 1982. Pressure Fluctuations on the Floor of Free and Forced Hydraulic Jumps. *Proc. Int. Conf. on the Hydraulic Modelling of Civil Engineering Structures, Paper C1. Coventry (England)*.
- Berzi D., Larcán E. & Orsi E. 2003. Analysis in frequency domain of pressure fluctuations over sills in stilling basins. *Proc. of the 2nd Fluid Structure Interaction, June 2003, Cadiz (Spain)*:375–384.
- Borsani, D., Larcán, E. & Orsi, E. 1998. Statistics of pressure fluctuations on a transversal sill due to supercritical flow. *Proc. of the 3rd Int. Conf. on Hydrosience and Engineering, August 31-September 3, Coptbus, Berlin (Germany)*.
- Borsani, D., Larcán, E., Mambretti, S. & Orsi, E. 2000. Pressure Fluctuation on Structures: Experimental Data Analysis. *Proc. of the 3rd Int. Conf. on Advances in Fluid Mechanics, May 2000, Montreal (Canada)*.
- Borsani, D., Larcán, E., Mambretti, S. & Orsi, E. 2001. Real Scale Investigation of Interaction between a Supercritical Flow and a Bottom Sill. 1: Physical Aspects and Time-Averaged Pressures on Sill. *Proc. of the Int. Conf. On Fluid Structure Interactions. Halkidiki (Greece)*.
- Bowers, C.E. & Tsai, F.Y. 1969. Fluctuating Pressures in Stilling Basins. *J. Hydr. Div., ASCE*, Vol. 95, No. HY6:2071–2079.
- Chen, B. & Luo, H. 1984. Model Test and Prototype Observation on Pressure Fluctuation in a Double-Deck Type Outlet. *Symposium on Scale Effects in Modelling Hydraulic Structures, IAHR conf. Esslingen am Neckar (Germany)*.

- Cigada, A., Guadagnini, A. & Orsi, E. 1996. Statistical Characteristic of Pressure Fluctuations Over Sills in Stilling Basins. *L'Energia Elettrica*, Vol. 73, No. 6.
- Fiorotto, V. & Rinaldo, A. 1992. Fluctuating Uplift and Lining Design in Spillway Stilling Basins. *J. Hydr. Eng.*, ASCE, 118(4):578–596.
- Guadagnini, A., Larcán, E. & Orsi, E. 1994. Analisi Sperimentale di Alcuni Aspetti del Comportamento di una Corrente a Superficie Libera su un Setto Continuo (in italian). *L'Energia Elettrica*, No. 2.
- Guadagnini, A., Larcán, E. & Orsi, E. 1998. Flow Conditions and Pressure Distributions Over Sills, *L'Energia Elettrica*, No.3.
- Karki, K.S. 1976. Supercritical Flow over Sills. *J. Hyd. Div.*, ASCE, Vol. 102, No. HY10:1449–1459.
- Lopardo, R.A. & Henning, R.E. 1985. Experimental Advances on Pressure Fluctuations Beneath Hydraulic Jumps. *Proc. of the 21st IAHR Congress*, Melbourne (Australia). Vol. 3:633–638.
- B.R. Munson, D.F. Young & T.H. Okiishi 1998. *Fundamentals of Fluid Mechanics (third edition)*. John Wiley & Sons.
- Narayanan, R. 1984. The Role of Pressure Fluctuations in Hydraulic Modelling. *Symposium on Scale Effects in Modelling Hydraulic Structures, IAHR conf., Essilngen am Neckar (Germany)*.
- Ohtsu, I., Yasuda, Y. & Yamanaka, Y. 1991. Drag on Vertical Sill of Forced Jump. *J. Hydraulic Research*, IAHR, Vol. 29, No. 1:29–47.
- Rajaratnam, N. 1964. The Forced Hydraulic Jump. *Water Power*: 14–19.

Analysis of the air rubber dam using “ANSYS”

H.Musavi-Jahromi

Assistant professor, Shahid Chamran University (SCU), Iran

A.H.Navabi

Master Engineer at Ministry of Jihad and Agriculture, Iran

A.M.Horr

Assistant professor, Emam Khomeni International University, Iran

Hydraulics of Dams and River Structures—Yazdandoost & Attari (eds)

© 2004 Taylor & Francis Group, London, ISBN 90 5809 632 7

ABSTRACT: Inflatable dams have been used as a storage system of water along seasonal and non-seasonal rivers for agriculture and the other uses from 50 years ago. Due to plasticity of the structure and continuous variation of its shape during operation, it's structural and hydraulic analysis is more complicated than the other dams such as concrete or earth dams. As a result, design of the rubber dam is very complicated.

This paper deals with analysis of the rubber dam using ANSYS. ANSYS is finite element based software capable of predicting behaviors of the rigid and flexible structures such as flexible rubber dams. In the present study, first, ANSYS is applied to an assumed rubber dam with some realistic characteristics. Then, it has been applied to the Babolsar rubber dam, Iran.

This paper has modeled a cantilever air rubber dam under the air internal pressure and the water external pressure. It is found that increasing of internal pressure causes a circular section of the dam up to a specified pressure. After this pressure, the dam starts to deform around its fixed axis and finally it will be ruined.

The rubber dam as a weir is very sensitive to the V-notch phenomenon on its crest. The V-notch is not stable and causes the continuous variation of the coefficient of discharge. It may be cause of instability of the structure. In this paper V-notch phenomenon and its effects on the dam hydraulics has been modeled by “ANSYS” as well. Finally, it is concluded that study and design of any rubber dam needs a mathematical modeling (or physical modeling) to find out its characteristics.

1 INTRODUCTION

Waters flowing over weirs and spillways are characterized by a rapidly varied flow (RVF) region near the crest. The broad-crested weir, the sharp-crested weir, the ogee crest weir and the circular-crested weir are the most common types of weir crest that are used. The crest of the rubber dam is a circular type. Advantages of the circular weir shape are the stable overflow pattern compared to sharpcrested weirs, the ease to pass floating debris, the simplicity of design, and the associated lower cost. For identical upstream head, circular-crested weirs have larger discharge than broad-crested weirs and sharp-crested weirs.

For small overflows it is not economical to apply gate for discharging the runoff overflow downstream. For the first time the inflated flexible membrane dam (rubber dam) was introduced in 1947. Rubber dam is a new form of weir that is flexible. They are used to raise the upstream water level by inflating the rubber membrane placed across a stream or along a weir crest. Small overflows are usually allowed without dam deflection and the overflow characteristics are somehow similar to those of circular weirs (Anwar, 1967; Chanson, 1996). Effects of inflow conditions on the discharge characteristics and flow properties at the crest of the rubber dam has been investigated (Chanson & Montes, 1998) and it is shown that discharge measurements with circular weirs are significantly affected by the upstream flow conditions. As a PhD research program, characteristics of curvilinear flow past circular-crested weirs have been undertaken and it is suggested that the

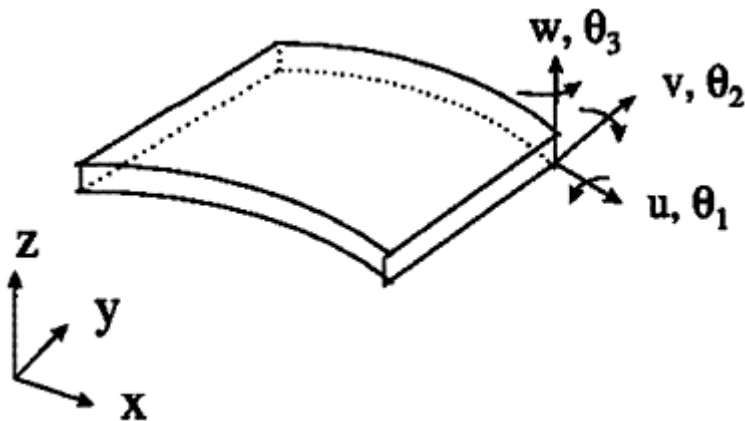


Figure 1. Element of Shell 63 in ANSYS.

flow field may be predicted by ideal fluid flow theory (Vo, 1992). In the present paper the structural behavior of the rubber dam and the flow pattern underneath of the structure and over the crest have been investigated.

2 MATERIALS AND METHODS

However, the rubber dam is non-homogenous in the field, to simplify the analysis it is assumed homogenous. Besides, it is assumed as a cantilever and rubber structure. Based on the literature survey, ANSYS has not been applied to rubber dam. In this paper it is used for analysis of this structure. Due to plasticity of the rubber dam, the Shell 63, 4 points element of ANSYS is selected to apply the analysis. Each node of the element includes 6 degree freedom that indicates 24 degree freedom for each element. Fig. 1 illustrates the applied element in the research.

In addition to structural analysis of the rubber dam, the flow pattern in the foundation and above the structure has been modeled using ANSYS. Finally, using field data, ANSYS has been applied to predict the suitable height of the Babolsar rubber dam, Iran.

2.1 Geometry and technical characteristics of the rubber dam

The assumed rubber dam includes two rubber sheets that are stuck together. ANSYS shell 63 is used for each sheet of the rubber dam. Some realistic characteristics have been assumed for the rubber dam including the length of 3.2 m, width of 1 m that indicates 2 m diameter of the structure. The mesh of the structure is assumed as squared element with 10 cm length that indicates 320 elements for each sheet and overall 640 elements for the structure. Rubber sheets on top of another with a 1 cm gap between them. Rubber sheets are stuck together from one side and the other side is jointed to the solid foundation. The other parameters are as follow: Yang's module= 1.037×10^3 ; rubber density= 1050 kg/m^3 ; Poisson's coeff.=0.3; thickness of rubber sheet=0.002 m. Fig. 2 shows the rubber dam before loading.

2.2 Flow regime in the foundation of the rubber dam

For analysis of the flow pattern underneath of the rubber dam, ANSYS plane 55 is selected. Transmissivity coefficient is substituted by the hydraulic conductivity and the temperature is substituted by the relative pressure. The model's mesh is extended in the mathematical model under upstream head of water from and infiltration of water from the initiation of the concrete blanket. The downstream head of water is neglected. Fig. 3 shows the, mesh for the mathematical model.

3 RESULTS AND DISCUSSIONS

Structural behaviors of the rubber dam are affected by internal and external pressures. Under internal pressure, rubber sheets start to stand up gradually, the shape and cross section of the rubber

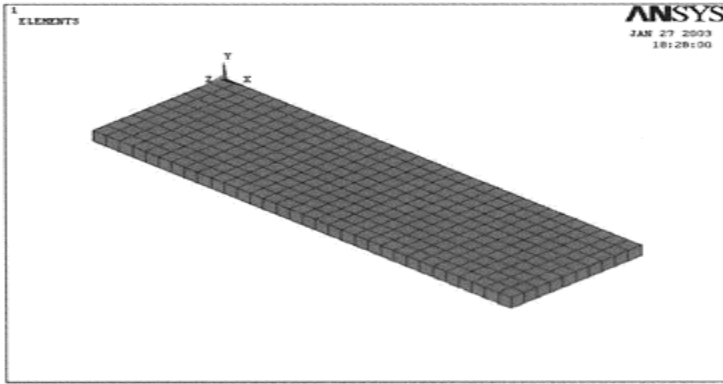


Figure 2. The assumed rubber dam model in ANSYS environment before loading.

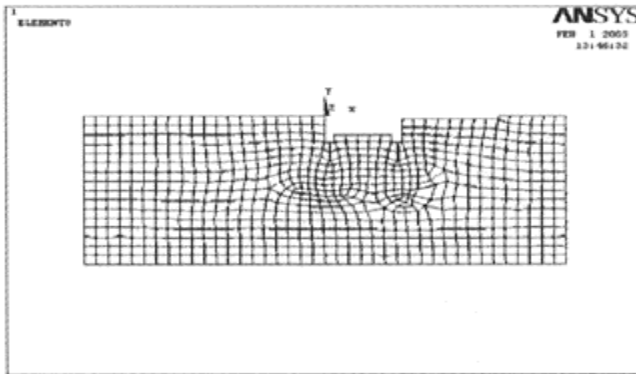


Figure 3. Mesh for the rubber dam foundation in the ANSYS environment.

dam will be varied. To find out variation of the shape and cross sectional area of the rubber dam under different loads, data of the assumed rubber dam have been entered in the ANSYS software. Fig. 4 shows the cross sectional variation of the rubber dam under continues variation of the internal pressure.

As shown in the figure, the cross sections start from ellipse shape and final shape is circular. The outputs of the finite element model are in agreement with previous researches (e.g., Anwar, 1967; Harison, 1970 and Chanson, 1998). The run of the ANSYS continued and after a certain pressure which depends to the thickness of the rubber sheet and the other characteristics of the project, there is no change in the height of the structure. After this certain height of the dam, if the internal pressure increases

above 25 KPa, the structure will be destroyed. Fig. 5 illustrates the percentage variation of displacement against the percentile variation of pressure.

As shown in the figure, the curve includes two parts, one with steep slope which denotes displacement of the structure is rapidly taken place. Another with mild slope that indicates, displacement of the structure is very slow. Finally, the curve is parallel to the horizontal axis that denotes no displacement of the rubber dam. Two ends of the rubber dam are stuck together that one end is bolted to the foundation and the other acts as a reflector of the structure.

In addition to analysis of the structure under internal pressure, it is analyzed under external hydrostatic pressure as well. This part of the research activity shows that increase in the

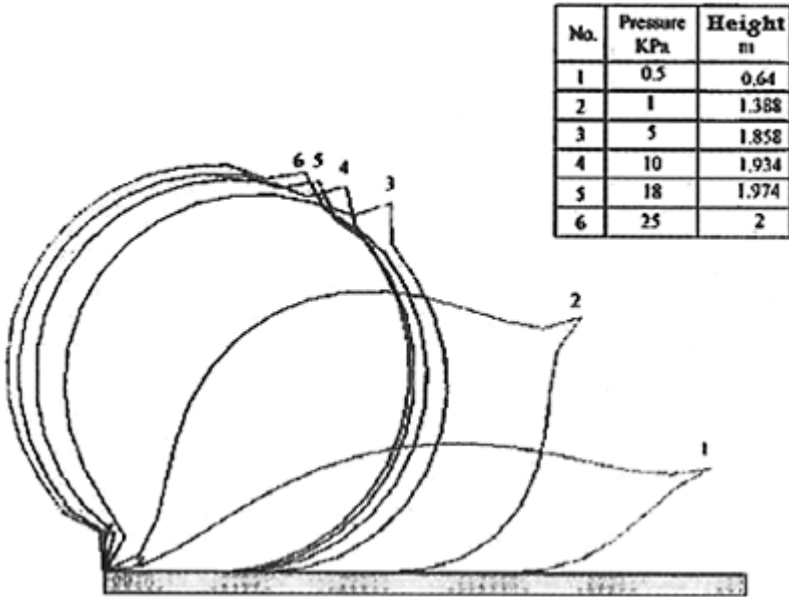


Figure 4. Cross sectional variation of the rubber dam height under continues variation of the internal pressure.

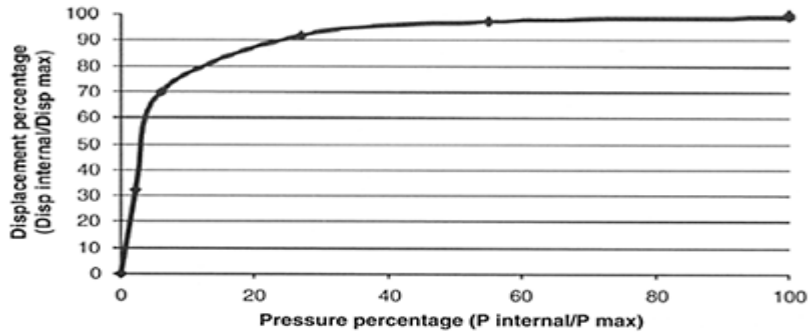


Figure 5. Percentile variation displacement of the rubber dam against internal pressure.

external hydrostatic pressure causes reduction in height of the dam and overflow above the structure. Fig. 6 shows the cross sectional profile of the rubber dam under internal and external loads.

The study shows that 2 m of upstream head causes 0.4 m reduction that is equivalent of 4 KPa. It does not cause the V-notch phenomenon in the structure. With increase in the upstream head of water to 2.2m, 0.7m reduction (Fig. 7) is observed (7 KPa), that indicates the inverse nonl relationship between upstream head and reduction of the rubber dam height. If the upstream head is increased, after a certain value, V-notch phenomenon on the structure will happen. The V-notch may cause instability of the structure.

The flow pattern under the rubber dam structure in the foundation is also investigated in this paper. Fig. 8 shows the flow velocity vectors in the foundation of the rubber dam.

As can be seen in the figure the flow pattern is in agreement with the ideal fluid flow pattern that denotes it can be analyzed with theory of the ideal fluid.

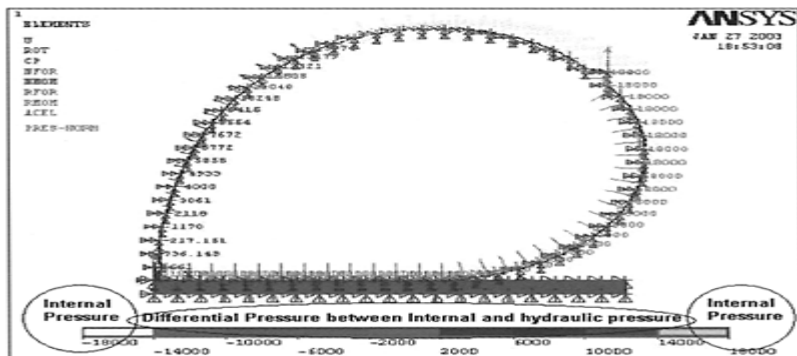


Figure 6. Internal and external loading of the rubber dam in the ANSYS environment.

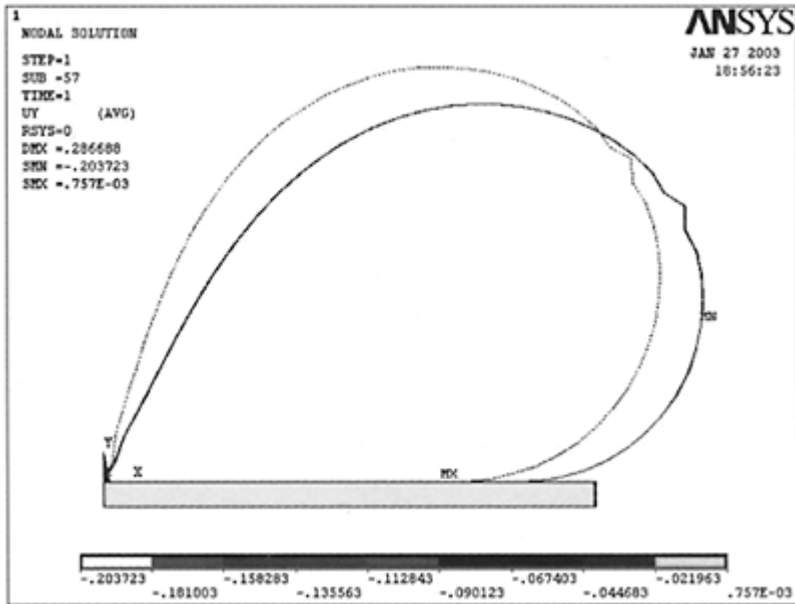


Figure 7. Effects of upstream head water on the height of the rubber dam.

4 APPLICATION OF THE DEVELOPED MODEL TO BABOLRSAR RUBBER DAM, IRAN

In this section, capability of ANSYS for estimation of the height of the Babolsar rubber dam that is already constructed on the Babolrood River, in the North of Iran is demonstrated. This dam is constructed to raise height of water for agricultural projects around the Babolrood River. The length of the dam is 60 m and its designed height is 3.1 m. The thickness of rubber sheet of the Babolsar rubber dam is 1.5 cm. The dam height is predicted by ANSYS using field data of the project. The predicted height is 3.22 m that is higher than designed height. The error is 4% that is satisfactory.

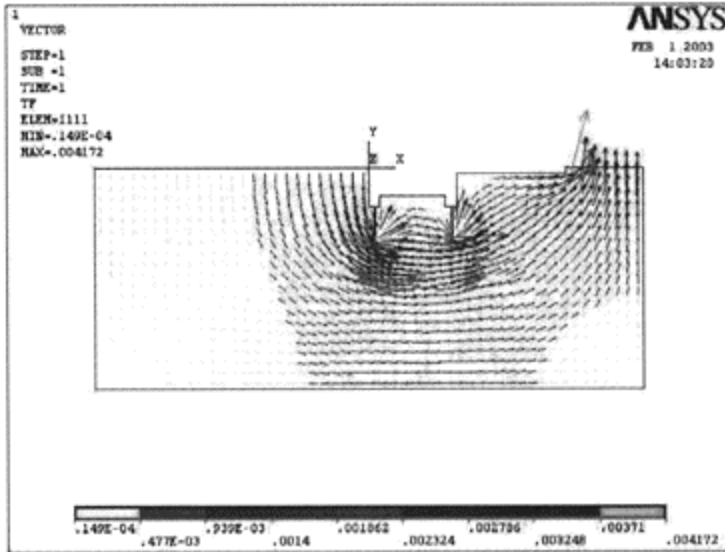


Figure 8. The velocity vectors and the flow pattern in the foundation of dam.

Several studies could be done related to this project but unfortunately lack of data limited the study to the ones present.

5 CONCLUSION

In the present paper, ANSYS software is applied to study the air rubber dam as a new hydraulic structure. Several characteristics of the rubber dam have been analyzed by this engineering software. The shape and cross sectional of the structure have been successfully modeled by ANSYS. It is shown that the cross sectional area of the rubber dam varied under load of the internal and external pressures. In the low internal pressure it is elliptic and increase in the internal pressure causes the circular cross sectional area for the structure. Depends on the rubber sheet properties, after a certain internal pressure there will be no change in the cross sectional area and the height of the rubber dam and finally increase of the internal pressure causes the structure to be destroyed. External loads such as hydrostatic pressure cause the reduction of height of the rubber dam. The correlation between the external pressure and height of the dam is inverse and nonlinear.

ANSYS successfully modeled the flow pattern in the foundation of the structure. Finally, as a field study, ANSYS was applied to the Babolsar rubber dam. The height of this rubber dam is predicted with 4% error that is satisfactory. Overall, it can be concluded that study and design of any rubber dam needs the project to be modeled by a mathematical model (such as ANSYS, or by a physical model. The experimental formula is not advised for this purpose.

REFERENCES

- Anwar, H.O. 1967. Inflatable Dams, *Journal of the Hydraulics Division, ASCE*, Vol. 93, pp. 99–119.
- Binnie, A.M. 1973. The Theory of Flexible Dams Inflated by Water Pressure, *Journal of Hydraulic Research*, Vol. 11, pp. 61–68.
- Chanson, H. 1996. Some Hydraulics aspects during overflow above inflatable flexible membrane dam, Rep.CH47/96, Dept. of Civil Engrg., University of Queensland, Australia.
- Chanson, H. 1998. Hydraulics of Rubber dam: A simple design approach, 13th Australasian Fluid Mechanics conference, Monash University, Melbourne, pp: internet pdf file.
- Chanson, H. and Montes. J.S. 1998. Circular weir, *Journal of Irrigation and drainage Engineering*, pp. 152–162.
- Harrison, H.B. 1970. The analysis and behavior of the inflatable Membrane dam under static loading, *Proceedings of the Institution of Civil Engineers*, Vol. 45, pp. 661–676.
- Vo, N.D. 1992. Characteristics of curvilinear flow past circular-crested weirs, PhD thesis, Concordia University, Montreal, Canada.

4.

Energy dissipators

Plunge pool scour in prototype and laboratory

Stefano Pagliara

Department of Civil Engineering, University of Pisa, Pisa, Italy

Willi H.Hager & Hans-Erwin Minor

VAW, ETH-Zentrum, Zurich, Switzerland

Hydraulics of Dams and River Structures—Yazdandoost & Attari (eds)

© 2004 Taylor & Francis Group, London, ISBN 90 5809 632 7

ABSTRACT: Scour is a major concern with flip buckets in hydraulic engineering, given the several serious incidents over the past 50 years. The present research is based on previous laboratory observations conducted at VAW, ETH-Zurich, Switzerland, to explore the effect of cross-sectional jet shape, the effect of tailwater jet submergence and the jet impact angle on the plunge pool scour features. All observations were conducted in a sediment bed. It was observed that the maximum scour depth may be significantly larger for so-called dynamic flow conditions than for static conditions when the jet action has seized. This was attributed to large dynamic forces with a twofold effect: (1) Suspension of sediment by the highly turbulent flow, and (2) Steeper scour hole slopes as compared with the natural angle of repose. The following thus intends to relate the static end scour depth to the maximum dynamic scour depth in order to allow prediction of the effective scour maximum for prototype conditions.

1 INTRODUCTION

Plunge pools are economic means to dissipate hydraulic energy for high-speed flows, provided the geological site conditions are favorable and the upstream jet velocity is larger than typically 20 m/s. For smaller velocities, stilling basins are often used, but these are highly unreliable for larger velocities because of concerns with cavitation damage, large spray production, unstable flow and tailwater wave generation (Vischer and Hager 1998). The limitations of plunge pools are dictated by large scour depth, its sufficient distance from other hydraulic structures to inhibit structural damages and control of spray action.

Plunge pools are usually at the end of either surface spillways or bottom outlets as applied in dam engineering. The flood discharge for surface spillways is first conveyed over a gated or ungated spillway crest that is followed by a chute. Once the discharge has reached an elevation close to the dam foot, it is directed onto a flip bucket to be ejected

into the air. Accordingly, an air-water jet travels through the atmosphere and eventually strikes the plunge pool, in which the hydraulic energy is dissipated, and a still tailwater may be conveyed to the downstream receiving water course.

Plunge pools are currently a standard design in hydraulic engineering, although its scour patterns are not yet fully understood. Therefore, a fundamental research project was initiated at Versuchsanstalt für Wasserbau, Hydrologie und Glaziologie VAW, at ETH-Zurich, Switzerland. Its purposes was: (1) Set-up of a laboratory installation to experimentally investigate such flows, (2) Define the main parameters of plunge pool scour and (3) Present design relations that may be applied in dam engineering. An exploratory study was provided by Canepa and Hager (2003), in which the complicated laboratory set-up was simplified in an air-water high-speed flow generated with a circular pipe, thereby profiting from well-defined upstream boundary conditions. Also, a three-phase Froude number was introduced that accounts for the effects of water, air and sediment involved in the flow. Minor et al. (2002) presented implications of this research and applied results to hydraulic practice. Recently, Pagliara et al. (2004) presented a large experimental study in which various points were further clarified. The main findings may be summarized as follows: (1) The effect of jet shape on plunge pool scour is small provided the cross-sectional average mixture velocity is considered, (2) the impinging jet angle has a relatively small effect provided it is included between 30° and 90° measured from the horizontal, and (3) there are distinct effects of both submergence of jet by the tailwater level and pre-aerated flow characteristics. The research is accompanied with generalized scour hole profiles and the effect of temporal scour depth development was also investigated. The present paper would like to add to previous research by relating maximum scour depths measured during scour progress, and as observed after jet flow was stopped. The motivation is simple: The prototype scour hole may exclusively be observed when floods have ended, and the true extent of prototype scour thus normally remains unknown. Using laboratory observations, this unknown may be determined. The present laboratory data are then compared with prototype observations to check the fit. A typical computational example is also added to explain the design procedure.

2 DESCRIPTION OF LABORATORY OBSERVATIONS

The experiments were conducted in a laboratory channel of 0.500 m width, 0.70 m height and 7 m length. The jet was generated with pipes of different diameters ranging up to 0.100m, in which also nozzle elements were placed to vary the cross-sectional jet geometry. Sands and gravels of almost uniform grain size of up to $d=0.007$ m were used to replace a completely disintegrated rock surface, of which the height was up to almost 0.35 m. Air was added to the pipe flow to simulate an air-water high-speed jet. Standard observations resulted in discharges for water Q_W and air Q_A . The water surface was recorded with a point gage, whereas the sediment surface was read with a special gage having a 0.04 m circular plate at its end to measure the sediment surface to approximately $d/2$ (Canepa and Hager 2003).

The ratio T between tailwater depth and jet diameter was set for all the tests in the range $3 < T < 4.5$.

Prior to experimentation, the sediment was horizontally inserted into the test channel, and air discharge was added by the in-house pressurized air supply system. Then, water discharge was

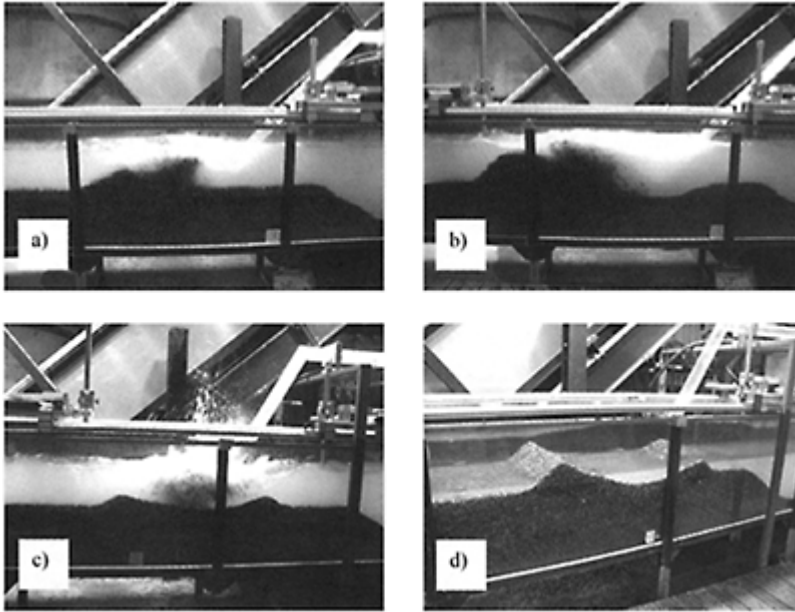


Figure 1. Photographs of plunge pool scour (45° jet angle) development (a) close to scour initiation, (b) close to scour end; view of a test with jet angle of 60° , (c) dynamic condition, (d) 'dry' conditions.

started, with the temporal start of a run set at the initiation of scour. It should be noted that scour initiated immediately once the air-water mixture flow impinged on the plunge pool. Readings of the sediment surface were made after 1, 5 and 20 minutes, and sometimes after longer time. For the present observations, the end scour was normally reached after 20, or even after 5 minutes. At the end of an experiment, the water flow was stopped, the jet at the same time deflected to inhibit further scour action and the resulting sediment surface measured after water had been drained from the test reach. This condition was referred to as the 'dry' scour measurement. Figure 1 shows typical photographs close to scour initiation, and scour end.

It was at once obvious that the scour profile close to end scour conditions, thus under a dynamic load, was significantly different from the 'dry' scour profile. Evidently, this difference results due to two reasons: (1) During jet flow, a considerable amount of sediment is in suspension that deposits as soon as the jet flow stops, and (2) much steeper

slopes of sediment surface may result due to dynamic jet forces, in addition to gravity. Figure 2 shows typical scour hole profiles for four jet impact angles α and three subsequent observational times, in addition to the 'dry' condition. It may be observed that both the maximum scour depth increases with time, as the maximum aggradation height increases to reach the final scour profile. Temporal changes for $\alpha=30^\circ$ appear to be larger than for $\alpha=90^\circ$. Also, the 'dry' scour profile reaches never the scour depth under dynamic conditions, although the maximum aggradation is normally larger, due to the deposition of suspended sediment after the jet being stopped. Note that differences between the 'dry' or static condition and the dynamic condition are relatively small for small jet angle, and increase as the jet angle α increases.

Figure 3 shows the cross-sectional shape of the scour hole under maximum scour depth. The tests involved a jet angle of 45° and 90° . As for the longitudinal scour hole profiles, this plot demonstrates the significant differences between the final dynamic and the dry scour hole geometries. In certain case, the dry scour surface was practically horizontal, and one might have thought that there was absolutely no scour action. Such a presumption may be dangerous because the real extent of scour

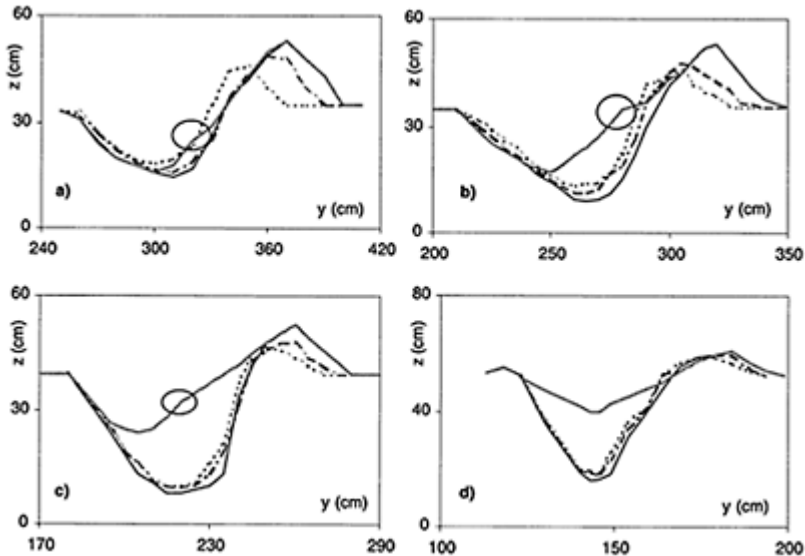


Figure 2. Scour profiles for dynamic and static conditions for (a) $\alpha=30^\circ$, Run BW30UB183, (b) $\alpha=45^\circ$, Run WW45UB21, (c) $\alpha=60^\circ$ Run WW60SC67, and (d) $\alpha=90^\circ$ Run BW90UC89 at times (····) 1, (---) 5, (- - -) 20 minutes and (—) 'dry' condition. Circles in (a) to (c) show the

impact region of the falling suspended material when flow is stopped.

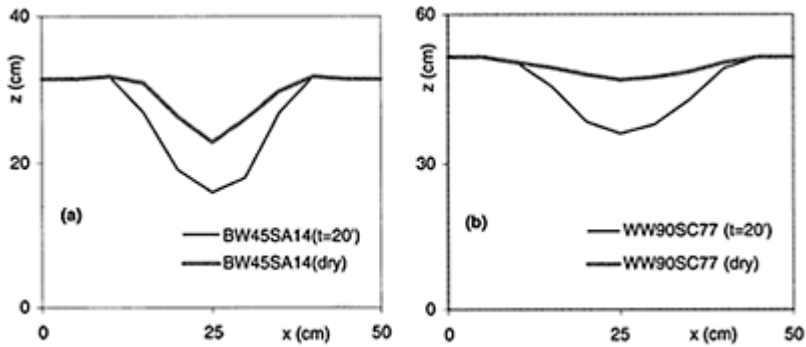


Figure 3. Cross-sectional scour profiles for (---) dynamic and (—) static conditions, (a) $\alpha=45^\circ$ (test BW45SA14) and (b) $\alpha=90^\circ$ (test WW90SC77).

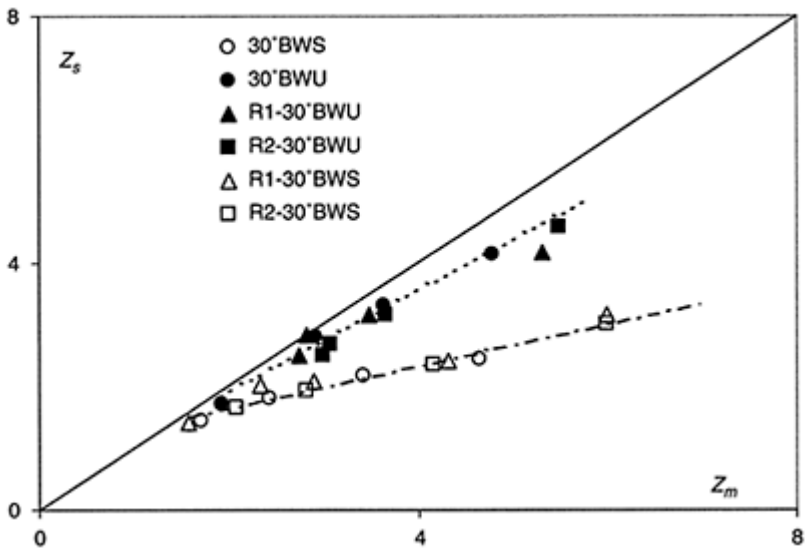


Figure 4. Shape effect for maximum static and dynamic scour depths, full symbols represent unsubmerged, open submerged impact conditions.

may be largely underestimated. Means to detect the maximum scour depth during dynamic scour action are thus an important basis for adequate hydraulic design.

3 EFFECT OF JET SHAPE

The effect of jet shape was further tested with a pipe nozzle 29 mm wide and 99 mm long in both the horizontal and vertical positions, for a jet angle of $\alpha=30^\circ$. Figure 4 compares the maximum scour depths for dynamic Z_m and static Z_s conditions, where $Z=z/D$ and D =equivalent pipe diameter. Note that the full symbols represent unsubmerged (U), and the open symbols submerged (S) impact conditions into the tailwater. These tests were made for blackwater (BW) flow conditions, i.e. there was no air addition to the water flow.

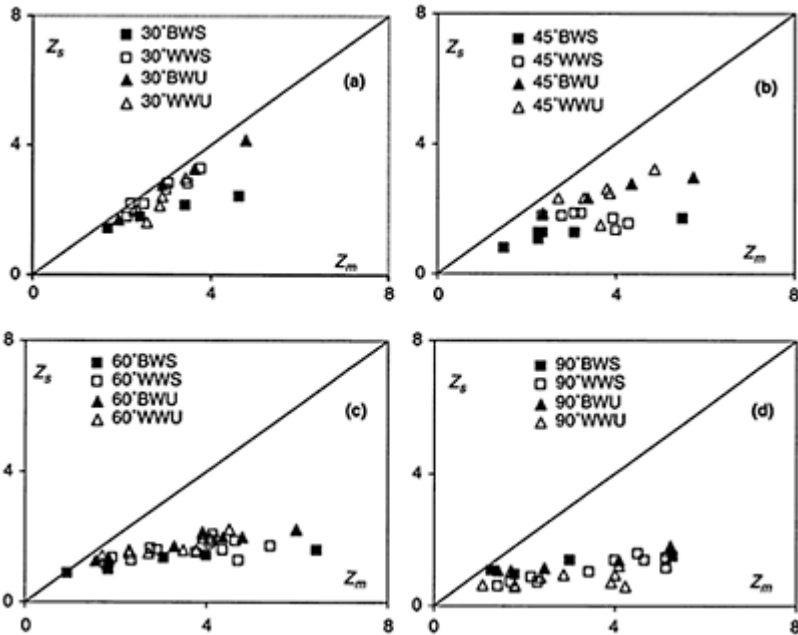


Figure 5. Maximum scour depths Z_s versus Z_m for α =(a) 30° , (b) 45° , (c) 60° , and (d) 90° and both blackwater BW and whitewater WW conditions, and submerged, and unsubmerged jets.

Figure 4 shows absolutely no shape effect because all respective data for submerged and unsubmerged conditions lie on well defined, yet different curves. Also included is the line $Z_s=Z_m$, from where it follows that all static scour depths are smaller than those under dynamic condition. In the following these differences are determined, based on a large

data series that involved four jet impact angles, submerged and unsubmerged tailwater conditions and whitewater (WW) and blackwater (BW) approach flow conditions. The 'dry' scour data are related to the dynamic scour data here, because the effects of the previous parameters on the dynamic scour depth have been determined previously by Pagliara et al. (2004).

4 STATIC VERSUS DYNAMIC SCOUR DEPTHS

The data relative to the static and dynamic conditions were further considered to propose a generalized correlation. Figure 5 shows all the data available for the four jet angles α , blackwater and whitewater conditions, and submerged and unsubmerged impact conditions. It may be noted that the angle $\alpha=30^\circ$ involves the smallest deviation, whereas $\alpha=90^\circ$ results in significant deviations between Z_s and Z_m , under otherwise identical conditions.

The data shown in figure 5 may be approximated with α [in deg.] as

$$Z_s = 0.75Z_m^\varepsilon, \quad \varepsilon = E\alpha^{-0.75}, \quad 30^\circ \leq \alpha \leq 90^\circ \quad (1)$$

where the coefficient $E=14$ for unsubmerged, and $E=10$ for submerged jet flow. Figure 6 is a summary plot in which the previous blackwater tests are shown again, together with the respective curves from (1). Accordingly, the impact angle has a significant effect on the reduction of the static, as compared with the dynamic scour depth. The effect of tailwater submergence is relatively

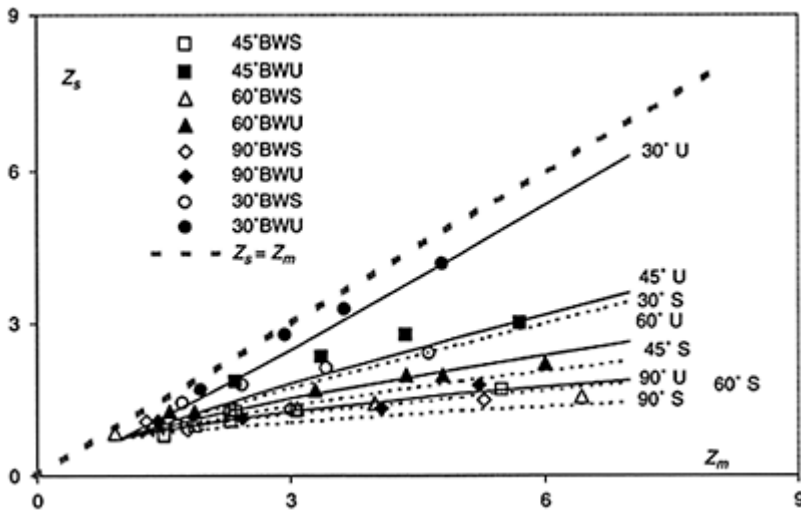


Figure 6. Regression of data for unsubmerged U and submerged S

conditions for different angles α (eq. 1).

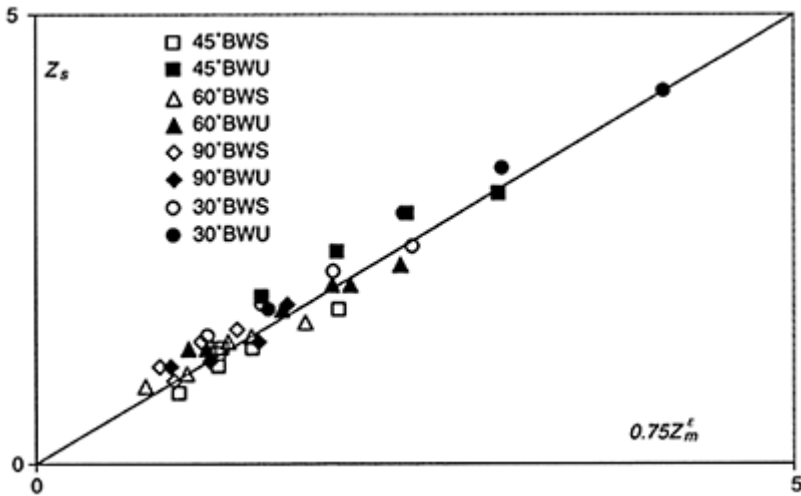


Figure 7. Condensed data plot $Z_s(0.75Z_m^E)$ according to (1) with (—) line of perfect agreement ($R^2=0.9$).

small for angles $\alpha \geq 45^\circ$, but considerable for small impact angles α of the order of 30° . Once the maximum dynamic scour depth Z_d is known from previous research (Pagliara et al. 2004), equation (1) may be applied to find the reduction of the static scour depth, in terms of all other hydraulic parameters involved in the plunge pool scour features. Also, a measured static scour depth recorded after a flood may be used to predict the effective dynamic scour depth that had occurred.

Figure 7 shows the data in a more concise arrangement, by using the abscissa proposed in (1). It is seen that the present data cover a wide range of the combined parameter Z_m^E , namely from 0.5 up to about 4. Both submerged and unsubmerged data lie evenly spaced along the straight of perfect agreement, indicating a small bias of (1). Figure 7 may be considered a condensed plot of a large number of data to determine the ratio of static to dynamic plunge pool scour depths. The application of (1) to cases of practice is straightforward, once the basic scour parameters such as

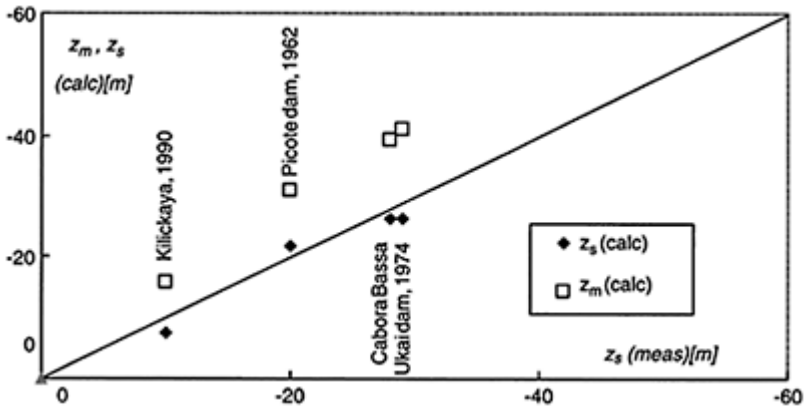


Figure 8. Comparison between prototype and calculated values of maximum scour depth Z_m and Z_s .

impact angle α , impact jet velocity V , determining median sediment size d_{90} , jet air content β and equivalent jet diameter D are known. The following intends to compare prototype data with (1).

5 COMPARISON WITH PROTOTYPE DATA

The previous results were applied to typical cases reported in the literature, to check whether agreement with the analysis may be obtained. Figure 8 compares data relative to Picote dam (Portugal), Ukai dam (India), Kilickaya dam (Turkey) and Cabora Bassa dam (Mozambique). In all evaluations, an unsubmerged air-water jet was assumed to occur, as is typical for hydraulic structures. The various parameters needed for the analysis according to Pagliara et al. (2004) were estimated based on Yildiz and Üzücek (1994) and Whittaker and Schleiss (1984), with the jet air content β calculated according to Ervine and Elsawy (1987) and a determining sediment size d_{90} of 0.30 to 2 m. It should be noted that this effect is relatively small and does not lead to a significant modification of the results. The Z_m values were calculated by means of Eq. (4) (Pagliara et al. 2004), while the corresponding Z_s values originate from (1).

Figure 8 indicates reasonable agreement between prototype observations and prediction according to laboratory measurements. The Z_s values calculated are close to the measurements (black squares), while the Z_m values calculated (white squares) indicate a deeper scour during flow as compared with the static condition.

It should be noted that the effects of jet impact velocity V and effective jet diameter D on both the static and the dynamic scour depths are significant, because both are linearly related to the maximum scour depth. Both of these parameters may be difficult to estimate, given that the exact development of cross-sectional average blackwater velocity and the air entrainment characteristics along the chute and over the flip bucket involve some degree of uncertainty, typically of the order of some 20%. Also, the jet

development across the atmosphere, from the bucket to the tailwater impact is actually not simple to predict, given a serious lack of research in this field. The present project may be considered a step forward in this direction.

6 CONCLUSIONS

Prototype scour may only be determined under static conditions, i.e. after a flood wave has passed and the scour hole is accessible again. This research was concerned with the maximum scour depth under dynamic conditions in a sediment bed, based on an extended laboratory program. It was found that the ratio between static and dynamic scour depths depends particularly on the jet impact angle, whereas the effect of jet submersion is relatively small except for small impact angles. The present results were verified with literature data of prototype static scour holes, of which reasonable agreement resulted. The present results may thus be a basis of future scour hole assessments, and can also be a design basis for plunge pools.

REFERENCES

- Ahmad, I., Chishti, M.I., Rasheed, M.A. 1979. Tarbela left bank irrigation tunnel: Some special features of design, construction and operation. *13th ICOLD Congress New Delhi Q50(R63)*: 13–32.
- Canepa, S., Hager, W.H. 2003. Effect of jet air content on plunge pool scour. *J. Hydraulic Engng.* 129(5): 358–365.
- Coleman, H.W. 1982. Prediction of scour depth from free falling jets. ASCE Conference *Applying Research to Hydraulic Practice* Jackson MI: 298–304.
- Ervine, D.A., Falvey, H.T. 1987. Behaviour of turbulent water jets in the atmosphere and in plunge pools. *Proc. Inst. Civ. Engrs.* 83:295–314; 85:359–363.
- Fahlbusch, F.E. 1994. Scour in rock riverbed downstream of large dams. *Hydropower & Dams* 1(4):30–32.
- Häusler, E. 1972. Der Kolk unterhalb der Kariba-Staumauer. *Tiefbau* 12(10):953–962 (in German).
- Häusler, E. 1980. Zur Kolkproblematik bei Hochwasser-Entlastungsanlagen an Talsperren mit freiem Überfall. *Wasserwirtschaft* 70(3):97–99 (in German).
- Kulkarni, V.N., Patel, I.C. 1981. Ski-jump spillway for India's Ukai dam. *Water Power & Dam Construction* 33(9):44–48.
- Lowe, J. III, Chao, P.C., Luecker, A.R. 1979. Tarbela service spillway plunge pool development. *Water Power & Dam Construction* 31(11):85–90.
- Mason, P.J., Arumugam, K. 1985a. Free jet scour below dams and flip buckets. *J. Hydraulic Engineering* 111(2):220–235; 113(9):1192–1205.
- Mason, P.J., Arumugam, K. 1985b. A review of 20 years of scour development at Kariba dam. *The Hydraulics of Floods & Flood Control* Cambridge A5:63–71.
- Minor, H.-E., Hager, W.H., Canepa, S. 2002. Does an aerated water jet reduce plunge pool scour? *Rock scour due to falling high-velocity jets*: 117–124, A.J. Schleiss & E. Bollaert, eds. A.A. Balkema: Lisse, the Netherlands.
- Pagliara, S., Hager, W.H., Minor, H.-E. 2004. Hydraulics of plunge pool scour. *J. Hydraulic Engng.* (Submitted).

- Quintela, A., de Carvalho, Fernandes, J., de Salvador, Cruz, A.A. da. 1979. Barrage de Cahora-Bassa: Problèmes posés par le passage des crues pendant et après la construction. *13th ICOLD Congress New Delhi Q50(R41)*: 713–730; 5:536–540.
- Sen, P. 1984. Spillway scour and design of plunge pool. *J. Irrigation and Power India* 41(1):51–66.
- Vischer, D.L., Hager, W.H. 1998. *Dam hydraulics*. John Wiley & Sons: Chichester.
- Whittaker, J.G., Schleiss, A. 1984. Scour related to energy dissipators for high head structures. *Mitteilung 73*, Versuchsanstalt für Wasserbau, Hydrologie und Glaziologie, ETH-Zurich: Zurich.
- Yildiz, D., Üzücek, E. 1994. Prediction of scour depth from free falling flip bucket jets. *Water Power & Dam Construction* 46(11):50–56.
- Zvorykin, K.A., Kouznetsov, N.V., Akhmedov, T.K. 1975. Scour of rock bed by a jet spilling from a deflecting bucket of an overflow dam. *16th IAHR Congress Sao Paulo* 2:418–422.

Experimental investigations on high-velocity jet characteristics and its influence on plunge pool rock scour

P.A.Manso, E.F.R.Bollaert & A.J.Schleiss

*Laboratory of Hydraulic Constructions, Swiss Federal Institute of
Technology Lausanne (EPFL), Switzerland*

Hydraulics of Dams and River Structures—Yazdandoost & Attari (eds)

© 2004 Taylor & Francis Group, London, ISBN 90 5809 632 7

ABSTRACT: In high dams, water spill operations for flood management by means of high-velocity jets often imply the dissipation of the flow energy directly on the rocky riverbed. This paper presents updated information on ongoing research on plunge pool scour. Experimental investigations have been conducted to estimate jet turbulence intensity at issuance for prototype velocities up to 30 m/s. This parameter is of key importance for the definition of the jet characteristics at impact downstream and for dynamic pressures in the pool bottom. Turbulence intensities of 3 to 14% were observed for velocities between 10 and 29.5 m/s. Furthermore, experimental work is underway to assess the influence of pool geometry (lateral confinement) on jet development and on pressures at the water-rock interface. Besides a better understanding of plunge pool scour formation, the research results aim at improving measures for rock scour management, such as pre-excavation and tailpond dams.

1 INTRODUCTION

Appurtenant structures of dams used for flood control and/or reservoir level management often include jet-issuing structures. The energy of high-velocity jets can be dissipated directly on the natural rocky riverbed allowing savings in the construction of concrete structures for energy dissipation. However, the evolution of the scour up to its ultimate equilibrium geometry should be assessed to guarantee the safety of the dam and its appurtenant structures. The estimation of the hydrodynamic loading induced by the falling jet is mandatory. In engineering practice, the assessment of rock scour is mainly

based on empirical and semi-empirical relationships. Despite providing an order of magnitude idea of the phenomena, these approaches cannot properly represent the characteristics of the rock mass, as well as the interaction with air and water.

Bollaert (2002) modeled both physically and numerically the different processes that govern rock scour, from jet issuance to rock fracturing and rock block uplift by hydrodynamic pressures. This resulted in a new and completely physically based scour evaluation method for both the ultimate scour depth and the time evolution of scour for plunge pools with flat bottoms. It is actually being applied to several dam scour problems worldwide. The present paper highlights the latest progress on jet issuing conditions and jet diffusion in plunge pools of realistic geometry.

Regarding jet characteristics, several authors like McKeogh & Elsayy (1980), Ervine & Falvey (1987) and May & Willoughby (1991) have analyzed the jet trajectory and impact in a downstream water cushion, for different issuing velocities. They indicated the jet turbulence intensity as the key parameter for jet behaviour. Turbulence intensity is defined by:

$$T_u = \frac{RMS(u')}{\bar{u}} \quad (1)$$

where u' is the RMS value of the velocity fluctuations and \bar{u} is the mean velocity. Yet, no direct measurements on prototype scale exist due to technical difficulties and cost. This paper intends to further clarify this topic by extensive experiments with jets at near prototype velocities.

2 IMPORTANCE OF JET TURBULENCE INTENSITY IN ROCK SCOUR FORMATION

Jet turbulence intensity at issuance strongly influences the spreading and eventual break-up of jets in the air. In the case of high dams, turbulence intensity defines the jet characteristics at impact in the downstream water cushion. As an example, a jet travelling in the air will disintegrate after a shorter distance the higher the issuing turbulence intensity is. Furthermore, the extension of the impact area (diameter at impact) is a function of the lateral spreading of the jet. The mechanisms and rate of air entrainment in the pool vary with the impact velocity but also with the turbulence intensity. Last but not least, jet turbulence intensity characterizes also the dynamic pressures impinging at the pool bottom for low tailwater levels. For increasing tailwater levels, the jet develops before impacting on the rock and its fluctuating pattern is intensified.

The propagation of pressure fluctuations inside rock joints contributes to crack opening, crack propagation and to block formation. Superposition of pressure waves can match the resonance frequencies of the joint system and build up very high-pressures (Bollaert 2002). Resonance frequencies of joint systems are normally in the range of 10 to 100 Hz. Rock block formation by hydraulic jacking occurs either instantaneously or by fatigue, when the dynamic stresses exceed the fracture toughness of the joints. Thus, the fluctuating characteristics of the jet merit further investigations.

3 INVESTIGATIONS ON JET TURBULENCE INTENSITY

3.1 Experiments

The objective of the investigation was to characterize the jet at the nozzle exit by means of pressure measurements along the diameter. Issuing conditions were investigated experimentally for nearprototype jet velocities of up to 30 m/s (max. Reynolds number of $2E+6$). Pressure measured were performed at the outlet of a circular shaped 72 mm diameter jet nozzle using piezoresistive micro-transducers type [®]KULITE XTL-190-17BAR-A. The 300 m m diameter upstream con supplies a maximum of 120 l/s by means of a 63 m high head pump. A pressure transducer was placed in a mobile structure right below the jet—Figure 1. Measurements were done at 15 positions along the diameter, spaced of 4 to 5 mm, for 10 exiting velocities from 7.5 to 30 m/s. The extreme points were 2 mm away from the sidewalls. The signal was sampled at 2 kHz during 32.5 s.

Two different supply conditions were tested. The upstream circuit having several bends, secondary currents were observed at the exit for the lowest velocities within the tested velocity range. The first series of tests were performed under these conditions.

For the second group of tests, an attempt was made to reduce the upstream secondary currents by placing a honeycomb grid immediately upstream of the last bend, made of 10 cm long and 10 mm diameter metallic tubes of 1 mm thickness. In addition, an air valve was added at the highest point of the supply system to assure a good and complete ventilation of the conduit.

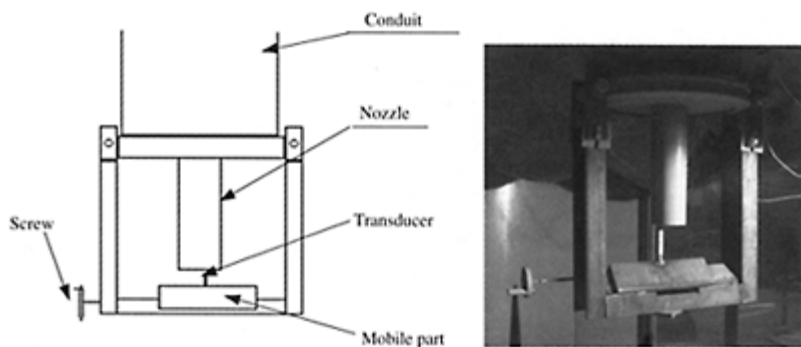


Figure 1. Overall view of the jet facility and detailed view of the measuring frame under the nozzle.

3.2 Results

The mean and RMS pressure values were computed at each position. The mean local velocity was derived from:

$$V_y = \sqrt{\frac{2(\bar{p} - p_{atm})}{\rho}} \quad (2)$$

where \bar{p} =mean local pressure [kN/m²], p_{atm} =atmospheric pressure [kN/m²] and ρ =water density (1000 kg/m³). The root-mean-square value of velocity fluctuations was computed from pressure fluctuations according to Arndt & Ippen (1970), Equation 3. This expression neglects higher order terms when converting pressures into velocities with an estimated error of 5% for a turbulence intensity level of 10%.

$$RMS(u') = \sqrt{u'^2} = \frac{\sqrt{p'^2}}{\rho u} \quad (3)$$

Finally, turbulence intensity at each measuring point was obtained with Equation 1. Section average and local turbulence intensities were computed replacing u by the mean average velocity V_j and by the local mean velocity V_y respectively. In Figure 2, average and local (at the jet axis) turbulence intensities are presented. Results from Bollaert (2002) from measurements performed exclusively at the jet axis are also shown for comparison and completion, including those with a convergent nozzle. Jet turbulence intensities tend to values below 8%, except for velocities lower than 12 m/s. For $V_j > 12$ m/s, the results tend to 4% for both supply conditions (with/without honeycomb grid). The use of a convergent nozzle reduces turbulence intensities to values of 2 to 3%.

On the other hand, the velocity distribution at the issuing section using the measured local mean velocities V_y was compared with theoretical profiles of turbulent flow (Figure 3) given by:

$$\frac{V(y)}{V_{max}} = \left(\frac{y}{D/2} \right)^{\frac{1}{n}} \quad (4)$$

where D =nozzle diameter and $n=7$ (typical value for turbulent rough flows).

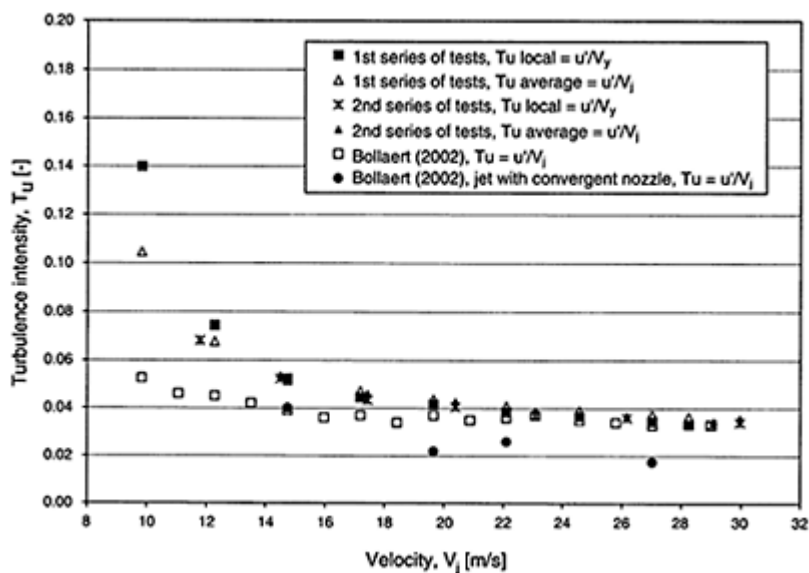


Figure 2. Initial turbulence intensity under the jet axis from experiments.

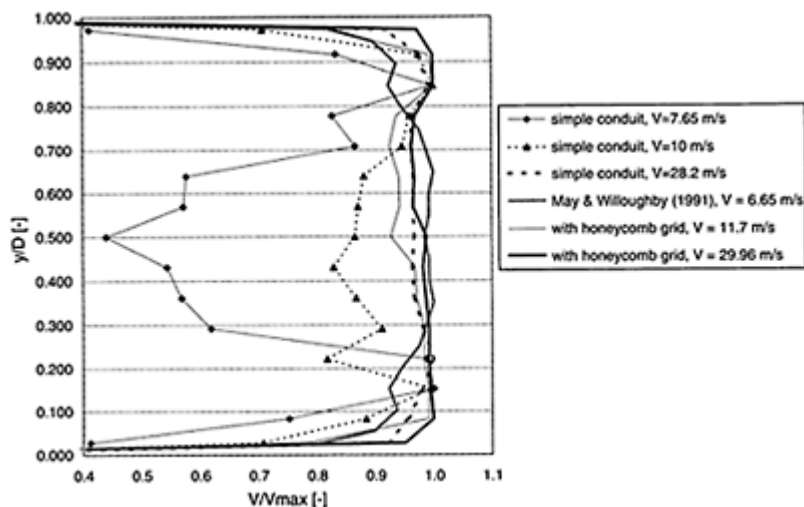


Figure 3. Velocity profiles from pressure measurements at the exiting nozzle of LCH facility (circular, 72 mm diameter) and from May &

Willoughby (1991, plane jet, largest jet
dimension of 101 mm).

Overall, the experimental profiles do not follow theoretical turbulent flow profiles. For velocities lower than 12 m/s, the profiles show very low velocities in the jet core. During the first series of tests, the secondary currents in the supply conduit tend to keep most of the flow close to the outer walls of the nozzle. For the second series of tests with the honeycomb grid and the air vent, a better flow distribution inside the conduit for low and intermediate velocities was obtained. The grid improves the flow repartition in the section, rendering turbulence more homogeneous and the operation of the outlet more regular. The additional head loss did not reduce the range of tested velocities.

For high velocities, the velocity profiles tend to be uniform, mainly due to the extreme contraction produced by the nozzle. This is more evident with the second experimental set-up, for which the flow is better distributed in the section and good air ventilation of the upstream circuit was assured. No secondary currents were observed during the second set of tests, most likely due to combined effect of the grid, the air vent and the contraction.

The velocity profiles allow also computing the kinetic energy correction factor:

$$\alpha = \frac{1}{A} \int_A \frac{v_x^3}{U^3} dA \quad (5)$$

This coefficient is used in the computation of dynamic pressure coefficients from the mean flow velocity, for the assessment of scour progression and design of protection measures as concrete linings, anchorages and pre-excavations. For the first series of tests, α varies from 1.0 to 1.1 for velocities higher than 15 m/s, for which no deflection of the velocity profiles (due to secondary currents) was observed. For lower velocities, α is unrealistic and less than 1 since the flow section is non-completely full and core velocities are dramatically low. For comparison, Bollaert (2002) found a values of 1.0 at low jet velocities and 1.05 at high jet velocities (up to 30 m/s) with similar supply conditions but performing measurements only under the jet axis and assuming a turbulent velocity profile as given by (4).

Using the honeycomb grid, α values higher than 1.0 are obtained at lower velocities, starting from 10 m/s. Values close to 1.1 correspond to well-developed turbulent profiles and values close to 1 are typical for uniform profiles. These values confirm the effect of the contraction in rendering the profiles more uniform. However, since the used contraction is rather sudden than smooth, the velocity profile presents slightly higher velocities close to the sidewalls.

Table 1. Initial jet turbulence intensity according to the type of outlet. Comparison with values proposed by Bollaert (2002) and Bollaert et al. (2002).

Type of outlet structure	T_u (present recommendations)	T_u (Bollaert, 2002)
Orifices (low head)	3–8%	3–8%
Orifices (with smoothly converging outlet or with high head)	2–4%	2–3%
Free overfall (without splitters)	3%	0–3%
Ski-jump (without deflectors)	4%	3–5%

3.3 Discussion and design recommendations

Compared to a theoretical pipe flow, the velocity profile is modified by the geometrical contraction in both test series. In fact, the (averaged) velocity profiles are rather uniform than turbulent and differences in impact kinetic energy of up to 10% were observed. This has direct repercussion on the assessment of the impact energy downstream.

Turbulence intensity depends mainly on the velocity and on the contraction at the nozzle. For increasing Reynolds, T_u increases when passing from the laminar to the turbulent flow regime. For the present case of turbulent rough flows, geometry starts playing a major role. In fact, the present measurements show that T_u values decrease asymptotically to values below 6%.

Based of the presented results, $T_u > 8\%$ should be considered if secondary currents are expected. For fully occupied sections, $T_u < 8\%$, tending to a value of 3–4% for rough jets as those produced in orifices of high head. For smoothly converging sections, as may be the case for bottom outlets, T_u values of 2–3% may be more appropriate at high prototype velocities (based on Bollaert 2002). For ski jump outlets, where no contraction is imposed but the effect of curvature uniforms the velocity profile, similar values to rough jets are recommended for feasibility purposes. Finally, for free overfalls, low T_u values are proposed according to the potential character of the flow. This, however, remains to be confirmed based on high-velocity jet data, which is only possible on prototype dam structures. In the meantime, upper values of about 3% are recommended for design.

A summary of T_u values is presented in Table 1. They may be considered as a first-hand indication for design purposes in practical cases.

Nevertheless, specific geometric characteristics (splitters, deflectors, etc.) of each type of outlet are not taken into account and may significantly alter the proposed values. The obtained results using 15 measuring points and modifying the supply conditions confirm the values obtained by Bollaert (2002) with a single point analysis at the jet axis.

For comparison, McKeogh & Elsayy (1980) obtained T_u values of less than 1% for laminar jets and 2% for turbulent jets with velocities lower than 5 m/s, using pressure transducers. May & Willoughby (1991) used a total-head Pitot tube to measure the RMS values of pressure fluctuations and estimated T_u in the range of 5.5 to 5.8% for velocities

between 4.9 m/s and 6.6 m/s. Ervine & Falvey (1987) present initial turbulence intensities of 0.3% for almost laminar plunging jets, 1.2% for smooth turbulent plunging jets and 5% for rough turbulent plunging jets, based on experiments using a laser Doppler velocimeter, velocities from 3.3 m/s up to 29 m/s and a smooth tapered nozzle. The values of T_u obtained in the present investigation with rough jets agree fairly well with those proposed by these authors and by Bollaert (2002).

4 INVESTIGATIONS ON JET INTERACTION WITH THE POOL BOUNDARY

4.1 Influence of plunge pool geometry on scour process

In what concerns rock scour, research and practice have just focused on the effect that an increasingly thick water cushion might have in protecting the underlying riverbed. No interaction between the diffusing jet and the pool geometry has formerly been considered aside from the impact at the bottom. This chapter highlights possible interactions with the pool boundaries.

The falling jet is diffused through a water cushion before impinging on the natural riverbed. Diffusion increases with increasing water depth. The water cushion is usually made thick enough to enhance the full development of the jet core for a predominant discharge. This condition is

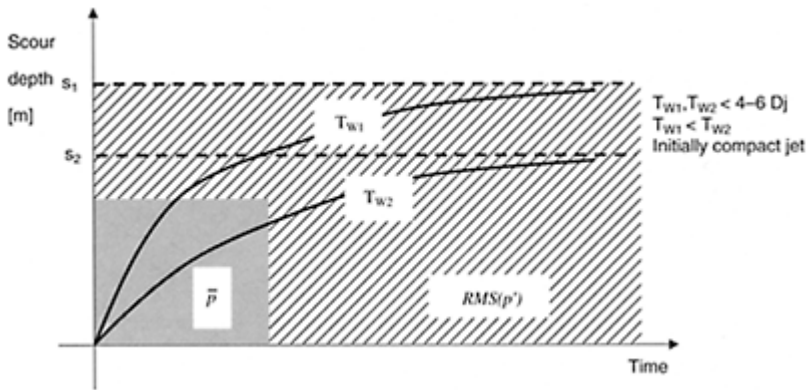


Figure 4. State-of-the-art knowledge diagram of scour evolution with time $s(t)$ for two different initial tailwater levels T_{w1} and T_{w2} and for initially compact jets. Predominant scouring agents are the mean pressure and the fluctuating pressures. S_1 and S_2 are the final depths of scour for each case.

normally achieved at a depth of 4 to 6 times the jet's diameter or thickness, eliminating the high mean pressures of compact jets at the water-rock interface. Since mean pressures are considered the driving agent in the preliminary stages of rock scour, this thickness is the main criterion for tailpond dam design. However, the fluctuating pressures of developed jets still have high energy content, even at high frequencies larger than 100 Hz (Bollaert 2002). According to this author, these fluctuations can excite rock joints to resonance frequencies and enhance crack opening and propagation. A thicker water cushion is thus needed to prevent further scouring.

All in all, scour process is expected to develop in two phases as represented in Figure 4. During the first stage, scour is due to high mean pressures of the jet core and evolves quite rapidly. On a second stage after full development of the jet, scour progresses by means of the fluctuating pressures and evolves asymptotically to a final pool water depth Y . Y is equal to the sum of the tailwater level T_w and the scour depth S in the deepest point of the pool.

However, for increasing pool depths, scour develops in rather irregular configurations. Plunge pools develop both vertically and laterally. Different pool geometries are created according to site specific geological and geotechnical characteristics of the rock. Some schematic examples are presented in a companion paper (Bollaert et al. 2004). The lateral jet confinement is thought to accelerate jet development locally under the jet, by effect of the re-circulating currents. Therefore, the interaction between jet turbulence and scour hole geometry is a key element for estimating the final equilibrium state of the scour. A given geometry may reach an equilibrium situation faster than other. For a progressively deeper scour hole, the scour geometry will modify the development of the jet. A reduction in impacting pressures may be expected by interference of the re-circulating flows reflected from the boundaries with the jet core. Thus, lateral confinement might slow down scour progression with depth. Once the confinement disappears by lateral erosion, the scour rate in depth might increase again. This, however, largely depends on the geomechanical characteristics of the rock.

4.2 Experimental work and preliminary results

Systematic experimental investigations were carried out to assess the effect of scour hole geometry on hydrodynamic pressures at the water-rock interface. The development of jets is studied for differently shaped scour holes. For the time being, flat and conical-stepped scour geometries have been tested. The conical pool geometry was obtained by placing cylinders of different diameters and heights in the basin presented in Figure 1 of the companion paper (Bollaert et al. 2004). A schematic representation of the two tested cases is presented in Figure 5. Preliminary results for a flat bottom and for a cylindrical-shaped bottom (20 cm high, 40 cm diameter) are discussed hereafter, focusing on the modification of the pressure fluctuation pattern at the water-rock interface.

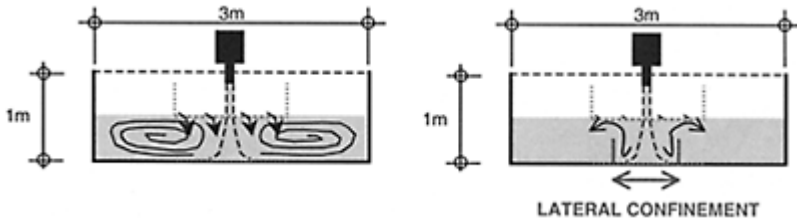


Figure 5. Tested pool geometries. On the left hand side, a flat pool bottom and on the right hand side, a lateral confinement of the jet corresponding $D_{\text{confinement}}/D_j=5.5$.

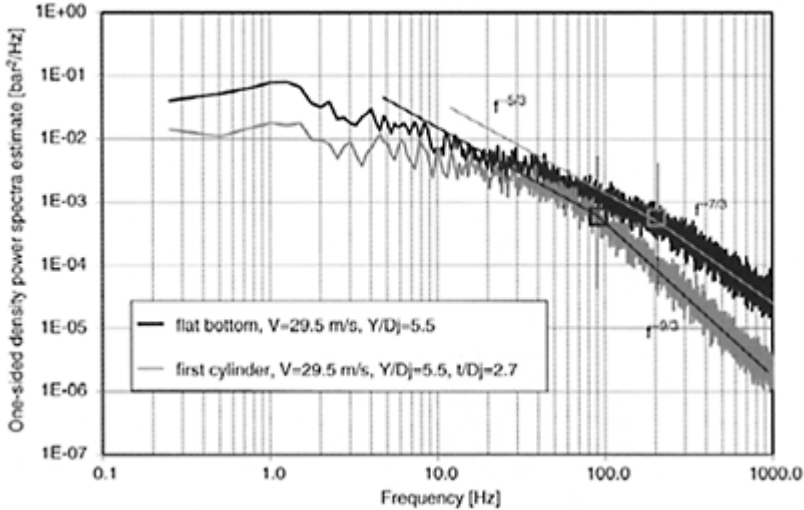


Figure 6. Density power spectra from pressure measurements, for a jet diameter $D_j=72$ mm and a tailwater level $Y=5.5 D_j$. Two cases are presented for a scour depth of $t/D_j=0$ and $t/D_j=2.1$.

Pressure fluctuations were measured at the bottom of the scour hole geometries, using micro piezoresistive pressure transducers. Pressures were sampled at 2 kHz. Power density spectra of the measured pressure fluctuations are compared in Figure 6, for the highest tested velocity of $V=29.5$ m/s.

The two spectra presented in Figure 6 correspond to developed jets and still have important energy content at frequencies higher than 100 Hz. For the flat bottom, the dissipation range is reached at a frequency of approximately 200 Hz. For the case of a lateral confinement of $D_{\text{cylinder}}/D_j = 5.5$, the transition from the redistribution to the dissipation range occurs at 80 Hz. Also, the low-frequency large-scale turbulent eddies seem to break-up more rapidly. Nevertheless, at frequencies that are able to stimulate rock joints to resonance and cracking, i.e. mainly between 10 and 100 Hz, the observed decrease in spectral energy (for cylindrical bottoms compared to flat bottoms) is for the time being very small.

The energy redistribution around the falling jet creates additional friction, increasing dissipation and decreasing the mean impact pressures at the bottom. The lateral confinement enhances the development of the jet and decreases the importance of very large scale (macroturbulence) and very small scale eddies. Its influence on intermediate scale eddies is not clear yet and needs further investigations.

5 CONCLUSIONS

The experimental investigations show that:

1. Jet turbulence intensities are generally below 8%, reaching larger values if the outlet section is either not fully occupied or if the outlet flows have some kind of helical pattern (secondary flows). For near-prototype velocities, jet turbulence intensities are close to 4% if the outlet has a pronounced contraction, and close to 2–3% if the outlet is smoothly convergent.
2. An abrupt contraction renders the mean velocity and pressure profiles almost uniform. The kinetic energy correction factor varies between 1.0 and 1.1. This may vary the kinetic energy downstream by $\pm 10\%$. Using a value of 1.1 for design purposes leads to conservative calculations.
3. The jet behaviour in the plunge pool is influenced by the pool geometry. Indeed, lateral confinement accelerates jet development by creating additional friction to the descending plunging jet. Its influence on the establishment of an equilibrium-scour situation is not clear yet, since enhanced jet development also increases pressure fluctuations. Further investigations are planned.

The present investigations will be included into the comprehensive scour model developed by Bollaert (2002) and described in Bollaert & Schleiss (2002).

ACKNOWLEDGEMENTS

The ongoing research project is co-funded by the Foundation for Science and Technology (Portugal) and the Federal Office for Water and Geology (Switzerland).

REFERENCES

- Arndt, R.E.A. & Ippen, A.T. 1970. Turbulence measurements in liquids using an improved total pressure probe. *Journal of Hydraulic Research*, 8(2): 131–157.

- Bollaert, E.F.R. 2002. Transient water pressures in joints and formation of rock scour due to high-velocity jet impact. *Communication N° 13 of the Laboratory of Hydr. Constructions* (LCH), EPFL, Lausanne.
- Bollaert, E.F.R. & Schleiss, A.J. 2002. A physically-based engineering model for the evaluation of the ultimate scour depth due to high-velocity jet impact. Proc. International Workshop on Rock Scour, A.A.Balkema, The Netherlands : 161–17
- Bollaert, E.F.R., Falvey, H.T. & Schleiss, A.J. 2002. Assessment of turbulent jet impingement in plunge pools: the particular characteristics of a near-prototype physical model study. *Proceedings of Riverflow 2002*. Louvain-la-Neuve. Belgique.
- Bollaert, E.F.R., Manso, P. & Schleiss, A.J. 2004. Dynamic pressure fluctuations at real-life plunge pool bottoms. Int. Conference on Hydraulics of Dams and River Structures, Teheran, Iran.
- Ervine, D.A. & Falvey, H.R. 1987. Behaviour of turbulent water jets in the atmosphere and in plunge pools. Paper 9136, Water Eng. Group, Proc. of the Institution of Civil Engineers, Part 2, 83:295–314.
- May, R.W.P. & Willoughby, I.R. 1991. Impact pressures in plunge pool basins due to vertical falling jets. Report SR 242, HR Wallingford, UK.
- McKeogh, E.J. & Elsayy, E.M. 1980. Air retained in pool by plunging water jet. *Journal of the Hydraulic Division*. 106(10): 1577–1593.

Effect of sill arrangement on maximum scour depth downstream of abruptly enlarged stilling basins

A.M.Negm

Professor of Hydraulics, Civil Engg. Dept., College of Engg., Garyounis University, Benghazi, Libya

Hydraulics of Dams and River Structures - Yazdandoost & Attari (eds)

© 2004 Taylor & Francis Group, London, ISBN 90 5809 632 7

ABSTRACT: Scour downstream (DS) of hydraulic structures (HS) may endanger the safety of the structures if the necessary precautions are not considered during the design stage. Normally, different measures produce different effects on reducing the maximum scour depth DS of HS. One important HS is the abruptly enlarged (or suddenly expanding) stilling basin. In this paper, the effects of different arrangements of sills inside an abruptly enlarged stilling basin will be treated. An experimental program was conducted to investigate the effects of a continuous end sill, one asymmetric side sill, double staggered asymmetric side sills, symmetric side sills, a central sill and a continuous central sill. The flow patterns were observed and the maximum scour depths were recorded. The results revealed that in most of the cases the flow patterns are asymmetric resulting in asymmetric scours. The reduction in the maximum scour depth depended on the sill arrangement and on the flow conditions represented by the Froude number. The central sill with limited width and the continuous central sill improved flow symmetry and the latter yielded the least depth of scour.

1 INTRODUCTION

Suddenly expanding stilling basins are effective in dissipating energy downstream of hydraulic structures. A disadvantage of such basins is that the corresponding flow patterns are mostly asymmetric, especially at high values of Froude number. This asymmetric flow causes asymmetric scour downstream of the basin where the soil is erodible, Negm et al. 2002a. Different measures may be used to improve the flow pattern

in a suddenly expanding stilling basin by forcing the flow to be symmetric and hence the expected downstream scour patterns may be improved. These methods may include the use of a central sill of limited width at a particular position, Negm et al. 2002b, one or more asymmetric side sills at certain positions with a particular orientation, Saleh et al. 2003b and symmetric side sills at particular positions with pre-specified orientation, Saleh et al. 2003c. All the above studies dealt with supercritical flow. The effect of subcritical flow ($F_1=0.48$ to 0.73) in a sudden expansion ($e = 1.5$ to 4.5) on movable bed topography (sediment size is 0.28 mm) was discussed by Nashta et al. 1987. In this paper, the effect of sill arrangement on the scour characteristics DS of suddenly expanding stilling basin is discussed based on experimental investigations.

2 THEORETICAL BACKGROUND

Figure 1 shows a definition sketch for the phenomenon under study. The maximum scour depth downstream of the stilling basin can be expressed as follows:

$$D_s = f(g, \rho, \rho_s, G, V_G, b, B, H_u, D_{50}, h_s, x_s, L_b, W, \phi) \quad (1)$$

in which g is the gravitational acceleration, ρ is the density of water, ρ_s is the density of the movable soil, G is the gate opening, V_G is the mean velocity under the gate, b is the approaching channel width, B is the width of the expanding channel, H_u is the upstream water depth, D_{50} is mean particle diameter, h_s is the height of the sill, x_s is the position of the sill from the expanding section, L_b is the length of the basin, W is the total length of the symmetric side sills normal to the flow direction

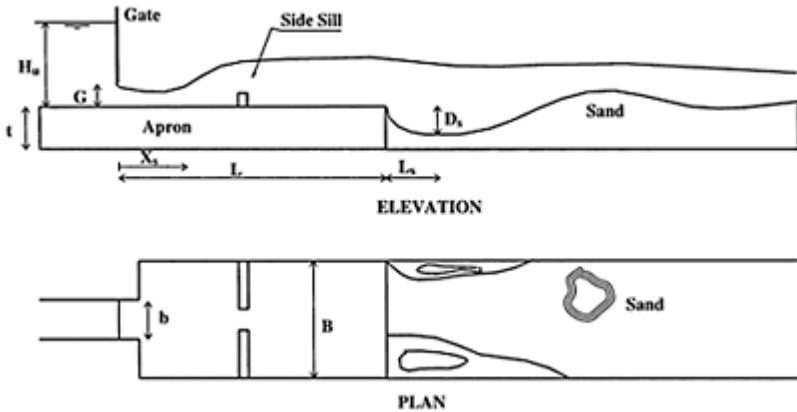


Figure 1. Definition sketch for a typical tested sill in a suddenly expanding stilling basin (SESB).

(W is twice the length of one side sill when two are employed), and ϕ is a factor to account for the sill arrangement.

Selecting ρ , G , V_G as repeating variables and employing the principle of Π theorem, Equation (1) can be written in dimensionless form as:

$$\frac{D_s}{G} = f\left(F_G, \frac{H_u}{G}, \frac{B}{G}, \frac{b}{G}, \frac{h_s}{G}, \frac{x_s}{G}, \frac{L_b}{G}, \frac{W}{G}, \frac{D_{50}}{G}, \frac{\rho_s}{\rho}, \phi\right) \quad (2)$$

The effect of the density ratio is excluded because only one fluid and only one soil were used during the course of experiments. The effects of sill height and particle size (since h_s and D_{50} are both constant) are neglected. Also, the effect of expansion was neglected because only one geometry was studied. Keeping in mind the properties of the dimensional analysis, Equation (2) may be reduced to

$$\frac{D_s}{G} = f\left(F_G, \frac{H_u}{G}, \frac{W}{B}, \frac{x_s}{L_b}, \phi\right) \quad (3)$$

where F_G is the Froude number at the gate. The validity of this equation will be assessed using the collected experimental data in a forthcoming section.

3 EXPERIMENTAL SET-UP

The experiments were carried out in a recirculating laboratory flume 0.20m wide, 0.25m deep and 3.5 m long. The discharge was measured using a pre-calibrated orifice meter installed in the feeding pipeline. The stilling basin model was made from perspex of thickness 10 mm with a length of 1.25 m. The length of the approaching channel was 50 cm while the length of the apron of the expanding stilling basin was 75 cm. The width of the approaching channel was kept constant at 13 cm, and the width of expanding channel was fixed to obtain an expansion ratio of 1.54, which is close to the one normally used in practice. A control sluice gate made from the same perspex was used to control the upstream depth and the gate opening. The gate was installed 5 cm upstream the sudden expansion section. The rest of the flume (2.5 m) was covered by sediment consisting of a 7.5 cm sand layer of median diameter, $D_{50}=1.17$ mm. The tailgate at the end of the flume was used to control the tailwater depth. During the course of the experiments, the tailgate was controlled such that the tailwater depth was about 5 cm. Nine models were tested. One model consisted of a smooth SESB (no sill case). A smooth SESB with an end sill of 2:1 US slope and vertical DS face with a height of 1.0 cm represented the second model. The third model consisted of a single side sill of height 1.5 cm and length of 7.4 cm fixed at $0.5L_b$. Adding another side sill of the same dimensions at the position of $0.25L_b$ to the third model represented the fourth model. The fifth and sixth models, each consisted of two symmetric side sills, the width of each was 7.4 cm with $W/B=0.74$, one fixed at $x_s/L_b=0.15$ and the second at $x_s/L_b=0.35$. The seventh and eighth models were similar to the sixth but with $W/B=0.90$ and $W/B=1.0$. The final model had a central sill of length 14.75 cm fixed at $x_s/L_b=0.35$ and of the same height of 1.5 cm. Since some of the tested sills consisted of two parts, the length of the sill W was obtained by doubling the length of one part to yield the width ratio W/B . The selection of the models was based on

researches conducted by Bremen and Hager (1994), Negm et al. (2002b), Saleh et al. (2003a,b,c) on the assumption that these previous studies had identified optimal arrangements.

A range of discharges and gate openings was used such that the Froude number under the gate ranged from 1.20 to about 3.9. About 90 runs were performed. The time of each run was chosen to be 45 min based on previous studies, Saleh et al. (2003a,b,c). A typical run consisted of leveling the movable soil, and fixing a particular tailwater depth in the downstream channel with the control gate in close position. The discharge was adjusted to the desired value and the gate was opened to obtain the required under-gate Froude number. During each run the flow pattern was observed and sketched and the deflection of the supercritical jet was recorded. After about 20 minutes, the water surface profile was recorded and its direction was noted. After 45 minutes, the control gate was closed and the pump was switched off. The topography of the movable bed was measured on 5 cm grid points to yield the scour pattern.

4 ANALYSIS AND DISCUSSIONS OF EXPERIMENTAL RESULTS

4.1 *Effect of sill arrangement on maximum scour depth*

The relationship between D_s/G and F_G is shown in Figure 2 for all tested arrangements of sill. In general the sills have a significant influence on the depth of scour, D_s/G regardless of the value of the Froude number. However, the Froude number had a remarkable effect on D_s/G for any particular sill arrangement. On the other hand, for a certain F_G , the effect of the sill on reducing D_s/G increased from the no sill case towards the continuous sill ($W/B=1.0$) in the following order (i) no sill case, (ii) asymmetric single side sill at $x_s=0.5L_b$, (iii) symmetric side sill at $x_s=0.15L_b$ and at $x_s=0.35L_b$, (iv) asymmetric staggered side sills at $x_s=0.25L_b$ and $x_s=0.5L_b$, (v) symmetric side sill at $x_s=0.35L_b$ with $W/B=0.9$, (vi) central sill of width $W/B=0.74$ positioned at $x_s=0.35L_b$ and (vii) continuous sill located at $x_s=0.35L_b$. Regarding the end sill, it increases the magnitude of the relative value of D_s/G . The values of D_s/G for end sill is larger than those of no sill case specially for values of $F_G > 2.2$ and produces similar values or lower at smaller values of F_G . Based on the present results and results by others, Saleh et al. (2003) the use of end sill in SESB basin is not recommended as a tool for reducing the maximum depth of scour DS of the basin.

4.2 *Effect of sill arrangement on flow and scour patterns*

4.2.1 *Case of no sill*

The scour patterns for a SESB under different flow conditions with no sill for $e=1.54$ indicated that the scour was asymmetric as a result of asymmetric flow pattern inside the basin. The main jet of supercritical flow inside the basin may be directed towards the left or right walls of the basin. This may be attributed to the instability of the hydrostatic pressure at the sluice gate section. Figure 3a shows a typical flow pattern for $e=1.54$ at $F_G=2.63$ while Figure 3b shows the corresponding scour pattern. It was observed that the

maximum scour occurred along the same direction of the main jet and another smaller scour hole was formed on the other side. These results compare well with those obtained by Negm et al. (2002a) for expansion ratios 2.0, 2.5 and 3.0.

4.2.2 Case of end sill

Inspection of the flow and scour patterns in the presence of an end sill revealed that both were asymmetric. An end sill is thus not recommended for improving either the flow or scour patterns DS of SESB.

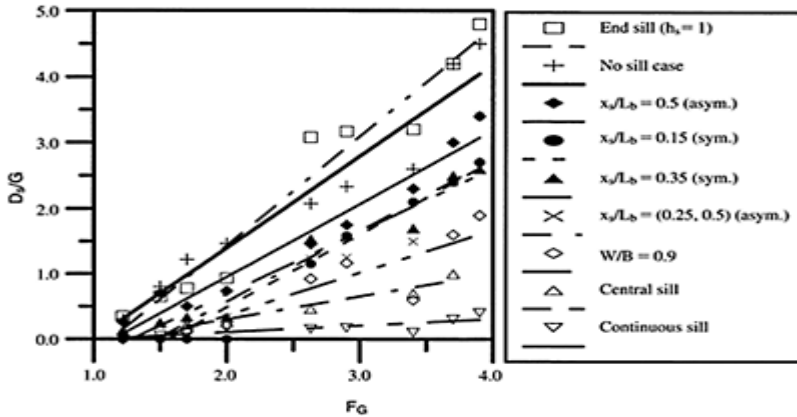


Figure 2. Relationship between D_s/G and F_G for different arrangements of sill inside SESB.

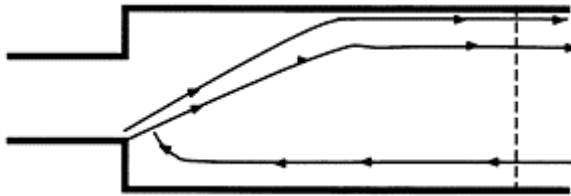


Figure 3a. Typical flow pattern for no sill case for $e=1.54$ at $F_G=2.63$.

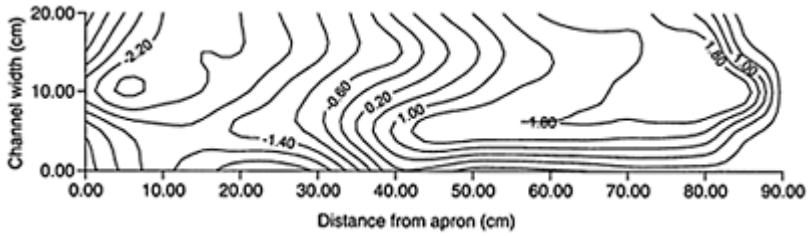


Figure 3b. Scour pattern DS of SESB with no sill for $e=1.54$ at $F_G=2.63$.

4.2.3 Case of asymmetric side sill

When the side sill was placed at $x_s/L_b=0.5$, the main jet of flow was deflected towards one of the basin sides. The deflection length for most values of the Froude number ($F_G < 3.4$) was less than $0.5L_b$. Consequently, the flow behaved as in the case of no sill with the exception that lower values of maximum depth of scour were observed when the direction of the main jet was on the same side of the sill and vice versa. At higher values of F_G , the sill forced the jet in the opposite direction to flow parallel to the bank and causing scour which is less than that of the no sill case. Furthermore, it was observed that a small portion of flow was reversed on the apron of the basin due to the formation of mound downstream of the SESB. For all flow conditions, the observed

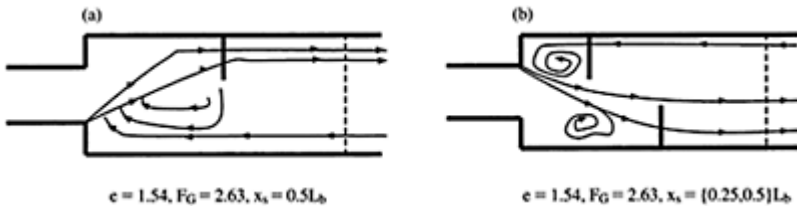


Figure 4. A typical flow pattern for (a) single side sill at $0.5L_b$ and (b) two asymmetric side sills at $0.25L_b$ and $0.5L_b$.

scour patterns were asymmetric because the main jet of flow was also asymmetric. A typical flow pattern at $F_G=2.63$ is shown in Figure 4a which confirms these features.

A second arrangement of asymmetric side sills was using two sills one at $0.25L_b$ and another at $0.50L_b$ on the opposite side. It was observed that the scour was greatly reduced when compared with only one sill. Here, both sills affect the flow because the first sill forced the flow to the other side, hence, the flow was affected by the other sill. At very low F_G , the flow is symmetric and causing little scour depth, which tends to be symmetric. An increased Froude number, caused the main jet to change its direction to the opposite sill passing over it and flowing parallel to the bank. At higher $F_G=3.9$, the

main jet was mostly symmetric up to the second sill but was then diverted to the bank in the direction of the second sill and flows parallel to the same bank. In all cases, the flow at the gate is partially submerged and two vortices were formed, one in front of the each side sill. A typical case of this type of flow pattern is indicated in Figure 4b.

The double side sills at 0.5 reduced greatly the extent of the scouring and deposition process to about the length of the basin. It is also observed that sometimes the maximum scour depth is reduced and sometimes it is increased by using the double side sills based on the behavior of the flow in the basin over the solid apron before reaching the movable soil. If both sills affect the main jet of flow, the scour depth is reduced and may be increased if the coming flow is affected by one of the two side sills.

4.2.4 Case of symmetric side sills with at $x_s/L_b=0.15$ and 0.35

For $W/B=0.74$ and F_G equals 1.22 to 2, the flow DS of sill is symmetric and mostly symmetric US of it with slight difference in the size and strength of the vortices US of each sill. The change in the bed topography occurred for a length of about 20% of the basin. For higher $F_G>2$, the main jet passed in between the two sills from the right one to the left one with the other portion of flow passing over the left sill. The length of scouring and deposition process increased up to about 55% of the basin length for $F_G<3.7$ and upto 85% of the basin length for $F_G>3.7$. The scour patterns were mostly symmetric although the depth of scour was smaller when one side sill was used but higher than when the same two sills were used in a staggered arrangement at positions $0.25L_b$ and $0.5L_b$. It is interesting to note that the flow and scour patterns in this case were not so different from those of $x_s/L_b=0.15$. A further increase in W/B from 0.74 to 0.90 improved both the flow and scour patterns and produced scour depths which were smaller than those of $W/B=0.74$ whether symmetric or asymmetric. Generally the flow in this case was more symmetrical than for other cases and the water surface of the flow is less fluctuating. The resulting scour was symmetrical about the flume centerline with smaller values and the scour processes end at shorter distances compared to all previous cases.

Typical flow patterns for $e=1.54$, $W/B=0.90$ at (a) $F_G=1.7$ and (b) $F_G=2.63$ are presented in Figures 5a,b while Figures 6a,b show scour patterns for $e=1.54$, $x_s/L_b=0.35$, $F_G=2.63$, at (a) $W/B=0.74$ and (b) $W/B=0.90$. A comparison of these patterns with that of no sill case at the same F_G indicates that the scour depth is reduced significantly and the extent of erosion is shortened due to the presence of the sill. Comparing these results with the previous ones, Saleh et al. (2003c) proved that the use of symmetric sills at $0.35L_b$ with a lateral length of more than 70% of the flume width enhances the flow patterns and the scour depth was considerably reduced. Moreover, the lengths over which the scour and deposition processes took place were significantly shortened. The use of wider sills as in the case of $W/B = 0.90$, both the depth of the scour and the

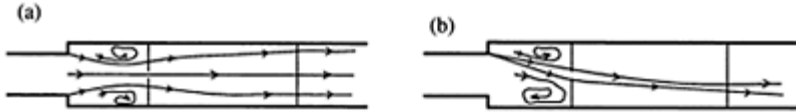


Figure 5. Typical flow patterns for (a) $e=1.54$, $x_s/L_b=0.35$, $W/B=0.90$, $F_G=1.73$ (b) expansion ratio $e=1.5$, $x_s/L_b=0.35$, $W/B=0.90$, at $F_G=2.63$

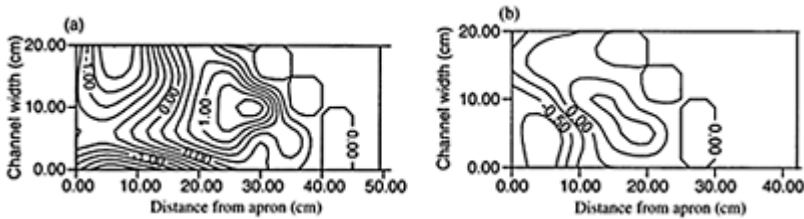


Figure 6. Scour pattern DS of SESB with symmetric side sill of height $h_s=1.50$ positioned at $0.35L_b$ for $e=1.54$ and (a) $W/B=0.74$ at $F_G=2.63$ (b) $W/B=0.90$ at $F_G=2.63$.

length of scouring and deposition processes are reduced more than when the width ratio of sill is greater than 0.74.

4.2.5 Case of central sill

The water surface was nearly smooth with very little fluctuations for low values of Froude number upto about 2.0. The issuing jet from under the gate was symmetric till it reached the sill and then the main jet was distributed to cover the full width of the channel forming a symmetric flow pattern with slightly higher velocity on one side than on the other. In front of the central sill, two vortices were formed but with differing strengths. The sill causes some back effect leading to partial submergence of the gate of about 16% for $F_G=1.7$ and about 20% for $F_G=2.0$. The stronger vortex is in the same side of the higher velocities. Downstream of sill, the water surface is almost smooth. The resulting scour was small and nearly symmetric around the channel centerline but slightly different in magnitude. The length of scouring and deposition processes extended to about 13% of the basin length. Further increase in the Froude number resulted in more turbulence near the sill but the flow in front and DS of the sill was still symmetric. Moreover, a length of about $0.13L_b$ was affected DS of the SESB in this case. A further increase in F_G led to more fluctuations in the water surface at and near the sill leading to unequal distribution of the flow over the channel width giving an indicator that the flow tends to be asymmetric for higher values of $F_G>3.4$. Although a length of about

$0.2L_b$ of the movable soil DS of SESB was affected for $F_G > 3.4$, the scour and deposition patterns were asymmetric forming the main scour in the same direction of the main jet.

4.2.6 Case of continuous sill

The flow in the basin for low values of $F_G < 2.0$ is symmetric both upstream and downstream of the sill. The water surface DS of the sill is smooth while US two vortices are formed which are slightly different in strength (one is weaker than the other). The gate is partially submerged by about 20% due to the effect of sill. The formed scour is small in magnitude and the length of the scour and deposition are also small about 5% of the basin length. For higher $F_G > 2.0$, the flow at the gates becomes free. The flow entering the expanding section forms one strong jet US of the sill which is divided again to pass over the sill with higher water surface and flows over the whole width of the channel (symmetric flow in the basin DS the sill). Two vortices formed US of the sill. The vortices are longer than those for lower F_G . The scour is symmetric around the centerline of the channel and smaller in magnitude than in the case of a central sill. For the highest F_G in this paper, the scour is overall symmetric and smaller compared to its corresponding one due to the central sill. Two typical cases of scour pattern are presented in Figures 7a, b for $F_G = 2.63$ and 3.90 respectively when $W/B = 1.0$ and $e = 1.54$.

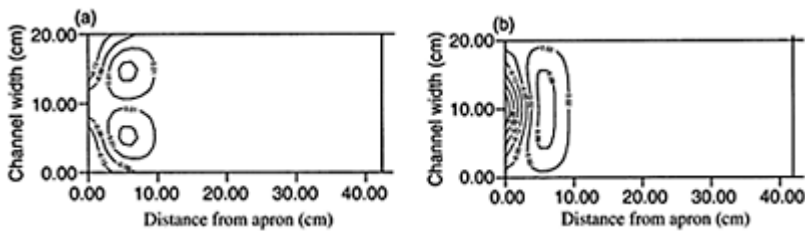


Figure 7. Scour pattern DS of SESB with continuous sill of height $h_s = 1.50\text{cm}$ positioned at $0.35L_b$ for $e = 1.54$ and $W/B = 1.0$ at (a) $F_G = 2.63$ (b) $F_G = 3.90$.

Table 1. Values of the regression coefficient of Equation (4).

Sill arrangement	W/B	x_s/L_b	Values of a, b and R^2		
			a	b	R^2
End sill	1.00	1.00	-1.871	1.655	0.952
No sill	—	—	-1.389	1.395	0.929
Asym sill	0.37	0.50	-1.280	1.117	0.957
Sym sill	0.74	0.15	-1.751	1.120	0.958

Sym sill	0.74	0.35	-1.238	0.964	0.951
Asym sills	0.74	0.25,0.5	-1.601	1.087	0.887
Sym sill	0.90	0.35	-0.955	0.658	0.833
Central sill	0.74	0.35	-0.393	0.349	0.937
Continuous sill	1.00	0.35	-0.099	0.102	0.655

5 ESTIMATION OF MAXIMUM SCOUR DEPTH RATIO D_s/G

Using the linear regression analysis both simple and multiple, several models were proposed and their coefficients were estimated using the experimental data. From all trials, it was concluded that simple linear regression model of the form of Equation (4) was the best one due to the wide variation in the data.

$$\frac{D_s}{G} = a + b(F_G) \quad (4)$$

where a and b are regression coefficients. Their values depended only on the value of x_s/L_b and W/B as shown in Table 1.

6 CONCLUSIONS

An experimental investigation was conducted in a laboratory flume to study the effect of sill arrangements in suddenly expanding stilling basin on scour characteristics downstream of the basin. It was concluded that the use of sill inside the basin affects significantly the maximum scour depth downstream of the basin. The reduction of scour depended upon the sill position, the type of arrangement of sill, the length of sill and the Froude number for a particular expansion ratio. The presence of sill inside the basin affects the flow pattern in the basin and affects also the scour pattern downstream of the basin. Two asymmetric staggered side sills at 0.25 and at 0.50 times the basin length were better than two symmetric side sills at the position 0.35 times the basin length and these two symmetric sills were better than one asymmetric side sill at 0.5 times the basin length. Much better than all sills, the central sill and the continuous sill at the position 0.35 times the basin length with the preference for the continuous sill. Both produced lower depths of scour and improved flow and scour patterns. However, the continuous yielded the minimum values of the maximum depth of scour and more improved flow and scour patterns compared to all investigated sills. An empirical Equation (4) was developed to estimate the maximum depth of scour downstream of the sudden expanding stilling basin for the various sill patterns.

REFERENCES

- Bremen, R. & Hager, W.H. 1994. Expanding stilling basin. *Proc. Instn Civ. Engrs Wat, Marit. & Energy*, Vol. 106 (9) pp. 215–228.
- Nashta, C.F. & Swamee, P.K. & Garde, R.J. 1987. Subcritical flow in open channel expansions with movable bed, *Journal of Hyd. Research*, Vol. 25 (1), pp. 89–102.
- Negm, A.M., Abdel-Aal, G.M., Saleh, O.K. & Sauida, M.F. 2002a. Effect of supercritical flow on scour characteristics downstream of sudden expanding stilling basins. *Egyptian Journal for Engineering Science and Technology EJEST*, Vol. 6, No. 1, 2002a, pp. 1–13.
- Negm, A.M., Saleh, O.K., Abdel-Aal, G.M. & Sauida, M.F. 2002b. Investigating scour characteristics downstream of abruptly enlarged stilling basins. *Proceedings of the International Conference on Fluvial Hydraulics, (River Flow 2002)* Sep. 4–6, Belgium, Published by D.Bousmar & Y.Zech, Editors, Swets & Zeitlinger, Lisse, The Netherlands.
- Saleh, O.K., Negm, A.M., Waheed-Eldin, O.S. & Ahmad, N.G. 2003a. Effect of end sill on scour characteristics downstream of sudden expanding stilling basins. *Proc. of 6th Int. River Engineering Conf.* Published on CD ROM, Ahvaz, Iran. 28–30 Jan.
- Saleh, O.K., Negm, A.M. & Ahmad, N.G. 2003b. Effect of asymmetric side sill on scour characteristics downstream of sudden expanding stilling basins. *Proc. of 7th Alazhar Engineering Int. Conf.*, 7–10 April, Faculty of Engineering, Alazhar University, Naser City, Cairo, Egypt.
- Saleh, O.K., Negm, A.M. & Ahmad, N.G. 2003c. Improving asymmetric scour patterns downstream of sudden expanding stilling basins using symmetric side sills. *Proc. 1st Int. Conf. of Civil Eng. Science (ICCES1'2003)*, 7–8 Oct 2003, Assuit, Egypt.

Energy dissipation and hydrodynamic forces of aerated flow over macro-roughness linings for overtopped embankment dams

S.André, J.-L.Boillat & A.J.Schleiss

Laboratory of Hydraulic Constructions (LCH), Federal Institute of Technology(EPFL), Lausanne, Switzerland

J.Matos

Technical University of Lisbon, IST, Portugal

Hydraulics of Dams and River Structures - Yazdandoost & Attari (eds)

© 2004 Taylor & Francis Group, London, ISBN 90 5809 632 7

ABSTRACT: A promising solution to control overtopping and limit the risk of damage at the toe of an embankment dam may consist in dissipating a significant part of the flow energy along the chute by macro-roughness linings. In fact, compared to a smooth chute, the drag form effects due to the macro-roughness elements increase considerably the flow resistance. In order to define an efficient macro-roughness system, not only the energy dissipation needs to be estimated but also the hydrostatic and hydrodynamic forces on the macro-roughness elements. With this aim, an experimental research is conducted at the Laboratory of Hydraulic Constructions (LCH-EPFL), in order to define the aerated flow characteristics for a stepped flume. The presented results allow to compare the energy dissipation efficiency of conventional steps, steps equipped with endsills and steps equipped with alternate rectangular blocks for a 30° sloping chute, as well as to estimate the forces on the latter lining.

1 INTRODUCTION

Recent advances in hydrology, namely those related to the evaluation of the Probable Maximum Flood (PMF), revealed a significant number of existing embankment dams which have inadequate spillway capacity and which are endangered by overtopping during flood events.

Before the eighties, conventional structural remedial measure consisted in increasing the spillway capacity. Nowadays, however, safe and controlled overtopping by surface protection linings has gained acceptance for the rehabilitation of small embankment dams (Manso & Schleiss 2002).

In parallel to development of Roller Compacted Concrete (RCC) techniques, researchers have shown that macro-roughness lining over the downstream slope is a promising solution to prevent erosion of the structure and to reduce significantly the flow energy along the chute. The energy dissipation rate for high velocity flow over stepped chutes is about 40% to 60% higher (Boes 2000, Chanson 2001, André et al. 2002) than that observed for a smooth chute.

In order to define the flow behaviour as well as to design an optimum energy dissipator lining system, an experimental study of flow over macro-roughness chutes was conducted at LCH-EPFL for different step configurations, namely conventional steps, steps equipped with endsills and steps equipped with alternate rectangular blocks. If an optimum macro-roughness system is to be obtained, in addition to estimate the energy dissipation efficiency, it is essential to evaluate the pressure field and resulting forces acting on the macro-roughness elements.

In this paper, estimates of the energy dissipation rate are proposed for the mentioned stepped linings over a 30° sloping chute. Hydrodynamic forces were also evaluated for the alternate blocks system.

2 EXPERIMENTAL STUDY

2.1 *Stepped flume and instrumentation*

The experimental tests were conducted in a 4 m high (H_f), 8 m long (L_f) and 0.5 m wide (B_f) flume with a variable slope and acrylic sidewalls to allow observation of the flow. The entrance of the flume consists in a jetbox which ensures a homogeneous distribution and a uniform height of the flow. The flume is long enough so that fully developed flow conditions are attained near the downstream end.

The tests were conducted for unit discharges (q_w) up to 0.28 m²/s, thus covering the nappe, transition and skimming flow regimes.

The results presented herein concern the tests conducted in a 30° sloping chute (θ). The bottom of the flume consists of 64 aluminum steps 0.06m high (h) and 0.104m (1) long.

A stilling rectangular and horizontal basin of width, B_{ba} , was fixed at the toe of the stepped flume, at the base of the last step. At the downstream end of the 6 m long and 1 m high basin, an adjustable gate allows an hydraulic jump to be formed at the toe of the stepped flume (Figure 3). According to Diez-Cascon et al. (1991) and Pegram et al. (1999), the upstream limit of the hydraulic jump should be located as close as possible but not drowning the last step. In addition, to minimize local head losses where the flow turns from the stepped flume to the basin, $B_{ba}=B_f$ (no contraction effect). Hence with the present facility, the residual energy can be estimated indirectly by using the sequent depths of the hydraulic jump.

The aerated flow characteristics, *i.e.*, local air concentration, longitudinal velocity and bubble chord lengths, were measured down the chute with a double fiber-optical probe (Matos et al. 2002, André et al. 2002). Vertical profiles of air concentration and velocity were obtained near the toe of the flume, in the quasi-uniform region (André et al. 2002).

In order to obtain the pressure field on the step faces as well as on the macro-roughness elements in the quasi-uniform flow region, eight Kulite silicon over silicon piezo-resistive micro-sensors of 2.6 mm of diameter (André et al. 2001) were fixed along the flume axis, in 1 to 2 cm intervals. Due to the instrumentation's good sensitivity (between 50 and 65 mV/bar), high resonance frequency (about 300 kHz) and accuracy (non-linearity and hysteresis error up to $\pm 0.1\%$ of the full scale of 0 1.7bars), reliable measurements of the pressure fluctuations and positive and negative peaks of pressures of the turbulent flow can be obtained.

Two automatic ultrasound limnimeters, fixed on the stilling basin, can measure the downstream sequent depth, Y_2 , in the non-aerated tail water of the hydraulic jump.

The step height commonly found in prototype of stepped protected embankment dams varies between 0.30 and 0.60 m (Ditchey & Campbell 2000). Therefore, the model data can be extrapolated to 1:5 to 1:10 scaled prototypes using the Froude similarity. The combination of large scale, large Reynolds and Weber numbers for the tested conditions allows significant mitigation of scale effects and the adequate extrapolation of results to prototype. In the following, results are given in model values.

2.2 Macro-roughness linings

The macro-roughness linings adopted in the present study are shown in Figure 1, for the 30° sloping chute. They are characterized by a density dimensionless number (m), given as the number of macro-roughness elements divided by the number of steps.

3 ENERGY DISSIPATION EFFICIENCY OF THE MACRO-ROUGHNESS LININGS

3.1 Influence of the macro-roughness elements on the flow structure

The three flow regimes of the aerated flow over a given stepped slope, namely the nappe, transition and skimming flow, have been described in detail in André et al. (2001, 2002, 2003).

The side views of the four configurations (Figure 2) show that the main macro-structures characterizing both nappe (air cavity, jet impact) and skimming regimes (vortices, internal jet) are similar for all linings. However the distinct effects of endsills fixed over the whole step width ($m = \frac{1}{2}$, $m=1$), as well as those related to the blocks ($m=4$) can be noticed.

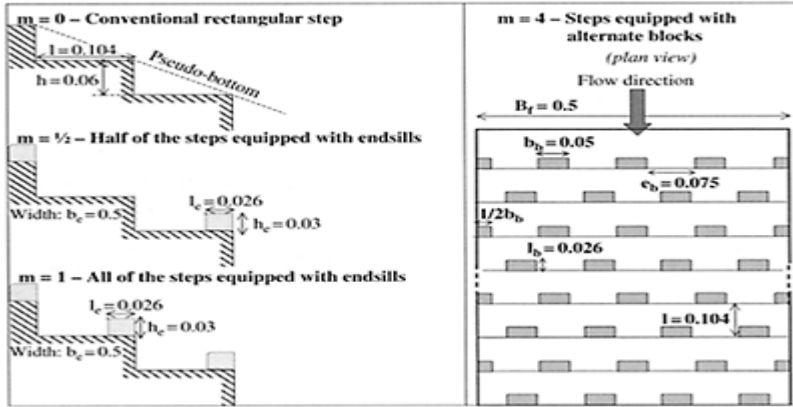


Figure 1. Sketch of the studied stepped macro-roughness linings, for the 30° sloping chute. The model scale dimensions are given in meters.

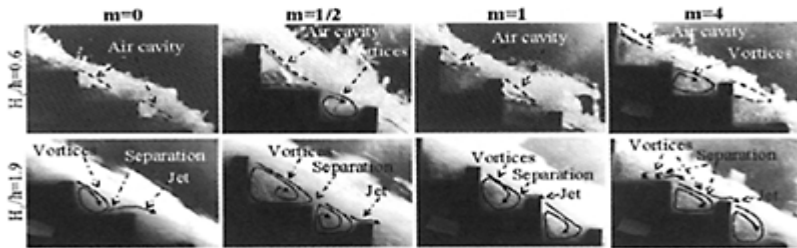


Figure 2. Fully developed aerated flow over a 30° sloping chute with conventional steps ($m=0$), half of the steps equipped with endsills ($m=\frac{1}{2}$), all steps equipped with endsills ($m=1$), and all steps equipped with alternate blocks ($m=4$).

For $m=\frac{1}{2}$ and $m=1$, the endsills do not contribute to a major modification of the flow macrostructures. However, their sizes are slightly modified, which has a direct effect on the contact length between recirculating cells and step faces as well as on the impact zone of the internal jet.

The situation of blocks leads to an increase of the 3-D flow features, due to their alternate position over the flume width. In fact, when passing between two blocks, the flow is contracted and deflected in the transversal axis. As a consequence, in addition to

the internal jet, blocks create a succession of transverse jets and the 3-D pattern of the recirculating cells is thus increased.

The macro-roughness elements might also modify the onset of flow regimes. On the basis the criterion used by Matos (2001) to distinguish the flow regimes, the conditions for their occurrence are given in table 1, where H_c is the critical depth and h the height of the step.

Table 1. Onset of transition and skimming flows for $h/1=0.58$.

Linings (as per Figure 1)	$m=0$	$m = \frac{1}{2}$	$m=1$	$m=4$
Onset of transition flow (H_c/h)	0.9	0.6	0.9	0.6
Onset of skimming flow (H_c/h)	1.2	1.9	1.2	0.9

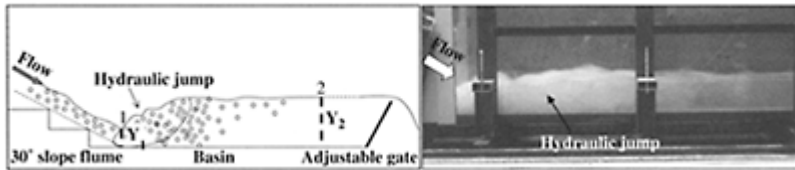


Figure 3. Schematic side view of the rectangular stilling basin.

When comparing the results against those for the situation of conventional steps, the following observations can be drawn:

- endsills on all steps ($m= 1$) do not appear to modify the onset of transition and skimming regimes. They have an effect similar to a displacement of the pseudo-bottom by a distance equal to the normal height of the endsill, $k_e=h_e \cos \theta$.
- endsills on half of the steps ($m=1/2$) influence significantly the onset of the skimming flow. In fact, the flow is subject to a larger acceleration prior to hitting the next endsills, where it is deflected. As a result, the air pocket in the subsequent downstream step (without endsill), remains in the cavity for higher unit discharges.
- alternate blocks ($m=4$) present the same criteria as that of endsills on half of the steps for the onset of transition flow, but the onset of skimming flow is rapidly attained, compared to the other linings. The transition regime occurs for a reduced range of discharges. It is judged that air cavities are rapidly filled of water because the flow is free to circulate between blocks.

3.2 Global energy dissipation

3.2.1 Methodology for estimating the energy dissipation

In order to compare the energy dissipation efficiency of the different linings, the global energy dissipation over the 30° sloping chute is estimated by the so-called “indirect” method. It consists in measuring the sequent depths of the hydraulic jump formed at the toe of the chute. This method, already applied by other researchers (Diez-Cascon et al. 1991, Pegram et al. 1999, Yasuda & Ohtsu 2003) is an adequate alternative for estimating the residual energy without encountering the difficulty of defining a representative depth for the aerated wavy flow. A schematic side view of the hydraulic jump at the toe of the stepped flume is given in Figure 3.

Because of the difficulty in measuring the upstream air-water mixture depth, Y_1 , the sequent depth of the hydraulic jump formed at the toe, Y_2 , measured with ultrasound sensors, is used to estimate Y_1 , from the mass and momentum conservation equations. Assuming an hydrostatic pressure distribution and a negligible wall friction, Y_1 is then obtained by:

$$Y_1^3 - Y_1 [\delta Y_2^2 (2Fr_2^2 + 1)] + 2\delta^2 Y_2^3 Fr_2^2 = 0 \quad (1)$$

where $\delta = \rho_2 / \rho_1$, $\rho_1 = (1-C)\rho_{\text{water}}$, C is the mean air concentration measured with the optical probe (André et al. 2002); g , the gravity acceleration; $\rho_2 = \rho_w$ and $Fr_2^2 = q_w^2 / g Y_2^3$, obtained from the measurements.

Assuming a hydrostatic pressure distribution, the residual energy at the toe of the chute is given by:

$$E_1 = Y_1 + \frac{\alpha q_w^2}{2g Y_1^2} \quad (2)$$

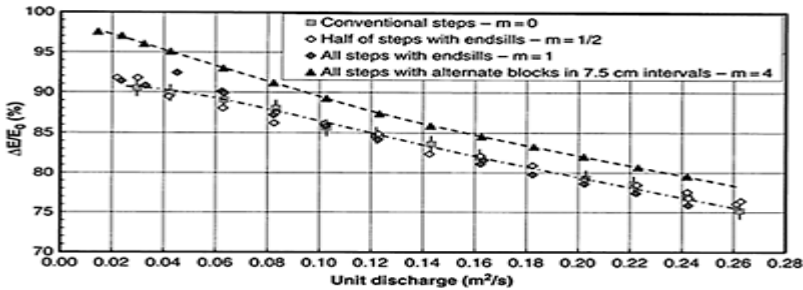


Figure 4. Energy dissipation rate (estimated according to Eq. 1–2) as a function of unit discharge.

with $a \approx 1.1$, the kinetic correction factor of turbulent flow, to take into account the non uniform vertical velocity profile.

Finally, the energy dissipation is given by $\Delta E/E_0 = (E_0 - E_1)/E_0$ and $E_0 = H_f + Z_0 \cos \theta + q_w^2 / (2gZ_0^2)$ where E_0 is the total energy head at the entrance of the flume and Z_0 the depth of the incoming flow.

3.2.2 Results

The evolution of the energy dissipation rate with discharge for all linings is given in Figure 4.

Comparison with smooth slope

The estimation of the energy dissipation of an equivalent smooth slope of 30° , based on Strickler's formula ($K_s = 95 \text{ m}^{1/3}/\text{s}$ for experimental installation), leads to rates from 60% to 30% for the range of high discharges tested (from 0.12 to 0.28 m^2/s respectively). The results shown on Figure 4 confirm that stepped protection allows a reduction of more than 40% of the residual energy at the toe.

Efficiency of the tested linings compared to conventional steps

For this embankment slope, it can be observed that:

- Endsills over all steps ($m=1$) or half steps ($m = \frac{1}{2}$) do not present relevant increase of the energy dissipation.

For $m=1$, as soon as the pool between adjacent steps is filled of water, even if the length of the friction under the vortices are larger ($l_{\text{fnt},m=1} \approx l_{\text{frict},m=0} + 32h$), the internal jets on the endsill edges are shorter and the separation zone vortices-internal jet is broken by the element itself. As a consequence, for well-developed skimming flow ($q_w = 0.16 \text{ m}^2/\text{s}$), this lining tends to be less efficient than conventional steps.

For $m = \frac{1}{2}$ the successive widening and narrowing of the flow, due to the passage from one step with endsill to the other step without endsill, seems to have no significant contribution in the energy dissipation process.

- Alternate blocks ($m=4$) lead to an increase of the head losses, with a dissipating rate of about 80% for the higher tested discharges. Globally, from nappe to skimming flow, the dissipation rate is improved by 6 to 3% compared to conventional steps. This interesting result may be attributed to the drag form effects (wakes, contractions) added by the blocks.

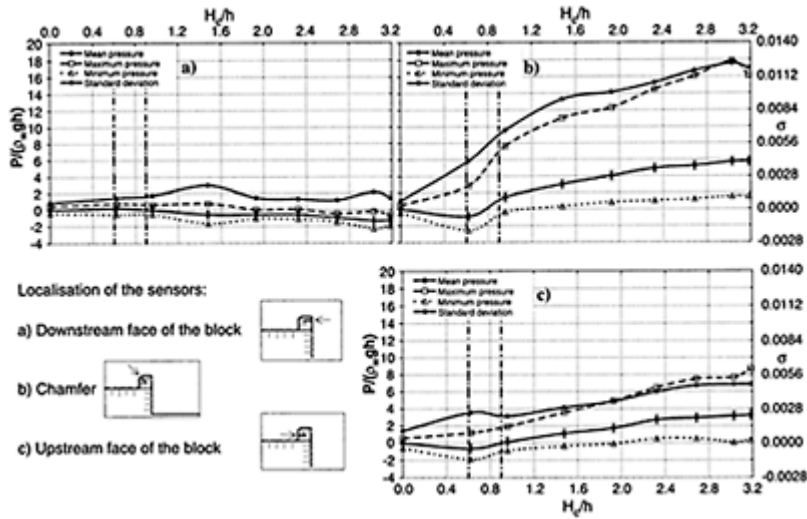


Figure 5. Evolution of the mean, maximum and minimum normalized pressure with the normalized critical depth for the 30° sloping stepped flume equipped with alternate blocks ($m=4$).

- For all linings, the energy dissipation efficiency decreases with discharge, suggesting that the drag form effects, of relevance in the dissipation process, are cushioned by the increasing flow depth.

The solution of blocks was found to be quite effective in terms of energy dissipation. A sensitivity analysis of dimensionless geometric characteristics as e_b/l_b or h_b/e_b (as per Figure 1) may lead to an optimum solution as far as energy dissipation is regarded.

4 FLOW PRESSURES ACTING ON THE MACRO-ROUGHNESS ELEMENTS

In the following, special attention is drawn to the order of magnitude of the loads on the blocks and to the verification that macro-roughness elements do not undergo important pressure fluctuation and negative pressures. The results focus on the alternate block system, the most efficient system as energy dissipation is regarded.

4.1 Pressure field

The evolution of the dynamic pressure on three selected block locations with the flow discharge (or normalized critical depth) is shown in Figure 5, covering the nappe,

transition and skimming flow regimes (distinct flow regimes were separated by vertical lines). The accuracy of the pressure measurements is about ± 3.4 mb.

The following observations can be made:

- A significant negative-pressure zone was observed at the upstream vertical face of the blocks (as in Figure 5a). In fact, both mean and minimum relative pressures are negative as soon as the skimming flow regime is attained.
- In the *aerated region*, the local air concentration is about 0.15 within one millimeter next to the block, which is higher than the minimum values of 0.05 to 0.08 proposed by Peterka (1953) to avoid cavitation damage. However, upstream and in the vicinity of the inception point, local air concentration is lower than 0.07. Considering that the minimum cavitation index for unit

Table 2. Estimated hydrostatic uplift and hydrodynamic drag forces for a prototype unit discharge of $7.6 \text{ m}^2/\text{s}$, $50 \text{ cm} \times 30 \text{ cm} \times 26 \text{ cm}$ blocks of 75 cm intervals and $60 \text{ cm} \times 104 \text{ cm}$ steps, over a 30° sloping chute.

Forces per block (kN)	Clear water region	Aerated uniform region
L: Uplift hydrostatic force	0.38	0.19
FD: Hydrodynamic drag force	11.4	8.9

discharges up to $0.26 \text{ m}^2/\text{s}$ is larger than about 10, the risk of cavitation might be considered negligible.

- The maximum load is located on the chamfer of the block. However, both the mean and the maximum pressures tend to reach an asymptotic value for well-developed skimming flow (Figure 5b). This may be explained by the cushion of the jet impact due to the high submergence of the block (mixture air-water depth larger than $3k_e$). It has been found that the maximum measured positive pressure corresponds, for a prototype, to an equivalent pressure force of 3.6 kN per block of 50 cm length and 30 cm high, for $q_w = 8.3 \text{ m}^2/\text{s}$.
- On the upstream vertical face of the block, the slight increase of the mean pressure (Figure 5c) may be the result of the increasing kinetic energy transported in the recirculating cells. The pressure fluctuation is low, despite the presence of the vortices.

When compared to conventional steps, the present results show that blocks induce negative pressure immediately downstream, but they are expected to be lower than the critical values for the onset of cavitation. They also lead to peaks of pressure about 3 times larger than those for conventional steps.

4.2 Hydrostatic and hydrodynamic forces

The resultant of the pressure field acting on the block includes the hydrostatic uplift L , normal to the flow direction, and a resultant force due to the hydrodynamic pressure field

F_R , which is composed by the drag force F_D , parallel to the flow direction, and the lift force, F_L , normal to the flow direction.

For the clear water region, the density $\rho = \rho_{\text{water}}$, the flow depth $Z = Z_w$ and the mean velocity $U = U_w = q_w / Z_w$. In the aerated region, the mixture density is given by $\rho = \rho_m = (1 - C)\rho_{\text{water}}$, $Z = Z_{90}$ (depth at 90% of air content) and the mean velocity is estimated as $U = q_w / ((1 - C)Z_{90})$. Assuming a hydrostatic pressure distribution in the sloped channel flow and steady flow conditions, the hydrostatic uplift is normal to the slope and it can be roughly estimated as $L = \rho g \cos \theta b_b l_b h_b$. Also considering the simplified assumption that the lift hydrodynamic force is considerably small compared to the resultant hydrodynamic force, the drag force will be parallel to the mean flow direction, similarly as adopted by Manso & Schleiss (2002), and it can be estimated as $F_D = C_D \rho b_b k_b U^2 / 2$, where $k_b = h_b \cos \theta$.

For Reynolds number higher than 10^4 , classical empirical tables, for roughly similar flow conditions and block geometry, give values of C_D ranging from 0.80 to 1.55 for $1 < l_b / b_b < \infty$. Considering the largest value of 1.55, the force values obtained for the maximum tested discharge are given in Table 2.

The obtained results show that the force due to the peak of pressure on the chamfer of a block is relatively low compare to the drag force. In the *aerated region*, the high air content reduces considerably the mass of the fluid mixture and then contributes to a decrease of the impacting forces.

Finally, the measurements suggest that the blocks will not experience severe critical pressure fluctuations and related minimum and maximum pressure. The uplift hydrostatic force was found to be small compared to the weight of the block, whereas the hydrodynamic drag force is of the same order of magnitude. Although it is judged that the forces acting on the blocks will not endanger their stability and resistance, a deepen study is needed to sustain the above reasoning.

5 CONCLUSION

Energy dissipation of four macro-roughness linings—conventional steps, all steps equipped with endsills, every second step equipped with endsills, all steps equipped with alternate rectangular blocks (slotted endsill)—has been assessed in a 30° sloping chute, using the indirect hydraulic jump method.

The results indicate that the drag form effects are a relevant source of energy dissipation. Then, the alternate blocks dissipator system is advantageous in order to reduce the residual energy at the toe of an embankment dam or spillway. At prototype scale, for unit discharge of $7.6 \text{ m}^2/\text{s}$ over a 30° sloping chute, with a lining consisting of four blocks per step (50 cm wide, 26 cm long and 30 cm high rectangular block in 75 cm intervals), the rate of energy dissipation is about 80%, compared to 35% for a smooth chute of identical slope.

The pressure fluctuation as well as the negative and the maximum pressures measured on the block faces and on the steps are not expected to be severe enough to produce cavitation or to destabilize the blocks.

Future research will focus on more detailed analysis on the most adequate geometric characteristics of the blocks and their density. Also, it will be studied a smaller slope, namely 18° .

REFERENCES

- André, S., Boillat, J.-L., Schleiss, A.J. 2001. High velocity two-phase turbulent flow over macro-roughness stepped chutes: focus on dynamic pressures. In ISEH (eds), *Proc. Int. Symposium on Environmental Hydraulics*: CD. Tempe, Arizona, 5–8 December 2001.
- André, S., Boillat, J.-L., Schleiss, A.J. 2002. Efficient surface protection by macro-roughness linings for overtopped embankment dams. In Llanos et al. (eds), Sweet & Zeitlinger Publishers. *Proc. Int. Congress on Conservation and Rehabilitation of Dams*: 407–415. Madrid, Spain, 11–13 November 2002. Rotterdam: Balkema.
- André, S., Dewals, B., Piroton, M., Schleiss, A.J. 2003. Quasi 2D-numerical model of aerated flow over stepped chutes. *Proc. XXX IAHR Congress on Water Engineering and Research in a Learning Society: Modern Developments and Traditional Concepts*: Theme D: CFD Models and Applications, pp. 671–678. Thessaloniki, Greece, 24–29 August 2003.
- Boes, R.M. 2000. Zweiphasenströmung und Energieumsetzung an Grosskaskaden. Minor H.-E. (eds). *WAV-Communication No 166, VAW-ETHZ, Zurich*.
- Chanson, H. 2001. The hydraulics of stepped chutes and spillways. Balkema, Lisse.
- Diez-Cascon, J., Blanco, J.L., Revilla, J. Garcia, R. 1991. Studies on the hydraulic behaviour of stepped spillways. *Water Power Dam Construction*: 22–26, September.
- Ditchey, E.J., Campbell, D.B. 2000. Roller compacted concrete and stepped spillways. In Minor & Hager (eds), *Proc. Int. Workshop on Hydraulics of Stepped Spillways*: 171–178. Rotterdam: Balkema.
- Manso, P.A., Schleiss, A.J. 2002. Stability of concrete macro-roughness linings for overflow protection of earth embankment dams. *Canadian J. of Civil Engineering*, No 29:76
- Matos, J. 2001. Onset of skimming flow on stepped spillways—Discussion. *J. Hydr. Engineering*, 127(7): pp. 519–521.
- Matos, J., Frizell, K.H., André, S., Frizell, K.W. 2002. On the Performance of Velocity Measurement Techniques in Air-Water Flows. *Proc. Int. ASCE—Hydraulic Measurements & Experimental Methods 2002*: CD. Estes Park, Colorado, USA, 07/28–08/01 2002.
- Pegram, G.S., Officer, A.K., Mottram, S.R. 1999. Hydraulics of skimming flow on modeled stepped spillways. *J. Hydr. Engineering*, ASCE 125(5): 500–510.
- Peterka, A.J. 1953. The effect of entrained air on cavitation pitting. *Joint Meeting Paper*, IAHR/ASCE Minneapolis, USA: 507–518.
- Yasuda, Y., Ohtsu, I. 2003. Effect of step cavity area on flow characteristics of skimming flows on stepped chutes. *Proc. XXX IAHR Congress on water Engineering and research in a learning society: Modern Developments and Traditional Concepts*: Theme D: Experiments on Stepped Spillways, pp. 703–710. Thessaloniki, Greece, 24–29 August 2003.

Experimental study of energy loss at drops

H.Musavi-Jahromi & M.Bina

Assistant professor, Shahid Chamran University (SCU), Iran

F.Salmasi

Assistant professor, Razi University, Iran

Hydraulics of Dams and River Structures—Yazdandoost & Attari (eds)

© 2004 Taylor & Francis Group, London, ISBN 90 5809 632 7

ABSTRACT: A vertical drop or free overfall is a common feature in both natural and artificial channels. Natural drops are formed by river's bed erosion while artificial drops are built in irrigation systems to reduce the channel slope to designed slope. Due to more energy dissipation, drops are also applied in stepped spillways. The more energy dissipation is caused by mixing of the jet with the pool at downstream of each drop. As a result, it will be the cause of the reduction in the size of the energy dissipator that is generally provided at the toe of drops and stepped spillways. In the present paper, the energy dissipation in drops has been investigated by physical models.

To reach the purpose of this study, after determination of effective parameters on the phenomenon, three drops with different heights have been constructed from plexiglas. They have been installed in two existing flumes in the hydraulic laboratory at Shahid Chamran university (SCU), Ahwaz, Iran. Several runs of physical models have been undertaken to measured required parameters for determination of the energy dissipation. Results showed that the energy dissipation in drops depends on the drop height and discharge. Predicted relative energy dissipations varied from 10.0% (for $y_c/h=0.94$) to 94.3% (for $y_c/h=0.02$). This work has also indicated that the energy loss at drop is mainly due to the mixing of the jet with the pool behind the jet that cause air bubbles entrainment in the flow.

Further a statistical model has been developed to predict the energy dissipation in drops using SPSS that denotes nonlinear correlation between effective parameters. Comparison between this study's results and results of Moore, Rand, White, Rajaratnam and Chamani, showed that White's model over estimates the energy dissipation in drops and Rand's model under estimates the energy dissipation in drops. The others can predict the energy dissipation in drops as same as the proposed statistical

model. The length of the downstream stilling basin predicted by White is 20% smaller than the others.

1 INTRODUCTION

A vertical drop located in a rectangular channel is illustrated in Fig. 1 where h is the height of drop. The upstream flow is subcritical and the flow immediately downstream of the drop is supercritical. q is the discharge per unit width of the channel and y_c is the critical depth. L_p is distance between hitting jet location on stilling basin and vertical drop wall and y_p is the average pool depth behind the falling jet. Moore (1943) performed an experimental study with drops of two heights and found that the energy loss at the drop could be significant depending upon the relative height of the drop h/y_c . As h/y_c increases from 1 to 12, the relative energy loss varies from zero to 0.53.

Moore also found that the Eq. 1 is good predictor for the depth of the pool behind the falling jet, y_p :

$$\frac{y_p}{y_c} = \sqrt{\left(\frac{y_1}{y_c}\right)^2 + 2\left(\frac{y_c}{y_1}\right)} - 3 \quad (1)$$

In a discussion of Moore's paper, White (1943) developed a method to predict the energy loss at the drop based on a number of assumptions. Using the momentum equation, White obtained the

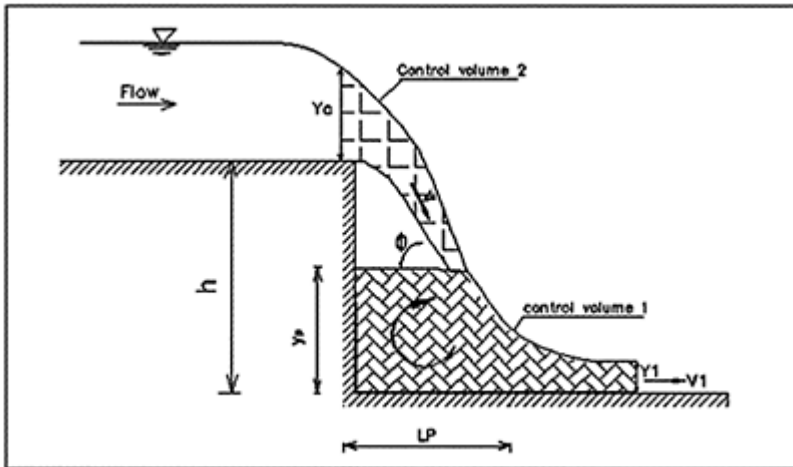


Figure 1. Characteristics of the flow over a vertical drop.

following equation:

$$\frac{y_1}{y_c} = \frac{\sqrt{2}}{1.061 + \sqrt{1.5 + h/y_c}} \quad (2)$$

Energy at downstream of drop and before hydraulic jump can be written as:

$$H_1 = y_1 + \frac{V_1^2}{2g} = y_1 + \frac{y_c^3}{2y_1^2} \Rightarrow \frac{H_1}{y_c} = \frac{y_1}{y_c} + \frac{1}{2} \left(\frac{y_c}{y_1} \right)^2 \quad (3)$$

By substitution of Eq. (2) in Eq. (3), White showed that:

$$\frac{H_1}{y_c} = \frac{\sqrt{2}}{1.061 + \sqrt{\frac{h}{y_c} + 1.5}} + \frac{1}{4} \left(1.061 + \sqrt{\frac{h}{y_c} + 1.5} \right)^2 \quad (4)$$

since the energy upstream of the drop H_t can be written as:

$$H_t = h + 1.5y_c \quad (5)$$

then it can be shown that energy dissipation ($\Delta H = H_t - H_1$) is a function of h/y_c . Gill (1979) attempted to modify the theory of White by refining his assumptions. Then Gill obtained the following equation for the depth below the drop y_1 as:

$$\frac{y_1}{y_c} = \frac{1}{\sqrt{\frac{(1 + \cos \phi)^2}{2} \left(\frac{h}{y_c} + 1.5 - \frac{y_p}{y_c} \right) + 2 \left(\frac{y_p - y_1}{y_c} \right)}} \quad (6)$$

where ϕ is the angle of the jet where it hits the pool. Gill also performed experiments on four drops with heights of 48.3, 74.0, 99.4 and 176.5 mm and measured primarily the pool depths and the angle of the impinging jet. Gill found that his method predicted values of H_1/y_c somewhat larger than those predicted by White.

Rand (1955) performed an experimental study on drops and developed a set of empirical equations for the drop characteristics in terms of the Drop Number (D) as follows:

$$D = \frac{q^2}{gh^3} = \left(\frac{y_c}{h} \right)^3 \quad (7)$$

$$\frac{y_1}{h} = 0.54 \left(\frac{y_c}{h} \right)^{1.275} \quad (8)$$

$$\frac{y_2}{h} = 1.66 \left(\frac{y_c}{h} \right)^{0.811} \quad (9)$$

$$\frac{y_p}{h} = \left(\frac{y_c}{h} \right)^{0.66} \quad (10)$$

Chamani and Rajaratnam (1995) performed an experimental study on two drops of heights 0.62 and 0.25 m were built in a rectangular channel of width of 0.46 m, 6.55 m length and depth of 0.91 m. For the third drop with height 0.25 m, a slot was cut in the back wall, so that no pool was formed behind the jet, thereby simulating an inclined jet.

Chamani and Rajaratnam presented a method to predict drop characteristics. Their analysis were based on a number of assumptions to simplify the problem. The effect of air entrainment on flow characteristic was ignored. With reference to Fig. 1, applying the momentum equation to the control volume 1, they obtained:

$$\rho q V \cos \phi + \frac{1}{2} \gamma y_p^2 = \rho q V_1 + \frac{1}{2} \gamma y_1^2 \quad (11)$$

where γ, ρ are respectively the specific weight and mass density of the fluid. It is assumed that the shear force at the bed is negligible. For the subcritical flow that approaches the drop structure at critical depth, the momentum and the energy equation for the control volume 2 reduce to:

$$\frac{1}{2} \gamma y_c^2 + \rho q V_c = \rho q V \cos \phi \quad (12)$$

$$h + \frac{3}{2} y_c = \frac{V^2}{2g} + y_p \quad (13)$$

The last relation is the continuity equation at supercritical condition of flow along the drop structure. As can be seen there are only four equations for five unknown including V, ϕ, y_p, V_1, y_1 . To complete the equations, Chamani and Rajaratnam used Eq. 14 that is an empirical equation.

$$y_p/h = 1.107(y_c/h)^{0.719} \quad (14)$$

2 MATERIALS AND METHODS

2.1 Air bubbles entrainment

Flow at downstream of drops contain air bubbles and it appears like white-water. Existing of air bubbles in the flow causes some error in reading of flow depth and as a result, reduction of the flow shear stress. Overall, this phenomena affects the calculation of the flow hydraulic characteristics.

To eliminate this error, Matos and Quintela (1995) try to calculate the flow energy dissipation in overfalls using conjugate water depth of hydraulic jump. They tried to reproduce the results obtained in investigation of Diez-Cascon et al (1991). This indirect or nonintrusive method has already been referred by Stephenson (1991) and Diez-Cascon et al (1991) and applied by Tozzi (1992) and Pegram et al (1999).

The present study tries to cope with this problem to reduce the error of the developing models.

2.2 Experimental apparatus and measurements

The experiments were conducted at the Hydraulic Laboratory at Shahid Chamran University (SCU), Ahwaz, Iran. Three drops were built from plexiglas. Two drops with heights of 18.5 cm and 31.6 cm

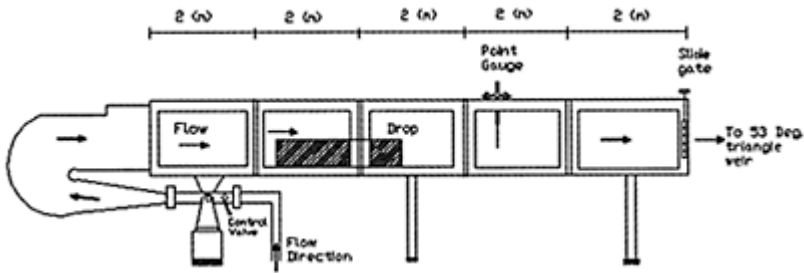


Figure 2. Longitudinal profile of the laboratory tilting flume.

that were installed in a tilting rectangular flume of 0.25 m width. Third drop with 70 cm height was installed in a rectangular flume with 0.50 m width. Fig. 2 shows the longitudinal profile of the tilting laboratory flume. The length of the first flume is 12 m and its height is 0.48 m. The length of the second flume is 8 m and its height is 1.5 m.

Water is pumped into 4.5 m constant head tank. Then, the subcritical flow was entered to the approach channel using a 10 inches pipe using a butterfly valve for adjusting the flow rate. Care was taken to minimize turbulence and swirl in the approaching channel.

Three drops were installed at 4.0 m downstream of the entrance section of the laboratory flume. At end of the laboratory flume, a vertical slide gate was installed for control of the water surface. In operation, the position of the slide gate was adjusted by a screwed rod to form a hydraulic jump in the basin and to locate the jump close to (but not drowning) the toe of the drops. The maximum discharge through the flumes was $0.06 \text{ m}^3/\text{s}$. The discharge was measured by a triangle weir with 53° installed in sidewall of a $1.5 \text{ m} \times 2 \text{ m}$ box at the downstream of flume. A total of 28 discharges were used for the three drops, providing a range of 0.02 to 0.94 for y_2/h . Water levels, drops elevations, and stream-bed elevations were measured with a manually operated point gauge equipped with a vernier, readable to within 0.1 mm accuracy. In each run test, water depth was measured at the upstream of drop, downstream before and after of hydraulic jump and above triangular weir. y_2 was measured where there were few bubbles in the tailwater, and the precision of measurement of y_2 was achieved to within a repeatable range of 3 mm for all flow conditions. All the measurements were made in the centreplain. The average flow velocity has been calculated using the measured flow rate and the depth.

3 RESULTS AND DISCUSSION

Several runs of the physical models were performed and a wide range of hydraulic variables were measured. The measured data have been analytically and statistically analysed. The following sections present these parts of the research program.

3.1 Effect of air bubbles entrainment

Total energy at the upstream of drops calculated with the following equation:

$$H_t = h + \frac{3}{2}y_c \quad (15)$$

Energy at downstream before hydraulic jump calculated with y_1 and y_2 . Where y_1 =depth before hydraulic jump and y_2 =depth after hydraulic jump. Energy at the toe of drop is expressed by:

$$H_1 = y_1 + \frac{V_1^2}{2g} = y_1 + \frac{q^2}{2gy_1^3} \quad (16)$$

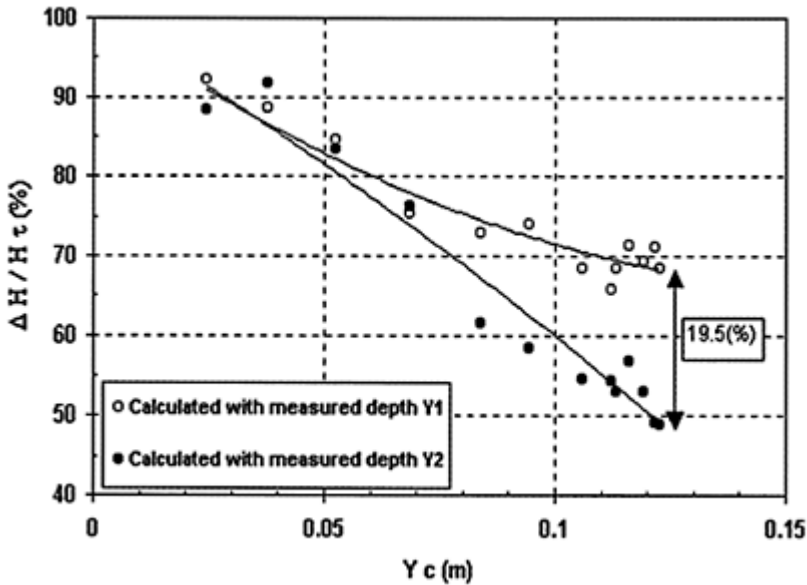


Figure 3. Effect of air bubbles on relative energy dissipation in drop with 70 cm height.

$$y_1 = \frac{1}{2}y_2 \left(\sqrt{1 + 8(y_c/y_2)^3} - 1 \right) \quad (17)$$

Relative energy dissipation is expressed by:

$$\frac{\Delta H}{H_t} = \frac{H_t - H_1}{H_t} \quad (18)$$

Relative energy dissipation between upstream of drop and downstream of drop (before hydraulic jump), are calculated using two methods as follows: a-Use of measured depth before hydraulic jump and equations 15, 16 and 18 b-Use of measured depth after hydraulic jump and equations 15, 17 and 18. To apply the second method, depth of clear water (without air bubbles) after hydraulic jump was measured.

Figure 3 illustrates the results of the energy dissipation analysis by both methods for the drop with 70cm height. As shown in Fig. 3, the relative energy loss is a function of discharge (or y_c). Increasing in discharge results the decreasing in relative energy loss and shows larger difference between calculated energy dissipation by two methods. The value of difference reaches 19.5% for the maximum discharge which denotes when the aerated-flow depth (y_1) is used to calculate the energy dissipation, it is significantly overestimated.

3.2 Comparison of different studies

To find the accuracy of this work, authors have compared findings of the present study with the others reported studies in the literature. Figure 4 has shown this comparative section results. Overall, Fig. 4 shows that the relative energy dissipation in drop structures is decreased with increasing in h/y_c .

Figure 4 illustrates very good agreement between the present study and Moore (1943), Chamani and Rajaratnam (1995) and Rand (1955). As shown in this figure, White's result is more higher than the present study results and the other studies findings. Rand results show lower energy dissipation and White results show higher energy dissipation. US Bureau of Reclamation suggested use of Eq. (2) for energy dissipation estimation for drop design. Average 11% energy dissipation for inclined jet in Chamani and Rajaratnam experiment, show that the energy dissipation at a drop is mainly due to the mixing of the jet with the pool behind the jet. It can be seen that the relative energy dissipation in this study varies from almost 8% (for $y_c/h=0.94$) to 94.3% (for $y_c/h=0.02$). Using SPSS software for regression the two best curve fitness for this study data are shown in as table 1.

In Fig. 5 the results of measured y_1 , y_2 , L_p and y_p with comparison the Rand's experiment were presented.

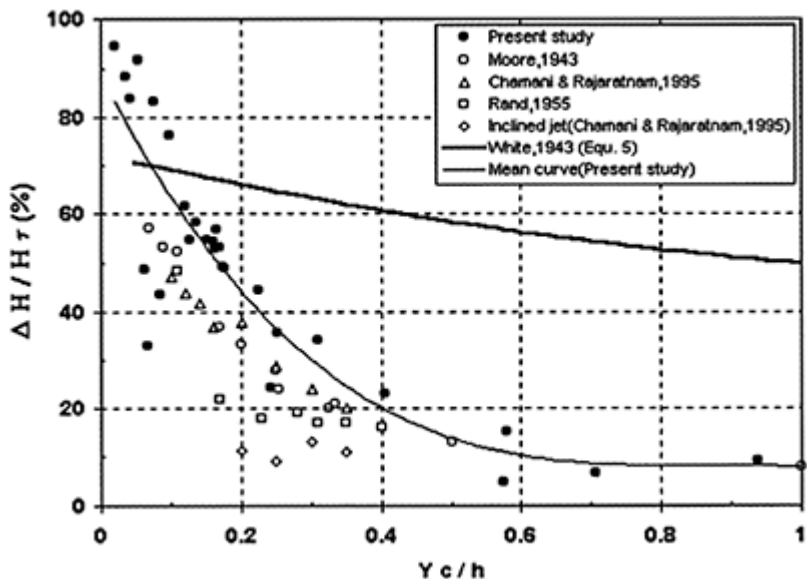


Figure 4. Comparison of different studies results.

Table 1. Results of the experimental data analysis using SPSS.

Equation number	n	Equation	r ²
19	28	$\frac{\Delta H}{H_t} = -245.15 \left(\frac{y_c}{h}\right)^3 + 554.22 \left(\frac{y_c}{h}\right)^2 - 390.92 \left(\frac{y_c}{h}\right) + 100$	0.74
20	28	$\frac{\Delta H}{H_t} = 12.521 \left(\frac{y_c}{h}\right)^{-0.6343}$	0.65

Present experiment results show that there are good fitness for y_1/h and y_2/h value with Rand experiments. But for L_p/h and y_p/h there are not fitness between present and Rand experiment. Probably high oscillated impinging jet in pool behind drop wall, reduces the accuracy of depth measurement. The regression analysis of the experimental data gave the best curve fitness for as table 2.

4 CONCLUSION

This paper presents an experimental study on the energy dissipation in three physical models that were built and installed in the hydraulic laboratory flume of Shahid Chamran University (SCU),

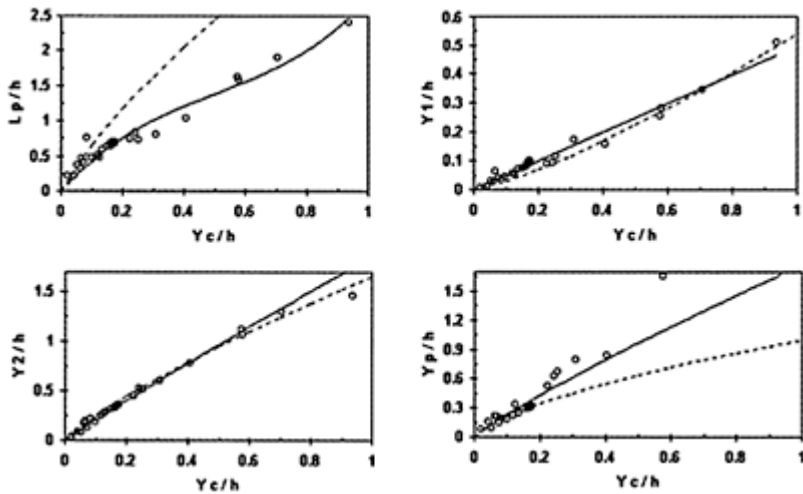


Figure 5. Relation between y_1/h , y_2/h , L_p/h and y_p/h vs. y_c/h in drop (— present experiment and -----Rand experiment).

Table 2. Results of regression analysis of the experimental data using SPSS.

Equation number	n	Equation	r^2
21	28	$\frac{L_p}{h} = 4.181 \left(\frac{Y_c}{h}\right)^3 - 6.288 \left(\frac{Y_c}{h}\right)^2 + 4.860 \left(\frac{Y_c}{h}\right)$	0.945
22	28	$\frac{y_p}{h} = 1.772 \left(\frac{Y_c}{h}\right)^{0.879}$	0.881
23	28	$\frac{y_1}{h} = 0.496 \left(\frac{Y_c}{h}\right)$	0.976
24	28	$\frac{y_2}{h} = 1.857 \left(\frac{Y_c}{h}\right)^{0.952}$	0.970

Iran. Several experiments were undertaken and a large amount of data was collected to handle statistical analysis. Relative energy dissipation on drops calculated by using both y_1 and y_2 (sequent depth). In section where y_1 was measured, there was air bubble in the flow, while in section that y_2 was measured there was little air entrainment. Results showed that:

- Application of measured depth y_1 instead of sequent depth (y_2), results more energy dissipation (Fig. 3). In fact air entrainment in flow (reduction in viscosity), causes to reduce shear stress and finally reduces the energy dissipation property. Also air entrainment causes to increase flow bulk and so flow depth. This problem causes error in calculating energy loss.

- Increasing in discharge, causes reduction in energy dissipation (Fig. 3, 4)
- There are good fitness among present study, Moore, Chamani and Rajaratnam studies.
- This work has also indicated that the loss at drop is mainly due to the mixing of the jet with the pool behind the jet.
- Comparison between this study's results and results of Moore, Rand, White, Rajaratnam and Chamani, showed that White's model over estimates the energy dissipation in drops and Rand's model under estimates the energy dissipation in drops. The others can predict the energy dissipation in drops as same as the proposed statistical model.

REFERENCES

- Chanson, H. 1994. "Comparison of energy dissipation between nappe and skimming flow regims on stepped chutes", *Journal of hydraulic research*. 32 (2): 213–218.
- Design of small canal structures. 1978. US Department of the interior, Bureau of Reclamation, USBR
- Diez-cascon, J., Blanco, I.L., Reviua, J., and Garcia, R. 1991. "Studies on the hydraulic be haviour spillways". *Int. water power and dam construction*. pp 22–26.
- Gill, M.A. 1979. Hydraulic of rectangular vertical drop. *Journal of Hydraulic Research*, Vol 17, No. 4, pp 289–302
- Hager, W.H. 1983. "Hydraulic of plane free overfall." *Journal of Hydraulic Engineering*, Vol 109, No.12, pp 1683–1697.
- Matos, J. and Quintela, A. 1994. "Jet flow on stepped spillways". *Discussion, Journal of hydraulic engineering*. 120 (2): 443–444
- Moore, W.L. 1943. "Energy loss at the base of free overfall". *Transactions, ASCE*, Vol 108, pp 1343–1360.
- Pegram, G.G.S and Officer, A.K., and Mottram, S.R. 1999. "Hydraulic of skimming flow on modeled stepped spillways". *Journal of hydraulic engineering*. 125 (5): 500–509.
- Rajaratnam, N., Chamani, M.R. 1995. "Energy loss at drops". *Journal of Hydraulic Research*, Vol.7, No.2, pp 373–384.
- Rand, W. 1955. "Flow geometry at straight drop spillway". *Proceedings, ASCE*, Vol.81, Paper 791, pp 1–13.
- Tozzi, M.J. 1992. Flow characterization/behavior on stepped spillways. PhD thesis, University of sao pauloBrazil (in portuguese).
- White, M.P. 1943. Discussion of Moore., *Transactions, ASCE*, Vol.108, pp 1361–1364.

Dam safety: the use of guidance documents for the training of Inspecting Engineers

R.Freer

Independent Consultant, Alleyn Crescent, London, UK

Hydraulics of Dams and River Structures—Yazdandoost & Attari (eds)

© 2004 Taylor & Francis Group, London, ISBN 90 5809 632 7

ABSTRACT: The best training for those engineers who wish to become qualified to undertake the inspection of dams would include the personal experience of having designed and built dams. But in Western Europe fewer dams are being built and therefore fewer engineers who wish to become Inspecting Engineers in the future will have had the opportunity to design and build a dam. To help compensate for this lack of personal experience dam engineers in Great Britain have prepared a series of documents which are intended to provide practical guidance for future Inspecting Engineers. These documents summarise the personal experiences of the present generation of Inspecting Engineers; they bring together and record the accumulated knowledge of those engineers who are at present responsible for dam safety and are intended to supplement the personal experience of new Inspecting Engineers.

The documents are non-prescriptive and the decision on the safety of the dam remains the personal judgement of the Inspecting Engineer. The documents were prepared for the use of Inspecting Engineers in Britain but may be of interest and value to engineers in other countries.

1 INTRODUCTION

Dam engineering in Western Europe is now at the mature stage at which the work of engineers will be more concerned with the operation and maintenance of existing dams than with the design and construction of new dams.

Dams start to age and deteriorate from the date of their completion and an essential part of their continuing maintenance is to establish a regular system of inspection which will provide the owner with the necessary assurance that the structures are being maintained in safe working order and that any potential problems are identified and solved in time.

The inspection system used in Great Britain relies on the exercise of the individual judgement of the Inspecting Engineer appointed to undertake the inspection. And the Inspecting Engineer's judgement depends, among other factors, on the breadth and depth of his personal experience in the design and construction of dams.

The opportunities to obtain this first hand experience are becoming fewer because fewer new dams are being built, while at the same time the need for inspection and (maintenance becomes more important as the existing dams become older and require more attention.)

Therefore Inspecting Engineers are increasingly required to understand the performance of a steadily ageing stock of dams without having had the personal experience of having designed and built one, and we need to address the problem of how a new Inspecting Engineer can build up the relevant knowledge and understanding of the behaviour of dams without this experience.

It is to help solve this problem that a number of practical guidance documents have been prepared in the UK in recent years to assist Inspecting Engineers in their work. These guidance documents are intended to supplement the personal experience of the Inspecting Engineers and they are essentially directed to the practical matters which engineers are concerned with in dealing with the regular surveillance, inspection and maintenance of dams.

It is important that the documents are recognised as being non prescriptive and are only advisory. They are intended to provide guidance which will supplement the Inspecting Engineer's experience and training, and will assist him in making his judgement.

The purpose of this paper is to explain the content of these documents and their use as part of the routine work of the Inspecting Engineer. These documents are essentially for practical guidance. For instance, the theoretical concepts of safety and risk assessment have attracted substantial academic interest in recent years and have generated serious analytical study in a number of countries, and in one of these guidance documents this theory has been applied and translated into a practical and useful guide.

2 RESERVOIR SAFETY PRACTICE IN GREAT BRITAIN

In most countries the development of the national policy for dam safety and the application of the inspection legislation reflects the political framework and the national concepts of insurance and structural responsibility adopted in that country. The information the Inspecting Engineer requires from these guidance documents will depend to some extent on the local inspection legislation.

Reservoir safety practice in Britain relies on legislation which puts the responsibility on the dam owner to employ an independent Inspecting Engineer to inspect the dam. The Inspecting Engineer has the freedom to exercise his professional judgement and to make independent decisions. This practice is intended to ensure that the national stock of dams is properly and adequately inspected in the most cost effective manner, and the Inspecting Engineer can make the best use of the dam owner's money and of his own time to concentrate the work of inspection on those dams which require the most attention.

The safety legislation applies to dams with a stored reservoir capacity in excess of 25,000 cu m and there are approximately 2500 such dams in Britain. The regular inspections are carried out by about 50 Inspecting Engineers supported by about 250 engineers in the junior grade of Supervising Engineer. Many of the Supervising Engineers are training to become Inspecting Engineers.

The relevant legislation originated with the *Reservoirs Act* of 1930 and has been updated since then, most recently in 1975. One of the requirements of the *Reservoirs Act* is that the dam owner shall appoint an engineer from a register of suitably qualified Inspecting Engineers.

Appointments to the register are made by the government but the important process of examining and recommending the appointment of Inspecting Engineers to the register is organised and managed by the Institution of Civil Engineers in London. The examination is based on an interview to assess the candidate's knowledge and experience and is conducted by a panel drawn from senior civil engineers, dam owners, contractors and staff of the enforcement authorities.

3 GUIDANCE DOCUMENTS

3.1 *Main documents*

The main guidance documents specifically produced for use by dam designers and Inspecting Engineers are:

- *Floods and Reservoir Safety* (Beaver et al. 1996)
- *Guide to the Reservoirs Act 1975* (Gosden et al. 2000)
- *Guide to seismic risk to dams in the UK* (Charles et al. 1991)
- *Guide to the Safety of Embankment Dams in the UK* (Johnston et al. 1999)
- *Engineering Guide to the Safety of Concrete and Masonry Dam Structures in the UK* (Kennard et al. 1996)
- *Valves, pipework and associated equipment in dams—guide to condition assessment* (Reader et al. 1997)
- *Risk management for UK Reservoirs* (Hughes et al. 2000).

Although these documents were prepared mainly for use in the UK much of their content may apply in other countries. In preparing these guides the objective has been to include the opinions and experiences of those engineers presently responsible for dam safety. The information has been collected, assessed and preserved as a general stock of reasoned opinion available as an aid for future Inspecting Engineers. It is a record of information more comprehensive than the experience of any single individual.

To illustrate the range of information and advice available in these documents some of the contents of the two guidance documents for embankment and for concrete and masonry dams (Johnston et al. 1999 and Kennard et al. 1996) are described in the following paragraphs.

The majority of British dams are embankment dams because the construction materials are widely available. Concrete dams are a minority and most of these are situated in the highland areas of Scotland and Wales.

3.2 Historical background

Part of the Inspecting Engineer's work is to give advice to the owner on a programme of planned surveillance to prevent or rectify any deterioration. To do this the Inspecting Engineer will need to know how the dam was designed and built, but it is an unfortunate fact that for many older dams the design drawings and construction records are no longer available. In these circumstances the Inspecting Engineer has no direct information about the construction of the dam to help him understand its subsequent behaviour. The next best alternative is for the Inspecting Engineer to study the general practice of dam construction at the time the dam was built and to make an intelligent assessment of how the dam may have been built.

Both these two guidance documents start with the historical background to the development and construction of dams and include a description of the equipment and materials used in their construction. These sections are intended to help understand the older practices, to identify the materials used in construction and to assist in the identification of probable details where there is no recorded information available. A knowledge and understanding of the design assumptions at the time of the construction of the dam, and also details of the specifications used, can provide insights into the cause of later defects.

Some of the embankment dams were built more than two hundred years ago at the end of the 18th century to provide reservoirs to supply water to the canals being built across the country. Some ornamental reservoirs for country estates were built even earlier. There was a great expansion of dam building in the 19th century to supply clean water to the factories and to the increasing populations in the industrial cities.

In contrast most concrete and masonry dams in the UK were built later, mainly in the hundred years span between about 1875 and 1975. Fewer conventional concrete dams are likely to be built in the future because of the changing economic conditions. Concrete dams built in the conventional manner are labour intensive and the higher labour costs in many Western countries today may make their construction unlikely except at sites which are particularly favourable. The alternative technique of building concrete dams using roller compacted concrete (RCC) is, in many instances, cheaper and quicker than using the conventional techniques.

3.3 Dam failures

Dams are usually categorised as high-hazard, low risk structures. That is, the consequences of a dam failure may be serious but the probability of a failure is remote. The consequences of a dam failure can be predicted by the use of dam break analysis, and in that respect the consequences of a failure are more predictable than some other accidents such as an accident at a chemical works or other industrial plant.

Dam failures in many countries are sufficiently uncommon for many of the public to be unaware of the potential hazard, but the engineer can learn from an analysis of these failures. The main causes of failure of an embankment dam are:

- Instability of the embankment or its foundation as a result of internal erosion or leakage of the reservoir water.

- Effect of external erosion of the embankment caused either by overtopping by the reservoir water or by water from some other source acting on the surface of the embankment.
- Instability of the embankment or its foundations by shear failure as a result of inadequate shear strength.

In certain locations there may be other sources of potential failure such as seismic activity or mining subsidence.

In contrast, concrete dams are by their nature inherently safe because the rock sites where they are built are usually non-erodible, and so are the materials of which they are made. Failures of concrete and masonry dams are usually attributed to foundation and abutment rock failures, but sometimes, as at the Vega de Tera dam in Spain in 1959, the failure can be due to excessive internal tension in the concrete.

3.4 *Construction materials*

Understanding the performance of materials and the construction methods is important in assessing the safety criteria for the dam. For instance, in an embankment dam the impermeability of the central clay wall is important and in understanding the performance of the older dams it may be helpful for an Inspecting Engineer to have access to the specifications used for the construction of dams in the 19th century and information about the sources of the materials. The guidance documents give examples of these earlier specifications and a comparison with modern specifications.

When assessing the potential safety of a concrete dam the foundation is important and should be considered as an integral part of the dam. The performance of the rock as a dam foundation is entirely dependent on the condition of the joints in the rock. These joints determine both the overall permeability and strength of the rock mass. Grouting the joints may help to fill them and to decrease the permeability, but the results may be unpredictable.

The source of the materials in a concrete dam is also relevant because reactive or harmful materials in aggregates and cement were less well recognised in the past and the assessment of these materials may be more difficult unless the original quarries are still available for inspection and there is information available about the cement used. Modern petrographic and chemical analysis can identify reactive materials in aggregates, or aggregates susceptible to drying shrinkage, and can identify the alkali content of cement which today is kept below 1% to meet the guidelines on alkali-silica reaction.

3.5 *Flood assessment*

The original design of the dam would have depended on the understanding at the time of the loads acting on the dam. The upstream water level and the uplift pressure under the dam give rise to two of the most significant loads, and these loads may have to be re-considered in the light of modern information about flood levels and their frequency.

Flood assessment from historical and present records has been studied thoroughly in Britain and the results published over the past 25 years. The third edition of the guidance document entitled *Floods and Reservoir Safety* was published in 1996.

The estimation of floods and the implications for dam safety refer mainly to catchment areas in Great Britain but the conclusions may be applicable to other similar areas.

In preparing this document the authors met members of other European national committees of ICOLD in order to exchange ideas on flood-protection standards. Although there is no common European Union standard to cover reservoir safety, international practice on reservoir floods is contained in the ICOLD bulletin 82, Selection of Design Flood.

3.6 Construction techniques

The working and record drawings for many of the older dams are no longer available and as the construction techniques have varied over the years it is useful for the Inspecting Engineer to know what construction methods were used at the time when the dam was built. Anomalies in the performance of a dam may be a consequence of the method of construction and this may not be visually apparent.

The guidance documents contain a summary of the various construction techniques used in the past to try to help the Inspecting Engineer to understand any such anomalies, but particularly with the older embankment dams the authors of the documents admit that a large proportion of the dams are of unknown construction.

The inspection of a dam should start with an understanding of how the river was diverted to enable the dam to be built. The method used can have a permanent effect on the behaviour of the dam.

For the construction of embankment dams or concrete arch dams the river is often diverted through tunnels on either side of the proposed dam site, but with concrete gravity dams the river may be diverted over a concrete monolith the foundation for which had already been placed. The final closure requires a plug of concrete to seal the diversion channel. In these conditions it is difficult to ensure a water tight seal and this may become a potential source of seepage.

The foundation of a dam is an important part of the construction but records are not usually kept of such matters as the depth of soft material removed to reach solid rock, or the location of any cut off trenches, fissures or soft pockets. And even where the records are available they are unlikely to be three dimensional and may give a misleading picture of the contact surface.

For embankment dams it was usual practice to excavate the cut-off trench to a stratum of material of low permeability, and the core wall was built of a very wet and remoulded clay fill known as puddle clay. Many of these dams were built before the theories of soil mechanics were understood and before heavy earth moving plant and rapid construction techniques were available.

The construction techniques of the time produced a clay core with an undrained shear strength as low as about 10 kN/sq.m placed in layers typically 0.15 m to 0.2 m thick. Some failures of the older dams were attributed to the fact that the clay core was too thin. This was remedied in the more modern dams and made necessary by the fact that the core needed to be sufficiently wide to accommodate the passage of modern vibrating rollers. On the upstream side the embankment slope was typically 1 vertical to 3 horizontal, and the downstream slope was 1 vertical to 2.5 horizontal.

In the earliest designs the outlet pipe was laid on the original ground surface beneath the embankment and controlled by a single valve at the downstream end. When the hazards of placing a pipe containing water under reservoir pressure beneath the dam were better understood it became more usual to place the valve controls at the upstream end.

With concrete dams the techniques of placing the large quantities of concrete required for the mass of the dam have changed over the years and to understand the performance of the older dams it is helpful to know what types of concrete were used and how the concrete was placed. Accurate specification of materials, mixing by weight and quality control of the process are comparatively modern techniques. Concrete mixes used in the past often contained large sized aggregates and coarsely ground cements, and the water cement ratio was adjusted on site to make the concrete easier to place.

The volume of concrete required was reduced for economy by placing large stones as displacers, or “plums”, in the concrete matrix. As a consequence the concrete in earlier dams was not as well compacted as it is today and there are likely to be more potential seepage paths through the concrete and particularly at lift joints.

3.7 Surveillance, monitoring and investigation

Surveillance is the regular visual observation of the structure for the purpose of ensuring that the dam and any control equipment is operating correctly. Surveillance is usually carried out by the same person at regular intervals so that any changes can be detected at an early stage.

On the other hand new peculiarities may be sometimes be spotted more quickly by a newcomer who is not familiar with the site.

Monitoring is concerned with the regular measurement and recording of a particular characteristic for the purpose of providing information which can be acted upon. Surveillance complements monitoring by observing the features that are not instrumented and by checking the operation of the instruments.

Instrumentation is most useful at three stages of the life of the dam, i.e. during construction, during first impounding and for long term monitoring.

Instruments designed and installed for the construction stage may not be suitable for long term monitoring.

The most usual measurements are:

- Seepage flow by using V notch weirs,
- Crest movement either by using pendulums or by surveying the movement of marker points,
- Chemical monitoring.

The best use of instrumentation is to ensure that the results are recorded, plotted, interpreted and acted upon without delay. Unless this happens the instruments are of little value.

4 CONCLUSIONS

A number of guidance documents have been prepared to assist Inspecting Engineers in undertaking the inspection of dams. These documents are intended to supplement the personal experience of new Inspecting Engineers, and those training to be Inspecting Engineers, by bringing together and recording the accumulated knowledge of the Inspecting Engineers who are at present responsible for dam safety.

The documents are a contribution towards maintaining a cost effective dam inspection system for the inspection of the national stock of dams.

Throughout the documents the authors emphasise the importance of the application of the Inspecting Engineer's personal judgement in making observations, and in interpreting and understanding the observations he has made and the information he has collected. The documents should not be used as checklists.

For instance the Inspecting Engineer is encouraged to understand the design and construction techniques at the time the dam was built, and he is also encouraged not only to examine the structures in details but to stand back and consider the setting of the dam as a whole entity in its surroundings.

All these techniques will help to give the Inspecting Engineer a better understanding of the performance of the dam and will enable him to give better advice to the dam owner to ensure the continued stability and safe operation of his dam.

REFERENCES

- Beaver, J.L. & Adamson, P.T. 1996. *Floods and Reservoir Safety*. Institution of Civil Engineers, 1 Great George Street, London SW1P 3AA, UK.
- Gosden, J.D., Brown, A.J. & Hockey, A.F. 2000. *Guide to the Reservoirs Act 1975*. Institution of Civil Engineers, 1 Great George Street, London SW1P 3AA, UK.
- Charles, J.A., Abbis, C.P., Gosschalk, E.M. & Hinks, J.L. 1991. *An Engineering Guide to Seismic Risk to Dams in the United Kingdom*. Building Research Establishment, Garston, Watford WD2 7JR, UK.
- Johnston, T.A., Millmore, J. P, Charles, J.A. & Tedd, P. 1999. *An Engineering Guide to the Safety of Embankment Dams in the United Kingdom, Report BR 363*. Building Research Establishment, Garston, Watford WD2 7JR, UK.
- Kennard, M. F, Owens, C.L. & Reader, R.A. 1996. *Engineering Guide to the Safety of Concrete and Masonry Dam Structures in the UK, Report No 148*. Construction Industry Research and Information Association, 6 Storey's Gate, London SW1P 3AU, UK.
- Reader, R.A., Kennard, M.F. & Hay, J. 1997. *Valves, pipework and associated equipment in dams-guide to condition assessment. Report No 170*. Construction Industry Research and Information Association, 6 Storey's Gate, London SW1P 3AU, UK.

5.

Reservoir sedimentation

Impacts of Sanmenxia Dam and management strategies

B.S.Wu & Z.Y.Wang

Dept. of Hydmulic Engineering, Tsinghua University, Beijing, China

Hydraulics of Dams and River Structures—Yazdandoost & Attari (eds)

© 2004 Taylor & Francis Group, London, ISBN 90 5809 632 7

ABSTRACT: Sanmenxia Dam is located in the middle reach of the Yellow River, which carries the highest sediment load of all the world's rivers. Due to the alarming rate of loss of reservoir storage capacity and the unacceptable negative impact induced by the rapid upstream extension of sediment deposited in the river's backwater region, the dam has been reconstructed to provide high sediment releasing capacity, and the reservoir operation has been substantially changed to achieve a balance between sediment inflow and outflow, and eventually to minimize the adverse effect of reservoir sedimentation. Complex sedimentation processes in response to the dam reconstruction and operation have been observed. Valuable experiences and lessons can be learned from the case study on sedimentation management.

1 INTRODUCTION

Sanmenxia Dam is located in the lower part of the middle reach of the Yellow River in China. It is a large-scale multipurpose hydro-project first constructed on the main stem of the Yellow River, as a main part of the Comprehensive Yellow River Basin Plan approved by the central government in the 1950s. The construction of the dam was initiated in 1957 and the impoundment of water commenced in September 1960. Due to the fact that the reservoir storage capacity was decreasing at an alarming rate and the unacceptable negative impact of rapid upstream extension of backwater sediment deposition, the dam had to be reconstructed to provide high sediment releasing-capacity of outlet structures and reservoir operation has been substantially changed to achieve a balance between sediment inflow and outflow, and eventually to minimize the adverse effect of reservoir sedimentation. This project not only demonstrates the perils of giving inadequate consideration to sediment management in the planning and design of a reservoir, but it also shows that a sediment balance may be achieved across an impounded reach even in a large reservoir built on a river with an extremely high sediment load.

This paper reports the complex river sedimentation responding to the management strategies applied. The unique engineering experience and lessons learned from the case study are particularly useful for sedimentation management and sustainable use of large dams built on heavy sedimentladen rivers.

2 THE SANMENXIA DAM

The Yellow River, with a drainage area of 795,000 km² and alength of 5,464 km, is the second largest river in China, as shown in Fig. 1. The river basin is mostly arid and semi-arid, with a long-term average annual runoff depth of 77 mm and a total annual runoff volume of 58 billion m³. The water resource per capita in the basin is 593 m³, only one quarter of the average in China. In the central part of the basin, the river cuts through a vast loess plateau with an area of 580,000 km², of which 439,000 km² suffers from severe soil erosion. The annual sediment yield of the gullied loess plateau area amounts to more than 10,000 tons/km². The long-term annual sediment load at Sanmenxia station is 1.6 billion tons, ranking first of all the world's rivers. The average sediment concentration is 35 kg/m³ and hyperconcentrated floods with sediment concentration over 100 kg/m³ occur quite



Figure 1. Sketch map showing the Yellow River basin and the location of Sanmenxia Dam.

often; a sediment concentration of 911 kg/m³ was measured on September 7, 1977. The majority of the sediment load consists of silt with a median diameter of about 0.03 mm.

As the river flow delivers a huge amount of sediment through the course of the lower reaches, which has a relatively small slope and a wide cross section, about 25% of the sediment load is deposited on the alluvial floodplain and another 50% is deposited on the delta prior to being discharged to the Bohai Sea. This has caused the riverbed of the lower Yellow River to consecutively rise; it is now more than 10m higher than the

surrounding land in some places, known as a “perched river”. This endangers the safety of communities and farmlands on both sides along the lower reaches of the river, bringing about serious problems for flood control and river management.

The Yellow River, recognized as the cradle of Chinese civilization, has been associated and famine throughout the history of China. In time, a perched river was formed that frequently breached its levees. From BC 602 to 1949 the river burst its dykes 1,593 times, flooding vast areas in those 543 years and claiming millions of human lives. The river shifted its major course (600–700 km long) by avulsion 26 times with the apex around Zhengzhou, causing devastating calamities. The course left numerous old channels, among them 8 major shifts (5 natural and 3 man-made) with river mouths alternating between the Bohai Sea and the Yellow Sea.

Chinese people have suffered from disastrous flooding of the Yellow River for centuries and have long dreamed of a dam to control the floods. Early in 1935, some river engineers and experts proposed the construction of Sanmenxia Dam on the middle reach of the Yellow River to control flood flows entering the downstream reaches. A landmark report entitled “Comprehensive River Basin Planning Report,” which officially proposed the construction of Sanmenxia Dam, was submitted to the National People’s Congress in 1955 and was immediately approved.

The Sanmenxia Dam was constructed within the period of 1957–1960. As a multipurpose project for flood control, hydropower, irrigation, navigation, and ice jam control, it is the first dam ever built on the Yellow River in China (see Fig. 1). The drainage area above the dam amounts to $688,400 \text{ km}^2$, which is 92% of the total drainage area of the Yellow River. It controls 89% of the runoff and 98% of the sediment coming into the lower Yellow River. The maximum historical floods records at the dam site were $22,000 \text{ m}^3/\text{s}$ in 1933 and $36,000 \text{ m}^3/\text{s}$ in 1843.

The reservoir consists of a dam, outlet structures and a power plant. In the original design, the maximum water level in the reservoir was set at an elevation of 360 m, with a total storage capacity of $64.7 \times 10^9 \text{ m}^3$, and an installed capacity of 116 MW. Under such conditions, $3,500 \text{ km}^2$ of the floodplains would be inundated, requiring the relocation of 870,000 people. To reduce this impact, the dam was built at an elevation of 353 m with a maximum dam height of 106 m and a maximum pool level of 340 m. The reservoir area extends upstream a distance of 246 km to Longmen. The Yellow River flows south from Longmen to Tongguan, then makes a 90° turn and goes east. As shown in Fig. 2, the dam site is located in a gorge section 113.5 km downstream of Tongguan, which is situated immediately downstream of the confluence of the Yellow and Wei Rivers. The river is constricted from a width of more than 10 km to less than 1 km at Tongguan, forming a naturally constricted river reach which acts as a hydraulic control section that influences the river’s stage, flow velocity, and thus the sediment transport capacity in the reaches of both the Yellow and Wei Rivers upstream of Tongguan. During floods, the stage at Tongguan rises rapidly and creates backwater conditions extending tens of kilometers upstream, thereby limiting the sediment transport capacity and promoting sediment deposition upstream of the constricted Tongguan reach. Because the bed elevation and stage at Tongguan exert hydraulic control on both the Yellow and Wei Rivers upstream, the control of sediment accumulation at Tongguan is the key to limiting sediment deposition and controlling backwater further upstream.

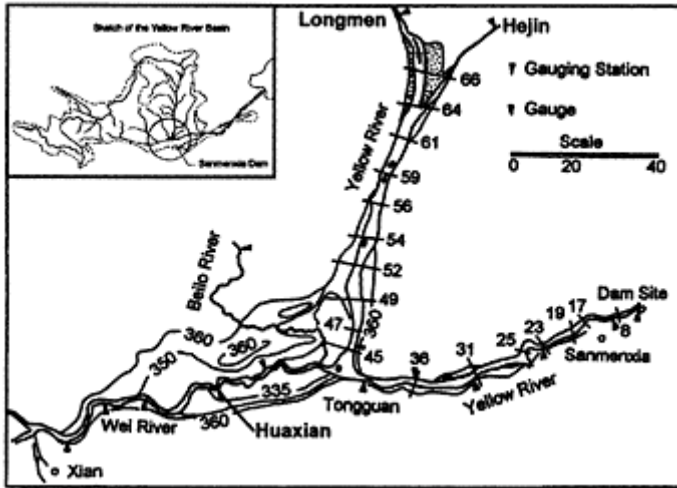


Figure 2. Plan view of the Sanmenxia Reservoir (after Wu, 1997).

3 RECONSTRUCTION OF SANMENXIA DAM

Following completion of the dam, the reservoir began to function as a storage basin from September 1960 to March 1962, when the maximum pool level reached 332.6 m. Severe sedimentation problems became evident immediately after impoundment. During the first 18 months after the dam's closure, 93 percent of the incoming sediment was trapped in the reservoir, representing a release efficiency of only 7 percent. The reservoir lost 17% of its capacity below an elevation of 335m and 26% of its capacity below an elevation of 330 m due to sedimentation.

To mitigate the sedimentation, the operation scheme of the dam was changed to detain only flood water in flood seasons. The primary function of Sanmenxia Dam was originally designed for flood control. For this purpose a capacity of 10 billion m^3 was still reserved to cope with floods that occur only once in a thousand years, such as that occurred in 1933. However, the flood-releasing capacity of the outlet structures was limited. Though the reservoir was operated at a low level during flood seasons with all the outlet structures fully opened, the reservoir stage was still high and serious sedimentation in the reservoir due to the detention of large amounts of flood water was still inevitable. A net accretion amounted to $2.04 \times 10^9 \text{ m}^3$ from April 1962 to May 1966. During this period, 16 floods lasting 89 days in the summer of 1964 caused $0.93 \times 10^9 \text{ m}^3$ of sediment to be deposited in the reservoir area (He *et al.*, 1987).

During the impounding period from September 1960 to March 1962, the "elevation of Tongguan," which indicates riverbed variations and is defined as the stage corresponding to a discharge of $1,000 \text{ m}^3/\text{s}$ at Tongguan station, was raised 4.5 m (Long & Chien, 1986; Long, 1996), finally reaching 327.2 m in March 1962. Backwater sediment deposition extended over Chishui in the lower Wei River, about 187 km upstream of the dam, and

extended 152 km in the Yellow River. After the mode of reservoir operation was changed, the backwater sediment deposition was still rapidly extending upstream, raising the bed elevation and flood levels in the Yellow River as far as 260 km upstream of the dam. This threatened the industrial and agricultural bases, and more importantly the capital city of Xi'an of Shanxi province, in the lower reaches of the Wei River. In addition,

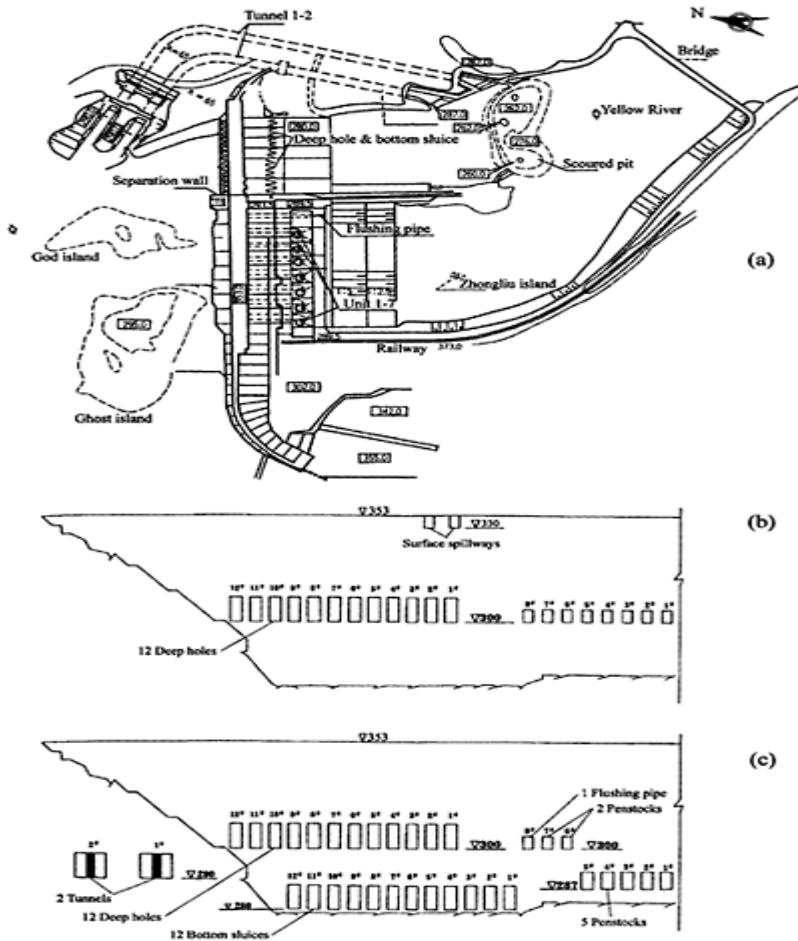


Figure 3. General layout and outlet structures of Sanmenxia Dam: (a) Plan view; (b) Front view of original design; (c) Front view after reconstruction.

it potentially required the relocation of an additional one million people. There was much pressure to improve the situation because of the dense population and the scarcity of farmland in China. In order to alleviate the serious reservoir sedimentation problem and to achieve a balance between sediment inflow and outflow, a special meeting was held in Xi'an City in December 1964 to find a solution to the sedimentation problem in the reservoir. The late Premier Zhou Enlai presided over the meeting, showing the high demand for a resolution to this problem. A policy was established to "ensure the safety of Xi'an City in the upstream as well as that of the lower Yellow River" and a decision was made on the reconstruction of outlet structures to increase the discharge capacity.

The reconstruction work was carried out in two stages. In the first stage, two tunnels at an elevation of 290 m were added on the left bank and four penstocks were remolded into outlets for the purpose of sluicing sediment, as shown in Fig. 3. After work on the first stage was in August

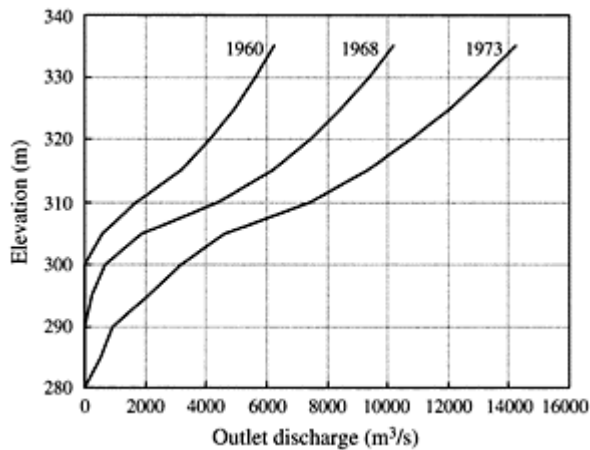


Figure 4. Increased discharging capacity of the outlets of Sanmenxia Dam.

1968, the discharge capacity had been increased from 3,080 m³/s to 6,100 m³/s at a water level of 315m. The reconstructed outlets were put into operation one after another and played a definite role in reducing sediment deposition in the reservoir area below Tongguan. However, the sills of the outlet structures were too high and the capability of the reservoir to release floodwater was inadequate. The ratio of outflow-inflow sediment reached 80%, the amount of backwater deposition increased accordingly and the bed elevation at Tongguan continued to rise.

The work of the second stage commenced in December 1970. In this stage, 8 bottom outlets at an elevation of 280 m previously used for diversions were reopened to sluice sediment at the lower elevation and to generate stronger headward erosion. In order to suit power generation at a low altitude by the river's current during the flood seasons, the intake of penstocks no. 1-5 were lowered from an elevation of 300 m to 287 m, and 5

generation units with a total installed capacity of 250 MW were installed. The first generating unit started to operate at the end of 1973, and the rest were put into operation by the end of 1978. After the second stage of reconstruction, the releasing capacity of all the outlets increased to 10,000 m³/s at an elevation of 315 m (Fig. 4). With this capacity, no significant backwater could accumulate immediately behind the dam in medium or minor flood conditions, and the outflow and inflow ratio of sediment had reached 105%. In the period from the beginning of summer in 1970 to the end of the flood season in 1973, about 4.1 million m³ of sediment was scoured away from the dam to Tongguan, and a part of the reservoir capacity was restored. Correspondingly the bed elevation at Tongguan dropped by 2 m.

After these two stages of reconstruction, the dam can discharge sediment-laden water and causes no significant detention of large amounts of flood water. However, due to surface abrasion and cavitation, the bottom sluices were severely damaged, and therefore they underwent repairs from 1984–1988. As a result the total discharge capacity of bottom sluice openings no. 1 to 8 was reduced by about 471 m³/s due to compression. To compensate for the reduction resulting from bottom sluice repairs, two more bottom sluices, no. 9 and 10, were opened in 1990. In an attempt to make the most of the dam by fully utilizing the potential for hydropower generation in the nonflood season, penstocks no. 6 and 7 were converted back to power generation in 1994 and 1997, respectively. Considering the effectiveness of sediment flushing by discharge at low levels, the last two bottom sluices, no. 11 and 12, were also opened in 1999 and 2000, respectively. To date, there are 27 outlets in Sanmenxia Dam for discharging flood flows, as summarized in Table 1.

4 MANAGEMENT OF RESERVOIR SEDIMENTATION

Sedimentation in the reservoir depends on the incoming water and sediment, the discharge capacity, and the operational mode. Reconstruction of outlet structures has significantly increased the discharge capacity, providing the dam with the necessary facility for avoiding significant detention of flood water which is important for maintaining sediment balance across the impounded reach in the reservoir. On top of this, the dam must be properly operated to maintain the reservoir level in order to increase the benefit of the project and to maintain sediment balance. For this purpose,

Table 1. Outlet structures in Sanmenxia Dam.

Outlet	Dimensions	Total number	Serial number	Invert elevation (m)	Discharge capacity at 335 m (m ³ /s)	Year of initial operation
Deep holes	w×d=3×8m	12	1–12	300	503/each	1960
Bottom sluices	w×d=3×8m	3	1–3	280	497/each	1970
		5	4–8	280		1971
		2	9–10	280		1990

		2	11–12	280		1 999 and 2000
Tunnels	Diameter=11 m	2	1–2	290	1410	1967 and 1968
Flushing pipe	Diameter=7.5m	1	8	300	290	1966
Penstocks*		2	6–7	300	230/each	1 994 and 1997
		5	1–5	287	210/each	1973–1978

* Penstocks no. 5–8 were converted to flushing pipes for discharging floodwater in 1966. Penstock no. 5 was converted back to power generation in 1978. Penstocks no. 6–7 were converted back to power generation in 1994 and 1997, respectively.

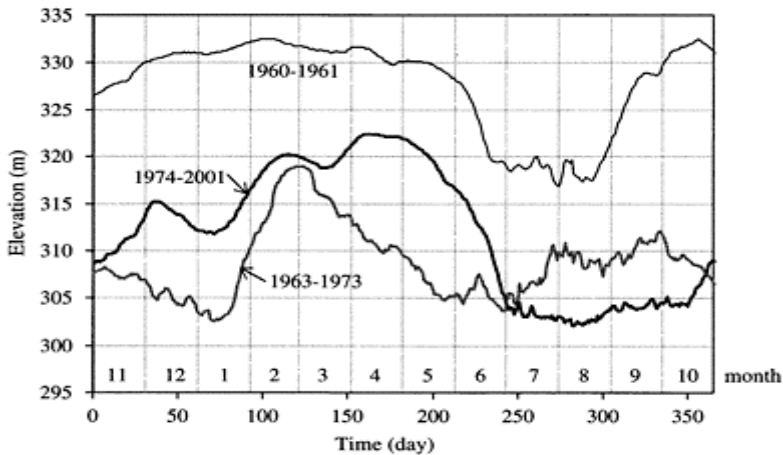


Figure 5. Variation of average pool level of Sanmenxia Reservoir in different time periods.

the Sanmenxia Reservoir has adopted three different modes of operation. The average pool levels corresponding to each operation mode are shown in Fig. 5.

- (1) Storage. The mode was employed during the initial period of reservoir impoundment, from September 1960 to March 1962, when the reservoir was operated at high storage level throughout the whole year, according to the original project design.
- (2) Flood detention. The mode was applied from March 1962 to October 1973, during which the reservoir was used for flood detention and sediment sluicing, water being released without restrictions. The reservoir was operated at a low storage level throughout the year, detaining floods only during flood seasons and sluicing sediment with the largest possible discharges.

(3) Controlled release. The mode has been used ever since November 1974, to store relatively clear water in non-flood seasons (November–June) and dispose muddy water in flood seasons (July–October). In this period, the reservoir has been operated at a high water level in non-flood seasons, and at a low storage level during flood seasons, and all the outlets were to be opened in times of flood peaks to sluice the sediment as much as possible.

Sedimentation in the reservoir is different corresponding to different operational modes and the outlet discharge capacities. Table 2 presents a summary of the amount of sediment deposited in

Table 2. Summary of sedimentation in different operation periods.

Time period	Mode of operation	Maximum discharge at 315m(m ³ /s)	Average annual runoff runoff (10 ⁹ m ³)	Average annual sediment sediment (10 ⁹ tons)	Mean annual deposition (10 ⁶ m ³)		
					Non-flood season (Nov.–June)	Flood season (July–Oct.)	Year
9/1960–10/1964	Storage	3080	46.2	1.34	70.11	550.27	620.38
11/1964–10/1973	Flood detention	6100	38.2	1.44	–63.61	–38.90	–102.51
11/1973–10/2001	Controlled release	10,000	31.6	0.86	129.02	–116.45	12.57

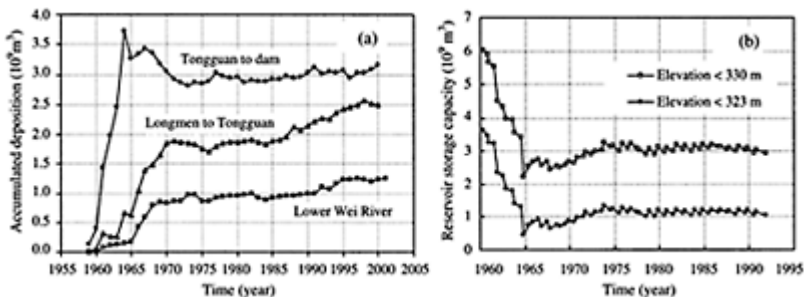


Figure 6. Variations of accumulated deposition and reservoir capacity in Sanmenxia Reservoir: (a) Accumulated deposition; (b) Reservoir storage capacity.

the reservoir from Tongguan to the dam during the periods of different operation modes. The mean annual deposition volumes in the reservoir area are 620.38×10^6 , -102.51×10^6 , and $12.57 \times 10^6 \text{ m}^3$ during the periods of storage, flood detention, and controlled release, respectively. Because the reservoir was operated at a low storage level and the discharge capacity was enlarged in the period of flood detention, the reservoir was changed from deposition to scouring. In the period of controlled release, deposition occurred during non-flood seasons while scouring occurred in flood seasons.

Fig. 6a shows the accumulated volume of sediment deposition in different reaches in the reservoir area and Fig. 6b shows the variation of reservoir storage capacity in the reservoir. Within the range of operation levels below 323 m, the capacity of 1.05 billion m^3 is available for controlling medium floods in the flood season whenever necessary. About 3 billion m^3 of reservoir capacity below the level of 330 m has been kept for use in the event of an extremely large flood. In the normal operation of the reservoir, the floodplain in the reservoir would be inundated only during extremely large floods; the major task of operation in the detention of such floods (Wu, 1992). The detained sediment would be eroded in the next several years. However, once the direct backwater effect reaches the confluence area above Tongguan during a flood event and lasts for a certain period of time, sediment deposition on the floodplain would be inevitable and a part of the reservoir capacity would become unavailable for use in the latter periods. It is obvious that for preserving a usable capacity in the reservoir, one of the guiding principles of the reservoir's operation is to prevent the direct backwater effect from exceeding Tongguan as much as possible.

The longitudinal and transverse profiles in the reservoir have been varied with the changes of operational conditions as shown in Figs. 7 and 8. The figures show that during the impoundment up to October 1961, i.e., the first year of operation, deposition was in the form of a delta with

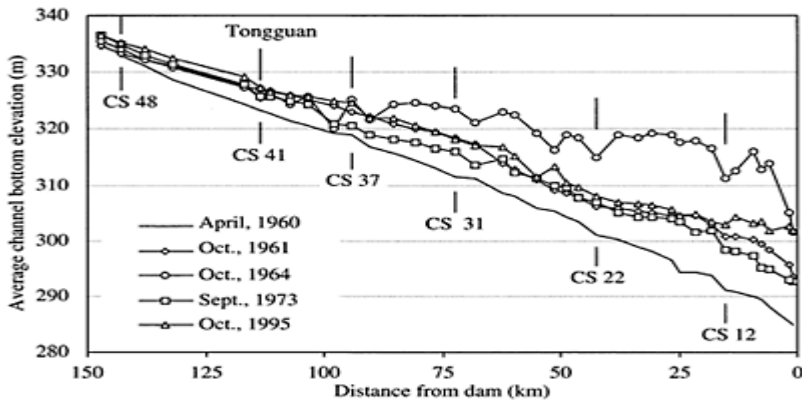


Figure 7. Typical longitudinal profiles in Sanmenxia Reservoir.

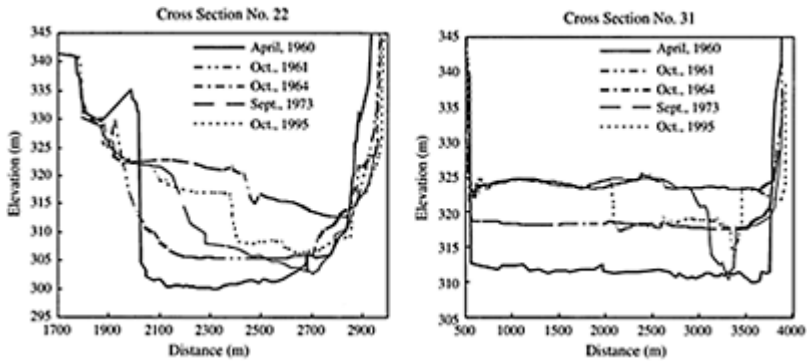


Figure 8. Typical transverse profiles in Sanmenxia Reservoir.

a topset slope of 0.00015–0.00017, nearly half the original river bed slope, and a forset slope of 0.0006–0.0009. The apex of the delta was near section 31, and the cross section was raised evenly in the transverse direction, making no distinction between the main channel and floodplain. During the wet year of 1964, the annual water and sediment inflows were 69.7 billion m^3 and 3.06 billion tons, respectively. The reservoir was severely silted because the outlet capacity was too small and the sluice holes were located too high. About 1.95 billion tons of oncoming sediment was deposited in the reservoir during the flood season, which was 70% of the total oncoming sediment. This was the most serious year of siltation. Longitudinal deposition was in the form of a cone, and a channel-floodplain configuration was formed. This can be seen from the transverse section, in which the floodplain rose simultaneously with the main channel. In 1973, the deposition occurred with the main channel being eroded because the reservoir was used for flood detention only during the flood season and the outlet discharge was enlarged after reconstruction. The figure reveals that the main channel had been lowered by erosion with basically no changes in the floodplain. The longitudinal bed slope of the main channel was 0.0002–0.00023 and that of the floodplain was 0.00012. A high floodplain and deep main channel had been formed; about one billion m^3 channel storage below Tongguan was recovered.

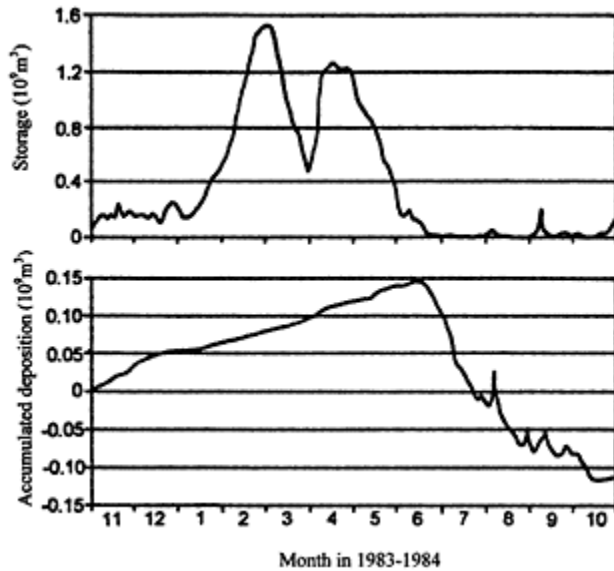


Figure 9. Variations of storage and deposition in the operational year of 1983–1984.

Since 1974 when the mode of controlled release has been used, the reservoir has been operated by storing only low concentration water in the non-flood season and discharging high concentration flow during the flood season. The longitudinal profile of the deposits has basically formed by superimposed deltas in the non-flood season. When the reservoir stage was lowered in the flood season, the deposits in the main channel were eroded along with the drawdown of the reservoir. If the oncoming flow in the flood season was too small, and, or, the operational stage in the non-flood season was relatively too high, depositions that took place at the head reach may not have been entirely eroded and thus would not be carried out of the reservoir in the same year. The residue would continue to erode until a large flood came the next year. In this case, the equilibrium of the deposition and erosion in the reservoir could not then be maintained within an operational year. A typical operational year of controlled release is shown in Fig. 9, which shows the variations of the storage of water and the processes of deposition in the reservoir.

In Fig. 7 the longitudinal profile of October 1995 shows the sedimentation associated with the operational mode of controlled release. The figure shows that there was no appreciable change in the longitudinal profile, except for a slight modification of the width and depth of the channel.

5 SEDIMENTATION AND FLOOD HAZARDS IN THE WEI RIVER

The most serious adverse effect caused by the impoundment of water at the Sanmenxia Reservoir is the sedimentation in the lower Weihe River and consequently the flooding risk to Xi'an, an ancient capital of China. The Wei River is the largest tributary of the Yellow River, and it empties into the Yellow River at Tongguan, as shown in Figs. 1 and 2. The lower Wei River is in the backwater region of Sanmenxia Reservoir. The elevation of Tongguan, acting as the base level of the bed profile of the lower Wei River, has been increasing since the operation of the Sanmenxia Reservoir. Fig. 10 shows the elevation of Tongguan varying with time from 1960 to 2001. There are three increasing periods, denoted by I, II, and III, and two decreasing periods, denoted by 1 and 2. The first increasing period was associated with high pools level in earlier periods of operation due to an unrealistic operation method and later limited outlet capacity. The second and third periods of increasing were mainly caused by reduction in inflow discharges, since in the controlled release period after 1973 the pool level was kept essentially the same within each operational year. On the other hand, the first decreasing period mainly resulted from the low pool level and the enlarged release capacity of the dam. And the second decreasing period mainly resulted from low discharges.

Generally speaking, sedimentation in the lower Wei River occurred during the periods of increased elevation of Tongguan and erosion occurred during the periods of decreased elevation of Tongguan. Fig. 6a shows the accumulated volume of sedimentation in the lower Wei River, indicated by the line with solid squares. The total deposition volume up to the year 2001 was about

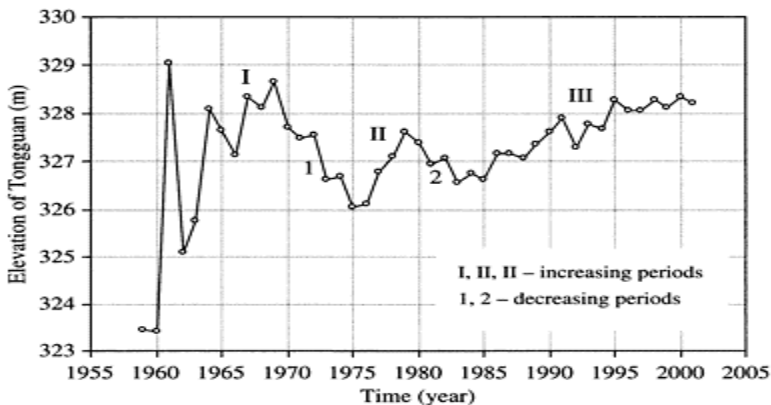


Figure 10. Variation of the elevation of Tongguan.

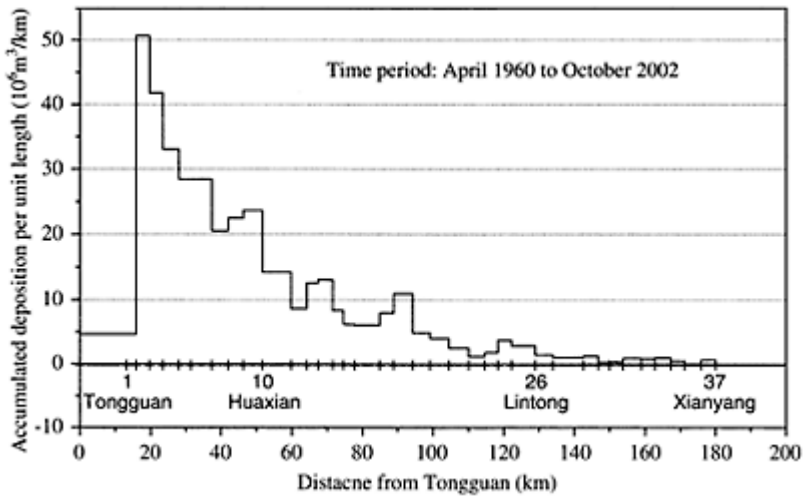


Figure 11. Longitudinal distribution of accumulated deposition volume per unit length in the lower Wei River.

1.3 billion m^3 . A comparison of the two curves given in Fig. 6a and Fig. 10 shows that sedimentation in the lower Wei River is closely related to the elevation of Tongguan. Accelerated sedimentation occurred as the elevation of Tongguan increased and erosion took place as the elevation of Tongguan decreased. The increased elevation of Tongguan prevented sediment transport from the tributary into the Yellow River, thus resulting in accumulated sedimentation in the lower Wei River. Fig. 11 shows that sedimentation was occurring mainly in a 100 km long reach upstream of Tongguan. The accumulated deposition volume per unit length was reduced to nearly zero at Xianyang, an ancient town near Xi'an.

Fig. 12 shows the transverse bed profiles of cross-sections no. 2 and 7 in the lower Wei River, measured in 1960 and 2001. The floodplain had risen by 3 to 5 m due to sedimentation and the main channel had shrunk and become unstable. The flood discharge capacity of the channel was thence reduced and the flood stage at the same discharge was substantially increased.

Erosion and sedimentation have been propagating upstream in a series of retrogressive waves. Figs. 13a, b and c shows the distribution of the deposition rate per unit river length in the periods of 1960–1969, 1969–1973 and 1973–1980.

In the period of 1960–1969, the elevation of Tongguan rose abruptly from 323 m to 328.5 m (see Fig. 10). As a result, sedimentation occurred in the reach around Huaxian station at a rate of up to 2.5 million tons per km per year (Fig. 13a). The mark "I" indicates that the sedimentation in

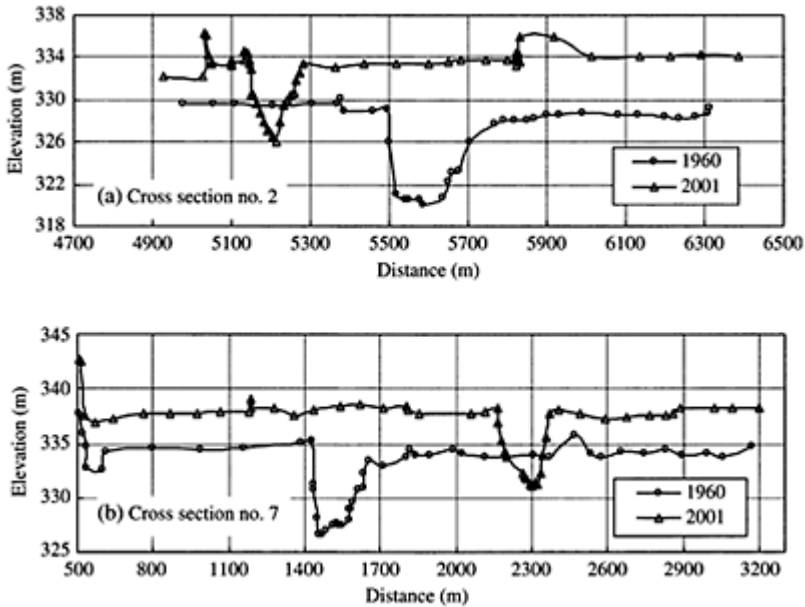


Figure 12. Channel bed aggradation at cross-sections no. 2 (a) and 7 (b) near Huaxian Station from 1960 to 2001.

this period corresponded to the first period in which the elevation of Tongguan increased. In the period of 1969–1973, the sedimentation moved upward to the reach between Huaxian and Lintong, but the rate of sedimentation decreased to about 0.75 million tons per km per year (Fig. 11b). In the meantime the first erosion wave occurred at the river mouth, which corresponded to the first period in which the elevation of Tongguan decreased, indicated by the mark “I”. In 1973–1980 the first sedimentation wave had moved upstream to Lintong and the first erosion wave had moved to Huaxian station, and the peaks had obviously decreased too. During this time period, the second sedimentation wave occurred in the reach between the river mouth and Huaxian station, indicated by the mark “II.” Of course this was associated with the second period of the increased elevation of Tongguan. The result described above clearly illustrated that the increase and decrease of the elevation of Tongguan generated erosion and sedimentation waves which could propagate retrogressively toward the upstream in the lower Wei River, at a speed of about 10 km per year.

Severe aggradations caused the flood stage to rise, and consequently escalating flood hazards occurred in the lower Wei River. Fig. 14 shows the stage rising at Huaxian station for flood discharges of 200 and 3,000–5,000 m³/s. A flow with a discharge of 200 m³/s is usually confined in the main channel, and therefore the corresponding stage rise reflects only the sedimentation and shrinking of the main channel. For a flood discharge between 3,000–5,000 m³/s the stage rise is due to sedimentation both on the floodplain and in the main channel. Sedimentation during the periods of increased elevation of

Tongguan made the low flow stage sharply increase because sediment was first deposited in the main channel. Similarly, during periods when the elevation of Tongguan decreased, erosion occurred in the channel. Therefore the low flood stage rise varied in a range of 1–4 m. In the meantime the high flood stage rise (for 3,000–5,000 m^3/s discharge) has also been increasing in a similar fashion. The flood stage is now 6 m higher than before the operation of Sanmenxia Dam, which poses a higher flood risk to the lower reaches of the Wei River. After 1990s, both the bankfull discharge and the frequency of inundation of floodplain have dropped significantly due to the reduced flood discharges, and the late resulted an increase in roughness values at the floodplain that had more crops. Consequently, the high flood stage rose significantly.

On Sept.1, 2003, a flood with a peak discharge of 3,570 m^3/s occurred in the lower Wei River and the stage at Huaxian station reached 342.76m, 0.51 m higher than the highest stage record at the station, even though the flood discharge was 230 m^3/s less than in the 1998 flood (3,800 m^3/s). Several factors contributed to the extremely high flood stage: (1) Continuous aggradation caused by high elevation of Tongguan in recent years; (2) Channel shrinking and bankfull discharge decreasing

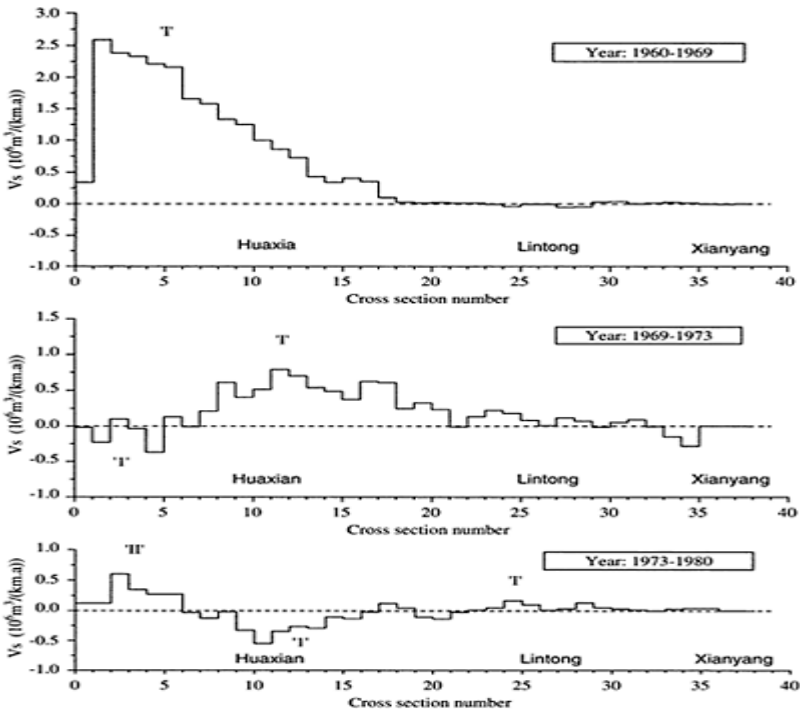


Figure 13. Erosion (–) and sedimentation (+) per unit length per year in a series of retrogressive waves in the lower Wei River, as a result of

increases and decreases of the elevation of Tongguan.

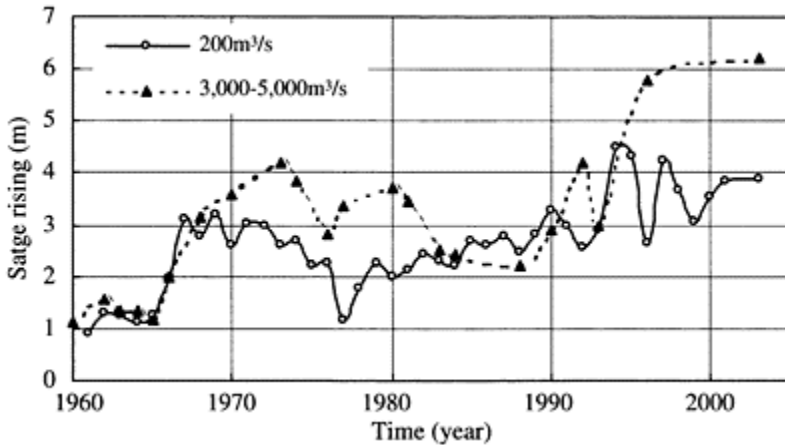


Figure 14. Flood stage rising at Huaxian station for discharges 200 m^3/s and 3,000–5,000 m^3/s .

due to a lack of high flow discharges which were necessary to maintain the channel; and (3) Unrealistic development and vegetation on the floodplain which increased the roughness. Five levee breaches occurred around Huaxian city and more than 20,000 people had to be evacuated. The record-breaking flood stage associated with a peak discharge of 3,570 m^3/s , which is only a 2-year flood, warns us of the severity of the sedimentation problem and the flooding hazard in the lower Wei River. One of the effective countermeasures is to change the operation of Sanmenxia Dam once again by lowering the pool level, consequently lowering the elevation of Tongguan as much as possible.

6 INFLUENCE OF WATER RESOURCES DEVELOPMENT

Briefly speaking, the severe sedimentation problems that occurred in the Sanmenxia Reservoir were mainly due to the following factors: (1) The original reservoir planning and design were performed according to the standards for and experiences with clear water. The principle of streamflow regulation that was adopted was basically the same as that used in reservoirs on non-sediment-laden rivers. Of course, the deposition of sediment in the reservoir was unavoidable. (2) The difficulties involved in resettling the inhabitants of the reservoir area were underestimated. (3) In the original design, anticipating that the sediment inflow of the reservoir would be rapidly reduced was too optimistic. The proposed sediment retention reservoirs were proposed to be built in the upland area and soil conservation works were also planned, and unrealistic, with a goal of

50% in less than 15 years. Through practice, it has become clear that the enormous amount of the sediment load could not be greatly reduced in a short period of time. A reservoir built solely for the storage of water and the retention of sediment on a river heavily laden with sediment is not the solution for water resources development. By the operational practice from 1974 on, it has been proven that the reconstruction of the outlets and the new operational mode are more suitable to the conditions of the Yellow River. The adopted operational mode presently in use has provided valuable experience for solving sediment problems of large sized reservoirs built on sediment-laden rivers. As a result, the Xiaolangdi Project, which is 130 km downstream of Sanmenxia Reservoir on the Yellow River, was planned and designed essentially based on the experience gained from the operation of Sanmenxia Reservoir.

The Yellow River is deficient in water and abundant in sediment. Due to the regulation of water in large reservoirs and the utilization of water resources for irrigation in recent years, the annual runoff and its temporal distribution within a year have been greatly modified (see Fig. 15 and Table 3). The mean annual runoff was reduced from $40.6 \times 10^9 \text{ m}^3$ in 1961–1985 to $28.7 \times 10^9 \text{ m}^3$ in 1986–1995, and further to $19.5 \times 10^9 \text{ m}^3$ in 1996–2001. Inflow in the flood season was reduced from 55.9% in 1961–1985 to 46.0% of the annual runoff in 1986–1995, and further to 42.8% in 1996–2001. After regulation of reservoirs in the upstream, the peak discharges of the flow have been attenuated. If the rainfall intensity is moderate, all the soil conservation measures are also effective in the detention of flood flow. Therefore, observations have shown that the peak discharge and the frequency of floodwaters entering the Sanmenxia Reservoir have been decreasing. Fig. 15b shows the number of days that had daily mean discharges was greater than $3,000 \text{ m}^3/\text{s}$ at Tongguan station. The results shown in the figure illustrate the decreasing frequency of flood flows entering the reservoir.

Table 3. Statistics of annual runoff and sediment load at Tongguan station.

Time period	Runoff (10^9 m^3)			Sediment load (10^9 tons)		
	Water year	Flood season	Ratio (%)	Water year	Flood season	Ratio (%)
11/1960–10/1969	45.07	26.41	58.6	1.420	1.203	84.7
11/1969–10/1975	33.03	17.19	52.0	1.244	1.013	81.5
11/1975–10/1979	39.62	23.15	58.4	1.439	1.286	89.4
11/1979–10/1985	41.50	24.75	59.6	0.806	0.655	81.2
11/1985–10/1995	28.71	13.20	46.0	0.800	0.600	75.0
11/1995–10/2001	19.52	8.35	42.8	0.594	0.440	74.1

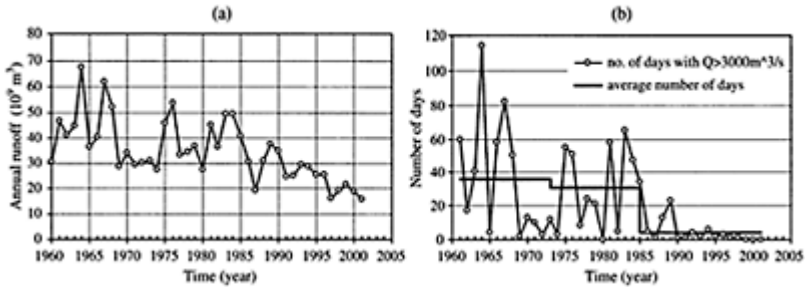


Figure 15. Variation of flow at Tongguan station: (a) Annual runoff; (b) Number of days with daily a mean discharge greater than $3,000 \text{ m}^3/\text{s}$.

Variation of the inflow has pronounced effects on the reservoir sedimentation. Increased inflow during the non-flood season has the ability to scour the alluvial channel, bringing more sediment into the reservoir. As a result, more sediment would be deposited at the backwater area of the reservoir, and this sediment probably could not be eroded during subsequent floods. Decreased runoff in flood seasons and fewer occurrences of floods are unfavorable to the scouring or transport of the deposited sediment from previous non-flood seasons. As a result, the backwater deposition again has been extending upstream since 1986, and the channel bottom elevation and water surface elevation have been gradually rising, as shown in Fig. 10. This has caused further sedimentation problems and exacerbated the flooding hazards in the lower reaches of the Wei River.

The variations of water and sediment inflows required that the operation level used from 1974 to 2002 be adjusted to properly regulate the water and sediment in order to maintain balanced deposition in the reservoir area. Debates on adjustments of the reservoir's operation level have continued for several years. Some experts argue that the upstream extension associated with backwater deposition in recent years was mainly caused by the reduction of runoff that resulted from excessive water resource development. Therefore, lowering the pool level has no effect on the backwater deposition. In addition, the reservoir has maintained a new balance between the newly established ecological system within the reservoir area below Tongguan and the backwater generated by the pool level. Any change in the operation level may disturb the newly formed ecological system and should be avoided.

Some other experts believe that the operation level used in the controlled release period was determined based on earlier inflow conditions. However, it is no longer compatible with the changed inflow conditions, notably the reduced annual runoff after 1986. Lowering the pool level could compensate, at least partially, for the negative effect of reduced runoff, and could also prevent the backwater extension.

An extreme plan proposed by a few agencies even suggests to decommission the Sanmenxia Dam and allow the flow to run freely without control. By doing so, it is estimated that the channel bed elevation at Tongguan station could be scoured down more than 2 m. A lower channel bed elevation at Tongguan would greatly slow down the

sedimentation process in the lower reaches of the Wei River, and consequently reduce the demand for flood control.

Research is being conducted to find the best operation level for preventing backwater deposition, without substantially affecting the newly formed ecological system in the reservoir area below Tongguan and without significantly losing the benefit of hydropower generation. The preliminary plan is to allow the flood flows to pass through the dam without any control in flood seasons, while lowering the maximum pool level from 318 m to a value between 312–315 m in non-flood seasons. As such, sediment would be deposited only within a shorter river reach near the dam in the non-flood season, and the deposited sediment could then be easily removed by the flood flows passing through the dam in the next flood season.

Besides the adjustment of the pool level, other countermeasures proposed for preventing the backwater deposition include:

- (1) River training in the river reaches upstream and downstream of the backwater zone. River training work could help to maintain a better channel configuration and to increase the flow's sediment transport capacity.
- (2) Dredging the channel in the vicinity of the backwater zone. Experimental work was conducted from 1996 to 2001 for flushing sediment using jet flows generated by specially designed ships. Some positive effects were observed during this ship operation.
- (3) Strengthening soil conservation practices in the loess plateau areas. Soil conservation can have a long-term effect on reducing the sediment load deposited in the reservoir. However, it may take a much longer time to show definite effectiveness.
- (4) Building sediment detention reservoirs on river reaches above Sanmenxia Dam. These reservoirs can directly trap the coarse sized sediment, and reduce the sediment load at the Sanmenxia Reservoir. They can also regulate the sediment and water, generating artificial floods to transport more sediment.

7 CONCLUDING REMARKS

Serious sedimentation occurred soon after the impoundment of water in Sanmenxia Reservoir, causing loss of reservoir storage capacity, backwater deposition, and flood risk in the lower Weihe River. These have posed difficulties and challenges for the management of the dam. Reconstruction of outlet structures has significantly increased the discharge capacity, and provided the dam with the necessary facility to allow flood flows to pass through the reservoir without significant sediment detention. Changes of reservoir operation have played a very important role in maintaining a balance of sediment across the impounded reach in the reservoir by using the transport capacity of the flow itself to flush and carry the sediment out of the reservoir, and eventually minimizing the adverse effect of reservoir sedimentation. Despite the unexpected sedimentation problems, the dam is still providing the basin with flood control, irrigation, and hydropower generation, even though some benefits are lower than the original design. Changing the management strategy is one of the key factors for the sustainable use of the dam. Study of further adjustments of the current operating rules continues, to

accommodate the changing inflow conditions into the reservoir that result from unrealistic basin development.

In the progression of our knowledge in the hydraulics of dams, the Sanmenxia Dam has served as a large-scale field experiment for dam design and sedimentation management for sediment-laden rivers. Experience gained from the reconstruction and operation of Sanmenxia Dam is a valuable asset for the sustainable use of dams by properly solving sediment problems of large sized reservoirs built on sediment-laden rivers.

ACKNOWLEDGEMENT

This study was supported by the Creative Research Team Foundation of the National Natural Science Foundation of China (Item: 50221903).

REFERENCES

- He, G.Z., Hua, Z. & Wang, G. (1987). "Regulation of Streamflow and Sediment Regime by Sanmenxia Reservoir and Particularities of Scouring and Deposition," Selected Papers of Researches on the Yellow River and Present Practice, Yellow River Press, Zhengzhou, China, pp. 106–175.
- Long, Y.Q. (1996). "Sedimentation in the Sanmenxia Reservoir," Proceedings of the International Conference on Reservoir Sedimentation, Vol. III, Fort Collins, Colorado, pp. 1294–1328.
- Long, Y.Q. & Chien, N. (1986). "Erosion and Transportation of Sediment in the Yellow River Basin," International Journal of Sediment Research, Vol. 1, No. 1, IRTCES, Beijing, China, pp. 2–28.
- Wu, B.S. (1992). "Optimal Operation of Reservoirs for Flood Control in the Yellow River," Journal of Wuhan University of Hydraulic and Electric Engineering (in Chinese), No.10.
- Wu, B.S. (1997). "Regulation of Sediment in the Sanmenxia Reservoir," Essays on River Mechanics, Colorado State University, pp. 199–209.

New approach in determining useful life of reservoirs

J.S.Yeoh & J.H.Lovel

Department of Civil Engineering, University of Bristol, UK

A.M.Siyam

University of Khartoum, Sudan

Hydraulics of Dams and River Structures—Yazdandoost & Attari (eds)

© 2004 Taylor & Francis Group, London, ISBN 90 5809 632 7

ABSTRACT: The primary use of a trap efficiency function (TEF) is to predict the useful life or remaining capacity of a reservoir. Currently TEFs for reservoirs are generally empirically based and are obtained by fitting data collected from existing reservoirs. The most widely used TEF is that of Brune (1953). Many researchers have questioned the use of the capacity to inflow ratio, (V/I) alone of the TEF of Brune (1953) to describe the dynamics of sedimentation in reservoirs (Gottschalk, 1964 and Heinemann, 1981). In this paper a newly developed generalised TEF in which the reservoir sedimentation problem is viewed as analogous to the mixer tank problem is presented. A sedimentation coefficient β is introduced to reflect the decay of storage capacity in reservoirs to relate the TEF of reservoirs to that of a mixer tank. Based on the new TEF, an analytical expression has been formulated for predicting the useful life or remaining capacity of reservoirs.

1 INTRODUCTION

Sediment deposition is an inevitable phenomenon in all reservoirs. Sedimentation gradually reduces the available storage and in many cases threatens the primary use of reservoirs in a time less than the expected lifespan. Accuracy in the prediction of the amount of sediment that will be deposited in a reservoir is very important for the planning, design and operation phases of reservoirs. In this respect the trap efficiency of the reservoir is a key factor in the estimation of the sediment distribution, storage loss and useful life. The trap efficiency, η is defined as the ratio of the retained sediment in the reservoir and the total incoming sediment. It depends on many factors such as (1) capacity and shape of reservoir, (2) inflow rate of sediment and water discharge, (3) type of reservoir operation and (4) fall velocity of sediment particles.

Currently empirical TEFs are employed in a step by step process to calculate the useful life of reservoirs, which were obtained by fitting data collected from existing reservoirs. As a result there have been TEFs, which do not share common parameters. This is clearly manifested in the most widely used trap efficiency curves of Brune (1953) which are based on data collected from 40 normally ponded USA reservoirs. The curves relate the η of the reservoir to the V/I ratio where V is the volume stored in the reservoir at normal retention level and I is the average annual inflow to the reservoir. Due to the generality of Brune's curves which uses the V/I ratio alone to describe the dynamics of sedimentation in reservoirs and no distinction made to the source of type of sediment has inspired the authors to develop a new TEF and process for direct prediction of the useful life or remaining capacity of reservoirs. Three design charts to ease the computation and visualisation of the dynamics of reservoir sedimentation are presented in this paper.

2 APPLICATION OF THE MIXER TANK MODEL TO THE TRAP EFFICIENCY IN RESERVOIRS

The following describes the derivation of the newly proposed TEF for reservoirs. It can be shown that the trap efficiency of a mixer tank is governed by a simple exponential law, which depends on a simple dimensionless parameter. The rate of change of concentration with time in a mixer tank can be expressed as

$$\frac{dc}{dt} = \frac{C_{in}Q_0 - CQ_0}{V} \quad (1)$$

where V =volume in the tank, C_{in} =inflow sediment concentration, Q_0 =inflow rate and C =uniform concentration in mixer tank. By integrating Eq. 1 and evaluating the arbitrary constant for the initial condition $C=0$ at $t=0$, Eq. 1 reduces to

$$C = C_{in} \left(1 - e^{-\frac{Q_0 t}{V}} \right) \quad (2)$$

The trap efficiency of the mixer tank is defined as

$$\eta = \frac{C_{in} - C}{C_{in}} \quad (3)$$

Substituting Eq. 2 into 3 yields

$$\eta = e^{-\frac{Q_0 t}{V}} \quad (4)$$

As mentioned earlier, the above trap efficiency of a mixer tank can be viewed as a function of a single dimensionless parameter, which is the inflow/capacity ratio, I/V (the inverse of the parameter used by Brune (1953)). In a mixer tank model, V and Q_0 are constant and efficiency, η changes with time, t . In reservoirs, the storage V also changes with time as a result of sediment deposition. However, since the siltation occurs over many years, the product $Q_0 t$ could be combined and introduced as average annual inflow, I . Eq. 4 can then be rewritten as

$$\eta = e^{-\frac{t}{T}} \quad (5)$$

Recognising the simple analytical equation for the trap efficiency of a mixer tank and its dependence on a single parameter, which does not include any of the properties of the mixed constituents, it is interesting to compare Eq. 5 with Brune's (1953) data on the trap efficiency of the normally ponded reservoirs. When the equation above was plotted against Brune's (1953) data, a similar trend with transitional shift was observed. This suggests the mechanics of trap efficiency in both systems belong to the same physical process for which Eq. 4 and 5 represent a particular solution for the case of a mixer tank. It is therefore suggested the term β , which is a sedimentation parameter that reflects the decay of the storage capacity of the reservoir due to the ongoing sedimentation process, is introduced into Eq. 5. Therefore the trap efficiency of an inefficient mixer tank or that of reservoirs can be expressed in the following form

$$\eta = e^{-\beta \frac{t}{T}} \quad (6)$$

Eq. 6 is the proposed generalised TEF, which could be adopted for any water retaining body likely to experience sediment deposition. It should be understood that β is not a universal physical constant but is governed by some hydraulic parameters of the reservoir mainly the settling velocity of sediments, strength of turbulence in the reservoir, type of reservoir operation, reservoir shape and area. When Eq. 6 is fitted with Brune's (1953) data, it was found that $\beta=0.0079$ gave a good coefficient of correlation $r^2=0.952$. Also, the η of the two semi-dry reservoirs cited by Brune fall close to that of an efficient mixer tank and are well fitted with $\beta=0.75$. This can be explained by the fact that in semi-dry reservoirs the flow is very turbulent. This produces efficient mixing that resembles similar processes in an efficient mixer tank ($\beta=1.0$). On the other hand desilting basins have a very low mixing effect and act predominantly in deposition. The two desilting basins, which resembles an inefficient mixer tank were fitted by a very low value of $\beta=0.00012$ (see Fig. 1). The normally ponded reservoirs fall between these two types.

3 NEW RELATIONSHIP FOR ESTIMATING THE USEFUL LIFE OF A RESERVOIR

In this section a relationship for estimating the storage capacity loss or the total useful life of a reservoir is formulated. Gill (1978) expressed three functional relationships (Eqs. 16, 17, 18) for

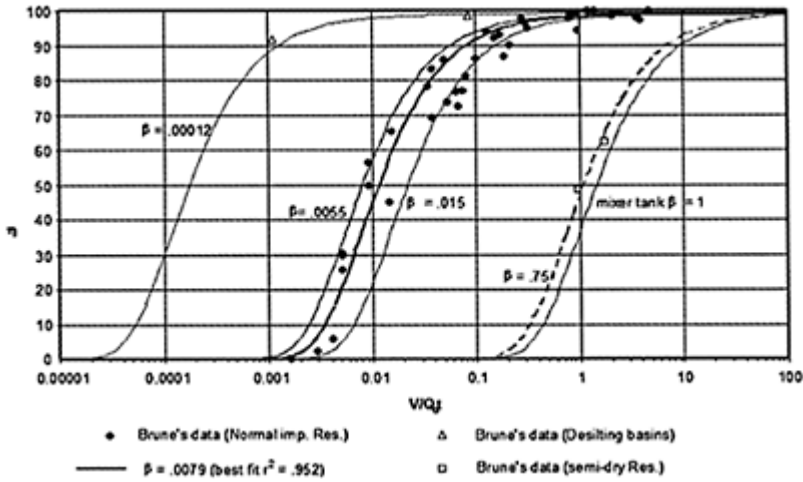


Figure 1. Comparison of Brune (1953) data with the proposed generalised trap efficiency function.

estimating the useful life of a reservoir by carefully fitting equations for the three curves of Brune (1953). It is shown here that these three relationships are, in fact, particular truncated solutions of a much generalised equation (Eq. 14) for estimating the useful life of reservoirs.

The change of capacity with time due to sedimentation of an operating normally ponded reservoir is given by

$$\frac{dV}{dt} = -\eta \frac{Q_s}{\gamma} \quad (7)$$

where Q_s is the average sediment inflow to a reservoir in kg, t is the time in years and γ is the average density of the deposited material in kg/m^3 which also varies with time. By substituting Eq. 6 into Eq. 7 yields

$$\frac{dV}{dt} = -e^{-\beta \frac{t}{V}} \frac{Q_s}{\gamma} \quad (8)$$

For the density, the expression proposed by Gill (1988) to simplify the integration process can be used

$$\gamma = \gamma_1 t^n \quad (9)$$

where n is given by

$$n = 0.5 \log \left(1 + \frac{2k}{\gamma_1} \right) \quad (10)$$

where k =compaction factor and γ_1 is the density of deposited sediment at the end of the first year of filling the reservoir. The recommended values for k and γ_1 by the USBR can be found in Yang (1996). Substituting Eq. 9 into Eq. 8 gives

$$\frac{dV}{dt} = -e^{-\beta \frac{I}{V}} \frac{Q_s}{\gamma_1 t^n} \quad (11)$$

It should be noted that the inflow I is in fact a function of time ($I=Q_0 t$). However, it can be argued that I is a parameter in its own right if the annual inflow is assumed constant. This allows Eq. 11 to be integrated by separating the variables. Thus

$$e^{\beta \frac{I}{V}} dV = -\frac{Q_s}{\gamma_1 t^n} dt \quad (12)$$

The LHS of Eq. 12 cannot be integrated directly but it can be truncated to any required degree of accuracy by expanding the exponential term i.e.

$$\left(\left(1 + \frac{\beta I}{V} + \frac{\beta^2 I^2}{2V^2} + \frac{\beta^3 I^3}{6V^3} + \dots H.O.T. \right) dV \right) = -\frac{Q_s}{\gamma_1 t^n} dt \quad (13)$$

Integrating Eq. 13 while neglecting the higher order terms and evaluating the integration constant with assumption of original reservoir capacity is V_0 at $t=0$ yields

$$V_0 - V + \beta I \ln \frac{V_0}{V} - \frac{\beta^2 I^2}{2} \left(\frac{1}{V_0} - \frac{1}{V} \right) - \frac{\beta^3 I^3}{12} \left(\frac{1}{V_0^2} - \frac{1}{V^2} \right) = \frac{Q_s t^{(1-n)}}{\gamma_1 (1-n)} \quad (14)$$

Hence Eq. 14 is the general relationship for predicting the capacity of the reservoir after t years of operation. The required inputs are (1) initial volume of the reservoir V_0 ; (2) the annual inflow of water I ; (3) the annual inflow of sediment, Q_s ; (4) initial density of the deposited sediment after first year of operation γ_1 ; and (5) appropriate value for the sedimentation factor, β . As mentioned earlier it would be useful to compare the LHS of Eq. 14 with the approximate algebraic equations of the three trap efficiency curves of Brune (1953) used by Gill (1979) to facilitate the integration of Eq. 7. Gill expressed the equivalent relation to Eq. 14 as

$$\phi \left(\frac{V}{I} \right) = \frac{Q_s}{I \gamma_1 (1-n)} t^{(1-n)} \quad (15)$$

where LHS of Eq. 15 is given by Eq. 16, 17 & 18 for the three curves of Brune (1953) for coarse, median and fine sediment respectively, coarse

$$\phi \left(\frac{V}{I} \right) = 0.9947 \left(\frac{V_0 - V}{I} \right) + 0.0063 \ln \left(\frac{V_0}{V} \right) - 0.000003 \left(\frac{I}{V_0} - \frac{I}{V} \right) \quad (16)$$

median

$$\phi \left(\frac{V}{I} \right) = 1.02 \left(\frac{V_0 - V}{I} \right) + 0.012 \ln \left(\frac{V_0}{V} \right) \quad (17)$$

fine

$$\phi\left(\frac{V}{I}\right) = 1.0266\left(\frac{V_0 - V}{I}\right) + 0.0262\ln\left(\frac{V_0}{V}\right) + 0.0013\left(\frac{I}{V_0} - \frac{I}{V}\right) - 0.00000051\left(\frac{I^2}{V_0^2} - \frac{I^2}{V^2}\right) \quad (18)$$

It is concluded here that the three trap efficiency curves of Brune's were best drawn to resemble an exponential decay function that can be described by Eq. 6 but with variable coefficient. These values can be read from comparing the coefficients of Eqs. 16, 17 & 18 with the generalised Eq. 14. Also it can be noticed that these equations corresponds with high accuracy to the generalised Eq. 14.

4 THE SEDIMENTATION COEFFICIENT

In general, any suitable TEF can be used in the prediction of the sediment distribution in reservoirs. The assumption of exponential decay of sediment concentration due to change in hydraulic conditions in the head of a reservoir is widely accepted. From analysis of forces that govern the sedimentation processes, it was found that there are two opposing forces that govern the value of β . The turbulence strength and the convection strength of the flow tend to decrease the trap efficiency and can be best represented by the shear velocity u^* and the average depth velocity U respectively. On the other hand the gravity force of sediment particles tends to increase the trap efficiency and can be represented by the settling velocity of the sediment particle w_s . In dimensionless form these

Table 1. Values of sedimentation factor β for some selected USA reservoirs.

No.	Normally ponded reservoir	Stream	Location	I/V ratio	β	Measured efficiency
4	Hales Bar (1935–3)	Tennessee R.	Chattanooga,	0.0051	0.00609	30.5
5	Hales Bar (193	Tennessee R.	Chattanooga,	0.0051	0.00612	29.7
6	Hales Bar (1938)	Tennessee R.	Chattanooga,	0.0051	0.00691	25.7
9	Wilson Lake	Tennessee R.	Florence,	0.0145	0.01164	44.9
12	Bullard's bar	No. Fk. Yuba	No. San Juan, Calif.	0.0378	0.00688	83.4
15	Corpus Christi(1942–1948)	Nueces R.	Corpus Christi, Tex.	0.0541	0.01652	73.7
16	Corpus Christi(1934–1942)	Nueces R.	Corpus Christi, Tex.	0.0638	0.01691	76.7
17	Lexington	Leonard's Creek	Lexington, N.C.	0.073	0.01886	77.2

19	Lake Michie	Flat River	Durham, NC	0.0998	0.01470	86.3
20	Lake Issaqueneena	Six-Mile Creek	Clemson SC	0.127	0.007567	94.2
21	Guernsey	North Platte R	Guernsey Wyo	0.151	0.012258	92.2
23	T and P	Town Creek	Weatherford Tex	0.191	0.026569	87
24	Hiwassee	Hiwassee R.	Murphy, NC	0.273	0.005235	98.1
24a	Imperial Dam	Colorado R.	Yuma, Ariz.	0.211	0.021743	90.2
25	Lake of Ozarks	Osage R.	Bagnell, Mo.	0.292	0.009771	96.7
26	Pardee	Mokelumme R	Buena Vista, Cali	0.313	0.016046	95
27	Possum Kingdom	Brazos R.	Palo Pinto, Tex	0.787	0.016156	98
29	Buchanan Lake	Colorado R.	Burnet, Tex	0.837	0.011824	98.6
30	Norris	Clinch R.	Norris, Tenn.	0.946	0.008556	99.1
31	Senecaville	Wills Creek	Senecaville, Ohio	0.947	0.055556	94.3
34	Lake Mead	Colorado R.	Boulder city, Nev	2.44	0.014714	99.4
35	San Carlos	Gila River	Globe, Ariz	3.59	0.072639	98
36	Conchas	So. Canadian R.	Tucumcari NM	3.82	0.104655	97.3

*Data on reservoirs are extracted from Brune (1953).

opposing roles are represented by U/w_s and u^*/w_s or can be bundled into a parameter as u^*U/w_s^2 . The following expression is proposed to relate this parameter with the sedimentation factor

$$\beta = \beta_c \left(\frac{u^*U}{w_s^2} \right) \quad (19)$$

where β_c is the constant of calibration and Eq. 6 can be rewritten as

$$\eta = e^{-\beta_c \left(\frac{u^*U}{w_s^2} \right) \frac{1}{T}} \quad (20)$$

It was noticed that the trap efficiency expression Eq. 20 is capable of simulating delta deposit at head of reservoir due to bed load transport. This criterion was used to adjust the value of the factor β_c by matching the location of the maximum deposition rate (i.e. delta apex) to that given by a bed load equation for the same sediment particle. The rate of deposition of several bed load transport at the head of a hypothetical reservoir with

vertical side walls were assessed. All formulae were found to give similar trend and magnitude of siltation. Hence Shield's formula was chosen for the calibration of factor β_c and was found to be 0.25. Although the calibrated value of β_c is found from bed load transport function, Eq. 20 seems valid as well for suspended sediment transport due to the presence of the settling velocity w_s . Laboratory experiments were carried out to assess the universality of the factor β_c in Eq. 20 and thereby testify the suitability of the TEF for predicting trap efficiency, useful life and sediment distribution. Details of the sedimentation tests are well documented in Siyam (2000). Some of the calculated values of β for normally ponded reservoirs used by Brune (1953) are presented in Table 1. Only reservoirs that were resurveyed in a period less than 20 years were chosen. The calculated values of sedimentation coefficients given here could only serve as a guide for defining β for another reservoir if the shape of the reservoir, operation type and incoming sediment characteristic matches with one of those listed in Table 1.

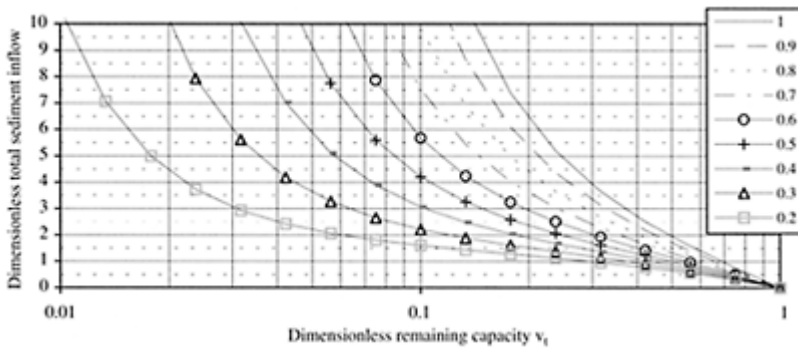


Figure 2. Time function of reservoir sedimentation with parameter $\beta I / V_0 = 0.2 - 1.0$.

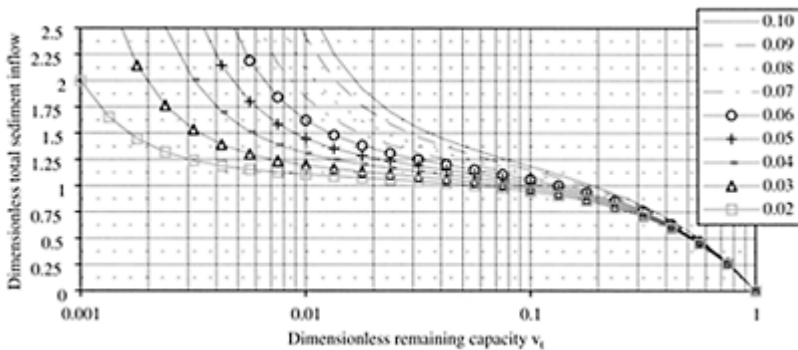


Figure 3. Time function of reservoir sedimentation with parameter $\beta I / V_0 = 0.02 - 0.1$.

5 DESIGN CHARTS FOR PREDICTION OF RESERVOIR SEDIMENTATION

The LHS of Eq. 14 consists of two dimensionless parameters. They are: (1) the ratio (V/V_0) which represents the ratio of the reservoir capacity at any time t to the original volume. This term will be known as the dimensionless remaining capacity, v_t . (2) the dimensionless group of β (I/V_0) which is the product of sedimentation factor and the inflow-original capacity. These terms emerge when dividing Eq. 14 by V_0 i.e.

$$1 - v_t + \frac{\beta I}{V_0} \ln \frac{1}{v_t} - \frac{\beta^2 I^2}{2V_0^2} \left(1 - \frac{1}{v_t}\right) - \frac{\beta^3 I^3}{12V_0^3} \left(1 - \frac{1}{v_t^2}\right) = \frac{Q_s t^{(1-n)}}{\gamma_1 V_0 (1-n)} \quad (21)$$

Thus RHS of Eq. 21 also emerges as a dimensionless group of parameters. The whole term resembles the ratio of the volume of the total sediment inflow during t years of operation to the original volume of the reservoir V_0 . This term will be known as the dimensionless total inflow sediment. Q_s is the annual sediment inflow in mass while the total inflow sediment is the volume of total incoming sediment during t year assuming all sediment is trapped in the reservoir. To avoid solving Eq. 21 each time for v_t for a given t , or vice versa, charts can be constructed to encompass the whole range of practical interest. This can be achieved by plotting the dimensionless total inflow sediment i.e. the RHS of Eq. 21 against the dimensionless remaining capacity of the reservoir, v_t with the dimensionless product β (I/V_0) as a single parameter. Figures 2, 3 and 4 are the charts constructed for selected values of β (I/V_0) ranging from 1 to 0.002.

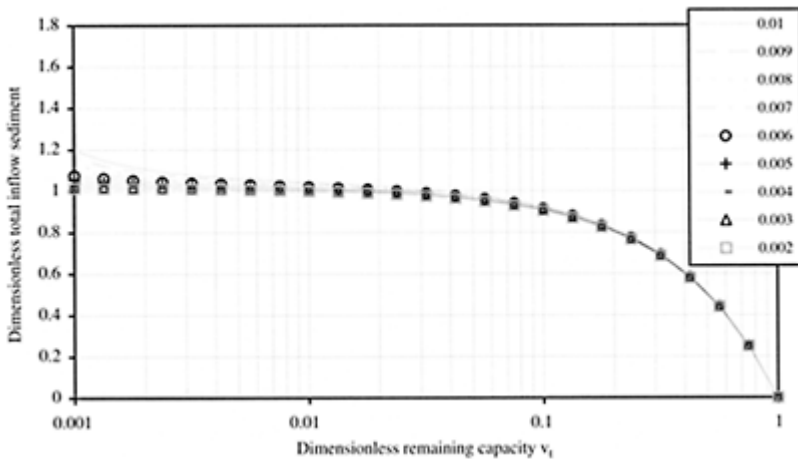


Figure 4. Time function of reservoir sedimentation with parameter $\beta I/V_0=0.002-0.01$.

6 DETERMINING THE CAPACITY OF RESERVOIR AFTER t YEARS OF OPERATION

The procedure for determining the remaining useful life capacity of the reservoir after t years of operation is presented in this section. The useful life can be determined in a similar way if the condition for terminating the reservoir life is given as when a certain percentage of the original reservoir volume is filled with sediment.

- (1) From hydrological data estimate the average monthly and annual inflows of sediment and water discharge.
- (2) Evaluate the appropriate mean sedimentation factor, β (use Table 1 as a rough guide or refer to methods of evaluating sedimentation coefficients in Siyam (2000)).
- (3) Estimate values of γ_1 and k for the inflow sediment mixture.
- (4) Determine Gill's number, n from Eq. 10.
- (5) Solve Eq. 14 to determine the capacity of the reservoir V after t years of operation noting that V_0 is the original volume of the reservoir.
- (6) If the design charts are used, calculate the total sediment inflow-original capacity ratio and using the appropriate curve of (I/V_0) calculate the dimensionless remaining capacity v_r . If the time, t is required for a given v_r , the chart can be used in reverse to determine the dimensionless total sediment inflow, from which t can be calculated.

7 CONCLUSION

Current empirical reservoir trap efficiency functions do not share the same parameters in describing reservoir sedimentation. They are applied in an iterative manner to estimate the useful life of reservoir. The most widely used trap efficiency curves of Brune (1953) have been criticised for their dependence on a single parameter. The authors have developed a generalised trap efficiency relationship (Eq. 6) by comparing reservoir with a mixer tank problem. Also the new relationship provides a theoretical justification for the use of the inflow capacity ratio, which is just the inverse of the parameter used by Brune (1953). It is shown that the general effects of all other significant parameters in reservoir sedimentation introduce a translational shift to the curve of trap efficiency versus the capacity-inflow ratio. Hence the trap efficiency curves for different reservoirs look similar and parallel to each other. The new TEF has accommodated this through an introduction of a sedimentation factor. Methods for evaluating this factor for any given reservoir can be found in Siyam (2000). A generalised relationship has been formulated to predict the useful life and the remaining capacity of a reservoir (Eq. 14). The relationship was compared with previous empirical relations (Eq. 16, 17 and 18) formulated based on the three curves of Brune (1953). Comparisons showed that the curves of Brune are only special case of the generalised TEF formulated by the authors. Design charts are proposed to simplify the design procedure. A general procedure for computation of the useful life and remaining capacity of reservoir is presented. Further research including field and laboratory tests are encouraged to substantiate the equations proposed.

REFERENCES

- Brune, G.N 1953. Trap efficiency of Reservoirs. *Transactions of the American Geophysics Union* 34(3)
- Brown, C.B 1943. Discussion of Sedimentation in Reservoirs by B.J Witzig. *Proceedings of ASCE* 69(6) 793–815, 1493–1499.
- Chen 1975. Design of Sediment Retention Curve. *Urban Hydrology and Sediment Control Symposium*. Lexington, USA 1975.
- Churchill, M.A 1948. Discussion of Analysis and Use of Reservoir Sedimentation Data by C.Gottschalk. *Proceedings of the Federal Interagency Sedimentation Conference, Denver, Colorado*, Jan 1948
- Dobbins, W.E. 1944. Effect of Turbulence on Sedimentation. *Transaction ASCE* 109:629–653
- Gill, M.A 1978. Analysis of Reservoir Sedimentation. *Water Power and Dam Construction*, Dec 1978:2
- Gill, M.A 1988. Planning the useful life of a Reservoir. *Water Power and Dam Construction*, May 1988:4
- Gill, M.A 1979. Sedimentation and Useful life of Reservoirs. *Journal of Hydrology* 44:89–95
- Gottschalk, L.C. 1964 Reservoir Sedimentation. *In Handbook of Applied Hydrology*, V.T.Chow (editor), s 17–1. New York. McGraw-Hill
- Graf, W.H. 1984. Storage Losses in Reservoirs. *Water Power and Dam Construction*, April 1984:3
- Heinemann, H.G. 1981. A new Sediment trap Efficiency Curve for Small Reservoirs. *Water Resources Bulletin* 17 (5): 825–830
- Lane, E.W & Koelzer, V.A. 1953. Density of sediments deposited in Reservoirs. *Report No 9*, Engineering District.
- Lianzhen, D & Qishun, Z. 1985. Computation of Deposition and Scouring in Reservoir. IRTCES Lecture Note of the Training Course on Reservoir Sedimentation. Beijing, China.
- Siyam, A.M. 2000. Reservoir Sedimentation Control. *PhD Thesis*. University of Bristol.

The use of a labyrinth weir in a reservoir flushing system

J.H.Loveless & J.S.Yeoh

Department of Civil Engineering, University of Bristol, UK

Hydraulics of Dams and River Structures—Yazdandoost & Attari (eds)

© 2004 Taylor & Francis Group, London, ISBN 90 5809 632 7

ABSTRACT: A novel reservoir flushing system known as the Submerged Straight Weir Closed Conduit (SSWCC) system has been proposed and successfully tested at the Hydraulics Laboratory at Bristol University. This paper presents further work on this flushing system where a new design incorporating a submerged labyrinth weir instead of a submerged straight weir flushing system is studied. The new system called a Submerged Labyrinth Weir Closed Conduit (SLWCC) flushing system consists of a type of submerged labyrinth weir connected to the main dam by closed conduit. Experimental tests were carried out on a physical model of the new proposed system and results were compared to the results obtained from previous experiments carried out on the SSWCC model. The performance of the physical model was simulated using SSIIM, a 3-D mathematical modelling package that is widely used in reservoir modelling.

1 INTRODUCTION

In designing a reservoir the basic considerations are hydrological conditions and the service requirements for the reservoir for a given period of time. To prevent premature loss of storage and services dependent on it, various methods for controlling reservoir sedimentation are currently employed to alleviate the problem of reservoir sedimentation around the world. These include watershed management, reduction in sediment influx by using check dams, density current venting, minimising sediment deposition through a reduction of trap efficiency by sluice draw down, allocation of additional storage volume and the removal of deposited sediment by flushing and dredging (Fan 1998). However in many cases, the success of these measures is either limited or cost prohibitive (Mahmood 1987). It is the view of the authors that the design of a system of reservoir sedimentation control should be incorporated as early as possible in the initial design of a reservoir and

dam; it should not be left as an after thought. This paper discusses a new reservoir design philosophy, which tackles the problem of reservoir sedimentation control at the outset. Recently the use of a pipeline to transport the incoming or newly deposited sediment in the reservoir has been more commonly advocated. (Eftekharzadeh & Laursen 1990, Singh & Durgunoglu 1991, Hotchkiss & Huang 1994). A novel flushing system known as the Submerged Straight Weir Closed Conduit (SSWCC) system similar to that suggested by Singh & Durgunoglu (1991) has already been successfully studied at Bristol University.

This paper describes some results of a physical and mathematical model study of a new Submerged Labyrinth Weir Closed Conduit system, (SLWCC) replacing the proposed SSWCC flushing system. The submerged labyrinth weir acts to block the advance of the delta into the reservoir and helps to flush the sediment downstream, thus fully preserving the storage capacity between the submerged weir and the main dam as shown in Figure 1. A suitable pipe flow theory has been developed and compared with a series of laboratory experiments to explore the performance of the proposed flushing system when the reservoir is undergoing sedimentation. The results were compared to SSIIM, a 3-D mathematical model that is widely used in reservoir sedimentation modelling. This is a useful duplication in order to validate both the numerical and physical model, which could be used independently for assessing the performance of similar prototype sedimentation control systems.

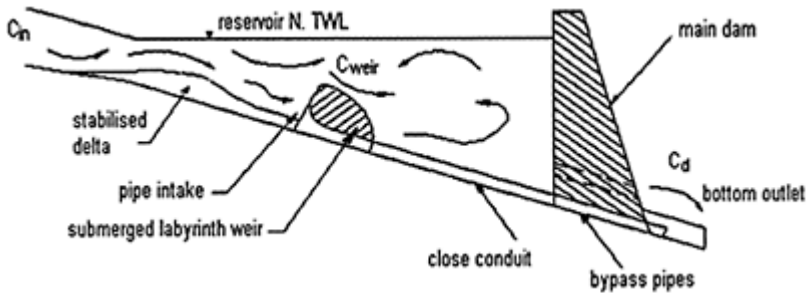


Figure 1. Submerged Labyrinth Weir Closed Conduit (SLWCC) flushing system.

2 PREVIOUS MODEL (SSWCC) AND MATHEMATICAL MODEL SSIIM

A previous SSWCC physical model study is described in Siyam (2000), where a submerged straight weir and intake with bellmouth entries is tested. In this design bypass pipes were also used to facilitate the flushing of the sediments from the straight weir to the downstream end of the main dam. The results obtained from this physical model have been compared to a 3-D Computational Fluids Dynamics (CFD) program called Sediment Simulation in Intakes with Multi-block option, SSIIM developed by Olsen in

1993. Two versions of the model, SSIIM 14 and 15b were used in this study. The software solves the Navier-Stokes equations with the $\kappa\text{-}\varepsilon$ model on a 3-D non-orthogonal structured grid and is specifically designed to solve water and sediment flow problems in rivers and reservoirs. Results are presented in graphical plots of velocity and sediment concentration fields with changes in channel geometry due to the morphological processes. In the previous study the simulated results obtained from SSIIM compared well with the results obtained from the physical modelling. The minor discrepancies in the mathematical and physical modelling of SSWCC were well explained and documented in Loveless & Siyam (2000).

3 NEW MODE—SUBMERGED LABYRINTH WEIR CLOSED CONDUIT SYSTEM (SLWCC)

Previous study of the SSWCC model has shown that it is feasible to reroute incoming sediments using a submerged weir and bypass pipes. However the limited reduction of trap efficiency of a whole reservoir system achieved in the SWCCC study prompted the authors to redesign the submerged weir. This new submerged weir should further increase the trap efficiency upstream of the weir hence preventing more sediment from moving into the deeper region of the reservoir. The design must also include flushing capability where the deposited delta formed in front of the weir can be flushed and subsequently carried downstream via the bypass pipes.

In this paper the authors propose a modified submerged labyrinth weir as the most suitable design both on the merits of its ability to increase the local trap efficiency and having effective flushing properties. The labyrinth design shown in Figure 2 is studied and results are compared to the previous SSWCC model. All experiments to date on the SLWCC model has been conducted in a rectangular flume 2360 mm long, 1560 mm wide and 380 mm deep. A general view of the SLWCC model set-up in the lab and a schematic layout of the flume are shown in Figures 3 & 4 respectively. A modified labyrinth weir 150 mm in height made from Perspex was constructed across the flume. Baffles were not used in the new model. However the inflow remains evenly distributed across the flume as the delivery pipe was made with many holes which produced the same effect as flow passing through baffles. The apron in the approach channel of the labyrinth weir has a slope of 7.5% to facilitate sediment flushing. The remaining part of the flume was horizontal. Special lightweight and fine plastic media ($D_{50}=145\text{ }\mu\text{m}$, specific gravity=1.5) was used to simulate the suspended sediment. The labyrinth model consisted of 5 equal sized channels. The width of each cycle was 300 mm. The

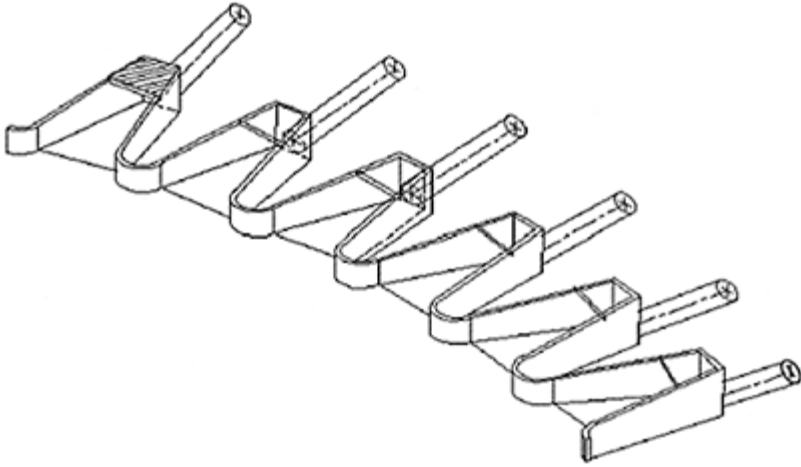


Figure 2. Modified labyrinth weir in flushing system.



Figure 3. Photograph showing SWLCC model setup in the laboratory.

labyrinth angle was fixed at 10 degrees. The approach apex was rounded off to minimise turbulence and to promote deposition in the immediate section upstream of the

submerged weir. Five Perspex pipes, each with an internal diameter of 45 mm were connected to the submerged weir to facilitate the bypassing of water and sediment. Perspex was chosen to ease visual observation of the mode of

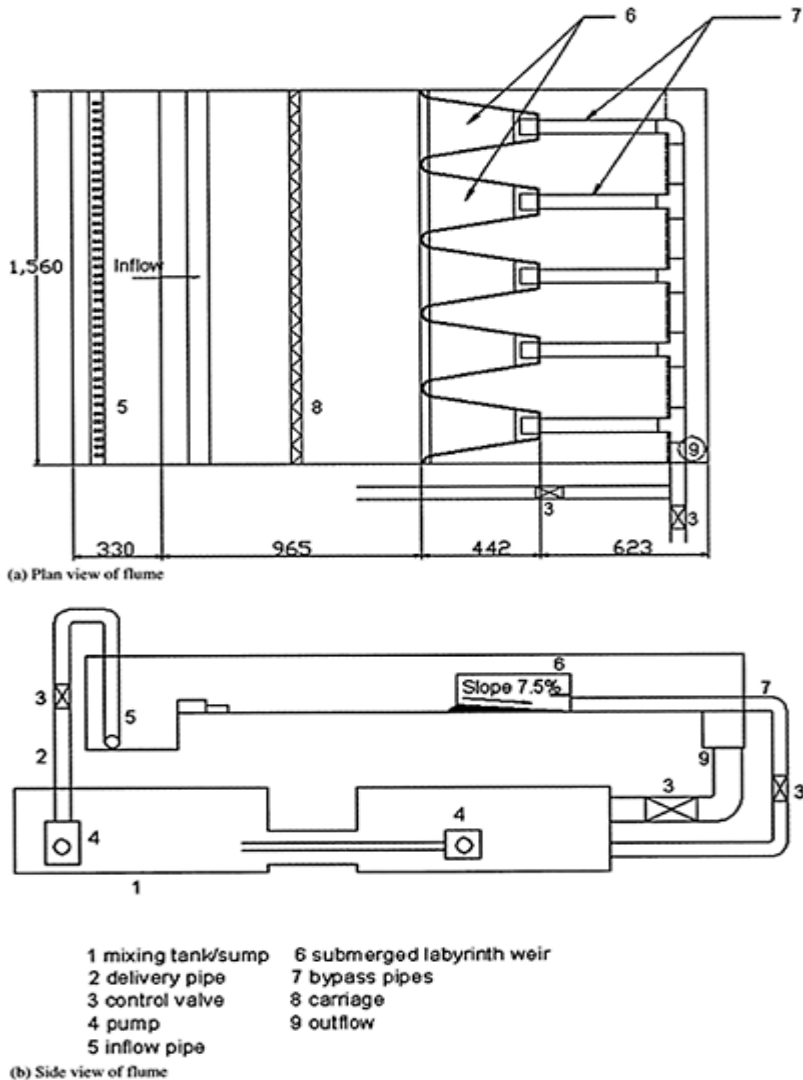


Figure 4. Schematic layout of the flume.

flow around the weir and in the pipes during operation. Each pipe has a flap gate acting as a flow control fixed onto the labyrinth weir at the end of the approach apron. All bypass pipes were connected to a manifold of similar size further downstream from the

weir. This enabled the combined outflow measurements to be taken when only one or many of the pipes were in operation. The flow passing through the reservoir and bypass pipes was returned to a sump tank before being recirculated to the flume by means of a single 40 l/s capacity pump. Also 2 separate 80 l/s pumps were used in the sump tank to mix and keep the sediment suspended. The inflow rate to the flume was adjustable by a control valve fitted to the delivery pipe. A two direction rolling carriage was used to hold all measuring equipment. An ADV probe was used to measure velocity profiles and to map the bed profiles. A turbidity meter was used to measure the concentration of the sediment-laden water while digital point gauges were used to measure the water levels. The inflow and bypass pipe discharges, Q_{in} & Q_p were measured using velocity meters connected to the intake pipe and the bypass manifold.

4 COMPARISON OF THE STRAIGHT WEIR AND LABYRINTH WEIR PERFORMANCE

As mentioned earlier the main objective of the experiments was to investigate and compare the new SLWCC model subjected to the same test conditions carried out on the SSWCC model. All the tests conducted on the SSWCC model published in Loveless & Siyam (2000) were duplicated and carried out on the new SLWCC model. In total 5 sedimentation runs and 2 clear water runs were carried out on the SLWCC model and results obtained were compared to the results obtained from the SSWCC model. A summary of all tests conducted is shown in Table 1. Clear water tests were conducted both to calibrate the initial configuration for the sedimentation tests and to assess the SSIIM performance in predicting flow patterns in the lab flume. Detailed description of tests CL1, CL2, 1, 2, 3, 8 and 11 carried out on the SSWCC model can be found in Loveless & Siyam (2000). The corresponding tests on the new SLWCC model were CLa, CLb, C, D, E, F, and G. These tests are briefly described in the following section. The only important difference between the tests was the total width (B) of the flume which in the first series of tests (SSWCC) was $B=750$ mm and in the second series (SLWCC) was $B=1560$ mm. This difference in the width was corrected by changing the actual flows in the 1560 mm wide flume from those indicated in Table 1.

The test procedures for all runs were similar except for the inflow discharge, amount of sediment, the outflow through the bypass pipes, initial bed level profiles and reservoir water levels were varied from one test to another. Sediment concentration in the flume during operation was measured using a turbidity meter. Samples of the inflow and outflow discharges were collected at regular intervals and their concentrations were measured later using the turbidity meter. In all the tests, bed profiles were measured before and after the test using the Acoustic Doppler Velocimeter, ADV probe. Sufficient time was allowed for the sediment to be deposited from suspension. All the experiments were found to give similar trend i.e. the measured concentration through the bypass pipes, C_p were higher and the measured concentration of the outflow C_d is lower for SLWCC when compared to SSWCC model.

Table 1. Summary of clear water and sedimentation tests.

SSWCC Test no	SLWCC Test no	Q_{in} (l/s)	Q_P (l/s)	Q_d (l/s)	Depth H(m)	Operation type
CL1	CLa	11.52	3.84	7.68	0.31	clear water
CL2	CLb	11.52	3.84	7.68	0.31	clear water
1	C	11.86	3.9	7.96	0.31	sedimentation
2	D	6.46	1.98	4.48	0.35	sedimentation
3	E	11.52	3.8	7.72	0.314	sedimentation
8	F	6.35	3.56	2.79	0.206	sedimentation
11	G	9.55	3.29	6.26	0.365	sedimentation

Q_{in} —inflow (l/s); Q_p —flow through bypass pipes (l/s)
 Q_d —outflow passing over submerged weir (l/s); H—reservoir depth at main dam/weir.

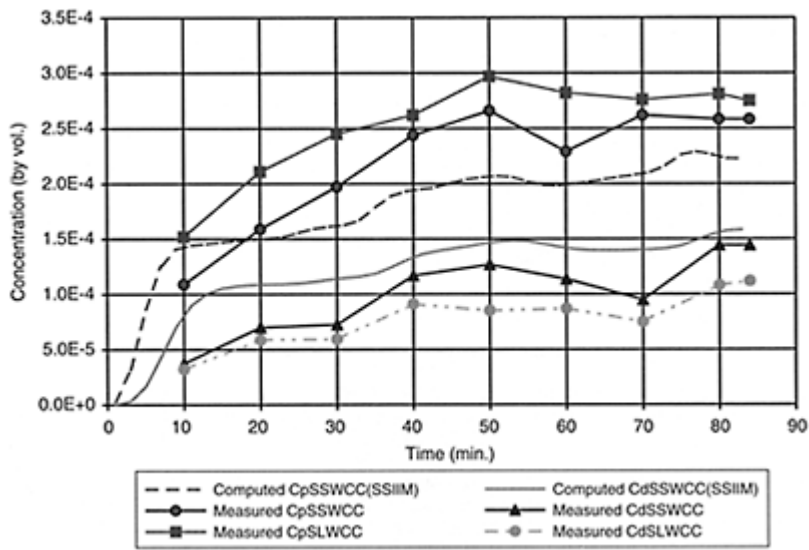


Figure 5. Comparison of the sediment concentration through the bypass pipes, C_p and the concentration of the outflow C_d for test 2 and the corresponding test D.

A detailed comparison of results is shown for test 2 and corresponding test D (Figure 5). It is observed that the sediment concentrations through the pipes in the SLWCC model,

C_{pSLWCC} were higher than the corresponding concentrations measured in the SSWCC model, C_{pSSWCC} . This is best explained by the increase of trap efficiency ahead of the labyrinth weir in the new design. Velocity profiles measured across the submerged labyrinth weir showed a greater drop in velocity close to the bed in front of the weir as opposed to the SSWCC model. The further reduction in velocity in the new design further promotes sedimentation ahead of the submerged weir. While it has been shown that the SLWCC system has the advantage over the SSWCC system in terms of stopping more sediment from moving downstream, it is also observed that the new system possesses great flushing ability. Experience in modelling reservoir flushing has shown that the region immediately in front of the outlets or bypass pipes is the most active region in the flushing condition where a cone of depression is formed and channels were incised into the formed delta. The shape of the modified labyrinth weir, which consists of a series of tapering channels (with apron slope), enhances the ability to flush the deposited sediment. In the presence of these channels the active zone of flushing has been extended further upstream from the weir when compared to the previous model. As a result more sediment was agitated and carried through the bypass pipes. While concentration immediately downstream of the labyrinth submerged weir was observed to be slightly higher mainly due to the presence of nappe interference from the labyrinth weir creating extra turbulence in the flow preventing the sediment from settling, the overall outflow concentration C_d downstream was in fact lower in the new model. The lower measured C_d value in the SLWCC model compared to the SSWCC model confirms that more sediment is now trapped by the submerged weir resulting in less sediment flow passing over the weir.

5 DISCUSSIONS AND CONCLUSIONS

The comparison of the overall performance of the SLWCC model and the SSWCC model undergoing sedimentation tests is summarised in Table 2. The table presents the computed and measured overall trap efficiency (η) for each run. Trap efficiency is taken as the percentage of the inflow

Table 2. Summary of measured and computed trap efficiencies for the five sedimentation tests.

Description	SSWCC		SLWCC		SSWCC		SLWCC	
	Run 1		Run C		Run 2		Run D	
	measured	SSIIM	measured	SSIIM	measured	SSIIM	measured	SSIIM
Inflow sediment (kg)	62.77	62.32	62.77		58.55	61.00	58.55	
Outflow through pipes (kg)	5.15	4.71	8.98		3.16	2.63	4.6	
Outflow over weir (kg)	4.72	4.27	3.81		3.29	4.02	3.15	
Overall trap efficiency	84.27	85.58	79.62		88.99	89.11	86.77	
Trap efficiency without pipes	90.01	90.88	90.18		92.66	91.40	92.02	

Reduction in trap efficiency	5.74	5.30	10.56	3.67	2.29	5.25
Run time (mins)	39.00	43.50	39.00	84.00	84.00	84.00
Percentage of bypass flow	32.88	32.88	32.88	30.65	30.65	30.65
	Run 3		Run E	Run 8		Run F
Description	measured	SSIIM	measured	measured	SSIIM	measured
Inflow sediment (kg)	76.77	82.38	76.77	45.03	44.44	45.03
Outflow through pipes (kg)	12.06	13.21	16.50	5.48	4.92	8.28
Outflow over spillway (kg)	11.21	14.39	10.98	1.05	1.52	1.04
Overall trap efficiency	69.69	66.50	64.21	85.50	85.51	79.3
Trap efficiency without pipes	80.58	76.77	81.20	96.36	94.66	95.48
Reduction in trap efficiency	10.89	10.27	16.99	10.86	9.15	16.18
Run time	88.00	88.00	88.00	32.00	32.00	32.00
Percentage of bypass flow	32.99	32.99	32.99	56.06	56.06	56.06
	Run 11		Run			
Description	measured	SSIIM	measured			
Inflow sediment (kg)	20.33	22.00	20.33			
Outflow through pipes (kg)	1.55	1.23	2.23			
Outflow over spillway (kg)	1.28	1.37	1.09			
Overall trap efficiency	86.06	88.19	83.66			
Trap efficiency without pipes	91.51	91.62	92.04			
Reduction in trap efficiency	5.44	3.42	8.38			
Run time	20.50	20.00	20.00			
Percentage of bypass flow	34.45	34.45	34.45			

sediment deposited in the reservoir. The trap efficiency without the submerged weir and bypass pipe system was calculated assuming that the flow concentration would be that measured or computed from the outflow discharge flowing into the sump tank. The reduction in η_3 due to the bypass system is taken as the difference between these two trap efficiencies.

It has been shown that the new model of SLWCC provides a larger reduction in η for the whole reservoir system when compared to the SSWCC model. On average the reduction in η in a reservoir system provided by the SLWCC model is about 50% higher than that of the SSWCC model. However both reductions in η are still considered low. One of the main reasons was most of the sediment was deposited in the upper region near the flume inlet. As a result the sediment concentrations that reached the submerged dam were low. This trend of exponential decay is widely accepted and consistent with the

observations of many other researchers (Siyam 2000). It is also worth pointing out that the main purpose of this facility is to stop the advancement of the deposited sediment further downstream and to preserve the volume between the submerged weir and the main dam. In this context it has been demonstrated that the use of the SLWCC system for the mitigation of reservoir sedimentation shows great promise in many cases and merits further research. While this paper only highlights the plus performance of submerged weirs subjected to deposition tests, an equally important factor for an efficient system of submerged labyrinth weir lies in the ability to flush successfully the deposited sediment. Such tests and results will be reported in future work.

REFERENCES

- Bechteler, W. 1996. Sedimentation in Low Head Reservoirs. *International Journal of Sediment Research* 11(13).
- Eftekharzadeh, S & Lauren. M. 1990. New method for removing sediment from reservoirs. *Journal of Hydro Review*: 80–84.
- Hay, N & Taylor, G. 1970. Performance and design of labyrinth weirs. *Journal of Hydraulic Engineering* 96 (11): 2337–2357.
- Hotchkiss, R.H. & Xi Huang. 1994. Reservoir sediment removal: Hydrosuction Dredging. *International Conference on Hydraulic Engineering*.
- Loveless, J.H & Siyam, A.M. 2000. Model assessment of a novel system of reservoir sedimentation control. *Proceedings of the Eighth International Symposium on Stochastic Hydraulics*. Beijing, China. 403–410.
- Mahmood, K. 1987. Reservoir Sedimentation: Impact, Extent and Mitigation. World Bank Technical report number 71. The World Bank, Washington, D.C.
- Olsen, N.R.B. 1997. A Three-Dimensional Numerical Model for Simulation of Sediment Movements in Water Intakes with Multiblock Option. SSIIM User's Manual, Version 21.5a. Division of Hydraulic Engineering, The Norwegian Institute of Technology.
- Olsen, N.R.B. 1999. Two Dimensional Numerical Modelling of Flushing Processes in Water Reservoirs. *Journal of Hydraulic Research* 37 (1): 3–13.
- Patankar, S.V & Spalding, D.B. 1972. A Calculation Procedure for Heat, Mass and Momentum Transfer in three-dimensional Parabolic Flows. *International Journal of Heat Mass Transfer* 15:1787.
- Singh, K.P & Durgunoglu, A. 1991. Remedies for sediment buildup. *Journal of Hydro Review* 90–97.
- Siyam, A.M. 2000. Reservoir Sedimentation Control. PhD Thesis. University of Bristol, U.K.
- Tullis, J.P. 1995. Design of Labyrinth Spillway. *Journal of Hydraulic Engineering* 121 (3): 247–255.

Numerical and physical modelling concerning the removal of sediment deposits from reservoirs

H.Scheuerlein

Univ. Prof. Dr., University of Innsbruck, Austria

M.Tritthart

Dipl. Ing., University of Technology, Vienna, Austria

F.Nuñez Gonzalez

Research Associate, National University of Mexico, Mexico

Hydraulics of Dams and River Structures—Yazdandoost & Attari (eds)

© 2004 Taylor & Francis Group, London, ISBN 90 5809 632 7

ABSTRACT: Removal of sediment deposits from reservoirs by means of flushing through lowlevel outlets is a widely used method to regain storage volume. However, the efficiency of flushing is very often highly overestimated. Flushing can only be effective when it is combined with substantial water level drawdown. However, even at favorable conditions and unregarded the excavation level which might have been reached, the lateral extension of flushing is rather limited. Analytical treatment of flushing processes is difficult due to the three-dimensional flow pattern in the vicinity of the flushing outlets, and due to the high number of parameters involved in the phenomena. In order to estimate flushing efficiency, a simplified approach was set up which was merely based on continuity equation applied on a 3D-grid of streamlines and isotachs, and on some stability criteria for granular sediment deposits against flow-induced eroding forces. The simplified approach rendered promising results. It could be proved very clearly that the lateral extension of the excavation must necessarily be restricted to a limited zone close to the outlet unless the water level is lowered drastically. In a separate approach, a 3D numerical model based on FVM was applied to evaluate the justification of the simplified approach. The simulation showed good agreement with the simplified approach as far as flushing at high water level was concerned, but rather poor agreement at water level drawdown. In addition to the two numerical approaches in a third step a physical

model was applied. As expected, the agreement with the simplified approach and the 3D FVM simulation was satisfactory for high water level conditions. The comparison of the three approaches with respect to flushing efficiency at drawdown is discussed.

1 INTRODUCTION

Sedimentation of man-made reservoirs is one of the most serious problems in dam engineering. In spite of considerable efforts to minimize sediment yield from the watershed by means of erosion control or check dams, the intrusion of sediment into the reservoir can never be avoided completely. Sediment enters the reservoir together with the river flow either as bedload or as suspended load. The coarse material moving close to the bed settles at the reservoir entrance forming a delta. Material moving in suspension is carried further and deposits rather uniformly all over the reservoir. Sometimes at favorable circumstances the entering sediment can be kept in suspension and sluiced through the reservoir towards downstream before it settles down (turbidity currents).

Unregarded how successful one may be in minimizing sediment yield and in sluicing turbidity currents the deposition of sediment in the reservoir will never be totally preventable. Once the sediment has settled down in the reservoir, its removal is difficult though not impossible. Besides applying costly dredging techniques there is also the possibility to take advantage of the available potential of the backed-up water in the reservoir which can be used for remobilization of the deposits and for flushing using the bottom outlet of the dam.

Removal of sediment deposits from reservoirs by opening the bottom outlet of the dam is practiced worldwide with largely varying success. The efficiency of flushing depends significantly on the water level in the reservoir during flushing action. Flushing at normal operational water level, i.e. without water level drawdown is rather ineffective. In general, it can be noted that flushing efficiency is mostly overestimated. This applies not only for flushing at high water level in the reservoir but also when the action is combined with water level drawdown. It must be suspected that the estimation of flushing efficiency is often governed by desire rather than by objective consideration (Scheuerlein, 1987).

2 SIMPLIFIED APPROACH TO ESTIMATE FLUSHING EFFICIENCY

Theoretical treatment of flushing processes is difficult for various reasons. The mechanism is complex and partly three-dimensional, verification of the numerous parameters involved is problematic due to the stochastic character of water and sediment data, random effects are hard to predict, etc.

In 1993 a simplified analytical approach was presented by Scheuerlein to identify the governing parameters of flushing actions and to develop criteria for the evaluation of the efficiency of flushing actions (Scheuerlein, 1993). The analysis is based on basic hydraulics applied to a three-dimensional grid of streamlines and isotachs combined with

some stability criteria of sediment deposits against flow induced eroding forces (Figure 1).

Referring to the notations given in Fig. 1 the application of the law of continuity by comparing the cross-section at the bottom outlet (Torricelli's law) and the cross-section at the distance r from the bottom outlet (assuming sphere-shaped isotachs), the following equation can be derived.

$$\frac{r}{D_G} = \frac{1}{2} \sqrt{\frac{\mu_G \sqrt{2gH_0}}{v_r}} \quad (1)$$

with r being the radial distance of the a sphere-shaped isotach from the bottom outlet, D_G being a diameter of the circular shaped bottom outlet, μ_G standing for a coefficient summarizing all possible losses at the outlet, H_0 representing the pressure head above the outlet, g the acceleration due to gravity, and v_r the flow velocity corresponding with the distance r of a quarter sphere shaped isotach from the outlet.

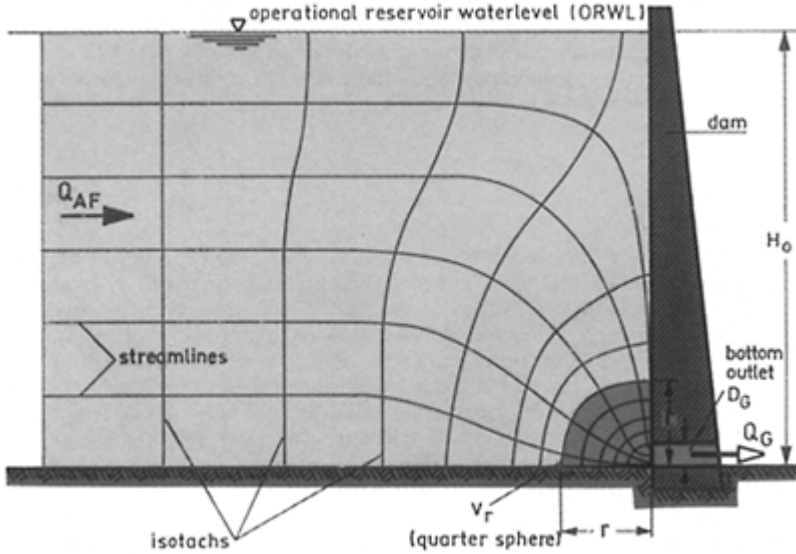


Figure 1. Simplified flow pattern at bottom outlet.

As distance r and flow velocity v_r are indirect proportional parameters, increasing distance means decreasing velocity. Sediment deposited in front of the outlet will be remobilized when the flowinduced forces exceed the resistance of the deposits. In this approach the criteria of Hjulstrom is used given as graph showing threshold velocity v_c versus grain size d_s (Scheuerlein, 1993). Substituting v_r by v_c , and r by r_c in (equ. 1), r_c represents the critical distance from the outlet within which a particle d_s can be remobilized. Figure 2 shows a case with a hypothetical sediment deposition which has reached already the bottom outlet. The remobilization has already taken place and a

funnel-shaped crater has developed in front of the outlet and stabilized at the distance r_c . The front slope of the crater should approximately correspond with the angle of repose β of the deposits. As soon as this stage is reached no further excavation of deposits will take place unless the water level will be lowered. It should be noted that even with water level drawdown for some time no further progress of excavation will occur as r_c is proportional to H_0 (equ. 1). In order to start excavation again a level somewhat above the sediment deposits (EFWL=effective flushing water level) must be reached.

With some simplifying premisses also for this stage of flushing a simplified approach was developed (Scheuerlein, 1993). With assumption of horizontal surface of the deposits (level H_s) and uniform approach flow towards the semi-circular rim of the crater (result of stage I), and introducing the threshold condition for beginning erosion as $V_{AF}=V_c$, one can derive a simple equation for the threshold drawdown (level HEF) at which stage 2 of the flushing process starts

$$H_{EF} = H_s + \frac{1}{2} \left(\frac{K D_G^2}{v_c} \right)^2 + \frac{K D_G^2}{v_c} \sqrt{H_s + \frac{1}{4} \left(\frac{K D_G^2}{v_c} \right)^2} \quad (2)$$

with K standing for

$$K = \frac{\mu_G \sqrt{2g}}{4 \left(\frac{H_s}{\tan \beta} + r_c \right)} \quad (3)$$

where r_c represents the final stage of flushing without water level drawdown according to equ. (1).

The simplified approach shown above may be used to reveal at least qualitatively the mechanism and the limits of flushing actions. Its usefulness for quantitative estimation of flushing efficiency with and without water level drawdown was still to be proved. Particularly, the simplifications incorporated in the analysis for water level drawdown left considerable room for uncertainties and questions. The investigations presented in the following chapters are used to evaluate the performance of the straight forward simplified approach by applying more sophisticated methods.

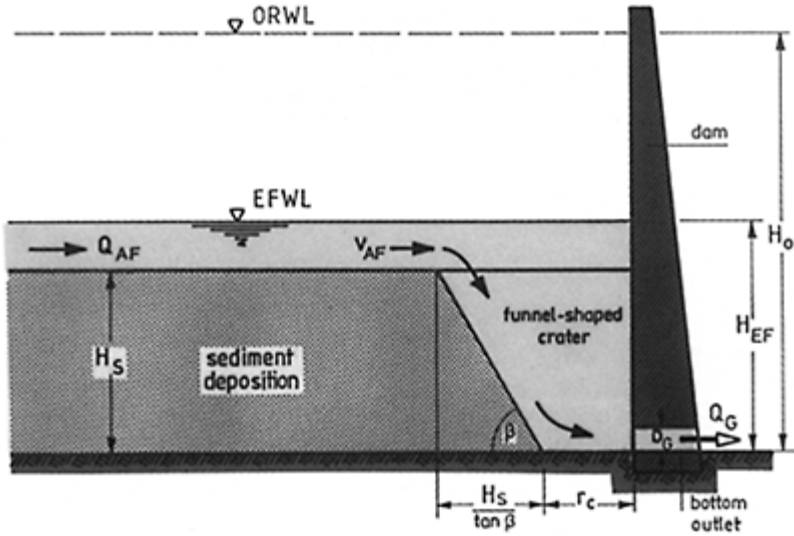


Figure 2. Flushing action at water level drawdown.

3 NUMERICAL MODELLING OF FLUSHING ACTIONS WITH 3D FVM

The approach presented in this chapter was carried out in the frame of a final project (Diplomarbeit) at the University of Innsbruck by Michael Tritthart (Tritthart, 2000).

3.1 Numerical model

In a numerical study the three-dimensional Finite Volume software SSIIM was used, developed by Olsen (2002). It solves the Reynolds-averaged Navier-Stokes equations to compute the water flow, using $k-\varepsilon$ turbulence closure (Rodi, 1984) and the SIMPLE method (Patankar, 1980) for determining the pressure field. As boundary condition at the bed and walls, the wall law for rough boundaries (Schlichting, 1979) is used. In order to compute the transport of sediments, the software simultaneously solves the convection-diffusion equation, using van Rijn's equations for sediment concentration near the bed (van Rijn, 1984b) and bed load transport (van Rijn, 1984a). SSIIM is available in two versions, allowing for both structured and unstructured grids to be used in the modelling process. Due to the nature of the problem investigated in this study, the version for unstructured grids was used.

3.2 Model geometry, properties and study cases

A simplified reservoir geometry as illustrated in Figure 3 was set up for the numerical study (Tritthart, 2000). The reservoir is of hexahedral shape, measuring 200 m in length, 100 m in width, with an initial water level of 60 m above ground. Half of the reservoir's height is filled with sediment that is characterized by an angle of repose of 35 degrees, with the average grain size diameter being varied throughout the study. The low-level outlet consists of a single rectangular opening, sized 2×2 m, with its lower edge situated at the bottom of the reservoir. In an approach to simulate the model being part of a larger reservoir, an inflow area was designed at the upper boundary, and flow continuity was enforced by setting the total inflow equal to the outflow through the low-level outlet.

Since grid refinement in the vicinity of the low-level outlet led to very unstable model behavior, the computational grid had to be chosen such that the maximum cell area in a cross section did not exceed the actual size of the outlet. Therefore, the grid was made up of 50 longitudinal sections and 50 cross sections with up to 30 layers in the vertical direction, resulting in hexahedral cell sizes between 4×2×1 m and 4×2×2 m. Wedge-shaped cells were used to spatially decompose the inclined portion of the sediment body. Even though such an approach is prone to lead to

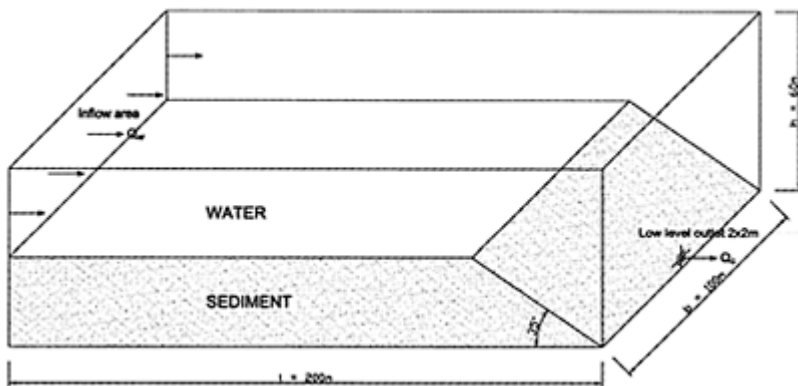


Figure 3. Reservoir geometry in the numerical study.

numerical instabilities, it performed better than allowing hexahedral cells to follow the bed because of the distortion to the elements in case of erosion taking place. At the bottom of the reservoir, an unerodible layer was introduced.

In the study, the average sediment grain size diameter d_s was varied between 0.0025 mm and 25.0 mm in steps of one order of magnitude. However, since cohesion effects that could not be taken into account in the numerical study were adversely affecting the results, only sediments larger than 0.25 mm in grain size diameter were finally considered useful for investigation. Rubey's equation (Rubey, 1933) was used to

compute the sediment settling rate from the average grain size, needed as input to the numerical model.

For the full set of grain sizes, in principle two different cases were investigated. A steady case with a fixed water level of 60 m above ground, used to simulate the effect of flushing without water level drawdown, and an unsteady case with step-wise water level drawdown from 60m above ground to the sediment layer at 30m. Assuming pressure-induced outflow for all relevant cases, discharge through the bottom outlet was calculated using Torricelli's equation with an inlet efficiency coefficient of 0.58. This assumption leads to a discharge of $80 \text{ m}^3/\text{s}$ at maximum water level, and approximately $56 \text{ m}^3/\text{s}$ at the lowest water level investigated in this study.

3.3 Calculations

In a first step, some parameters and components of the numerical model had to be adjusted to yield useful results: size and shape of the inflow area and treatment of the free surface condition, especially in the unsteady cases.

The overall shape of the inflow area of the model heavily influences the flow conditions and morphological changes in the vicinity of the upstream boundary of the reservoir. Best agreement with the natural situation was finally found with an inflow area occupying approximately one third of the total upstream boundary, coupled with an additional unerodible layer on top of the first couple of meters of the sediment body in order to avoid local scour effects to take place in that region affecting the results further downstream the reservoir. Local recirculation areas in the reservoir corners near the inflow, induced by the choice of location of the inflow area, did not influence the results in the area of interest in the vicinity of the low level outlet.

The numerical model unfortunately showed instabilities when transient computations were performed with free surface conditions being enabled at the same time. In order to overcome this problem, the free surface option was disabled and all computations were performed using an immovable surface. While the results of the steady state variants were not influenced to a notable extent by this simplification, the unsteady cases had to be subject to some modifications. The water level was drawn down manually in steps of 5 m from 60 to 40 m above ground, and steps of 2 to 1 m below that level. This was done by modifying the grid using an external program after steady state was reached in the transient computations of each water level, and using the altered computational grid for the next step.

3.4 Results

Results of the study for cohesionless sediments are being presented in Figure 4, where the radius of the flushing crater, defined as flushing range in the simplified approach of Scheuerlein (1993) is plotted versus the grain size diameter. This comparison is justifiable since for granular material the vertical projection of the flushing crater appears to be almost circular in the numerical results, right as assumed for the simplified approach, thus a radius can be defined.

A good agreement of the results of the steady case without water level drawdown with the simplified approach can be seen for average grain size diameters of 2.5 mm and

above, whereas the agreement for smaller grain sizes is not satisfying. This effect is explicable by the fact that the simplified approach assumes the isotachs to be distributed in the shape of a quarter sphere in the vicinity of the outlet of the reservoir, but the numerical results have shown that the larger the flushing crater becomes, the isotachs move towards ellipsoidal shape, no longer satisfying the requirements for the simplified calculation. Therefore the agreement is best for smaller flushing craters at large grain size diameters and becomes worse for larger craters at small grain sizes.

The results for the unsteady cases after water level drawdown showed that the radius of the final flushing crater was approximately twice the size of the flushing range in the steady cases without water level drawdown, being consistent over all grain sizes investigated in the presented study.

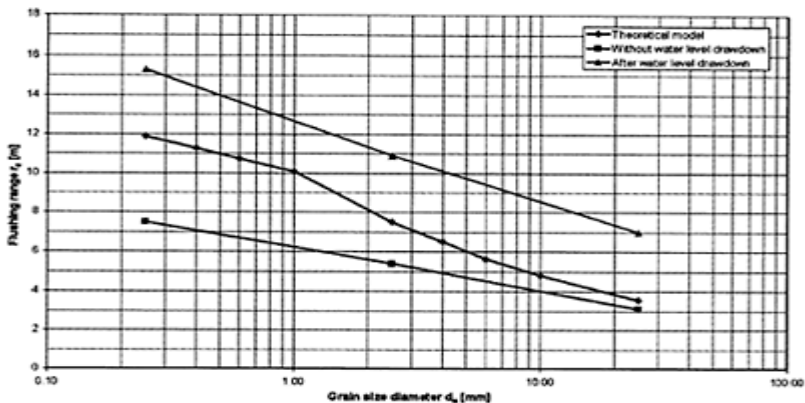


Figure 4. Flushing range with and without water level drawdown dependent of the grain size diameter.

However, it appears that the results of the simplified approach fit well into the range defined by the results of the numerical investigations with and without water level drawdown.

By making use of the simplified approach, also an effective flushing water level can be defined at which erosion of the sediment top layer becomes effective in case of a water level drawdown. In a final step, the results of the simplified approach regarding this water level were compared to those gathered from the numerical study, but no satisfying agreement could be found. To a high extent, this may be due to the inappropriate water level drawdown method chosen in the numerical study, but also due to the fact that the water level at which erosion starts again could only be defined by visual interpretation of the numerical results.

4 HYDRAULIC MODEL TESTS ON RESERVOIR FLUSHING

The model study presented in this chapter was executed at the Hydraulics Laboratory of the University of Innsbruck in the frame of the MSc study of Francesco Nuñez Gonzalez from the National University of Mexico (Nuñez Gonzalez, 2003).

In order to analyze the main characteristics of reservoir flushing technique and to obtain conclusions about the interaction between the different variables involved, diverse tests were carried out in an experimental setup. The model used did not represent a scaled physical model for a specific reservoir in the field, but an idealized silted reservoir in which sediment deposition has reached the bottom outlet. Flushing with high water levels in the reservoir and flushing with water level drawdown were tested with three bottom outlets of different sizes.

4.1 Experimental setup

The model used for the experiments simulated a rectangular reservoir, in which sediments have reached the dam and accumulated regularly along the reservoir, so that the top layer of the sediment deposits was flat and horizontal at a certain height over the low-level outlet. Two out of three tested outlets had a square section of 5 and 10 cm sides respectively and the third one had a 5×2.5 cm rectangular section, obtained by closing the 5×5 outlet half. The outlets were opened and closed by a plastic plate sliding rapidly up and down on rails attached to the front wall that simulated the dam. Water was supplied by a 0.2 m diameter tube situated at the base of the model. An electronic flowmeter at the model entrance regulated the flow rates, while a triangular spillway at the model exit was used for control. Discharges for the different tests varied from 1 l/s, for the smallest outlet, to 24 l/s for the biggest one. The highest possible water level above the center of the outlets was 53 cm. The sediment used was quartz sand, with a 0.884 mm mean diameter, 1.77 geometric

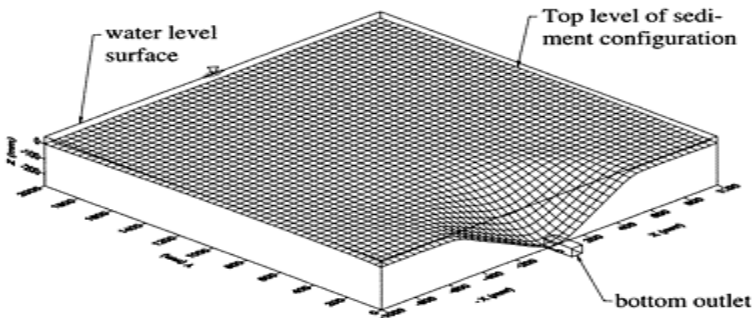


Figure 5. Schematic view of the flushing crater configuration after the

first stage of an experiment: flushing without water level drawdown.

standard deviation and 2.7 relative density. Its submerged repose angle was approximately of 35° . Measurements of the sediment profile were performed with an optic electronic device.

4.2 Model parameters and test procedure

For each of the three bottom outlet sizes tests were performed in two stages. The first stage was dedicated to study the variation of flushing extension for different high water levels in the reservoir, while during the second one, water level was drawn down in order to determine the water level at which sediment removal begins and to observe the main features of the flushing process when back-cutting erosion occurs.

At the first stage of the experiments, the reservoir was slowly filled with water to the water level H_0 to be tested. When the water level reached the required H_0 , the outlet was opened and it was closed only when no further particle motion was observed. Then, the incoming discharge was set to zero and the sand configuration in front of the outlet was surveyed with the optic device. The procedure was repeated for different water levels, which were increased gradually by controlling the inflow discharge.

The second stage of the experiments began with a high water level in the reservoir, a constant inflow discharge and the sand configuration as it was left after the last step at the first stage of the experiment. After opening the flushing outlet, the inflow discharge was slowly decreased, as a consequence of which the water table in the reservoir descended at short steps. The moment particle motion was perceived on the sediment deposit in front of the outlet, the water level was registered and the inflow discharge was set constant and with a value that corresponded to a water level equal or lower than the level of the sediment deposits for the corresponding outlet. Also, from that moment on, time was taken to register chronologically the evolution of the sediment deposit configuration. At short intervals a survey of the bed profile, at different distances from the outlet, was performed, along the perpendicular axis to the dam. At the end of the experiment, the width of the developed flushing channel was measured. For all tests, the hydraulic conditions in the flushing outlet were pressurized flow, that means, the water stage in the reservoir never was lower than the top level of the outlet.

4.3 Experimental results

Experimental flushing with high water levels in the reservoir confirmed that the action is limited to the development of a funnel shape crater in front of the outlet. Figure 5 shows a schematic 3D view of the crater, reconstructed using the data of the survey for one of the experiments performed. Development of the flushing crater, at the first stage of the tests, appeared to be an extremely fast process, which varied from 30 to 50 seconds for the range of values tested in the physical model. From the measured points of the crater configuration, it was found, on the one hand, that the slopes of the crater were always similar to the repose angle of the submerged material. On the other hand, the plan shape of the curve described by the crater over the sand surface was close to half a

circumference, while the horizontal curve at the level of the outlet was closer to half an ellipse.

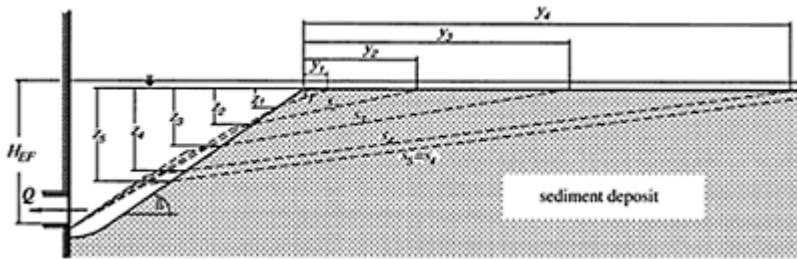


Figure 6. Schematic development of the flushing process with water level drawdown.

An explanation for this behavior is that, at the outlet level, the extension of the eroding capacity is approximately equal in all directions from the outer limits of the outlet; that means, the distance until which sediment can be removed, is the same in front of the outlet and at its sides and thereby the longitude of the outlet base decides to some extent the final geometry of the curve. Only if the longitude of the outlet base were zero, that is, a suction line (vertical group of consecutive sinks), then the shape of that curve would be a circumference.

Comparisons with the simplified approach described in chapter 2 showed a good agreement as far as the lateral dimensions of the crater were concerned. Nevertheless, to increase accuracy, adjustments should be made to account for a better description of the 3D-grid of streamlines and isotachs because, as it was experimentally demonstrated, strictly the 3D of isotachs would not describe a sphere but an ellipsoid. In agreement with the simplified approach, the experimental tests showed that the crater size depends strongly and directly on the flushing outlet dimensions, much more than on the water level over the outlet.

Experimental tests proved that once the crater for the highest water level in the reservoir was formed, no further sediment motion was possible unless the water level was substantially lowered until it was close to the surface of the sediment deposit. The effective flushing water level EFWL, that is, the minimum water level drawdown for which there would be sediment motion near the crater, was very similar for tests with the same bottom outlet, but had a slight variation between different outlet sizes, since, at the same water level, the larger the size of the outlet, the larger the flow velocity in the reservoir, thus the EFWL grows with the size or discharge capacity of the flushing outlet. This behavior was well reproduced by the simplified approach, showing average calculated values of the relation $EFWL/DH$ (DH =hydraulic diameter of the outlet) of 0.18, 0.27 and 0.29 for the 2.5, 5 and 10cm base outlets, respectively, while the average $EFWL/DH$ values obtained experimentally were 0.24, 0.36 and 0.43, respectively.

After the beginning of sediment motion near the crater, excavation of the bed proceeded rapidly through back-cutting erosion, until an apparent equilibrium was

reached for which the slope of the bed tended to be constant. Figure 6 describes this process with an idealized scheme of what was experimentally observed. In this scheme, subscripts for the variables correspond to the stage of the process with respect to time. Time zero (t_0) corresponds to the beginning of sediment motion; at that time the depth of excavation near the crater (z_0) with respect to the original horizontal level, was zero. Sediment transport began on the apex of the crater and quickly extended laterally, while sediment was carried into the crater, filling it progressively. Thus, the diameter of the crater diminished and its plan shape deformed tending to become elliptical. The geometry of the crater reached an equilibrium when the base of the front material was close to the outlet and its slope tended to be equal to the repose angle of the submerged material. The slopes of the bed, on the profile in front of the outlet, were very steep in the beginning of the process, but gradually their angle decreased, until at a certain time t_e an apparent equilibrium was reached for which the slopes tended to be constant, while erosion proceeded in a more stable development. Erosion of the sediment deposit in the reservoir during the very initial moments of the back-cutting erosion process was general in the areas near to the crater, but soon a straight flushing channel developed and erosion concentrated between its limits. The channel widths varied from 30 to 200 cm, and apparently the most important parameter to define its size was the water discharge passing through the reservoir, as channel width increased with the size of the outlets. For the moment at which equilibrium is reached, there appears to be a relation between the water discharge, sediment size, flushing channel width and energy slope that determines the sediment discharge passing through the outlet.

5 COMPARISON OF RESULTS

In this paper three different approaches to evaluate flushing efficiency are presented, namely

- (1) a simplified analysis using basic hydraulics,
- (2) a numerical model using 3D FVM simulation,
- (3) a hydraulic model study.

It was to be expected that the simplified analysis would necessarily have deficiencies compared with the more sophisticated approaches using numerical and physical modelling. The performance of the three approaches shall be compared by means of the two principally differing scenarios: flushing without and with water level drawdown, respectively.

5.1 *Flushing without water level drawdown*

The formation of a funnel-shaped crater in the vicinity of the bottom outlet was generally confirmed by all three approaches. However, the assumption of a sphere-shaped grid of isotachs and streamlines in (1) was slightly corrected by (2) as well as (3) in an ellipsoidal pattern which makes sense as the shape of the bottom outlet (circular in (1), rectangular in (2) and (3)) should have some influence. Comparison of (1) and (2) shows better agreement for larger grain sizes of deposits ($d_s > 2.5$ mm) than for smaller ones.

This deviation may be explained by the fact that (1) works with Hjulstrom (Scheuerlein, 1993) and (2) with Rubey (1933) criteria of cohesion, respectively. The assumption concerning the slope angle of the funnel-shaped crater as equivalent to the angle of repose of the deposits in (1) is also confirmed by (3).

In summary it may be stated that there is no serious disagreement between the three approaches dealt with in this paper.

5.2 Flushing with water level drawdown

Considering the case of flushing with water level drawdown there was in principle agreement of (1) and (3), at least in such that an effective flushing water level (EFWL see chapter 2) should exist. However, the simplified analysis describing the calculation of this level seems to contain some deficiencies. In (3) it was confirmed that a strong correlation of EFWL and outlet size exists indeed, but that the development of the channel incised into the deposits is an unsteady process which is not considered in (1). The back-cutting erosion process of the channel with continuously decreasing slopes proceeds until equilibrium of discharge and channel slope is reached (see also Fig. 6 in chapter 4). In (3) it was also confirmed that the lateral extension of the flushing action was restricted to a width which was rather in the order of magnitude of the width of the outlet than to the size of the reservoir.

Comparison of (1) and (2) does not show satisfying agreement for flushing with water level drawdown. According to Tritthart (2000), the cause may be the method of water level drawdown chosen in the numerical study or the problem to identify the water level (EFWL) at which erosion starts again.

6 CONCLUSIONS

Summarizing the findings derived from the different approaches to describe flushing actions through low-level outlets flushing efficiency is governed by the following parameters:

- the capacity of the low-level outlets
- the water level in the reservoir
- the time of the flushing action

Flushing actions at operational reservoir water level (ORWL) are restricted to very limited efficiency. As soon as the funnel-shaped crater in front of the outlet has developed the action has reached its final stage. For cohesionless material the slope of the crater corresponds with the angle of repose of the deposited material.

For successful continuation of the flushing action drawdown of the water level is compulsory. At water level drawdown the flushing action will not be continued until a certain stage of water level has been reached (EFWL, effective flushing water level). Remobilization of deposits will only start when the drag forces of the flow approaching the bottom outlet are capable to start back-cutting erosion at the rim of the funnel-shaped crater. This means that the EFWL has to come very close to the surface of the sediment deposits.

The back-cutting erosion is an unsteady process and its lateral extension is very limited, rather corresponding with the size of the bottom outlet than with the width of the reservoir.

REFERENCES

- Núñez Gonzalez, F. (2003) Lavado de sedimentos en embalses azolvados, MSc Thesis, Universidad Nacional Autonoma de Mexico.
- Olsen, N.R.B. (2002) A three dimensional numerical model for simulation of sediment movements in water intakes with multiblock option. User's manual, The Norwegian University of Science and Technology, Norway.
- Patankar, S.V (1980) Numerical Heat Transfer and Fluid Flow. Taylor & Francis Publ.
- van Rijn, L.C. (1984a) Sediment Transport Part I: Bed load transport. *Journal of hydraulic engineering*, Vol. 110, No. 10.
- van Rijn, L.C. (1984b) Sediment Transport Part II: Suspended load transport. *Journal of hydraulic engineering*, Vol. 110, No. 11.
- Rodi, W. (1984) Turbulence models and their application in hydraulics. IAHR state-of-the-art publication.
- Rubey, W.N. (1933) Settling velocities of gravel, sand and silt particles. *Amer. Jour. Sci.*, Vol. 25.
- Scheuerlein, H. (1987) Sedimentation of Reservoirs—Methods of Prevention, Techniques of Rehabilitation, First Iranian Symposium on Dam Engineering, Tehran.
- Scheuerlein, H. (1993) Estimation of flushing efficiency in silted reservoirs. Proceedings of the First International Conference on Hydro-Science and Engineering, Washington D.C., USA.
- Schlichting, H. (1979) Boundary-layer theory. McGraw-Hill.
- Tritthart, M. (2000) Anwendung von dreidimensionalen numerischen Methoden beim Sedimentmanagement in Talsperrenreservoirs. Master's thesis, University of Innsbruck, Austria.

Application of fine sediment behavior to sedimentation management in Miwa Dam, Japan

M.Umeda & M.Okano

Japan Water Resources Environment Technology Center, Tokyo, Japan

G.Yokomori

Ministry of Land, Infrastructure and Transport of Japan, Nagano, Japan

Hydraulics of Dams and River Structures—Yazdandoost & Attari (eds)

© 2004 Taylor & Francis Group, London, ISBN 90 5809 632 7

ABSTRACT: Sediment bypass systems have recently been planned and constructed in several reservoirs as effective countermeasures against sedimentation. Nowadays how to control the behaviors of fine sediment has made an important issue on reservoir sedimentation management systems. In this study, field measurements and numerical analyses were conducted on behavior of fine sediment in Miwa Dam, Japan, where a redevelopment project is just being carried out. First, typical time variation was confirmed on fine suspended solid concentration by means of field measurements during flood events since 1988. Then behavior of fine suspended load in the reservoir was analyzed by using a vertical 2-dimensional reservoir hydraulic simulation model. We also observed movement of fine sediment mass on reservoir bed caused by lowering reservoir water level. Consequently we are going to propose practical methods to prevent inflow of fine suspended load and to reduce sedimentation in the reservoir.

1 INTRODUCTION

Sediment bypass systems have recently been planned and constructed in several reservoirs as effective countermeasures against sedimentation. On the other hand, reservoirs working for flood control and water supply have to store flood water, which also brings suspended sediment load into the reservoirs. In these reservoirs, although rough sediment load can be trapped in check dams installed just upstream of the reservoir, fine sediment inevitably flows into the reservoir and deposits. Nowadays how

to control the behaviors of fine sediment has made an important issue on reservoir sedimentation management systems.

In this study, field measurements and numerical analyses were conducted on behavior of fine sediment in Miwa Dam, Japan, where a redevelopment project is just being carried out. Consequently we are going to propose practical methods to prevent inflow of fine suspended load and to reduce sedimentation in the reservoir.

2 SITE DESCRIPTION

2.1 Catchment and sedimentation of the Miwa Dam

The Miwa Dam Reservoir is a multi-purpose reservoir constructed in 1959. The nominal water storage capacity of the reservoir is about $3.0 \times 10^7 \text{ m}^3$ and the catchment area is 311 km^2 . The dam is located in the central area of the main island of Japan (Honshu). The catchments contain a part of Japan Alpine Mountains; some of the mountains are higher than 3000m, and median tectonic line and many faults. Because of these catchments conditions, sediment yield counts quite a large.

Total sediment deposit in the dam measured in 1999 was $1.45 \times 10^7 \text{ m}^3$. This sedimentation occupies half of the reservoir capacity. The sediment deposit in the reservoir is mostly composed of silt and clay, which make up to 75% of total sediment deposit. The Miwa Dam has experienced several deluges and their sediment greatly reduced the reservoir capacity. For example, the annual

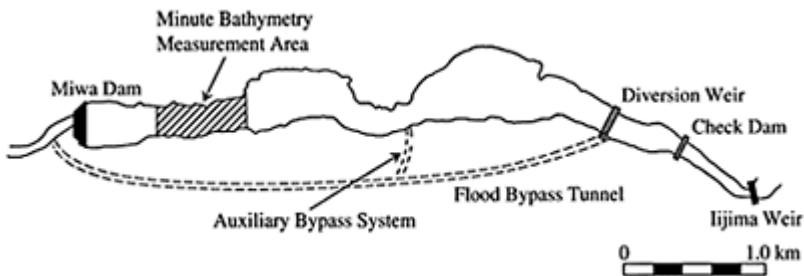


Figure 1. Plan view of the Miwa Dam Reservoir and the redevelopment project facilities.

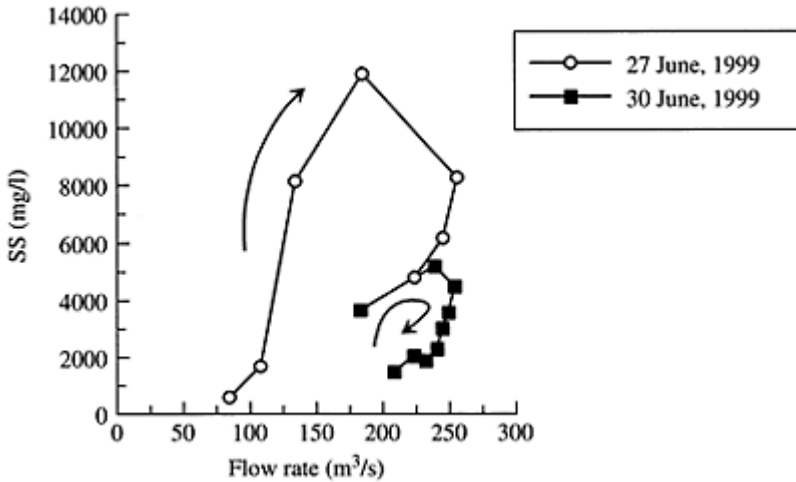


Figure 2. Loop correlation of rate of inflow and suspended sediment concentration in a sequence of floods in 1999.

sedimentation in 1982, when the largest flood ever since the construction of the dam occurred, reaches as much as $4.3 \times 10^6 \text{ m}^3$.

2.2 Redevelopment project

To ensure the reliability on flood control and water supply, a project to reduce sedimentation has been being undertaken in the Miwa Dam since 1988 (Urakami & Sugiyama 2000). It is composed of excavation of sediment and construction of flood bypass system. Figure 1 shows the plan view of the Miwa Dam reservoir including the facilities of the redevelopment: the check dam, the diversion weir and the bypasses.

3 CHARACTERISTICS OF FINE SEDIMENT ENTERING INTO THE MIWA DAM

Typical concentration variation was confirmed by means of field measurements on fine suspended solids flowing into the reservoir during a flood period. Water sampling and analysis of suspended sediment have been conducted since 1988 during flood events at the upstream end of the reservoir. Water was sampled at the station of the Iijima Weir station shown in Figure 1. Suspended solid concentration was analyzed for the sediment whose diameter is between 1 μm and 2 mm by GFP filtration. Grain size distributions were also analyzed for samples obtained at times around the flow rate peak of each flood event.

In most of the floods, correlations between suspended sediment concentration and flow rate draw clockwise loops when plotted in order of time. Figure 2 shows a typical variation of the loop characteristics. The data were obtained for two flood events that occurred sequentially in a short

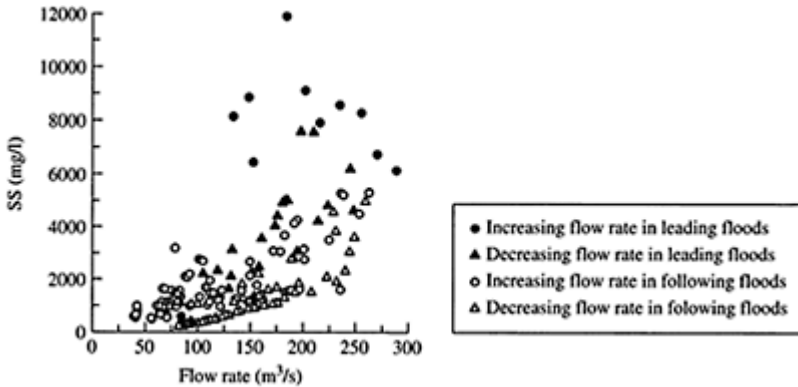


Figure 3. All the data of flow rate and suspended sediment concentration of reservoir inflow since 1988.

span of time. The first flood had a larger loop of time variation. A higher sediment concentration was observed in the leading flood when compared at a same flow rate and a stage of flood.

Data from 21 flood events are plotted in Figure 3. As shown in Figure 2, when a flood occurs after another, the loop becomes smaller than the previous one and the mean concentration also becomes lower. In Figure 3, flood events are classified into two groups: a) leading floods that do not have a flood ahead of itself for half a year, b) following floods, and in each group of flood, data is also divided considering increasing or decreasing of flow rate.

The figure indicates that increasing stage of leading flood has much higher sediment concentration. Considering this characteristics of the inflow, if we can manage to handle this sediment load, such as bypassing or sluicing the flood water, sedimentation in the reservoir is largely restrained.

4 NUMERICAL ANALYSIS OF FINE SEDIMENT BEHAVIOR IN THE RESERVOIR

4.1 Model description

The behavior of fine suspended load in the reservoir was analyzed using numerical simulation model. Density current in the reservoir caused by suspension of sediment typically shows a flow pattern in longitudinal and vertical directions (Akiyama & Stefan

1985, Parker et al. 1987). Two dimensional models have been applied to simulate current in reservoirs (e.g. Farrell & Stefan 1988, Chung & Gu 1998). In this study, a vertical 2-dimensional reservoir hydraulic simulation model is employed that includes the effect of buoyancy caused by water temperature and suspended sediment. The basic equations are as follows:

$$\frac{\partial(Bu)}{\partial t} + u \frac{\partial(Bu)}{\partial x} + w \frac{\partial(Bu)}{\partial z} = -\frac{1}{\rho} \frac{\partial Bp}{\partial x} + \frac{\partial}{\partial x} \left(A_x B \frac{\partial u}{\partial x} \right) + \frac{\partial}{\partial z} \left(A_y B \frac{\partial u}{\partial z} \right) \quad (1)$$

$$\frac{\partial p}{\partial z} = -\rho g \quad (2)$$

$$\frac{\partial(Bu)}{\partial x} + \frac{\partial(Bw)}{\partial z} = 0 \quad (3)$$

$$\frac{\partial(BT)}{\partial t} + u \frac{\partial(BT)}{\partial x} + w \frac{\partial(BT)}{\partial z} = \frac{\partial}{\partial x} \left(D_x B \frac{\partial T}{\partial x} \right) + \frac{\partial}{\partial z} \left(D_z B \frac{\partial T}{\partial z} \right) + \frac{Bh}{\rho C_W} \quad (4)$$

$$\frac{\partial(BC)}{\partial t} + u \frac{\partial(BC)}{\partial x} + (w - w_s) \frac{\partial(BC)}{\partial w} = \frac{\partial}{\partial x} \left(D_x B \frac{\partial C}{\partial x} \right) + \frac{\partial}{\partial z} \left(D_z B \frac{\partial C}{\partial z} \right) + \frac{F_C}{n_x \cdot n_z} \quad (5)$$

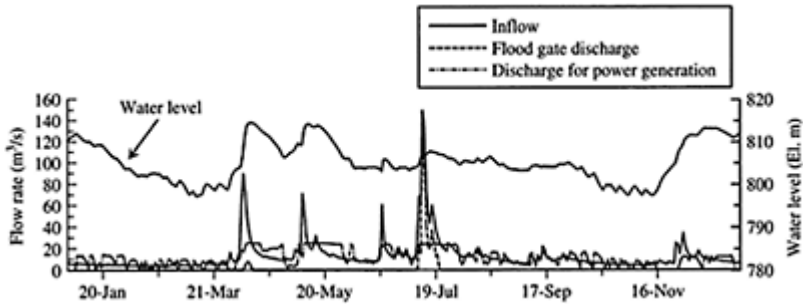


Figure 4. Time series of the rates of inflow and discharge and water level in 1997.

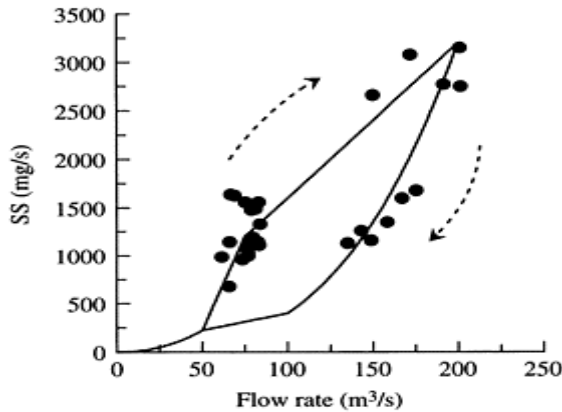


Figure 5. Relation of rate of inflow and suspended sediment concentration used as the boundary condition in the model calibration.

where x =longitudinal coordinate, z =vertical coordinate, u =longitudinal velocity component, w =vertical velocity component, p =pressure, ρ =density of water, T =water temperature, C =sediment concentration, B =local width of the reservoir, A_i =eddy viscosity for i -direction, D_i =eddy diffusion coefficient for i -direction, w_s =settling velocity of sediment, h =heat flux from the water surface caused by latent and sensible heat and short and long wave radiation (Huber et al. 1972), C_w =specific heat of water. The last term of Equation 5 denotes sedimentation flux onto the bed slope of the reservoir.

Buoyancy effect caused by water temperature and suspended sediment concentration is taken into account as density ρ is calculated as

$$\rho = f(T, C). \quad (6)$$

Settling velocities of suspended sediment relative to the ambient water are estimated from the Stokes' law of particle settlement.

4.2 Model calibration

The model is verified by simulating time and space variations of water temperature and suspended solid concentration in 1997, when a flood occurred in July. The calculation was conducted for the whole duration of the year, since the thermal stratification condition in the reservoir before intrusion of the flood can influence much on the behavior of the density current. Figure 4 shows the reservoir conditions (flow rate and water surface level) in 1997.

Table 1. Grain size distribution for model verification.

Range of diameter μm	Representative diameter μm	Proportion %
>1.0	1.0	12.2
1.0–5.0	5.0	24.1
5.0–10.0	10.0	16.4
10.0–20.0	15.0	19.1
20.0–40.	25.0	18.5
40.0<	50.0	9.7

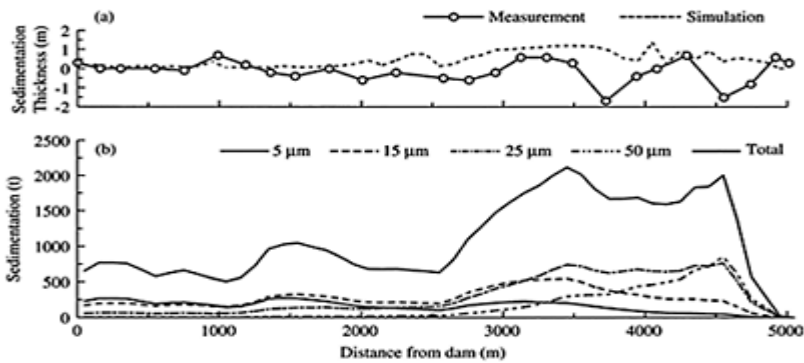


Figure 6. Longitudinal distribution of sedimentation in the reservoir in 1997.

- (a) Sedimentation thickness comparing the measurement and the simulation
(b) Simulated distribution of sedimentation plotting each grain size component.

In the verification, the loop characteristic of inflow load during the flood was applied on basis of observations conducted for the flood in July 1997 as shown in Figure 5. The flood is divided into four stages to form a loop correlation. Grain size distribution, i.e. settling velocity, of fine sediment is estimated from the measurement conducted in 1989. Table 1 shows the grain size sections and proportions for calculation.

The annual sediment deposition distribution was also validated by comparing the measurement and the calculation. Figure 6 (a) compares the result of simulation and the measurement of longitudinal sedimentation distributions. The measurement result shown in this figure was estimated by taking the difference of deepest lines of bed observed in 1996 and 1997. The simulated result in Figure 6 (a) assumes the void fraction as 0.7 and the soil fraction density as 2650 kg/m^3 .

Figure 6 (b) shows sedimentation amount distributions of each grain size component. Larger sediment deposits in the upstream area of the reservoir and finer sediment is distributed quite uniformly in the reservoir.

4.3 Analysis of the redevelopment effect

Then simulations were conducted to analyze effects of the redevelopment systems assuming that the redevelopment project had been completed. Simulations were conducted for the flood event in August 1982 that has the largest flow rate ever occurred in the Miwa Dam. The maximum flow rate of the flood is $1210\text{m}^3/\text{s}$, which is nearly as large as the design flood. The redevelopment

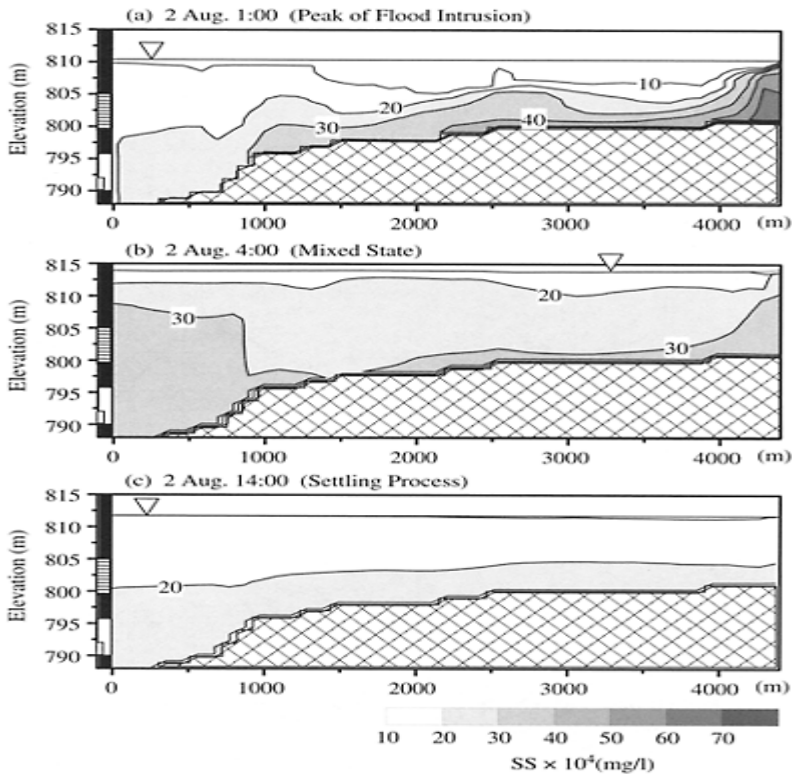


Figure 7. Spatial distribution of suspended sediment concentration in the reservoir during the flood event in 1982. Conditions in the reservoir are assumed that the redevelopment project is completed.

system bypasses inflow of up to 300 m³/s so that inflow of 910 m³/s at its maximum enters into the reservoir.

For this flood event, effects of relocated spillway and bed excavation were analyzed on discharge efficiency of sediment. According to the redevelopment plan, two cases on the excavation were configured for the analysis: bed higher than elevation 800 m and 792 m is excavated. As for the elevation of the spillway, current elevation of 799 m and lowered elevation of 790 m are simulated.

Examples of sediment concentration distribution are shown in Figure 7 for the case of lowered spillway and 800 m elevation excavation. The flood event analyzed is so large that the reservoir water body is completely mixed soon after the flood water enters into the reservoir. After half a day has passed, a stratification caused by settlement of suspended sediment is formed. The lowered spillway can discharge more sediment than the current spillway because of this stratification.

Results of all the four cases of analysis are shown in Table 2. The effects of sediment sluicing represented here do not seem very large. This is partly because the flood is so large compared with the reservoir capacity that the reservoir water body is mixed by the flood intrusion. If the density underflow were maintained throughout the flood, the effect of the lower spillway would be larger (Fan & Morris 1992).

In spite of this unfavorable condition, the relocated flood gate can reduce reservoir deposition of 20,000–40,000 ton (about 10,000–22,000 m³). Including the work of check dam and flood bypass systems, effects of the redevelopment are not little.

5 MOVEMENT OF BED SEDIMENT DURING DRAWDOWN

We also observed movement of fine sediment mass on reservoir bed caused by drawdown of reservoir water level. The measurements were carried out twice in September and November 2002, during which the reservoir water level was lowered 8 m. The region of the measurement is the downstream area in the reservoir as shown in Figure 1. The area extends 0.7 km in the longitudinal direction and the most upstream point of measurement is 1.2 km from the dam. The water level declined from 805.9 m elevation to 798.5 m elevation between the measurements. When the water level was lowered the most, the water edge came around the center of the measurement area.

Bed shapes were minutely measured by using echo sounder and GPS. Water level was lowered 8 m in this period, which might have caused the sediment movement. Figure 8 shows measured bathymetries and the bed variation that is estimated by taking the difference of the two measurements. The bathymetry difference indicates fine sediment mass movement, which reaches as much as 4.5×10^4 m³. If the sediment is efficiently gathered to a certain area in the reservoir by water level controls, discharging, dredging or trucking sediment can be more easily achieved.

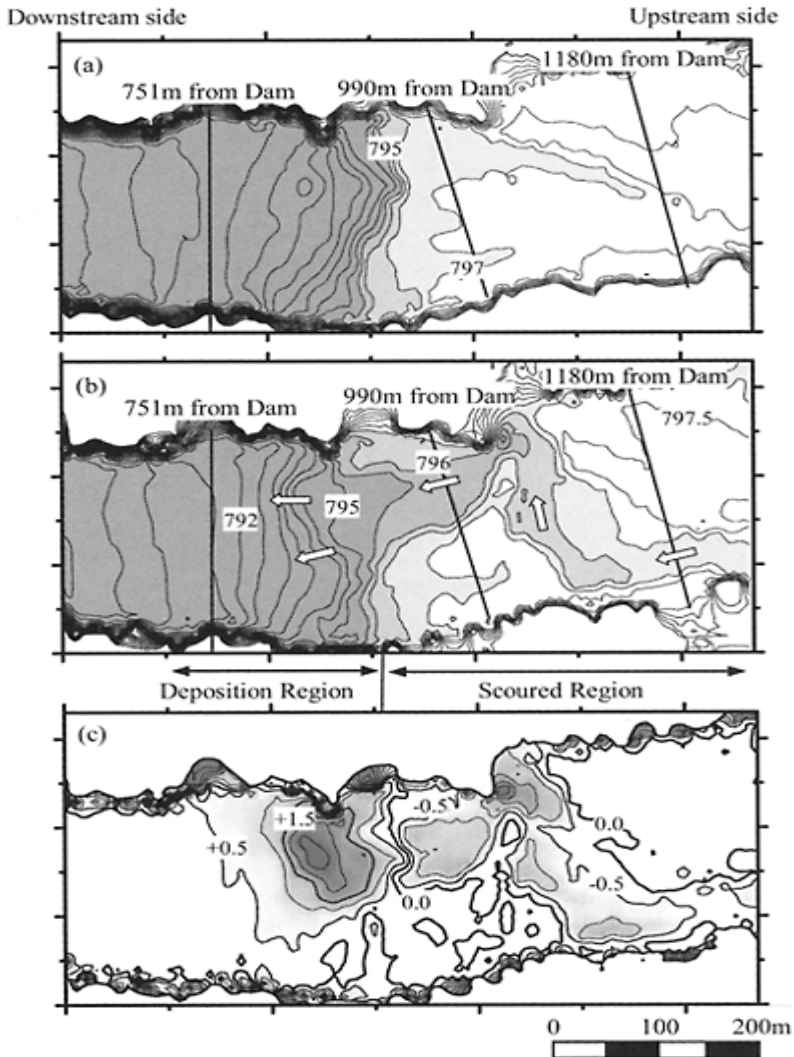


Figure 8. Measurement results on redistribution of deposited sediment caused by drawdown. (a) Bathymetry measured on 18–20 Sep. 2002. (b) Bathymetry measured on 17–18 Nov. 2002. (c) Variation of bathymetry as a difference between (a) and (b).

Table 2. Sensibility of excavation and spillway location on sedimentation.

Elevation of excavation El.m	Spillway elevation El.m	Sediment deposition in reservoir		Trap efficiency (%)
		1000 ton	1000 m ³	
800	799	537.8	364.8	51.5
800	790	517.8	351.1	49.6
792	799	579.5	728.9	55.5
792	790	539.5	678.6	51.7

6 CONCLUSIONS

Behaviors of fine sediment in the Miwa Dam Reservoir, Japan were extensively examined for flood events and drawdown. The achievements in this study are going to be applied to the redevelopment project of the dam where good and proper treatment of sedimentation is seriously needed. Conclusions of this study are summarized as follows.

Suspended sediment concentrations entering into the Miwa Dam Reservoir vary widely on account of flood scales, intervals of flood occurrences and so on. Taking these characteristics into management of flood bypass systems and water level controls, intrusion of fine sediment into the reservoir can be efficiently reduced.

Behaviors of density current during flood events can be utilized to route and sluice the high concentration sediment laden flow out of the reservoir. Location of spillway and excavation of reservoir bed have effects to reduce trap efficiencies of fine sediment so that more investigations are needed to decide an optimum facility design.

Fine sediment deposited in upstream area of the reservoir can be gathered to some area by using the effect of redistribution of sedimentation during drawdown of the reservoir water. If the sediment redistribution is controlled properly, discharging the sediment by the redevelopment facilities including the auxiliary bypass is more effectively achieved.

REFERENCES

- Akiyama, J. & Stefan, H. 1985. Turbidity current with erosion and deposition. *Journal of Hydraulic Engineering* 111 (12): 1473–1496.
- Chung, S. & Gu, R. 1998. Two-dimensional simulations of contaminant current in stratified reservoir. *Journal of Hydraulic Engineering* 124 (7): 704–711.
- Fan, J & Morris, L.M. 1992. Reservoir sedimentation. II: Reservoir desiltation and long-term storage capacity. *Journal of Hydraulic Engineering* 118 (3): 370–384.
- Farrell, G.J. & Stefan, H.G. 1988. Mathematical modeling of plunging reservoir flows. *Journal of Hydraulic Research* 26 (5): 525–537.
- Huber, W.C., Harleman, D.R.F. & Ryan, P.J. 1972. Temperature prediction in stratified reservoirs. *Journal of the hydraulics division, ASCE* 98:645–666.

- Parker, G., Garcia, M., Fukushima, Y. & Yu, W. 1987. Experiments on turbidity currents over an erodible bed. *Journal of Hydraulic Research* 25 (1): 123–147.
- Urakami, M. & Sugiyama, T. 2000. The Miwa Dam redevelopment project. *Engineering for Dams* 108: 75–87. (in Japanese)

Management of reservoir sedimentation due to turbidity currents by technical measures

Ch.D.Oehy

Cat Perils, Swiss Re, Zurich, Switzerland

A.J.Schleiss

Laboratory of Hydraulic Constructions (LCH), Swiss Federal Institute of Technology Lausann (EPFL), Switzerland

Hydraulics of Dams and River Structures—Yazdandoost & Attari (eds)

© 2004 Taylor & Francis Group, London, ISBN 90 5809 632 7

ABSTRACT: The growing demand of water and food all over the world can be satisfied in arid regions only by artificial reservoirs. They supply water for drinking and irrigation, but may be endangered by sedimentation. Without effective measures their sustainability is questioned. Deposits of sediments not only affect the loss of life storage, but also the proper functioning of outlet structures such as intakes and bottom outlets. In narrow reservoirs with rather steep bottom slopes, turbidity currents are often the main process in the reservoir sedimentation. The highly sediment-laden density current not only transports the sediments along the thalweg to the dam but also erodes already deposited fine sediments. Technical measures to influence and govern turbidity currents are therefore very important in view of a sustainable reservoir sedimentation management. To control the sedimentation within the reservoir, the effects of obstacles, screens, water jets and bubble curtains on the turbidity current were investigated with physical experiments and numerical simulations. In the physical experiments, measurements of the spatial and temporal evolution of the deposits, of vertical velocity profiles and of the front velocities were recorded. The investigated measures were simulated using a three-dimensional numerical model, based on the flow solver CFX-4.4. The investigations showed that turbidity currents could be influenced effectively by properly designed constructive measures. Based on the results of the physical experiments and numerical simulations, some design recommendations as rules of thumb are given for the application of the investigated measures.

1 INTRODUCTION

The today's worldwide annual mean loss of storage capacity due to sedimentation is already higher than the increase of capacity by construction of new reservoirs for irrigation, drinking water and hydropower. Thus the sustainable use of the reservoirs is not guaranteed in long term. In narrow reservoirs with rather steep bottom slope, turbidity currents are often the main process for the transport and deposit of sediments (Schleiss & Oehy 2002, De Cesare 1998). These turbidity currents with high sediment concentrations mainly occur during floods and follow the thalweg to the deepest zones of the reservoir near the dam, where the sediments are deposited (Figure 1).

Depending on the slope of the thalweg, the density currents can reach rather high velocities up to 0.5–0.8 m/s. Thus sediments, which have already settled down, can be eroded again and transported in the direction of the dam. The introduction of additional suspended sediments into the turbidity current due to this process increases its density and consequently its velocity. On the other hand, on low slopes the turbidity current slows down which causes the sediments to settle down and finally the current to die (De Cesare et al. 2001).

If turbidity currents can be entirely stopped in a reservoir or influenced in such a way, that the sediments are not transported at critical locations, such as intakes and bottom outlets, the

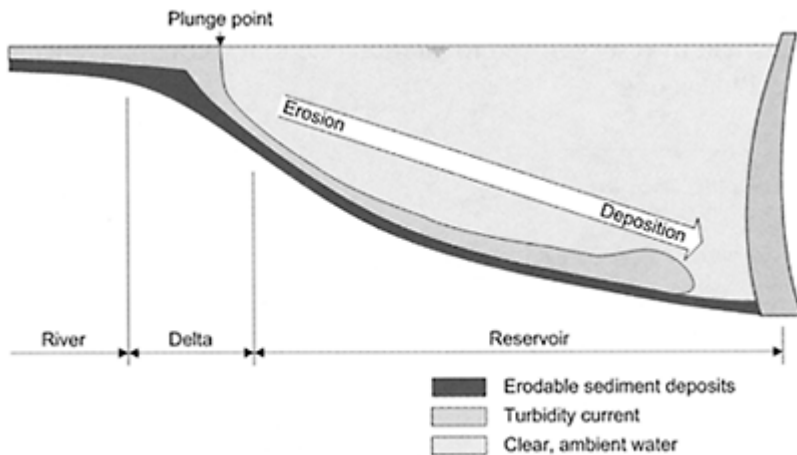


Figure 1. Schematic sketch of a turbidity current in a reservoir.

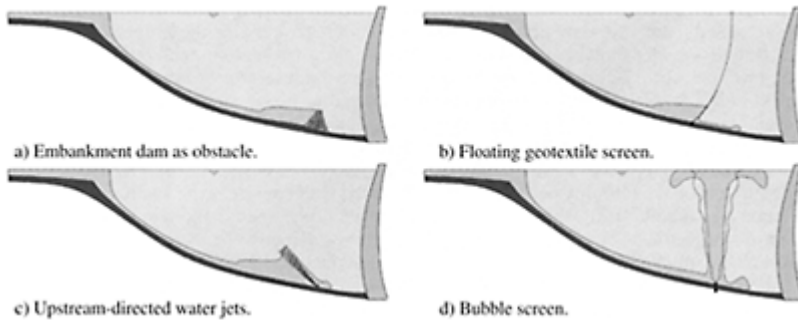


Figure 2. Technical measures for the management of turbidity currents in a reservoir.

sustainability of the use of the reservoir can be increased considerably. In the framework of a research project, technical measures were identified and investigated with which the reservoir sedimentation due to turbidity currents can be managed. These technical measures have in principal the purpose to stop, dilute or divert the density current. This can be done by obstacles or by energy-dissipation elements such as screens and grids placed in the reservoirs as well as by the supply of external energy by the help of water jets and bubble curtains.

Obstacles placed along the thalweg of the reservoir can stop the turbidity currents and cause the fine sediments to settle. Small concrete walls or embankment dams can be used as obstacles, which need to have openings to prevent water storage behind when the reservoir level is low (Figure 2a).

Turbidity currents can be stopped also by energy-dissipation elements, for example by a geotextile screen. This screen can be spanned by steel ropes over the lower part of a reservoir cross-section or be suspended at floats or booms in order to follow reservoir level variations. The geotextile screen has not to be absolutely impermeable but can be a mesh with certain porosity. In this case the turbidity current will be partially stopped, slowed down and diluted in such a way that it dies out (Figure 2b). With obstacles and screens the turbidity current can also be diverted in reservoir regions where sediment deposits do not harm operation.

As a third measure the turbidity current can be stopped, diluted or diverted by supply of external energy (Figure 2c). If upstream-directed water jets have a certain minimum momentum, the turbidity current is fully stopped. Otherwise at least a certain storage and dilution effect can be obtained, which slows down the turbidity current until it dies out. For this local water injection by jets at the reservoir bottom, the energy of the water of collecting tunnels entering the reservoir on a certain height above the operation level, can be used, which.

The idea of air bubble screen is to whirl up the approaching turbidity current and to keep the sediments in suspension, so that they can be evacuated through the powerhouse intakes (Figure 2d). Of course, the sediment concentration in the water entering the intakes has to be limited, in order to limit abrasion at turbine runners and ecological

problems in the tailwater. Turbidity currents attain a sediment concentration of some volume percentages. By the entrainment of clear water by the bubble screen, the concentration will be reduced in order to avoid the above-mentioned problems. Furthermore, turbine runners of high head power plants coated with new high abrasion resistant materials can withstand rather high sediment concentrations of 2–5 g/l under normal maintenance cycles (3 to 5 years).

2 PHYSICAL AND NUMERICAL MODELLING OF TURBIDITY CURRENTS

The effects of the technical measures as shown in Figure 2 on the turbidity currents in a reservoir were studied with physical model tests and numerical simulations.

The physical model tests were performed in a rectangular flume of 7.1 m length, 27 cm width and 90 cm depth. Tests were carried out with a horizontal and an inclined bottom with a slope of 4.64%. In order to measure the evolution of the deposited sediments at the bottom, a new measurement device based on the electrical resistance of the sediment layers was developed following the ideas of De Rooij et al. (1999). This measurement method allowed observing the spatial and temporal evolution of deposits with an accuracy of about 0.15mm. Furthermore, vertical velocity profiles across the turbidity current were measured with ultrasonic probes (UVP) and front velocities were analyzed from video recordings. The following series of physical model tests were performed:

- Series A: Behaviour of a not influenced turbidity current on horizontal and inclined bottom (10 tests).
- Series B: Effect of an obstacle with 24 cm height (5 tests).
- Series C: Effect of a permeable vertical geotextile screen (5 tests with 2 porosities).
- Series D: Effect of a vertical water jet (4 tests).
- Series E: Effect of a 45°-upstream inclined water jet (4 tests).
- Series F: Effect of a bubble curtain (2 tests).

The different characteristics and the detailed results of the physical model tests can be found in Oehy & Schleiss (2003a, 2003b) and Oehy (2003).

In general it has to be distinguished between subcritical and supercritical conditions of the turbidity current flow depending if the densimetric Froude number Fr_d is lower or higher than 1. This characteristic number is defined as follows

$$Fr_d^2 = \frac{U^2}{g'h} \quad (1)$$

where U is the average velocity and h the height of the turbidity current. g' corresponds to the reduced gravitational acceleration, which for a sediment concentration of 1 g/l is about 1000 times smaller than the normal gravitational acceleration g . It is defined as

$$g' = \frac{\Delta\rho}{\rho_a} g = \frac{\rho_t - \rho_a}{\rho_a} g \quad (2)$$

where ρ_t is the density of the turbidity current and ρ_a the density of the clear water.

The numerical simulations had the purpose to further quantify the effect of obstacles, screens, water jets and bubble curtains and compare the results with the physical model tests. The 3D-solver CFX-4.4 (AEA Technology 2001), which is based on the Reynolds averaged Navier-Stokes equation with variable density (RANS) was used. The transport of the suspended sediments was calculated by a convection-diffusion equation for the sediment concentration, where the settling

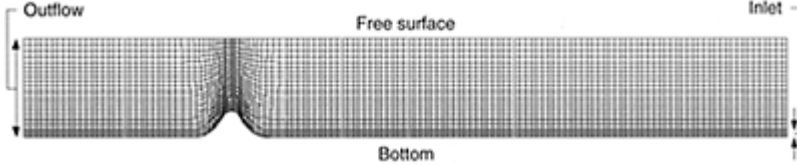


Figure 3. Computational grid with Gaussian-shaped obstacle (6762 cells).

velocity is considered in the convective term

$$\frac{\partial c}{\partial t} + (U_i - w_i) \frac{\partial c}{\partial x_i} - \frac{\partial}{\partial x_i} \left(\Gamma_T \frac{\partial c}{\partial x_i} \right) = (S_E - S_D)_b \quad (3)$$

with the sediment concentration c , the velocity components U_i and the sink velocity of the suspended sediments w_i . S_E and S_D correspond to the eroded or deposited sediments at the bottom and Γ_T to the eddy diffusivity, which is determined with the k - ϵ turbulence model. In order to model the erosion and deposition terms the approach of Garcia & Parker (1993) was used. In addition, the program was completed with user-defined routines, which allowed considering a fractional sediment transport and the effect of a density layered fluid in the turbulence model (Oehy & Schleiss 2001). For the numerical simulations of the obstacles, screens and water jets and bubble curtains further modifications were introduced into the computer program and are described below (Oehy 2003).

3 EFFECT OF OBSTACLES

The effect of an obstacle was investigated in the laboratory tests by means of a obstacle of 24 cm high with a form of a Gaussian shape as shown in Figure 3. For the numerical simulation the laboratory flume was discretized with a mesh of 6772 cells, which was denser near the bottom and at the obstacle. Since the influence of the wall roughness could be neglected, only a 2D calculation was required. The results of the numerical simulations were in good agreement with the velocities and the heights of the deposits measured in the laboratory tests (Oehy 2003). In order to illustrate the unsteady turbidity current, the sediment concentrations are represented in Figure 4 with time steps of 20 sec, whereas the lines of equivalent concentration have a difference of density of 0.1 g/l. The

envelope of the approaching turbidity current was assumed with a minimum concentration of 0.1 g/l.

For subcritical conditions the obstacle produces an internal bore, which travels upstream and successively produces a backwater curve. Once quasi-steady conditions are reached, the volume upstream of the obstacle is fully filled up and acts like a desilting basin. Only a small part of the approaching turbidity current, namely about 10%, passes the obstacle. In the case of supercritical approaching conditions the obstacle is less efficient and about 50% to 80% of the sediments cannot be retained. The obstacle produces an internal hydraulic jump, which travels upstream and consequently reduces the velocity of the turbidity current.

Based on the tests and simulations it may be concluded, that obstacles can retain the turbidity current only for subcritical approaching conditions. In this case the obstacle has to be two times higher than the height of the approaching turbidity current. This results in obstacle heights of about 20 m for turbidity currents in alpine reservoirs, which are typically 10m high. The storage volume upstream of the obstacle should be as large as possible. Therefore, obstacles should be placed at the downstream end of flat reservoir bottom zones or, if present, at the end of negative slopes (see example of Grimsel reservoir in Oehy & Schleiss 2001b).

Obstacles can be built as embankment dams which need to have an open breach in order to allow free drainage of water when the reservoir level is low. During each flood event for which a turbidity current occurs the storage volume upstream of the obstacle is reduced. Typically obstacles with heights of 20 m will loose their retaining capacity after about 50 years. Then heightening of the obstacle could be considered. An alternative solution could be the construction of several obstacles along the reservoir.

In principal an obstacle can also be used to divert turbidity currents in reservoir zones where the deposits do not harm the operation of intake and outlet structures. If the intake of the bottom outlet is sufficiently far away from the power intake, the turbidity currents can be directed by means of obstacles to the bottom outlet. This increases efficiency of regular flushing operations by the help of the bottom outlet, especially if they are carried out during flood events.

4 EFFECT OF SCREENS AND GEOTEXTILE CURTAINS

The effect of a permeable vertical geotextile screen was studied with 5 hydraulic laboratory tests using two different porosities of the geotextile. In the numerical simulation the geotextile screen was modelled as a porous area, which reduces the volume available for the flow and produces additional drag forces on the flow. These forces were determined by the help of empirical relationships depending on Reynolds number and the porosity of the geotextile (Oehy & Schleiss 2003b). The

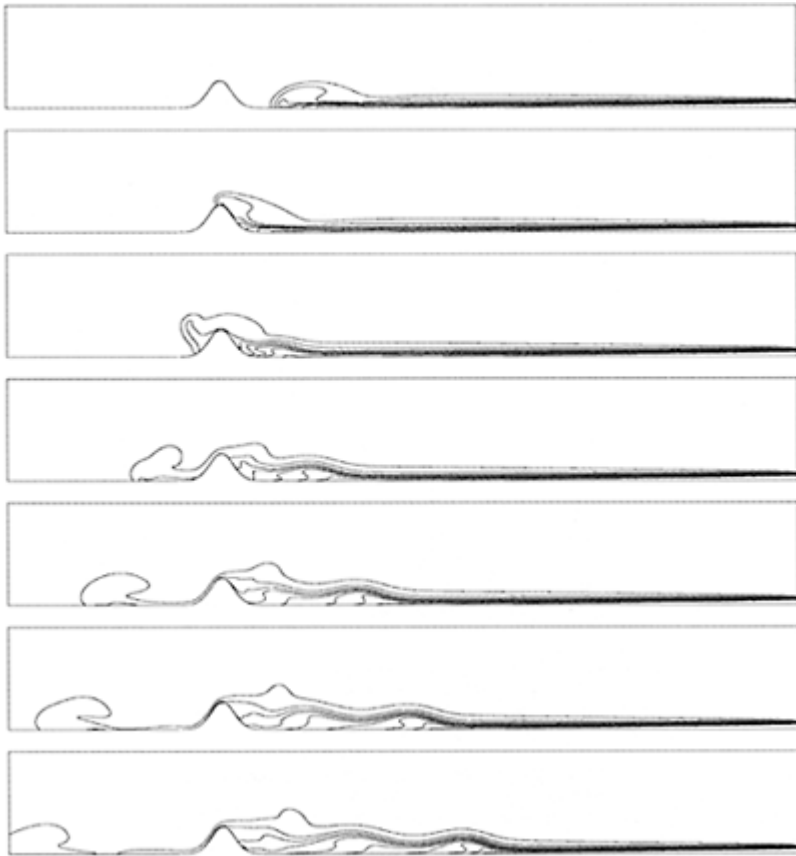


Figure 4. Numerical simulation of a turbidity current influenced by an obstacle for time steps of 20 sec. The lines of equivalent concentration are shown with a difference of density of 0.1 g/l, whereas the most upper line corresponds to a minimum concentration of 0.1 g/l.

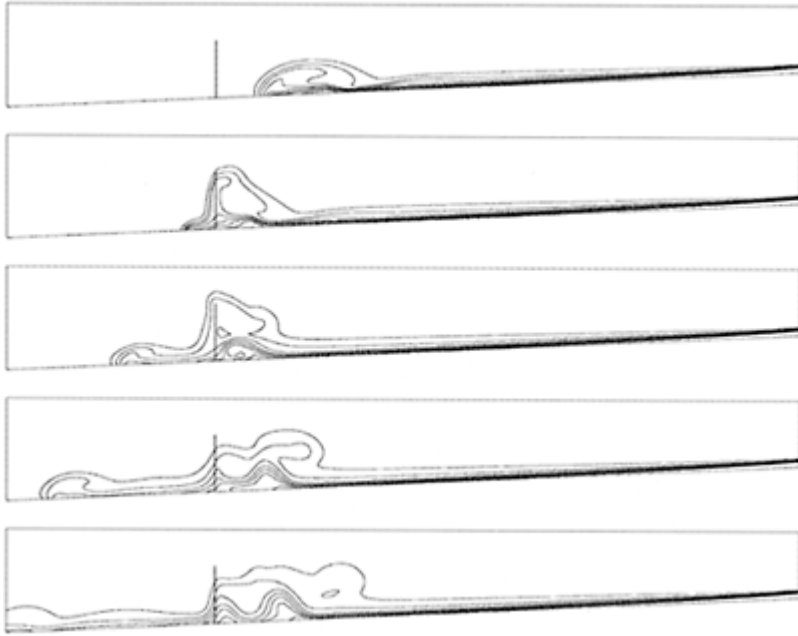


Figure 5. Numerical simulation of a turbidity current influenced by a screen for time steps of 20 sec. The lines of equivalent concentration are shown with a difference of density of 0.1 g/l, whereas the most upper line corresponds to a minimum concentration of 0.1 g/l (slope 4.64%).

results of the numerical simulations were again in good agreement with the measurements in the laboratory tests. Figure 5 illustrates the sediment concentration distribution in a supercritical turbidity current passing a geotextile screen. It can be seen that the turbidity current partially seeps through the geotextile but that it is reflected as a bore travelling upstream. At the end of the test, i.e. a flood event, the region upstream of the screen is fully filled up and sediments settle down like in a desilting basin. For the tested porosity, which was about 35%, 30% to 50% of the sediments seeped through the screen in the case of subcritical approaching conditions. In the case of supercritical conditions these values increase slightly to 40% to 70%. This shows that a screen is more adapted for supercritical conditions than an obstacle.

The efficiency of a screen or a geotextile curtain depends mainly on its porosity and the mesh openings. In order to retain significant amount of sediments of the turbidity current, the porosity should be lower than 30%. Furthermore, the screen should be three times higher than the height of the approaching turbidity current. For typical practical

applications this would lead to 30 m high curtains. The mesh openings should be in the range of 5 to 10 cm in order to avoid clogging by the sediments.

The highest pressure on the curtain occurs when the turbidity current bounds against the curtain. The pressure can be divided in a hydrostatic and a dynamic part. The hydrostatic pressure remains moderate since the difference in the density of the turbidity current and the clear reservoir water is small. The dynamic pressure on the geotextile curtain comes up to 70 to 150 N/m² for practical applications depending on the approaching velocity of the turbidity current.

Screens or geotextile curtains have similar applications in reservoirs as obstacles. Nevertheless compared to embankment dams or concrete walls the installation of geotextile screens is less time consuming and requires only a short lowering of the reservoir level. Installing several screens in series can increase the sediment retention efficiency. The screens can be made of fiber-reinforced

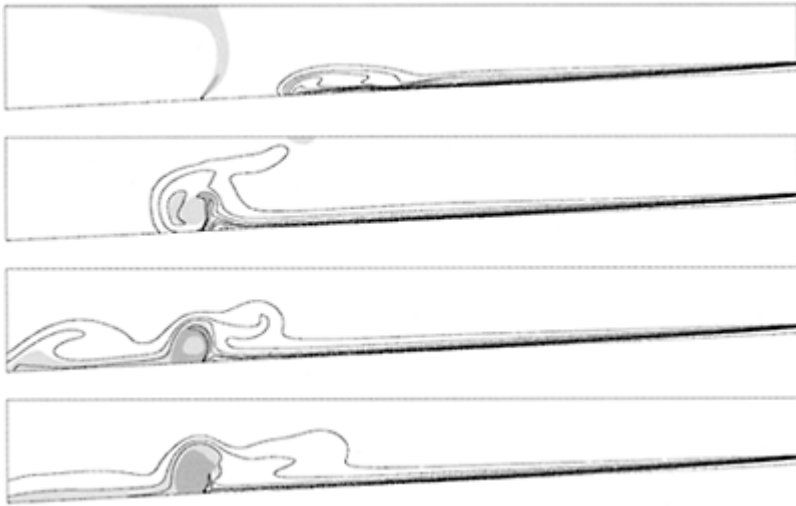


Figure 6. Numerical simulation of a turbidity current influenced by a water jet inclined 45° in upstream direction for time steps of 20 sec. The lines of equivalent concentration are shown with a difference of density of 0.1 g/l, whereas the most upper line corresponds to a minimum concentration of 0.1 g/l (slope 4.64%).

geotextile bands. It can then be fixed at horizontal steel cables spanned over the reservoir valley and/or fixed with vertical steel cables and floats.

When the sediment deposits upstream of the screen have attained a certain height, the screen has to be replaced. The old screen or geotextile curtain can be placed horizontally on the deposits and stabilize similar to reinforced earth concepts.

5 EFFECT OF WATER JETS AND AIR BUBBLE SCREENS

The physical model tests showed that a 45° upstream-inclined water jet is more effective than a vertical one. In the numerical simulation the water jet screen was modelled with a slot at the channel bottom through which clear water was injected. Again good agreement between the physical model test and the numerical simulation was obtained. Figure 6 shows the effect of a water jet on an approaching supercritical turbidity current. The lines of equivalent sediment concentration reveal that the turbidity current partially crosses the water jet whereas the other part forms an internal hydraulic jump travelling upstream.

In the case of a supercritical turbidity current in general the efficiency of the water jet screen is low and about 70% to 100% of the sediments are flowing across. For subcritical conditions these values decrease considerably to only 10% to 20%. Thus, water jets can be recommended only for subcritical conditions.

For typical turbidity currents in a reservoir with a height of 10 m and a mean velocity of 20 cm/s, the 45° upstream-inclined nozzles should have a diameter of 0.5 m and should be spaced by about 5 m. An outlet velocity of the water jet of 4.2 m/s results in a discharge of about 7.5 m³/s for a 50 m wide water jet screen. As mentioned in the introduction the energy of the water of collecting tunnels could be used. This water has to be guided by a penstock down to the reservoir bottom to the nozzles. The energy head between the highest reservoir level and the outlet of the collecting tunnels has to be higher than the head losses in the penstock and at the nozzles.

The physical and numerical analysis with air bubble screens revealed that its buoyancy flux has to be several times (in the test 22 times) higher than the buoyancy of the turbidity current. For practical applications in deep reservoirs (>30 m) the energy demand to supply the compressed air would be considerable and in most cases not economical.

6 CONCLUSIONS

In order to ensure the sustainable use of reservoirs created by dams the management of sedimentation is a challenge. Very often turbidity currents are the main process for the transport and deposit of suspended sediments in reservoirs.

The results of a systematic research program show that turbidity currents can be slowed down and most of the sediments can be retained upstream efficiently by obstacles, screens or geotextile curtains or water jets. For typical turbidity currents of 10 m to 20 m height as they occur in reservoirs, the preliminary design of the technical measures can be based on the following criteria:

- The obstacle should be only used for subcritical conditions and be two times higher than the turbidity current.

- Geotextile curtains or screens should be three times higher than the turbidity current and should have a porosity below 30%. They are also effective for supercritical conditions.
- Water jet screens should be 45° inclined in upstream direction and have a momentum, which is 50% higher than the momentum of the approaching turbidity current.

The local conditions of the reservoir determine which measure is most successful in practice. The developed numerical models produce reliable results for real reservoir geometries and can be used for detailed design of the technical measures. If possible such measures should be already considered in the early stage of the reservoir planning.

ACKNOWLEDGEMENTS

The research project was funded by the PSEL foundation of the Swiss Union of Electricity Producers, grant N° 175 and by the Swiss Committee on Dams (SCD).

REFERENCES

- AEA Technology: CFX-4.4 2001. Solver Manual, AEA Technology, Oxfordshire, UK.
- De Cesare, G. 1998. Alluvionnement des retenues par courants de turbidité, Communication No 7 du Laboratoire de constructions hydrauliques (LCH), EPFL, Lausanne.
- De Cesare, G.; Schleiss, A.; Hermann, F. 2001. Impact of turbidity currents on reservoir sedimentation, *Journal of Hydraulic Engineering* 127 (1), p. 6–16.
- De Rooij, F; Dalziel, S.B.; Linden, P.F. 1999. Electrical measurement of sediment layer thickness under suspension flows, *Experiments in Fluids* 26, p. 470–474.
- Garcia, M.H.; Parker, G. 1993. Experiments on the entrainment of sediment into suspension by a dense bottom current, *Journal of Geophysical Research (Oceans)* 98 (C3), p. 4793–4807.
- Oehy, Ch. 2003. Effects of obstacles and jets on reservoir sedimentation due to turbidity currents, PhD Thesis, No 2684 and Communication No 15 du Laboratoire de constructions hydrauliques (LCH), Swiss Federal Institute of Technology (EPFL), Lausanne, Switzerland.
- Oehy, Ch.; Schleiss, A. 2001a. Comparative study between two buoyancy-extended and the standard k- ϵ model for simulating turbidity currents, *Proceedings of the 2001 International Symposium on Environmental Hydraulics*, Tempe AZ, USA.
- Oehy, Ch.; Schleiss, A. 2001b. Numerical and physical modeling of a turbidity current passing over an obstacle—practical applications in the Lake Grimsel, *Proceedings of the 2001 International Symposium on Environmental Hydraulics*, Tempe AZ, USA.
- Oehy, Ch.; Schleiss 2003a. A Physical and numerical modelling of a turbidity current flowing through a permeable screen, *Proceedings of the XXXth IAHR Congress*, 24–29 August 2003, Thessaloniki, Greece.
- Oehy, Ch.; Schleiss 2003b. Beherrschung von Trübeströmen in Stauseen mit Hindernissen, *Gitter, Wasserstrahlund Luftblasenschleier, wasser, energie, luft—eau, énergie, air*, Heft 5/6, p. 143–152.
- Schleiss, A.; Oehy, Ch 2002. Verlandung von Stauseen und Nachhaltigkeit, *wasser, energie, luft—eau, énergie, air*, Heft 7/8, p. 227–234.

6.

Stepped spillways

Energy dissipation along stepped spillways

G.Valentin, P.U.Volkart & H.-E.Minor

*Laboratory of Hydmulics, Hydrology and Glaciology (VAW), Swiss
Federal Institute of Technology (ETH), Zurich, Switzerland*

Hydraulics of Dams and River Structures—Yazdandoost & Attari (eds)

© 2004 Taylor & Francis Group, London, ISBN 90 5809 632 7

ABSTRACT: In the past years considerable research was done on stepped spillways. Investigations were conducted to understand the hydraulics on the stepped face of Roller Compacted Concrete (RCC) dams and overlays for embankment dams. Significant energy losses occur along the stepped chute so that the energy dissipation structure, e.g. the stilling basin, becomes smaller and more economic. Therefore, energy losses and energy dissipation along the chute must be known. Experimental investigations were conducted at the Laboratory of Hydraulics, Hydrology and Glaciology (VAW) of the Swiss Federal Institute of Technology (ETH), Zurich, using a hydraulic scale model. The analyzed data lead to a simple equation for estimating energy losses of stepped spillways.

1 INTRODUCTION

1.1 *Motivation*

The interest in stepped spillways is still growing, because of the cost efficient construction method using Roller Compacted Concrete (RCC). Compared with smooth spillway chutes the unit flood discharge is smaller and limited so far up to some 20 m²/s for which no cavitation damage was observed. Some dams do not allow wide chutes because of particular site condition. The placement of the Conventional Vibrated Concrete (CVC) on the stepped face for a smooth chute is more cost extensive and needs more time for placement.

In principle a stepped dam chute dissipates more energy than a smooth chute. Therefore, the downstream energy dissipation structure often is smaller. Extended research was done to explore the hydraulics, especially the energy loss on stepped spillways.

1.2 Recent research

At stepped spillways two different flow types may occur, namely nappe flow and skimming flow. Nappe flow involves a sequence of free falling water jets over steps. The energy dissipation process is mainly affected by turbulent interaction of these plunging jets. Skimming flow occurs at higher discharges. It appears as a coherent stream flowing over the steps. The external corners of the steps form a pseudo-bottom over which the flow skims. Underneath the pseudo-bottom, vortices develop and recirculation is maintained through the transmission of shear stress from the main stream (Chanson 2002). Small-scale vorticity is also generated at the step corners. Most of the hydraulic energy is dissipated by maintaining the circulation of the vortices.

The flow is aerated and the mean air concentration is:

$$C_{mean} = \int_0^{Y_{90}} C \, dy \quad (1)$$

where Y_{90} =distance perpendicular to the pseudo-bottom where air concentration $C=90\%$; and y =coordinate perpendicular to the pseudo-bottom.

Form drag is important for estimating energy losses at stepped spillways, whereas skin friction is almost negligible. The flow resistance factor for air-water flow f_e is (Chanson 2002):

$$\frac{f_e}{f_d} = 0.5 \left[1 + \tanh \left(2.5 \frac{0.5 - C_{mean}}{C_{mean}(1 - C_{mean})} \right) \right] \quad (2)$$

$$f_d = \frac{2}{\sqrt{\pi}} \frac{1}{k}, \quad \text{for steep chutes } (\phi > 22^\circ) \quad (3)$$

where f_d =clear-water friction factor; C_{mean} =depth-averaged air concentration; k =inverse of the spreading rate of a turbulent shear layer; and ϕ =angle of pseudo-bottom relative to horizontal. Equations (2) and (3) characterize the form drag of air-water flows.

Various crest geometries have been investigated so far. Mateos and Elviro (1995), among others, investigated standard Waterways Experiment Station (WES) profiles with smaller steps above the tangent point to prevent jet deflection for small discharges. Yasuda and Ohtsu (1999) used a broadcrested weir at the beginning of the stepped chute. Most research related to aeration and energy losses in fully developed uniform flow.

Figure 1 shows all relevant parameters of a stepped spillway.

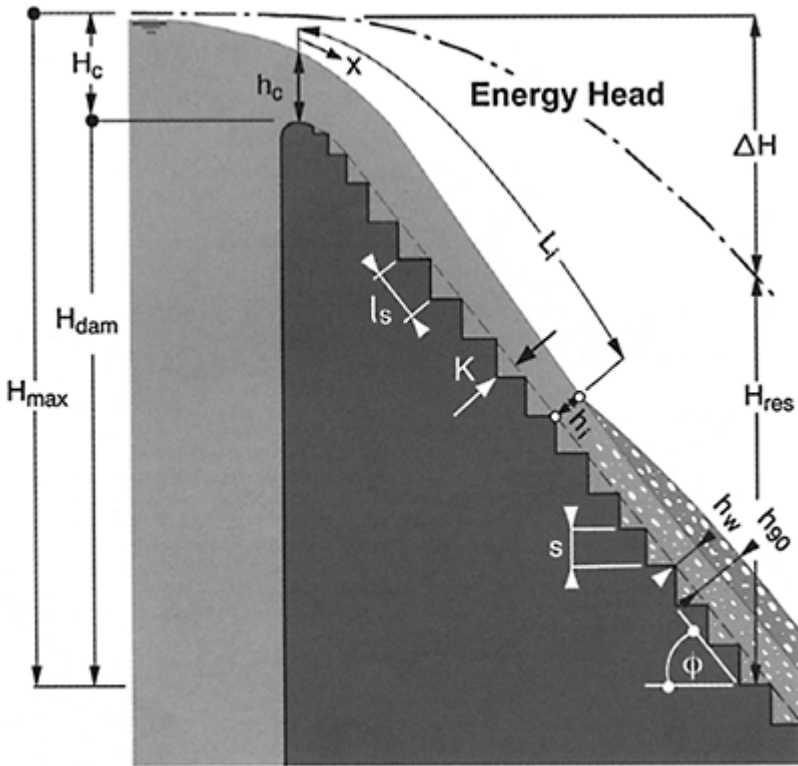


Figure 1. Definition sketch of a stepped spillway, --- pseudo-bottom (Boes 2000).

2 VAW MODEL INVESTIGATIONS

2.1 Investigations of a model with a jet-box

All experiments were conducted in a prismatic rectangular channel of width $b=0.50$ m and length $L=5.7$ m of bottom angles measured from the horizontal of $\phi = 30^\circ, 40^\circ, 40^\circ$ and 50° or slopes (V:H) of 1:1.73, 1:1.19 and 1:0.84 (Figure 2). Uniform flow conditions were reached in all tests. Three different vertical step heights $s=23.1, 46.2$ and 92.4 mm were investigated for the 30° cascade, steps of 31.1 and 93.3 mm for the 50° chute and of 26.1 mm for $\phi = 40^\circ$. The model scales were equivalent to 1:26.4, 1:13.2 and 1:6.6 for $\phi = 30^\circ$, 1:19.6 and 1:6.5 for $\phi = 50^\circ$ and 1:23.4 for $\phi = 40^\circ$ referred to a typical prototype value of $5=0.61$ m (2 feet). In accordance with Kobus (1985) and Chanson et al. (2002), the geometric scale of the model was in the range of 1:5 to 1:30. This range of

scale factors is presently considered adequate to suppress scale effects in the air-water mixture flow. The discharges Q were in the range of 201/s up to 1901/s.

In contrast to all other studies, the spillway face had a constant bottom slope with the jet-box at its upstream end. The jet-box transformed the pressurized approach flow into a free surface open channel flow of pre-calibrated approach flow depth h_o and approach velocity u_o (Schwalt and Hager 1992). The jet-box allows for an independent variation of h_o and the approach Froude number $Fr_o = u_o / (g h_o)^{1/2}$, where g =acceleration of gravity. The approach velocity u_o was in the range of 2.0 to 5.7m/s depending on the discharge. The vertical velocity distributions, as well as the air-concentration distributions were measured using a fiber-optical probe.



Figure 2. Upstream portion of hydraulic model (Boes 2000).

3 MAIN FLOW CONDITIONS

3.1 Flow resistance and energy dissipation

The flow resistance of stepped chute flow depends on the specific discharge q , the chute angle ϕ and the step height s . The boundary layer grows up to the free surface at the inception point.

The bottom roughness friction factor f_b , can be computed with (Boes and Hager 2003):

$$\frac{1}{\sqrt{f_b}} = \frac{1}{\sqrt{0.5 - 0.42 \sin(2\phi)}} \left[1.0 - 0.25 \log \left(\frac{K}{D_{h,wu}} \right) \right] \quad (4)$$

where $D_{h,wu} \approx 4h_{wu}$ is the uniform hydraulic diameter for a wide, rectangular chute; $K = s \cos \phi$ step roughness perpendicular to the pseudo-bottom; and h_{wu} =uniform equivalent clear water depth.

Further, the energy dissipation depends on the mean air-concentration. The more air is entrained the smaller is the energy dissipation rate (Chanson 2002). Figure 3 shows the energy dissipation for fully developed aerated flow characterized by the relative energy dissipation H_{res}/H_{max} where $H_{max} = H_{dam} + 1.5h_c$ =maximum reservoir energy head. The residual energy head H_{res} can be written as:

$$H_{res} = h_w \cos \phi + \alpha \frac{q^2}{2gh_w^2} \quad (5)$$

where $h_w = (1 - \bar{C})h_{90}$ =equivalent clear water depth; and α =energy correction coefficient.

The equation for the friction factor can be deduced from Chanson (2002):

$$f_e = \frac{8\tau_o}{\rho_w U_w^2} = \frac{8g \left(\int_{y=0}^{y=Y_{90}} (1 - C) dy \right) S_f}{U_w^2} \quad (6)$$

where $U_w = q/b$ mean water velocity; S_f =friction slope; and H =mean total energy head.

For the calculation of the residual energy head on stepped chutes, a distinction should be made between conditions whether uniform flow is attained, or not. For uniform flow, that is for

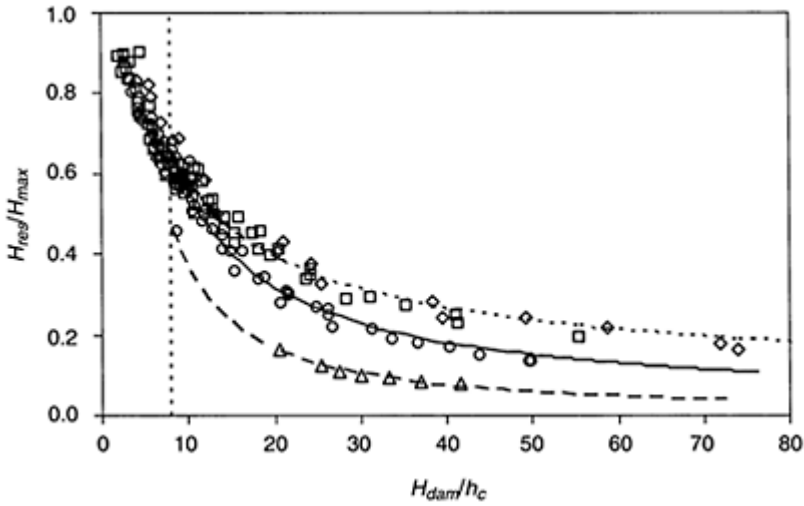


Figure 3. Relative residual energy head ratio H_{res}/H_{max} as a function of relative spillway height H_{dam}/h_c for $\phi = (\Delta)$ 19° (Yasuda 1999) step roughness $K=23.6$ mm, (O) 30° (Boes 2000), (\square) 40° (Schläpfer 2000) and (\diamond) 50° (Boes 2000), step roughness $K=20$ mm (model), eq. (9) for (---) 19°, (—) for 30°, (....) for 40° and 50°. Eq. (9) is valid for $H_{dam}/h_c > 8$.

$H_{dam}/h_c \geq 15$ to 20 according to $H_{dam}/h_c \approx 24(\sin \phi)^{2/3}$ the normalized residual energy head can be expressed as (Boes and Hager 2003):

$$\frac{H_{res}}{H_{max}} = \frac{F}{\frac{H_{dam}}{h_c} + F} \quad (7)$$

with the friction factor f_b , according to equation (4), $\alpha \approx 1.1$ and

$$F = \left(\frac{f_b}{8 \sin \phi} \right)^{1/3} \cos \phi + \frac{\alpha}{2} \left(\frac{f_b}{8 \sin \phi} \right)^{-2/3} \quad (8)$$

3.2 Novel equation for energy dissipation

Computing of energy dissipation according to the procedure described in 3.1 is somewhat complicated, though perfectly correct. Therefore, the available data was analyzed in order

to find a simple relation based on the major geometrical and hydraulic parameters to allow for a simpler design process.

Figure 3 shows the relative residual energy head H_{res}/H_{max} as a function of relative spillway height H_{dam}/h_c for various chute angles, namely 19° (Yasuda 1999), 30° (Boes 2000), 40° (Schläpfer 2000) and 50° (Boes 2000).

The measured data can be described by the following relation if the data for higher relative dam heights, $H_{dam}/h_c > 8$, only is considered:

$$\frac{H_{res}}{H_{max}} = a \left(\frac{H_{dam}}{h_c} \right)^b \quad (9)$$

where H_{dam} =vertical spillway or dam height; and $h_c=(q^2/g)^{1/3}$ critical depth. For smaller relative dam heights Boes and Hager (2003) recommended a more generalized relation.

The variables a and b in equation (9) depend exclusively on the chute angle (Table 1).

The analysis shows an identical result for 40° and 50° chute angles corresponding to the finding of Boes and Hager (2003) represented in equation (4).

Model results show to a certain extent a difference in energy dissipation, depending on step roughness as shown in Figure 4 for a chute angle of $\phi = 30^\circ$. Whereas energy dissipation for various step roughnesses of 40 mm and 80 mm is almost identical, energy dissipation for a step roughness of 20 mm is somewhat smaller. It is not completely clear whether this is a genuine influence of the step roughness or a model scale effect.

Nevertheless the following is true: For practical application it is possible to use equation (9) with the variables given in Table 1. Should steps be larger than 0.3m corresponding to a model scale of about 1:15, which according to Boes (2000) seems to be an upper limit, and which very often will be the case, then the computed energy loss will be slightly smaller than predicted by equation (9). For practical application, e.g. for designing the stilling basin, this result is on the safe side.

4 CONCLUSIONS

The presented data analysis shows a clear dependence of the relative energy dissipation on the chute angle, whereas the step height plays a minor role. The energy loss for chute angles of $\phi = 40^\circ$

Table 1. Variables for Equation (9).

Chute angle	Factor (a)	Exponent (b)
19°	5.0	-1.14
30°	3.6	-0.81
40°, 50°	2.1	-0.56

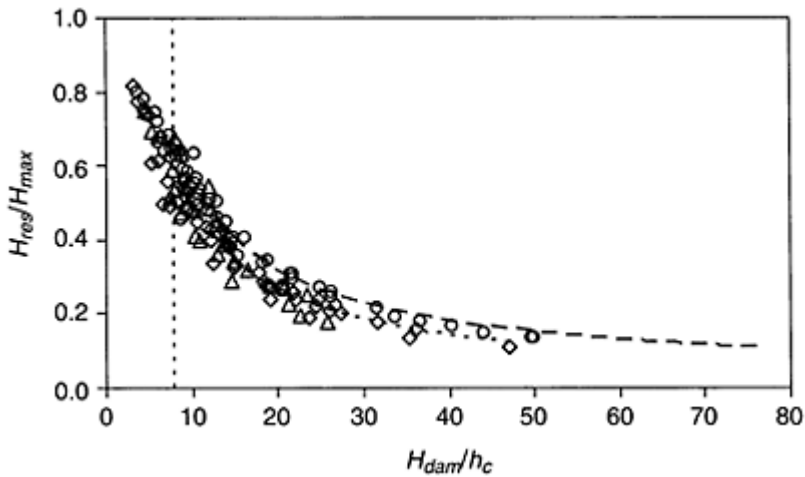


Figure 4. Relative residual energy head ratio H_{res}/H_{max} as a function of relative spillway height H_{dam}/h_c for $\phi = 30^\circ$.

$K=20$ mm, $\diamond K=40$ mm and $(\Delta) K=80$ mm (Boes 2000), eq. (9) (---) with $a=3$ $b=-0.81$ for $K=20$ mm, (....) with $a=3.8$ and $b=-0.89$ for $K=40$ mm and 80 mm.

and $\phi = 50^\circ$ are equal which confirms the result of Boes and Hager (2003) according to which the friction factor f_b depends exclusively on $\sin(\sin(2\phi))$. This may be explained by a different distance $L_s = s/\sin \phi = K/(\sin \phi \cos \phi)$ between two adjacent step corners for a given step roughness K (Figure 1). Since L_s determines the shear length between the recirculating vortices in the step niches and the main flow along the pseudo-bottom.

The proposed novel explicit relation depends on simple parameters only and is based on model test of a step roughness $K=20$ mm. It can be used for larger steps than $s=0.3$ m in practice, too. Thereby the residual energy head is slightly underestimated for higher step roughness (Figure 4).

For a designer it is now possible to compute easily the energy losses of stepped spillway flow for various chute angles on gravity dam profiles and including embankment dam overlays.

REFERENCES

- Boes, R. 2000. Zweiphasenströmung und Energieumsetzung an Grosskaskaden (*Two-phase-flow and energydissipation at cascades*). VAW-Mitteilung Nr.166, Zurich: VAW (in German).

- Boes, R., Hager, W.H. 2003. Hydraulic design of stepped spillways. *Journal of Hydraulic Engineering* 129(9): 671–679.
- Chanson, H. 2002. *The hydraulics of stepped chutes and spillways*. Rotterdam: Balkema.
- Chanson, H., Yasuda, Y., Ohtsu, I. 2002. Flow resistance in skimming flows in stepped spillways and its modelling. *Canadian Journal of Civil Engineering* 29 (6): 809–819.
- Kobus, H. 1985. *Wasserbauliches Versuchswesen*. DVWK-Schrift 39, Stuttgart: DVWK (in German).
- Mateos, C., Elviro, V 1995. Stepped spillways. Design for the transition between the spillway crest and the steps. *Proceedings of 26 IAHR Congress, Hydra 2000*, London, Vol. 1: 260–265.
- Schläpfer, D. 2000. *Treppenschussrinnen (Stepped spillways)*. Zurich: Diploma thesis, unpublished (in German).
- Schwalt, M, Hager, W.H. 1992. Die Strahlbox (The jet-box). *Schweizer Ingenieur und Architekt* 110 (27/28): 547–549 (in German).
- Yasuda, Y., Ohtsu, I.O. 1999. Flow resistance of skimming flow in stepped channels. *Proceedings 28 IAHR Congress*, H. Bergmann, R. Krainer, and H. Breinhälter (eds.). Theme B14 (CD-ROM), Graz, Austria.

Velocity and pressure field in skimming flow in stepped spillways

A.Amador, M.Sánchez-Juny & J.Dolz

*Hydraulic, Maritime and Environmental Eng. Dep., UPC, Barcelona,
Spain*

F.Sánchez-Tembleque & J.Puertas

*Centro de Innovación Tecnológica en Edificación e Ingeniería Civil
(CITEEC), University of La Coruña, La Coruña, Spain*

Hydraulics of Dams and River Structures—Yazdandoost & Attari (eds)

© 2004 Taylor & Francis Group, London, ISBN 90 5809 632 7

ABSTRACT: In stepped spillways the presence of steps enhance the flow turbulence and hence the growth of the boundary layer. The earlier inception of air entrainment in this type of hydraulic structures, compared with a smooth spillway is considered an advantage in terms of cavitation risk. Nevertheless the point of inception is also a function of the discharge, increasing the non aerated zone for higher flow rates. The existence of sufficient air content next to the solid boundaries prevents cavitation damage, the region upstream and next to the inception point will be then critical for evaluation of cavitation risk. In this work, velocity and pressure field in the non aerated region of the spillway were measured. For the velocity field it is used the Particle Image Velocimetry (P.I.V) technique, this non intrusive measurement can bring some insight about the internal flow features that fill the cavities between the main flow and the faces of the steps.

1 INTRODUCTION

Since the first RCC dams in the early 1980's, the method of construction has spread throughout the world, being nowadays a new alternative in the world. The benefits of the RCC method, in terms of construction time and costs of concrete, cause as soon as a RCC dam is built in any country, a rapid expansion of the number of this type of dams within that country (Dunstan 1996). According to the annual data base published in *Handbook of Water Power & Dam Construction* at the end of 1986, there were only 15 completed

RCC dams in the world, by the end of 2002 there were at least 199, showing a rapid development of RCC dams.

The stepped spillways are very suitable hydraulic structures for the RCC method, only needing at the crest a smooth ogee shape followed by some smaller steps (fitted to the ogee shape) before the spillway changes into the stepped chute that is in fact the ogee downstream face of the RCC dam. Besides these economic and time construction advantages this kind of hydraulic structure permits much higher energy dissipation along the chute than a conventional (smooth) spillway, reducing the dimensions of the downstream stilling basin.

Spain is one of the leading countries in construction of RCC dams, from the 24 completed, only 11 have stepped spillways. For high flow rates ($q=15\text{--}20\text{m}^2/\text{s}$), design engineers prefer a more costly conventional spillway than a stepped chute where there is a lack of elements that assure prevention against possible damages on the structure caused by the dynamic loads induced by the flow.

2 SKIMMING FLOW IN STEPPED SPILLWAYS OVER RCC DAMS

Skimming flow regime is usually present in stepped spillways over RCC dams, being the nappe flow limited for small specific discharges. This flow regime is characterized by a coherent stream that skims over the steps, where the edges form a so called “pseudo-bottom”. In the cavity delimited by the faces of the steps and the pseudo-bottom, there is a formation of recirculation vortices. At irregular time intervals momentum exchanges occurs between the main stream and the cavity flow.

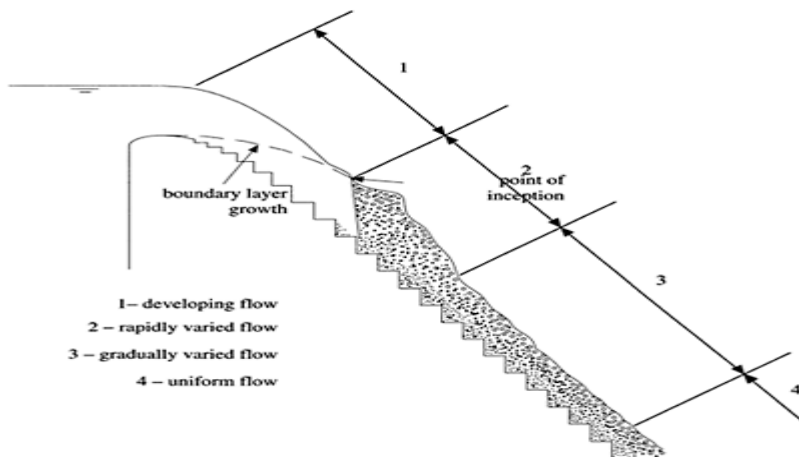


Figure 1. Flow regions in skimming flow regime in a stepped spillway over a RCC dam.

Distinct regions in skimming flow regime can be identified along the stepped chute (Fig. 1). In the initial flow stage there is no air entrainment, the free surface is smooth and glassy. Next to the steps, flow turbulence is generated and starts the growth of the boundary layer. When the thickness of the boundary layer equals the flow depth, it defines the point of inception of air entrainment on the chute.

Downstream the inception point, a rapidly varied flow region is observed. Matos (1999) based on air concentration measurements, showed a convex curvature of the streamlines causing a sudden aeration followed by concave flow that favours the buoyancy of the bubbles and hence causes a slight decrease in the mean air concentration. This region is not usually identified in self aerated flow over conventional spillways, constituting an unique characteristic of stepped spillways. A gradually varied flow region follows the previous described rapidly flow region. Finally far downstream equilibrium will be reached (uniform flow), where the flow depth, velocity and air concentration values will not vary along the chute.

In the present paper focus will be given to the developing and rapidly varied flow regions.

3 EXPERIMENTAL SETUP

The experiments were performed at the Hydraulic Laboratory of the University of La Coruña. The stepped spillway is 2.0m high (H), with a bottom inclination of 51.3° , width (B) of 0.5m and the step height (h) of 0.05 m. The side walls as well as the steps are made of transparent methacrylate to realise optical access from all directions.

The flow conditions analysed are shown in Table 1.

3.1 Particle Image Velocimetry (P.I.V.)

The P.I.V system is used to obtain the velocity field in the zone upstream of the inception point. Ceramic micro spheres with 70 μm diameter were introduced into the flow as tracers. The flow

Table 1. Flow conditions.

	H	B	h	q		
α	m	m	m	m^2/s	y_c/h	Re
53.1°	2.0	0.5	0.05	0.03 up to 0.11	0.90	$0.3 \cdot 10^5$
					2.15	$1.1 \cdot 10^5$

* q—flow discharge per unit width, y_c —critical flow depth, Re—Reynolds number.

is illuminated by a double pulsed Nd-Yag laser with maximum energy level of 450 mJ per pulse. Charge coupled device (CCD) camera with a resolution of 1280×1024 pixels, was positioned normal to the light sheet to capture the flow field. An optical filter was placed in front of the camera lens that allowed only a narrow band of wavelengths around 532nm scattered by the seeding particles.

The images covered one or two steps, bigger measurement areas using the PIV system available implied a loose of accuracy. The camera and laser were synchronized to capture double frame double exposure particle images. The time between two successive images was adjusted in order to give maximum particle displacement of 8 pixels. A digital cross correlation method is used to find the particles images displacements. The algorithm is a multi pass scheme that starts with a predictor step with large interrogation cell size of 128×128 pixels and finishes in a last it where the final interrogation cell size is 32×32 pixels. This interrogation algorithm has shown to be the more adequate for the case in study, more details can be found in Amador et al. (2002) & Bolinder (2000). The cell overlap was 50%, which gives a vector spacing of 16×16 pixels. The spurious vectors were detected using the local median test (Westerweel 1994). The vector is considered incorrect if the displacement deviates more than an accepted amount from the median displacement in the local neighbourhood about the vector.

3.2 Pressure transducers

The fluctuating pressures over the steps were measured by means of Druck PTX 1830 pressure transducers, with a linear working range of -150 mbar to 200 mbar. The non-linearity and hysteresis error is $\pm 0.1\%$ of the range scale. At the steps faces series of pressure taps with diameter of 0.006 m were made. The pressure transducers were connected to the taps by rigid tubes of 0.006 m inside diameter and 0.10 m length. The natural frequency of the measuring system was estimated and considered sufficiently high in comparison with the dominant frequencies of the pressure fluctuations (1 – 5 Hz) found by Sánchez-Juny (2001).

4 VELOCITY FIELD

Velocity fields over six steps located in the developing flow region were obtained. These measurements permit to study the growth of the boundary layer upstream the inception point.

To analyse the mean flow velocity fields and the time mean turbulence quantities, sequences of 500 up to 1000 double frame particle images were taken at intervals of 1 s.

In Figure 2 is shown a map with the contour lines of the average velocity (V) constructed from 1000 instantaneous velocity fields, for a discharge equal to $y_c/h=2.15$. The time between the two successive pulse lasers was $200 \mu\text{s}$. The velocity vector spacing is 2.0 mm (16 pixels) and the kriging method was chosen to create the grid.

The map clearly illustrates the presence of a large size eddy at the corner of the step faces, delimiting the zone of the step affected by recirculation zone and locating shear layer impingement process at the downstream end of horizontal face of the step. It is interesting also to notice the difference between velocity profiles at the steps edges and in between the steps. A concentration of velocity contour lines occur at the step edges having the velocity distribution a sharper increase to the potential flow velocity existent near the free surface than the profile in between the steps were the velocity contour lines are more spaced. Here a more gradual growth of the velocity is observed

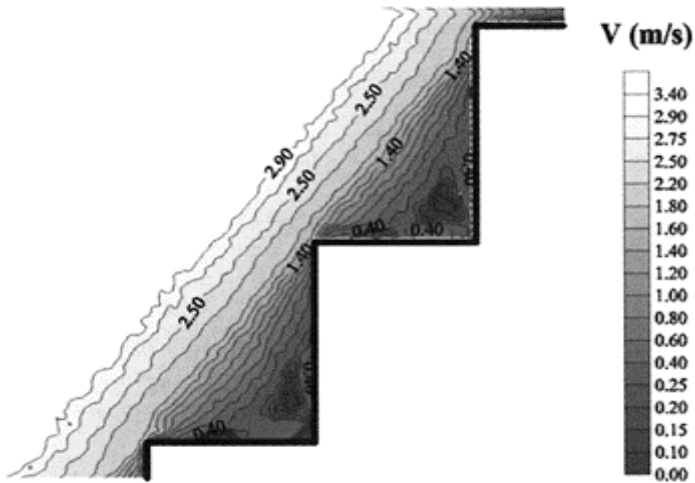


Figure 2. Mean velocity contour lines over steps 30 ($L/k_s=23.28$) and 31 ($L/k_s=21.23$) for the discharge $y_c/h=2.15$, where L (m) is length from spillway crest and $k_s=h.\cos\alpha$ (m) is the roughness height.

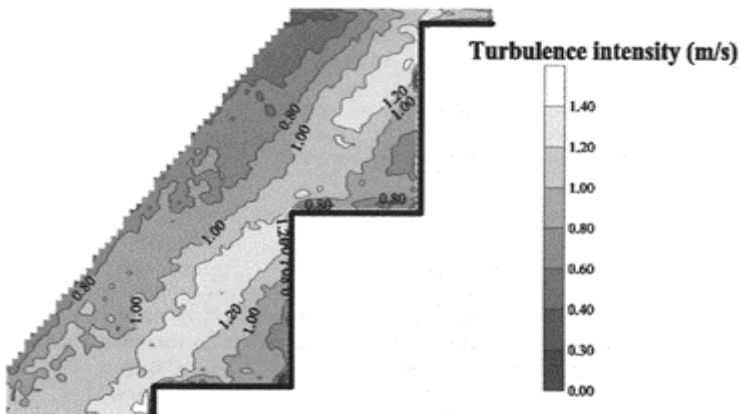


Figure 3. Turbulence intensity contour lines over steps 30 ($L/k_s=23.28$) and 31 ($L/k_s=21.23$) for the discharge $y_c/h=2.15$.

up to the free surface. Also Matos et al. (2001) observed the influence of the recirculation over the air concentration distribution, showing the differences existent between the step edges and in between the steps.

Also it was constructed the detailed field of the turbulence intensity (I), defined as:

$$I = \sqrt{u'^2 + v'^2} \quad (1)$$

where the u' (m/s) is the turbulent velocity in the flow direction and v' (m/s) is turbulent velocity normal to the flow direction.

In Figure 3 is presented the turbulence intensity field for the discharge $y_c/h=2.15$ at steps 30 ($L/k_s=23.28$) and 31 ($L/k_s=21.23$) constructed from 1000 instantaneous velocity fields.

The maximum levels of turbulence intensity are located, like it was expected, near the pseudobottom where important momentum exchanges takes place between the main stream that flows over the steps and the cavity flow. In this zone the dimensionless turbulence intensity, defined as the ratio of the turbulence intensity by the local mean velocity, gets to values around 100%.

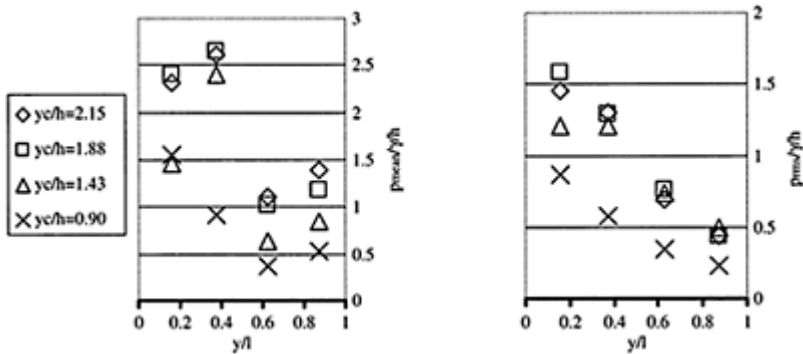


Figure 4. Profiles of mean ($p_{mean}/\gamma/h$) and standard deviation ($p_{rms}/\gamma/h$) over the horizontal face of step 30 ($L/k_s=23.28$).

A decrease in the turbulence intensity is observed in the normal direction up to the free surface where the dimensionless turbulence intensity is about 20 to 30%. Important also are the turbulence levels near the corner of the steps that are connected with the oscillations of the recirculation zone interacting with the shear layer.

Different turbulent intensity profiles were obtained by Chanson (2002), for the air-water flow zone. The results exhibit high turbulence levels across the entire air-water flow mixture ($0 < y < Y_{90}$), the mention author refers that the increase in turbulence levels is directly linked with the number of entrained bubbles/droplets.

5 PRESSURE FIELD

After characterizing the velocity field, it would be interesting to study the relationship between the flow conditions and the pressures induced by the flow over the faces of the step.

The pressures were registered over steps mainly located in the upstream zone of the stepped spillway, where depending on the discharge different flow regions of the skimming flow (developing flow, rapidly varied flow or gradually varied flow regions) could be found.

The time of data acquisition was 60 seconds and the sampling rate adopted was 100Hz. In the present paper profiles of the mean and root mean square of the pressures over the horizontal and vertical faces of the steps will be shown.

In Figure 4 the mean pressure and standard deviation profiles over the horizontal face of step 30 ($L/k_s=23.28$) for the four discharges studied ($y_c/h=2.15, 1.88, 1.43, 0.90$) are presented.

The pressure profiles show that the flows impacts in the downstream half ($y/1<0.4$) of the horizontal face. In this zone the mean pressures are bigger than in the upstream half ($0.4<y/1<1$) where the pressures are governed by the cavity flow. The standard deviation profiles, that reflect the spread of the pressure distribution around the mean, indicate that it is also on the downstream half where occurs a higher variability of the pressures. Nevertheless, like the mean pressures are smaller at the upstream half, the amplitudes of the existent fluctuations are sufficient for appearing negative pressures at the inner region of the step (Sánchez-Juny 2001).

In relation to the vertical face, is shown in Figure 5 the mean and standard deviation profiles obtained at step 31 ($L/k_s=21.23$).

In the vertical face, near the outer edge, there is a separation flow region and negative pressures occur in this zone. The mean pressures are negative or close to zero but the fluctuations are important like indicated by the standard deviation profiles, increasing the amplitudes for higher discharges. So the pressures over the vertical faces are affected by the separation of the shear layer and the recirculation zone in the cavity. Near the step corner it can be noticed a region of positive mean pressures, which can be explained by the formation of a small corner eddy that is impacting on the wall of the steps.

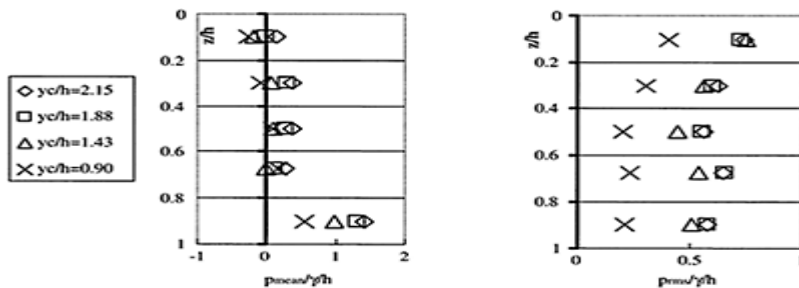


Figure 5. Profiles of mean ($p_{mean}/\gamma h$) and standard deviation ($p_{rms}/\gamma h$) over

the vertical face of step 31
($L/k_s=21.23$).

Comparing the standard deviation profile obtained in the developing and rapidly varied flow regions with the presented by Sánchez-Juny (2001) for the case of fully developed aerated flow, it can be concluded that higher pressure fluctuations on the vertical faces should be expected for the first case, emphasizing the cushion effect that the presence of air introduces on the acting pressures.

6 CONCLUSIONS

In the present paper, velocity and pressure field measurements for a skimming flow regime over a stepped spillway are described. Special attention was devoted for the developing flow and rapidly flow regions of the skimming flow region, where it is believed that are present the higher dynamic efforts acting on the structure and where the evaluation of the cavitation risk should be done.

The measurements with P.I.V technique give an insight about the internal flow features in the cavities of the steps and provide a better understanding of how the flow conditions influence the pressures field over the step faces.

The pressure measurements indicate that negative pressures may occur over the steps, especially over the vertical faces. Further study of the statistical parameters of the turbulence in the skimming flow is needed in order to define the magnitudes and extents of the pressure fluctuations over the steps.

ACKNOWLEDGMENTS

This research was financed by a scholarship of the Fundação para a Ciência e Tecnologia (FCT, Praxis XXI/ BD/3056/2000).

REFERENCES

- Amador, A., Tembleque, F., Sánchez-Juny, M., Puertas, J., Dolz, J. 2002. Aplicación de la técnica particle Image Velocimetry al estudio de aliviaderos escalonados. *Proc. of XX Hydraulic Congress, Latinameri Ciudad La Habana, Cuba*.
- Bolinder, J. 2000. Optimization of PIV in flows with strong velocity gradients. *PDF publication available at internet site of Lavision (www.lavision.de)*.
- Chanson, H., Toombes, L. 2002. Air-water flows down stepped chutes: turbulence and flow structure observations. *International Journal of Multiphase Flow* N° 28, Ed.Pergamon, Oxord. 1737–1761.
- Dunstan, M. 1996. The state of the art of RCC dams. *Proc. of 1st Portuguese Conferences of RCC dams. Lisboa, Portugal*
- Matos, J. 1999. Emulsiónamento de ar e dissipação de energia do escoamento em descarregadores em degraus. *Phd thesis, Instituto Superior Técnico, Lisboa. Portugal*.

- Matos, J., Yasuda, Y., Chanson, H. 2001. Interaction between free-surface aeration and cavity recirculation in skimming flows down stepped chutes. *Proc. 29th IAHR Congress, Beijing, China.*
- Sánchez Juny, M. 2001. Comportamiento hidráulico de los aliviaderos escalonados en presas de hormigón compactado. Análisis del campo de presiones. *PhD thesis, UPC, Barcelona. Spain.*
- Westerweel, J. 1994. Efficient detection of spurious vectors in particle image velocimetry data. *Experiments in Fluids, N° 16.* Ed. Springer. Heidelberg. 236–247.

Stepped spillways for embankment dams. Review, progress and development in overflow hydraulics

H.Chanson & C.A.Gonzalez

The University of Queensland, Dept. of Civil Eng., Brisbane, Australia

Hydraulics of Dams and River Structures—Yazdandoost & Attari (eds)

© 2004 Taylor & Francis Group, London, ISBN 90 5809 632 7

ABSTRACT: In recent years a number of embankments were designed with concrete overtopping protection shaped in a stepped fashion. During large overflows on stepped chutes, there is no skin friction between mainstream and steps, and flow resistance is basically form drag. Alterations of flow recirculation and of fluid exchanges between free-stream and cavity flow are discussed in this study. A comprehensive series of air-water flow measurements on embankment dam stepped chute are presented. The introduction of vanes demonstrates turbulence manipulation and form drag modification that could lead to more efficient designs.

1 INTRODUCTION

In recent years, the design floods of a number of dams were re-evaluated and the revised flows were often larger than those used for the original designs. In many cases, occurrence of the revised design floods would result in dam overtopping because of the insufficient storage and spillway capacity of the existing reservoir. This is unacceptable for embankment structures without overtopping protection systems. During the last three decades, a number of embankment dam spillways were designed with concrete overtopping protection shaped in a stepped fashion (e.g. CHANSON and TOOMBES 2001, CHANSON 2001 pp. 220–230). Although some overflow systems were made of timber cribs, sheet-piles, riprap and gabions, and reinforced earth, recent structures were designed with concrete slabs and formed concrete (CHANSON 2001). During the 1990s, the construction of secondary stepped spillways for embankment accounted for nearly two-thirds of dam construction in USA (DITCHEY and CAMPBEL 2000). The preferred construction method was roller compacted concrete overlays placed on the downstream slope (Fig. 1).

While most modern stepped spillways were designed as prismatic rectangular chutes with flat horizontal steps, recent studies hinted means to enhance the rate of energy

dissipation (see next paragraph). In skimming flows on stepped chutes, there is no skin friction between free-stream



Figure 1. Stepped overflow protection system for a detention basin in west Las Vegas under construction (Courtesy of M.R. DELCAU and USACE-LA District).

and stepped invert, but at the step edges which are hydrodynamic singularities. Flow resistance is basically form drag. Alterations of flow recirculation and of fluid exchanges between free-stream and cavity flow may affect drastically the form losses and in turn the rate of energy dissipation. In the present study, new experiments were conducted at near full-scale with a 22° slope. Interactions between free-surface and cavity recirculation were thoroughly investigated in the skimming flow regime, while the effects of turbulence manipulation were systematically detailed.

1.1 *Energy dissipation enhancement: prototype and laboratory experience*

During the 19th century, overflow stepped spillways were selected frequently with nearly one third of the dams built in USA being equipped with a stepped cascade (e.g. SCHUYLER 1909, WEGMANN 1922, CHANSON 2001). Most structures had flat horizontal steps (e.g. Gold Creek dam, Titicus dam), but some were equipped with devices to enhance energy dissipation. Some spillways had pooled steps with vertical walls (Sorpe dam, 1932) or rounded edges (Le Pont dam, 1882) (Fig. 2). Recently ANDRE et al. (2001) suggested an alternance of pooled steps and flat steps for maximum energy dissipation. PEYRAS et al. (1991) demonstrated greater energy dissipation with inclined upward steps. All these techniques add considerable structural loads to the stepped structure and might not be economical.

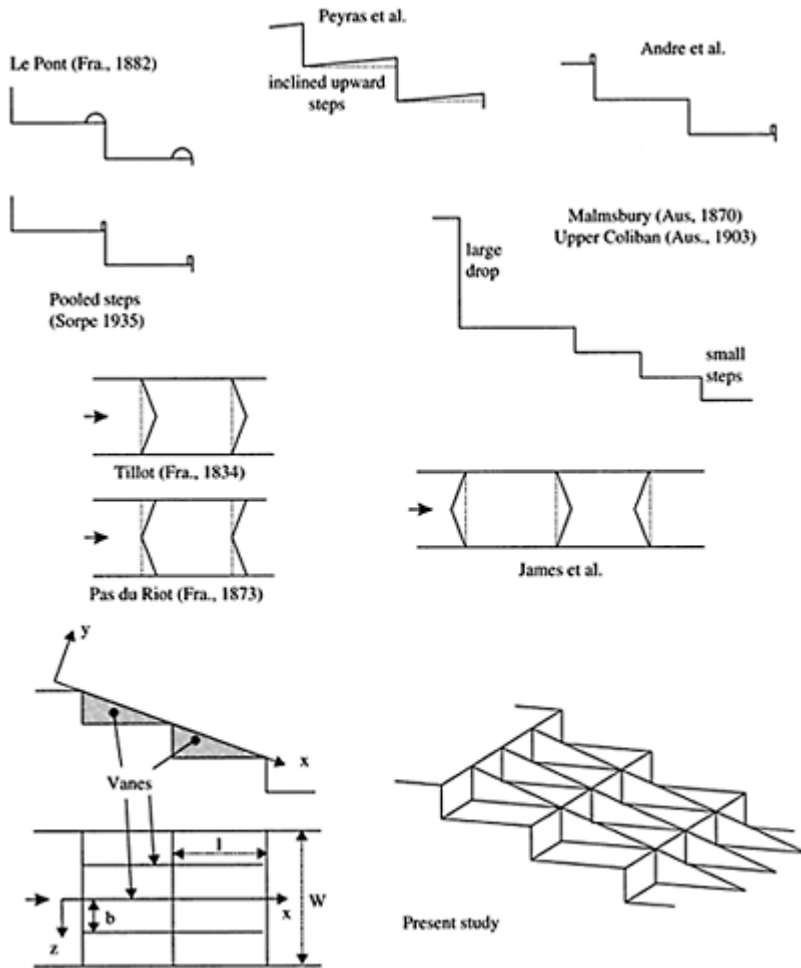


Figure 2. Examples of step configurations for energy dissipation enhancement.

Enhancement of energy dissipation may be provided by superposition of small and large steps. In Australia, the Malmsbury (1870) and Upper Coliban (1903) dam spillways were designed with a combination of large drops ($h=2$ to 4 m) and stepped chutes ($h=0.305$ m). At design flows, the drops operate with a nappe flow and the chutes in skimming flow regime. Their successful operation for more than a century suggests that the design is sound. On the model of the Kennedy's Vale dam ($h/l=1$), STEPHENSON (1988) superimposed occasional large steps to smaller steps and he observed a 10% increase in energy dissipation for this model. JAMES et al. (2001) observed larger rates

of energy dissipation with V-shaped step edges (Fig. 2). Two early French stepped spillways were also equipped with V-shaped steps: Tillot dam (1834) and Pas du Riot dam (1873). Both stepped spillways are still in use. CHANSON (2002b) argued however that step lateral deflections induce complicated three-dimensional flow patterns.

2 EXPERIMENTAL SETUP

New experiments were conducted at the University of Queensland in a 3.3 m long, 1 m wide, 21.8° slope chute previously used by CHANSON and TOMBES (2002). Waters were supplied from a large feeding basin (1.5-m deep, surface area 6.8 m×4.8 m) leading to a sidewall convergent with a 4.8:1 contraction ratio. The test section consisted of a broad-crested weir (1 m wide, 0.6 m long, with upstream rounded corner (0.057-m radius)) followed by ten identical steps ($h=0.1$ m, $l=0.25$ m) made of marine ply. The stepped chute was 1 m wide with perspex sidewalls followed by a horizontal concrete-invert canal ending in a dissipation pit. For two series of experiments, the step cavities were equipped with vanes (Fig. 2, Table 1).

The flow rate was delivered by a pump controlled with an adjustable frequency AC motor drive, enabling an accurate discharge adjustment in a closed-circuit system. The discharge was measured from the upstream head above crest with an accuracy of about 2%. Clear-water flow depths were measured with a point gauge. Air-water flow properties were measured using a double-tip conductivity probe ($\phi=0.025$ mm) designed at the University of Queensland (CHANSON 1995). The probe sensors were aligned in the flow direction and excited by an air bubble detector

Table 1. Detailed experimental investigations of air entrainment on embankment dam stepped chutes.

Reference (1)	θ (deg.) (2)	q_w (m^2/s) (3)	h (m) (4)	Flow regime (5)	Instrumentation (6)	Remarks (7)
Chanson and Toombes (2002)	21.8	0.06 to 0.18	0.1	Transition, Skimming	Double-tip conductivity probe ($\phi=0.025$ mm)	$L=3.0$ m. $W=1$ m. Inflow: uncontrolled broad-crest. Experiments TC200.
	15.9	0.07 to 0.19	0.1	Transition, Skimming	Double-tip conductivity probe ($\phi=0.025$ mm)	$L=4.2$ m. $W=1$ m. Inflow: uncontrolled broad-crest. Experiments TC201
Gonzalez and Chanson (2004)	15.9	0.020 to 0.200	0.05	Transition, Skimming	Double-tip conductivity probe ($\phi=0.025$ mm)	$L=4.2$ m. $W=1$ m. Inflow: uncontrolled broad-crest. Experiments CG202.
		0.075 to 0.220	0.10	Transition, Skimming		Incl. detailed measurements between step edges.

Present study	21.8	0.10 to 0.22	0.1	Skimming	Double-tip conductivity probe (Ø=0.025 mm)	L=3.3 m. W=1 m. Inflow: uncontrolled broad-crest. Experiments CG203.
				Type		b=W=1 m (no vane).
				Type		b=W/4=0.25m(3vanes).
				Type		b=W/8=0.125 m (7 vanes).

Notes: b: spacing between vanes; L: chute length; W: chute width.

(UQ82.518). The probe signal was scanned at 20 kHz for 20 seconds. The translation of the probes in the direction normal to the channel invert was controlled by a fine adjustment traveling mechanism connected to a Mitutoyo™ digimatic scale unit (Ref. No. 572–503). The error on the vertical position of the probe was less than 0.025 mm. The accuracy on the longitudinal probe position was estimated as $\Delta x < \pm 0.5$ cm. The accuracy on the transverse position of the probe was less than 1 mm. Flow visualisations were conducted with high-shutter speed digital still- and video-cameras.

2.1 Data processing

The basic probe outputs were the void fraction, bubble count rate, velocity, turbulence intensity and air/water chord size distributions (e.g. CHANSON 2002a). The void fraction C is the proportion of time that the probe tip is in the air. The bubble count rate F is the number of bubbles impacting the probe tip. The bubble chord times provide information on the air-water flow structure. With a dual-tip probe design, the velocity measurement is based upon the successive detection of air-water interfaces by two tips. In turbulent air-water flows, the detection of all bubbles by each tip is highly improbable and it is common to use a cross-correlation technique (e.g. CROWE et al. 1998). The time-averaged air-water velocity equals: $V = \Delta x / T$, where Δx is the distance between tips and T is the time for which the cross-correlation function is maximum. The turbulent intensity $Tu = u' / V$ may be derived from the broadening of the cross-correlation function compared to the auto-correlation function (CHANSON and TOOMBE S 2002

$$Tu = 0.851 \times \frac{\sqrt{\Delta T^2 - \Delta t^2}}{T} \quad (1)$$

where ΔT as a time scale satisfying: $R_{xy}(T + \Delta T) = 0.5 \times R_{xy}(T)$, R_{xy} is the normalised crosscorrelation function, and Δt is the characteristic time for which the normalised autocorrelation function R_{xx} equals 0.5. The autocorrelation function itself provides some information on the air-water flow structure. A time series analysis gives further information on the frequency distribution of the signal which is related to the air&water (or water&air) length scale distribution of the flow.

Chord sizes may be calculated from the raw probe signal outputs. The results provide a complete characterisation of air and water chord streamwise distribution and may be analysed in terms of particle clustering and grouping. CHANSON and TOOMBES (2002) considered two air bubbles to form parts of a cluster when the water chord separating the bubbles is less than one tenth of the mean water chord size. The

measurement of air-water interface area is a function of void fraction, velocity, and bubble sizes. For any bubble shape and size distribution, the specific air-water interface area a defined as the air-water interface area per unit volume of air and water may be derived from continuity: $a=4 \times F/V$

2.2 Stepped configuration

Experimental observations highlighted the three-dimensional nature of recirculation vortices in the step cavities beneath the pseudo-bottom formed by the step edges. In absence of vane (see below), three to four cavity recirculation cells were observed across the channel width. The finding was consistent with similar observations by MATOS (Pers. Comm.) and YASUDA (Pers. Comm.) on steeper slopes. In the present study, three stepped geometries were tested systematically. All had ten identical flat horizontal steps. In the first configuration, no vane was installed. In the second and third geometries, vanes were placed across the step cavity from steps 2 to 10 as illustrated in Figures 2 and 3. The second and third configurations had 3 and 7 vanes respectively (Table 1, Fig. 3). The vanes were made of aluminum, with few in perspex next to the sidewall for flow visualisation. The vanes did not interfere with the free-stream.

Experimental observations were conducted for flow rates ranging from 0.1 to 0.22 m³/s corresponding to a skimming flow regime (Table 1, column 5). Measurements were performed at step edges and between adjacent step edges (i.e. above the recirculation cavity).

3 BASIC AIR-WATER FLOW RESULTS

In skimming flows, the flow was smooth and no air entrainment occurred at the upstream end of the cascade. After a few steps the flow was characterised by strong air entrainment. Downstream the two-phase flow behaved as a homogeneous mixture and the exact location of the interface became undetermined. There were continuous exchanges of air-water and of momentum between the main stream and the atmosphere, while intense cavity recirculation was observed. The mainstream air-water flow consisted of a bubbly flow region ($C < 30\%$), a spray region ($C > 70\%$) and an intermediate flow structure for $0.3 < C < 0.7$.

At inception of free-surface aeration, the flow was rapidly varied. Side view observations suggested that some air was entrapped by a flapping mechanism in the step cavity (ies) upstream of the visual location of free-surface aeration. In presence of vanes, aeration of two to three cavities were seen upstream of inception: that is, more than in absence of vanes for identical flow rates. Flow visualisations next to the chute sidewall and next to the inception point of free-surface aeration highlighted the effects of vanes onto cavity recirculation. Although the vanes did not interfere with the stream flow, they were subjected to strong transverse pressure forces: i.e., in the horizontal direction z normal to the stream flow direction. The pressure load fluctuations appeared to be of the same period and in phase with cavity fluid ejections described by CHANSON et al. (2002).

3.1 Void fraction and velocity distributions

Detailed measurements of void fraction and air-water velocity were conducted downstream of air entrainment inception. For the stepped configurations with vanes, measurements were conducted systematically at $z=0$, $b/4$ and $b/2$, where z is the transverse direction with $z=0$ on the channel centreline above a series of vanes and b is the spacing between vanes (Fig. 2).

For all stepped configurations, air concentration distributions highlighted smooth profiles that followed closely an analytical solution of the bubble advective diffusion equation. Between step edges, strong aeration was recorded in the step cavities. The results showed little effects of the vanes on the void fraction results (Fig. 4). Figure 4 presents typical dimensionless distributions of air concentrations C and velocity V/V_{90} at step edge, where V_{90} is the characteristic velocity at $y=Y_{90}$, y is the distance normal to the pseudo-bottom formed by the step edges and Y_{90} is the distance where $C=0.9$. In Figure 4, the mean air content C_{mean} was 0.36 (no vane), 0.33 (7 vanes, $z/b=0$) and 0.37 (7 vanes, $z/b=0.5$).

Velocity measurements demonstrated that the effect of vanes extended far into the main stream. The velocity distributions showed some marked difference with 3 and 7 vanes for $y/Y_{90} < 0.6$ to 0.7 at all transverse positions ($z/b=0$, 0.25 & 0.5). This is illustrated in Figures 4 and 5. Figure 5 shows typical dimensionless distributions of velocity V/V_{90} and turbulence intensity Tu between step edges. Data for $y < 0$ were recorded in the step cavity. Velocity measurements between step edges highlighted further the developing mixing layer downstream of each step edge (GONZALEZ and CHANSON 2004). Above vanes, the mainstream turbulence levels were usually lower than between vanes and than in absence of vanes.

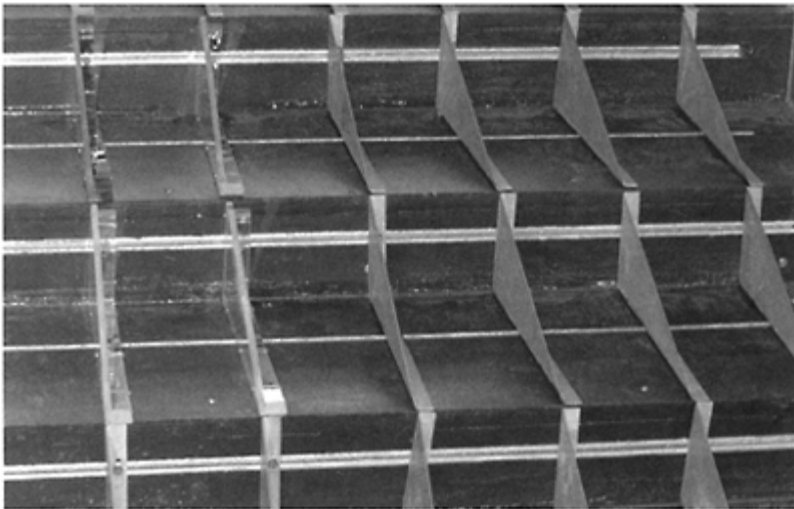


Figure 3. Photograph of the stepped invert with 7 vanes (Configuration 3).

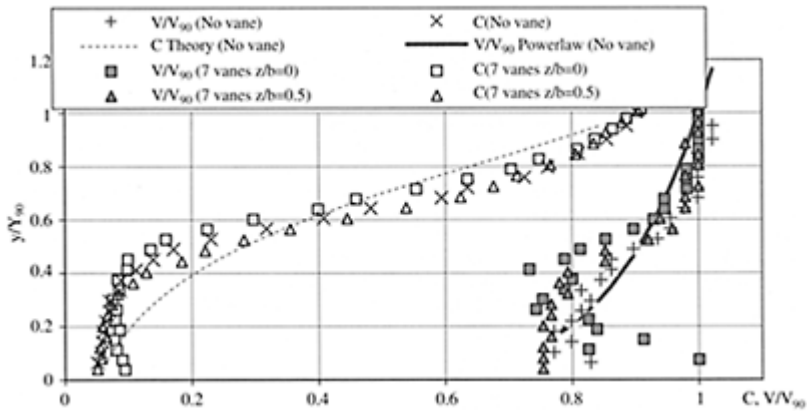


Figure 4. Dimensionless distributions of air concentrations and velocity at step edge 9 ($d_c/h=1.5$)—Comparison between Configuration 1 (no vane) and Configuration 3 (7 vanes, $z/b=0$ & 0.5).

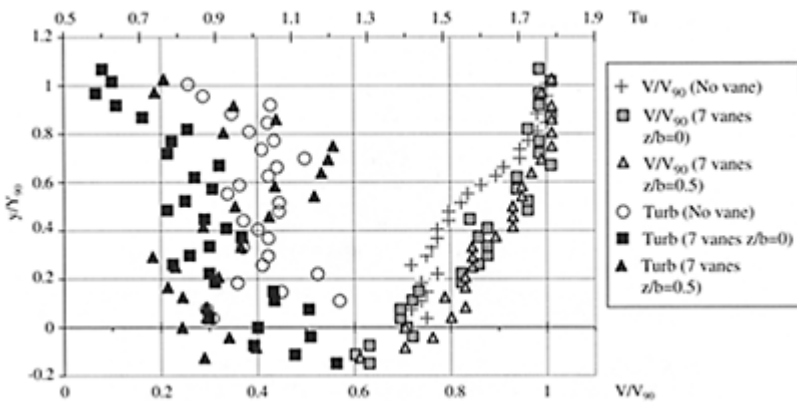


Figure 5. Dimensionless distributions of velocity and turbulence intensity at half-distance between step edges 9 and 10 ($d_c/h=1.5$)—Comparison between Configurations 1 and 3 (7 vanes, $z/b=0$ & 0.5).

3.2 Flow resistance and energy dissipation

Flow resistance was deduced from the average friction slope (e.g. CHANSON et al. 2002). For the stepped configurations with vanes, the flow resistance was calculated at $z/b=0$ (above vane), $z/b=0.25$ and $z/b=0.5$. Results are presented in Table 2 for all configurations. In average they implied equivalent Darcy friction factors of about 0.25, 0.32 and 0.29 for no vane, 3 vanes and 7 vanes respectively suggesting that the presence of vanes increased the flow resistance and the rate of energy dissipation. It is believed that the vanes prevent the development of transverse turbulence in the cavities. The inhibition of large transverse vortical structures is associated with enhanced vertical mixing between recirculation zones and mainstream that is characterised by irregular fluid ejections, turbulent bursts and sweeps. Turbulent mixing enhancement yields greater rate of energy dissipation and flow resistance.

Table 2. Flow resistance estimates in air-water flows

d_c/h	No vane	f_e					
		3 vanes			7 vanes		
		$z/b=0$	$z/b=0.25$	$z/b=0.5$	$z/b=0$	$z/b=0.25$	$z/b=0.5$
(1)	(2)	(3)	(4)	(5)	(6)	(7)	(8)
1.1	0.234	0.355	0.304	0.337	–	0.297	0.301
1.3	0.244	0.340	0.318	0.314	–	0.312	0.293
1.5	0.281	0.373	0.301	0.272	0.281	0.31	0.273
1.7	0.249	0.408	0.287	0.259	–	0.273	0.259

4 SUMMARY AND DISCUSSION

In skimming flows on stepped channels, there is no skin friction between mainstream and step surfaces, but at the flow singularities generated by the step edges. Flow resistance is basically form drag. Alterations of flow recirculation and fluid exchanges between free-stream and cavity flow affect drastically form losses and in turn the rate of energy dissipation. This study presents a comprehensive series of air-water flow measurements on an embankment dam stepped chute. The introduction of vanes demonstrated simple turbulence manipulation and form drag modification that could lead to more efficient designs in terms of rate of energy dissipation without significant structural load on the chute.

However the design of embankment overflow stepped spillway is a critical process. Any single failure of the spillway system can lead to a total dam failure. A number of specific key issues must be assessed accurately and these include stepped chute operation and erosion, embankment seepage, drainage beneath steps, sidewall design (overtopping,

scour), chute geometry (effects of chute convergence), and downstream energy dissipation and scour (CHANSON and TOOMBES 2001). Today some hydrodynamic processes are still inadequately understood. For example, the secondary currents at the connection between steps and (smooth) abutment walls, chute convergence effects, the interactions between seepage and free-surface flows, and downstream energy dissipation in a plunge pool. At the connection between steps and abutment walls, the differences in flow resistance between stepped invert and smooth concrete abutment generate transverse velocity gradient and secondary currents, associated with high shear forces. During overflows, seepage takes place in the embankment. Appropriate provision for drainage is required and drains are usually installed on the vertical face of the steps. With form drag, fluid injection in the separated region (i.e. the wake) does reduce drastically the drag (e.g. WOOD 1964, NAUDASCHER and ROCKWELL 1994). CHANSON and TOOMBES (2001) hypothesised that a similar mechanism may exist in skimming flows above embankment stepped spillway. At the downstream end of the spillway, submerged steps may be damaged during high tailwater level conditions. BAKER (2000) observed major damage to stepped block spillway sections submerged by a hydraulic jump and a plunge pool. YASUDA and OHTSU (2000) investigated the characteristics in the plunge pool downstream of a stepped chute as a function of the tailwater level. Although their results did not include efforts on the submerged steps, they observed some energy dissipation contribution from the submerged steps, suggesting some loads on the steps.

In most cases, physical modeling of embankment stepped spillway is strongly advised. Physical models are usually based upon a Froude similitude, but recirculation flows and free-surface aeration may induce significant scale effects in small-size laboratory models. The geometric scaling ratio should be no greater than 10:1, and preferably less than 5:1.

ACKNOWLEDGMENTS

The writers thank Mr G.ILLIDGE for his assistance and Professor C.J.APELT his valuable advice. The second writer acknowledges the financial support of the National Council for Science and Technology of Mexico (CONACYT) and of the University of Queensland.

REFERENCES

- ANDRE, S., BOILLAT, J.L., and SCHLEISS, A. (2001). "High velocity two-phase turbulent flow over macroroughness stepped chutes: focus on dynamic pressures." *3rd Intl Symp. Environmental Hydraulics*, Tempe, 6 pages (CD-ROM).
- BAKER, R. (2000). "Field Testing of Brushes Clough Stepped Block Spillway." *Intl Workshop on Hydraulics of Stepped Spillways*, Zürich, Switzerland, Balkema Publ., pp.13–20.
- CHANSON, H. (1995). "Air Bubble Entrainment in Free-surface Turbulent Flows. Experimental Investigations." *Report CH46/95*, Dept. of Civil Engrg., Univ. of Queensland, Australia, 368 pages.
- CHANSON, H. (2001). "The Hydraulics of Stepped Chutes and Spillways." *Balkema*, Lisse, The Netherlands, 418 pages

- CHANSON, H. (2002a). "Air-Water Flow Measurements with Intrusive Phase-Detection Probes. Can we Improve their Interpretation?" *Jl of Hyd. Engrg.*, AS CE, Vol. 128, No. 3, pp. 252–255.
- CHANSON, H. (2002b). "Enhanced Energy Dissipation in Stepped Chutes. Discussion." *Proc. Instn Civ. Engrs Water and Maritime Engrg*, UK, Vol. 154, No. 4, pp. 343–345 & Front cover.
- CHANSON, H., and TOOMBES, L. (2001). "Experimental Investigations of Air Entrainment in Transition and Skimming Flows down a Stepped Chute. Application to Embankment Overflow Stepped Spillways." *Research Report No. CE158*, Dept. of Civil Eng., Univ. of Queensland, Brisbane, Australia. 74 pages.
- CHANSON, H., and TOOMBES, L. (2002). "Air-Water Flows down Stepped Chutes: Turbulence and Flow Structure Observations." *Intl Jl of Multiphase Flow*, Vol. 27, No.11, pp. 1737–1761.
- CHANSON, H., YASUDA, Y., and OHTSU, I. (2002). "Flow Resistance in Skimming Flows and its Modelling." *Can Jl of Civ. Eng.*, Vol. 29, No. 6, pp. 809–819.
- CROWE, C., SOMMERFIELD, M., and TSUJI, Y. (1998). "Multiphase Flows with Droplets and Particles." *CRC Press*, Boca Raton, USA, 471 pages.
- DITCHEY, E.J., and CAMPBELL, D.B. (2000). "Roller Compacted Concrete and Stepped Spillways." *Intl Workshop on Hydraulics of Stepped Spillways*, Zürich, Switzerland, Balkema Publ., pp. 170–178.
- GONZALEZ, C.A., and CHANSON, H. (2004). "Interactions between Cavity Flow and Main Stream Skimming Flows: an Experimental Study." *Can Jl of Civ. Eng.*, Vol 31 (accepted for publication).
- JAMES, C.S., MAIN, A.G., and MOON, J. (2001). "Enhanced Energy Dissipation in Stepped Chutes." *Water & Maritime Engineering, Proc. Instn. Civ. Engrs.*, UK, Vol. 148, No. 4, pp. 277–280.
- NAUDASCHER, E., and ROCKWELL, D. (1994). "Flow-Induced Vibrations. An Engineering Guide." *IAHR Hydraulic Structures Design Manual No. 7*, Hydraulic Design Considerations, Balkema Publ., Rotterdam, The Netherlands, 413 pages.
- PEYRAS, L., ROYET, P., and DEGOUTTE, G. (1991). "Ecoulement et Dissipation sur les Déversoirs en Gradins de Gabions." *Jl La Houille Blanche*, No. 1, pp. 37–47.
- STEPHENSON, D. (1988). "Stepped Energy Dissipators." *Proc. Intl Symp. on Hydraulics for High Dams*, IAHR, Beijing, China, pp. 1228–1235.
- SCHUYLER, J.D. (1909). "Reservoirs for Irrigation, Water-Power and Domestic Water Supply." *John Wiley & sons*, 2nd edition, New York, USA.
- WEGMANN, E. (1922). "The Design and Construction of Dams." *John Wiley & Sons*, New York, USA.
- WOOD, C.J. (1964). "The Effect of Base Bleed on Periodic Wake." *Jl Roy. Aer. Soc.*, Vol. 68, pp. 477–482.
- YASUDA, Y., and OHTSU, I. (2000). "Characteristics of Plunging Flows in Stepped Channel Chutes." *Intl Workshop on Hydraulics of Stepped Spillways*, Zürich, Switzerland, Balkema Publ., pp. 147–152.

Part 2:
River Structures

7.

*Scouring and sedimentation
around structures*

Recent views on the origin of river meandering and braiding

M.S.Yalin

Emeritus Professor, Department of Civil Engineering, Queen's University, Kingston, Ontario, Canada

Hydraulics of Dams and River Structures—Yazdandoost & Attari (eds)

© 2004 Taylor & Francis Group, London, ISBN 90 5809 632 7

ABSTRACT: Using the expression of energy of an alluvial stream conveying a constant flow rate in conjunction with the entropy increment principle it has been demonstrated that the regime formation is by the minimization of flow velocity, and thus of the flow Froude number. In the case of meandering the minimizations mentioned are achieved by the reduction of channel slope, in the case of braiding, by the reduction of friction factor. The criteria for meandering and braiding are also revealed.

1 INTRODUCTION

Regime channels, meandering and braiding are still regarded by many researchers as independent from each other fluvial phenomena, and they are investigated and formulated by them as such. Although the views that the regime formation should be due to the increment of entropy, that a stream is meandering because it tends to reduce its slope to the regime value,... have already been proposed (see e.g. Yang 1976, 1992, 1994, Yang et al. 1981, Song & Yang 1982, Chang & Hill 1977, Chang 1979, White et al. 1981, 1982, Davis & Sutherland 1980, 1983), they have not been readily accepted by the professionals. And the reason for this may lie in the fact that these views were literally *views* only—no theory, or even a convincing explanation, was offered by their authors to support them. The first attempt to unify these disjoint views in the form of a coherent explanation is apparently due to Yalin 1992 and Yalin and da Silva 1999, 2001. They maintain that any alluvial stream having a constant energy and flow rate is either in the regime state, or it is in the process of attaining that state—the process is motivated by the entropy-increment principle, meandering and braiding being the “methods” used by the stream to achieve its regime state.

The present paper is the updated and improved outline of the approach of the last cited authors.

2 TOTAL ENERGY OF AN ALLUVIAL STREAM: THE FIRST LAW

i) Consider the system S formed by the hydrological cycle of a river (Figure 1): \bar{Q}_{sol} , \bar{Q}_{int} , \bar{Q}_{rad} are the long-range average time-rate of heat received by S from the sun, the long-range average time-rate of heat received by S from the earth's interior, and the long-range average time-rate of heat lost by radiation, respectively. Since the "overall average temperature of the earth surface ($\approx 300^\circ\text{K}$) hardly changes over hundreds or even thousands of years..." (Goldstein & Goldstein 1993, p.251) we can write

$$\bar{Q}_{sol} + \bar{Q}_{int} + \bar{Q}_{rad} = 0 \quad (1)$$

The analogous is valid for the long-range heat and wind work-rates \bar{Q}'_* and \bar{W}'_* crossing the side boundaries bc and da :

$$\bar{Q}'_* - \bar{W}'_* = 0 \quad (2)$$

But if the long-range work and heat rates crossing the boundary of S are zero, then, according to the *First Law of Thermodynamics* (Spalding & Cole 1973, Wark 1971, Moran & Shapiro 1992,

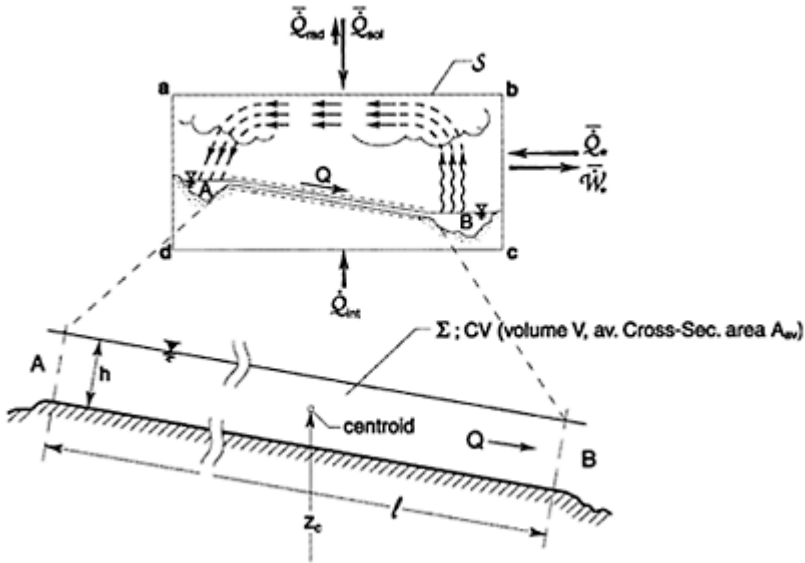


Figure 1. Idealized river-system S and the sub-system Σ .

Munson et al. 1994), the long-range average time-rate of the energy E (of S) must also be zero:

$$\frac{d\bar{E}}{dt} = \frac{d\bar{E}}{dt} = 0 \quad \text{i.e.} \quad \bar{E} = \text{const} \quad (3)$$

The same is valid for the energy of any constituent part of S , and thus for the energy E of the “river” AB forming the subsystem Σ . (The heat and wind-work exchange between the river and its surroundings is quasi-periodically alternating, and its long-range time-average is zero). Hence

$$\frac{d\bar{E}}{dt} = 0 \quad \text{i.e.} \quad \bar{E} = \text{const} \quad (4)$$

ii) The *basic* mechanism of the river formation process can be revealed best if the attention is focused on the simplest idealized “river” in Figure 1. Here the river system Σ is coincidental with the control volume CV : each of them has, at any instant t , the same volume V . The initial channel at $t=0$ is prismatic. The flow rate Q , the temperature T° , and the fluid density ρ are treated as constants: the width-to-depth ratio B/h of the flow is assumed to be “large” at all stages (larger than ≈ 10 to 15). [In natural rivers, $Q=f(t)$, and $Q=\text{const}$ usually is identified with the “bankfull Q ”. $\rho=\text{const}$, because the (dimensionless volumetric) concentration C of the suspended-load does not exceed ≈ 0.02 (even near the bed Soo 1967)).]

The duration T_R of the regime development is by orders of magnitude larger than the average period of the seasonal fluctuation of Q_* , W_* and E . Hence the regime development will be in terms of the long-range dimensionless time

$$\Theta = \frac{t}{T_R} \quad (\in [0; 1]) \quad (5)$$

3 ENERGY COMPONENTS AND ENTROPY: GIBBS' EQUATION

Identifying the actual (fluctuating) E with its constant time-average value \bar{E} , and considering (4), we can write for any Θ

$$E = E_k + E_p + E_i = \text{const} \quad (6)$$

and thus,

$$\left(\frac{dE}{d\Theta} \right) = \frac{dE_k}{d\Theta} + \frac{dE_p}{d\Theta} + \frac{dE_i}{d\Theta} = 0 \quad (7)$$

where E_k , E_p and E_i are the kinetic, potential, and internal energy components of E (at that Θ). The first two terms in (7) can be expressed as,

$$\frac{dE_k}{d\Theta} + \frac{dE_p}{d\Theta} = \rho \frac{d}{d\Theta} [V((u_{av}^2/2) + gz_c)] \quad (8)$$

where u_{av}^2 is the averaged over V value of the flow velocities u , and z_c is the averaged over V value of the elevations z (it is the elevation of the centroid of V).

If the system is formed by an incompressible fluid, then the time increments of its internal energy E_i and its entropy S_* are interrelated by the following form of the Gibbs' Eq. (Spalding & Cole 1973, Wark 1971, Moran & Shapiro 1992, Munson et al. 1994)

$$\frac{dE_i}{d\Theta} = T^\circ \frac{dS_*}{d\Theta} \quad (9)$$

where T° is the (always positive) absolute temperature.

Substituting (8) and (9) in (7), we obtain

$$T^\circ \frac{dS_*}{d\Theta} + \rho \frac{d}{d\Theta} [V(u_{av}^2 + gz_c)] \quad (10)$$

where T° and ρ are to be treated as positive constants. No systematic up or down displacement of a stream as a whole has been observed in the course of its regime development. Hence one has no alternative but to adopt $z_c = \text{const}$. And since the z -datum is arbitrary, one can just as well take $z_c = 0$. By doing so (10) can be reduced into

$$2T^\circ \frac{dS_*}{d\Theta} + \rho \frac{d}{d\Theta} (Vu_{av}^2) = 0 \quad (11)$$

4 TIME-EVOLUTION OF AN ALLUVIAL STREAM: THE SECOND LAW

The *Second Law* of Thermodynamics (Spalding & Cole 1973, Wark 1971, Moran & Shapiro 1992, Munson et al. 1994) states that

The Entropy S_ of an isolated irreversible System monotonously increases with the passage of time ($dS_*/d\Theta > 0$).*

Since $dE/d\Theta = 0$ our system Σ is *isolated*, and since it is formed by a real (frictional) fluid it is irreversible. Hence

$$\frac{dS_*}{d\Theta} > 0 \quad (\text{for any } \Theta \in [0; 1]). \quad (12)$$

This inequality indicates that the first term in (11) is positive, and that the second *must* thus be negative:

$$\frac{d(Vu_{av}^2)}{d\Theta} < 0 \quad (13)$$

Let ℓ and A_{av} be the length and the average cross-sectional area of the stream. Since $V = \ell A_{av}$ (see Fig. 1) and $Q = A_{av} u_{av}$, we have $(Vu_{av}^2) = Qu_{av}\ell$ which means that (13) can be expressed as

$$\frac{du_{av}}{d\Theta} \ell + u_{av} \frac{d\ell}{d\Theta} < 0 \quad (14)$$

Here the second term cannot be negative, for the channel length ℓ either increases (as in meandering and braiding) or it remains as it is (as in aggradation-degradation). But then (14) and thus (13) can be fulfilled only if

$$\frac{du_{av}}{d\Theta} < 0 \quad (15)$$

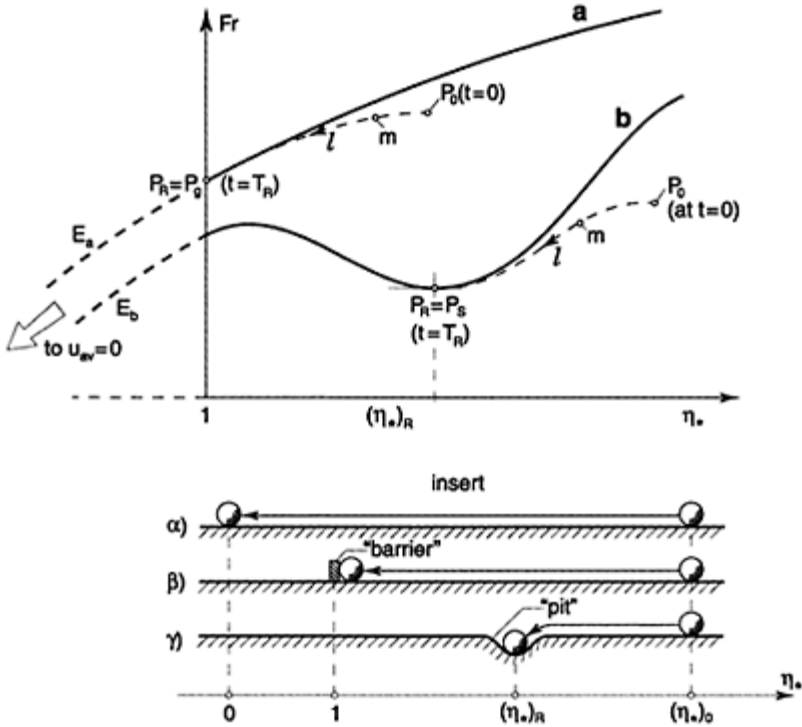


Figure 2. Regime development on the $(Fr; \eta_*)$ -plane.

i.e. only if the velocity u_{av} of the flow (having constant values of E and Q) progressively decreases during the regime development.

5 MINIMIZATION OF AVERAGE FLOW VELOCITY

From the content of the preceding Section one infers that an isolated stream having a constant Q tends to increase its entropy S_* , and thus to reduce its velocity u_{av} . However,

the reduction of u_{av} can be achieved only if the stream appropriately alters its channel. The regime development is the process of this “appropriate alteration”. The regime development terminates when the smallest possible value of u_{av} , or of its dimensionless counterpart, the Froude number

$$Fr = \frac{u_{av}^2}{gh} \quad (16)$$

is reached (more on the topic in Yalin and da Silva 2001).

For a given granular material and a specified Q , Fr varies as a function of $\eta_* = \tau_0/(\tau_0)_{cr}$ only (Figure 2). If alluvium is gravel, then the curve $Fr = \varphi(\eta_*)$ is monotonous (curve a in Figure 2), and if it is sand, then the curve has a “deep” (curve b). The regime development can be reflected by the “motion” of the point m on the $(Fr; \eta_*)$ -plane. The point m , starting from its initial location P_0 , moves towards the regime point P_R which corresponds to the smallest Fr of “its” curve a or b . If the curve a , then $P_R = P_g$ where $\eta_* = 1$; if the curve b , then $P_R = P_s$ where $dFr/d\eta_* = 0$ (“deep”). The regime state is thus not really the state of the final thermodynamic equilibrium which corresponds to $u_{av} = \eta_* = 0$ (as indicated by the broken lines E_a and E_b). It is merely the state where channel deformation (“aiming” to achieve $u_{av} = \eta_* = 0$) is compelled to terminate because of the physical constraints. The existing conditions are illustrated, in the insert of Figure 2, by the “rolling ball”-analogy (Yalin and da Silva 2001).

The frictional rolling ball cannot reach its target location $\eta_* = 0$, for it is stopped before that either by the “barrier” $\eta_* = 1$ (no transport—no channel deformation) or by the “pit” at $(\eta_*)_R$ (the

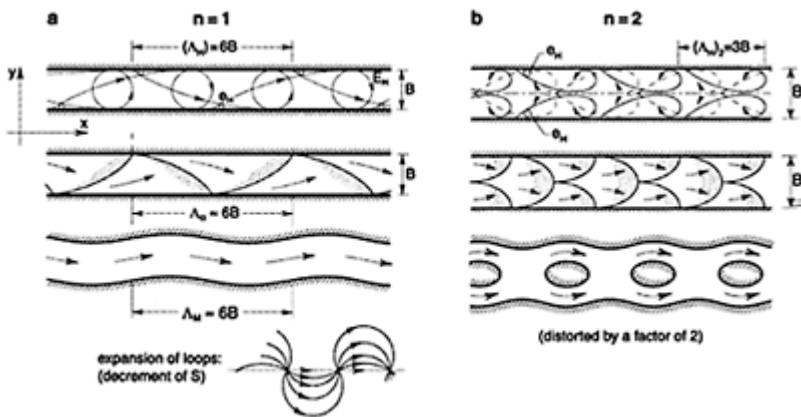


Figure 3. Initiation of meandering and braiding by the large-scale horizontal turbulence.

channel configuration corresponding to $(u_{av})_{min}$ (at P_s) cannot alter itself spontaneously, for it would lead to the *increment* of u_{av} (which is impossible by virtue of the second law)).

6 MEANDERING AND BRAIDING CRITERIA

i) Before entering the topic of this section, the reader is reminded that the resistance equation of the wide channels, viz

$$u_{av} = c\sqrt{gSh} \quad (17)$$

can be expressed as

$$Fr = c^2 S \quad (\text{where } Fr = u_{av}^2/gh) \quad (18)$$

which indicates that the minimization of $Fr \sim u_{av}^2$ can be achieved by the minimization of the stream-slope S or/and of the dimensionless Chézy resistance factor c . (See Yalin 1992, Yalin and da Silva 2001 for the evaluation of c).

ii) Whether the regime development of an initially straight alluvial stream will be by meandering or braiding depends on the structure of its large-scale horizontal turbulence. If the aspect ratio B/h of the channel is smaller than a certain upper limit β (which will be disclosed at the end of the Section), then the disk-like bed-rubbing eddies eH of channel's horizontal turbulence form the *onerow horizontal bursts*, having the largest eddy diameters $\approx B$ and the burst-lengths $(\Lambda_H)_1 \approx 6B$ (Figure 3a). In this case the flow manifests itself as a “coherent” (correlated) totality throughout the flow width. Its horizontal bursts “imprint” themselves on the bed surface as *alternate bars*, and it begins to deform the banks in a wave-like manner (meandering). Clearly

$$(\Lambda_H)_1 = \Lambda_a = \Lambda_M (\approx 6B) \quad (19)$$

The further development of the so initiated meandering (which is motivated by the regime trend $Fr \sim u_{av}^2 \rightarrow \min$) is by the expansion of loops (insert in Figure 3a). The expansion of loops, i.e. the increment of their length (see insert), means the decrement of the channel slope S and thus of the Froude number $Fr \sim u_{av}^2$ (see (18)). The development stops when $S=SR$ is achieved (Yalin 1992, Yalin and da Silva 2001).

If $B/h > \beta$, then the bed-rubbing eddies e_h , originated at one of the banks, cannot grow up to the size B : they will be destroyed before that by the bed friction. Consequently, these eddies form *n-row horizontal bursts* ($n \geq 2$) having $(\Lambda_H)n = 6B/n$ (Figure 3b). These bursts “imprint” themselves on the bed surface as *multiple bars*. The flow impeded by the bars “attacks” the banks

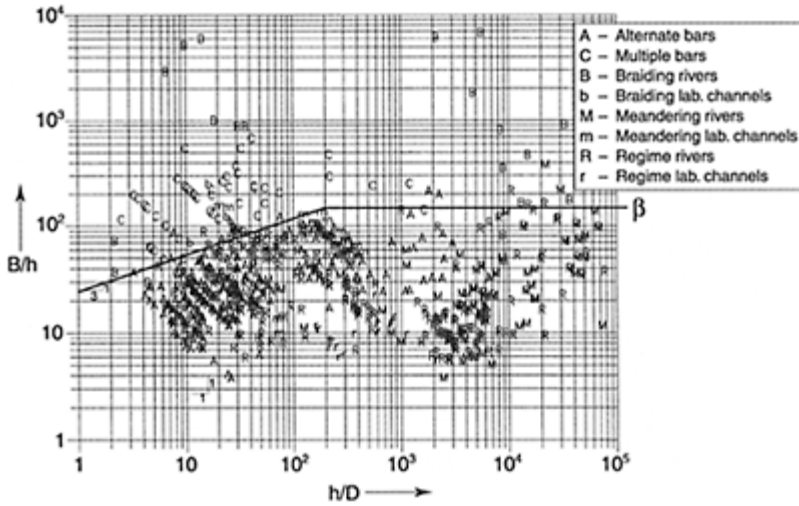


Figure 4. $(B/h; h/D)$ -plane.

and widens (B increases): consequently, h decreases. The continual increment of B and consequent decrement of h results into the emergence of bars as “islands” (initiation of braiding). Moreover it results into the progressive decrement of the overall resistance factor c and thus of $Fr \sim u_{av}^2$ (see (18)). The development stops when $c=C_R$ is achieved (Yalin 1992, Yalin and da Silva 2001). (iii) The B/h - and h/D -values of all the available field and laboratory data of various sources are plotted versus each other in Figure 4 (Yalin 1992, Yalin and da Silva 2001).

In spite of a substantial scatter, this graph clearly conveys that the region $B/h > \beta$ tends to be populated indeed by the multiple-bar points C and the braiding points B and b (i.e. by the “outcomes” of flows having n -row horizontal bursts), whereas the region $B/h < \beta$ is populated mainly by the creations of flows having one-row horizontal bursts (the points A , M , m , R and r). (Here R and r represent those (conventional) regime streams where the regime state is achieved either by meandering or by aggradation-degradation; M and m being the meandering streams which may or may not be in regime).

The boundary β separating the regions mentioned can be approximated, for the present, as

$$\text{if } Z \lesssim 200, \text{ then } \beta \approx 25Z^{1/3}$$

$$\text{if } Z \gtrsim 200, \text{ then } \beta = 150$$

where $Z=h/D$ (see Yalin and da Silva 2001, Yalin 1992).

7 SUMMARY AND CONCLUSIONS

The present paper conveys that whether an initially straight alluvial stream will be meandering or braiding depends on the structure of its large-scale horizontal turbulence.

If the aspect ratio B/h of the initial stream does not exceed a certain limit β (and it has thus one-row horizontal bursts), then it will be meandering. And if $B/h < \beta$ (and the stream has thus more than one-row horizontal bursts), then it will be braiding. The locations of the available field and laboratory data in the $(B/h; h/D)$ -plane (in Figure 4) are, in general, in agreement with these predictions.

The meandering and braiding, which *initiate* as outlined above, grow in their “amplitude” (they *develop*) until the regime state is achieved.

The present paper adheres to the view that the regime development is motivated by the Entropy increment principle, and demonstrates analytically that the increment of the entropy of an alluvial stream (corresponding to the constant energy and flow rate) can be achieved only by the reduction of flow velocity u_{av} (or of the flow Froude number $Fr = u_{av}^2/gh = c^2S$). In the case of meandering, the reduction of u_{av} is realized by the reduction of the stream slope S , in the case of braiding, by the reduction of the resistance factor c .

REFERENCES

- Chang, H.H. 1979. Minimum stream power and river channel patterns. J.Hydrol, Vol. 41.
- Chang, H.H., Hill, J.C. 1977. Minimum stream power for rivers and deltas. J.Hydr. Div., ASCE, Vol. 103, No. HY12, Dec.
- Davies, T.H.R., Sutherland, A.J. 1983. Extremal hypothesis for river behaviour. Water Resour. Res., Vol. 19, No. 1.
- Davies, T.H.R., Sutherland, A.J. 1980. Resistance to flow past deformable boundaries. Earth Surf. Proc., Vol. 5.
- Goldstein, M., Goldstein, I.E. 1993. Understanding the laws of energy. Harvard University Press, Cambridge.
- Moran, M.J., Shapiro, H.N. 1992. Fundamentals engineering thermodynamics. (2nd edition), John Wiley and Sons.
- Munson, B.R., Young, D.F., Okiishi, T.H. 1994. Fundamentals of fluid mechanics. (2nd edition) John Wiley and Sons.
- Song, C.C.S., Yang, C.T. 1982. Minimum stream power: theory. J.Hydr. Div., ASCE, Vol. 106, No. HY9, July.
- Soo, S.L. 1967. Fluid dynamics of multiphase systems. Blaisdall Publishing Co., Toronto, London.
- Spalding, D.B., Cole, E.H. 1973. Engineering thermodynamics. (3rd edition) Edward Arnold (Publishers) Ltd.
- Wark, K. 1971. Thermodynamics. (2nd edition) McGraw-Hill Book Company.
- White, W.R., Bettess, R., Paris, E. 1981. Analytical approach to river regime. J.Hydr. Div., ASCE, Vol. 108, No. HY10, Oct.
- White, W.R., Paris, E., Bettess, R. 1981. River regime based on sediment transport concept. Rep. IT 201, Hydraulic Res. Stn., Wallingford.
- Yalin, M.S., da Silva, A.M.F. 2001. Fluvial Processes. IAHR Monograph, IAHR, The Netherlands.
- Yalin, M.S., da Silva, A.M.F. 1999. Regime channels in cohesionless alluvium. Special Issue on River Morphology, Journal of Hydraulic Research, IAHR, Vol. 37, No. 6.
- Yalin, M.S. 1992 River Mechanics. Pergamon Press, Oxford.
- Yang, C.T. 1994. Variational theories in hydrodynamics and hydraulics. J.Hydr., Engrg., ASCE, Vol. 120, No. 6, June.

- Yang, C.T. 1992. Force, energy, entropy and energy dissipation rate. in "Entropy and energy dissipation in water resources", V.P.Singh and M.Fiorentino eds., Kluwer Academic Publishers, London, United Kingdom.
- Yang, C.T. Song, C.C.S., Woldenberg, M.J. 1981. Hydraulic geometry and minimum rate of energy dissipation. Water Resour. Res., 17.
- Yang, C.T. Minimum unit stream power and fluvial hydraulics. J.Hydr. Engrg., ASCE, Vol. 102, No. HY7, July.

Time-dependent local scour at piled bridge foundations

G.Oliveto & A.Rossi

DIFA, Università della Basilicata, Potenza, Italy

W.H.Hager

VAW, ETH-Zentrum, Zurich, Switzerland

Hydraulics of Dams and River Structures—Yazdandoost & Attari (eds)

© 2004 Taylor & Francis Group, London, ISBN 90 5809 632 7

ABSTRACT: This paper aims at analysing the local scour processes at piers founded on piles. Experiments were conducted at DIFA in two rectangular channels. All tests were run under steady flow conditions and clear-water scour regime. Several scenarios involving different distances from the initial bed level to the top of the pier footing were analysed. Based on the experimental data collected, the effects of the foundation on the temporal scour evolution are highlighted. All the results are given in terms of equivalent pier or pile diameters, as synthetic parameters of the whole geometry of the composite pier structure. Thus, a straightforward design procedure is provided. A previously established scour equation for the temporal progress of scour at uniformly shaped piers was assumed as framework for this analysis.

1 INTRODUCTION

Bridge piers are frequently founded on piles mainly due to geotechnical and economic reasons. This kind of foundation is commonly considered a guarantee for the safety of the bridge structure against any scouring problems. However, pier footings may often project above the streambed as result of either long-term degradation, lateral shifting of the stream, contraction scour, or local scour during a runoff event. For such cases piles should be designed to resist to a certain exposure to the flow and the footing location should be designed on structural and hydraulic bases. Moreover, when general scour produces a significant bed lowering, the safety reassessment of the bridge requires a new local scour prediction that must consider the combined pier/foundation pile geometry.

Papers dealing with the effects of such a combined geometry on scour depth are rare in literature. Based on a laboratory study, Jones *et al.* (1992) evaluated how the effect of footing location can be taken into account in scour-prediction equations that use a single characteristic pier size. They found that a weighted width technique provides simple and

accurate estimations. Their analysis did not account for the scour-arresting effects for footings located below the streambed. HEC-18 (*Richardson & Davis, 1995*) provides some guidelines for evaluating local scour at exposed pile caps. It is recommended that the pier width should be used in a scour equation if the top of the pile cap is at or below the streambed. If the pile cap is placed into the flow, its width should be considered instead of the pier width. However, the HEC-18 procedure is based on few data and many engineers consider it conservative, especially for large piers. *Martin-Vide et al* (1998) undertook an experimental investigation of scouring at rectangular piers founded on two circular cylindrical piles. Their research was thus focused on a pure two-width problem not considering the more complex geometries. Finally, preliminary results on physical models composed by pier, pile cap and pile group were given by *Jones & Sheppard* (2000).

All these studies mainly focused on conditions of quasi-equilibrium scour depth. Moreover, the proposed design procedures are specific and preliminary because of the complexity of the problem and the large number of parameters involved. In this context, a research project was initiated at DIFA for developing general and straightforward design criteria. In the following, some methods of estimating scour depth are introduced which appear effective throughout a wide range of possible pier and foundation geometries.

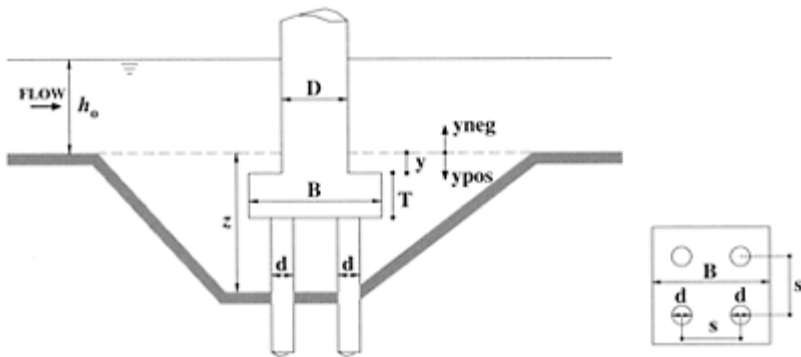


Figure 1. Definition sketch of the scour element and hydraulic variables.

2 EXPERIMENTS

Experiments were performed at University of Basilicata in two rectangular channels here denoted by A and B. The A channel had a width of 1 m and a total length of 20 m with a working section of about 10m. The bed material was a nearly uniform sand of density $\rho_s=2.65 \text{ t/m}^3$, median grain size $d_{50}=1.7\text{mm}$ and sediment gradation $\sigma=(d_{84}/d_{16})^{0.5}=1-5$. The B channel, described in detail elsewhere (*Oliveto et al.* 2003), had a width of 0.5 m and a total length of 10 m with a working section of about 7 m. The bed material was gravel with $\rho_s=2.65 \text{ t/m}^3$, $d_{50}=2.4 \text{ mm}$, and $\sigma=1.6$.

The scour elements were three-width models consisting of a cylindrical pier of diameter D , a square pile cap of width B and thickness T , and 4 cylindrical piles of diameter d , spaced each other by s . A definition sketch is given in Figure 1.

Two models were tested, one for each channel. The model used in the A channel had $D=0.12$ m, $B=0.24$ m, $T=0.08$ m, and $d=0.04$ m, the one used in the B channel had $D=0.06$ m, $B=0.12$ m, $T=0.04$ m, and $d=0.02$ m. All model dimensions were multiples of the piles diameter.

All experiments were run under steady flow, plane bed conditions, and just below incipient sediment motion (upstream of the structure) in the clear-water scour regime. Several scenarios involving different distances y from the initial bed level to the top of the footing were analysed. Discharges Q ranged from 10 to 50 l/s and were measured with an orifice plate of $\pm 3\%$ accuracy. The water surface was read with a conventional point gage, typically to ± 0.5 to 1 mm, whereas the scour hole was contoured, with an accuracy of ± 1 mm, with a so-called shoe-gage having a 4 mm by 2 mm wide horizontal plate at its base.

Both channels were equipped with an adjustable sharp-crested weir located at their downstream ends to control the approach flow depth. Once the bed was accurately levelled and the pier model properly mounted, the experiment initiated submerging the working section by setting the sharpcrested weir up. This was lowered within 10 to 20 seconds to the pre-selected flow depth and the temporal start of the experiment was set at scour inception. Subsequent measurements were usually taken at least each hour. For the experiments conducted in the B channel the duration was typically between 4 and 9 hours. The A channel allowed experiments of easily 1 week duration and a maximum period of 12 days was investigated.

Test conditions and measured scour depths are presented in Table 1, with y =elevation of the top of the pile cap measured from the initial bed level (y is positive if the top of the foundation is below the initial bed level and vice versa, see Fig. 1), h_0 =approach flow depth, $F_0=V_0/(gh_0)^{1/2}$ =approach Froude number, V_0 =approach velocity, g =gravitational acceleration, $F_d=V_0/(g'd_{50})^{1/2}$ =approach densimetric Froude number, $g'=[(\rho_s-\rho)/\rho]g$, ρ =fluid density, z =maximum scour depth at the time t , and t_t =test duration.

3 ANALYSIS OF DATA

A previously established scour equation by *Oliveto & Hager* (2002) for the temporal progress of scour at uniformly shaped piers was assumed as framework for this analysis. This equation involves the maximum scour depth z as a function of time t and the dominant parameter governing scour processes is the densimetric particle Froude number F_d . Using that dimensionless number, and

Table 1. Test conditions and measured scour depths.

Run	Channel	s cm	y cm	h_o cm	F_o	F_d	cm	t_t h
1	B	4.00	0.00	10.51	0.46	2.37	3.30	8.0
2	B	4.00	-3.00	10.70	0.43	2.23	4.40	8.0
3	B	4.00	-4.00	11.23	0.42	2.21	3.98	8.4
4	B	4.00	-5.75	10.12	0.41	1.83	2.78	3.3
5	B	4.00	-5.95	11.22	0.42	2.22	4.02	7.5
6	B	4.00	-11.42	11.42	0.41	2.18	3.52	8.0
7	B	4.00	0.00	20.00	0.25	1.80	1.90	3.0
8	B	4.00	-6.76	20.00	0.31	2.18	3.80	4.0
9	B	4.00	-7.20	20.00	0.31	2.22	4.32	4.5
10	B	4.00	-9.78	20.30	0.31	2.20	4.04	4.8
11	B	4.00	-8.10	16.00	0.28	1.80	2.92	8.4
12	B	2.00	-16.50	11.35	0.41	2.20	5.78	5.4
13	B	4.00	-16.50	11.35	0.41	2.18	2.89	8.0
14	B	6.00	-16.50	11.35	0.41	2.18	2.15	5.0
15	B	8.00	-16.50	11.35	0.41	2.18	2.52	9.0
16	B	10.00	-16.50	11.35	0.41	2.18	2.13	8.0
17	A	8.00	7.30	12.04	0.36	2.41	7.35	21.7
18	A	8.00	3.40	10.40	0.43	2.65	4.05	4.3
19	A	8.00	1.90	10.85	0.40	2.54	8.62	16.6
20	A	8.00	0.00	10.80	0.41	2.61	12.60	19.7
21	A	8.00	0.00	11.70	0.36	2.36	16.50	295.1

scaling depths involving the approach flow depth h_o and the pier diameter D allows to determine the time scale $t_R = z_R / (\sigma^{1/3} (g' d_{50})^{1/2})$ in which effects of density, sediment size distribution and element geometry are contained. It may be written as

$$Z = z/z_R = 0.068 \sigma^{-1/2} F_d^{1.5} \log T \quad (1)$$

where $z_R = (h_o D^2)^{1/3}$ and $T = t/t_R$ is the relative time.

The proposed procedure for predicting local scour at piled pier foundations consists in finding an equivalent pier diameter producing the identical clear water scour depth as the actual structure produces according to Equation (1).

3.1 Top elevation of the pile cap at or below the streambed

One experimental series (runs 17 to 21) was performed in the A channel in which the flow approach conditions were held constant while the top elevation of the pile cap was placed at or below the initial bed level. Additional experiments (runs 1 and 7) were also conducted in the B channel. According to the above procedure, Figures 2a, b were obtained in which the equivalent pier diameter D_{eq} appears to be a function of the ratio y/D as follows

$$D_{eq}/D = 1 - y/D + 0.5 (y/D)^2 \quad (2)$$

Curves in Figure 2a are relative to the scour depth development starting from the time in which the top of the foundation was reached. From Equation (2) emerges that the scour depth is sensitive to the foundation level. In particular, $D_{eq} = D$ for $y=0$, then as the top of foundation descends below the streambed it decreases until a minimum first and then increases tending to D for $y/D=2$. Note that this latter value of y/D is commonly considered the maximum scour depth to be expected at a uniformly shaped pier. These evidences are in agreement with findings of Melville & Raudkivi (1996) for piers founded on caisson. A reason of this similar behavior may be that even for the long-term experiment (run 21) the maximum scour depth was always located at the upstream side

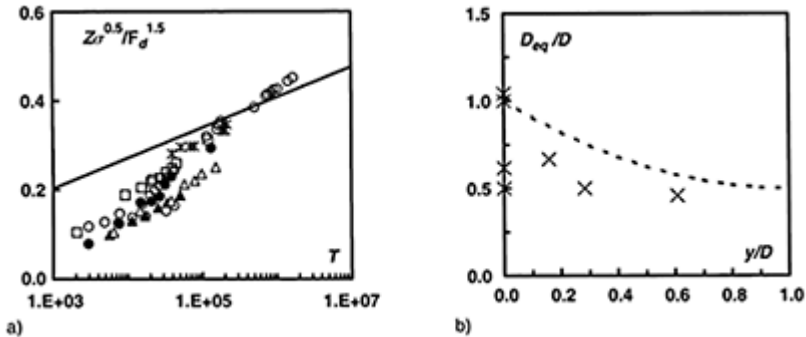


Figure 2. (a) $Z\sigma^{0.5}/F_d^{1.5}$ as a function of T for runs (Δ) 1, (\blacktriangle) 7, ($*$) 17, (\diamond) 18, (\bullet) 19, (\square) 20, and (\bigcirc) 21; (b) D_{eq}/D as a function of the ratio y/D with (---) Equation (2).

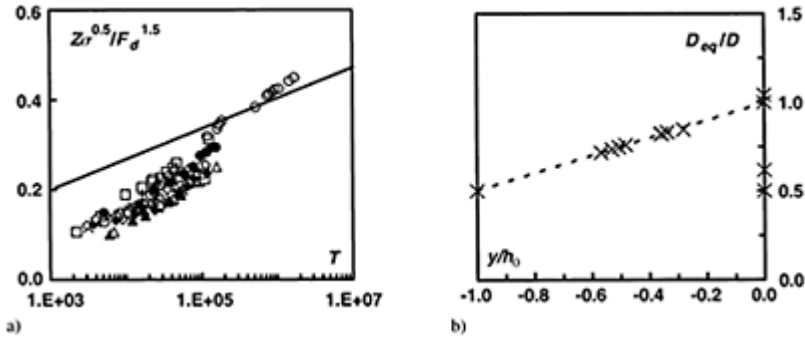


Figure 3. (a) $Z\sigma^{0.5}/F_d^{1.5}$ as a function of T for runs (Δ) 1, (\bullet) 2, (\ast) 3, ($+$) 4, (\diamond) 5, (\circ) 6, (\blacktriangle) 7, (\ast) 8, (\blacklozenge) 9, (\times) 10, (\blacksquare) 11, (D) 20, and (\bigcirc) (Q) 21; (b) D_{eq}/D as a function of the ratio y/h_0 with (----) Equation (3).

of the foundation where the scour development followed the same logarithmic trend even when piles have begun to be exposed. This latter condition determined a change of the scour trend at the downstream side of the foundation structure with an increasing of the scour-depth rate.

3.2 Top elevation of the pile cap between the streambed level and the water surface

Two experimental series (runs 2 to 6 and runs 8 to 10) were performed in the B channel. For each series the approach flow conditions were held constant while the elevation y was systematically changed. An additional experiment (run 11) was also conducted at an intermediate approach flow depth. Diagrams in Figure 3 provide the equivalent uniform pier diameter D_{eq} as a function of the ratio y/h_0 and D as

$$D_{eq}/D = 1 + 0.5y/h_0 \quad (3)$$

with a slight overprediction of the scour depth for low values of T . In agreement with the previous findings it was also noted that $D_{eq}=D$ for $y=0$. From Equation (3) the conservatism of the

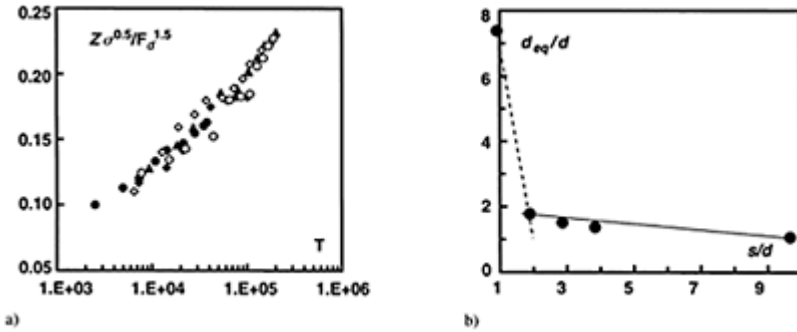


Figure 4. Exposed piles: (a) $Z\sigma^{0.5}/F_d^{1.5}$ as a function of T for runs (•) 12, (◊) 13, (◆) 14, (○) 15, and (▲) 16; (b) d_{eq}/d as a function of the ratio s/d .

HEC-18 assumption $D_{eq}=B$ becomes obvious, at least when the effect of debris lodged between piles is confidently neglected.

3.3 Completely exposed pile groups

Some experiments (runs 12 to 16) were conducted for pile groups capped above the water surface (i.e. only the piles obstructed the flow). The effect of spacing between piles was tested for selected values of the ratio s/d .

Diagrams in Figure 4 provide an equivalent pile diameter, d_{eq} producing the same maximum clear water scour depth as resulting from the actual pile group. Here, d_{eq} is defined as the multiple of d that would induce, for any T , the same dimensionless value $Z\sigma^{0.5}/F_d^{1.5}$ of the single pile. The values of d_{eq}/d were found as shown in Figure 4b. In particular, these values give a maximum coefficient of determination r^2 of the two dimensionless variables $Z\sigma^{0.5}/F_d^{1.5}$ and T (see Fig. 4a). These results, substantially consistent with the findings of *Salim & Jones* (1995), show that the more the spacing between piles, the less the scour depth, due to the reduced interference and contraction created by nearby piles. Furthermore, the rate of decrease depends on s/d , being higher for smaller values of s/d . A slight increase in scour depth should even occur for $1 < s/d < 2$, as observed by *Salim & Jones* (1995). Thus, $s/d > 2$ or 3 should be applied in designing piles.

According to Figure 4a, observed scour depths for single pile were found approximately 30% smaller than the corresponding ones from Equation (1), but substantially within the percentage intervals suggested by *Oliveto & Hager* (2002) in the application of their model.

4 CONCLUSIONS

Several studies have been conducted on scour at bridge piers, however most of them did not consider the effect of foundations when exposed to the flow as a consequence of long term degradation and/or local scour. This experimental study was carried out to analyse the temporal scour evolution at piers founded on piles.

Although the limited number of experiments, findings seem to suggest straightforward design procedures that appear to be effective throughout a wide range of possible pier and foundation configurations. In particular, the results of this study show that:

- scour depth is sensitive to changes in foundation location;
- piled foundations tend to alleviate the scour process when placed below the undisturbed bed level; the same occurs when foundations protrude above the streambed if the interdistance s between the pile is greater than 2 and debris lodging effects can be neglected;
- time-dependent local scour is given by Equation (1) with the effective pier width given by equations similar to Equations (2) and (3).

ACKNOWLEDGEMENTS

The authors would like to thank Domenico Fiore and Beniamino Onorati for their help during the experimental phase. The project was financially supported by CNR-GNDCI, Italy (contract No. 01.01043.42).

REFERENCES

- Jones, S.J. & Sheppard, D.M. 2000. Local scour at complex pier geometries. In R.H. Hotchkiss & M. Glade (eds), *Joint Conference on Water Resources Engineering and Water Resources Planning & Management; Proc. intern. conf., Minneapolis, July 30-August 2 2000*. Reston, Va: ASCE.
- Jones, S.J., Kilgore, R.T. and Mistichelli, M.P. 1992. Effects of footing location on bridge pier scour. *Journal of Hydraulics Engineering*, ASCE 118(2): 280–290.
- Martin-Vide, J.P., Hidalgo, C. and Bateman, A. 1998. Local scour at piled bridge foundations. *Journal of Hydraulic Engineering*, ASCE 124(4): 439–444.
- Melville, B.W. & Raudkivi, A.J. 1996. Effects of foundation geometry on bridge pier scour. *Journal of Hydraulic Engineering*, ASCE 122(4): 203–209.
- Oliveto, G. & Hager, W.H. 2002. Temporal evolution of clear-water pier and abutment scour. *Journal of Hydraulics Engineering*, ASCE 128(9): 811–820.
- Oliveto, G., Rossi, A. & Hager, W.H. 2003. Local scour at a partly-full flow culvert outlet. In I. Nezu & N. Kotsovinos (eds), *Inland Waters: Research, Engineering and Management; Proc. of XXXIAHR Congress, Thessaloniki, 24–29 August 2003*. Madrid: IAHR.
- Richardson, E.V. & Davis, S.R. 1995. *Evaluating scour at bridges*; Publ No. FHWA-IP-90-017, Washington, D.C.: Federal Hwy. Admin.

Salim, M. & Jones, S.J. 1995. Effects of exposed pile foundations on local pier scour. *First International Conference on "Water Resources Management"; Proc. intern. conf., San Antonio, 14–18 August 1995*. Reston, Va: ASCE.

Time evolution of scour at comparatively long abutments

C.M.S.Fael

Universidade da Beira interior, Covilhã, Portugal

A.H.Cardoso

Instituto Superior Técnico, Lisboa, Portugal

Hydraulics of Dams and River Structures—Yazdandoost & Attari (eds)

© 2004 Taylor & Francis Group, London, ISBN 90 5809 632 7

ABSTRACT: The effects of the approach flow velocity and obstacle-length on the time evolution of scour depth at comparatively long abutments are discussed in the framework of the equations suggested by Ettema (1980) and by Franzetti *et al.* (1982). This discussion stands for clear-water flow conditions and vertical wall abutments in rectangular mobile-bed open-channels. The evaluation of the coefficients involved in the equations leads to conclude that those of Franzetti *et al.* (1982) seem to be universal, while those of Ettema (1980) clearly depend on the approach flow intensity and on the dimensionless obstacle length. Time to equilibrium also depends on the same parameters.

1 INTRODUCTION

Scour around obstacles inserted in riverbeds, namely bridge piers and abutments, has attracted the attention of researchers mainly because this phenomenon can lead to the collapse of bridges.

The topic has mobilized bridge specialists, particularly since the fifties of the last century. Its importance is reflected in the countless studies developed in the last few decades with the purpose of characterizing the phenomenon and of quantifying the scour depth. However, there are still doubts concerning the accuracy of the predictions supplied by existing formulations. The effect of some factors is even not yet unequivocally established. The available knowledge differs with the obstacle type. The literature on local scour at bridge piers is abundant. The existing literature on obstacles protruding from river margins (spur-dikes and bridge abutments) is less extensive.

The gaps in knowledge are particularly important in the case of long abutments. This fact justifies an effort for additional investigation on this type of structures. This paper deals with new experimental results obtained in a large flume for comparatively long abutments; time evolution of the depth of the associated scour holes is discussed.

2 BACKGROUND

Several authors have suggested empirical formulas for the time evolution of scour depth. Most of them apply to the principal phase of the erosion process. One of these formulas was suggested by Ettema (1980); Franzetti *et al* (1982) suggested another one that predicts finite scour depth, d_{se} , for $t=\infty$. In practice, it can also be adjusted to the principal phase. The mentioned contributions are strictly valid for piers.

Restricting the study of the scour phenomena to very wide rectangular channels where the effect of flow contraction due to the presence of obstacles is negligible, whose bed is composed of uniform sand incompatible with the formation of ripples ($\sigma_D < \approx 2.0$, where σ_D is the sediment gradation coefficient, and $D_{50} > \approx 0.6$ mm, where D_{50} is the median diameter of the bed material), the non-dimensional relation for the study of the time evolution of scour holes is as follows (Santos & Cardoso, 2001):

$$N_{ds} = \varphi(N_L, N_U, N_t) \quad (1)$$

where $N_{ds} = d_s/L$ is the non-dimensional parameter associated with scour depth at instant t ; $N_L = L/d$ is the obstacle length parameter; $N_U = U/U_c$ represents the flow intensity; N_t is any non-dimensional time parameter; L is the obstacle length (pier diameter or abutment length); d is the approach flow depth; U is the mean velocity of the undisturbed approach flow; and U_c is the critical mean velocity for the beginning of motion.

Equation 1 is valid under the assumption that the effect of the bed material size is negligible. For threshold conditions, i.e. for $U/U_c \approx 1.0$, and cylindrical piers of diameter D_p , Ettema (1980) proposed the following equation for describing the time evolution of the scour depth:

$$\frac{d_s}{D_p} = k_1 \times \log \left[\frac{D_{50} t v}{D_p^3} \right] + k_2 \quad (2)$$

where k_1 and k_2 are coefficients and v is the kinematic viscosity of the water.

Franzetti *et al.* (1982) proposed the following exponential function:

$$\frac{d_s}{d_{se}} = 1 - \exp \left[a_1 \left(\frac{U t}{D_p} \right)^{a_2} \right] \quad (3)$$

where $a_1 = -0.028$, $a_2 = 1/3$ and d_{se} is the equilibrium scour depth.

In the previous formulations, the non-dimensional parameter N_t includes the cylinder diameter, D_p , as a characteristic length. In the case of obstacles protruding from channel walls, Cardoso & Bettess (1999) generalised the previous formulations by assuming the obstacle length as the characteristic length. They have also studied the influence of

$N_L=L/d$ on the temporal evolution of scour depth close to obstacles for the condition of beginning motion in the approach flow. In other words, they have characterized the equation

$$N_{ds}=\varphi(N_L, N_U) \text{ for } N_U \approx 1.0 \quad (4)$$

They have shown that, k_1 , k_2 and a_1 vary with $N_L=L/d$, while a_2 seems to be a universal constants. Their study was carried out for $N_i=L/d \approx 17$. For this reason, the specific objective of this work is to evaluate the dependence of the same coefficients (a_1 , a_2 , k_1 and k_2) on parameters N_L and N_U in the attempt of further characterizing Equation 1 for higher values of N_L and for values of N_U other than $N_U=1$, in the clear-water range.

3 EXPERIMENTAL SET-UP

Experiments were carried out in a 4.0 m wide, 28.0m long and 1.0 m high concrete flume. The right lateral wall is made of glass panels that allow the observation of the flow, namely in the central reach where the local scour develops. This reach includes a 3.0m long and 0.6m deep recess, where scour is free to develop. The recess box was filled with natural quartz sand ($D_{50} \approx 1.28$ mm; $\sigma_D \approx 1.46$). The obstacles were installed at the mid cross-section of the recess box. Thin obstacles were used to simulate abutments. The study was made for reasonably high, practically constant flow depths and for different flow velocities in the clear-water range.

The flume includes a closed hydraulic circuit where the discharge can be varied continuously up to 0.18 m³/s. Another, smaller, circuit exists where the discharge goes up to 5l/s. This circuit makes it possible to fill the flume very slowly, from its bottom, this way avoiding the occurrence of uncontrolled phenomena of scour in the beginning of the tests. At the downstream end of the main hydraulic circuit, at the entrance of the flume, a diffuser tube exists which distributes evenly the flow along the whole width of the flume. At the downstream end of the flume, a manually operated tailgate allows the regulation of the water level inside the flume.

The flume is equipped with a moving carriage. It allows the bottom leveling and serves as a support to the measuring equipment. Scour depth evolution with time was measured with a specially adapted point gauge until equilibrium was identified in a log-scale representation of the measurements.

Table 1. Characterization of the tests carried out in this study.

Test	d (m)	L (m)	d_{se} (m)	T_e (h)	T_d (h)	U/U_C (–)	L/d (–)
CF.1	0.062	1.86	0.426	59.1	149.7	1.12	30.097
CR2	0.062	1.86	0.381	87.5	166.2	0.90	30.097
CF.3	0.051	1.86	0.344	115.5	161.9	0.81	36.328
CF.4	0.055	1.71	0.330	160.7	169.0	0.75	30.888

CF.5	0.062	1.71	0.357	72.3	177.3	0.90	27.679
CF6	0.068	1.71	0.421	127.5	167.0	1.02	25.185
CF.7	0.069	1.55	0.423	163.7	172.2	1.00	22.591
CF.8	0.060	1.55	0.337	54.4	129.2	0.92	25.695
CF9	0.064	1.55	0.237	54.6	184.0	0.65	24.250
CF.10	0.067	1.40	0.230	105.7	168.1	0.62	20.958
CF.11	0.071	1.40	0.295	125.4	146.3	0.79	19.858
CF.12	0.065	1.40	0.407	150.1	509.1	1.06	21.440
CF.13	0.066	1.25	0.199	75.9	263.8	0.63	18.879
CF.14	0.069	1.25	0.294	91.2	216.7	0.80	17.980
CF.15	0.066	1.25	0.372	49.2	200.9	1.04	18.822
CF.16	0.070	1.09	0.160	129.4	189.5	0.58	15.592
CF.17	0.069	1.09	0.273	78.1	173.1	0.81	15.841
CF.18	0.066	1.09	0.359	70.6	166.9	1.05	16.687
CF.19	0.067	0.94	0.334	90.5	167.7	1.04	14.135
CF.20	0.070	0.94	0.243	91.5	168.7	0.79	13.371
CF.21	0.070	0.94	0.131	111.9	167.9	0.59	13.506
CF.22	0.069	0.79	0.312	88.7	167.6	1.01	11.474
CF.23	0.071	0.79	0.231	134.5	168.8	0.79	11.102
CF.24	0.071	0.79	0.104	96.2	147.4	0.57	11.055
CF.25	0.070	0.64	0.297	143.8	169.4	0.99	9.097
CF26	0.070	0.64	0.080	112.9	170.0	0.58	9.033
CF27	0.072	0.64	0.208	83.8	168.4	0.78	8.881

4 DISCUSSION

4.1 Data characterization

As a complement to the data obtained during this study some data were also compiled from the literature. Tables 1 and 2 summarize, respectively, the experiments carried out in this study and those selected in the literature. They include the values of d , L , equilibrium scour depth, d_{se} , time to equilibrium, T_e , test duration, T_d , and parameters $N_U = U/U_C$ and $N_L = L/d$.

Tests presented in Table 1 are characterized by values of abutment lengths ranging from $L=0.64$ m to $L=1.86$ m. This way, L/d varied between ≈ 9 and ≈ 36 , which is not very

common in previous studies. It can be seen that $N_U=U/U_C$ ranged from 0.57 to 1.12, while the flow depth, d , is practically constant and equal to 0.05 m-0.07 m.

In Table 2, data are identified according to the corresponding authors' names: JS stands for Santos & Cardoso (2001), VC, for Da Cunha (1973), C&B, for Cardoso & Bettess (1999) and K, for Kwan (1984). These data correspond to test durations, T^{\wedge} , higher than equilibrium time, T_e . Besides, in all cases, the obstacles were thin vertical walls placed at the right angle with the flow direction; sandy bottom ($D_{50}>0.6$ mm; $\sigma_D<2.0$) channels with rectangular cross-section were used and clear-water condition ($U/U_C<1$) was observed. Values of U/U_C are of the same order of magnitude as for the tests carried out in the present study and the values of T_d were always greater than those of T_e , which means that tests lasted long enough for equilibrium to be reached.

4.2 Time evolution ofscour depth

4.2.1 Effect ofthe approach flow velocity

The effect of the approach flow velocity on the time evolution of scour depth will be discussed in the framework of the parameters used by Ettema (1980). Thus, Figure 1 shows the variation of

Table 2. Characterization of the data selected in the literature.

Test	d (m)	L (m)	d_{se} (m)	T_e (h)	T_d (h)	U/U_c (-)	L/d (-)
JS-A1	0.071	0.18	0.211	110.0	150.0	1.06	2.535
JS-A2	0.071	0.18	0.176	94.4	94.5	0.96	2.535
JS-A4	0.069	0.18	0.049	80.2	125.8	0.75	2.609
JS-A5	0.070	0.18	0.021	40.0	70.6	0.66	2.571
JS-B1a	0.071	0.40	0.295	120.0	237.1	1.05	5.634
JS-B2a	0.072	0.40	0.243	110.0	166.6	0.93	5.556
JS-B3a	0.069	0.40	0.156	54.1	91.7	0.85	5.797
JS-B3b	0.069	0.40	0.171	45.0	91.7	0.85	5.797
JS-B4a	0.070	0.40	0.124	52.8	138.9	0.75	5.714
JS-B4b	0.070	0.40	0.119	62.5	138.8	0.75	5.714
JS-B5a	0.069	0.40	0.087	60.9	114.1	0.65	5.797
JS-B5b	0.069	0.40	0.088	55.4	114.1	0.65	5.797
JS-B6a	0.070	0.40	0.035	40.0	91.7	0.54	5.714
JS-B6b	0.070	0.40	0.040	35.0	91.8	0.54	5.714
JS-C1	0.071	0.50	0.308	101.1	150.1	1.06	7.042

JS-C2	0.071	0.50	0.223	72.1	94.5	0.96	7.042
JS-C4	0.069	0.50	0.137	44.7	126.0	0.75	7.246
JS-C5	0.070	0.50	0.099	27.8	118.7	0.66	7.143
VC1	0.090	0.20	0.039	31.5	96.0	0.59	2.222
VC2	0.090	0.20	0.056	41.0	133.0	0.65	2.222
VC3	0.090	0.20	0.087	59.5	144.0	0.7	2.222
VC4	0.090	0.20	0.202	70.0	120.0	0.86	2.222
VC9	0.090	0.20	0.289	102.0	120.0	1.02	2.222
C&B1	0.031	0.15	0.122	50.0	101.0	0.95	4.742
C&B2	0.073	0.15	0.220	120.0	142.0	0.93	2.014
C&B4	0.078	0.27	0.242	75.0	118.0	0.92	3.462
C&B5	0.028	0.40	0.123	22.0	105.0	0.95	14.286
C&B6	0.079	0.40	0.246	55.5	70.0	0.92	5.063
K1	0.100	0.16	0.220	90.0	100.0	0.92	1.640
K12	0.050	0.52	0.194	44.6	98.0	0.93	10.320
K13	0.050	0.72	0.234	37.2	127.0	0.90	14.340
K19	0.050	0.87	0.263	34.0	72.0	0.90	17.400

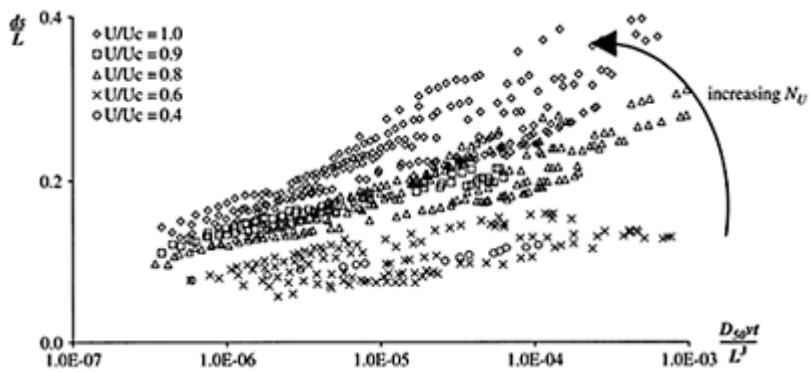


Figure 1. Effect of $N_U=U/U_C$ on time the evolution of scour depth.

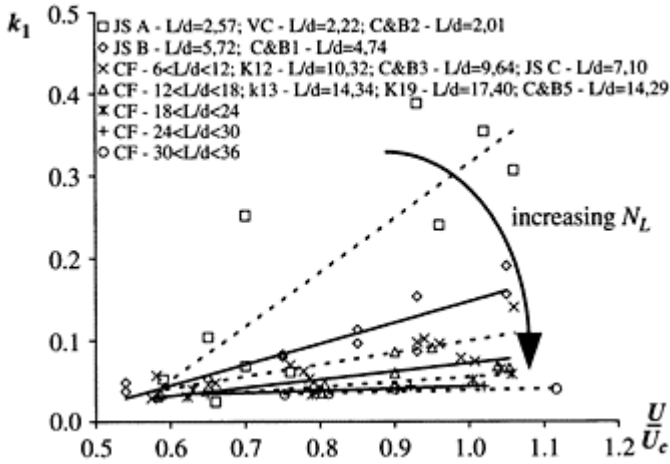


Figure 2. Variation of k_1 with $N_U = U/U_C$.

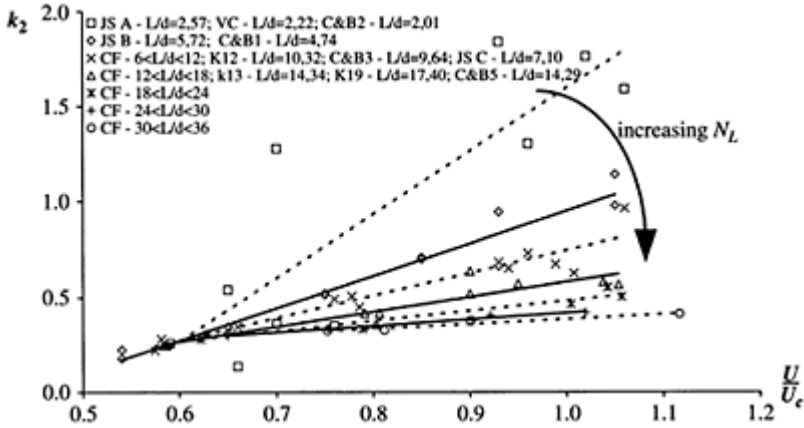


Figure 3. Variation of k_2 with $N_U = U/U_C$.

$Nd_s = d_s/L$ with $N_i = D_{50}vt/L^3$ (Eq. 2) for the principal phase of the tests carried out during the present study.

From Figure 1, it can be concluded that the scour process time evolution is affected by $N_U = U/U_C$, i.e. by the approach flow velocity. Santos & Cardoso (2001) showed that this conclusion is also valid in the framework defined by the parameters used by Franzetti *et al* (1982). This is the reason why the dependence of coefficients k_1 , k_2 , a_1 and a_2 on N_U , for $N_L = \text{const.}$, was evaluated. Those coefficients (k_1 , k_2 , a_1 and a_2) were calculated through regression analysis applied to the data of the principal phase written as N_{ds} vs. N_i .

It should be noted that the definition of both N_{ds} and N_t are not the same for the equations of Ettema (1980) or Franzetti *et al.* (1982).

Figures 2 and 3 show, respectively, the variation of coefficients k_1 and k_2 with $N_U = U/U_c$. These coefficients were grouped into classes of approximately constant values of N_L . The first class includes tests of series JS-A- $L/d \approx 2.57$, VC- $L/d=2.22$ and C&B2- $L/d=2.01$. The second includes tests of series JS-B- $L/d \approx 5.72$ and test C&B1- $L/d=4.74$. The third represents the tests of the present study CF- $6 < L/d < 12$, K12- $L/d \approx 7.10$, C&B3- $L/d=9.64$ and JS-C- $L/d \approx 7.10$. The fourth one includes tests of series CF- $12 < L/d < 18$, K13- $L/d=14.34$, K19- $L/d=17.40$ and C&B5- $L/d=14.29$. The other series are composed by the tests of the present study grouped into three classes $18 < L/d < 24$, $24 < L/d < 30$ and $30 < L/d < 36$. Figures 2 and 3 also show regression lines of the coefficients k_1 and k_2 with N_U , calculated for each group.

From Figures 2 and 3 it can be concluded that, for each class the $N_L = L/d$, the coefficients k_1 and k_2 decrease with increasing N_L and tend to becoming practically constant for high values of N_L .

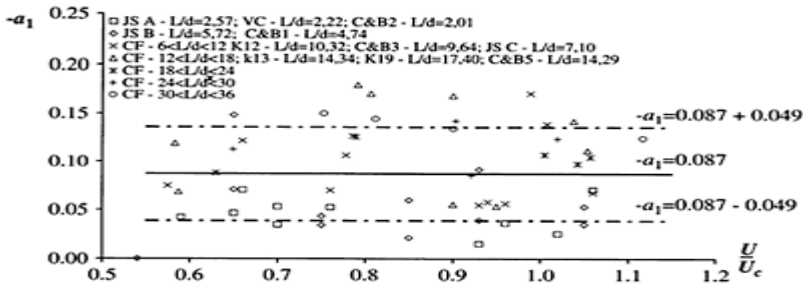


Figure 4. Variation of $-a_1$ with $N_U = U/U_c$.

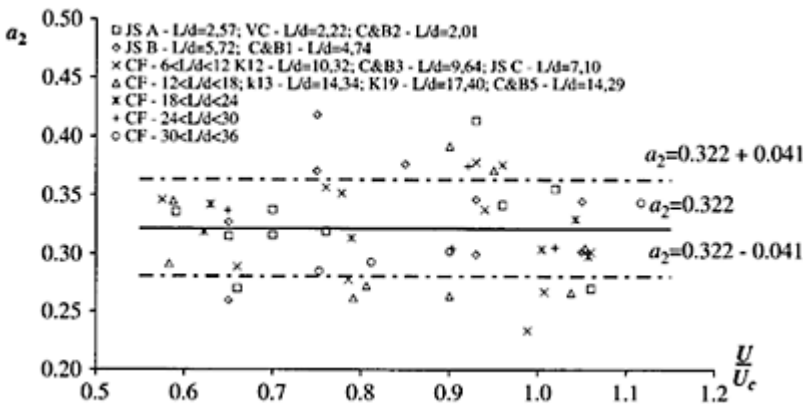


Figure 5. Variation of a_2 with $N_U = U/U_c$.

For $N_L > 30$, the values of coefficients k_1 and k_2 are, respectively, ≈ 0.03 and ≈ 0.26 . The maximum observed k_1 and k_2 correspond to the threshold flow condition, *i.e.* to $N_U \approx 1.0$.

Figures 4 and 5 present, respectively, the variation of $-a_1$ and a_2 with $N_U = U/U_C$. The values of a_1 and a_2 were calculated for the same tests as k_1 and k_2 . The figures do not allow the identification of any tendency for the variation of the coefficients a_1 and a_2 . These coefficients take the values $a_1 = -0.087 \pm 0.049$ and $a_2 = 0.322 \pm 0.041$ (mean \pm standard deviation), independently of N_U . This result clearly differs from the one of Cardoso & Bettess (1999) who claimed that a_1 would vary with N_U . The coefficient a_2 is similar to the one suggested by Franzetti *et al.* (1982), namely $a_2 = 1/3$.

From above, it can be concluded that k_1 and k_2 depend on both L/d and U/U_C while a_1 and a_2 seem to be universal constants. However, a_1 is apparently smaller than the value suggested by Franzetti *et al.* (1982) (according to whom a_1 would be $a_1 \approx -0.028$).

4.2.2 Effect of the obstacle length

Figures 6 and 7 present the variation of coefficients k_1 and k_2 with $N_L = L/d$. In this analysis, only data close to the threshold condition were considered ($0.90 \leq U/U_C \leq 1.12$). Equations suggested by Cardoso & Bettess (1999) and the ones obtained in the present study,

$$k_1 = 0.579 (L/d)^{-0.786} \text{ and } k_2 = 2.345 (L/d)^{-0.542} \quad (5)$$

were also included in the figures. For these equations, R^2 is respectively 0.938 and 0.946.

It is clear that curves obtained in the present study are similar to those proposed by Cardoso & Bettess (1999) in spite of the patent discrepancies in the case of the coefficient k_1 .

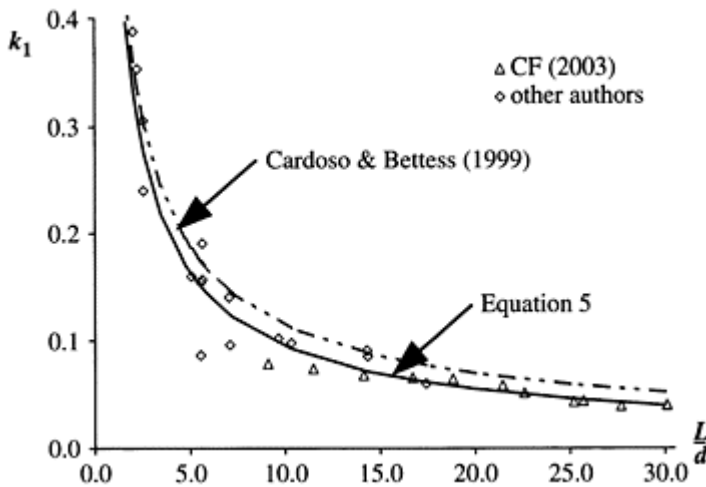


Figure 6. Variation of k_1 with $N_L = L/h$.

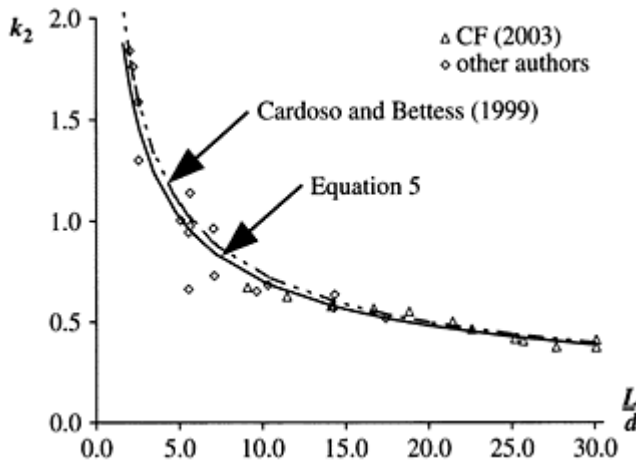


Figure 7. Variation of k_2 with $N_L=L/d$.

The variation of coefficients a_1 and a_2 with $N_L=L/d$ was also analyzed. Only data close to the threshold condition were considered ($0.90 < U/U_c < 1.12$). The values obtained for a_1 and a_2 were observed to be independent of N_L . Again, the coefficient a_1 was similar to the one suggested by Franzetti *et al.* (1982).

In what concerns the coefficient a_1 , the present study seems to indicate that it is a universal constant, since it does not vary neither with $N_U=U/U_c$ nor with $N_L=L/d$ unlike what Cardoso & Bettess (1999) have suggested. However, it should be pointed out that the value of a_1 obtained in this study ($a_1=-0.087$) is about the triple of the one suggested by Franzetti *et al.* (1982) ($a_1=-0.028$).

4.2.3 Time to equilibrium

Since the contributions of Ettema (1980) and Franzetti *et al.* (1982) apply to the principal phase of the scour process, the definition of the equilibrium time is crucial. One can assume

$$\frac{UT_e}{L} = \varphi(N_U, N_L) \quad (6)$$

Under this Hypothesis, Figure 8 shows the variation of UT_e/L with $N_U=U/U_c$ for the seven classes of N_L previously defined. The associated regression lines are also presented.

From Figure 8 it can be concluded that UT_e/L decreases with increasing N_L and tends to become practically constant for high values of N_L (for $N_L > 30$, the value of UT_e/L is approximately constant and equal to 1.05×10^5). The maximum observed UT_e/L values correspond to the threshold flow condition, i.e. to $N_U=U/U_c \approx 1.0$.

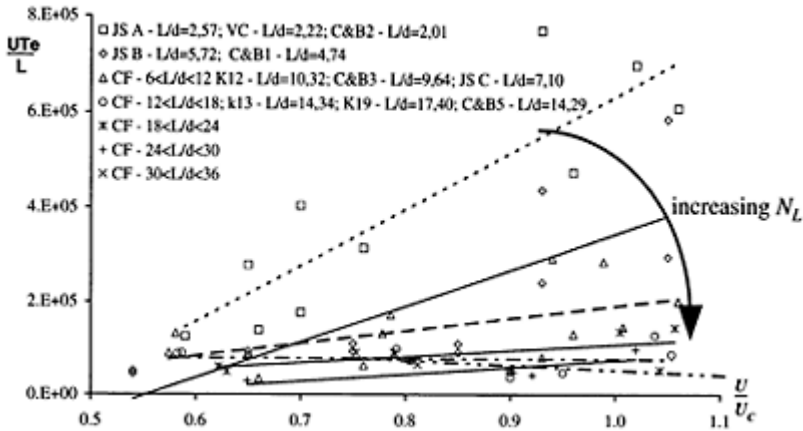


Figure 8. Variation of UT_e/L with $N_U = U/U_c$.

5 CONCLUSIONS

This study applies to thin vertical obstacles protruding at right angle from the walls of rectangular, non-ripple forming sand-bottom channels. For the range of data covered in this study, the following conclusions can be drawn:

1. Coefficients a_1 and a_2 of Franzetti *et al.* (1982) are independent of $N_U = U/U_c$ and $N_L = L/d$. These coefficients take the values $a_1 = -0.087 \pm 0.049$ and $a_2 = 0.322 \pm 0.041$.
2. Coefficients k_1 and k_2 of Ettema (1980) vary with both N_L and N_U . For $N_U \approx 1$, the dependence curves of k_1 and k_2 on N_L are similar to those proposed by Cardoso & Bettess (1999).
3. Time to equilibrium depends on both N_U and N_L according to Figure 8.

REFERENCES

- Cardoso, A.H. & Bettess, E. 1999. Time evolution and effect of channel geometry on local scour at bridge abutments, *Journal of Hydraulics Engineering*, ASCE, Vol 125, No. 4, April, pp. 388–399.
- Da Cunha, L. V 1973. Local scour at obstacles protruding from lateral walls (in Portuguese), *Memoria No. 428, Laboratorio Nacional de Engenharia Civil*, Lisboa, Portugal.
- Ettema, R.E. 1980. Scour at bridge piers, *The University of Auckland, School of Engineering, Rep. No. 236*, New Zealand.
- Franzetti, S. & Larcen, E. & Mignosa, P. 1982. Influence of tests duration on the evaluation of ultimate scour around circular piers, *International Conference on the Hydraulic Modelling of Civil Engineering Structures, paper G2*, Coventry, U.K.

- Kwan, T.F. 1984. Study of abutment scour The University of Auckland, *School of Engineering, Rep. No. 328*, New Zealand.
- Santos, J.P. S. & Cardoso A.H. 2001. Time evolution of local scour at obstacles protruding from channel side walls, *International Journal of Sediment Research*, Vol 16, No. 4, pp. 460–472.

Local scour downstream of grade control structures

C.Adduce, M.La Rocca & P.Mele

*Department of civil Engineering Sciences, University of Roma TRE Via
Vito Volterra, Rome, Italy*

Hydraulics of Dams and River Structures—Yazdandoost & Attari (eds)

© 2004 Taylor & Francis Group, London, ISBN 90 5809 632 7

ABSTRACT: Grade control structures are used to prevent from excessive channel-bed degradation, but the erosive action of the flowing water causes downstream local scour. This scour can endanger the stability of the structure and cause the risk of a failure, if the foundations are not designed taking into account the maximum scour depth. This study investigates experimentally the scour downstream of a grade control structure, followed by a rigid apron, in clear water scour conditions. Eight experiments are run, changing the discharge and the tailwater depth of the flow, in order to investigate the influence of these parameters on the development of the scour hole. The temporal evolution of the scour, its maximum depth and length are recorded by a video camera and measured using image analysis techniques. The velocity field, measured by an ultrasonic velocity profiler, both on the rigid apron and in the scour hole is shown.

1 INTRODUCTION

Local scour downstream of hydraulic structures is an important problem concerning the hydraulic engineering. As a matter of fact, during the design of an hydraulic structure, it is necessary to take into account the scouring process which could undermine the stability of the structure. However, the flow downstream of an hydraulic structure in a channel with a mobile bed is very complex, not uniform and turbulent. As a consequence, the investigations concerning local scour phenomena are usually run in laboratory. Such research trend is shown in many recent scientific works (Gaudio and Marion 2003, Farhodi and Smith 1985, Kurniawan, Altinakar and Graf 2001), in which experimental studies of local scour problems downstream of different structures (such as bed sills, energy dissipators, gates) are shown.

The aim of this experimental study is to give a contribution for a better understanding of the scouring process downstream of a grade control structure, followed by a rigid apron. The experiments were carried out in the laboratory of Hydraulics at the Department of Civil Engineering Sciences of the University RomaTRE. The temporal evolution of the scour profile, registered by a CCD camera and obtained using image analysis techniques, is shown. The velocity field, measured by an ultrasonic velocity profiler at the end of the mn, when the asymptotic state is reached, is presented. A predicting formula, obtained interpolating the experimental data, is proposed.

2 EXPERIMENTAL SET-UP

The experiments were carried out in the hydraulic laboratory of RomaTRE University, using a tilting flume (17m long, 1 m high and 0.8 m wide) with a rectangular cross section. The slope of the flume bed was close to zero. A test section, 0.3 m high and 3 m long, positioned 7 m downstream the inlet of the flume, was created raising artificially the flume bed. A uniformly graded sand, with a mean diameter $d_{50}=0.6$ mm, was used to fill the test section, in order to have a mobile bed. The same sand was glued both to the upstream and downstream fixed-bed sections, in order to have a bed with homogeneous roughness.

A sill, with a height of $D_p=0.15$ m, followed by a $L_p=0.5$ m long rigid apron, was positioned upstream of the test section (see Figure 1). A weir, positioned at the end of the flume, was used to change the tailwater conditions.

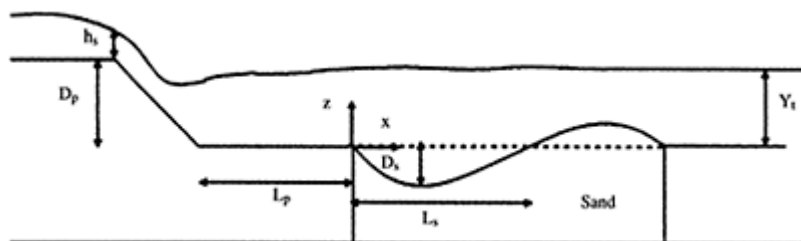


Figure 1. Definition sketch for model tests.

Before starting the experiments, the level of the mobile sand bed, positioned in the test section, was set to the same height of the fixed bed, the weir was completely closed and the flume was slowly filled with the water pumped from the laboratory water reservoir. The discharge was slowly increased and set to the desired experimental value, paying attention to avoid any movement of the sand bed. The experiment started at $t=0$, having the tailwater depth been rapidly set to the desired experimental value opening the weir. The discharge was maintained constant for the whole duration of the experiment.

The evolution of the scour hole was registered on a mini DV, using a CCD camera (Sony XC-77CE) connected to a digital videocassette recorder (Sony DSR-11). A detailed study of the temporal evolution of the scour hole was possible using image

analysis techniques. The water level in flume was measured using a capacitive point gauge with a precision of 0.1 mm, mounted on a carriage which could move along the flume.

At the end of the experiment, when the scouring process is assumed to have reached an asymptotic state, velocity measurements were performed by an ultrasonic velocity profiler (Signal-Processing DOP2000). The Acoustic Doppler Velocity Profiler (ADVP), first developed for medical studies on blood flow (Willemetz), is today used to perform measurements both in transparent (Ito, Tsuji, Nakamura, Kukita 2001, Hurther 2001, Alfonsi 2001) and optically opaque fluids and high temperature fluids (Ecker & Gerberth 2002), giving spatio-temporal velocity information. The ADVP is constituted by a piezoelectric probe, which works both as emitter and receiver of a signal consisting of ultrasonic pulses travelling across the fluid and backscattered by the targets, i.e. small air bubbles or particles, moving with the flow. Evaluating the time elapse between the emission of the pulse and its reception it is possible to determine the position of the target. The received backscattered pulses are shifted in frequency, due to the Doppler effect, so it is possible to calculate the velocity component of the flow along the probe axis evaluating this frequency shift. For a detailed description of the ADVP technique see Takeda (1990,1999). For these experiments the pulses are repeated with a pulse repetition frequency (PRF) of 2200 Hz and the number of emissions used to compute one profile is 40, corresponding to a final sampling frequency of about 25 Hz. The size of the measurement volume depends on the characteristics of the probe (emitting frequency and diameter) and increases far from the probe, due to the lateral spreading of the pressure wave. During these runs probes with an emitting frequency of 2 MHz and with a diameter of 14 mm were used, being the divergence angle equal to 1.83° . The ADVP allows a quasi-instantaneous measurement of the velocity in different volumes (gates), positioned along the axis of the probe. The distance between the center of these gates used for the experiments is 3.52mm. The longitudinal size used for the sampling volume is 2.96 mm, while its lateral size depends on the distance from the transducer. For the measurement of the profiles of the two velocity components, the horizontal and the vertical one, three probes with the same emitting frequency were used (Longo, Losada, Petti, Pasotti, Lara 2001).

Velocity profiles were measured in different longitudinal sections (-25, -15, -5, 5, 15, 25, 35, 45, 55, 65, 75, 85, 95 and 105 cm following the reference system as shown in Figure 1) in the center of the flume. Due to instrument configuration, the data can not be obtained in regions closer to 5 cm from the water surface and 1.5 cm from the eroded bed. For the same reason in it was not possible to perform velocity measurements in a zone approximately positioned 25 cm upstream of the end of the rigid apron.

Measurements of the water surface elevation along the center line of the flume were performed using a capacitive point gauge. At the end of the experiments, measurement of the bed profile were made in the center of the flume.

Table 1. Summary of the experimental runs.

Run	Q [l/s]	h_s [m]	Y_t [m]	D_s [m]
1	11.0	0.021	0.126	0.042
2	12.3	0.024	0.129	0.044
3	14.2	0.023	0.134	0.050
4	16.2	0.023	0.137	0.061
5	18.4	0.028	0.143	0.067
6	20.5	0.029	0.145	0.069
7	24.8	0.032	0.151	0.077
8	25.8	0.034	0.156	0.082

3 RESULTS

3.1 *General considerations*

Several experiments were performed, each one of them characterised by a different value of the discharge. In particular 8 values of the discharge were considered, resumed in Table 1.

Each considered experiment was performed in clear water scour condition. After the desired tailwater was reached, the formation of a submerged hydraulic jump was observed on the rigid apron immediately downstream of the sill. The scouring process started contemporaneously with the formation of such hydraulic jump and was characterised by a very rapid increase during the first minutes of the experiment, followed by a slower and slower increasing, until the asymptotic state was reached, defined as that condition in which no more sediment are moved. From a phenomenological point of view the scouring process is due to the presence of a jet which is caused by the presence of the sill. In fact, the flow accelerates on the sill, where the Froude number is always greater than 1, and in correspondence of the rigid apron causes the formation of a submerged hydraulic jump. It was experimentally observed the presence of a wall jet over the apron. Such wall jet meets the mobile bed and starts the scouring process, which, due to the high value of the magnitude of the velocity, goes very rapidly. However, while the scouring process is going on, the wall-jet becomes a free-jet, being its maximum velocity not in correspondence of the mobile bed (Hoffmans 1997). For this reason, the scouring process, goes slower and slower, until an asymptotic state configuration is reached, defined as a configuration in which no more sediments are moved. Such phenomenological description is valid for each considered experiment. Detailed analysis of the velocity field as well as of the temporal evolution of the scouring process were performed for each considered experiment. In the following the analysis of run 4, characterised by 16.2 l/s of discharge will be considered.

3.2 The velocity field

The velocity field, measured by the ADVP, the bed profile, measured in the center of the flume and the free water surface profile are shown in Figure 2. The horizontal and vertical distances are made nondimensional dividing them by the water depth over the sill, h_s . The jet created by the flowing water over the sill first moves over the rigid apron, positioned immediately downstream of the sill, with a wall-jet velocity distribution.

It is possible to observe the presence of a flow, with a backward direction close to the water surface in the zone of the rigid apron. This backward flow is due to the presence of the submerged hydraulic jump, positioned over the rigid apron. The backward flow becomes stronger and stronger, decreasing the distance from the sill. The flow which moves over the mobile bed has a free-jet velocity distribution and its maximum velocity continues to decrease increasing the distance from the sill. In a zone between 0 cm from the end of the rigid apron and about $L_{\max}/2$, being L_{\max} the length of the scour, the velocity vectors close to the mobile bed have small values. Moving downstream of the maximum depth, the velocity vectors start to have a constant positive value (considering the frame of reference shown in Figure 1) all over the depth. The flow in this region has a slightly upward movement, due to the upward slope of the eroded-deposited bed. Downstream of the dune, created by the deposition of the bed material, the flow continues with an uniform vectors distribution all over the water depth.

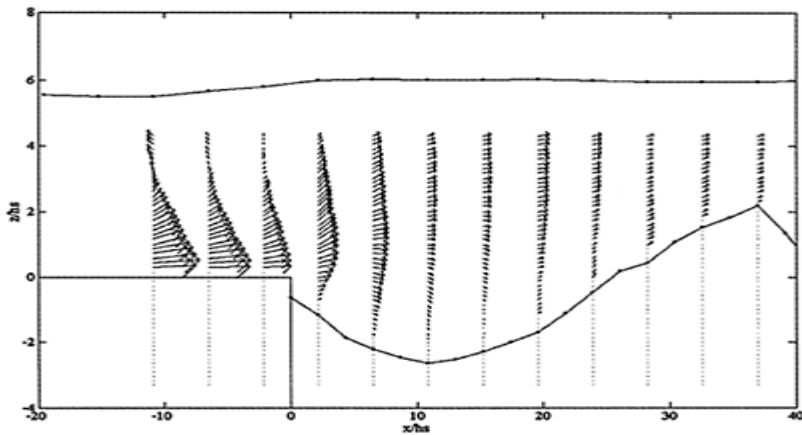


Figure 2. The velocity field.

3.3 Temporal evolution of the scour hole

The temporal evolution of the scour hole, from the beginning of the experiment, was recorded on a mini-DV, using a CCD camera and a videocassette recorder. Applying an image analysis technique, it was possible to measure the temporal evolution of the scouring process at the wall of the flume. This technique has the advantage of making scouring measurements in many different points simultaneously and is very important in order to study the fast evolution of the scour during the first minutes from the beginning of the run. The disadvantage of the technique is that the scour on the glass wall is always

bigger than the scour in a plane in the center of the flume. However, different measurements of the bed profile, made in 5 different transversal planes of the flume, showed that the bed profile was approximately 2D, the differences between a measurement close to the wall and another one in the center of the flume being very small compared to the total eroded depth, so it is possible to use the data obtained by the camera as a reasonable estimate of the scouring process.

In Figure 3 is plotted the temporal evolution of the maximum depth of the scour (triangles) and the time rate of the scour (circles), being the measurements performed during the run. Six different profiles, measured at 1, 4, 16, 66, 260 and 501 minutes, are plotted. It is possible to observe how the scouring process evolves very fast during the first minutes of the experiment, while it is getting slower and slower increasing the time. The asymptotic state was reached after 351 min (5.85h) since the start of the experiment. After that time, no sediment transport was observed throughout the measuring section. The maximum scour depth measured was 0.061 m and the length of the scour hole was 0.60 m. Almost 90% of the total scour depth needed about the 28% of the total time. A similar behaviour was observed by Kurniawan, Altinakar and Graf (2001).

In Figure 4 is plotted the temporal evolution of the scour profiles, measured by the camera. After only 1 minute a scour hole with a maximum depth of 0.025 m is formed and it is possible to observe the presence of a small dune downstream of the hole. A lot of suspended material was observed during the first minutes of the run. It is possible to distinguish two different phases of the scour evolution. During the first one, which ends at a time of about 351 minutes, when the scour hole reaches the asymptotic state, the scour profile changes very fast, increasing both of its depth and

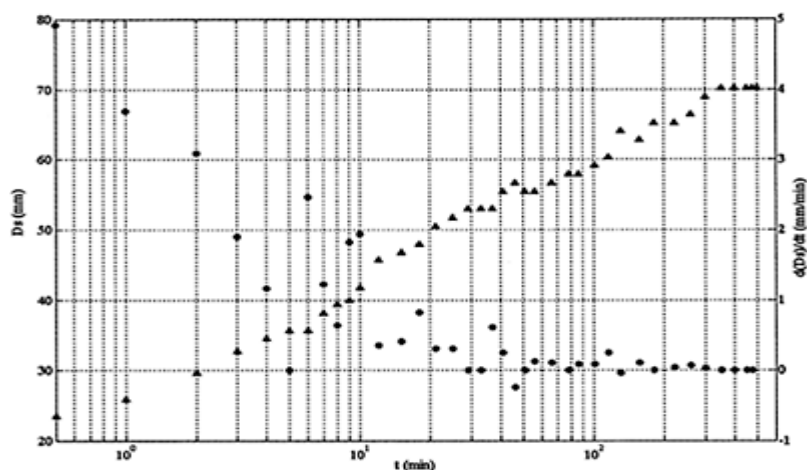


Figure 3. Temporal evolution of the maximum scour depth (triangles) and time rate of its increasing (dots).

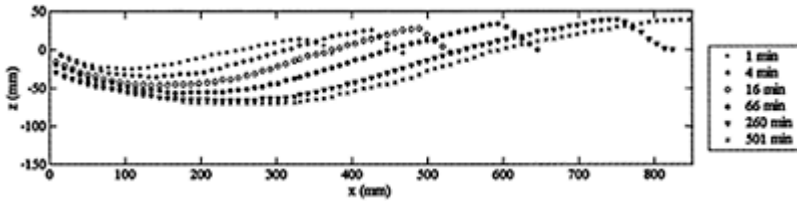


Figure 4. Temporal evolution of the scour profile.

its length. The dune increases its height and length, moving downstream. During the second phase the maximum scour depth is always the same, while the scour hole continues its developments increasing its length. During the evolution of the scour hole, it is possible to observe that the point of maximum scour depth was moving downstream.

3.4 An interpolating formula

In order to have a general idea on the behaviour of the considered phenomenon, a formula, which interpolates the experimental results, is proposed. Such formula is obtained by applying the dimensional analysis to the considered problem which shows that the maximum scour depth at the asymptotic state can be expressed as a function of non-dimensional parameters. Following the work of Mossa (1998), the following choice is proposed for the non-dimensional parameters:

$$\frac{D_s}{Y_t} = f(Fr_d, Fr_s, \Delta H) \quad (1)$$

The influence of other parameters has been excluded either because the parameter is assumed not influencing the phenomenon or because its variation is not sensible along

the scour. In (1) $\frac{D_s}{Y_t}$ is the ratio of the maximum scour on the tailwater downstream, Fr_d is the densimetric Froude number, Fr_s is the Froude number at the sill, ΔH is the ratio of the difference between the tailwater in correspondence of the sill and the tailwater downstream ($\Delta H = \frac{h_s + D_p - Y_t}{Y_t}$). The latter quantity gives the variation of the hydraulic grade line, due to the crossing of the flow along the sill. The densimetric Froude number is defined as:

$$Fr_d = \frac{Q}{bh_s \sqrt{\psi \left(\frac{u_* d_{50}}{v} \right) \left(\frac{\rho_s - \rho}{\rho} \right) g d_{50}}} \quad (2)$$

being $\psi \left(\frac{u_* d_{50}}{v} \right)$ the Shields parameter, in which d_{50} is the characteristic diameter of the sediment, ρ , ρ_s respectively the density of the water and the sediment. In the present work u_* , the shear velocity, is calculated as:

$$u_* = \sqrt{\frac{d_{50}}{h_s^{7/3}} \frac{Q}{bn}} \quad (3)$$

being n the Manning factor, which is closely related to d_{50} by means of:

$$u_* = 0.13 \frac{(2d_{50})^{1/6}}{\sqrt{g}} \quad (4)$$

As a matter of fact, the values assumed by $Re_* = \frac{u_* d_{50}}{\nu}$ for each experiments are in the range:

$3.93 \leq Re_* < 7.18$, in correspondence of which the Shields parameter is approximately constant ($\psi \approx 0.035$). The Froude number Fr_s is defined adopting the tailwater measured in correspondence of the first section of the sill:

$$Fr_s = \frac{Q}{bh_s \sqrt{gh_s}} \quad (5)$$

By adopting a monomial formula:

$$\frac{D_s}{Y_t} = K Fr_d^\alpha Fr_s^\beta \Delta H^\gamma \quad (6)$$

It is straightforward to apply a least squared approximation technique to determine the coefficients K , α , β , γ . The following values were obtained: $K \approx 2.9 \times 10^{-5}$, $\alpha \approx 3$, $\beta \approx -1.6$, $\gamma \approx 0.57$ which highlight the most important features of the considered phenomenon: the maximum scour depth increases with the discharge and decreases with the tailwater depth.

The validity of the interpolation is shown in Figure 5, where the predicted values of $\frac{D_s}{Y_t}$ are plotted versus the experimental ones.

4 CONCLUSIONS

The local scour downstream of a grade control structure with a rigid apron was experimentally investigated at the hydraulic laboratory of the University RomaTRE. The evolution of the scouring process was recorded by a CCD camera and the profiles of the scour hole were obtained using image analysis techniques. The experiments show that the temporal evolution of the maximum scour depth is very fast during the first minutes of the run and decreases with time increasing. Velocity profiles, both of the horizontal and the vertical component, were measured in the center of the flume when the asymptotic scour depth was reached. The velocity measurements show the presence of a wall jet, which moves downstream on the rigid apron, related to the submerged hydraulic jump. A formula, obtained interpolating the measured maximum scour depth, is proposed. This work contributes to a better understanding of the velocity field, which develops

downstream of a grade control structure with a rigid apron. A possible development of this work could be a numerical model which simulates the temporal evolution of the scour hole, due to the wall jet observed by these velocity measurements.

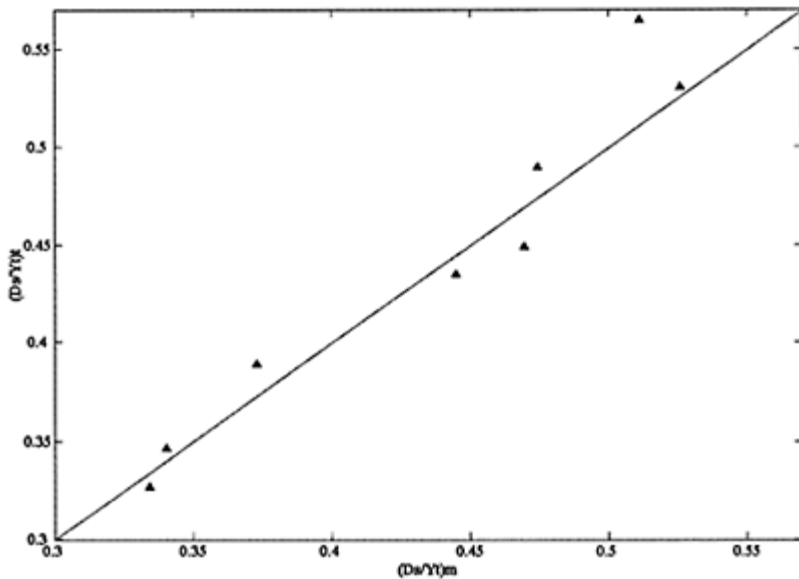


Figure 5. Comparison between experimental and predicted values of the maximum scour depth divided by the tailwater depth.

REFERENCES

- Alfonsi G. 2001. Analysis of streamwise velocity fluctuations in turbulent pipe flow with the use of an ultrasonic Doppler flowmeter. *Flow, Turbulence and Combustion*. 67:137–142.
- Eckert S. and Gerbeth G. 2002. Velocity measurements in liquid sodium by means of Ultrasound Doppler Velocimetry. *Experiments in Fluids*. 32 (5): 542–546.
- Farhodi J. and Smith K. V H. 1985. Local scour profiles downstream of hydraulic jump. *Journal of hydraulic research*. 23:343–358.
- Gaudio R. and Marion A. 2003. Time evolution of scouring downstream of bed sills. *Journal of hydraulic research*. 41:271–284.
- Hoffmans G.J. C.M. and Verheij H.J. 1997. *ScourManual* Rotterdam: Balkema.
- Hurth D. 2001. 3-D Acoustic Doppler velocimetry and turbulence in open-channel flow. These N° 2395, EPFL Lausanne, Switzerland.
- Ito T., Tsuji Y., Nakamura H. and Kukita Y. 2001. Application of ultrasonic velocity profile meter to vortex shedding and empirical eigenfunctional analysis, *Experiments in fluids*. 31:324–335.
- Kurniawan, A., Altinakar, M.S. and Graf, W.H. 2001. *Flow Pattern of an Eroding Jet*, Proc. of XXIX IAHR Congress, Beijing, China: 537–544.

- Longo S., Losada I.J., Petti M., Pasotti N. and Lara J.L. 2001. Measurements of breaking waves and bores through a USD velocity profiler. Technical Report UPR/UCa_01_2001. University of Parma, E.T.S.I.C.C. y P, Ocean & Coastal Research Group Laboratory, Universidad de Cantabria, Spain, 2001.
- Mossa M. 1998. Experimental study on the scour downstream of grade-control structures. *XXVI Convegno di idraulica e costruzioni idrauliche; proc. Nat. symp.*, Catania, 9–12 September 1998. CUECM.
- Takeda Y. 1995. Velocity profile measurements by ultrasonic Doppler method. *Experimental thermal and fluid science*. 10:444–453.
- Takeda Y. 1999. Ultrasonic Doppler method for velocity profile measurements in fluid dynamics, *Experiments in fluids*. 26:177–178.
- Willemetz J.C., Etude Quantitative de l'Hémodynamique de Vaisseaux Profonds par Echographie Doppler Ultrasonore. These No 893, EPFL Lausanne, Switzerland.
- Willemetz J.C. *DOP 2000 Users manual*.

S.M.Borghei & A.Nazari
Civil Engineering Department, Sharif University of Technology

A.R.Daemi
Water Planning Bureau, Ministry of Energy

Hydraulics of Dams and River Structures—Yazdandoost & Attari (eds)

© 2004 Taylor & Francis Group, London, ISBN 90 5809 632 7

ABSTRACT: The flow pattern at channel junctions is a complicated matter specially when loose boundary is included. There are many parameters which influence the scouring profile due to junction. Some of the important ones, which have been studied in this research, are: channels and junction geometry, discharge ratio, downstream Froude number, as well as, sediment size. The results from experimental tests at channel junction are presented. The experiments were carried out with 3 different ratios of branch to main channel width. The results show that maximum scouring depth happens further downstream of the junction (longitudinal and transverse) and not at the junction itself. This is more extreme for smaller grain size. Also, when branch channel has smaller width to main channel, the length of scour hole becomes larger while the depth does not change much. Another important result is the effect of connection geometry of the channels which, a chamfer or non-sharp edge reduces the scouring dramatically. Finally, the complete results are presented as graphs.

1 INTRODUCTION

Channel junction is a phenomenon that occurs frequently in rivers and open-channels. The flow pattern and flow characteristic changes at channel junction due to confluence of two flows. Different factors affect flow at channel junction, such as; channel and sediment geometry (layout of channel junction, width ratio of tributary to main channel, size, type and degree of sediment erodability), tributary to main channel discharge ratio and downstream Froude number. Sediment scour and deposition are very important and complicated problems in channel junction hydraulics. Previous investigations show that the maximum scour happens at threshold motion with clear water condition (Yang 1996). It is very difficult to define threshold. There is no definite or exact condition under which a particular sediment size can be displaced but, a range for threshold values exist. Mason

and Armugum (1985) performed many investigations on different relations with 47 experimental models. They concluded that d_{50} is more suitable than d_{95} and d_{10} in order to study the sediment scour. Silvia & Gerardo (1999) studied one of the common features of deep-scour holes at the junction of tidal channels in the Bahia Blanca Estuary (Argentina), in order to find the possible origin and evolution of scour holes. The tests were investigated on the two largest known holes in the estuary. According to their observations, the evolution of the holes is related to flood dominance acting on the steep side (inner face) and ebb dominance over the gentle side (outer). So, holes migrate headward in a pattern opposite to similar holes in fluvial reaches. Paphitis (2000) studied sediment movement under unidirectional flow using empirical threshold curves. His new modified curve can predict sediment threshold.

In this paper, laboratory tests were performed using experimental flume with two channel confluence at right angle. The flow is subcritical and the tests were done in clear water condition and particle movement threshold.

Table 1. Test variables.

Variable	Set-up
W_u =Upstream main channel width (cm)	40
W_d =Downstream main channel width (cm)	40
W_b =Branch channel width (cm)	20, 30, 40
q =Branch discharge/Total discharge	0.25, 0.5, 0.75
L =Length of main channel (cm)	600
l =Length of branch channel (cm)	200
Q_t =Total discharge (lit./sec.)	14.38
(d_1, d_2, d_3) =Sediment size (mm)	0.25, 0.5, 1.5
Downstream Froude Number (Fid)	<1

2 BED MATERIAL AND EXPERIMENTAL SET-UP

(1) The assumptions for the sediments are:

- (a) To eliminate the effect of materials nonuniformity in scour depth, the selected material should be uniform, and for this purpose the parameter σ_g is less than 1.5 or:

$$\sigma_g = \sqrt{d_{84.1}/d_{15.9}} < 1.5$$

- (b) Since the cohesion of bed materials, is a different phenomenon and produces completely different results (Raudkivi 1998), this study has been concentrated with cohesionless materials.
- (c) Three sizes mean particle diameter ($d_1=0.25$ mm, $d_2=0.5$ mm, $d_3=1.5$ mm) were selected for the experiments. So that, scour can occur due to flow at junction

(Mason 1985, Breusers & Raudkivi 1991). The materials used are from crushed burned tile as cohesionless. In order to observe the maximum scour depth, the flume had 10 cm thickness of the sediment materials for the tests.

- (2) The variables of the set-up used are shown in Table 1. Three ratio of branch to total discharge ($q=Q_b/Q_d$) of 0.25, 0.5, 0.75 were employed.

3 RESULTS

3.1 Timeeffect

One of the main parameters dealing with scour experimental work is the running time for each test. In order to determine the effective time for this study, the scour was measured at intervals up to maximum of 48 hours. As shown in Figure 1, time of 3 hours is a good estimate and were selected since, more than 90 percent of scour relative to 48 hours happens in the first hour. The figure shows the scour with time initially has a steep trend which after a stage tends asymptotically to final depth. The scour process for fine materials is faster compared to coarse materials but, this process decrease as the time increases. With a good approximation, the effect of discharge rate (q) on the scour process does not have much influence and, thus, can be neglected (Paphitis 2001, Stephen 1995, Nazari 2003).

3.2 Effect ofchamfer

The existence of chamfer at the junction cause the score hole depth to be smaller than the case with no chamfer at the junction. The reason is that the separation dimensions decrease at the junction due to the chamfer and, therefore, decreasing the intensity of formed turbulence and vortices at this point (Borghei et al. 2003). Figure 2, shows the way in which chamfer, or 45° connection, affect the maximum scour depth.

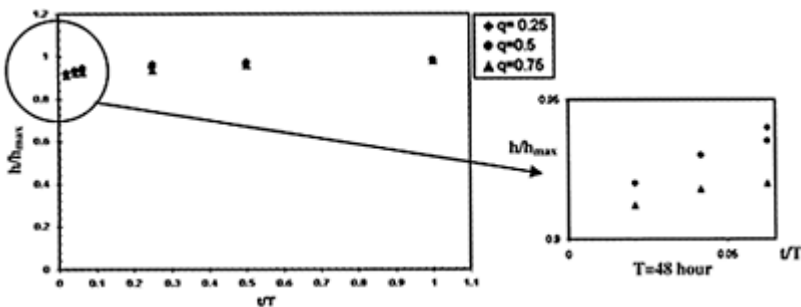


Figure 1. The effect of time on scour depth, h_{max} =Scour depth at end of 48 hours, h =Scour depth at time t

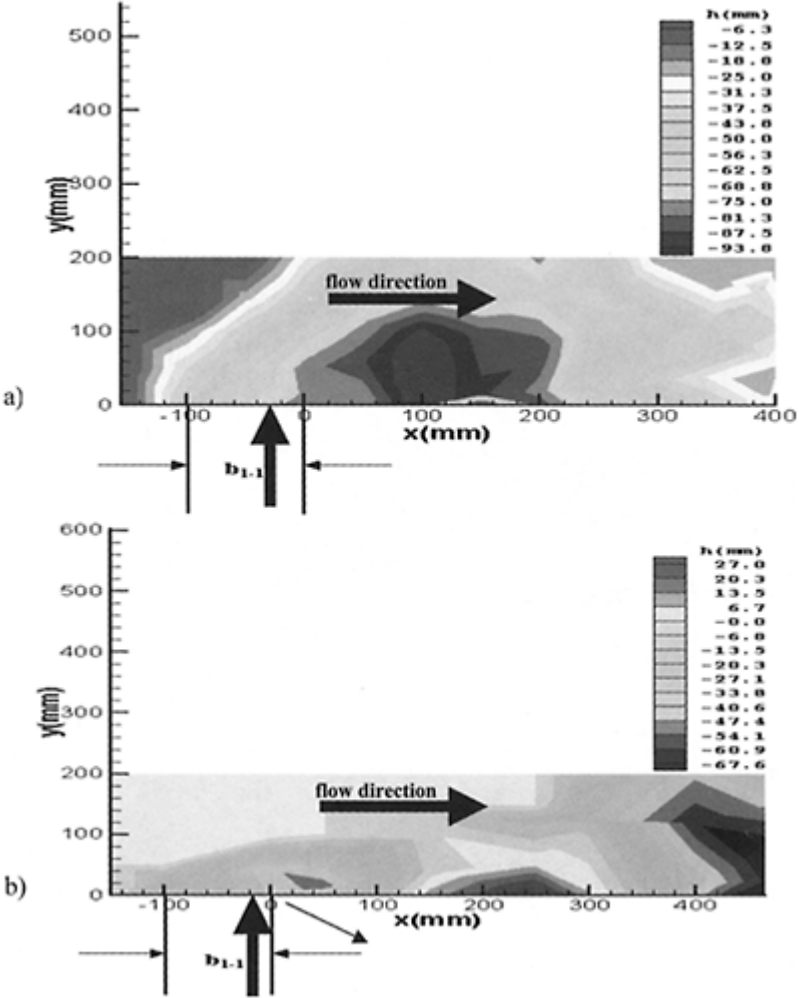


Figure 2. Scouring map for $d=0.25$ mm and $q=0.5$; (a) sharp connection $\theta=90^\circ$, (b) $\theta=45^\circ$

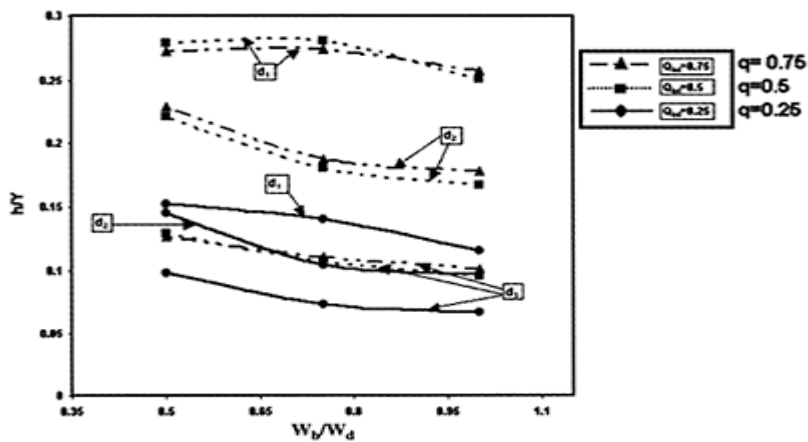


Figure 3. Maximum scour depth for three discharges and different width ratio (Y =Water depth).

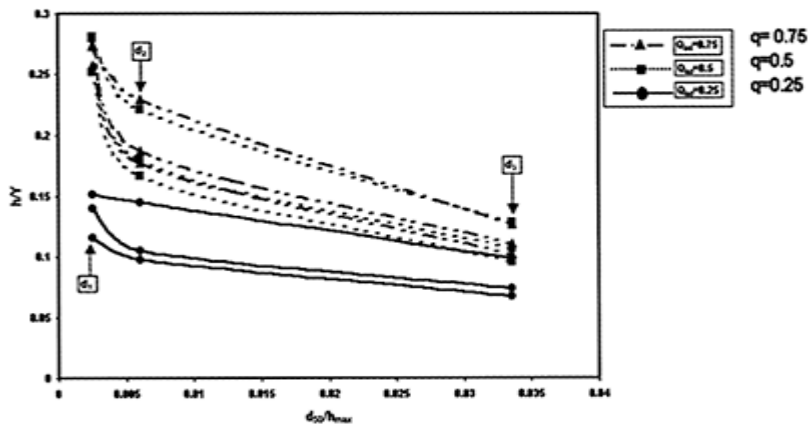


Figure 4. Effect of bed material mean diameter on maximum scour depth.

3.3 Effect of tributary channel widths

The effect of tributary width to main channel width on maximum scour depth (h_{max}) is shown in Figure 3. As it can be seen, in general with increase of tributary branch width, maximum scour depth decreases. The results show that q and sediment size (d), are more influential than width ratio.

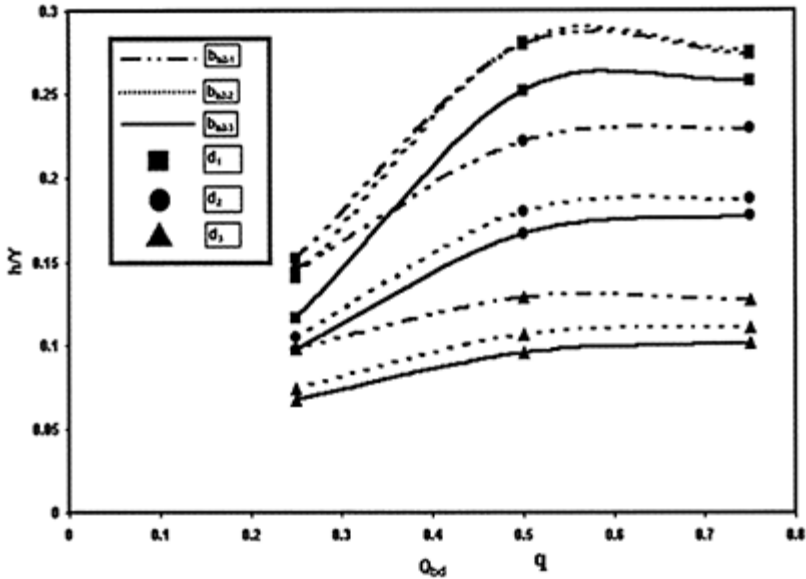


Figure 5. The effect of tributary branch discharge ratio (q) on maximum scour depth.

3.4 Sediment size

Another variable which is studied, was material mean diameter. Figure 4, shows the effect of nondimensional parameter d_{50}/h_{\max} on the maximum scour depth ($h_{\max}=100$ mm). It is seen that, as expected, for a fixed discharge ratio, with increase of d_{50} , the scour depth decreases. Since, the necessary force for initial motion and their movement increases.

3.5 Effect of discharge ratio

An important parameter studied for the present study, is the effect of discharge ratio, q (Figure 5). With increase of q or increase of discharge from the tributary channel to the main discharge, the scour depth increases. However, an important result is that for the same conditions the changes for $q \geq 0.5$ is very small.

4 CONCLUSION

1. For this study, running time of 3 hours for each test was chosen which, completes more than 95% of scour due to 48 hours tests.
2. Simple 45° connection of the channels has great effect on scouring. This can be further studied.

3. With the decrease of tributary branch width to main channel the scour depth reaches to its maximum value. However, the ratio of 0.5 influence the scour only by 10%.
4. The smaller the size of sediment the bigger the scour depth is.
5. Increase of q up to $q=50\%$, increase maximum depth sharply but, after that, q is less influential.
6. Finally, scour depth has an inverse relation with particle size d_{50} , tributary width and discharge ratio from tributary channel to total discharge, while it is directly related to the geometry of the chamfer.

ACKNOWLEDGMENT

The authors would like to thank Sharif University of Technology and Water Resource Management Organization affiliated to Ministry of Energy for their financial support of this project.

REFERENCES

- Yang, C.T. 1st ed. 1996. Sediment Transport; Theory and Practice. New York: Mc Graw Hill.
- Mason, P.J. & Arumugam, K. 1985. Free Jet Scour Below Dams and Flip Bucket. *J. Hydraulics Engineering*. ASCE 11:220–235.
- Silvia, S.G. & Gerardo, M.E.P. 1999. Deep-Scour Holes at Tidal Channel Junctions, Bahaia Blanca Estuary, Argentina. *J. Marina Geology* 160:171–182.
- Paphitis, D. 2001. Sediment Movement Underctional Flow: an Assessment of Empirical Threshold Curves. *J. Coastal. Eng.* ASCE 43:227–254.
- Raudkivi, A.J. 1998. Loose Boundary Hydraulics. Rotterdam: Balkama.
- Breusers, H.N.C. & Raudkivi, A.J. 1991. Scouring. Rotterdam: Balkama.
- Stephen, T.K. & Bruce, L.R. 1995. Hydraulic Control of Spatial Patterns of Suspended Sediment Concentration at a Stream Confluence. *J. Hydrology*. 168:251–263.
- Nazari, A.G. 2003. Sediment Erosion and Deposition in Channel Junction at Subcritical Flow. M.Sc. Thesis (in Farsi). Sharif University Of Technology. Tehran. Iran.
- Borghei, S.M., Behrang, A. & Daemi, A.R. 2003. Open Channel Flow Junction with Different Channel Width. Proc. of the XXXth IAHR Congress, Thessaloniki, Greece, Aug. 573–580.

8.

*Numerical approaches in
hydrodynamics of river flow*

An improved implicit solution for the two dimensional shallow water equations using unstructured grids

S.Komaie & W.Bechteler

German Armed Forces University Munich, Munich, Germany

Hydraulics of Dams and River Structures—Yazdandoost & Attari (eds)

© 2004 Taylor & Francis Group, London, ISBN 90 5809 632 7

ABSTRACT: In this paper, an implicit unstructured grid algorithm for solving 2-D Shallow Water Equations (SWE) has been developed. It is based on cell-centered Finite Volume Method (FVM) and can handle cells of triangular type. The model uses Roe's approximate Riemann solver to compute fluxes. In addition, a new technique is introduced to prevent instabilities and oscillations caused from the bed slope terms in the case of problems with arbitrary topography and hydraulic structures. The proposed method is validated and verified via solving an example and comparison of the results obtained from the new method with the physical model measurements. Second order accuracy in time and second or higher order accuracy in space can be achieved in this method.

1 INTRODUCTION

Flows in open channels are often modelled by a set of hyperbolic partial differential equations, i.e. the well known Shallow Water Equations (SWE). Algorithms for solving SWE on structured grids have become widespread in recent years (Delis et al. 2000; Fennema and Chaudhry 1989; Panagiotopoulos and Soulis 2000; Valiani et al. 1999). However, these algorithms have shown difficulties in predicting satisfactory results in complex geometries due to mesh irregularities. As a result, attention has turned to the development of solution algorithms on arbitrary unstructured grids.

A major hurdle remaining for unstructured algorithms is the increased computational cost of these methods over those incurred by existing structured mesh solvers. Many current unstructured algorithms utilize explicit time integration (Anastasiou and Chan 1997; Beffa and Connell 2001; Nujic 1995; Zhao et al. 1996) that can be computationally expensive if a long period of time has to be simulated. On the other hand, the explicit approach is computationally efficient when applied to meshes that are coarse. For cases where finer meshes are used, the time of computations significantly increases. For the sediment transport problem, which is not a high gradient phenomenon, the simulation

takes a lot of time therefore, an implicit scheme could be more useful which allows large time steps to obtain solutions in a computationally efficient manner. Flood simulation is less concerned than sediment transport. The first one takes a time in the range of one day to one week but the later one often needs a time range of several years or decades.

The application of the implicit schemes in SWE is often an extension of the schemes used in CFD. As pioneers, Fennema and Chaudhry (Fennema and Chaudhry 1989) have used implicit finite difference schemes, developed by Beam and Warming (Beam and Warming 1976; Warming and Beam 1978) for hyperbolic systems in conservation law form, for the solution of two-dimensional SWE without source terms. In general, good results are reported, even though quite dissipative. However, these schemes are only first order accurate in space and employ the flux splitting in a nonconservative way. Later, Jha et al. (Jha et al. 1996) proposed a modification for achieving full conservation, employing the use of the Roe-average approximate Jacobian (Roe 1981). Molls and Chaudhry (Molls and Chaudhry 1995) have developed a mathematical model to solve two-dimensional SWE on structured grid using boundary-fitted coordinates. The model uses a second order accurate Beam and Warming approximation for the time differencing, while the spatial derivatives are approximated by second-order accurate central differencing. MacCormack (MacCormack 1982) presented an implicit analog of his earlier widely used explicit method (MacCormack and Paullay 1972) for solving the equations of compressible viscous flow. Panagiotopoulos and Soulis (Panagiotopoulos and Soulis 2000) have extended the implicit MacCormack scheme to integrate the flow equations. They developed a numerical method to solve SWE in generalized coordinates describing the depth-averaged, steady, subcritical and supercritical free-surface flows with the presence of hydraulic jumps. In the other paper, Klonidis and Soulis (Klonidis and Soulis 2001) have developed another finite volume scheme to calculate steady, two-dimensional SWE. The formulation is based on transformation of the flow equations into a non-orthogonal, boundary-fitted coordinate system. Therefore, the method is suitable for structured grids.

In this paper, an implicit robust model for numerical solving of SWE on unstructured grids is introduced. The proposed method has a special treatment of the bed source terms therefore it is able to model flow over an initially dry and irregular bed and hydraulic structures.

2 SYSTEM OF GOVERNING EQUATIONS, SWE

The system of SWE in the conservative form is given by:

$$\frac{\partial \mathbf{q}}{\partial t} + \frac{\partial \mathbf{f}(\mathbf{q})}{\partial x} + \frac{\partial \mathbf{g}(\mathbf{q})}{\partial y} = \mathbf{S}(\mathbf{q}) \quad (1)$$

with

$$\mathbf{q} = \begin{Bmatrix} h \\ hu \\ hv \end{Bmatrix} \quad \mathbf{S}(\mathbf{q}) = \begin{Bmatrix} 0 \\ gh(S_{0x} - S_{fx}) \\ gh(S_{0y} - S_{fy}) \end{Bmatrix} \quad (2)$$

$$\mathbf{f}(\mathbf{q}) = \begin{Bmatrix} hu \\ hu^2 + gh^2/2 \\ huv \end{Bmatrix} \quad \mathbf{g}(\mathbf{q}) = \begin{Bmatrix} hv \\ huv \\ hv^2 + gh^2/2 \end{Bmatrix}$$

where $\mathbf{F}(\mathbf{q})=[\mathbf{f}(\mathbf{q}), \mathbf{g}(\mathbf{q})]^T$ is the flux vector, h is the water depth, u, v depth averaged velocity in x - and y -direction, respectively, S_{0x}, S_{fx} are bed and friction slope in x -direction and S_{0y}, S_{fy} are bed and friction slope in y -direction. The bed slope is defined in x -direction as:

$$S_{0x} = -\frac{\partial Z_b(x, y)}{\partial x} \quad (3)$$

and the friction slope is estimated using the Manning's formula. For example, in x -direction, it is:

$$S_{fx} = \frac{n^2 u \sqrt{u^2 + v^2}}{h^{4/3}} \quad (4)$$

S_{0y}, S_{fy} are defined in a similar way.

3 NUMERICAL ALGORITHM

3.1 Discretization of the governing equations

The system of governing equations is discretized using the Finite Volume Method (FVM). Integrating Equation (1) over an arbitrary triangular cell Ω and using the divergence theorem, the basic equation of the FVM is obtained as:

$$\iint_{\Omega} \mathbf{q}_t dA = - \int_{\Gamma} \mathbf{F}(\mathbf{q}) \cdot \mathbf{n} dl + \iint_{\Omega} \mathbf{S}(\mathbf{q}) dA \quad (5)$$

in which \mathbf{n} is unit outward vector normal to the boundary Γ (see Figure 1); dA, dl are area and arc element, respectively. After some manipulation, the semi-discrete form of the equation is:

$$A_i \frac{d\mathbf{q}_i}{dt} + \sum_{m=1}^{N_i} \mathbf{F}_m \cdot \mathbf{n}_m, l_m = A_i, \mathbf{S}(\mathbf{q}_i) \quad (6)$$

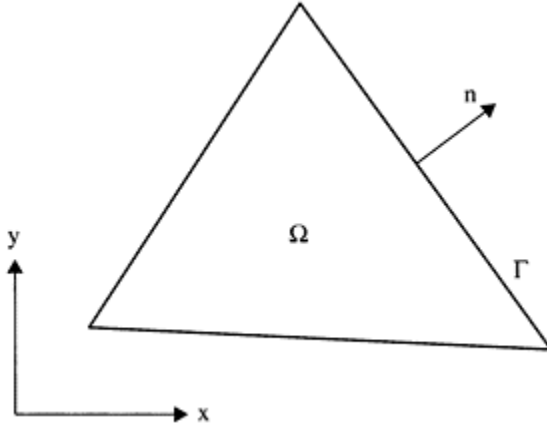


Figure 1. Notation for finite volume method.

where the subscripts i and m denote quantities for the i -th cell and m -th face of the cell, respectively and N is the total number of the faces for that cell.

In an implicit scheme, the flux vector \mathbf{F} is computed at the new time level $k+1$. Using implicit scheme, Eq. (6) can be rewritten in the following form:

$$A_i \frac{\mathbf{q}_i^{k+1} - \mathbf{q}_i^k}{\Delta t} + \sum_{m=1}^{N_i} \mathbf{F}_m^{k+1} \cdot \mathbf{n}_m l_m = \mathbf{R}_i \quad (7)$$

where $\mathbf{R}_i = A_i \mathbf{S}(\mathbf{q}_i)$ is the right hand side terms evaluated in cell i at the known time level k . Expanding \mathbf{F} about a known time level, we get:

$$\begin{aligned} \mathbf{F}^{k+1} &= \mathbf{F}^k + \left(\frac{\partial \mathbf{F}}{\partial \mathbf{q}} \right)^k (\mathbf{q}^{k+1} - \mathbf{q}^k) + O(\Delta t^2) \\ \mathbf{F}^{k+1} &= \mathbf{F}^k + \mathbf{J} \Delta \mathbf{q} + O(\Delta t^2) \end{aligned} \quad (8)$$

where $\mathbf{J} = \partial \mathbf{F} / \partial \mathbf{q}$ is the flux Jacobian matrix. Substituting Eq. (8) into (7) leads to:

$$A_i \frac{\mathbf{q}_i^{k+1} - \mathbf{q}_i^k}{\Delta t} + \sum_{m=1}^{N_i} (\mathbf{J} \Delta \mathbf{q}) \cdot \mathbf{n}_m l_m = \mathbf{R}_i - \sum_{m=1}^{N_i} \mathbf{F}_m^k \cdot \mathbf{n}_m l_m \quad (9)$$

Following Jameson and Turkel (Jameson and Turkel 1981) and Yoon and Kwak (Yoon and Kwak 1992), the flux Jacobian matrices are splitted as follows:

$$\mathbf{J}^\pm = \frac{\mathbf{J} \pm \mathbf{I} \alpha \lambda_{\max}}{2} \quad (10)$$

with:

$$\lambda_{\max} = |\mathbf{V} \cdot \mathbf{n}| + c \quad (11)$$

where \mathbf{V} and $c = \sqrt{gh}$ are the velocity vector and speed of the wave, respectively and α is a relaxation factor of order unity. Eq. (9) now becomes:

$$A_i \frac{q_i^{k+1} - q_i^k}{\Delta t} + \sum_{m=1}^{N_i} (\mathbf{J}^+ \Delta \mathbf{q}_i) \cdot \mathbf{n}_m / m = \mathbf{R}_i - \sum_{m=1}^{N_i} \mathbf{F}_m^k \cdot \mathbf{n}_m / m - \sum_{m=1}^{N_i} (\mathbf{J}^- \Delta \mathbf{q}_m) \quad (12)$$

or written in matrix notation:

$$\mathbf{M} \Delta \mathbf{q}_i = \mathbf{RHS}^k \quad (13)$$

in which:

$$\Delta \mathbf{q}_i = \mathbf{q}_i^{k+1} - \mathbf{q}_i^k = [\Delta h, \Delta(hu), \Delta(hv)]^T \quad (14)$$

is the unknown vector. The formulation of the matrix \mathbf{M} and the vector \mathbf{RHS} are given by Komaie (Komaie 2003). To numerically solve the discretized Eq. (12), the major steps of the solution procedure are reconstruction, flux computation and evolution. These steps are illustrated below.

3.2 Reconstruction

For the first step, reconstruction, a cell-centered scheme is used. The piecewise linear, least-square reconstruction procedure used here is similar to those used by Barth (Barth 1993) and Coirier (Coirier 1994). Each of the three primitive variables h ; u and v is assumed to linearly vary within a finite volume as:

$$U(x, y) = \bar{U} + U_x(x - \bar{x}) + U_y(y - \bar{y}) \quad (15)$$

where U can be any of the above variables. The bars in Eq. (15) denote cell-averaged values as defined in the last equations. In high gradient regions, a gradient limiter is normally used in Eq. (15) to ensure that the reconstruction polynomial does not produce new extrema near a flow discontinuity such as a shock wave. Limiters can also control the numerical oscillation that are common with second and higher order numerical schemes. In this paper, the limiter is applied to the gradient terms (Anastasiou and Chan 1997) so that:

$$U = \bar{U} + \Phi \nabla U \cdot \bar{\mathbf{r}} \quad (16)$$

where \mathbf{r} is the vector from cell centroid to the midpoint of the edge and $0 < \Phi < 1$ is a chosen limiter. When Φ is set to zero, the computation domain is characterized by

piecewise constant regions resulting in a first-order scheme. The non-linear limiter is given by:

$$\Phi = \max [\min (\beta D_j, 1), \min (D_j, \beta)] \quad (17)$$

where:

$$D_j = \begin{cases} (U_j^{\max} - U_j)/(U_L - U_j) & \text{if } U_L > U_j \\ (U_j^{\min} - U_j)/(U_L - U_j) & \text{if } U_L < U_j \\ 1 & \text{if } U_L = U_j \end{cases} \quad (18)$$

with:

$$U_j^{\min} = \min(U_j, U_i), \quad U_j^{\max} = \max(U_j, U_i) \quad (19)$$

This procedure is carried out sequentially for the two cells separated by the common edge. These values are then used in the Riemann solver to estimate the flux across the edge in the flux computation phase. When $\beta=1$, Φ is the *Minmod* limiter and when $\beta=2$, the limiter is *Roe's Superbee* limiter. The *Minmod* limiter is used in this paper.

3.3 Flux computation

In the next step, the normal component of the flux vector, i.e. $\mathbf{F}_m \cdot \mathbf{n}_m$ in Eq. (12), should be estimated. With the piecewise linear reconstruction, the unknown variables are continuous and assumed to linearly vary within a finite volume. However, no guarantee exists that the variables will be continuous across adjacent finite volumes because a different polynomial is used in each finite volume. As a result, a flux formula is needed to compute a single flux at a finite volume boundary using fluxes from the adjacent volumes. In this paper the Roe's approximate Riemann solver is used (Roe 1981). Roe's method may be the most famous Riemann solver in CFD and SWE (Brufau et al. 2002; Erduran et al. 2002; Roe 1981; Sanders 2001; Toro 2001; Tseng and Chu 2000). Define the normal component of the flux vector as:

$$\mathbf{F}_n = \mathbf{F} \cdot \mathbf{n} \quad (20)$$

Then \mathbf{F}_n can be computed using the Roe FDS method as:

$$\mathbf{F}_{n,i+1/2} = \frac{1}{2} \left[\mathbf{F}_{n,L} + \mathbf{F}_{n,R} + \left| \hat{\mathbf{A}}_{i+1/2} \right| (\bar{\mathbf{q}}_L - \bar{\mathbf{q}}_R) \right] \quad (21)$$

where the subscripts L and R denote the flow conditions to the left and right sides of the cell face and $\hat{\mathbf{A}}_{i+1/2}$ is Roe flux difference splitting matrix.

3.4 Evolution

Now it is possible to solve the Eq. (12) for each cell. There is a part of RHS in Eq. (12) that relates to the unknowns of the neighbour cells. Therefore, the system of the algebraic equations should be solved iteratively. The nature of the method enables us to implement it on parallel computer systems. In addition, it is efficient because no block or scalar tridiagonal inversions need to be calculated. After achieving convergence, the solution is updated to find the flow variables at the end of a time step. The main question is whether there is any condition to restrict the time step of the computation for the proposed implicit scheme. It is clear that the CFL condition is not applicable here. But from the mathematics it is well known that to achieve a numerically stable method, the Matrix $\mathbf{M}=[m_{ij}]$ should be diagonally dominant. It means:

$$|m_{ii}| \geq \sum_{j \neq i} |m_{ij}| \quad \forall i \quad (22)$$

3.5 Treatment of the bed source terms

Here, the new developed method for numerical implementation of the bed source terms is presented. The proposed method is simple and robust and it is independent of the Riemann solver. It also holds the conservation property that is defined by Bermudez et al. (Bermudez et al. 1998). For the description of the method, two options should be considered:

- How the method deals with the terms $0.5 gh^2$ in the flux terms.
- Which scheme is used to numerically compute $\mathbf{S}_b(\mathbf{q})$.

3.5.1 Flux modification

The flux vector on the edge can be computed with a desired Riemann solver but after that, the term $0.5 gh^2$ should be recomputed for the sloped edge (Komaie 2003):

$$\frac{1}{2}gh^2 = \frac{1}{2}g\bar{h}^2 = \frac{1}{2}g \frac{h_i^2 + h_i h_j + h_j^2}{3} \quad (23)$$

which h_i and h_j are the water depth at the two ends of the edge based on the constant water level assumption over the edge.

3.5.2 Source terms

Now it is required to compute the integral of the bed source term vector over a cell Ω :

$$\iint_{\Omega} \mathbf{S}_b(\mathbf{q}) dA = \iint_{\Omega} \begin{pmatrix} 0 \\ ghS_{0x} \\ ghS_{0y} \end{pmatrix} dA = g \iint_{\Omega} h \begin{pmatrix} 0 \\ -\frac{\partial Z_b(x,y)}{\partial x} \\ -\frac{\partial Z_b(x,y)}{\partial y} \end{pmatrix} dA \quad (24)$$

If we assume that the bed slope in x- and y-direction in every cell Ω is constant, then we have

$$\iint_{\Omega} \mathbf{S}_b(\mathbf{q}) dA = g \left(\iint_{\Omega} h dA \right) \begin{pmatrix} 0 \\ S_{0x} \\ S_{0y} \end{pmatrix} = g Vol_{water} \begin{pmatrix} 0 \\ S_{0x} \\ S_{0y} \end{pmatrix} \quad (25)$$

It means that the bed term integral is converted to the multiplication of two parameters: cell bed slope and the volume of water in the cell between water surface level and bed level. For the case of wet cell, i.e. all three nodes are under the water surface (Figure 2), the volume of water is:

$$Vol_{water} = \left(\frac{h_1 + h_2 + h_3}{3} \right) \cdot A \quad (26)$$

which A is the cell area and h_i where $i=1, 2, 3$ is the water depth at i -th node of the cell. For the partially wet cell the above Eq. should be modified so that the real volume of water is obtained.

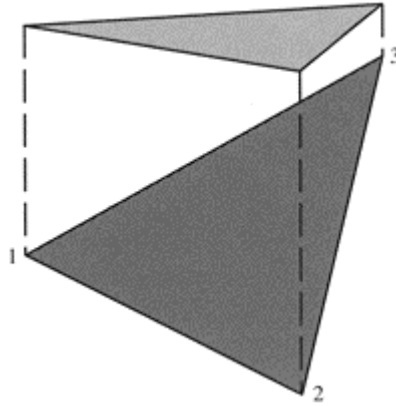


Figure 2. Sloped wet cell and the water surface level, 3D imagination.

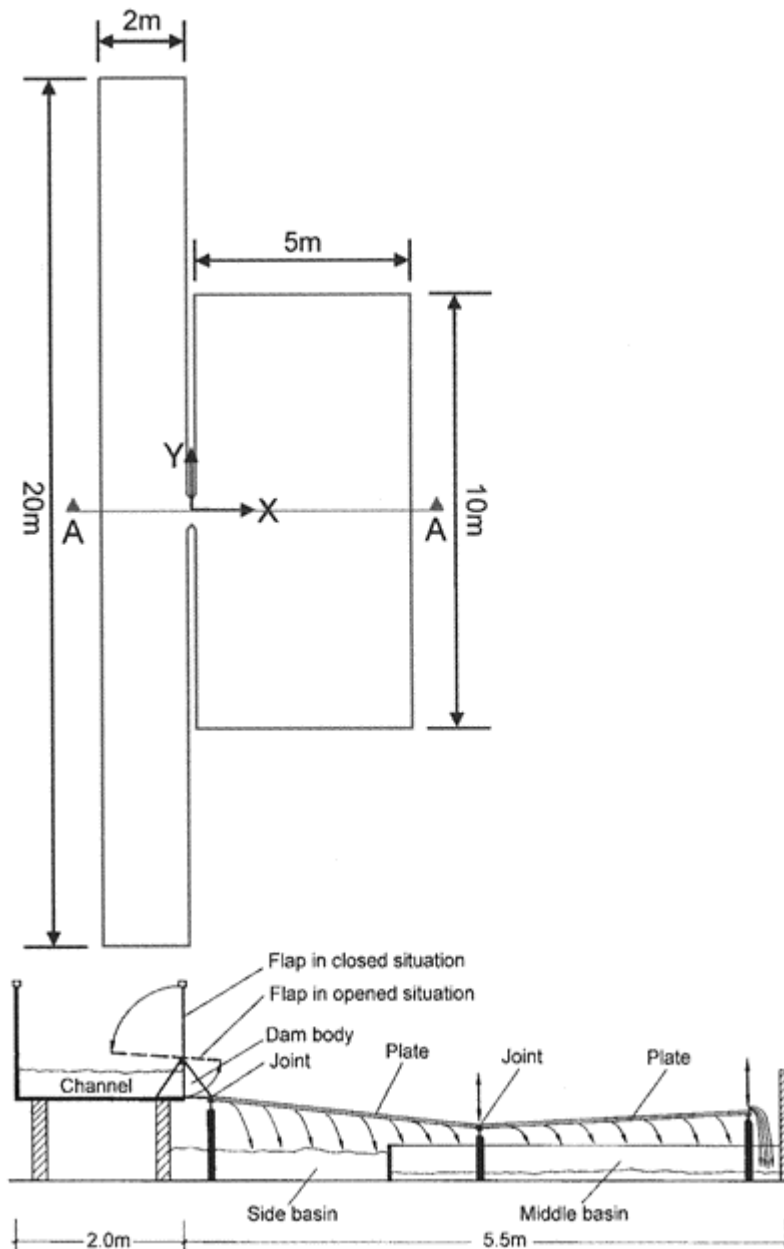


Figure 3. Sketch of the physical model (Kulisch 2002).

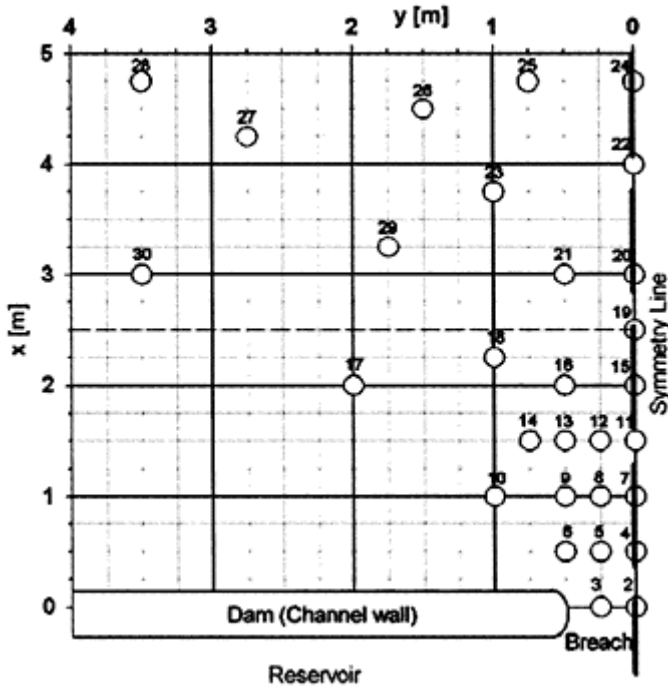


Figure 4. Positions of the pressure sensors (Kulisch 2002).

4 NUMERICAL EXAMPLE

For the ability of the proposed method to simulate the applications with the large time steps, see the last paper (Komaie and Bechteler 2002). Hereafter the capability of the method for the modeling of the dam-break problem is only shown.

A physical model of dam-break was built at the hydraulic laboratory of hydro-science Institute, German Armed Forces University Munich (UniBwM) (Bechteler et al. 1992; Kulisch 2002). The main purpose of the model was validation and verification of different numerical algorithms. The model was capable to simulate the two-dimensional propagation of a flood wave caused by sudden breach of a dam.

The model consisted of a channel (2 m width and 30m long), that represented a river and of a flat plate (5 m×10 m) with changeable inclination that simulated the area alongside the river. The plate was limited at three sides by open boundaries where the water could fall into a basin. The geometry of the model is shown in Figure 3.

The channel sidewall had a breach, which was initially closed by a flap. The sudden removal of the flap simulated a dam-break and the flood wave propagated over the plate.

The time history of the free surface flow was measured. This was achieved using 29 pressure sensors installed under the plate at positions shown in Figure 4. Simultaneously the flood wave propagation was video-taped by a camera installed above the plate. The

time data which was needed for the analysis afterwards was generated by a video-script. Using a video analyzing system, it is possible to obtain the coordinates of the wave front at different times. Using these coordinates together with the water depths measured at the same time, the shape of water surface can be reconstructed. The main parameters affected the shape of water surface are the initial water depth in the reservoir, plate roughness and the slope of the plate. These parameters were varied systematically and the results were measured.

We focused on the case with horizontal plate and initial water depth in the channel of 0.2 m. Based on that, a computational grid had been constructed. A part of the grid near by the dam-breach is shown in Figure 5. It is unstructured and contains 9379 nodes and 18028 triangular cells. The mesh size varies from 0.10m to 0.14m. The initial water depth in the reservoir is 20cm. After calibration, the Manning's coefficient was selected as $n=0.015$. The problem was run with the average Courant number of 0.8.

After remove of the gate, the water spreads over the plate symmetrically to the main flow direction (X-direction in Figure 3). Figure 6 shows the comparison between the computed flooded

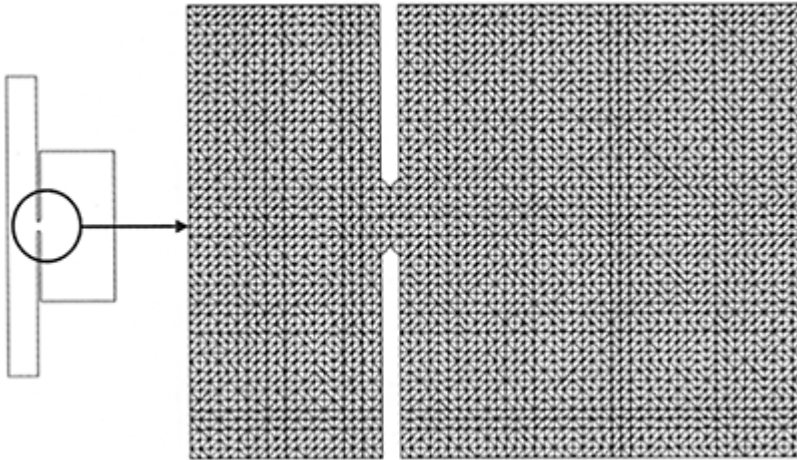


Figure 5. Computational grid near dam breach.

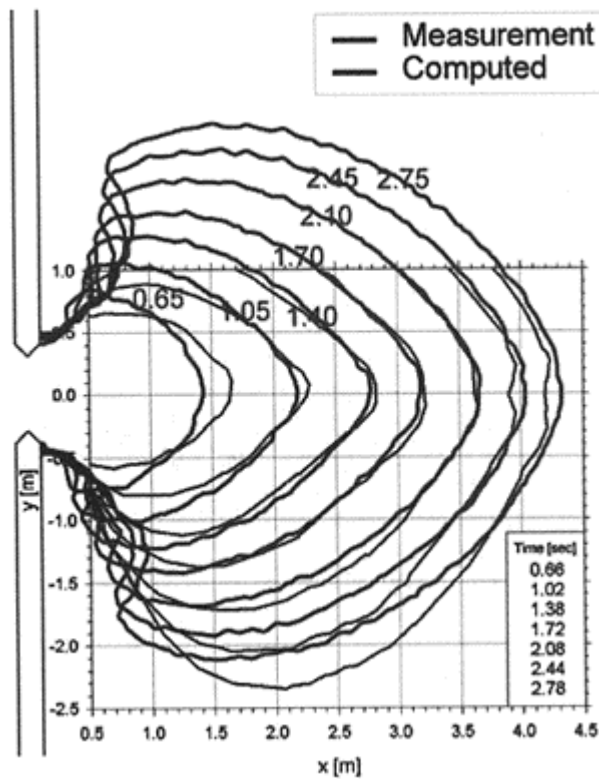


Figure 6. Flooded area at different times.

areas versus the measured ones at different times. In this Figure, the red numbers and blue contours are the results of computation while the black numbers and contours come from measurements (Kulisch 2002).

The wave front velocity reduces in the main flow direction while it approximately remains constant in the transverse direction (Y-direction). This phenomenon is shown in Figure 7.

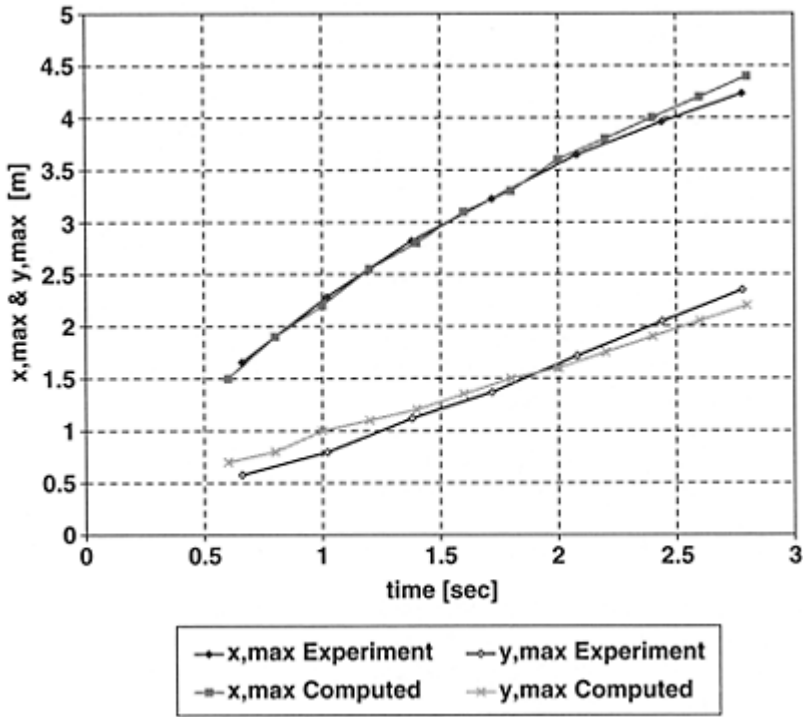


Figure 7. The positions of the flood wave front at different times in X- and Y-direction.

5 CONCLUSION

A new implicit numerical scheme has been introduced and applied for SWE. The method can be applied on unstructured grids with triangular cells. In addition, a new simple treatment of source terms is proposed. The results show a good agreement of the proposed method with the comparable sources. The new method gives a well-computed velocity distribution that could result quite reasonable bed shear stresses. For the high gradient applications, the new method needs more run-time than explicit methods. The main advantage of this method is for the quasi steady state conditions in which the much higher time steps could be used.

REFERENCES

- Anastasiou, K., and Chan, C.T. (1997). "Solution of the 2D shallow water equations using the finite volume method on unstructured triangular meshes." *International Journal for Numerical Methods in Fluids*, 24 (11), 1225–1245.
- Barth, T.J. "Recent developments in high order K-Exact reconstruction on unstructured meshes." *31st Aerospace Sciences Meeting & Exhibit*, Reno, NV
- Beam, R.M., and Warming, R.F. (1976). "An implicit finite difference algorithm for hyperbolic systems in conservation law form." *Journal of Computational Physics*, 22, 87–110.
- Bechteler, W., Kulisch, H., and Nujic, M. "2D dam-break flooding waves comparison between experimental and calculated results." *3rd International Conference on Floods and Flood Management*, Florence, Italy.
- Beffa, C., and Connell, R.J. (2001). "Two-Dimensional Flood Plain Flow. I: Model Description." *Journal of Hydrologic Engineering*, ASCE, 6 (5), 397–05.
- Bermudez, A., Dervieux, A., Desideri, J.-A., and Vazquez, M.E. (1998). "Upwind schemes for the two-dimensional shallow water equations with variable depth using unstructured meshes." *Computer methods in applied mechanics and engineering*, 155, 49–72.
- Brufau, R., Vazquez-Cendon, M.E., and Garcia-Navarro, P. (2002). "A numerical model for the flooding and drying of irregular domains." *Int. J. Numer. Meth. Fluids*, 39, 247–275.
- Coirier, W.J. (1994). "An adaptively-refined, cartesian, cell-based scheme for the Euler and Navier-Stocks equations," The University of Michigan.
- Delis, A. L, Skeels, C.P., and Ryrle, S.C. (2000). "Evaluation of some approximate Riemann solvers for transient open channel flows." *Journal of Hydraulic Research*, 38 (3), 369–382.
- Erduran, K.S., Kutija, V., and Hewett, C.J.M. (2002). "Performance of finite volume solutions to the shallow water equations with shock-capturing schemes." *Int. J. Numer. Meth. Fluids*, 40, 1237–1273.
- Fennema, R.J., and Chaudhry, M.H. (1989). "Implicit methods for two-dimensional unsteady free-surface flows." *Journal of Hydraulic Research*, 27 (3), 321–332.
- Jameson, A., and Turkel, E. (1981). "Implicit schemes and LU decompositions." *Mathematics of Computation*, 37(156), 385–397.
- Jha, A., Akiyama, J., and Ura, M. (1996). "A fully conservative Beam and Warming scheme for transient open channel flow." *Journal of Hydraulic Research*, 34 (5), 605.
- Klonidis, A.J., and Soulis, J. (2001). "An implicit scheme for steady two-dimensional free-surface flow calculation." *Journal of Hydraulic Research*, 39 (4), 393–402.
- Komaie, S. (2003). "A Robust Implicit Shallow Water Equations Solver on Unstructured Grids," German Armed Forces University Munich, Munich.
- Komaie, S., and Bechteler, W. "An implicit scheme for the two-dimensional shallow water equations using unstructured meshes." *RiverFlow 2002*, Universite catholique de Louvain, Belgium, 271–275.
- Kulisch, H. (2002). "Ausbreitung von Dammbruchwellen in physikalischen Modell (in German)," Universität der Bundeswehr München, Munich.
- MacCormack, R.W. (1982). "A numerical method for solving the equations of compressible viscous flow." *AIAA Journal*, 20 (9), 1275–1281.
- MacCormack, R.W., and Paullay, A.J. (1972). "Computational efficiency achieved by time splitting of finite difference operators." *Paper 72-154*, AIAA, San Diego.
- Molls, T., and Chaudhry, M.H. (1995). "Depth-averaged open-channel flow model." *ASCE, Journal of Hydraulic Engineering*, 121 (6), 453–465.
- Nujic, M. (1995). "Efficient implementation of non-oscillatory schemes for the computation of free surface flows." *Journal of Hydraulic Research*, 33 (1), 101–111.

- Panagiotopoulos, A.G., and Soulis, J.V. (2000). "Implicit biadiagonal scheme for depth-averaged free-surface flow equations." *ASCE, Journal of Hydraulic Engineering*, 126 (6), 425–436.
- Roe, P.L. (1981). "Approximate riemann solvers, parameter vectors, and difference schemes." *Journal of Computational Physics*, 43, 357–372.
- Sanders, B.F. (2001). "High-resolution and non-oscillatory solution of the St.Venant equations in non-rectangular and non-prismatic channels." *Journal of Hydraulic Research*, 39 (3), 321–330.
- Toro, E.F. (2001). *Shock-Capturing Methods for Free-Suface Shallow Flows*, Wiley and Sons Ltd.
- Tseng, M.H., and Chu, C.R. (2000). "Two-dimensional shallow water flows simulation using TVDMacCormack scheme." *Journal ofHydraulic Research*, 38 (2), 123–131.
- Valiani, A., Caleffi, V, and Zanni, A. "Finite Volume Scheme for 2D Shallow-Water Equations Application to The Malpasset Dam-Break." *CADAM*, Zaragoza.
- Warming, R.F., and Beam, R.M. "On the construction and application of implicit factored schemes for conservation laws." *Proc. Symposium on Computational Fluid Dynamics, SIAM-AMS, Vol 11*, New York, 85–129.
- Yoon, S., and Kwak, D. (1992). "Implicit Navier-Stokes solver for three-dimensional compressible flows." *AIAA Journal*, 30 (11), 2653–2659.
- Zhao, D.H., Shen, H.W., Lai, J.S., and TabiosIII, G.Q. (1996). "Approximate Riemann solvers in FVM for 2D hydraulic shock wave modeling." *Journal of Hydraulic Engineering, AISC*, 122 (12), 692–702.

A fully mesh-less Lagrangian numerical method for prediction of free water surface

Leila Farhadi & B.Ataie-Ashtiani

*Department of Civil Engineering, Sharif University of Technology,
Tehran, Iran*

Hydraulics of Dams and River Structures—Yazdandoost & Attari (eds)

© 2004 Taylor & Francis Group, London, ISBN 90 5809 632 7

ABSTRACT: Euler's equation is the governing equation of the irrotational flow of ideal fluids; this equation can be considered for the free surface water flow in open channels. The two dimensional Euler's equation is solved by a mesh-less method of *Smooth Partide Hydrodynamics* (SPH). A fractional step method has been applied which consist to split each time step in two steps. The numerical method is based on Moving Particle Semi-implicit method (MPS) for simulating incompressible inviscid flows with free surfaces. The motion of each particle is calculated through interactions with neighboring particles covered with the kernel function. The numerical model results are verified with the available experimental results for the collapse of a water column. Agreement with experimental results is excellent. Finally the effect of height of dam and the kernel size on the time the bore is formed is investigated and an estimate for the time of bore formation is presented. The present model is a very useful utility for solving problems in hydraulic and river engineering that an accurate prediction of free water surface is required.

1 INTRODUCTION

Free surface hydrodynamic flows are of significant industrial and environmental importance but are difficult to simulate because the surface boundary conditions are specified on an arbitrarily moving surface. The marker and cell (MAC) and volume of fluid (VOF) methods are two of the most flexible and robust approaches for treating such flows in which the Navier-Stokes equations are solved on a fixed Eulerian grid. The former uses marker particles to define the free surface while the latter solves a transport equation for the volume fraction of the fluid. They have been successfully applied to a

wide variety of flow problems involving free surfaces. Hirt *et al.* (1981) applied them to dam break problem and Lin *et al.* (1998) used these methods to simulate wave break in the surf zone. In spite of the recent advances in numerical modeling of free surface flows, still there are difficulties to analyze problems in which the shape of the interface changes continuously or fluid structure interactions where large deformations should be considered.

Recently particle methods have been used in which each particle is followed in a Lagrangian manner. Moving interfaces and boundaries can be analyzed by mesh-less methods much easier than with the Finite Element Methods because it is difficult to fit and move a grid continuously. Furthermore, in Lagrangian formulations the convection terms are calculated by the motion without any numerical diffusion. The first ideas in this way were proposed by Monaghan (1994) for the treatment of astrophysical hydrodynamic problems with the method called Smooth Particle Hydrodynamics (SPH) in which kernel approximations are used to interpolate the unknowns. This method was later generalized to fluid mechanic problems.

A modified particle method, called the moving particle semi implicit (MPS) method was proposed by Koshizuka *et al.* (1996). In the MPS method, fluid is represented by moving particles. Convection is calculated by the motion of these particles. Thus, numerical diffusion, which is a large problem in finite difference method, does not take place. The interfaces are always clear even if fragmentation or merging of the fluid occurs. Recently, a large number of researchers are paying attention to this method, for example Koshizuka *et al.* (1998) have applied this method for the numerical analysis of breaking waves and Heo *et al.* (2001) employed the MPS method for numerical simulation of growth of the bubble in the transient pool boiling.

In this paper the application of MPS method for free surface problems in hydrodynamics and hydraulics is re-visited. A numerical model based on MPS method is developed and the performance of two different kernel functions is compared. Collapse of water column experiment is used for numerical results verification and comparison. The developed model is used to study the effect of height of dam and the kernel size on the time the bore is formed and to estimate the time of bore formation.

2 MATHEMATICAL AND NUMERICAL FORMULATIONS

The governing equations of non-viscous fluid flow including mass conservation and momentum conservation are presented in Equations 1 and 2.

$$\frac{1}{\rho} \frac{D\rho}{Dt} = -\nabla \cdot \mathbf{u} \quad (1)$$

where ρ [KgL⁻³] is the density and \mathbf{u} =[LT⁻¹] is the velocity vector.

$$\frac{D\mathbf{u}}{Dt} = -\frac{1}{\rho} \nabla p + \mathbf{f} \quad (2)$$

where p [ML⁻¹T⁻²] is the pressure and \mathbf{f} [LT⁻²] is a source term.

In particle methods, the mass and momentum conservation equations are transformed to particle interaction equations. All interactions between particles are limited to a finite distance. The weight of interaction between two particles that are distance r apart can be described by a kernel function. In this paper two different type of kernel functions proposed by Koshizuka *et al.* (1996) are considered. These kernel functions are presented in Equations 3 and 4.

First type:

$$w(r) = \begin{cases} \frac{r_e}{r} - 1 & 0 \leq r < r_e \\ 0 & r_e \leq r \end{cases} \quad (3)$$

Second type:

$$w(r) = \begin{cases} -(2r/r_e)^2 + 2 & 0 \leq r < \frac{1}{2}r_e \\ (2r/r_e - 2)^2 & \frac{1}{2}r_e \leq r < r_e \\ 0 & r_e \leq r \end{cases} \quad (4)$$

where r is the distance between two particles i and j . Since the area that is covered with these kernel functions is bounded, a particle interacts with a finite number of neighboring particles. The radius of the interaction area is determined by parameter r_e . The particle number density can be computed as:

$$\langle n \rangle_i = \sum_{i \neq j} w(|r_j - r_i|) \quad (5)$$

In this equation, the contribution from particle i itself is not considered. When the number of particles in a unit volume is denoted by N_i , the relation between n_i and N_i is written as

$$\langle N \rangle_i = \frac{\langle n \rangle_i}{\int_v w(r) dv} \quad (6)$$

The denominator of Equation 6 is the integral of the kernel in the Whole region, excluding a central part occupied by particle i . Assuming that the particles have the same mass m , we can see that the fluid density is proportional to the particle number density:

$$\langle \rho \rangle_i = m \langle N \rangle_i = \frac{m \langle n \rangle_i}{\int_v w(r) dv} \quad (7)$$

Thus, the continuity equation is satisfied if the particle number density is constant. This constant value is denoted by n^0 .

If ϕ and u are arbitrary scalar and vector respectively, particle interaction models for differential operators are expressed as:

$$\langle \nabla \phi \rangle_i = \frac{d}{n^0} \sum_{i \neq j} \frac{\phi_j - \phi_i}{|r_j - r_i|^2} (r_j - r_i) w(|r_j - r_i|) \quad (8)$$

$$\langle \nabla^2 \phi \rangle_i = \frac{2d}{\lambda n^0} \sum_{i \neq j} [(\phi_j - \phi_i) w(|r_j - r_i|)] \quad (9)$$

where d is the number of space dimensions, n^0 is a particle number density fixed for incompressibility and λ is

$$\lambda = \frac{\int_V w(r) r^2 dv}{\int_V w(r) dv} \quad (10)$$

The gradient model is obtained as the average of gradient vectors which are determined between particle i and its neighboring particles j . The Laplacian model is derived from the physical concept of diffusion. Part of a quantity at particle i is distributed to neighboring particles j . Parameter λ is introduced to keep the same variance increase as that of the analytical solution.

The MPS method can be summarized in a simple algorithm, combined of 6 steps.

1. Initialize fluid: $\mathbf{u}^0, \mathbf{r}^0$

For each time step dt :

2. Compute forces and apply them to particles. Find temporary particle positions and velocities $\mathbf{u}^*, \mathbf{r}^*$.

$$\mathbf{u}^* = \mathbf{u}^n + \Delta t \mathbf{f} \quad (11)$$

$$\mathbf{r}^* = \mathbf{r}^n + \mathbf{u}^* \Delta t \quad (12)$$

3. Compute particle number density w^* using new particle locations

4. Solve Poisson equation of pressure after discretizing it into a system of linear equations.

5. Compute velocity correction \mathbf{u}' from the pressure equation

$$\mathbf{u}' = -\frac{dt}{\rho} \nabla p^{n+1} \quad (13)$$

6. Compute new particle positions and velocities

$$\mathbf{u}^{n+1} = \mathbf{u}^* + \mathbf{u}' \quad (14)$$

$$\mathbf{r}^{n+1} = \mathbf{r}^n + \mathbf{u}^{n+1} \Delta t \quad (15)$$

End for.

The boundary conditions used in this paper are similar to those used by Koshizuka *et al.* (1996) and Koshizuka *et al.* (1998) and Young Yoon *et al.* (1999). The particle density number decreases for particles on the free surface. A particle which satisfies a simple condition $n_i^* < \beta n^0$ is considered on the free surface. In this paper, we use $\beta=0.97$, which is investigated with test calculations. Pressure $p=0$ (or atmospheric pressure, if applicable) is applied to these particles on the free surface in the pressure calculation. Solid boundaries such as walls or other fixed objects are represented by fixed particles. Velocities are always zero at these particles. Three layers of particles are used to represent fixed objects to ensure that particle density number is computed accurately and the particles on the inner first line of walls are involved in the pressure calculations.

Parameters used in the current particle interaction models are investigated with test calculations of the collapse of a water column. The free surface parameter β which is used to judge whether the particle is on the free surface or not can have a value between 0.8–0.99. In this study $\beta=0.97$ was selected. For the first type of kernel, the size of weight function which is used for the particle number density and the gradient model is $r_{en}=2.1 l_0$. l_0 is the distance between two adjacent particles in the initial configuration. The size which is used for the Laplacian model is $r_{elap}=4.0 l_0$. For the second type of kernel function the calculation is successful when $1.4 l_0 \leq r_{en}=r_{elap} \leq 1.7 l_0$. When $r_{en}=r_{elap} \geq 1.8 l_0$, the trajectory deviates upward from the correct one, even though it might simulate the movement of water front acceptably. These values were selected from the viewpoint of accuracy (Koshizuka *et al.* 1996). Parameter λ is calculated by direct integration. For the first weight function represented by Equation 3 the value of λ is:

$$\lambda = \frac{1}{6} r_e^2$$

And for the second kernel function represented by Equation 4 the value of λ is:

$$\lambda = \frac{31}{140} r_e^2$$

Different methods are used to solve the linear equation derived from the discretization of the Laplacian equation. Two different methods used in this paper are the direct Gauss elimination method and the iterative method of Gauss-Seidel.

3 MODEL APPLICATION

3.1 Broken dam analysis

In this example, a rectangular column of water is confined between two vertical walls. The removable board, which supports the initial water column in the experiment, is pulled up and collapse starts from $t=0$. In the calculation, the height of the water column

is two times its width. The column is represented by 648 particles, which are located like a square grid. The distance between two neighboring particles l_0 is 8.0×10^{-3} m. The height of the left and right walls is the same as the height of the water liquid and the width of the bottom wall is four times the width of the liquid. The left, right and bottom walls are represented by 447 particles. Both kernel functions give a good estimate for the collapse of water column as shown in Figures 1, 2. In the second kernel function, the value of weight function is finite at $r=0$. This means that two particles can occupy the same position, satisfying the incompressibility condition of $2w(0) < \beta n^0$. These particles are regarded as the free surface and no repulsive force acts between them, therefore particles are clustered. This problem can be avoided such as in the first kernel type. In this kernel function, the value of the weight function increases to infinity when the distance approaches zero, this characteristic shows good stability in the incompressibility calculation and clustering of particles does not occur. Koshizuka

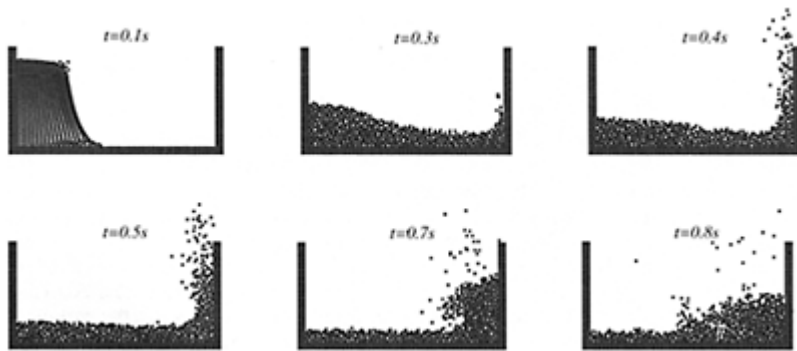


Figure 1. Simulation results of the collapse of water column using the first kernel function (Equation 3).

et al. (1996) used the method of incomplete cholesky conjugate gradient (ICCG) for solving the linear equation derived from discretizing the Laplacian equation of pressure and concluded that by using the first type of kernel function, numerical stability and computation speed are markedly improved.

In our investigation we have concluded that the method used for solving the linear equation of $AX=b$ highly affects the numerical stability and computation time of the MPS method, especially for modeling the fragmentation and coalescence of water after it impinges the right vertical wall. Two different methods of Gauss elimination and Gauss-Seidel linear equation solver are considered in this work. According to our studies if the second type of kernel function is used, by using the Gauss-Seidel method for solving the linear equation of $AX=b$, numerical instability occurs, but the numerical results are acceptable if Gauss elimination method is used. In the first type of weight function if we use Gauss elimination method for solving the linear equation of $AX=b$, the particles are dispersed and a large number of particles are regarded as the free surface. By using GaussSeidel method and inserting an artificial error in to the solution, this problem is

solved, as shown in Figure 3, and not only the shape of the free surface agrees well with experimental results, but also the computation speed and stability improves. The results of numerical simulation using the

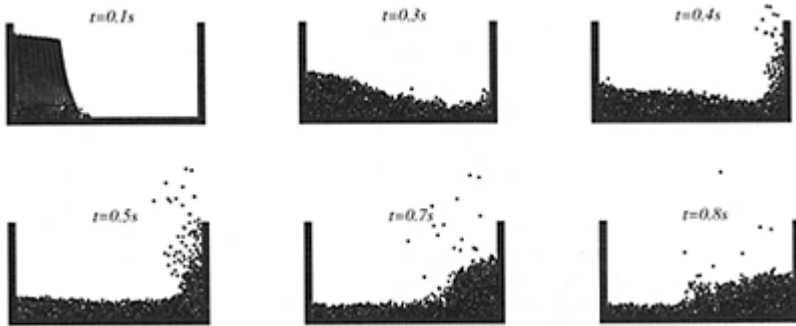


Figure 2. Simulation results of the collapse of water column using the second kernel function (Equation 4).

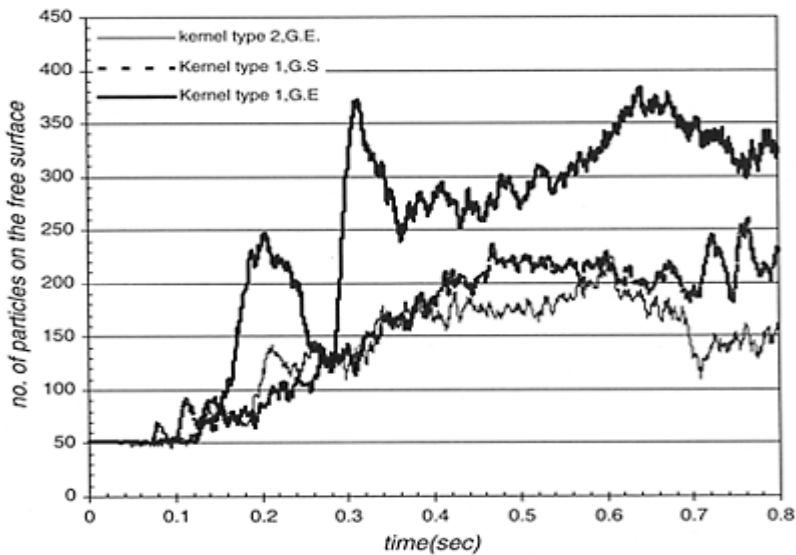


Figure 3. Effect of kernel type and linear equation solvers on number of particles on the free surface. (G.E. stands for the Gauss elimination and G.S. stands for Gauss-Seidel).

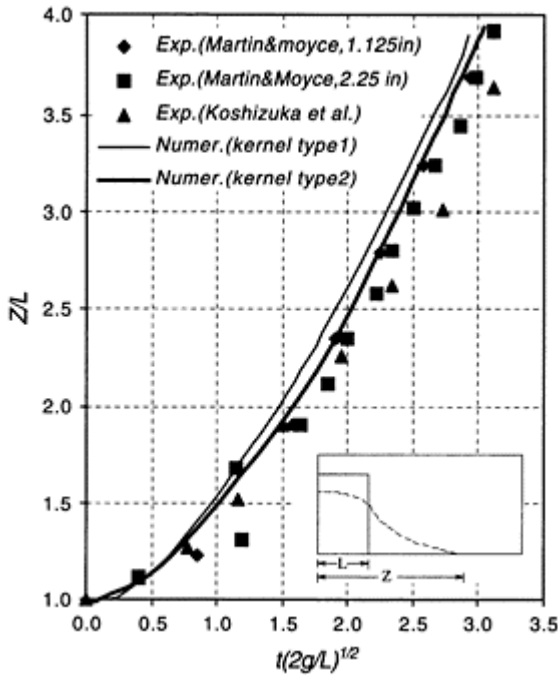


Figure 4. Comparing the motion of leading edge with experimental results

first type of kernel function (Equation 3) and Gauss-Seidel equation solver with acceptable error of (10^{-3} Pmax) are shown in Figure 1. Figure 2 shows the results of numerical simulation using Gauss elimination method the second type of kernel function (Equation 4) with effective kernel size of $1.5 l_0$. For both types of kernel functions the shape of the free surface agrees well with the experimental results of Koshizuka *et al.* (1996).

At 0.4 s, the water goes up losing its momentum, at 0.5 s it begins to come down. A breaking wave is clear at 0.7 s and the wave falls down in to the remaining water at 0.8 s.

For both types of kernel functions the shape of the free surface agrees well with the experimental results of Koshizuka *et al.* (1996). A comparison between the results gained from the MPS method and the previous experimental results is illustrated in Figure 4.

3.2 Estimating the time of bore formation

Instantaneous removal of the dam causes an abrupt adjustment of the pressure field, This adjustment of the pressure causes the resulting unsteady motion, eventually producing a propagating bore. Figures 1 and 2 clearly show that a jet is being formed at the lower right corner on the free surface around 0.1 s, which is similar to that observed experimentally by Stansby *et al.* (1998). Meanwhile the velocity changes rapidly and the pressure distribution inside the fluid deviates significantly from hydrostatic. At larger

times the initial large acceleration decreases and the velocity gradually becomes stable, until a bore develops downstream. During this period, the magnitude of the pressure also gradually increases until the pressure distribution is nearly hydrostatic. (Shao *et al.* 2003).

In order to estimate the time of bore formation, various numerical tests are performed by changing the width and height of the dam. The legend in the figure denotes the number of particles representing the width and height of the dam. From the numerical results and the figure it is seen that the formation of the bore is around time $t/(2H/g)^{1/2}$ equals 0.6 from which point the slope of the curves tends to be almost constant, which means that water is propagating downstream with a constant velocity. For consistency, the starting particle spacing is constant for all runs at 8.0×10^{-3} m. Thus, the total number of particles differ from run to run. In the computation, the dam width is constrained to be greater than half of the dam height in order to diminish the influence of the negative wave reflecting from the left wall, (Shao *et al.* 2003). The relation between the time normalized by $(2H/g)^{1/2}$ and leading edge from the dam site normalized by dam height H is shown in Figure 5a. As seen in Figure 5a, the bore formation develops later with increasing dam height and the time of bore formation after dam-break can be approximately evaluated by $(2H/g)^{1/2}$.

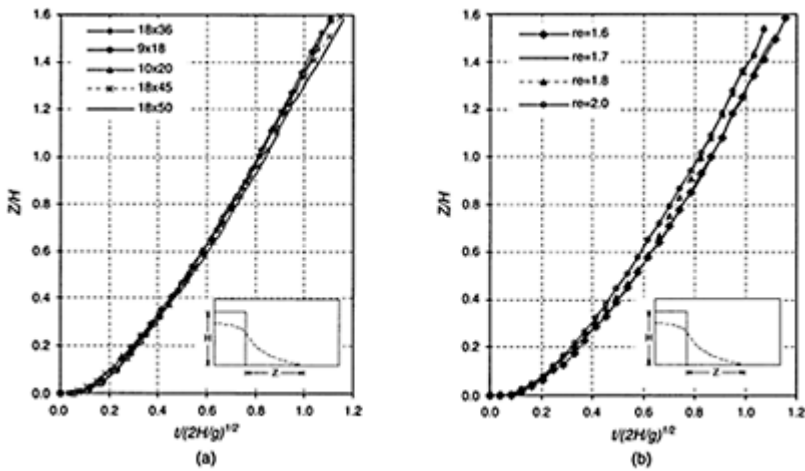


Figure 5. Relation between non-dimensional leading edge and time after dam break. (a) different width and height of water column, (b) different effective radius of kernel function.

The effect of effective radius on the time of bore formation is shown in Figure 5b. It is seen that the formation of bore for the second kernel type is also around $t/(2H/g)^{1/2}$ equals 0.6. Therefore in MPS method the time for the formation of bore is not sensitive to the kernel type and effective radius of the kernel function when the simulations are tested to give proper results for the motion of water after dam break.

4 CONCLUSION

The paper presents an incompressible MPS method to simulate incompressible inviscid flows with free surfaces. The method employs particles to discretize the Navier-Stokes equations and the interactions among particles simulate the flows. Two different kernel functions are presented. A dam break problem is considered and the computations are in good agreement with available experiment data for both types of kernel functions. The effect of the method of solving the linear equation of $AX=b$, derived from discretizing the Laplacian equation of pressure is studied on the numerical stability of the dam break problem. In the next step the formation of bore is considered. The effect of height of dam and different kernel size, on the time of bore formation is shown and an estimate for the time the bore is formed is proposed.

REFERENCES

- Dilts, G.A. 1999. Moving least squares particle hydrodynamics. i. Consistency and stability. *Int. J. Numer. Meth. Eng.* 44:1115–1155
- Hirt, C.W & Nichols, B.D. 1981. Volume of fluid (VOF) method for the dynamics of free surface boundaries. *J. Comput. Phys.* 39:201–225
- Idelsohn, S.R., Storti, M.A. & Onate, E. 2001. Lagrangian formulation to solve free surface incompressible inviscid fluid flows. *Comput. Methods. Appl. Mech. Engrg.* 191:583–593
- Koshizuka, S. & Oka, Y. 1996. Moving-Particle Semi-Implicit Method for Fragmentation of Incompressible Fluid. *Nuclear Science and Engineering* 123:421–34
- Koshizuka, S., Nobe, A. & Oka, Y. 1998. Numerical Analysis of Breaking waves using the moving particle Semi-Implicit Method. *Int. J. Numer. Meth. Fluids.* 26:751–769
- Lin, P.Z. & Liu Philip, L.F. 1998. A numerical study of breaking waves in the surf zone. *J. Fluid. Mech.* 26:751–769
- Monaghan, J.J. 1994. Simulating Free Surface Flows with SPH. *J. Comput. Physics.* 110:399–106
- Shao, S. & Lo, E.Y.M. 2003. Incompressible SPH method for simulating Newtonian and non-Newtonian flows with a free surface. *Advances in water resources.* 26:787–800
- Stansby, P.K., Chellini, A. & Barnes, T.C.D. 1998. Initial stages of dam-Break flow. *J. FluidMech.* 370:203–220
- Young Yoon, H., Koshizuka, S. & Oka, Y. 1999. A particle-gridless hybrid method for incompressible flows. *Int. J. Numer Meth. Fluids.* 30:407–124

Numerical study of flood routing in compound channels

S.A.Ayyoubzadeh

Dept. of Irrig. Hydra. Struc. Eng., TMU, Tehran, Iran

A.Zahiri

*PhD Student of TMU, Engineer of Khozestan Water and Power Authority,
Iran*

Hydraulics of Dams and River Structures—Yazdandoost & Attari (eds)

© 2004 Taylor & Francis Group, London, ISBN 90 5809 632 7

ABSTRACT: Recent advances in two-stage compound channel flow aspects improves our knowledge to take into account many complex features involved in this special type of river flow and hence to increase our ability to cope with more efficiently the flood flows. However, among these only a few studies under unsteady flow conditions are available. Due to the difference of the hydraulic and geometric characteristics between the main river channel and its floodplains, flood waves are differently routed in these two parts of the river cross section. Hence, a modified flood routing of the Saint-Venant equations is needed to deliberate this distinctive peculiarity. In this paper, a finite difference method to solve the modified Saint-Venant equations in some homogenous and heterogeneous typical compound channel cross sections are presented. Both explicit and implicit schemes are used in the numerical solution of the basic equations. No difference was observed between the results of these schemes.

1 INTRODUCTION

There are many investigations on flood routings in rivers and many mathematical models have been developed so far. In most of these studies, the well known 1D Saint-Venant equations have been used. The Saint-Venant equations give accurate results in most natural channel conditions. However, in some cases, such as flooding in alluvial rivers with compound sections, the flood flow exceeds the bankfull level and enters the floodplains. Due to the high difference of the hydraulic and geometric characteristics between the main river channel and its floodplains, inundation of floodplains involves

with much complexities. In previous numerical models only the river compound channel is divided to main channel and floodplain sections and donot take into account any interaction effects between these two sub-areas. Many researchers have investigated the flow hydraulics in compound open channels. However, most of these studies carried out under steady and uniform flow assumptions. Due to the great importance of flooding and its problems, it is essential to consider the unsteady flow condition in study of flow hydraulics of compound channels. There have been a few studies on unsteady flow simulation in compound channels, e.g. Garbrecht and Brunner 1991, Mizanur and Chaudhry 1995, Tang et al. 1999, Tuitouk and Hicks 2001, Abril and Knight 2003. In this paper, using the numerical solution of modified Saint-Venant equations (Horritt and Bates 2002) and by taking into account the flow interactions in hydraulics of compound channels (Shiono-Knight 1990), the full dynamic flood routing developed by authors is presented. Both explicit and implicit schemes are used in the numerical solution of the basic equations.

2 MODIFIED SAINT-VENANT EQUATIONS

For flood routing in natural rivers, the 1D Saint-Venant equations may be read as follows:

$$\frac{\partial Q}{\partial x} + \frac{\partial A}{\partial t} = 0 \quad (1)$$

$$\frac{\partial Q}{\partial t} + \frac{\partial}{\partial x} \left(\frac{Q^2}{A} \right) + gA \frac{\partial h}{\partial x} + gA(S_f - S_0) = 0 \quad (2)$$

where Q =flow discharge; A =flow area; g =acceleration due to gravity; h =depth of flow; S_0 =slope of channel bed in longitudinal direction; S_f =friction slope; x =longitudinal coordinate; and t =time coordinate. These equations give accurate results when flood is below the bankfull level. When flood exceeds the main channel capacity and propagates along the floodplain, these equations are inaccurate (French 1986). In such a situation, equation 2 is modified to account for the differences in flood wave properties of flow occurring simultaneously in the main channel and floodplain section (Fread 1982):

$$\frac{\partial Q}{\partial t} + \frac{\partial}{\partial x} \left(\beta \frac{Q^2}{A} \right) + gA \frac{\partial h}{\partial x} + gA(S_f - S_0) = 0 \quad (3)$$

where β =momentum correction factor.

$$\beta = \frac{\sum_{i=1}^N \left(\frac{K_i^2}{A_i} \right) \sum_{i=1}^N A_i}{\left(\sum_{i=1}^N K_i \right)^2} \quad (4)$$

where i refers to discrete sub-area (main channel and floodplains); N =number of sub-areas; and K =conveyance factor. The conveyance factor is calculated separately for main channel and floodplains as:

$$K = \frac{A^{5/3}}{nP^{2/3}} \quad (5)$$

where P =wetted perimeter; and n =Manning's roughness coefficient. Another form of the equation 3 is (Horritt and Bates 2002):

$$\frac{\partial Q}{\partial t} + \frac{\partial}{\partial x} \left(\frac{\phi^2 Q^2}{A_c} + \frac{(1-\phi)^2 Q^2}{A_f} \right) + gA \frac{\partial h}{\partial x} + gA_c S_c + gA_f S_f - gAS_0 = 0 \quad (6)$$

$$\phi = \frac{K_c}{K_c + K_f} \quad (7)$$

$$S_c = \frac{\phi^2 n_c^2 Q^2}{R_c^{4/3} A_c^2} \quad (8a)$$

$$S_f = \frac{(1-\phi)^2 n_f^2 Q^2}{R_f^{4/3} A_f^2} \quad (8b)$$

where R =hydraulic radius; and S =friction slope. The c and/subscripts refer to main channel and floodplain respectively. ϕ determines how flow is partitioned between the floodplain and main channel (Horritt and Bates, 2002). These equations are discretized using the finite difference method and are solved using both explicit (Graf 1998) and implicit schemes (French 1986).

3 FLOW HYDRAULICS IN COMPOUND CHANNELS

According to the high difference of flow depth and Manning's roughness coefficients in main channel and floodplains of compound channels and hence the large velocity difference between these subsections in certain natural conditions, a strong lateral momentum transfer induced across the interface. The traditional methods such as divided channel method (DCM) ignore this phenomenon. Many enhanced methods are presented to take into account this flow interaction (Shiono and knight 1990, Ackers 1993, Lambert and Sellin 1996, Lambert and Myers 1998, Bousmar and Zech 1999, Ervine et al. 2000, Haydera and Valentine, 2002). The 2D Shiono-Knight model (SKM) is used in this paper due to its good results in many applications (Knight et al. 1989, Abril 2002). The 2D Shiono-Knight model (1990) uses the depth-averaged turbulent Navier-Stocks equations to predict the lateral distribution of velocity and bed shear stress as:

$$\rho g H S_0 - \rho \frac{f}{8} u_d^2 \sqrt{1 + \frac{1}{s^2}} + \frac{\partial}{\partial y} \left\{ \rho \lambda H^2 \left(\frac{f}{8} \right)^{1/2} u_d \frac{\partial u_d}{\partial y} \right\} = \frac{\partial H(\rho \bar{U} \bar{V})_d}{\partial y} \quad (9)$$

where ρ =fluid density; u_d =depth-averaged velocity; H =local water depth; s =channel side slope of the banks (1: s , vertical:horizontal); f =Darcy-Weisbach friction factor, λ =dimensionless eddy viscosity; $\{UV\}$ =velocity components in the $\{xy\}$ directions, x =streamwise parallel to the bed; and y =lateral coordinate. The right hand side of the equation 9 is the secondary flow term. Calibration of Shiono-Knight model with experimental data and numerical simulations shows that the secondary flow term in the main channel and floodplains may be estimated from equation (10):

$$\frac{\partial H(\rho \bar{U} \bar{V})_d}{\partial y} = \beta_s \rho g S_0 H \quad (10)$$

where β_s =the calibration coefficient. β_s is constant in the main channel and floodplains. The value of this coefficient is 0.05 in main channel for inbank flow. In the overbank flow, these values are 0.15 and -0.25 for main channel and floodplains respectively (Shiono and Knight 1990, Knight and Abril 1996, Abril 2002). The analytical solution of equation 9 is presented by Shiono and Knight (1998, 1990). However, for simplicity, the numerical solution of this equation is used in this paper (Ayyoubzadeh and Zahiri 2003). Equation (9) is a non-linear differential equation, hence using the transform of

$$u \frac{\partial u}{\partial y} = \frac{1}{2} \frac{\partial u^2}{\partial y} \quad (11)$$

and assumption of $X = u_d^2$ a linear differential equation is obtained:

$$\rho g H S_0 - \rho \frac{f}{8} X \sqrt{1 + \frac{1}{s^2}} + \frac{1}{2} \frac{\partial}{\partial y} \left\{ \rho \lambda H^2 \left(\frac{f}{8} \right)^{1/2} \frac{\partial X}{\partial y} \right\} = \beta_s \rho g H S_0 \quad (12)$$

4 CASES OF SIMPLE AND COMPOUND CROSS SECTIONS

In this paper, some cases of simple and compound cross sections with different hydraulic and geometric characteristics are used. These geometries are shown in Figure 1. For study of effect of floodplain/main channel ratio of roughness coefficients, both the homogenous and heterogeneous compound channels are considered. For computation of friction factor and dimensionless eddy viscosity in the floodplains for each water depth, Abril's relationships are used (Abril 2002):

$$f_f = f_c R_f \text{ and } \lambda_f = \lambda_c R_\lambda \quad (13)$$

$$R_f = R_n^2 (0.669 + 0.331 Dr^{-0.719}) \quad (14)$$

$$R_\lambda = -0.20 + 1.2 Dr^{-1.44} \quad (15)$$

where R refers to the ratio of floodplain to the main channel value (friction factor, dimensionless eddy viscosity and Manning's roughness coefficient) and Dr = relative depth (ratio of depth of flow

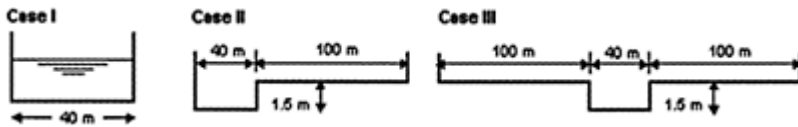


Figure 1. Sketch of the simple and compound channel geometries.

in floodplain to the main channel). The main channel friction factor for inbank flow is calculated based on the Manning coefficient. For overbank flow, this parameter is constant with stage and equal to bankfull flow value. The main channel dimensionless eddy viscosity may be considered to be constant with stage, equal to 0.07 (Abril 2002). The floodplain value of dimensionless eddy viscosity is the same in homogenous and heterogeneous compound channels (Knight et al., 1989).

For flood routing computations, a reach length of 10 km with longitudinal bed slope of 0.001 is considered. In all cases, the Manning roughness coefficient of main channel is considered 0.03. For homogenous and heterogeneous compound channels, the Manning roughness coefficient of floodplain are assumed to be 0.03 and 0.06, respectively. The flood is generated using a triangular hydrograph imposed at the upstream end of the reach. During the flood, the discharge in the channel increases linearly to peak of 200 m³/s in a time period of 2/3 hour and decrease linearly back to its initial value during a time period of 1 1/3 hour. The initial flow assumed to be uniform flow with a depth of 1.2 m over the entire reach. The lateral distribution of depth mean velocity simulated by the SKM for water depth of 2 m is illustrated in Figure 2 for all cases of geometries for both homogenous and heterogeneous conditions. From Figure 2, it can be seen that the heterogeneous conditions represent very lower velocity in the floodplain comparing to the homogenous conditions. Lateral integration of velocity distribution for each water level gives the rating curve shown in Figure 3

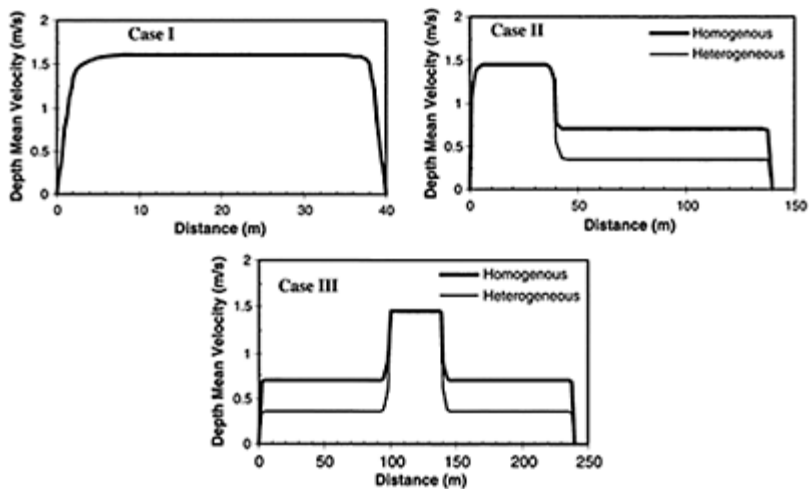


Figure 2. Lateral distribution of depth mean velocity in homogenous and heterogeneous conditions for water depth of 2.0m.

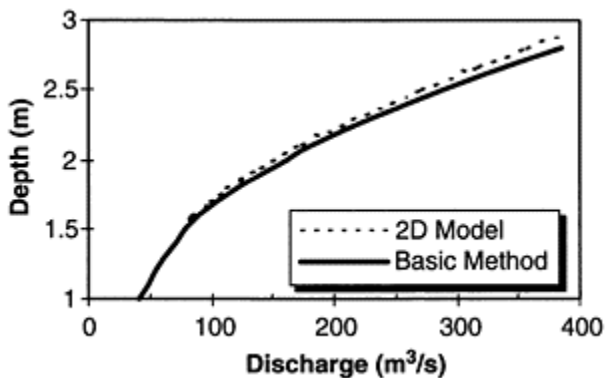


Figure 3. Rating curves of case III obtained by DCM (Basic method) and SKM (2D Shiono-Knight model).

only for heterogeneous condition of case III. This figure is also illustrated for comparison the rating curve calculated using the DCM. No significant difference is observed at the either methods.

5 HYDRAULIC FLOOD ROUTING RESULTS

In numerical solution of equations (1) and (6), the conveyance factors for main channel and floodplains are calculated using the DCM. To take into account the interaction effects of flow between subsections, these conveyance factors should be improved by the SKM:

$$K_c^* = \frac{Q_c^*}{Q_c} K_c \quad (16)$$

$$K_f^* = \frac{Q_f^*}{Q_f} K_f \quad (17)$$

where Q and Q^* refer to flow discharges obtained by the DCM and SKM, respectively.

5.1 Results of explicit scheme

In this scheme, a fixed time step of 0.15sec and space discretization of 100 elements are adopted. These values are nearly the same values used by Graf (1998). The results of routed depth and discharge hydrographs for homogenous condition of all cases obtained by this scheme are illustrated in Figure 4. At the upstream end of the reach, only the depth hydrograph of the case I is shown. It is interesting to observe the high deformation of the outflow hydrographs in compound channel cases for bankfull level 1.5 m and bankfull discharge $54.8 \text{ m}^3/\text{s}$. This behaviour is associated with overbank flood routing. From this Figure it can be seen that the attenuation of the peak depth and discharge in the case I are 10 and 29 percents, respectively. This attenuation is so obvious for the compound channels. The attenuation of the peak depth are 12 and 14 percents and for peak discharge are 35 and 40 percents for cases II and III, respectively. Also the time to peak discharge of the cases of II and III are so increased. The increase of time to peak discharge are 2.25 and 3.14 hours for cases II and III, respectively.

Results for heterogeneous condition are illustrated in Figure 5. The shapes of the outflow hydrographs are very different relative to the homogenous ones. In this case, the attenuation of peak discharge in compound channels are 40 and 48.5 percents for cases II and III respectively. The increase of time to peak is 2.7 and 3.9 hours, respectively.

The rating curves obtained by the hydraulic flood routing at the middle of the reach are illustrated in Figure 6 only for case I and III. The unsteadiness of the flow conditions are obvious. Great difference observed between the rating curves of the cases I and III.

5.2 Results of implicit scheme

Similar to the explicit scheme, in the implicit scheme the conveyance factors in the main channel and on the floodplains are corrected using the SKM. The results of flood routing using this scheme

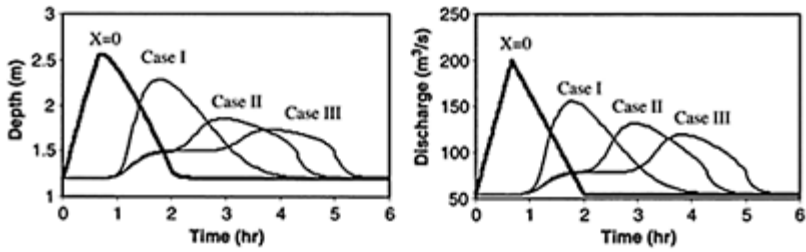


Figure 4. The routed depth and discharge hydrographs for the homogenous condition and by the explicit method.

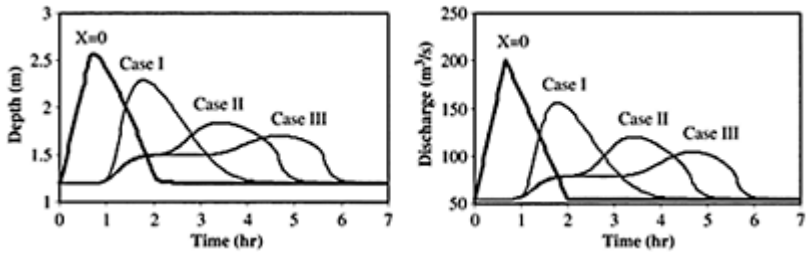


Figure 5. The routed depth and discharge hydrographs for the heterogeneous condition and by the explicit method.

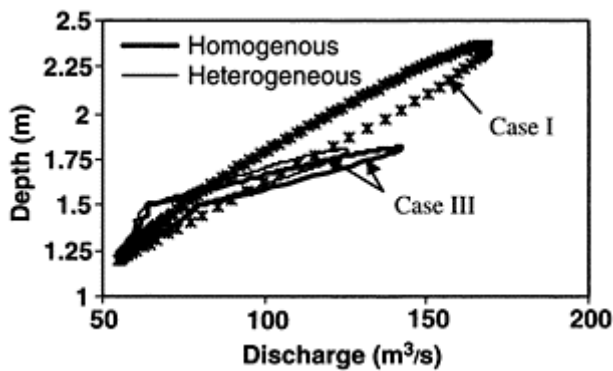


Figure 6. The rating curves of cases I and III in the middle of the reach by the explicit method.

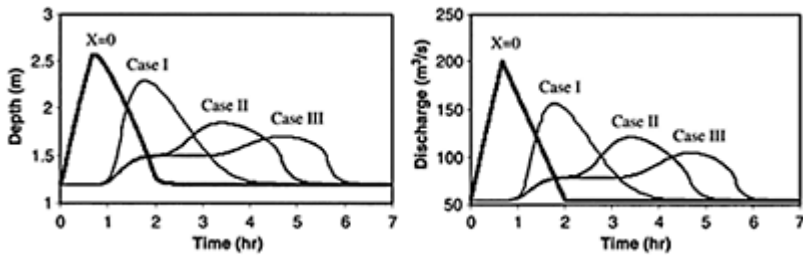


Figure 7. The routed depth and discharge hydrographs for the heterogeneous condition and by the implicit method.

are illustrated in Figure 7 only for heterogeneous condition. These results are exactly matched with explicit scheme ones. In this scheme, the time step of 30 sec and disCrete length of 500 m are adapted. These values are very larger than the explicit scheme ones.

6 CONCLUSION

The hydraulics of compound channels under steady and uniform flow assumption has received much attention in recent research literature. In this paper, using Shiono-Knight model (1991), a model for unsteady flow simulation in these types of channels is presented. For flood routing in compound channels, the modified Saint-Venant equations with correction of conveyance factors of main channel and floodplains are used. In fact, the flow discharge distribution between main channel and floodplains are corrected using the SKM. Both explicit and implicit schemes are used to solve numerically the fiill dynamic flood routing. The results of flood routing shows high deformation of outflow depth and discharge hydrographs especially in the heterogeneous roughness condition under certain conditions. Furthermore, the attenuation of peak discharge along the reach of 10 km assumed length is obtained about 50 percent that is so considerable. Also, the time to peak is increased from 2/3 hours to the 42/3 hours in the case III of the numerical example.

ACKNOWLEDGMENTS

The authors would like to thank the research administrations of the Tarbiat Modares University and also the Engineering Research Committee of Khozestan Water and Power Authority for their supports.

REFERENCES

- Abril, J.B. 2002. Overbank flood routing analysis applying jointly variable parameter diffusion and depth-averaged flow finite element models, Proceedings of the International Conference on Fluvial Hydraulics, Belgium, 4–6 September: 161–167.
- Ackers, P. 1993. Stage-Discharge functions for two-stage channels. *Water and Environmental Management*, Vol. 7:52–61.
- Ayyoubzadeh, S.A. & Zahiri, A. 2003. Numerical solution of depth-averaged lateral distribution of velocity and bed shear stress in simple and compound channels. 6th River Engineering International conference, Ahvaz, Iran, 285–293 (in Persian).
- Bousmar, D. & Zech, Y. 1999. Momentum transfer for practical flow computation in compound channels. *Journal of Hydraulic Engineering*, ASCE, Vol. 125(7), 696–700.
- Ervine, D.A., Babaeyan-Koopaei, K. & Sellin, R.H. J. 2000. Two-Dimensional Solution for Straight and Meandering Overbank Flows. *Journal of Hydraulic Engineering*, ASCE, Vol. 126, No. 9, PP. 653–669.
- French, R.H. 1986. *Open-Channel Hydraulics*, McGraw-Hill Book Company.
- Garbrecht, J. & Brunner, G. 1991. Hydrologic channel-flow routing for compound sections. *Journal of Hydraulic Engineering*, ASCE, Vol. 117, No. 5:629–642.
- Graf, W.H. 1998. *Fluvial Hydraulics*, John Wiley & Sons Ltd, Chichester, UK.
- Haidera, M.A. & Valentine, E.M. 2002. A practical method for predicting the total discharge in mobile and rigid boundary compound channels. Proceedings of the International Conference on Fluvial Hydraulics, Belgium, 4–6 September: 153–160.
- Horritt, M.S. & Bates, P.D. 2002. Evaluation of 1D and 2D numerical models for predicting river flood inundation. *Journal of Hydrology*, Vol. 268, 87–99.
- Knight, D.W. & Abril, J.B. 1996. Refined calibration of a depth-averaged model for turbulent flow in a compound channel, *Proc. Instn Civ. Engrs Water, Maritime & Energy*, Paper 11017, Sep., Vol. 118:151–159.
- Knight, D.W., Shiono, K. & Pirt, J. 1989. Prediction of depth mean velocity and discharge in natural rivers with overbank flow. *International Conference Hydraulic and Environmental Modelling of Coastal, Estuarine and River Waters*. Bradford, England.
- Lambert, M.F. & Myers, R.C. 1998. Estimating the discharge capacity in straight compound channels. *Engrs., Wat, Marit. and Energy*, 130:84–94.
- Lambert, M.F. & Sellin, R.H.J. 1996. Discharge Prediction in Straight Compound Channels Using The Mixing Length Concept. *J. of Hydraulic Research*, Vol. 34:381–394.
- Mizanur, R. & Chaudhry, M.H. 1995. Flood routing in channels with flood plains. *Journal of Hydrology*, Vol. 171:75–91.
- Shiono, K. & Knight, D.W. 1990. Mathematical models of flow in two or multi stage straight channels. *International Conference on River Flood Hydraulics*. 17–20 September: 229–238.
- Shiono, K. & Knight, D.W. 1988. Two dimensional analytical solution for a compound channel. 3rd International Symposium on Refined Flow Modeling and Turbulence Measurements, 26–28 July: 1–8.
- Tang, X., Knight, D.W. & Samuels P. 1999. Variable parameter Muskingum-Cunge method for flood routing in a compound channel. *Journal of Hydraulic Research*, IAHR, Vol. 37(5), 591–614.
- Tuutoek, D.K. & Hicks, F.E. 2001. Modelling of unsteady flow in compound channels. *African Journal of Civil Engineering*, JKUAT, Vol. 6.

A finite volume method for solving SWE in rivers of complex topographies

D.Farshi & H.-E.Minor

*The Laboratory of Hydraulics, Hydrology and Glaciology (VAW), Swiss
Federal Institute of Technology Zurich (ETH)*

Hydraulics of Dams and River Structures—Yazdandoost & Attari (eds)

© 2004 Taylor & Francis Group, London, ISBN 90 5809 632 7

ABSTRACT: A numerical model based on cell-centred finite-volume method is developed for unsteady, two-dimensional, shallow water flow on triangular meshes for calculating the depth and velocities in a natural river. The model uses special form of Riemann solver as a building block to compute fluxes, and an explicit predictor-corrector time stepping is used to provide a second-order accurate solution in time. Special approach in Riemann solver is used to take into account the presence of variable bottom topography and hydraulic structures such as a weir. The approach has been successfully verified for different examples.

1 INTRODUCTION

Shallow water equations (SWE), which explain two-dimensional shallow water flow, play an important role in hydraulic engineering. Many problems, such as the prediction flood due to dam breaks, currents and water elevation in coastal estuaries, bays and rivers can be modeled by the SWE. The solution of these equations also provides the necessary data for the determination of sediment and pollutant transport for use in water quality models. In order to apply the solution of SWE for Natural River, it is necessary for a model to be able to handle the internal conditions such as weirs and culverts in a convenient form.

For many years finite difference methods have been extensively used to solve problems governed by the SWE (Fennema & Chaudhry 1990). In the last decade the finite-volume and finite-element methods appear as new and powerful alternatives in the context of fluid dynamics and in particular of SWE. (Bechteler *et al.* 1993, Ribeiro *et al.* 2001, Bradford & Sanders 2002).

Finite-volume schemes solve the integral form of SWE in computational cells. Therefore, mass and momentum are conserved in each cell, even in the presence of flow discontinuities. The cell shapes can be triangular, quadrilateral etc. and generate a structured or an unstructured grid. *The unstructured grid, which is used in the present*

study, enables one to accurately handle the geometries that are complex in planform. This is clearly an important advantage of the method and also in contrast to the Finite Element, the solution on the cell is not strongly linked to the geometric representation of the computational cell. Therefore, the Finite-Volume Method (FVM) has been utilized in this work to solve the SWE.

2 GOVERNING EQUATIONS

2.1 Shallow water equations (SWE)

By assuming a hydrostatic pressure distribution and neglecting wind shear and Coriolis acceleration, the following form of SWE can be derived by integrating the three-dimensional Navier-Stokes equations over the flow depth (Rodi 1982):

$$\mathbf{U}_t + \nabla \cdot \mathbf{Q} + \mathbf{S} = 0 \quad (1)$$

Where \mathbf{U} , \mathbf{Q} and \mathbf{S} are the vectors of the primitive variables, fluxes in the x and y directions and source term respectively, given as:

$$\mathbf{U} = \begin{pmatrix} \zeta \\ uh \\ vh \end{pmatrix} \quad (2)$$

$$\mathbf{Q} = (F, G); \quad F = \begin{pmatrix} uh \\ u^2h + \frac{1}{2}gh^2 - vh\frac{\partial u}{\partial x} \\ uvh - vh\frac{\partial v}{\partial x} \end{pmatrix}; \quad G = \begin{pmatrix} vh \\ uvh - vh\frac{\partial u}{\partial y} \\ v^2h + \frac{1}{2}gh^2 - uh\frac{\partial v}{\partial y} \end{pmatrix}$$

$$\mathbf{S} = \begin{pmatrix} 0 \\ gh(S_{fx} - S_{Bx}) \\ gh(S_{fy} - S_{By}) \end{pmatrix}$$

Here h represents the water depth, ζ the water elevation, u the velocity component in x direction, v the velocity component in y direction and g the acceleration due to gravity.

Bottom slopes in x and y directions are defined as

$$S_{Bx} = -\frac{\partial z}{\partial x}; \quad S_{By} = -\frac{\partial z}{\partial y} \quad (3)$$

where z represents the bottom height.

Friction slopes are taken care of by Manning's formula as:

$$S_{fx} = \frac{n^2 u \sqrt{u^2 + v^2}}{h^{4/3}}; \quad S_{fy} = \frac{n^2 v \sqrt{u^2 + v^2}}{h^{4/3}} \quad (4)$$

in which n =Manning's roughness coefficient.

The viscosity factor ν is defined as

$$v=0.60 V^*h \quad (5)$$

where the V^* is the total shear velocity.

2.2 Initial and boundary conditions

Due to the mathematical reasons, it is necessary to define both, initial and boundary conditions (BC). In this context, the stability of utilized boundary conditions is the important question, which is not easy to answer. Defining too much or few and wrong BC could cause a ill-conditioned problem. There are two types of BC.

2.2.1 Closed boundary

The flux through the closed boundaries is equal to zero. In addition to this, the non-slip condition is used in this work.

2.2.2 Open boundary

The number of open boundaries of a partial differential equation system depends on the type of system. From the mathematical point of view, the SWE establish a quasi-linear hyperbolic differential equation system. If the temporal derivatives vanish, the system is elliptical for $F_r < 1.0$ and hyperbolic for $F_r > 1.0$, where F_r is the Froude number. On the open boundary the two types of inflow and outflow boundaries can be respectively distinguished.

Based on the behaviour of the system of equations, the theoretical number of open boundary conditions is listed in Table 1 (Agoshkov *et al.* 1993, Beffa 1994).

However, in practical applications of boundary conditions, the number of the implemented conditions is often more or less than the theoretical criteria (Nujić 1998).

Table 1. The correct number of boundary conditions in SWE.

Flow Types	Inflow	Outflow
Subcritical ($F_r < 1$)	2	1
Supercritical ($F_r > 1$)	3	0

2.3 Internal condition (hydraulic structures)

There are often different hydraulic structures within the computational area. Some of these structures, e.g. large bridge openings, can be two dimensionally modeled. As long as the water level height does not reach the lower edge of the bridge, in principle computational results do not change and it can be simulated directly. Otherwise the water flow fills the bridge opening and therefore the water depth does not change more in the bridge region. In this case the flow under the bridge takes place as pressure flow.

Most other structures require a special treatment in the model, particularly for two important reasons. On the one hand, the dimensions of the hydraulic structures are clearly smaller than the computational area. Even if it were meaningful, an exact two-dimensional modeling of these structures would require a relatively fine computation mesh with very small node distances. This would be then connected under given circumstances with relatively high computing times.

On the other hand, in these regions, important assumptions of the SWE are violated. Therefore, important modeling errors can occur. For these reasons in such regions, it is appropriate to use empirical relations instead of directly solving SWE. There are the following two special importance structural types.

2.3.1 Overflow structures (Weir)

The computation of overflow structures such as weirs, ramps etc can be done through the following formula:

$$q = C \cdot h^{2/3} \quad (6)$$

where C is the discharge factor and h denotes the water depth upstream of the weir crest.

2.3.2 Culverts

The discharge through the culverts can be calculated by following formula:

$$q = c \cdot \sqrt{2g\Delta h} \quad (7)$$

where c is the discharge factor and Δh denotes the difference between the water level height of upstream and downstream of the defined cross section.

It is in general difficult to cover different hydraulic structures and their entire discharge regime correctly with the help of empirical relations. It is therefore particularly advisable to accomplish flow control with possibly more exact parameter adjustments.

3 NUMERICAL MODEL

3.1 Finite-volume method (FVM)

The numerical representation of the physical domain is obtained by using an unstructured mesh, composed of triangular elements. Each of them must be considered as an elementary control volume (cell). The outward normal unit vector to each face is called \mathbf{n}_s (Fig. 1).

Equation (1) can be integrated over an arbitrary cell Ω of unit height as

$$\int_{\Omega} U_t d\Omega + \int_{\Omega} \nabla \cdot \mathbf{Q} d\Omega + \int_{\Omega} \mathbf{S} d\Omega = 0 \quad (8)$$

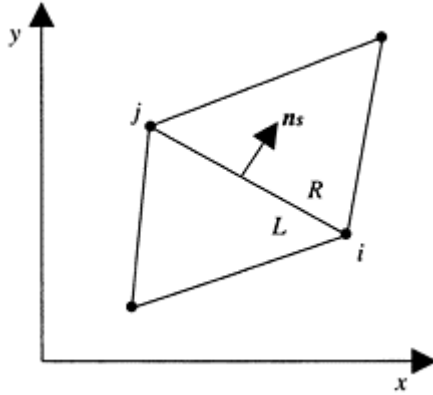


Figure 1. Cell-centred finite-volume element.

Applying the Gauss theorem to the second integral of Equation (8), assuming U_i and S_f are constant over the domain for first order accuracy, one obtains

$$U_i + \frac{1}{\Omega} \int_{\partial\Omega} \mathbf{Q} \cdot \mathbf{n}_s dl + S_f + \int_{\Omega} S_B d\Omega = 0 \quad (9)$$

The Equation (9) can be discretized by a two-phase solution, namely the corrector-corrector scheme as follows:

$$U_i^p = U_i^n - \frac{\Delta t}{\Omega} \sum_{j=1}^3 \mathbf{Q}_{i,j}^n \cdot \mathbf{n}_{sj} dl_j - \Delta t S_f^n - \Delta t \bar{S}_{Bi}^n \quad (10)$$

$$U_i^c = U_i^p - \frac{\Delta t}{\Omega} \sum_{j=1}^3 \mathbf{Q}_{i,j}^p \cdot \mathbf{n}_{sj} dl_j - \Delta t S_f^p - \Delta t \bar{S}_{Bi}^p$$

$$U_i^{n+1} = 0.5 (U_i^n + U_i^c)$$

where $\mathbf{Q}_{ij} = (\mathbf{F}_{i,j}, \mathbf{G}_{i,j})$ = numerical flux through each edge; \mathbf{n}_{sj} = unit vector of each edge and \bar{S}_B the modified form of the bed slope term.

In the FVM, the key problem is to estimate the normal flux through each face of computational cell namely $(\mathbf{Q} \cdot \mathbf{n}_s)$. The set of SWE being hyperbolic and, therefore, it has an inherent directional property of propagation. Algorithms to estimate the flux should appropriately handle this property. The *Riemann solver*, which is based on characteristic theory, is one such algorithm (Zhao *et al.* 1996).

3.2 Flux estimating based on Riemann solver

Based on the *rotational invariance* property for $F(U)$ and $G(U)$ on the boundary of each cell, the two dimensional problem in Equation (1) can be handled as a series of local Riemann problems in the normal direction (n_s) to the cell face (Toro 2001). The Riemann solvers can be categorized into two types: exact and approximate. It is computationally expensive to solve the Riemann problem exactly at the interface; therefore, an approximate Riemann solver which retains the relevant features of the exact solution is desirable.

3.2.1 Roe's approximate Riemann solver

Roe's approximate Riemann solver was first constructed for the Euler equations. Glaister (1988) appears to be the first to have applied the Roe approach to the SWE in one dimensional form. We use also this solver for the flux calculation over edges:

$$Q^* = \frac{1}{2} [Q_R + Q_L - |\tilde{J}^*| (U_R - U_L)] \quad (11)$$

where $|\tilde{J}^*| = \tilde{R}|\tilde{A}|\tilde{R}^{-1}$; \tilde{R} is the eigenvectors matrix \tilde{J}^* , denoted by $\tilde{e}^1, \dots, \tilde{e}^m$ with corresponding eigenvalues $\tilde{a}^1, \dots, \tilde{a}^m$, $|\tilde{A}| = \text{diag}(|\tilde{a}^1|, \dots, |\tilde{a}^m|)$, subscripts R and L refer to the right and left side of the cell interface respectively (Fig. 1). The following averaged values are used to determine the over bar parameter (\tilde{J}^*) (Zhao et al 1996):

$$\begin{aligned} \tilde{h} &= \frac{h_L + h_R}{2} \\ \tilde{u} &= \frac{u_L \sqrt{h_L} + u_R \sqrt{h_R}}{\sqrt{h_L} + \sqrt{h_R}} \\ \tilde{v} &= \frac{v_L \sqrt{h_L} + v_R \sqrt{h_R}}{\sqrt{h_L} + \sqrt{h_R}} \end{aligned} \quad (12)$$

3.2.2 Bottom slope source term

The numerical treatment of the bottom slope source term SB is not trivial and needs to pay special attention to its discretization. The numerical problems, which rise from source term is known and has been already discussed by different researcher (Nujic 1995, Bemudez *et al.* 1995, Hubbard & Garcia-Navarro 2000). We used a new solution for this problem, which is developed by Komaie (2003) the first author. It has been observed that the new approach is stable and robust. It is independent of the type of Riemann solver. In the new approach the depth (h) on each edge in bed slope term $SB \rightarrow \bar{S}_B$ is considered variable along the edge and the integral will be directly calculated. In addition to it the depth in pressure term of the flux has been substituted by following relation:

$$h_p = \frac{h_i^2 + h_j^2 + h_i h_j}{3} \quad (13)$$

where h_i and h_j are the depths in nodes i and j respectively (Fig. 1) and h_p is the depth in pressure term of flux ($1/2gh^2$)

4 APPLICATION AND VALIDATION

For the verification of the numerical model, comparisons are made between the computational predictions of the numerical model against measured data from laboratory models.

4.1 Meander main channel with flood plains

Experiments using a physical model were conducted at the Aachen University of Technology (RWTH) in Germany to understand the fundamental flow behaviour in meandering channels and rivers with overflow onto floodplains (Stein, 1990). The experimental program enclosed two basis variants whose essential difference was the existence or non-existence of vegetation on floodplains. In the present work, it is the experiment with smooth conditions on the floodplains that have been chosen for the purpose of simulation.

The qualitative process of mass and momentum exchange between the main channel and floodplains as well as the initiated secondary roller system by centrifugal forces is a fully three-dimensional flow process, which is not possible to completely simulate by a 2D model. However, the quality of measured data makes it possible to determine how far the numerical model is able to compute the considered phenomena and to describe the influence on the averaged flow parameters.

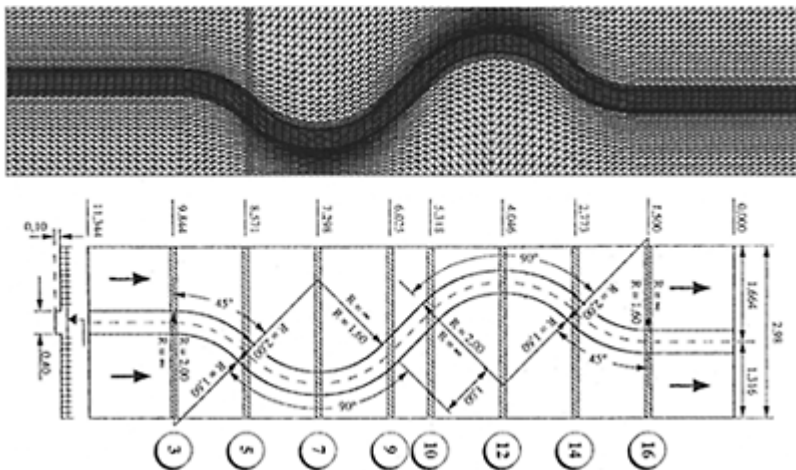


Figure 2. The geometrical dimensions and numerical grid of the hydraulic model of meander channel.

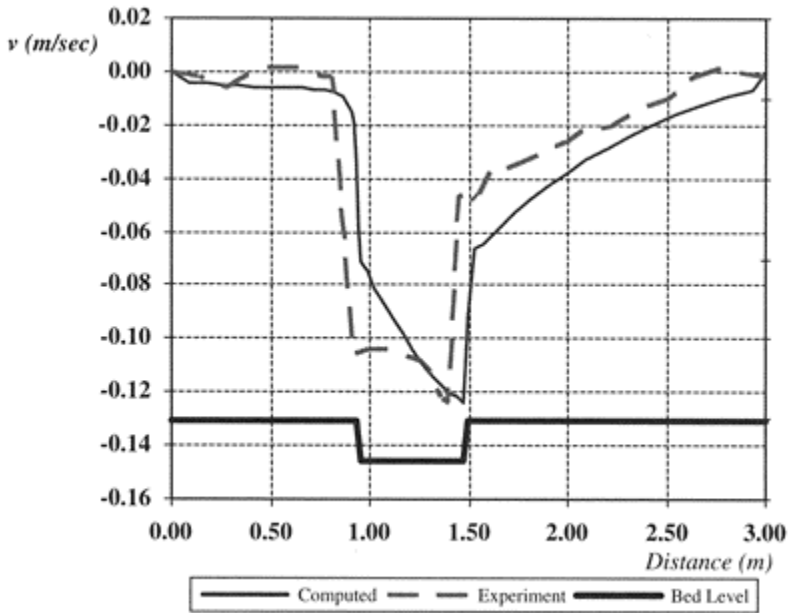


Figure 3. y-component of velocity at section 10.

The triangular computational grid, as well as the geometry of the test flume is illustrated in Figure 2. The numerical grid has been extended at inflow and out flow boundaries to prevent the effects of the boundary conditions on flow structure in the channel. The outflow BC has been adopted as a weir and regulated to reach the experimental depth in the main channel.

The velocity components of the computational results and measured data are presented in Figures 3 and 4. As can be seen in Figure 4, the interaction of floodplain flows and the main channel has retarded the flow velocity in the main channel and the velocity in left flood plain is larger than that in the main channel. This effect could be also reproduced by the numerical model.

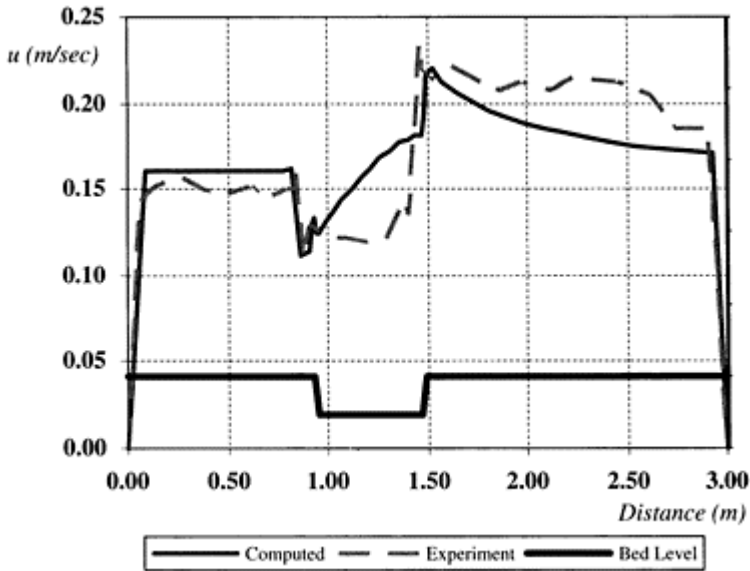


Figure 4. x-component of velocity at section 10.

5 CONCLUSION

A finite volume method coupled with Riemann solver to compute the interfacial fluxes is introduced for solving the SWE over arbitrary topography with unstructured grids. Efficient corrections and treatments are presented to correctly discretize the pressure and bed slope terms by a new method, which allows for accurate, stable and conservative simulation of flows over strongly variable bottoms.

The proposed model has been successfully applied to complicated flow problems such as meandering channel flow with floodplains. The model is quite general and may also be applied to simulate other shallow water flows without any additional modification.

ACKNOWLEDGEMENT

The first author would like to express his best thanks to Professor Dr.-Ing. Wilhelm Bechteler, director of the Hydrosience Institute of German Armed Forces University in Munich, where most of this work was done.

REFERENCES

- Agoshkov VI., Ambroni D., Pennati V., Quateroni A. & Saleri F. (1993) "Mathematical and Numerical Modelling of Shallow Water Flow", Computational Mechanics (11), pp. 280–299
- Bechteler W., Nujić M. & Otto A.J. (1993) "Program Package FLOODSIM and its Application" Advances in Hydro-Science and-Engineering, Volume I, Ed. Wang, Sam S.Y., pp. 762–76, June 7–11, Washington, USA
- Beffa, C.J. (1997) "Praktische Lösung der tiefengemittelten Flchwassergleichungen", Mitteilungen Heft 133, Versuchsanstalt für Wasserbau, Hydrologie und Glaziologie (VAW), ETH Zürich, Switzerland (in German)
- Bermudez A., Dervieux A., Desideri J.A. & Vazquez M.E. (1995). "Upwind Schemes for the Two-Dimensional Shallow Water Equations with Variable Depth using Unstructured Meshes" Rapport de recherche, No. 2738, INRIA, France
- Bradford S.F. & Sanders B.F. (2002). "Finite-Volume Model for Shallow-Water Flooding of Arbitrary Topography", Journal of Hydraulic Engineering, Vol. 128, No. 3, pp. 289–298
- Hubbard M.E. & Garcia-Navarro P. (2000). "Flux Difference Splitting and the Balancing of Source Terms and Flux Gradients", Journal of Computational Physics, Vol. 165, pp. 89–125
- Fennema R. & Chaudhry M.H. (1990). "Explicit Methods for 2-D Transient Free-Surface Flows", Journal of Hydraulic Engineering, Vol. 116, No. 8, pp. 1013–1034
- Glaister P. (1988) "Approximate Riemann Solution of the Shallow Water Equations", Journal of Hydraulic Research, Vol. 26, No. 3
- Komaie S. (2003) "A Robust Implicit Shallow Water Equations Solver on Unstructured Grids" Ph.D. Thesis, Institute of Hydro science, German Armed Forces University Munich—in press
- Nujić M. (1995) "Efficient Implementation of Non-Oscillatory Schemes for the Computation of Free-Surface Flows." Journal of Hydraulic Research, IAHR Vol. 33, No. 1, pp 101–111
- Nujic M. (1998) "Praktischer Einsatz eines hochgenauen Verfahrens für die Berechnung von tiefengemittelten Strömungen", Mitteilungen Heft 62, Institut für Wasserwesen, Universität der Bundeswehr München (in German)
- Ribeiro F.L.B., Galeão A.C. & Landau L. (2001) "Edge-Based Finite Element Method for Shallow Water Equations", International Journal for Numerical Methods in Fluids, 36, pp. 659–685
- Rodi W. (1993). "Turbulence Models and Their Applications in Hydraulics." Balkema
- Stein, C.J. (1990). "Mäandernde Fließgewässer mit überströmten Vorländern- Experimentelle Untersuchung und numerische Simulation.", Mitteilung des Instituts für Wasserbau und Wasserwirtschaft, RWTH Aachen, Nr. 76 (in German)
- Toro E.F. (2001) "Shock-Capturing Methods for Free-Surface Shallow Flows", John Wiley & Sons, Ltd., 2001, U.K
- Zhao D.H., Shen H.W., Lai J.S. & Tabios III G.Q. (1996) "Approximate Riemann Solvers in FVM for 2D Hydraulic Shock Wave Modeling", Journal of Hydraulic Engineering, Vol. 122, No. 12, pp. 692–702

Application of a Boussinesq-type equation to flow over trapezoidal profile weirs

Y.T.Zerihun & J.D.Fenton

Department of civil and Environmental Engineering, The University of Melbourne, Australia

Hydraulics of Dams and River Structures—Yazdandoost & Attari (eds)

© 2004 Taylor & Francis Group, London, ISBN 90 5809 632 7

ABSTRACT: Flow over embankment shaped weirs commonly encountered in large 2-D flow problems cannot be simulated by most of the common flow models which assume uniform velocity and hydrostatic pressure distributions. A Boussinesq-type momentum equation, which allows for curvature of the free surface and a non-hydrostatic pressure distribution, is considered in this paper for the numerical simulation of steady flow over short- and broad-crested trapezoidal profile weirs as well as for the establishment of head-discharge relationships under free flow conditions. An implicit finite difference scheme is applied. Computed and measured results of flow surface profiles and rating curves for these types of weirs are presented. The numerical results of the flow surface profiles and rating curves show good agreement with the corresponding experimental data. The model results also demonstrate the detailed dependence of the flow characteristics of these weirs on the curvature of the streamlines.

1 INTRODUCTION

Flood flows over highway and railway embankments are analogous to flow over short- and broad-crested weirs. The hydraulic advantage of higher discharge capacity of these trapezoidal profile weirs compared to broad-crested weirs with vertical faces makes them very attractive in practice as a discharge measuring device. Thus, the development of head-discharge relationships of such weirs assumes considerable practical importance. Also in the applications of two-dimensional flow models, these weirs often provide important boundary conditions. However, flow over such types of weirs cannot be simulated by most of the common flow models, which assume uniform velocity and hydrostatic pressure distributions over the depth. These assumptions restrict the

application of the models to flow simulation problems that involve insignificant curvature of streamlines. These models do not retain accuracy for flow situations where the effects of non-hydrostatic pressure distribution are significant and essential, such as rapidly varied flows past hydraulic structures. The two-dimensional nature of this flow problem requires relatively accurate methods for exact simulation of the flow situation. In this study a model based on a higher-order Boussinesq-type equation will be employed for the simulation of such types of flow problem numerically.

A review of the literature shows that little effort has been made to study the numerical modelling of flow over trapezoidal profile weirs particularly for the establishment of rating curves. Contrary to this, the problem of flow over such weirs has been extensively studied experimentally. Most of the experimental works were performed towards the understanding of the flow characteristics of these weirs and also the determination of the coefficients of discharge under free and submerged flow conditions (see e.g. Kindsvater 1964, Fritz & Hager 1998). A simple numerical procedure was applied to develop rating curves for flow over broad-crested weirs by incorporating directly the discharge coefficients. The procedure was formulated based on the energy equation which assumes uniform flow at the gauging station and control section, and constant head between this station and section (see Bos 1985 #3.7). This rating procedure provides solution to irrotational flow problems with negligible curvature of streamlines since its application is limited by the ratio of the total energy head, H_0 , to weir crest length, L_w ($H_0/L_w \leq 0.50$). However, the procedure is inappropriate to develop a rating curve for flow over short-crested weirs where the effects of non-hydrostatic pressure and non-uniform velocity distributions are significant. More recently Collins & Catalano (2001) studied the ability of the DELFT-FLS model to predict accurately the crest-referenced head of a broad-crested weir. The study aimed to explore the capabilities and limitations of the model. The discharge rating curves of the weir were simulated for free flow condition and the predicted results were compared with the results of the common broad-crested weir formula for the range in which this equation estimates the discharge accurately ($0.08 \leq H_0/L_w \leq 0.33$). However, the study did not include flow simulations over short-crested weirs ($0.33 \leq H_0/L_w \leq 1.50$) where the curvature of the streamlines above the weir crest has a considerable influence on the head-discharge relationships. This review demonstrates that a general model, which includes the effects of the curvature of the streamlines implicitly or explicitly, is necessary to provide head-discharge relationships for short-and broad-crested weirs. In this work a numerical model based on a higher-order equation will be used for flow simulation over trapezoidal profile weirs with smooth transition curves introduced at the four corners of the profile for the purpose of integrating the equation continuously at these points.

Therefore the main objectives of this paper are: (i) to model transcritical flow over trapezoidal profile weirs using a higher-order equation numerically for establishing head-discharge relationships; (ii) to assess the influence of the curvature of the streamlines on the head-discharge relationships as well as on the flow profile solutions of the governing equation; (iii) to examine the accuracy of the model results by a number of laboratory experiments.

2 GOVERNING EQUATION

Fenton (1996) developed a Boussinesq-type momentum equation based on the assumption of a constant centrifugal term at a vertical section to model relatively short length scale flow problems. For steady flow in a rectangular channel, the equation reads as

$$\begin{aligned} \frac{\beta q^2}{4} \frac{d^3 H}{dx^3} + \frac{\beta Z_b' q^2}{2H} \frac{d^2 H}{dx^2} + (1 + Z_b'^2) \left(\left(gH - \beta \frac{q^2}{H^2} \right) \frac{dH}{dx} + gH (Z_b' + S_f) \right) \\ + \omega_0 \beta q^2 \left(\frac{Z_b'''}{2} + \frac{Z_b' Z_b''}{H} \right) = 0, \end{aligned} \quad (1)$$

in which H is the depth of flow; Z_b' , Z_b'' and Z_b''' are the first, second and third derivatives of the bed profile respectively; S_f denotes the friction slope, calculated from the Manning equation or smooth boundary resistance law; q is the discharge per unit width; β refers to the Boussinesq coefficient; g is gravitational acceleration; and ω_0 is a constant factor to reflect the effect of the bed in determining the elevation of the surface and the associated dynamic pressures due to slow moving flow near the bottom of the flow boundary. Fenton (1996) suggested a value of slightly less than one for ω_0 . In the formulation of this equation, the curvature, κ at the surface is approximated by $\kappa \cong d^2 H / dx^2 + Z_b''$ and at the bed by $\kappa \cong Z_b''$.

This equation implicitly includes the effect of the vertical acceleration to model two-dimensional flow problems where more vertical details are significant and essential. For the case of weakly curved free surface flow with negligible curvature of streamlines in a constant slope channel, the flow surface and bed curvatures terms vanish to zero. Under this flow condition, the above equation reduces to the gradually varied flow equation. Equation (1) will be used in this study to simulate transcritical flow over trapezoidal profile weirs for the purpose of developing discharge rating curves. These weir profiles are characterized by the presence of discontinuous bed geometry properties at the four corner points. Smooth transition curves should be fitted at these points in order to integrate equation (1) continuously within the solution domain. A simple curve described by a polynomial function of degree five was used. The length of this curve was fixed based on the criteria that the error associated with the prediction of the bed profile elevation around the discontinuous point is less than 5%.

3 PROBLEM FORMULATION

The computational domain for the numerical solution of the weir flow problem is shown in Figure 1. In this figure AB is the inflow section, CD is the outflow section and BM is the approaching channel

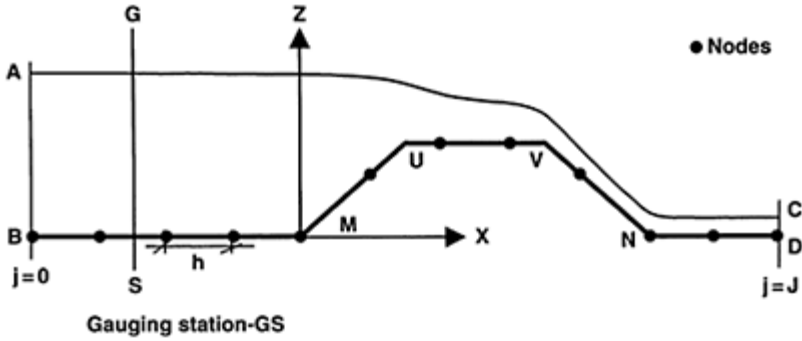


Figure 1. Computational domain for flow over weir.

bed. Also, MUVN is the trapezoidal profile weir. The inflow section of the computational domain is located in a region where the flow is assumed to be nearly horizontal, with uniform velocity and hydrostatic pressure distributions. This pseudo-uniform flow condition before the inflow section of the solution domain simplifies the evaluation of the boundary values at this section using the gradually varied flow equation, equation (2). Thus, for a given depth at the inflow section the slope of the water surface, dH/dx , can be evaluated from the following equation

$$\frac{dH}{dx} = \frac{S_0 - S_f}{1 - \beta Fr^2}, \quad (2)$$

in which Fr is the Froude number; and S_0 is the bed slope. For the subcritical flow upstream of the weir, the Froude number squared is sufficiently small and can be neglected. Using this approximation, the curvature of the flow surface, k_s , at inflow section after differentiating equation (2) with respect to x becomes

$$k_s = \frac{-2q^2 B^2}{K^3} \frac{dK}{dH} \frac{dH}{dx}, \quad (3)$$

where K is the conveyance factor, can be determined from the Manning equation; B is the width of the channel. Similarly, the gauging station GS should be situated sufficiently far upstream of the weir to avoid the influence of the curvature of the water surface on the magnitude of the estimated overflow depth. According to Bos et al. (1984 p. 36) this section is located at a distance of the larger of the following two values: (i) between two and three times the maximum crest referenced head from the upstream edge of the weir crest; (ii) the maximum crest referenced head from the heel of the embankment shaped weir. From the computational point of view, however, the maximum overflow head is not known a priori to fix the position of the gauging station. For this numerical simulation problem, the overflow head corresponding to the given discharge at the heel of the embankment shaped weir will be used to locate approximately the gauging station.

For the given flow depth, AB , and discharge at the inflow section, it is required to determine the flow surface profile, AC , and the corresponding overflow head at the

gauging station GS. For this purpose, the computational domain ACDNVUMB is discretized into equal size steps inx as shown in Figure 1.

4 DEVELOPMENT OF THE NUMERICAL MODEL

Finite difference approximations are used to replace the derivative terms in the above flow equation. This formulation is very simple to code and extensively used to solve linear or non-linear differential equations. For the purpose of discretization, equation (1) can be represented by a simple general equation as

$$\frac{d^3 H}{dx^3} + \xi_0 \frac{d^2 H}{dx^2} + \xi_1 \frac{dH}{dx} + \xi_2 = 0, \quad (4)$$

where ξ_0 , ξ_1 and ξ_2 are the non-linear coefficients associated with the equation. It is a third-order differential equation which needs to employ third- or higher-order accurate methods to solve the equation numerically. This is necessary in order to reduce the truncation errors introduced in the formulation due to the finite difference approximation of the derivative terms of the equation (see Abbott 1979 #4.12). Therefore, five point finite difference approximations are employed here to replace the derivative terms in the governing equation.

The upwind finite-difference approximations (Bickley 1941) for derivatives at node j in terms of the nodal values at $j-3, j-2, j-1, j$ and $j+1$ are introduced into equation (4) for the purpose of discretising the equation. After simplifying the resulting expression and assembling similar terms together, the equivalent finite difference equation reads as

$$\begin{aligned} & H_{j-3} (12 - 2\xi_0 h - 2\xi_1 h^2) + H_{j-2} (-72 + 8\xi_0 h + 12\xi_1 h^2) \\ & + H_{j-1} (144 + 12\xi_0 h - 36\xi_1 h^2) + H_j (-120 - 40\xi_0 h + 20\xi_1 h^2) \\ & + H_{j+1} (36 + 22\xi_0 h + 6\xi_1 h^2) + 24\xi_2 h^3 = 0, \end{aligned} \quad (5)$$

where h is the size of the step. In the solution domain, equation (5) is applied to evaluate nodal values at different points. However, the use of equation (5) at $j=1$ and $j=J$ will introduce unknowns external to the computational domain. Using the backward difference approximations in terms of nodal points $j, j-1, j-2, \dots$ for the derivative terms in equation (4), the finite difference equation at the outflow section after simplifying the resulting expression becomes

$$\begin{aligned} & H_{j-1} (36 + 22\xi_0 h + 6\xi_1 h^2) + H_{j-2} (-168 - 112\xi_0 h - 32\xi_1 h^2) \\ & + H_{j-3} (288 + 228\xi_0 h + 72\xi_1 h^2) + H_{j-4} (-216 - 208\xi_0 h - 96\xi_1 h^2) \\ & + H_j (60 + 70\xi_0 h + 50\xi_1 h^2) + 24\xi_2 h^3 = 0. \end{aligned} \quad (6)$$

Since the value of the nodal points at $j=0$ is known, the values of the imaginary nodes at $j=-1$ and $j=-2$ can be determined from the estimated water surface slope, S_H , and curvature of the free surface, k_H , at the inflow section. Using similar discretization equations as above for the water surface slope and curvature at inflow section and the expanded form of equation (5) at $j=0$, the explicit expressions for the nodal value at $j=-1$ and $j=-2$ are

$$H_{-2}=6hS_H+12H_{-1}-15H_0+4H_1-6h^2k_H, \quad (7)$$

$$H_{-1} = \left(\frac{1}{\Phi - \Omega} \right) \left(A (24hS_H - 80H_0 + 27H_1 - 36h^2\kappa_H) + B (6hS_H - 15H_0) \right) + B (4H_1 - 6h^2\kappa_H) + H_1E + H_0\Gamma + Y \quad (8)$$

where:

$$\begin{aligned} A &= 6h^2\xi_{1,0} + 22\xi_{0,0} + 36; B = 20h^2\xi_{1,0} - 40h\xi_{0,0} - 120; \\ \Omega &= 36h^2\xi_{1,0} + 10h\xi_{0,0} + 144; \Phi = -54A - 12B; E = -2h^2\xi_{1,0} - 2h\xi_{0,0} + 12; \\ \Gamma &= 12h^2\xi_{1,0} + 8h\xi_{0,0} - 72; Y = 24h^3\xi_{2,0}. \end{aligned}$$

The solution of the non-linear flow equation based on a boundary value technique requires an initial estimate of the position of the free surface profile. This makes the solution of the flow problems relatively more difficult due to the fact that the location of the free surface profile is not known a priori. Generally, such problems must be solved by iterative methods, which proceed from an assumed initial free surface position. Convergence of the iteration procedure to a final profile that satisfies the boundary condition may be dependent to some extent on the choice of the initial flow surface profile. In this work the Bernoulli and continuity equations are employed to obtain the initial flow surface profile for commencing the iteration solution. To simulate the flow surface profile, equations (5) and (6) are applied at different nodal points within the solution domain and this results a sparse system of non-linear algebraic equations. These equations together with equations (7) and (8), and a boundary value at the inflow section, are solved by the Newton—Raphson iterative method with a numerical Jacobian matrix. The convergence of the solution is assessed using the following criterion:

$$\sum_{j=1}^m |\delta H_j| \leq \text{tolerance},$$

where δH_j is the correction depth to the solution of the nodal point^y at any stage in the iteration; m is the total number of nodes in the solution domain excluding nodes having known values. In this case study, a tolerance of 10^{-6} is used for the convergence of the numerical solution. The overflow head at the gauging station can be determined from the predicted flow depth at this station and a known height of the trapezoidal profile weir above the upstream floor level. In this model equations (5), (6), (7) and (8) constitute the one-dimensional finite difference equivalent equations.

5 EXPERIMENTAL SET-UP AND PROCEDURE

The experiments were performed in a horizontal flume 7100 mm long, 380 mm high, and 300 mm wide in the Department of Civil and Environmental Engineering at the University of Melbourne. The flume and the trapezoidal profile weirs were made of Plexiglass. The water was supplied to the head tank from a sump through 115 mm diameter pipe with a valve for controlling the discharge. Various flow improving elements were provided upstream of the trapezoidal profile weirs to obtain a smooth flow

without large-scale turbulence. Symmetrical trapezoidal profile weirs of 150mm high, crest length 100mm and 400mm respectively and side slope 1V:2H were tested at different discharges.

A volumetric tank system was used to measure the discharge. The system consists of a tank with plan dimensions of 200 cm by 150 cm and depth of 450 cm, and an inclined manometer (56.62° to the horizontal) for water level measurement in the tank. Tank filling time longer than one minute was used to minimize errors associated with the starting and stopping of the stopwatch. The longitudinal flow surface profile was observed with a manual point gauge of reading accuracy ± 0.1 Omm. For recording the bed pressure, steel pressure taps of external diameter 3 mm were fixed along the centreline of the weir model with maximum horizontal spacing of 100mm, but the spacing was much closer near to the edges of the weir crest. These pressure taps were connected to vertical water piezometers of reading accuracy to 1 mm by long plastic tubes. For each experiment, the base reading for the pressure taps was obtained immediately after the flow was shut off. According to the criteria given by Ranga Raju et al. (1990), the effects of viscosity and surface tension on the experimental results were negligible.

6 RESULTS AND DISCUSSION

In this work the numerical model, which was developed in the previous section, is used to simulate steady flow over short- and broad-crested trapezoidal profile weirs for transcritical flow situation. In order to assess the effect of the streamline curvature on the solution of the model, free flow situations with different H_0/L_W values were considered. The magnitude of this ratio directly measures the degree of the curvature of the flow over the crest of the weir. For $H_0/L_W \leq 0.50$, the curvature of the streamline over the crest is insignificant except near to the edges of the weir crest (see e.g. Bos 1978 p. 15). Since the experiment was performed in a laboratory flume, a smooth boundary resistance law was applied to estimate the friction slope for the numerical model. For computational simplicity β is taken as unity in the above flow equation. All computational results presented here were independent of the effect of spatial step size.

The comparison of the computed and experimental free surface profiles for transcritical flow over short- and broad-crested trapezoidal profile weirs is shown in Figures 2–3. A good agreement is seen between the observed and predicted free surface profiles in both the subcritical and supercritical flow regions, and for all cases of curvatures of the flow surface over the crest of the weirs. This numerical experiment indicates that the model simulates the weir flow problem accurately irrespective of the degree of curvature of the streamlines. It also suggests that the effect of the curvature approximation on the numerical solutions of the equation is insignificant.

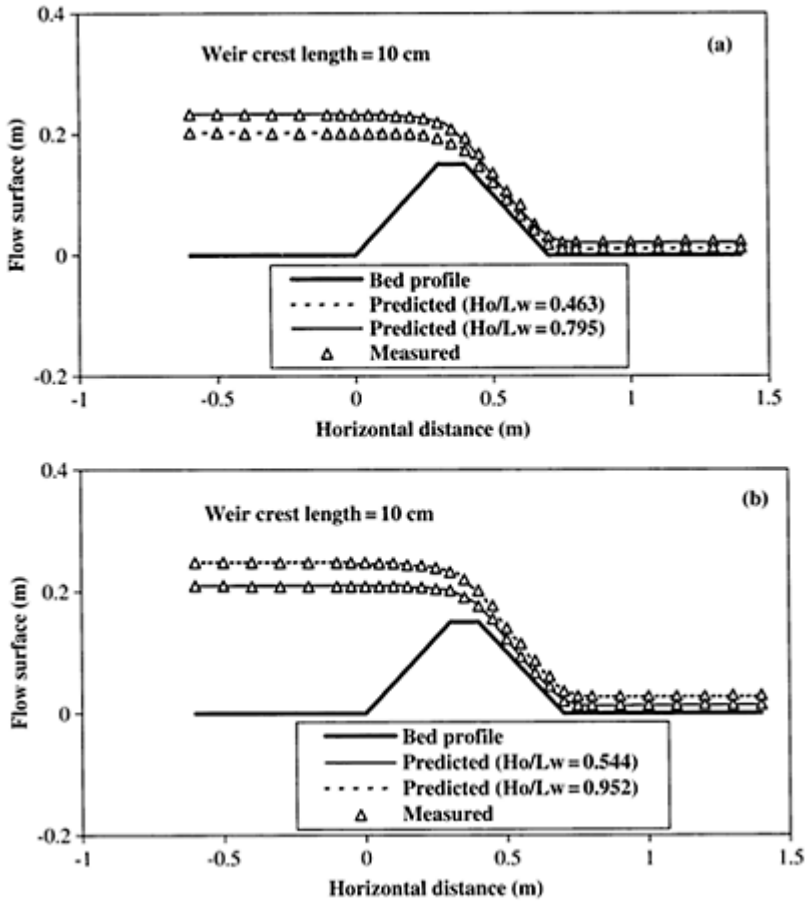


Figure 2. Flow surface profiles for free flow over short-crested weir.

The computed head-discharge curves obtained for the case of flow over trapezoidal profile weirs is compared with the experimental results in Figure 4. The numerical solutions demonstrate good agreement with the experimental data for both weirs. This figure also compares the simulated discharge rating curves of the short- and broad-crested type of trapezoidal profile weirs. Depending on the magnitude of H_o/L_w , the same type weir can act as a broad-crested or a short-crested weir. At low flow rates the rating curve for the short- and broad-crested type of trapezoidal profile weirs are identical; indicating the insignificance of the influence of the curvature of the streamlines on the discharge characteristics of both weirs at this level of the flow rates (see Fig. 4). As the discharge increases, clear differences between the head-discharge curves of the broad-crested and short-crested weirs are observed. This difference is due to the large increase of curvature of the streamlines of the flow over the crest of the short-crested trapezoidal profile weir. It can be observed from Figure 4 that in the region of relatively high flow rate, the

overflow depth required to pass the given discharge over the broad-crested weir is larger than the corresponding overflow depth for the short-crested weir. This implies that less energy is required to pass a given flow over the short-crested types than the broad-crested weirs. This result suggests that the curvature of the streamlines of the flow over the crest of the trapezoidal profile weir has significant impact on the discharge capacity of the weir.

7 CONCLUSIONS

A numerical model has been developed using a higher-order Boussinesq-type momentum equation to simulate transcritical flow over short- and broad-crested trapezoidal profile weirs as well as to

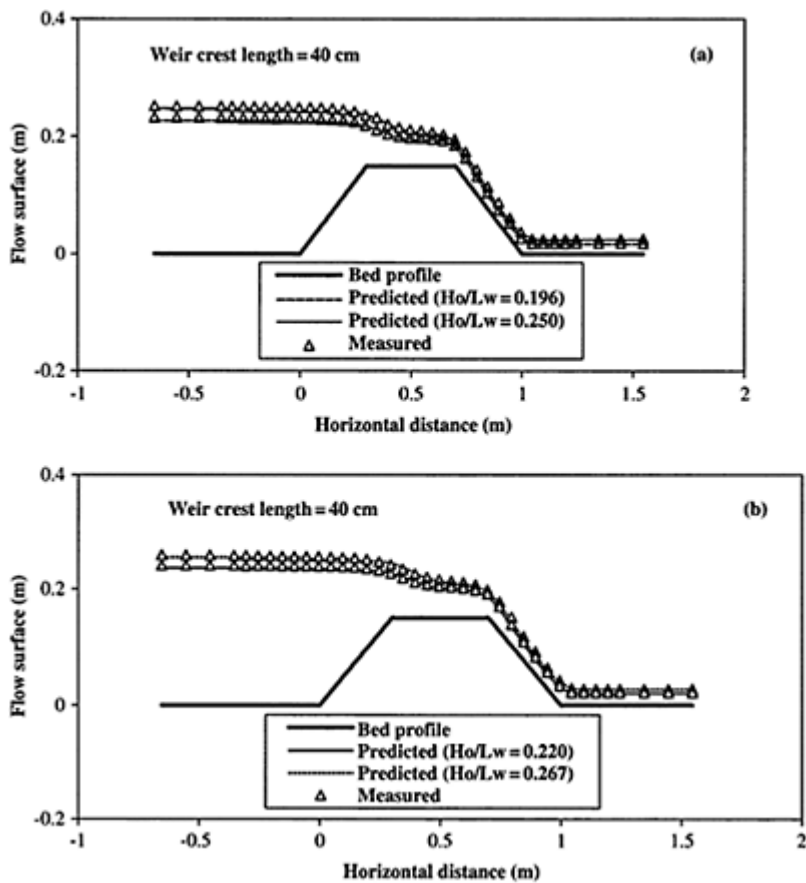


Figure 3. Flow surface profiles for free flow over broad-crested weir.

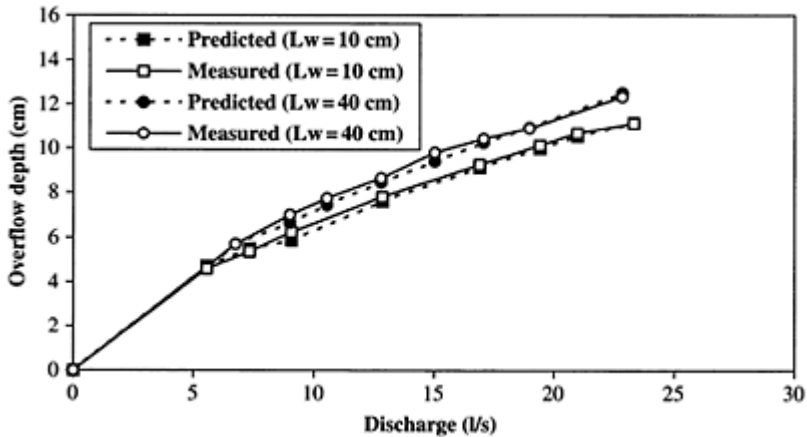


Figure 4. Discharge rating curves for the short- and broad-crested trapezoidal profile weirs.

predict the upstream overflow depths for the given discharges for the purpose of establishing head-discharge relationships for these weirs. It should be emphasized that this one-dimensional model is capable of treating free flow over any type of weir profile providing the profile does not have vertical faces. Analysis of numerical and experimental results was also presented. Good agreement was observed between the predicted and measured values. The model predicts accurately the free surface profiles regardless of the curvature of the streamlines. The model result also shows the influence of the curvature of the streamlines on the discharge characteristics of the trapezoidal profile weirs. The existing flow model for developing discharge rating curves under free flow condition, which is valid only for broad-crested weir, was extended using the Boussinesq-type momentum equation model.

REFERENCES

- Abbott, M.B. 1979. *Computational Hydraulics; Elements of the Free Surface Flow*. London: Pitman Publishing limited.
- Bickley, W.G. 1941. Formulae for Numerical Differentiation. *Math. Gaz.* 25:19–27.
- Bos, M.G. (2nd ed.) 1978. *Discharge measurement structures*. Wageningen: ILRI.
- Bos, M.G., Replogle, J.A. & Clemmens, A.J. 1984. *Flow Measuring Flumes for Open Channel Systems*. New York: John Wiley & Sons.
- Bos, M.G. 1985. *Long-throated Flumes and Broad-crested Weirs*. Dordrecht: Martinus Nijhoff/Dr. W. Junk Publishers.
- Collins, N. & Catalano, C. 2001. Specialized 2-D modelling in floodplains with steep hydraulic gradients. *Proc. Conf. on Hydraulics in Civil Engrg.*, Hobart, 28–30 November, The Institution of Engineers, Australia.
- Fenton, J.D. 1996. Channel flow over curved boundaries and a new hydraulic theory. *Proc. 10th congress, Asia and Pacific Division of the IAHR*, Langkawi, 26–29 August, Malaysia, 2:266–273.

- Fritz, H.M. & Hager, H.W. 1998. Hydraulics of embankment weirs. *J. Hydr. Engrg.*, ASCE, 124 (9): 963–971.
- Kindsvater, C.E. 1964. Discharge characteristics of embankment shaped weirs. *Geological Survey Water Supply Paper 1617-A*. Washington: U.S. Government Printing Office.
- RangaRaju, K.G., Srivastava, R. & Porey, P.D. 1990. Scale effects in modelling flows over broad-crested weirs. *Journal of Irrigation and Power*, 47 (30): 101–106.

Hydrodynamics of three-dimensional density currents

B.Firoozabadi

*Mechanical Engineering Department, Sharif University of Technology,
Tehran, Iran*

Hydraulics of Dams and River Structures—Yazdandoost & Attari (eds)

© 2004 Taylor & Francis Group, London, ISBN 90 5809 632 7

ABSTRACT: Density current is a dense fluid, which is continuously released from a source of rectangular cross section and spreads down a sloping surface inside a lighter, motionless fluid. A CFD code has been developed to describe salt solution density current, which propagates three-dimensionally in deep ambient water. The equations of continuity, momentum conservation, and diffusion are solved simultaneously in the fixed Cartesian directions, on a non-staggered grid using finite volume scheme. The velocity-pressure coupling is handled by SIMPLEC model. Comparison of the computed width of the density currents at the different bed slopes and inlet buoyancy fluxes, with the experimental data, shows a good agreement between them. The center-plate velocity profiles are compared with experiment. Results show the three-dimensional dense layer approaches a normal state shortly after release and the flow behaves as two-dimensional. At low bed slope, lateral propagation increases with concentration and decreases the 3-D length. This solving provides a physical understanding of such complex phenomena.

1 INTRODUCTION

Density current is formed when fluid heavier than ambient, flows down an inclined bed. These flows, which are common phenomena in nature, can be produced by salinity and temperature in homogeneities, or suspended particles of silt and clay. Turbidity current is one of the important mechanisms for the transport of sediment from continental rim to the abyssal plain in oceans. These currents are often observed in oceans and large lakes, powder snow avalanches in mountain area, and pyroclastic flows in volcanic zones [1, 2].

Driven by density differences between the sediment-laden inflow and clear water in the reservoirs, the turbid density current plunges the clear water and moves toward the

dam as a submerged current. This flow consists of a head with complex three-dimensional structure at the leading edge, followed by a thinner flow. Real-fluid effects influence the propagation of the head at a bottom so that its analysis requires a realistic approach. The no-slip condition causes the frontal stagnation point to rise above the bottom, and the front speed, relative to the ambient velocity, decreases as this velocity increases.

In hydraulic engineering, two-dimensional density or turbidity currents propagation on a slope has been investigated by many researchers. Tsihrintzis and Alavian [3] have a complete review of 2-D turbidity currents. For density currents flowing in a submarine channel, the vertical spreading due to water entrainment plays an important role in determining the propagation rate in longitudinal direction. However, in case of the non-channelized density currents, which flow without lateral restriction, one more degree of freedom is added to the longitudinal propagation. That is, the longitudinal spreading rate of such currents is highly dependent on the lateral spreading as well as the vertical mixing [4].

This paper presents the solution of the governing equations of three-dimensional turbid density currents without any special assumptions for simplifications of equations. The obtained results are compared with the experimental data and have reasonable agreement.

2 GOVERNING EQUATIONS

Figure 1 shows the schematic view of 3-D density current. In solving the equations, the depth of the lighter fluid, H , is assumed remarkable compared to that of the turbidity current height, h .

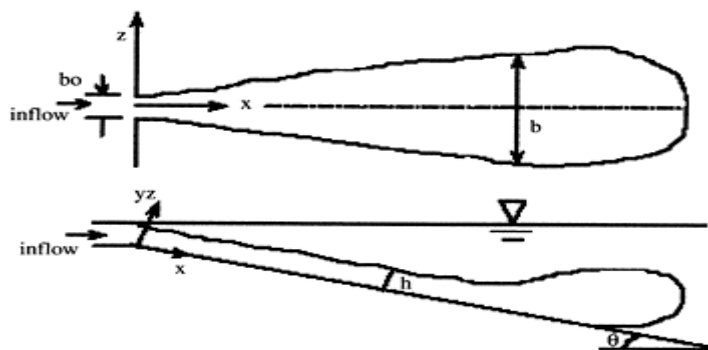


Figure 1. The schematic diagram of three-dimensional density current.

Because the density difference is very small compared to the density of inflow fluid itself, the density current caused by saline water is analyzed by Boussinesq approximation. Due to the low concentration of the salt solution, the fluid could be

assumed as Newtonian. The equations, which describe the motion of a density current, can be expressed as

$$\frac{\partial U_i}{\partial x_i} = 0 \quad (1)$$

$$U_j \frac{\partial U_i}{\partial x_j} = -\frac{1}{\rho} \frac{\partial p}{\partial x_i} + g' \sin \theta_i + \nu \nabla^2 U_i \quad (2)$$

$$U_j \frac{\partial C}{\partial x_j} = \lambda \nabla^2 C \quad (3)$$

These equations are continuity, momentum, and diffusion, respectively. The U_i are components of velocity in x_i directions; g' is reduced acceleration of gravity and is defined as $g((\rho - \rho_w)/\rho) \cdot \rho$ and ρ_w are the density of saline solution and pure water, respectively. C is the concentration of the mixture and is defined as

$$C = \frac{\rho - \rho_w}{\rho_s - \rho_w} \quad (4)$$

ρ_s is the density of salt. θ_i are the components of the bed slope and are $(\theta, \theta - \pi/2, 0)$. ν and λ are the viscosity and diffusivity of the fluid, respectively. The pressure term, P , is defined as

$$\frac{P}{\rho_w} = \frac{P_0}{\rho_w} + g(H - h) + \frac{\rho g(h - y)}{\rho_w} \quad (5)$$

P_0 is the surface pressure. Due to the formation of shear layer and vortices at the interface of the current with surrounding fluid, the entrainment is occurred in addition to creation of density gradient. It also causes the increase of density current depth. The appearance of the pressure term in these equations is due to the variation of density and depth of current; hence its gradient cannot be omitted even at the presence of a free surface.

3 BOUNDARY CONDITIONS

The boundary conditions at the inlet are known. It is similar to the Alavian models [5], the salt solution flow with uniform velocity and concentration enters the channel under the still bodies of water via a sluice gate, onto a surface inclined at angle θ . At the outflow-boundary, the streamwise gradients of all variables are set to zero. It is expected that modeling of the outlet have only a local effect on the flow field [6]. At the free surface, the rigid-lid approximation is made. Then, the symmetry condition is applied that includes zero gradients and zero fluxes perpendicular to the boundary [6]. At the rigid walls, due to the no slip conditions, and a pure depositing assumption, velocities and concentration gradients are set zero. For the concentration equation, zero gradient conditions normal to the vertical walls and zero-flux conditions normal to the bottom are applied.

4 SOLUTION PROCEDURE

The governing equations are solved by a finite-volume method using boundary fitted coordinates. The continuity, momentum, and diffusion equations are solved for the velocity components and concentration U_i , C in the fixed Cartesian directions on a non-staggered grid. All the variables are thus stored at the center of the control volume. The velocity components at the control volume faces are computed by the Rhie-Chow interpolation method [7] and the pressure-velocity coupling is handled by SIMPLEC method. The convective terms are treated by the hybrid scheme. TDMA-based algorithms are applied for solving the algebraic equations. Further details are provided by Farhanieh and Sunden [8]. The solution procedure is iterative and the computations are terminated when the sums of absolute residuals normalized by the inflow fluxes were below 10^{-4} for all variables. To achieve convergence in the solutions, under-relaxation factors of 0.5 were chosen for all the variables. Depending on inlet velocity and bed slope, around 3000–5000 iterations are required to achieve convergence in the velocity fields. However, for concentration field, convergence is much quicker. The mesh points are chosen as uniform in the flow direction, but in the normal direction, the grid points are distributed in a non-uniform manner with higher concentration of grids close to the bed surface. Each control volume contains one node at its center, but the boundary adjacent volumes contain two nodes. The effects of different mesh sizes on the flow characteristics are tested and mesh independency was obtained [6].

5 RESULTS AND DISCUSSION

To validate the computer program, the inlet boundary conditions are set as Table 1 [5]. Salt solution with uniform velocity and concentration is continuously released from a source of rectangular cross section and spreads down a sloping surface inside a lighter, motionless fluid. The inlet height of density current is 7.5 mm and inlet width is 4.5 cm.

Figure 2 shows the lateral propagation of density current in comparison with Alavin [5]. It can be seen that the agreement is quiet well, except entrance zone. In addition, it is observed from the figure that at low inlet fluxes, the present model could detect the experimental data. When the inlet fluxes are high enough, the density current enters via sluice gate with internal hydraulic jump and makes some instability. In addition, due to the formation of shear layer and vortices at the interface of the current with surrounding fluid, high entrainment is occurred. In other words, there were local stabilities in this flow region and the laminar solution could not capture them. Nevertheless, after entrance region, the present model was capable to show the lateral propagation of density current. The Fig. 2, also, shows that lateral propagation increase with inlet flux and after 3-D propagation, the density current flows as two-dimensional current.

The effects of bed slope on lateral propagation can be seen from Fig. 3. It is observed that propagation increase when the bed slope decrease. This is due to the increase of gravity forces.

For complete verification of the present code, the streamwise velocity and concentration profiles at $b/b_0=7.0$ and $\theta=10^\circ$ are shown in Fig. 4a,b in comparison with

Alavian data [5]. The agreement is well, especially in concentration profile. Due to entrainment, it was seen a slightly

Table 1. The inlet conditions.

Inlet conditions	$(\rho-\rho_w)/\rho_w$	$Q_0(\text{cm}^3/\text{s})$	$B(\text{cm}^4/\text{s}^3)$	Ri_0	Re_0
High flux	0.004	14.90	58.5	0.15	330
Medium flux	0.004	8.60	33.7	0.44	190
Low flux	0.004	2.40	9.4	5.90	55

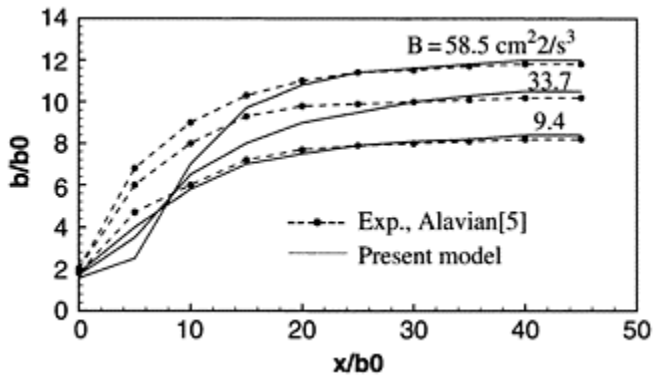


Figure 2. Lateral propagation of 3-D density current, the bed slope is 10° in comparison with experimental data.

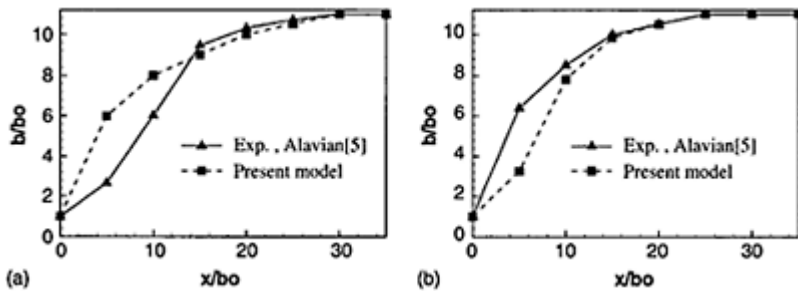


Figure 3. The lateral propagation of density currents in comparison with experiments [5]. (a) $\theta=10^\circ$ (b) $\theta= 15^\circ$.

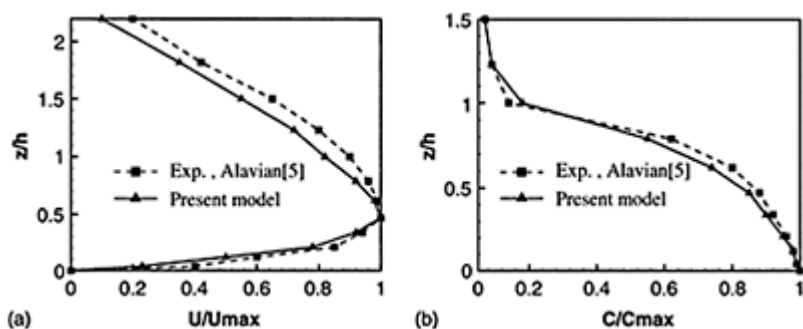


Figure 4. The velocity and concentration profiles at $b/b_0=1.0$ and $\theta=10^\circ$ in comparison with Alavian experiments [5]. (a) velocity profile, (b) concentration profile.

overestimation in velocity profile near the interface of density current and clear water. The Fig. 4a, also, shows that the momentum diffusion in normal direction is larger than concentration.

Figure 5 shows the effects of bed slope and concentration on lateral propagation. It is revealed that the lateral propagation increases with concentration in $\theta=5^\circ$ and the 3-D density current changes to 2-D by increasing the bed slope (15°), the effect of concentration is insignificant in lateral propagation and this is agreed with Fukushima [1].

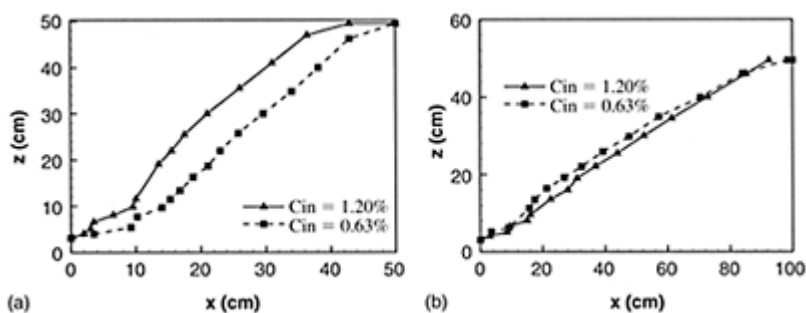


Figure 5. The effects of concentration and bed slope on lateral propagation of density currents. (a) $\theta=5^\circ$ (b) $\theta=15^\circ$.

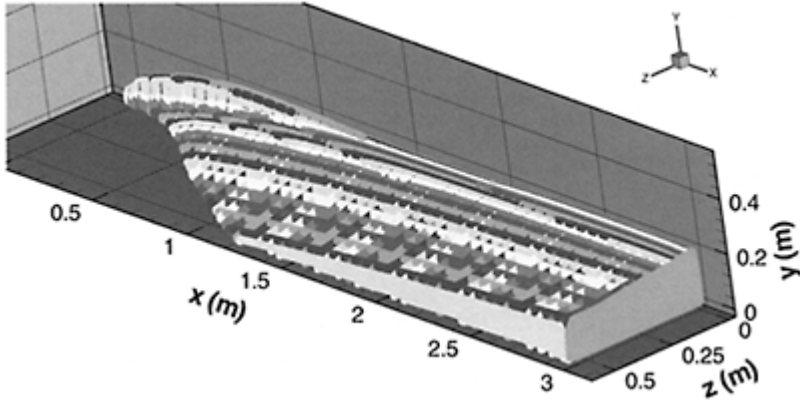


Figure 6. The conetration contours of 3-D density current.

Figure 6 shows the concentration contours of three-dimensional density current. This figure indicates the propagation and height of the density current. It is seen that the current height increase after passing gate.

6 CONCLUSION

In this work, a numerical model is developed to simulate the density current. The viscous analysis is based on the three-dimensional Navier-Stokes equations. The equations for the mass continuity, momentum conservation, and diffusion are solved simultaneously in the fixed Cartesian directions, on a non-staggered grid using finite volume scheme. The velocity-pressure coupling is handled by SIMPLEC model. Density currents with uniform velocity and concentration enter the channel via a sluice gate into a lighter ambient fluid and move forward down the slope on the bed of the channel. The results are compared with the experiments and showed good agreement. The solution can show the distribution of concentration and velocity profiles of the current. The height, and width of the density current are compared with the laboratory experiments. This comparison shows good agreement. This method is capable to determine the span wise entrainment and propagation of the current.

7 NOMENCLATURES

b	width of the sluice gate
C	concentration, $C=(\rho-\rho_w)/(\rho_s-\rho_w)$
ds	Particles diameter
Fr	densimetric Froude number, $Fr = u/\sqrt{g'h\cos\theta}$
g	gravitational acceleration

g'	reduced gravitational acceleration, $g' = g(\rho - \rho_w)/\rho_w$
h	density current depth
P	pressure
Re	Reynolds number, $Re = uh/\nu$
Ri	Richardson number, $Ri = g'h \cos \theta / u^2$
u	velocity in x direction
v	velocity in y direction
v_f	settling velocity of particles
u_{av}, c_{av}	average value of velocity and concentration
x	stream wise co-ordinate
y	vertical co-ordinate
λ	molecular diffusion
ρ	density of turbidity current
ρ_w	water density
ρ_s	particle density
θ	angle of the bed

REFERENCES

- Y.Fukushima, "Dynamics of three dimensional inclined thermal", J. of Hydraulic Eng., ASCE, V 121, N. 8, 1995, pp. 600–607.
- S.Altinakar, W.H.Graf, E.J.Hopfinger, "Weakly depositing turbidity current on a small slope" J. of Hydraulic Research, V 28, N. 1, 1990, pp. 55–80.
- V.Tsihrintzis, V.Alavian, "Spreading of three-dimensional inclined gravity plumes", J. of Hydraulic Research, V 34, N. 5, 1996, pp. 695–711.
- S.Choi, "Layer-averaged modeling of two-dimensional turbidity currents with a dissipative-Galerkin finite element method. Part 2: Sensitivity analysis and experimental verification", J. of Hydraulic Research, V37,N.2, 1999, pp. 257–271.
- V.Alavian, "Behavior of density Current on an Incline," J. of Hydraulic Eng., ASCE, V 112, N. 1, 1986, pp. 27–42.
- B.Firoozabadi, B.Farhanieh, M.Rad, "Hydrodynamics of two-dimensional, laminar turbid density currents", J. of Hydraulic Research, (in printing).
- L.Davidson, B. Farhanieh, "A Finite Volume Code Employing Collocated Variable Arrangement and Cartesian Velocity Components for Computation of Fluid Flow and Heat Transfer Complex Three-Dimensional Geometry", Chalmers University of Technology, Goteborg, Sweden, 1991.
- B.Farhanieh, B.Sunden, "Laminar Heat Transfer and Fluid Flow in Stream wise-Periodic Corrugated Square Ducts for Compact Heat Exchangers," HTD-V201, Compact Heat Exchangers for Power and Processes Industries, Editors: Shah, R.K., et al., and ASME BookNo. H00759, 1992.
- Y., Fukushima, "Numerical simulation of gravity current front", J. of Hydraulic Eng., ASCE, V 124, N. 6, 1998, pp. 572–578.

9.

*River response to hydraulic
structures*

Experimental analysis on the hydraulic efficiency of mudflow breakers

A.Armanini, C.Dalri, F.Della Putta, M.Larcher, L.Rampanelli &
M.Righetti

*CUDAM, Dept. of Civil and Environmental Engineering, University of
Trento,
via Mesiano, Trento, Italy*

Hydraulics of Dams and River Structures—Yazdandoost & Attari (eds)

© 2004 Taylor & Francis Group, London, ISBN 90 5809 632 7

ABSTRACT: The paper analyses the hydraulic efficiency of mudflow breakers. These structures are usually located inside a deposition basin with the purpose to localize dissipative phenomena in restricted areas and to reduce the destructive power of mudflow. In this way it is possible to minimize the part of the bottom of the basin to be protected, reducing negative environmental impacts and building costs. The investigation provides for the positioning of mudflow breakers in two rows being sufficient to absorb most of the kinetic energy of the incoming debris flow.

Results were finalized to design some defense structures for the village of Sarno (Campania—Italy) that was partially destroyed by a mudflow on May 5th 1998.

1 INTRODUCTION

In the technical literature there are few references about mudflow breakers design criteria. Some simple criteria were mentioned by Baldwin *et al.* (1987), concerning some defence structures built in the San Francisco Bay. The authors suggested the construction of breakers composed by small elements of wood, steel or concrete, dimensioned to bear the impact forces. They are fixed in the terrain with concrete foundations, with a lateral spanning of 2 or 3 m. In general the relative position of the elements, the distance between two elements and the number of rows are defined on the basis of the morphology and the characteristics of the catchment; moreover, to increase the resistance to the flow, every single element can be connected to the others by chains or metallic nets.

Because of the shortage of information on mudflow breakers, the problem is studied here by means of an experimental approach on physical model. In the construction of the hydraulic model, the choice of the type of material to be employed is very important as,

in the case of mudflows, both the stress regime and the dissipative processes have characteristics completely different with respect to the case of clear water, though affected by ordinary sediment-transport phenomena. Generally a distinction has to be made on the rheological characteristics of the mixture, which presents a remarkable variability as a function of the solid-phase concentration. An important parameter to be taken into account in mudflow breaker design is the solid concentration. The mudflow characterized by relatively low values of the solid phase concentration shows generally high velocities and small flow depths: in this case the dynamic impact on the blocks can be particularly devastating. On the other side, mudflows with relatively high solid concentration are characterized by thick flow depths and low flow velocities that may lead to overflow problems (Armanini *et al.*, 2001).

The estimation of the correct concentration that could occur during a mudflow event is the focal aspect to be evaluated in order to test the efficiency of a defense structure.

Herein the experimental investigation on different kinds of mudflow breakers is presented. The aim of the experiments is to verify that for low concentration of the fluid the interventions effected were able to locate the dissipation of most of the energy in a localized area, so as to reduce the costs for the construction of the works without compromising the overall security level obtained. Moreover the works must be able to spread out the more dense flows inside the area destined for the accumulation, blocking the regular flowing of the possible subsequent flood event and the consequent flooding of upriver areas.

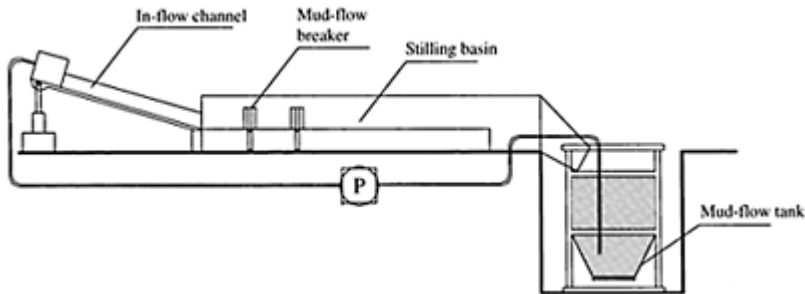


Figure 1. Scheme of the experimental apparatus used during the experiment.

2 EXPERIMENTAL APPARATUS

The experimental apparatus was composed of a rectangular tilting channel, 40 cm wide and 2 m long, that flows into a 140 cm wide, 2 m long tank (Figure 1). The fluid was recirculated through a properly designed closed circuit system, able to produce steady-flow conditions inside the model. The hydraulic model represented a mountain valley leading into a stilling basin. All the tests with clear water were performed according to Froude similarity, while those with mud respecting also Reynolds similarity. The channel was long enough to assure uniform flow conditions before entering into the stilling basin.

The experiments were done both with clear water and mudflow: in particular experiments performed with clear water, the extreme case of low concentrations, enabled to highlight the erosive capacity of the current. In the first case the discharge was fixed ($Q=0.018 \text{ m}^3/\text{s}$) and the Froude number of the in-flow channel was varied tilting the channel. In the second case three different mudflow concentration were tested ($c_1=24\%$, $c_2=28\%$, $c_3=40\%$); for each concentration the discharge was constant ($Q=0.018 \text{ m}^3/\text{s}$) and only the Froude number was changed. Some preliminary tests were carried out both in movable bed and fixed bed conditions. Concerning the tests on movable bed four uniform granular materials were used with different diameters: $d_{50}=50 \text{ mm}$, $d_{50}=31 \text{ mm}$, $d_{50}=10 \text{ mm}$ and $d_{50}=4.4 \text{ mm}$.

3 MEASURING TECHNIQUE

To calculate the value of the specific energy, the flow depth was measured by means of a point gauge placed on a trolley movable both in the longitudinal and transversal direction. The hydrodynamic field has been surveyed through the reconstruction of the trajectories, obtained tracking tracers floating on the surface of the fluid. To this purpose, a digital high-speed CCD camera was used, shooting from above of the motion field. The position of the particle centroids has been detected with sub-pixel precision ($1/84 \text{ pxl}$). For the reconstruction of the trajectories covered by the centres and the subsequent assessment of the particle velocity, an opportunely modified version of the Particle Tracking Velocimetry algorithm by Hassan & Canaan (1995) was used (Serafini, 2003). The investigated flow field has been divided into 8 sub-shots, captured in subsequent times, in order to increase the spatial resolution of the measured velocities. The statistical ergodicity of the stationary-motion field examined permits the reconstruction of the whole flow field coupling the data measured for each shot. Afterwards, starting from these data, the specific energy associated with the section of interest was calculated.

The analysis of the digital images allows the determination of the streamlines and the calculation of the length of the rollers and the depth of the lateral jets formed by the breakers.

A system of load cells has been developed and used, able to measure the force exerted by the flow on the breakers with a confidence interval ranging between 0.3% and 0.6%.

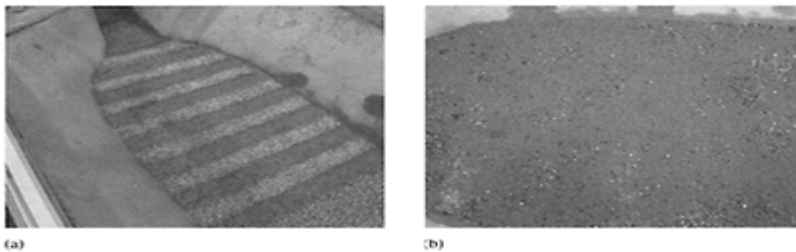


Figure 2. Striped coloured bed of the sedimentation basin: (a) before the experimental run; (b) after having

carefully removed the mud at the end of the test (Armanini, 2001).



Figure 3. *M-30-d1* type mudflow breakers.

4 RESULTS

4.1 *Results in movable bed configuration*

Some initial tests, carried out on a movable bed composed by uniform grain size material, led to show that high density mudflows tend to form a deposition layer over the erodible bed near the entrance of the stilling basin, preventing in this area the bed from any successive erosion.

However if the mud is not sufficiently dense a localized scouring should form. In this case it is necessary to design structures able to localize this phenomenon to mitigate possible damages. The results of the experimental analysis allowed concluding that the optimal arrangement of the flow breakers provides for a system composed by several rows of breakers disposed normally to the undisturbed velocity direction.

The first one has the function of deviating the current, while the second one reduces significantly the available cross section of the basin and enhances the transition of the flow into sub-critical conditions. The successive rows have the function to absorb possible jets, which are likely to form.

4.2 Results in fixed bed configuration

The purpose of this series of experiments is to evaluate the dissipation efficiency of the breakers, as a function of the characteristics of the flow and of the blocks geometry. In order to pursue this

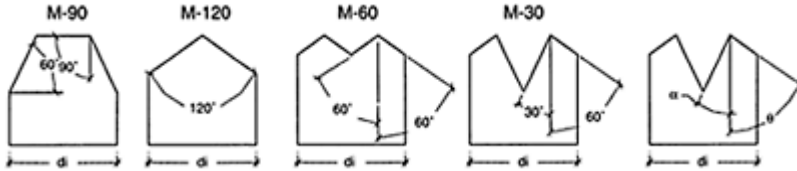


Figure 4. Schematic representation of the various typologies of breakers used in the experiment.

aim, different geometries of breakers (Figure 4) and different configurations have been tested. Two different cases have been observed:

- if the deviation angle is small enough ($\theta < 45^\circ$, where θ is represented in Figure 4), two lateral jets form;
- if the deviation angle is large enough ($\theta > 45^\circ$) a third vertical jet forms, which overtakes the breaker.

Moreover it has been observed that:

- a single wedged breaker, as the M-120 type in Figure 4, is not suitable to deflect the incoming flow, because it induces the formation of strong lateral jets. Moreover, the addition of one more than a single wedged breaker, the problem is not resolved: locally each breaker behaves as described above;
- the double wedged blocks, as the M-30 type in Figure 4, force the formation of a roller just upstream the breaker and this causes a strong reduction in the jets dimension, so leading to a significant reduction of the extension of the localized scouring zone and an increase in energy dissipation;
- the shape and the location of the hydraulic jump are influenced by the shape and arrangement of the first row of breakers.

Moreover, the performed analysis allows evaluating the optimal location (i.e. the one able to maximize energy dissipation) for the first row of breaker, in order to characterize the extension of the area interested by erosion, and to quantify the flow overpressures on the defence structures.

The determination of the dissipative capacity of the system has been calculated in a section just downstream the breakers and by calculating the specific energy of the flow in that section. It is possible to define a non-dimensional parameter E_j/E_0 , in which E_0 represents the value of the specific energy in the reference section when mudflow breakers are not present, while E_j is the energy value of every configuration tested.

In Figure 5a the dissipation efficiency is presented for different kinds of mudflow breaker ($R_1 = bD/b_m$ where b_D represents the breaker width and b_m the width of the in-flow channel). The data refer to the clear water and incoming Froude number equal to 2.5. It is possible to note that:

- for breakers with a narrowing ratio $R_1 = 0.25$ the shape of the breaker employed determines significant difference in energy dissipation;
- considering simultaneously the two series of values, the M-30 shape allows to maximize the dissipative capacity.

From the considerations above the M-30-d1 is the most efficient breaker among those studied because of its capacity to damp the lateral flows and to dissipate the kinetic energy of the current.

In Figure 5b results are reported for a test performed in clear water with Froude number equal to 2, and for a test with a 24% volume concentration and a slope of the in-flow channel equal to 5%. Energy is dissipated above all by the first two rows of breakers, while the contribution given by the third row is negligible, therefore flow-breaker configurations composed by more than two rows can be considered not necessary. From Figure 5b it emerges that for a given flow-breaker less kinetic energy is dissipated by mudflow than by clear water. One possible explanation of this is that, due to the small scale, in the mudflow case the fluid viscosity influences the flow, while in clear water Reynolds number is high enough for the flow to be independent on it.

In designing these works, it is very important to know the zone of the basin where the dissipative phenomena take place, in order to protect the foundation of the structures from possible scouring.

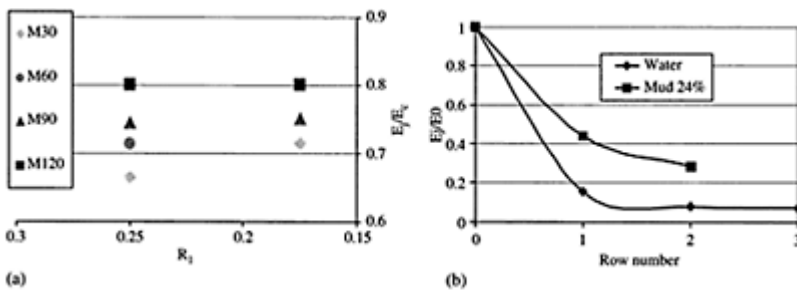


Figure 5. (a) Dissipative effect of the first row of breakers as a function of the local narrowing ratio R_1 for a Froude number of the incoming current equal to 2.5. E_j is the specific energy of the current measured using various types of breakers. (b) Relative energy dissipation produced using different numbers of rows of flow

breakers in the presence of a mud flow with concentration equal to 24% and in the presence of water. Note that the cross section in which the specific energy in figure (a) was measured is different than the cross section in figure (b) was measured.

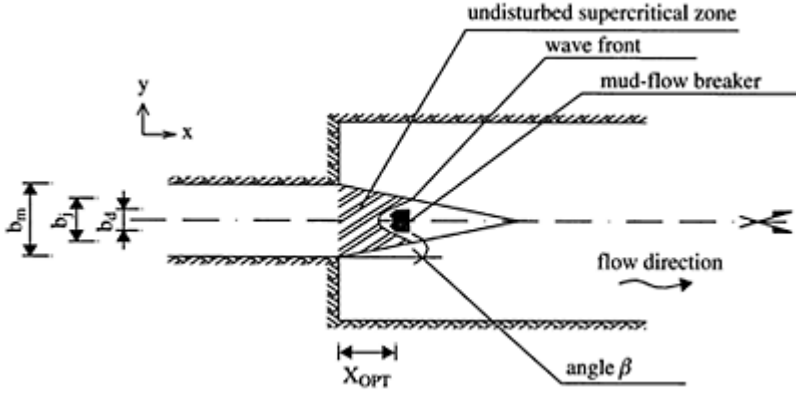


Figure 6. Constant supercritical flow fields at the confluence. The angle β of the characteristic decreases for increasing Froude numbers.

The minimum distance X_{OPT} , at which placing the first row of breakers in order to minimize the lateral jets and maximize the energy dissipation, has been determined by the following procedure:

- the breaker with shape M-30-d1 has been positioned at different distances from the outlet of the upstream channel inside the area where the in-flow stream is not yet affected by the section widening, according with field theory of supercritical flows (Knapp & Ippen, 1938);
- the intensity of the lateral jets depends also on the difference between the width of the undisturbed field b_j (linearly decreasing in the downstream direction) and the width of the block b_d ;
- for $Fr_1 > 1$ the following empirical formula has been obtained for X_{OPT} :

$$\frac{X_{OPT}}{b_D} = 0.69Fr_1 - 0.59 \quad (1)$$

The impact of a flow against the block can be assimilated to the impact of a debris surge against a vertical wall. In this case two types of impact have been observed by Armanini

& Scotton (1993): either a vertical jet or a reflected wave. In the experiments we noted that the presence of the breakers enhanced the formation of a phenomenon, which can be considered neither a reflected wave nor a vertical jet. The problem has a two-dimensional characterization, and further experimental investigations are needed for a deep comprehension of this phenomenon. In this case, however, our interest is limited to define the extension of the zone subjected to erosion. For this

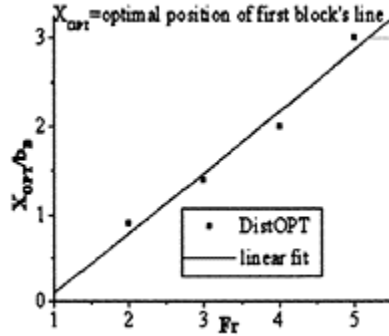


Figure 7. Relation between the ideal distance X_{OPT} from the inlet-channel outlet at which the breaker has to be placed.

reason a simplified approach has been proposed with reference to the rollers of an hydraulic jump studied by Hager (1990), which is a case quite similar to the one presented here. The expression proposed by Hager is:

$$\frac{l_r}{h_1} = 160 \cdot \tanh\left(\frac{Fr_1}{20}\right) - 12 \quad (2)$$

with the following limits of validity:

$$\begin{cases} 2 \leq Fr_1 \leq 16 \\ \frac{h_1}{b_m} \leq 0.1 \end{cases} \quad (3)$$

where l_r is the roller length; h_1 the upstream flow depth; Fr_1 is the Froude number of the upstream current and b_m is the inflow channel width.

According to this procedure, the length of the roller is independent from the type of the breaker. For this reason the theoretical length l_r has been corrected with a reduction coefficient k , defined as:

$$k = \frac{l_{r_CALC}}{l_{r_MIS}} \quad (4)$$

in which l_{r_CALC} is the roller length calculated utilizing relation (2) and l_{r_MIS} is the measured value. The value of k is a function of the main parameters of the problem: namely of the shape factor represented by the internal shape angle α (Figure 4), by the Froude number of the incoming current Fr_1 and by the dimensionless contraction ratio $R_1 = b_n/b_m$. The following empirical relation has been obtained for the coefficient k :

$$k = - \left[0.17 + 3.7 \cdot \ln R_1 \cdot \sin \alpha - 1.9 \cdot (\ln R_1)^3 \cdot \frac{\sin \alpha}{Fr_1} \right] \quad (5)$$

with the following limits of validity:

$$\begin{cases} 2 \leq Fr_1 \leq 5 \\ 0^\circ \leq \alpha \leq 90^\circ \\ R_1 < 1 \end{cases} \quad (6)$$

In Figure 8b the experimental values of the reduction coefficient are compared to the theoretical ones given by equation (5). Inserting equation (5) into (4) and (2), the following formula is proposed for the length of the area interested by the roller and, therefore, to be protected:

$$\frac{l_r}{h_1} = \frac{160 \cdot \tanh\left(\frac{Fr_1}{20}\right) - 12}{k} \quad (7)$$

An analysis of the forces acting onto each breaker has been carried out in order to optimize the structural design of the works. This analysis allows determining a dimensionless parameter cd

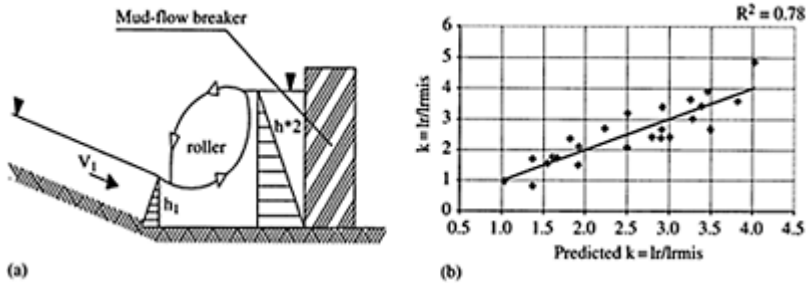


Figure 8. (a) Representation of the roller forming upriver with respect to the flow breaker; (b) Comparison between the calculated and measured values of k .

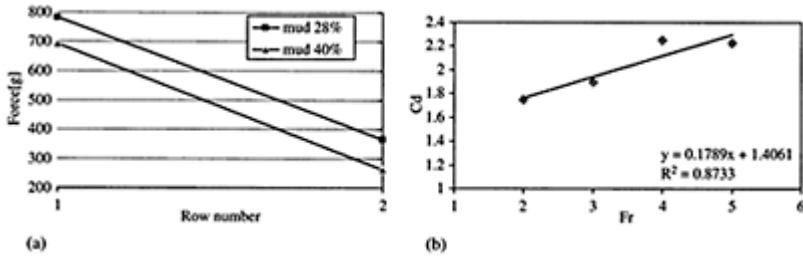


Figure 9. (a) Comparison between the mean values of the forces acting on the different rows of breakers produced by a mud flow with volume concentration equal to 28%, to 40% and with water; (b) Drag coefficient analysed for the first row of breakers: peak impact forces.

(drag coefficient of the structure) to be adopted for design purposes. The mean values of the forces acting onto both rows are greater in the case in which the works are affected by a flow with lower concentration, according to the hypothesis of possible influence of Reynolds number (Figure 9a).

The relation adopted is the following:

$$S = c_d \rho A \frac{v_1^2}{2} \quad (8)$$

in which $A = b_d h_1$ represents the main section; b_d the breaker width; h_1 the flow depth of the upriver current; v_1 the velocity of the undisturbed upriver current; ρ the density of the fluid; S the pressure onto the breaker and c_d the resistance coefficient.

In principle c_d should depend on the shape of the structures, on the geometrical characteristics of the in-flowing current and on Reynolds number. Figure 9a shows an decreasing of impact forces for increasing mud concentration. This fact suggests that the increasing of Reynolds number produces an increasing of impact forces and this result agrees with the possible influence of Reynolds number on drag coefficients. The same figure suggests that the clear water should determine the highest force values. For this reason clear water has been considered the most severe condition. In Figure 9b the clear-water drag coefficient for the first row of breakers has been reported as a fimction of Froude number: the experiments in clear water condition correspond to $Re > 10^4$, for which c_d should depend no more on Reynolds number.

From the data analysis the following linear equation is derived, obtained with clear water for $Fr_1 > 1$. It should be noted that the expression is asymptotically independent from the Reynolds number:

$$c_d = 0.18 Fr + 1.4 \quad (9)$$

5 CONCLUSIONS

Some indications are given for the design of mudflow breakers to be located at the entrance of a deposition basin. The most efficient configuration is composed by two rows of breakers. The role of the second row of blocks is capturing the jets formed by the first row. The shape of the first breaker results to be the most important parameter.

The use of the breakers permitted to reduce the zone to protect from erosion. The necessity to place the works at a definite distance from the inflow channel in order to optimize the functioning of the works was shown. A formula to calculate the extension of the dissipative processes upstream the first block is given.

This work is not aimed to propose a general solution for possible cases of mudflow breakers design, but has to be intended as a particular application.

The research presented in this paper was carried out thanks to financial support provided by the Struttura Commissariale per l'Emergenza Idrogeologica nella Regione Campania. The authors wish to thank prof. Pasquale Versace for his support and his precious discussion on some points.

REFERENCES

- Armanini, A. 2001. Verifica su modello fisico in scala ridotta di manufatti speciali, quali vasche di laminazione o dissipazione o di deposito delle colate di detriti e di fango, da realizzarsi in località San Felice a Canello come piano rimodulato ex ordinanza commissariale N. 415/99. CUDAM—Department of Civil and Environmental Engineering, Trento University, Italy.
- Armanini, A., Larcher, M., Fraccarollo, L., Papa, M. 2001. Considerazioni sulla dinamica delle colate di fango e sulle opere per il loro controllo. *Forum per il rischio idrogeologico in Campania: fenomeni di colata rapida di fango nel maggio '98, Napoli 22 giugno 2001*.
- Armanini, A., Scotton, P. 1993. On the dynamic impact of a debris flow on structures. *Proc. XXVIAHR Congress, Tokyo, vol. B, paper n. 1221*.
- Baldwin II, J.E., Howard, F.D., Terry, R.H. 1987. On debris flow/avalanche mitigation and control, San Francisco Bay area, California. In J.E. Costa & G.F. Wieczorek (eds), *Debris flows/avalanches: process, recognition, and mitigation: 223–236*. Colorado: The Geological Society of America.
- Della Putta, F. 2003. Analisi sperimentale dei dispositivi frangicolata. *M. Eng. Thesis*, University of Trento, Italy.
- Hager, H.W., Bremen, R., Kawagoshi, N. 1990. Classical hydraulic jump: length of roller. *Journal of Hydraulic Research*, 28, 591–608.
- Okamoto, K., Hassan, Y.A., Schmidl, W.D. 1995. New tracking algorithm for particle image velocimetry. *Experiments in Fluids*, 19, 342–347.
- Knapp, R.T., Ippen, A.T. 1938. Curvilinear flow of liquids with free surfaces at velocities above that of wave propagation. *5th Int. Congress. Of Appl. Mech.*, Cambridge, Mass. 531.
- Rampanelli, L. 2002. Verifica sperimentale per il controllo di colate di detriti. *M. Eng. Thesis*, University of Trento, Italy.
- Serafini, A. 2003. Messa a punto di un sistema di Particle Tracking Velocimetry per la determinazione di campi di moto. *B. Eng. Thesis*, University of Trento, Italy.

Sub-critical flow in open channel junction

A.Behrangi

MSc Graduate, Sharif University of Technology, Civil Engineer, SABIR Co.

S.M.Borghei

Associate Professor, Civil Engineering Department, SUT

A.R.Daemi

General Director of Water Planning Bureau, Ministry of Energy, Iran

Hydraulics of Dams and River Structures—Yazdandoost & Attari (eds)

© 2004 Taylor & Francis Group, London, ISBN 90 5809 632 7

ABSTRACT: Hydraulics of open-channel junction concerns many disciplines in engineering such as; river engineering, environmental hydraulics, sedimentation and scouring problems. Although, ample study are available in this field but, due to many parameters involved, more studies are needed. Among the variables, different channel width ratio (branch to main) and connection geometry (sharp and non-sharp) have been less studied. In this paper, experimental results of these two matters are of main interest. The results show that a non-sharp edge junction reduces dramatically the separation zone dimensions. Also, the separation shape index cannot be assumed constant for all situations contrary to previous suggestions. A new relation for separation zone dimension with inflow angle (instead of junction angle which has been suggested by previous works) is introduced which has resulted a better correlation with present data.

1 INTRODUCTION

Study of flow combination in open channels is an important subject in hydraulic engineering with direct application in design of many hydraulic systems. Junctions with equal channel width have been studied by many researchers in three categories, analytical approach (Gurram et al. 1997, Taylor 1944), experimental or field studies (Best & Reid 1984, Biron et al. 1996, Weber et al. 2001) and numerical models (Weerkoon et al. 1991, Huang et al. 2002). However, the actual flow is complicated since many variables are involved, such as; the ratio of lateral discharge (Q_b) to total or downstream discharge (Q_d), the geometry of the channel connection (sharp and non-sharp or, S and NS) and especially the channel widths ratio ($W_{bd}=W_b/W_d$, W_b is branch width, W_d is main channel width).

Geometry of separation zone, just downstream of the junction, is one of the main hydraulic interests in the rigid boundary junctions. Thus, many attempts have been done to introduce equations to estimate the dimensions of the separation zone (Gurram et al. 1997). Few published works are available on different connection angle (θ), Figure 1, or width ratio but, no work has been seen for non-sharp connection. Present paper is an experimental study of the effect of two important variables, which have been less considered, i.e. different widths ratio and non-sharp connection (NS) as well as sharp connection (S).

2 EXPERIMENTAL SET-UP AND EQUIPMENTS

The tests have been carried out with two channels connected at right angle ($\theta=90^\circ$). The main channel upstream and downstream had 40 cm width ($W_u=W_d=40$ cm), while the lateral channel (W_b) has three variable widths (20, 30 and 40 cm). For 20 and 30 cm width, sharp and 45 degree connections were tested (Fig. 1). The channel walls were made of Plexiglas and the bed of wood. Triangular sharp-crest weirs were used to measure the discharge of the two channels.

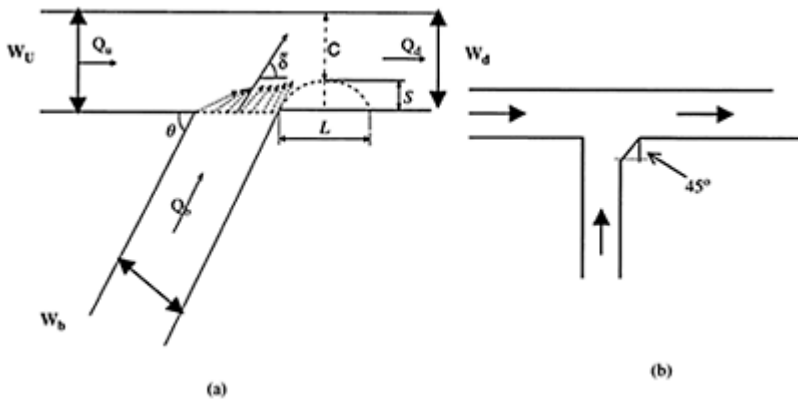


Figure 1. Definition sketch, a) important parameters, b) non-sharp connection.

The depths were measured with an electronic depth-meter with an accuracy of 0.01 mm. For the flow direction or velocity components, ADV (Acoustig Doppler Velocimeter) and micro propeller velocimeter were used. Also, dye injection was used for observation and measurement of the separation zone dimensions.

3 TEST VARIABLES

The tests were carried out with total discharge of 14.381/s for six different discharge ratios ($Q_{bd}=Q_b/Q_d$ from 0.05 to 0.95), four different values of downstream Froude number ($Fr_d=0.22, 0.39, 0.46$ and 0.53), three different branch channel widths ($W_{bd}=W_b/W_d=0.5, 0.75$ and 1) and two different channel connections (sharp edge and 45°). In these tests the subscript u, d, and b are for upstream, downstream and branch channels respectively. Also subscript with two letters is for non-dimensional values, e.g.; $Q_{bd}=Q_b/Q_d$ when Q is the discharge.

4 RESULTS

4.1 Separation zone

The momentum of lateral flow ensures that the flow detaches from the sidewall as it enters the main channel and a separation zone of lower speed with circulating flow introduces. This zone varies in size and, therefore, is of considerable importance in limiting the effective channel width (Fig. 1a). The results from experimental study of length (L) and width (S) of separation zone for different variables are the main objective of this study. It should be mentioned again that the zone was measured with the help of dye injection. For low Fr_d the measurement of exact dimensions of separation zone was difficult and not very accurate using dye. However, for higher values of Fr_d the accuracy is within few millimeters or less than 5%.

4.2 Width of the separation zone (S)

Results in Figure 2 shows that for the two kind of connections the non-dimensional width of the separation zone (S/W_d) increases as Q_{bd} increases and Fr_d decreases when $W_{bd}=0.75$. From another view, the influence of W_{bd} and Fr_d on S/W_d are shown in Figure 3 (in the figure, S is for sharp, NS is for non-sharp and the coefficient for S or NS is the width ratio, W_{bd}). Figure 4 is an illustrative example of a hydraulic jump when the lateral flow is larger than the main channel flow and $Fr_d>0.35$. If hydraulic jump happens, it has a great influence on separation zone specially when W_{bd} is small (i.e. when $W_{bd}=0.5$).

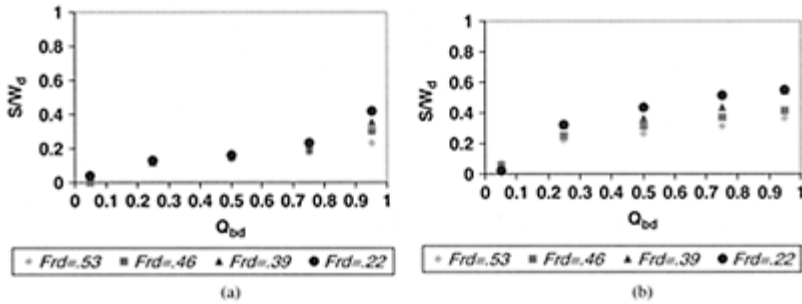


Figure 2. Dimensionless separation width versus discharge ratio for $W_{bd}=0.75$ and different Fr_d , a) sharp edge connection, b) non-sharp edge connection.

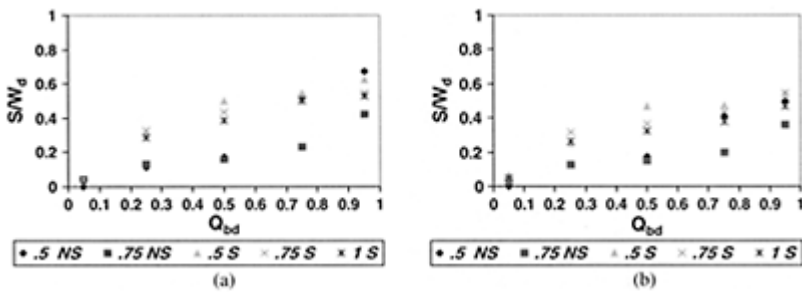


Figure 3. Dimensionless separation width versus discharge ratio for different width ratio and edge connection, a) $Fr_d=0.53$, b) $Fr_d=0.39$.

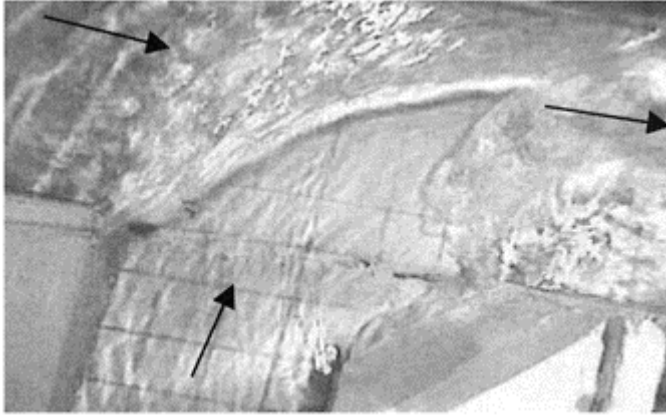


Figure 4. Hydraulic jump near the non-sharp edge connection.

4.3 Length of separation zone (L)

As mentioned, measuring length of separation zone is more accurate than its width through dye injection. The values of non-dimensional separation length L/W_d versus Q_{bd} for different W_{bd} (0.5 & 0.75) are shown in Figure 5. The value of L/W_d increases with increasing of Q_{bd} up to 0.5 when Fr_d is 0.53. Also for other values similar limitations exist.

Infact, as Q_{bd} increases there is a limitation to growth of separation length. This is because as the flow from the lateral branch increases ($Q_{bd} \geq 0.5$ depending on Fr_d), reflection of the flow from main channel wall (opposite wall) influences the downstream end of the separation zone and shortening it (Fig. 6). This phenomenon is called “reflection effect” which reduces the separation length. Another effect of this phenomena is an abrupt increase of water depth or a sort of hydraulic jump, which happens in a length of about 1.7–1.85 W_d downstream of the junction, as shown in Figure 7. This discontinuity separates upstream flow from downstream and therefore it has an important effect on flow pattern. This effect is also mentioned in pervious studies but, no quantitative range is provided (Christodoulou 1993). Experimental measurements of flow velocity using ADV show that higher speed of flow occurs near the bed of the main channel downstream of the junction and before hydraulic jump commencement. Also, shape of connection (sharp or non-sharp) and W_{bd} have major effect on L , as illustrated in Figure 8. It is seen that non-sharp (NS) edge reduces the length dramatically. Also, the present study shows that the separation zone is larger near the water surface, both in length and width.

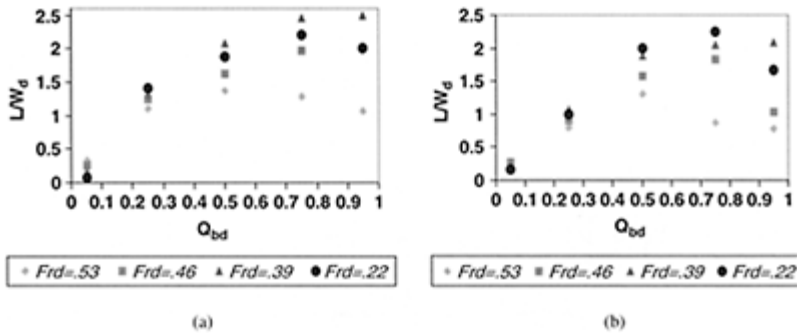


Figure 5. Dimensionless separation length for different Froude numbers, a) $W_{bd} = 0.5$, b) $W_{bd} = 0.75$.

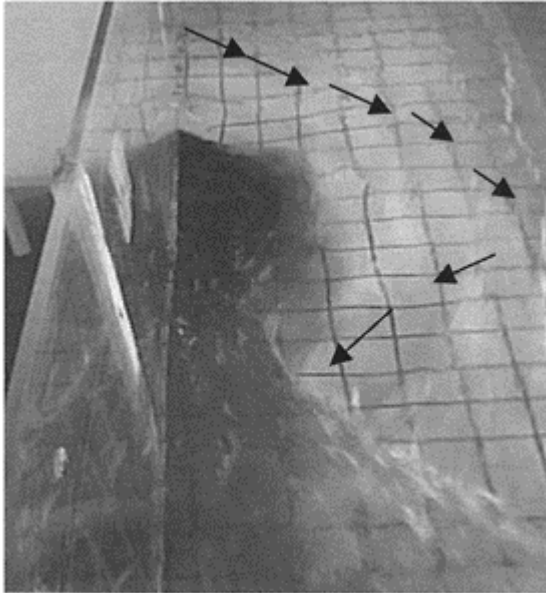


Figure 6. Reflection effect from opposite wall.

4.4 Comparison with previous works

Gurram et al. (1997) have done a valuable study and presented the separation zone geometry in the form of equations;

$$\frac{S}{W_d} = \frac{1}{2} \left(Fr_d - \frac{2}{3} \right)^2 + 0.45 Q_{bd}^{0.5} \left(\frac{\theta}{90^\circ} \right) \quad (1)$$

$$\frac{L}{W_d} = 3.8 \sin^3 \theta \left(1 - \frac{1}{2} Fr_d \right) Q_{bd}^{0.5} \quad (2)$$

However, since θ is a fixed angle but the separation zone should depend on a variable relative to the flow characteristics, therefore, probably a substitution for θ in the equations would be the average entrance angle, $\bar{\delta}$. Figure 9 shows $\bar{\delta}$ versus Q_{bd} for different W_{bd} ratios together with the study of Hsu et al. (1998). Also, Borghei et al. (2003) have shown that Froude number has no considerable influence on $\bar{\delta}$.

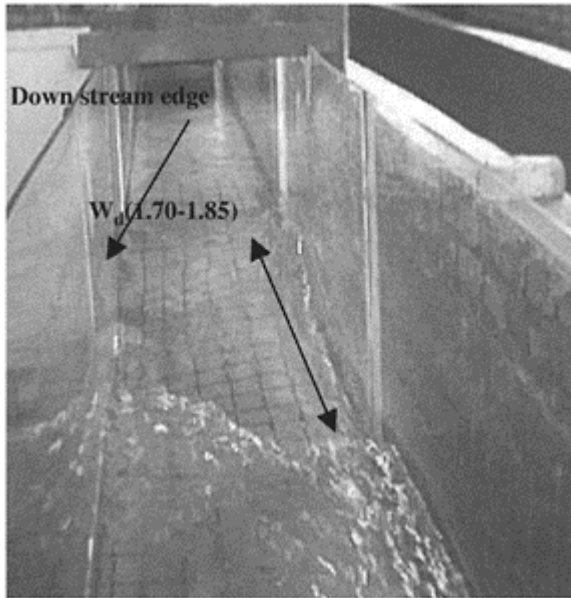


Figure 7. Position of hydraulic jump.

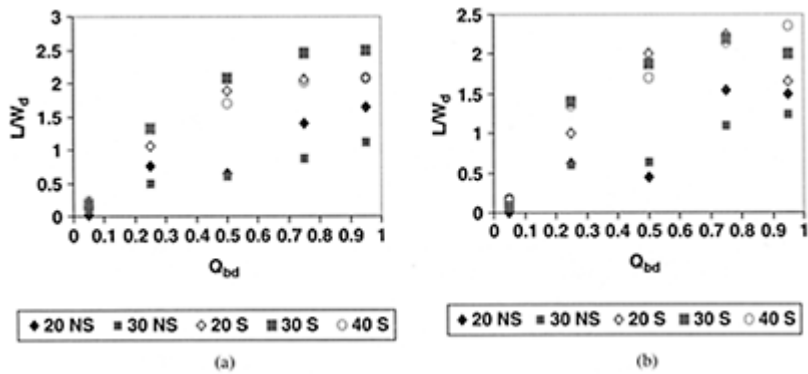


Figure 8. Dimensionless separation length for different connections including width of the branch channel (20, 30 and 40 cm) and the connection shape (sharp S and non-sharp NS), a) $W_{bd}=0.5$, b) $W_{bd}=0.75$.

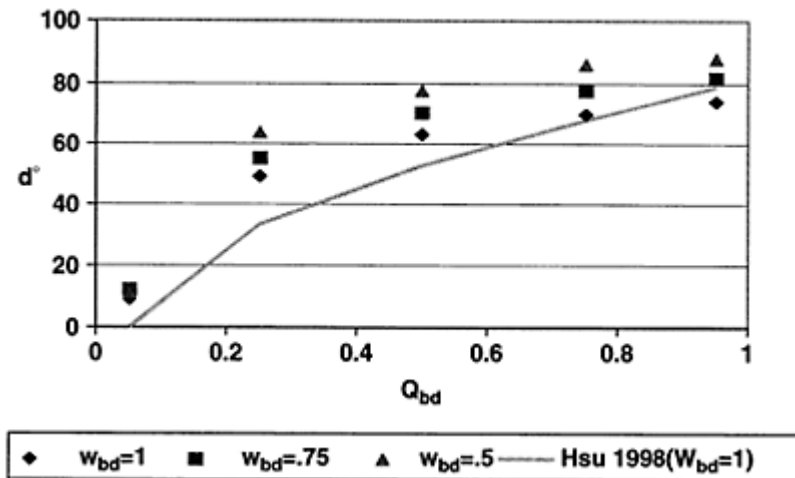


Figure 9. \bar{d} value for different W_{bd} ratios.

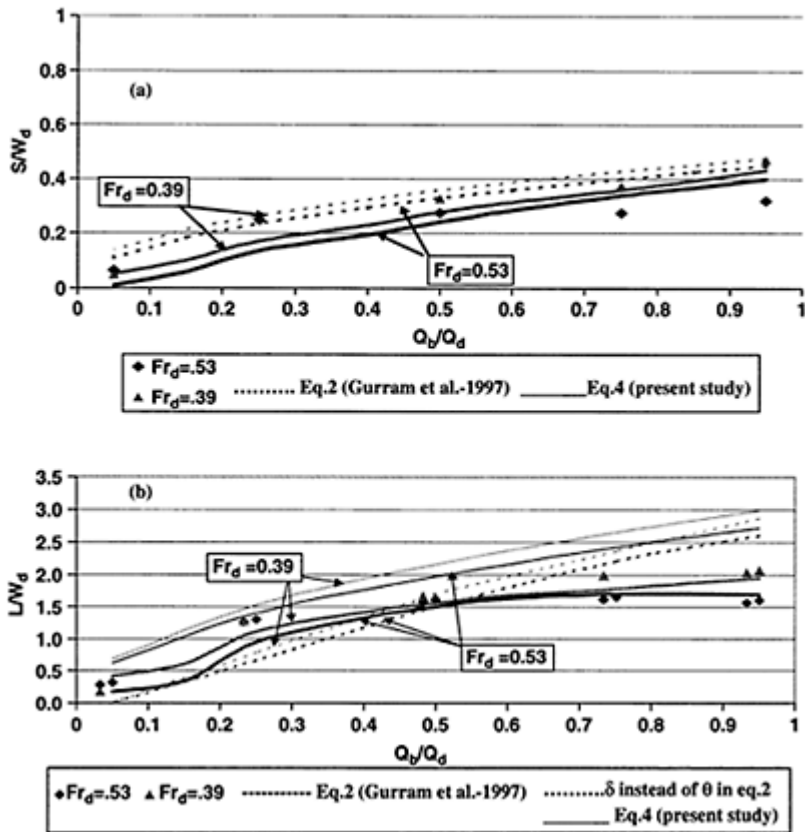


Figure 10. Comparison between present data, proposed equations and Gurram et al. (1997), a) width of separation zone, b) length of separation zone.

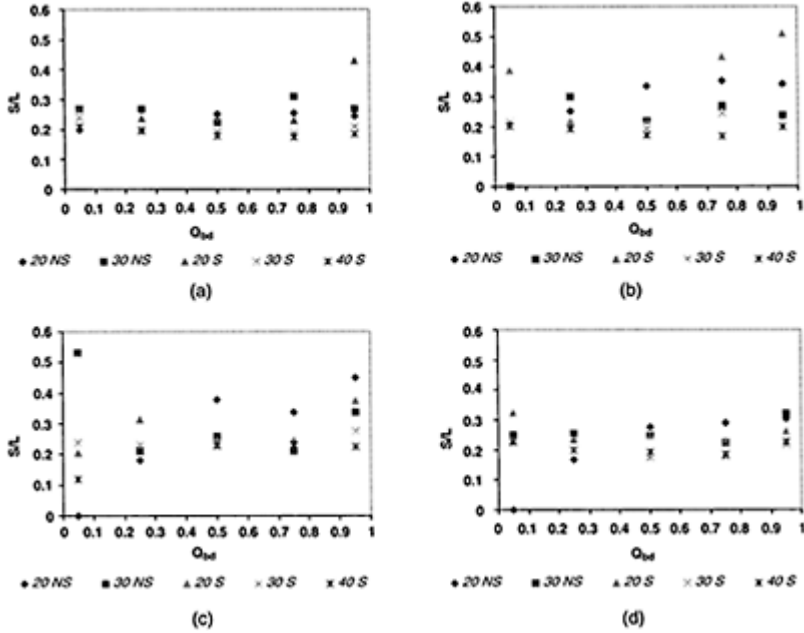


Figure 11. Shape index versus relative discharge, a) $Fr_d=0.46$, b) $Fr_d=0.53$, c) $Fr_d=0.22$ and d) $Fr_d=0.39$.

Thus, the following relations, according to the present data are proposed;

$$\frac{S}{W_d} = \frac{1}{2} \left(Fr_d - \frac{2}{3} \right)^2 + 0.45 Q_{bd}^{0.5} \left(\frac{\delta}{90^\circ} \right) \quad (3)$$

$$\frac{L}{W_d} = \begin{cases} 3.8[(\sin^3 \delta (1 - \frac{1}{2} Fr_d) Q_{bd}^{\frac{1}{2}} - (1 - Fr_d)^3 (Q_{bd} - 0.5)), Q_{bd} < 0.5 \\ 3.8[(\sin^3 \delta (1 - \frac{1}{2} Fr_d) Q_{bd}^{0.5} - Fr_d (Q_{bd} - 0.5)), Q_{bd} \geq 0.5 \end{cases} \quad (4)$$

These results together with Gurram et al. (1997) are shown in Figure 10.

4.5 Shape index (S/L)

Shape index (width to length of separation zone, S/L) for different Fr_d , W_{bd} and connections are shown in Figure 11.

Best et al. (1984) and Hsu et al. (1998) suggested that the mean value of shape index (S/L) is 0.19 and 0.17 respectively for equal width ($W_{bd}=1$). Present study shows that other variables have considerable effects on shape index value, as shown in Figure 12. Therefore, the assumption of $0.17 < S/L < 0.19$ has a very limited workability.

5 CONCLUSIONS

Concluding results from the present experimental tests of equal ($W_{bd}=1$) and non-equal width ($W_{bd}=0.5$ and 0.75) and, also, sharp (S) and non-sharp (NS) connections at 90° open channel

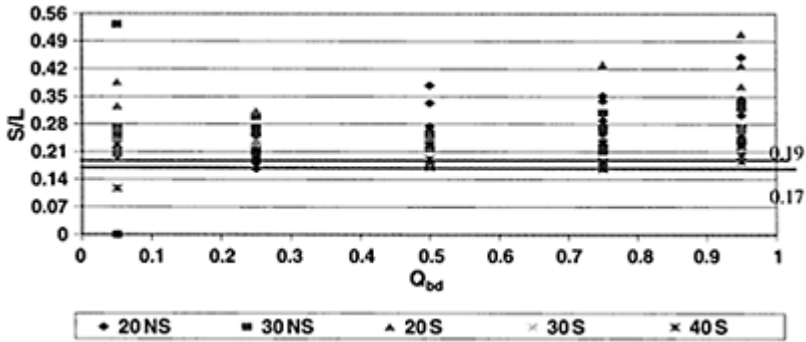


Figure 12. Shape index for all data in present study.

junction are:

- Non-sharp connection at 90° junction reduces the separation zone dimensions and hence a limited disturbed area is obtained.
- Decreasing branch to main channel width ratio has the following effects: a) Reflection effect and shortening the separation zone length. b) Increasing the average inlet flow angle from branch to main channel.
- Using flow entrance angle δ rather than channel connection angle (θ), gives a better estimation of the length and width of separation zone.
- The shape index value (S/L) depends on channel geometry and has a variable value contrary to previous assumptions of 0.17 to 0.19. The value can be as high as 0.45 depending on the conditions.

ACKNOWLEDGEMENTS

The support of Sharif Univ. of Technology, Iran Water Resources Management Organization and Sabir Co. affiliated to the Iranian Ministry of Energy are acknowledged.

REFERENCES

- Best, J. L. & Reid, I. 1984. Separation zone at open-channel junction. *Hydraulic Engineering*. ASCE, Vol. 110, No. 11:1588–1594.
- Biron, R, Best, J.L. & Roy, A.G. 1996. Effects of bed discordance on flow dynamics at open-channel confluence. *Hydraulic Engineering*, ASCE, Vol. 122, No. 12: pp. 676–682.
- Borghei, S.M., Behrangi, A., Daemi, A. 2003. Open-channel junction with different channel width. *Proc. of 30th Intern. IAHR Congress*, 24–29 August, Greece, Theme C: 573–580.
- Christodoulou, G.C. 1993. Incipient hydraulic jump at channel junctions. *Hydraulic Engineering*. ASCE, Vol. 119, No. 3: pp. 409–421.
- Gurram, S.K., Karki, K.S. & Hager, W.H. 1997. Subcritical junction flow. *Hydraulic Engineering*. ASCE, Vol. 123, No. 5: pp. 447–455.
- Gurram, S.K., Karki, K.S. 2000. Discussion of Subcritical open-channel junction flow by Hsu, C.C., Lee, W.J. & Chang, C.H. *Hydraulic Engineering*. ASCE: pp. 87–89.
- Hsu, C.C., Wu, F.S. & Lee, W.J. 1998. Flow at 90 equal width open-channel. *Hydraulic Engineering*. ASCE, Vol. 124, No. 2: pp. 186–191.
- Huang, J., Weber, L.J. & Lai, Y.G. 2002. Three dimensional numerical study of flows in open-channel junctions, *Hydraulic Engineering*. ASCE, Vol. 128, No. 3: pp. 268–280.
- Taylor, E.H. (1944). Flow characteristics at rectangular open-channel junctions. *Trans. ASCE*, 109:893–912.
- Weber, L.J., Schumate, Eric, D & Mawer, N. 2001. Experiments on flow at a 90 open-channel junction. *Hydraulic Engineering*. ASCE, Vol. 127, No. 5: pp. 340–350.
- Weerakoon, S.B., Kawahara, Y. and Tamai, N. 1991. Three dimensional flow structure in channel confluences of rectangular section, *Proc. 25th IAHR Cong.*, A: pp. 373–380.

Boundary shear stress distribution in a V-shaped channel

Mirali Mohammadi

Dept. of Civil Eng., Faculty of Eng., The University of Urmia, Urmia, Iran

Donald W.Knight

*School of Civil Engineering, Birmingham University, Edgbaton,
Birmingham, England*

Hydraulics of Dams and River Structures—Yazdandoost & Attari (eds)

© 2004 Taylor & Francis Group, London, ISBN 90 5809 632 7

ABSTRACT: To understand the lateral distribution of boundary shear stress, a series of measurements was undertaken for velocity and boundary shear stress in fully developed turbulent flow for a V-shaped bottom channel. The distribution results show that for the mild slope channels they are fairly flat, but that for the steep ones this is not the case. The distributions for the steep channels point to the role of secondary currents and cross sectional shape. The percentage shear force carried by the walls, $\%SF_w$, was analyzed. Previous experimental data for other channels were reassessed and were compared with the new experimental data. The results reveal that $\%SF_w$ is favorably correlated with the geometry parameter, P_b/P_w . It was also found that the present channel gives low values of $\%SF_w$ as the aspect ratio, B/h , increases. This result again ratifies the cross sectional shape effects.

1 INTRODUCTION

In open channel flow, it is possible to derive a simple formula that allows evaluation of the mean boundary shear stress acting over the wetted perimeter of the channel. In order to understand the general 3D flow structures, however the lateral distribution of boundary shear stress needs to be explored. The well-known Navier-Stokes equations have already been used for extraction of turbulent flow structures (see Schlichting, 1979), where express the mean and fluctuating velocity components. In this case, the boundary shear stress, τ_b , has an important role. The pattern and number of secondary flow cells as well

as channel cross sectional shape will influence the lateral distribution of boundary shear stress.

Einstein (1942) developed the first method to estimate mean shear stresses at the bed and at the walls in an open channel. Meyer-Peter and Muller (1948) presented a similar method to Einstein's, without making any reference to it. Taylor (1961) concluded that the Einstein method was appropriate to evaluate friction with an aspect ratio smaller than 0.5. Johnson (1942) admitted the convenience of using the friction logarithmic law with Einstein's method. Vanoni & Brooks (1957) refined Johnson's method and explained how to separate bed and wall shear stresses. The ASCE (1975) recommended to using the Vanoni & Brooks method, warning about possible deficiencies in the estimation of the friction factor. ASCE, however advises about making direct measurements to obtain true values of shear stress at the bed and at the walls since there is not any experimental support in Vanoni & Brooks's method.

Many researches have considered the shear distribution problem by obtaining local shear stress as a fraction of the total shear stress and as a function of the aspect ratio B/h , where B is the channel width and h is the flow depth, e.g. Lundgren & Jonsson (1964), Rajaratnam & Muralidhar (1969), Ghosh & Roy (1970 & 1972), Knight & MacDonald (1979a & 1979b), Knight (1981), Knight & Demetriou (1984), Knight & Patel (1985), Knight et al. (1992 & 1994), Sterling (1997), and Mohammadi (1998, 2000 & 2002). These authors studied smooth channels, separately from rough channels.

In this paper, to investigate the hydraulic characteristics of a V-shaped bottom channel, several series of experiments were conducted for measuring boundary shear stress around wetted perimeters (see Fig. 1 for channel cross-section). A Preston tube was used for measuring dynamic pressures

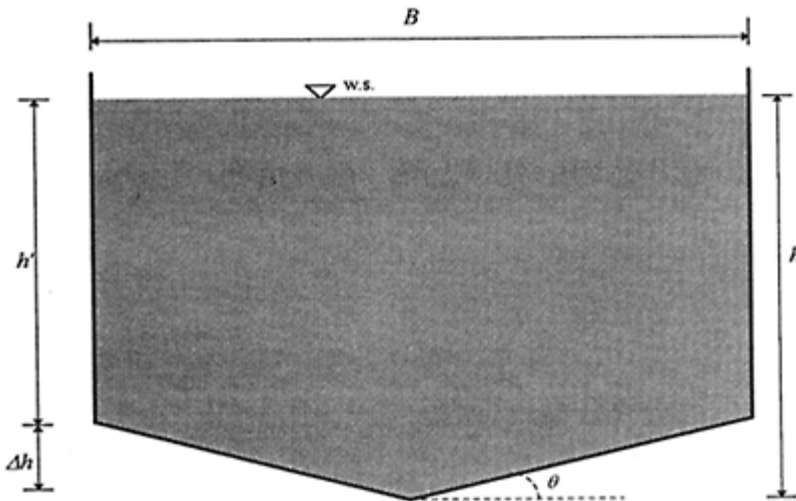


Figure 1. Geometry of the V-shaped channel and notation: $B=460$ mm, $\Delta h=50$ mm; $h_{max}=300$ mm.

to evaluate boundary shear stress and shear force. For a certain channel bed slope, a discharge was introduced and uniform flow was established using stage-discharge results and discharge-tailgate relationships. For every set of flows both point velocities in cross section and dynamic pressures in contact with channel boundary were measured at the same flow condition. For both velocity and boundary shear stress, the data are analyzed from a variety of different perspectives, and the results from each analysis are used to interpret the mechanics occurring in the flow. The findings from each perspective complement each other and highlight the consistency of the experimental data.

It is intended to verify that the experimental data related to shear stress show similar results for open channels and rectangular ducts if they keep geometric similitude. It is also intended to find the influence of cross sectional shape on shear stresses at the boundary. Finally, the paper deals with the presentation of some existing experimental data on boundary shear stress, together with analysis of the results obtained so far. The associated discussions will also be presented.

2 BOUNDARY SHEAR STRESS MEASUREMENTS TECHNIQUE

Various techniques have been developed to determine boundary shear stress, a thorough review of which is given by Winter (1977). The most widely adopted and applicable technique for use in water was first proposed by Preston (1954) and consists of placing a Pitot tube in contact with a boundary surface. The technique is based on the law of the wall outlined by Mohammadi (1998) or elsewhere which assumes that near the surface the velocity distribution can be expressed as:

$$\frac{u}{u_*} = f\left(\frac{zu_*}{\nu}\right) \quad (1)$$

Using dimensional analysis, Preston assumed that the pressure acting on the open end of the tube could be expressed by

$$\frac{\Delta P \cdot d^2}{\rho \nu^2} = F\left(\frac{\tau_0 \cdot d^2}{\rho \nu^2}\right) \quad (2)$$

where ΔP is the difference between the dynamic and static pressures, d is the external diameter of the tube, ν is the liquid kinematics viscosity, and τ_0 is the local boundary shear stress. The function F is not universal and inevitably depends on the function f used in equation (1). Although Preston provided various expressions for F , experiments undertaken by Smith & Walker (1958), Bradshaw & Gregory (1958) cast doubt on these expressions, while data from Haeed & Rechenberg (1962) supported the earlier relationships. This lack of consistency promoted Patel (1965) to “*produce what is currently regarded as a definitive calibration*”, (Winter, 1977). Patel’s calibration is given in terms of x^* and y^* where:

$$x^* = \log\left(\frac{\Delta P \cdot d^2}{4\rho \nu^2}\right) \quad y^* = \log\left(\frac{\tau_0 \cdot d^2}{4\rho \nu^2}\right) \quad (3)$$

Since the velocity distribution can effectively be considered to consist of three different regions (i.e. a viscous sublayer, buffer layer and logarithmic layer), the calibration for x^* and y^* is expressed by three different formulas, For example, when

$$\begin{aligned} y^* < 1.5y^* &= 0.5x^* + 0.037 \\ 1.5 < y^* < 3.5y^* &= 0.8287 - 1.1381x^* + 0.1437x^{*2} - 0.0060x^{*3} \\ 3.5 < y^* < 5.3x^* &= y^* + 2 \log(1.95y^* + 4.10) \end{aligned} \quad (4)$$

For many years the Preston tube has been used as outlined above. The technique adopted for this series of experiments follows the method and calibration by Patel (1965). For fully developed turbulent flow boundary layer encompasses the whole depth of flow.

3 EXPERIMENTAL APPARATUS AND PROCEDURE

To investigate the hydraulic characteristics of a V-shaped bottom channel, several series of experiments were conducted for measuring boundary shear stress around wetted perimeters. The experimental channels were built inside the existing 15 m long tilting flume. A Preston tube was used for measuring dynamic pressures to evaluate boundary shear stress and shear force. For a certain channel bed slope, a discharge was introduced and uniform flow was established using stagedischarge results and discharge-tailgate relationships. The flume was supported by two hydraulic jacks and rotated about a hinge joint beneath the middle of the channel. The flume also had a motorized slope control system with a mechanical visual read out on a ruler at the upstream end of the flume used for determining the precise channel bed slope.

The maximum slope obtainable was $S_0=2\%$. The experimental channels, with a V-shapedbottom cross section built by using PVC panels to make a 14.5 m long channel having 50mm crossfall, were built along the inside centerline of the existing flume. Water was supplied to the channel by an overhead tank through a 101.6 mm pipeline for discharges up to 30 l/s and a 355.6 mm pipeline for discharges higher than 30 l/s. To reduce large-scale disturbances, and in order to ensure that the flow was uniformly distributed, a system of honeycombing was placed at the upstream end of the channel where the entrance tank and bell-mouth shaped inlet transition section were located. However for the case of supercritical flow i.e. $Fr>1$ the honeycomb was not very useful. Individual bell-mouth shaped transition sections were designed and made for each channel types and served to reduce separation and improve the development of the mean flow into the channels. Discharge measurements (up to 30 l/s) were made by means of a Venturi meter connected to mercury and air/water manometers at the head of the flume. An electromagnetic flow meter was also installed in the supply line after the Venturi and was used to check discharges. For the case of higher discharges a dall-tube connected to an air/water manometer was used in the 355.6 mm diameter supply line.

The flume had a very rigid bottom designed for high loads, and therefore it was not necessary to do any deflection tests. A slatted tailgate weir was installed in the downstream end of the channel in order to minimize upstream disturbance of the flow, and hence allowed a greater reach of the channel to be employed for experimental measurement in subcritical flows. The test section consisted 12m long zone, commencing at a distance of 1.25m from the channel entrance and 1.85 m from the flume entrance.

However, for supercritical flows, because of the S2 profiles, the test length was reduced to about 7 m. A trolley was mounted on rails running along the flume with a depth probe, having an electrical contact to the water surface level (accurate to 0.1 mm) and hence the channel bed slope was obtained. It has also been possible to do lateral measurements using the same trolley. The depth was measured at 1 m and sometimes half a meter intervals in the test length by means of a centerline pointer probe moved down from the instrument carriage.

The present research work deals with the boundary shear stress measured around the wetted perimeter. Local boundary shear stress was measured using the Preston tube technique with a probe having 4.705 mm outer diameter. The tube was mounted on a carriage and aligned vertically near the walls and normal to the bed. It was also placed on the channel boundary every 10mm intervals on the vertical walls and every 20 mm intervals on the bed in the spanwise direction. The total pressure arising from the difference between the static and dynamic pressures were recorded by connecting the tube to a simple manometer inclined at 12.52° to the horizontal. The static pressure was measured separately using a Pitot static tube at the centerline of the measuring section, and at least 5 minutes allowed to achieve an accurate reading.

4 BOUNDARY SHEAR STRESS DISTRIBUTION

It is important to notice the general 3D flow structures that exist in straight or curved prismatic channels, in order to understand the lateral distribution of boundary shear stress. The distributions are well established by reference to the governing equations and illustrative sketches published by various researchers. Mohammadi (1998 & 2002) highlight some of the significant studies related to the subject. The pattern and number of secondary flow cells however can affect the lateral distribution of boundary shear stress, as described elsewhere by Perkins (1970), Gessner (1973), Knight et al (1982), and Knight & Patel (1985). Figure 2 shows an example of isovel plots and the relationship between boundary shear stress distribution, secondary flow cells and primary flow in a trapezoidal channel, for the case of $Fr < 3.24$, $B/h = 1.52$. The phenomenon is very difficult to examine without referring to both the flow cells and the shear stress distributions. In order to achieve this, various tests were carried out in a V-shaped bottom channel and in a part-full pipe channel, using a Preston tube and the method described by Mohammadi (1998). From experimental results, it is therefore possible to analyze such parameters as percentage wall shear force, apparent shear stress & shear force, local friction factor and eddy viscosity using the velocity and boundary shear stress data.

4.1 *Boundary shear stress results and analysis*

Local dynamic pressures were measured using a 4.075 mm outer diameter Preston tube at 10mm interval spacing in the spanwise direction along the bed perimeter. Although the channel cross sections are symmetric, the measurements were carried out along the whole wetted perimeter for all tests conducted. Thus the lateral distribution results presented in this paper are the actual measured data for both sides of the channels central axis line.

The recorded dynamic pressures were converted to the local boundary shear stress values using the Patel calibration equations given by equations 3 & 4.

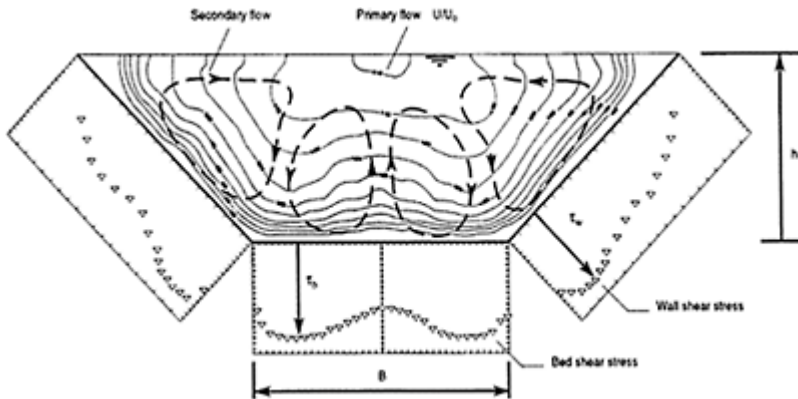


Figure 2. A typical relationship between boundary shear stress distribution, secondary flows and primary flow in a trapezoidal channel, $Fr < 3.24$, $B/h = 1.52$ (after Knight et al. 1994).

Figures 3 & 4 show the boundary shear stress distributions adjusted to the mean energy slope, $pgRS_0$ for flow rates of 50 & 125.891/s respectively, at different channel bed slopes, S_0 , of 0.2%, 0.4%, 0.9% & 1.6%. These Figures are some examples of the experimental results undertaken for this channel shape. The Froude numbers are less than 1.0 for 0.2% and 0.4% bed slopes and consequently the flows are in subcritical condition. For the cases of 0.9% and 1.6% bed slopes, the Froude numbers are higher than 1.0 and consequently the flows are in super critical condition. As can be seen from those Figures, the distributions are very flat along the spanwise direction. However when the flow discharge increases i.e. the flow depth decreases for a certain channel bed slope, the perturbations about the mean begin to appear. This is because the aspect ratio changes and consequently the cross sectional shape and secondary flow cells size or perhaps cells numbers influence the flow behavior. It has also been seen that the maximum value of bed shear stress tends to occur at around the channel centerline for higher flow rates. However its position alters with flow discharge. The minimum values of bed and wall shear stresses belong to the corner regions of the channel cross section close to the vertical walls. The maximum value of wall shear stress and its location also varies, as the flow depth increases.

In the case of higher Froude numbers i.e. steeper channels and even large discharges, there are more severe perturbations in the distributions. There is also a significant variation of boundary shear stress across the channel bed and walls, especially at high Froude numbers. The perturbations in those Figures may indicate the size and number of

the secondary flow cells as suggested by Perkins (1970), Knight & Patel (1985) and others. These perturbations have already been observed

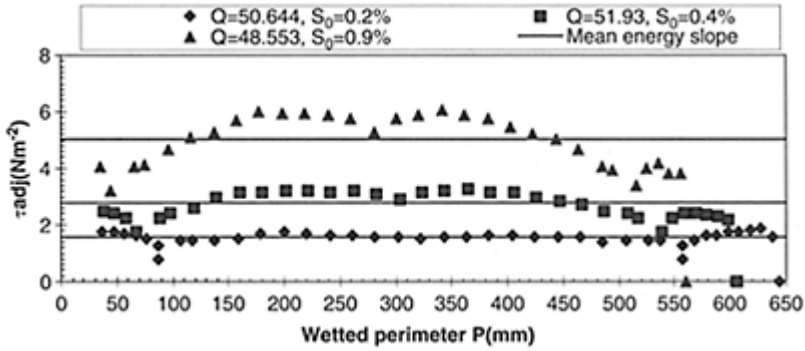


Figure 3. Lateral distribution of boundary shear stress, adjusted to the mean energy slope value: $Q=50$ l/s.

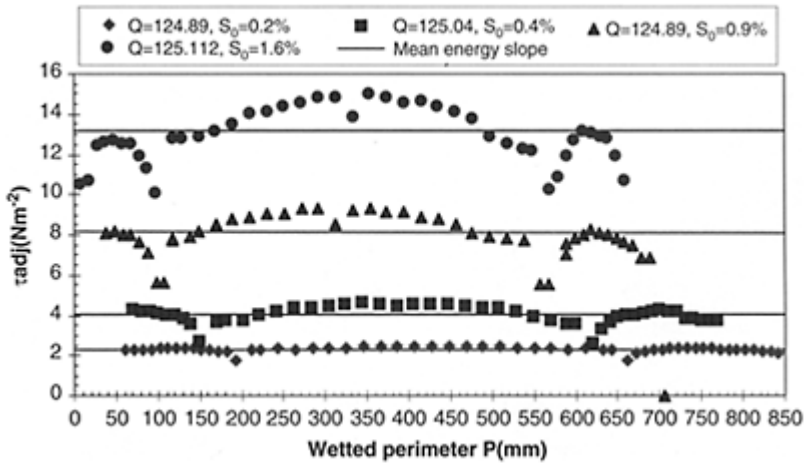


Figure 4. Lateral distribution of boundary shear stress, adjusted to the mean energy slope: $Q=125$ l/s.

in the velocity contours and depth-averaged velocity results (see Mohammadi, 1998). This leads to a view that for a certain flow depth, as the channel gets steeper, the number of secondary flow cells are more than those for a mild slope, but the size of the cells for mild slope channels are greater than that of the steeper ones. It should be noted that the small size of secondary flow cells with increasing numbers may generate more energy than those of the larger cells with decreasing numbers. This phenomenon plays an

important role in the sediment-laden channels and also affects the incipient motion of the sediment particles, as described by Mohammadi & Knight (1999) and Mohammadi (2002).

The Figures also indicate that the values of wall shear stress are sometimes higher than that of the mean energy slope values at low Froude numbers. This means that the effect of wall should not be ignored for low aspect ratios in terms of shear stress analysis as well as sediment transport issues.

5 BOUNDARY SHEAR FORCE ANALYSIS

Applying the concept of shear force, based on the reach shear force acting on the wetted perimeter per unit streamwise length, the mean bed and wall shear forces may be separated along the channel boundary. The total shear force per unit length, SF_t , acting on the total wetted perimeter, P , of a prismatic channel may be obtained. Thus for any channel cross section it can be written as

$$\begin{cases} SF_t = SF_w + SF_b \\ SF_w = P_w \bar{\tau}_w \\ SF_b = P_b \bar{\tau}_b \\ \%SF_w = 100SF_w/SF_t \\ \%SF_b = 100SF_b/SF_t \end{cases} \quad (5)$$

where, SF is the shear force, $\%SF$ is the percentage of shear force multiplied by 100, $\bar{\tau}$ is the mean shear stress, and the subscripts w and b denote walls and bed, respectively. SF_t is the total shear force acting on the whole wetted perimeter given by

$$SF_t = \tau_0 \cdot P = (pgRS_f) \cdot P = pgAS_f \quad (6)$$

To obtain the relationship between the percentage of the shear force carried by the walls an alternative approach is to use

$$\%SF_w = \frac{100}{\left(1 + \frac{P_b}{P_w} \frac{\bar{\tau}_b}{\bar{\tau}_w}\right)} \quad (7)$$

based on the regression analysis using a power law for the application of this approach to duct flows). Flintham & Carling (1988) utilized the Knight et al (1984) equation for $\%SF_w$ in rectangular channels to the trapezoidal ones by substituting (bed length over total wall length) for the aspect ratio, Blh . They proposed an equation for smooth and uniformly roughened trapezoidal channels, and by modifying one of the constants, it was applied to the differentially roughened channels. The same type of equations may be applied for any V-shaped bottom channel given by (see Fig. 1 for channel cross section and notation)

$$\frac{\bar{\tau}_w}{\rho ghS_f} = \left\{ \frac{\%SF_w}{100} \right\} \left[\frac{B(h + h')}{4hh'} \right] \quad (\text{for the walls}) \quad (8a)$$

$$\frac{\bar{\tau}_b}{\rho g h S_f} = \left\{ \frac{\%SF_b}{100} \right\} \left[\frac{s(h+h')}{2h\sqrt{1+s^2}} \right] \quad (\text{for the bed}) \quad (8b)$$

where, h is the whole depth, h' is the length of vertical wall, and s is the side slope of the bottom side sections on bed ($=\cot\theta$).

5.1 Percentage wall shearforce, $\%SF_w$, analysis and discussion

As mentioned in the previous section, the total shear force per unit length of the wetted perimeter, SF_b , is the sum of the individual shear forces carried by the walls and bed, which can be obtained from the integrated mean boundary shear stress values multiplied by the perimeters of their related

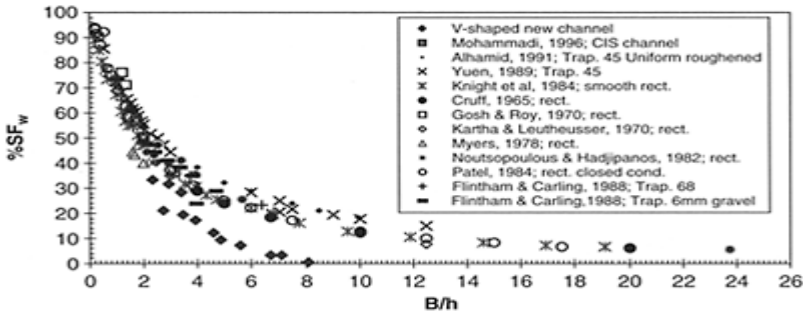


Figure 5. A comparison of $\%SF_w$ versus B/h for the V-shaped bottom channels together with data from other channel shapes.

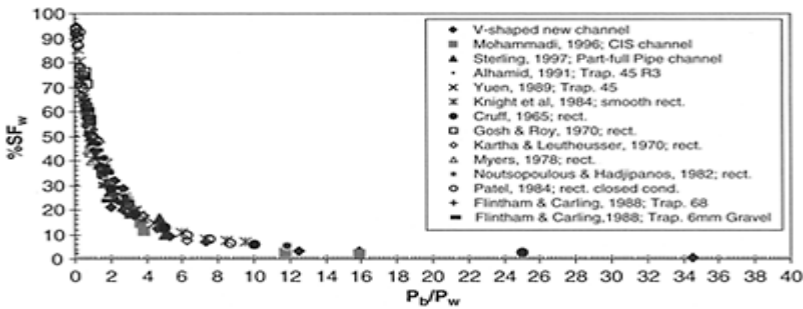


Figure 6. A comparison of $\%SF_w$ versus P_b/P_w for the V-shaped bottom channels together with data from other channel shapes.

sub areas (see eq. 5). The corresponding equation used for calculating the $\%SF_w$ in a V-shaped bottom channel is given by equation 8a. This equation shows that the $\%SF_w$ only varies in the same way as the geometry of the channel, i.e. in proportion to the perimeter ratio if $\bar{\tau}_b = \bar{\tau}_w$.

It has often been suggested that the aspect ratio, B/h , and the wetted perimeter ratio, P_b/P_w , should be used to characterize the channel shape. The percentage shear force carried by the walls, $\%SF_w$, of such a channel shape may be related to the mean boundary shear stresses $\bar{\tau}_b$ and $\bar{\tau}_w$ acting on the bed and walls. There is much evidence such as Replogle & Chow (1966), Perkins (1970), Naot & Rodi (1982), Knight et al. (1982, 1984, 1992 & 1994), Flinham & Carling (1988), and Shiono & Knight (1991) to suggest that even in smooth and homogeneously roughened channels, the mean shear stress varies considerably due to the 3D turbulence and streamwise velocity effects. A comparison of the $\%SF_w$ relationship for a V-shaped bottom channel and a comparison made with the other channel shapes.

To compare the present channels results with previous work carried out for the other channel shapes, the $\%SF_w$ values are shown plotted versus B/h and P_b/P_w in Figs. 5 & 6, respectively. It can be seen from Figure 5 that regarding different cross sectional channel shapes the present channel data follows trends in previous data. For example, Figure 5 clearly shows that the trapezoidal channel gives a higher $\%SF_w$ than that of the rectangular channel for a given value of B/h , and the V-shaped bottom channels give a lower $\%SF_w$ than that of the rectangular channel, especially as the aspect ratio increases. The reason for this is that as the flow discharge increases in a trapezoidal channel, the aspect ratio decreases, while for a rectangular and V-shaped bottom channels the aspect ratio reduces. This is also true for the V-shaped channel i.e. in a certain value of B/h . This finding verifies that the V-shaped bottom channels have almost a similar behavior as homogeneously smooth and roughened rectangular open channels and duct flows at low aspect ratios. However, at large aspect ratios there is some disagreement. This is due to a particular V-shaped bottom of such a channel which arises its effect at low flow depths i.e. higher aspect ratios.

Another argument is due to the separation of bed and walls for these channel shapes, because there is no clear distinction between wall and bed regions for this channel shape. Thus the question is that: can the whole triangular bottom be accounted as a bed part for a V-shaped bottom channel? Figure 6, however, illustrates that the present channel data is in good agreement with previous studies on rectangular, trapezoidal and part-full pipe channels, provided the wetted perimeter ratio is used instead of aspect ratio. This finding supports the previous discussion that for any channel shapes the wetted perimeter ratio, P_b/P_w , is more representative than the aspect ratio, B/h .

6 CONCLUDING REMARKS

Boundary shear stress measurements have been undertaken in the uniform flow condition for five target flow discharges of 10, 25, 50, 85 & 125 l/s at four different channel bed slopes of 0.2%, 0.4%, 0.9% & 1.6%. In addition 16 different flow conditions were examined for velocity and the same 16 for boundary shear stress, in a V-shaped bottom channel. Herein, some sets of experiments are presented. Therefore a considerable

amount of data has been collected and the associated parameters have been analyzed. The main results and findings are as follows:

1. It appears from the boundary shear stress results that the lateral distributions are very flat at low Froude numbers. Thus for a certain flow discharge the active width decreases as the Fr number increases (i.e. the channel gets steeper).
2. The distributions of boundary shear stress show that at the free surface, the boundary shear is not necessarily zero, as often assumed in certain computational models.
3. The effect of multiple pairs of secondary flow cells was evident in the perturbations of the boundary shear stress for both subcritical and supercritical flows. Although at low flow depths where the Froude number is not so high, i.e. greater aspect ratios. Perturbations in the boundary shear stress distributions were more easily detected using the Preston tube technique.
4. The number of perturbations, and hence the number of secondary flow cells, has been shown to be dependent on the flow depth and discharge i.e. the aspect ratio. Up to three pairs of flow cells can be detected at a large discharge in a steep channel with a V-shaped bottom (see Figs. 3 & 4).
5. The proportion of the total shear force which acts on the walls have been shown to be dependent on the Froude number, Reynolds number and aspect ratio. The percentage wall shear force, $\%SF_w$, depends primarily upon the aspect ratio, B/h , and the bed to wall wetted perimeter ratio, P_b/P_w , in an exponential manner, as first introduced by Knight (1981).
6. A comparison of the $\%SF_w$ results for the V-shaped bottom channels with previous work on rectangular, trapezoidal, and part-full pipe channels are presented (Figs. 5 & 6). These Figures show that there is a significant difference for the different channel shapes. For example, at high aspect ratios the trapezoidal channel gives a higher $\%SF_w$ than that of rectangular channel, and the V-shaped bottom channels give a lower $\%SF_w$ in a certain aspect ratio.
7. It can be seen from Figures 5 & 6 that the wetted perimeter ratio, P_b/P_w , was found to account for the channel shapes properly, and that the $\%SF_w$ correlated better with this ratio than the aspect ratio, B/h . This is also the case for trapezoidal channels, as pointed out by Yuen (1989), Alhamid (1991), and Knight et al (1994).
8. The $\%SF_w$ values increase as the Re numbers increases. However, the $\%SF_w$ values decrease as the Fr numbers increases.
9. There is a strong evidence of cross sectional shape effects on the distribution of boundary shear stress.
10. The information in this paper may prove useful to any computational modelers dealing with channels with a similar shape. The work may also be valuable to river engineers trying to solve stable channel problems as well as sediment transport in channels with side slopes, similar to channels with a V-shaped bottom.

REFERENCES

- ASCE, 1975. *Sedimentation Engineering*. Edited by Vanonni V. , Denver, Colorado.
- Bradshaw, P. & Gregory, N. 1959. The Determination of Local Skin Friction fro Observations in the Viscose Sublayer, *National Physics Laboratory, Reports and Memoranda*, No. 3203, March.

- Cruf, R.W. 1965. Cross section Transfer of Linear Momentum in Smooth Rectangular Channel, *Geological Survey Water Supply*. paper 1592-B, U.S. Government Printing Office, Washington D.C.
- Einstein, H.A. 1942. Formulas for the Transportation of Bed-Load. *Transactions of the ASCE*, Vol. 107, 2140.
- Flintham, T.P. & Carling, P.A. 1988. The Prediction of Mean Bed and Wall Boundary Shear in Uniform and Compositely Rough Channels. International Conference on River Regime, ed. White W.R., Hydraulic Research Ltd., pp. 153–162, May.
- Gessner, F.B. 1973. The Origin of Secondary Flow in Turbulent Flow along the Corner. *J. of FluidMechanics*, Vol. 58, Part 1, pp. 1–25.
- Ghosh, S.N. & Roy N. 1972. Boundary Shear Distribution in Channels with Varying Bed Roughness. *Proceeding of the Institution of Civil Engineers*, Vol. 53, Paper 7572, pp. 529–544. London, England.
- Ghosh, S.N. & Roy, N. 1970. Boundary Shear Distribution in Open Channel Flow. *J. Hydraulics Div., ASCE*, Vol. 96, HY4, pp. 967–994.
- Head, M.R. & Rechenberg, I. 1962. The Preston Tube as a means of Measuring Skin Friction. *J. Fluid Mechanics*, Vol. 14, UK.
- Johnson, J.W. 1942. The Importance of Side Wall Friction in Bed-load Investigation. *Proceeding of the Institution of Civil Engineering*. June. Vol. 12, No. 6, 339–331, London, England.
- Kartha, V.C. & Leuthesser, H.J. 1970. Distribution of Tractive Force in Open Channels, *J. Hydr. Div., ASCE*, Vol. 96, HY7, pp. 1469–1483, July.
- Knight, D.W. & MacDonald J.A. 1979a. Open Channel Flow with Varying Bed Roughness. *J. of Hydraulics Division, ASCE*, Vol. 105, No. HY9, Proc. Paper 14839, pp. 1167–1183.
- Knight, D.W. & Macdonald, J.A. 1979b. Hydraulic Resistance of Artificial Strip Roughness. *J. of Hydraulics Division, ASCE*, Vol. 105, No. HY6, Proc. Paper 14635, pp. 675–690.
- Knight, D.W. & Patel, J. 1985. Boundary Shear in Smooth Rectangular Ducts. *J. of Hydraulics Division, ASCE*, Vol. 111, Proc. Paper 19408, pp. 29–47.
- Knight, D.W. 1981. Boundary Shear in Smooth and Rough Channels. *J. of Hydraulics Division, ASCE*, No. HY6, Proc. Paper 16364, pp. 839–852.
- Knight, D.W., Alhamid, A.A.I & Yuen, K.W.H. 1992. Boundary Shear in Differentially Roughened Trapezoidal Channels, in Hydraulic and Environmental Modeling. Estuarine and River Waters, Ch. 1, (eds. R.A. Falconer, K.Shiono & R.G.S.Mathew), aSHGATE, pp. 3–14.
- Knight, D.W., Demetriou, J.D. & Hamed, M.E. 1984. Boundary Shear in Smooth Rectangular Channels, *J. of the Hydraulic Eng., ASCE*, Vol. 110, No. 4, April, pp. 405–422.
- Knight, D.W., Patel, H.S. Demetriou, J.D. & Hamed, M.E. 1982. *Boundary Shear Stress Distributions in Open Channel and Closed Conduit Flows*, Proc. Euromech 156 the Mechanics of Sediment Transport, Istanbul, July, A.A.Balkema, Rotterdam, Netherlands, pp. 34–40.
- Knight, D.W. Yuen, K.W.H. & Alhamid, A.A.I 1994. *Boundary Shear Stress Distributions in Open Channel Flow*, in *Physical Mechanisms of Mixing and Transport in the Environment*, Ch. 4, (ed. K. Beven, P.Chatwin & J.Millbank), J.Wiley, pp. 51–87.
- Lundgren, H. & Jonsson, I.G. 1964. Shear and Velocity Distribution in Shallow Channels, *J. Hydraulics Div., ASCE*, Vol. 90, HY 1, January.
- Meyer-Peter, E. & Muller, R. 1948. Formulas for Bed-Transport. *Second Meeting of the IAHR*, Annex 2, pp. 39–64. Stockholm, Sweden.
- Mohammadi, M. & Knight, D.W. 1999. Threshold Condition for a V-shaped Channel. *Proceeding XXVIII IAHR Congress*, Graz, Austria.
- Mohammadi, M. 1998. *Resistance to Flow and the Influence of Boundary Shear Stress on Sediment Transport in Rigid Boundary Channels*. PhD Thesis, School of Civil Engineering, The University of Birmingham, England.
- Mohammadi, M. 2000. Shape Effects on Boundary Shear Stress Distribution in Open Channels, *Proceeding 5th International Conference on Civil Eng.* Ferdosi University, Mashhad, Iran.

- Mohammadi, M. 2002. *Boundary Shear Stress Distribution in Open Channels having Different Cross Sections*. A Research Report submitted to the Research Department of Urmia University, Urmia, Iran.
- Patel, VC. 1965. Calibration of the Preston Tube and Limitations on Its Use in Pressure Gradients, *J. Fluid Mechanics*, Vol. 23, Part 1, pp. 185–208.
- Perkins, H.J. 1970. The Formation of Streamwise Vorticity in Turbulent Flow, *J. Fluid Mechanics*, No. 44, Part 4, pp. 721–740.
- Preston, J.H. 1954. The Determination of Turbulent Skin Friction by Means of Pitot Tube, *J. Royal Aeronautical Society*, Vol. 58, February.
- Rajaratnam, N. & Muralidhar, D. 1969. Boundary Shear Distribution in Rectangular Open Channels, *La Houille Blanche*, No. 6, pp. 603–609.
- Replogle, J.A. & Chow, V-T. 1966. Tractive Force Distribution in Open Channels, *J. Hydr. Div., ASCE*, Vol. 192, No. 2, pp. 169–191.
- Rhodes, D.J. 1991. *An Experimental Investigation of the Mean Flow Structure in Wide Ducts of Simple Rectangular and Trapezoidal Compound Cross-section, Examining in Particular Zones of High Lateral Shear*, PhD Thesis, University of Birmingham, Birmingham, England.
- Schlichting, H. 1979. *Boundary Layer Theory*, Seventh ed., McGraw-Hill Classic Text Book Series, New York.
- Shiono, K. & Knight, D.W. 1991. Turbulent Open Channel Flows with Variable Depth across the Channel, *J. Fluid Mechanics*, Vol. 222, pp. 617–646.
- Smith, D.S. & Walker, J.H. 1958. The Use of Surface Pitot Tube as Skin Friction Meters at Supersonic Speeds. *Aero Research Council & M*: 3361.
- Sterling, M. 1997. *The Distribution of Boundary Shear Stress in an Open channel Circular Conduit running Part-full*, PhD Thesis, University of Birmingham, Birmingham, England.
- Taylor, R.H. 1961. Critical Analysis of Open Channel Resistance. *J. of Hydraulics Division, ASCE*, HY4.
- Vanoni, VA. & Brooks, N.H. 1957. *Laboratory Studies of the Roughness and Suspended Load of Alluvial Streams*, Sedimentation Laboratory Report NO. E68, California Institute of Technology, California.
- Winter, K.G. 1977. An outline on the techniques available for the measurements of skin friction in turbulent boundary layers. *Prog Aerospace Science*, Vol. 18, pp. 1–57.
- Yuen, Y.H.K. 1989. *A Study of Boundary Shear Stress, Flow Resistance and Momentum Transfer in Open Channels with Simple and Compound Trapezoidal Cross-section*, PhD Thesis, Birmingham University, Birmingham, England.

10.
Hydroinformatic applications

Cardiff Bay barrage and managing the impounded water quality

R.A.Falconer & B.Lin

School of Engineering, Cardiff University, Cardiff, UK

Hydraulics of Dams and River Structures—Yazdandoost & Attari (eds)

© 2004 Taylor & Francis Group, London, ISBN 90 5809 632 7

ABSTRACT: Cardiff is the capital city of Wales, U.K., with the city having a population of approximately 300,000 and being located some 2 km from its waterfront. In the 1990s, and following an Act of Parliament, a tidal exclusion barrage was built across the mouth of Cardiff Bay, with the aim being to regenerate 1100 ha in the area to the south of Cardiff. The Cardiff Bay Barrage impounded the estuaries of the rivers Taff and Ely, creating a 200 ha freshwater lake and about 13 km of attractive waterfront. In the paper brief details are given of the barrage structure, the loch gates and the auxiliary structures, followed by details of a numerical hydro-environmental model study to predict the hydrodynamic and water quality characteristics within the Bay. Details are also given of a physical model study and a field monitoring programme.

1 INTRODUCTION

Cardiff is the Capital City of Wales and owes much of its prosperity to the coal and iron and steel industries from the early 1800s onwards, see Crompton (2002). Welsh coal was used to power the early iron and steel sea vessels and Welsh iron and steel were used throughout the world. With the rapid expansion of these industries Cardiff developed into one of the world's largest ports with the port reaching its full potential in the period from 1910–1920 see Figure 1.

From the 1920s onwards the coal trade started to decline and shipping moved to oil for power. More competition developed for steel across the U.K. and world-wide, with this decline leading to a



Figure 1. Illustration of Cardiff Port taken in its heyday around 1900.



Figure 2. Illustration of Cardiff Bay and Barrage, showing land-based developments and Cardiff City.

significant closure of steel works in South Wales. The decline in the demand for coal and increased competition for iron and steel led to a severe depression in South Wales from about 1930 and the port of Cardiff was one of the most affected areas. The area continued to decline until the 1980s, when there was growing public opinion that Cardiff needed to be re-connected with its waterfront and that the urban area around the port needed to be regenerated.

In 1987 the UK government decided to set up the Cardiff Bay Development Corporation with a brief to regenerate the area. The Corporation prepared a strategy for regenerating the area with the aim of creating 30,000 new jobs, 840,000m² of industrial development and commercial premises and 6,000 new homes. The strategy was underpinned with a tourism potential of bringing 2 million visitors annually to Cardiff's waterfront (see Crompton, 2002). However, the major problem with Cardiff's existing waterfront at that time was that Cardiff Bay was sited along the Bristol Channel, which experienced the second highest tidal range in the world, with spring tidal ranges being typically 14 m. At low tide Cardiff Bay was virtually dry and the Bay exposed mud-flats for typically 12 h per day. In overcoming the challenge of developing a waterfront in such conditions, it was decided to propose a 1.3 km long tidal exclusion barrage across the mouth of the Bay, impounding the rivers Taff and Ely and creating a 200 ha fresh water lake, with a constant water level. In 1987 the initial legislation was commenced and in 1993 the Cardiff Bay Barrage Act was passed through parliament and given Royal Assent. The barrage was then designed and constructed, and completed in 2001 as shown in Figure 2, with regeneration in the region now well underway, as indicated in Figure 3.

In addition to the barrage and lock gate structures etc, the impoundment of the two rivers and the change of the Bay from an estuary, with extensive flooding and drying, to a freshwater lake would have major changes on the hydro-environmental characteristics and management issues upstream of the impoundment. In particular, following impoundment the main water quality issues needing to be addressed can be summarized as follows:

- The Bay would now experience long retention times, whereas previously the estuary was well flushed with substantial tidal variations—up to 14m during spring tides;
- Several combined sewer overflows (CSOs) discharge directly into the watercourses under wet weather flow conditions, thereby leading to effluent discharges reaching the Bay;
- Nutrient and pathogenic inputs were expected in the form of diffuse source discharges from agricultural runoff etc, which in turn would flow via the rivers into the Bay; and
- Low dissolved oxygen levels were expected in the lower layers of the water column, particularly in the summer months, leading to stratification and interaction with the contaminated sediments.

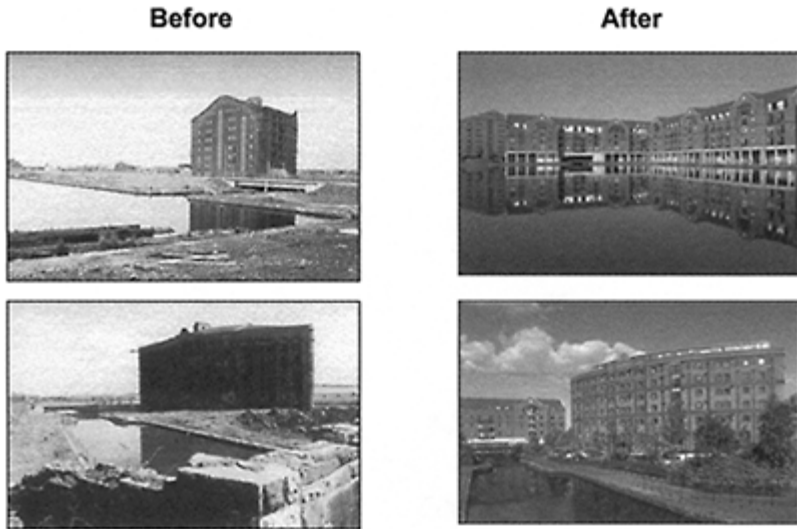


Figure 3. Typical examples of urban regeneration of Cardiff Bay following construction of the barrage.

As a result of some of these concerns the Environmental Water Management Research Centre at Cardiff University undertook a substantial research study to refine and apply an integrated modelling tool for hydro-environmental management of the Bay. The project strategy consisted of integrating a CSO model (namely SWMM), with a 1-D river model (namely FASTER—Flow And Solute Transport in Estuaries and Rivers) and a 3-D numerical model (namely TRIVAST—Three-dimensional layer Integrated Velocities And Solute Transport). The latter two models have been developed by staff within the Research Centre, whereas the model SWMM is a stormwater rainfall-runoff model developed by the U.S. Environmental Protection Agency. In the second part of the paper details are given of this modelling study and the application of the integrated modelling tool to predict faecal coliform levels in the Bay for various scenarios. The numerical modelling was complemented with an extensive field monitoring programme to establish more precise values for the kinetic decay rate and thereby provide enhanced predictions of coliform levels in the Bay. A laboratory model study was also undertaken to establish retention times and provide an indication of dispersion values within the basin.

2 BARRAGE DETAILS

The key components of the barrage consisted of: the embankment, the fish pass, the sluices and the navigation locks, as shown in Figure 4. Full details of the planning and design, and the construction of the barrage and its components are respectively given in Hunter & Gander (2002) and Platt (2002).

The embankment is approximately 800 m long and 100 m wide and is protected on the seaward face from wave action by rock armour. The structure of the embankment was similar to that of a rock-fill dam. Rock-fill was placed on top of a sand bed, and then on the Bay side of the embankment a substantial sand-fill column was constructed. The sand was covered with rock armour protection and the embankment was landscaped to provide a local amenity, with a service road, footpath and cycle path on top of the dam. The impounded lake upstream of the barrage, i.e. Cardiff Bay, had a design water elevation level of 4.5 m above Ordnance Datum (OD), with the highest and lowest astronomical tidal elevations seaward of the barrage being +7.96 m and -6.3 m relative to OD respectively.



Figure 4. Illustration of barrage embankment, fish pass, sluices and navigation locks.

The fish pass was required by the regulatory authority, namely Environment Agency Wales, to allow migratory fish to pass from the Bristol Channel through the Barrage and up the rivers Taff and Ely (see Figure 5). In order to ensure that fish were attracted to the

fish pass it was designed to have a flow of $10 \text{ m}^3/\text{s}$, plus an additional gravity flow of $5 \text{ m}^3/\text{s}$ in a culvert below the fish pass. The fish pass is cited as being the largest in Europe and had the unique feature, in that it had to be designed to accommodate a head difference in either direction, and depending upon the state of the tide. The fish pass was constructed of concrete, with there being 11 steps, each 1 m high, forming fish entrances from -5 m to $+6 \text{ m}$ relative to OD.

There are five sluice gates enabling the river flows through Cardiff Bay to discharge into the Bristol Channel, see Figure 5. Each sluice is 9 m wide and 7.5 m high and they have a total capacity of $2,300 \text{ m}^3/\text{s}$, which is more than twice the maximum probable flood for the rivers Taff and Ely combined. The steel gates are housed in concrete headworks and there is a large concrete stilling basin downstream. To control leakage and uplift pressures, the upstream end of the sluices and locks included a sheet pile cut-off wall, with this wall being driven into the underlying mudstone. The sluices are computer controlled enabling far greater protection for Cardiff from high tides, surges in the estuary and high river flows. Computer model predictions were undertaken to ascertain the impact of the barrage on flood inundation levels in Cardiff as a result of peak anticipated conditions and the results indicated that the flood inundation elevation would be 2 m lower as a result of the barrage.

Finally, three navigation locks were included in the design of the barrage to enable safe passage of yachts and small boats etc from the Bristol Channel to the bay and vice-versa. Sector gates were selected as being the most appropriate and efficient solution. The lock chambers were 40 m long and 10.5 m wide between fender faces. One lock was made shallower than the other two as it was

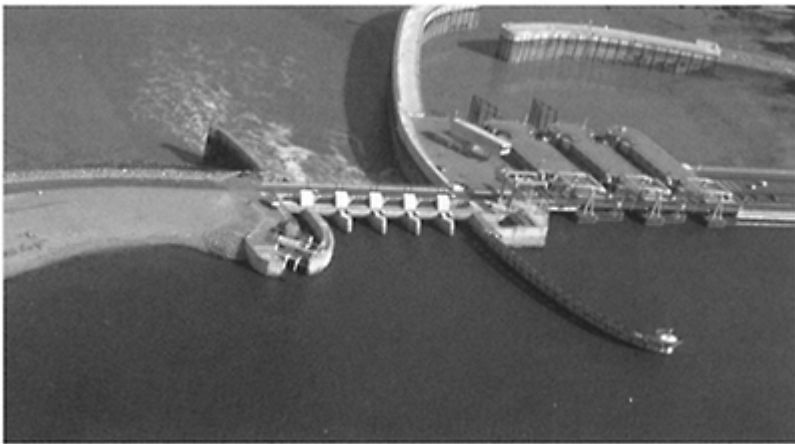


Figure 5. View of fish pass, sluice gates and navigation locks as seen from Cardiff Bay.



Figure 6. Illustration of aerator system used to oxygenate Cardiff Bay.

not necessary for all three locks to be available to operate at low tide. Full details of the locks and the other hydraulic structures cited above are given in Hunter & Gander (2002).

In addition to the structural features of the Cardiff Bay Barrage, low dissolved oxygen levels were anticipated potentially to cause a problem in the summer months and the Cardiff Bay Barrage Act required the authority responsible for managing the Bay (namely Cardiff Harbour Authority) to ensure that at all times the dissolved oxygen level was maintained at 5 mg/l minimum. This was primarily required for fisheries management, with salmon and trout requiring this level of dissolved oxygen as a minimum for survival. In order to achieve this required threshold of dissolved oxygen, a complex aerator system was put in place across the bed of the Bay, with a typical aerator being shown in Figure 6.

3 HYDRO-ENVIRONMENTAL MODELLING STUDIES

3.1 *General*

In studying the potential hydro-environmental challenges associated with such a hydraulic structure as Cardiff Bay Barrage, research studies have been undertaken between the Environmental Water Management Research Centre at Cardiff University and the Centre for Research into Environment and Health at the University of Wales, Aberystwyth. The post impoundment effects on the hydrodynamics and water quality characteristics in the Bay have been investigated by the refinement and application of a three-dimensional hydrodynamic and water quality model, which included inputs from stormwater rainfall-runoff software (namely SWMM). The modelling suite has also been

extended to include epidemiological models to provide quantifiable health risk assessments and management strategies for optimizing recreational opportunities in such urban water bodies. The numerical model was complemented by limited experimental studies and field measurements.

3.2 Physical model details

The physical model of Cardiff Bay was sited in the Hyder Hydraulics Laboratory at Cardiff University. The model was located in a large 7 m by 5 m tidal basin, with an oscillating overflow weir being driven by computer and generating tides of varying or constant amplitude and period. The physical model also included a scaled removable barrage at the mouth of the bay to replicate the impounded waters, with the presence of the barrage preventing the tidal influence from affecting the waters inside the model bay, see Figure 7. The physical model was a distorted scale model, with the horizontal and vertical scale ratios being 1:1500 and 1:75 respectively. Tracer measurements were undertaken of a conservative substance being discharged into the rivers and the plume trajectories were observed and monitored accordingly. These measurements were compared with computer model predictions at the same model scale and the comparisons were used to assess the dispersion and diffusion coefficients, before being scaled to equivalent prototypes. The physical and numerical model predictions were in close agreement and further details being given in Harris et al. (2002).

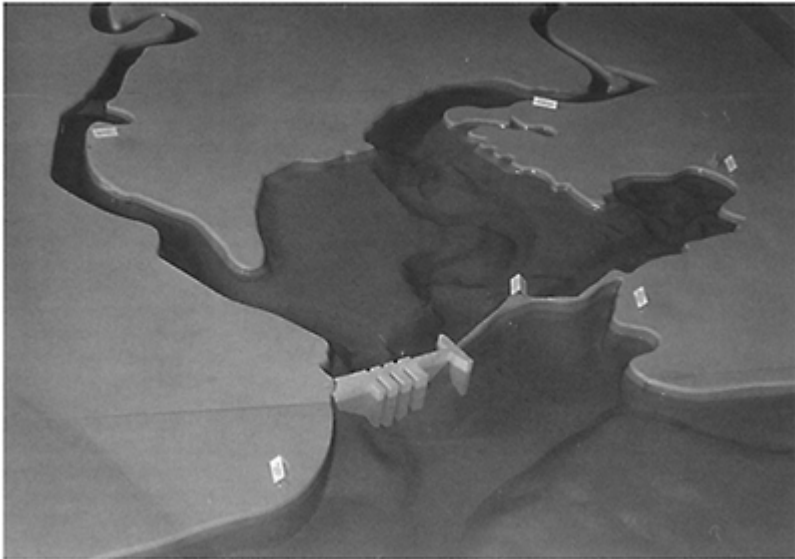


Figure 7. Cardiff Bay physical model as sited in tidal basin and with barrage in place.

3.3 Numerical model details

The main numerical model used for predicting the hydrodynamic and water quality indicator levels in the Bay was based on the research Centre's 3-D numerical model TRIVAST. The model first solves the three-dimensional Navier-Stokes equations written for mass conservation and momentum as:

$$\frac{\partial u}{\partial x} + \frac{\partial v}{\partial y} + \frac{\partial w}{\partial z} = 0 \quad (1)$$

$$\frac{\partial u}{\partial t} + \frac{\partial u^2}{\partial x} + \frac{\partial uv}{\partial y} + \frac{\partial uw}{\partial z} = +fv - \frac{1}{\rho} \frac{\partial P}{\partial x} - \left[\frac{\partial \overline{u'u'}}{\partial x} + \frac{\partial \overline{u'v'}}{\partial y} + \frac{\partial \overline{u'w'}}{\partial z} \right] \quad (2)$$

$$\frac{\partial v}{\partial t} + \frac{\partial uv}{\partial x} + \frac{\partial v^2}{\partial y} + \frac{\partial vw}{\partial z} = -fu - \frac{1}{\rho} \frac{\partial P}{\partial y} - \left[\frac{\partial \overline{u'v'}}{\partial x} + \frac{\partial \overline{v'v'}}{\partial y} + \frac{\partial \overline{v'w'}}{\partial z} \right] \quad (3)$$

$$\frac{\partial P}{\partial z} + \rho g = 0 \quad (4)$$

where u, v, w =velocity components in x, y, z co-ordinate directions respectively, t =time, f =Coriolis parameter, ρ =fluid density, P =fluid pressure, $\overline{u'u'}, \overline{u'v'}, \overline{u'w'}$ =Reynolds stresses in x direction on x, y, z planes respectively. For the Reynolds stresses these terms were solved using a two-layer mixing length model. For further details of the mixing layer model and the three-dimensional formulation see Lin and Falconer (1997).

The governing equations (1)–(4) were solved using a finite difference technique on a square mesh, covering the region of interest in the horizontal plane and a layer integrated finite volume scheme in the vertical plane. The number of grid squares varied according to the depth across the domain, with the option to set the grid size as regular or irregular in the vertical. The depth integrated equations were used to determine the water surface elevation field using the layer integrated velocities. The layer integrated equations were then used to determine the velocity field using the corresponding water elevation field. The alternating direction implicit method was modified to solve the depthintegrated equations. A description of the bathymetry and bed roughness was given for each grid square and water elevations or currents included along the open boundaries.

In modelling numerically the flux of water quality indicator organisms, the conservation of solute mass equation has been solved, with the three-dimensional form of the equation being given as:

$$\frac{\partial \varphi}{\partial t} + \frac{\partial \varphi u}{\partial x} + \frac{\partial \varphi v}{\partial y} + \frac{\partial \varphi w}{\partial z} + \frac{\partial \overline{u'\varphi'}}{\partial x} + \frac{\partial \overline{v'\varphi'}}{\partial y} + \frac{\partial \overline{w'\varphi'}}{\partial z} = \varphi_s + \varphi_d \quad (5)$$

where φ =time averaged faecal solute concentration, φ_s =source or sink solute input (e.g. an outfall), and φ_d =faecal coliform decay term.

The cross-produced terms $\overline{u'\varphi'}$ etc. represent the mass flux of solute due to the turbulent fluctuations and, by analogy with Fick's law of diffusion, can be assumed to be proportional to the mean concentration gradient and in the positive direction of decreasing concentration. Hence, the terms can be written as:

$$\overline{u'\phi'} = -D_x \frac{\partial \phi}{\partial x} \quad (6)$$

where D_x , etc.=turbulent diffusion coefficient in x direction etc. These coefficients are often associated with the eddy viscosity ε_t by a Schmidt number, with its value found to vary between 0.5 and 1.0.

For the variation of concentration distributions of faecal coliform, the solute transport equation was integrated over a layer of the water column depth with the inclusion of turbulent diffusion, source and sink inputs and decay rate constants. In numerical model simulations relating to the transport of faecal coliform indicator organisms, the solute mass conservation equation was often applied to, and solved for, faecal coliform distribution fields where high concentration gradients exist. The numerical representation of the advective terms in the solute mass conservation equation are critical in terms of the degree of numerical diffusion introduced into the scheme and the occurrence of grid scale oscillations, or undershoot and overshoot, arising in the vicinity of large concentration gradients. Cahyono (1993) undertook an extensive study in comparing 36 of the most popular finite difference schemes for modelling high concentration gradients, with comparisons showing that the ULTIMATE scheme was particularly attractive since it was more general than the other schemes considered and was relatively easy to apply. The ULTIMATE (Leonard, 1991) and the third order QUICKEST schemes were combined to represent the advective terms in the solute mass conservation equation. This algorithm reduces considerably the introduction of numerical diffusion and eliminates undershoot or overshoot in regions of high concentration gradients. This factor is particularly important for point sources (such as the riverine inputs into Cardiff Bay) and the episodic discharges from combined sewer overflows.

For the faecal coliform decay rate this term is generally written in most numerical models as a simple first order decay rate. However, extensive reviews of the literature show that this kinetic process is at least a function of:- sunlight intensity, irradiance, depth, pH, temperature, and suspended particulate matter. In particular, the work of Gameson and Saxon (1967) showed that the faecal coliform decay rate was highly dependent upon light intensity. The identification of sunlight as a major bactericidal agent has many ramifications with the expected survival rate of sewageborne bacteria in the natural environment. Bellair et al. (1977) undertook a series of experiments that commenced at 6:30 am, when it was found that the die-off was low. However, it was found to increase rapidly, reaching a maximum around noon. Recorded values ranged from 19 h to 40 h, with the inactivation rate varying greatly, particularly over a diurnal cycle, and with the rate of die-off at any time of the year being approximately proportional to the intensity of irradiance received by the sample. The effect of sunlight on the mortality of faecal coliform die-off was approximated by being related to the irradiance through a power law function as given by:

$$k_s = \alpha I^\beta \quad (7)$$

where k_s =die-off rate due to sunlight intensity (day^{-1}), I =irradiance (W/m^2), α =constant of proportionality and β =slope of the log plot of die-off against irradiance. The degree of sunlight penetration into the water column has a significant effect on the bacterial die-off

beneath the water column. The turbidity of the water interferes with the light penetration through the water column and effects the bactericidal effectiveness of sunlight. Therefore in more turbid waters the bacteria survival time is increased, mainly because of the decreased effect of UV light, which is partially adsorbed by the suspended matter. The penetration of incoming solar irradiation is usually described by an extinction coefficient. This coefficient is proportional to the water depth and may be calculated from solar radiation measurements taken at a range of water depths and represented by the Lambert law, given as:

$$I_z = I_0 e^{-k_e z} \quad (8)$$

where I_0 =irradiance at the surface (W/m^2), I_z =irradiance at depth z (W/m^2), z =depth (m) and k_e =vertical light extinction coefficient (m^{-1}).

To enable the inclusion of a dynamic method for determining the survival rates of bacteria in the numerical model, two field measurement exercises were undertaken to determine the key environmental parameters affecting the faecal indicator organism levels in the bay and the rivers Taff and Ely. These surveys were conducted in March (characterizing cold, overcast conditions) and July (characterizing hot, sunny conditions). The surveys involved the deployment of two survey boats within the bay, as well as land based survey teams to sample the rivers and other inputs. The surveys were conducted over the period dawn to dusk, to provide information on the diurnal variability of relevant parameters. The main parameters measured, at various depths, included bacterial concentrations, solar irradiance in air and water, water temperature, turbidity, pH, salinity, conductivity, suspended particulate matter and water depth. The hydro-environmental model was set up with field values of the vertical light extinction coefficient for the March and July surveys and the die-off rate directly related to the solar intensity, implying that the die-off rate in darkness would be zero. Gameson and Gould (1975) reported that the effects of sunlight on coliform die-off were additive and independent of temperature, hence the die-off rate was expressed as the sum of the die-off rate for darkness, k_d , and the die-off rate due to sunlight, k_s . Assuming that the total faecal coliform mortality rate, k , can be defined by a simple relationship, taking into account darkness and sunlight mortality, then this relationship gives:

$$k = k_d + k_s \quad (9)$$

where typical values for k_d and k_s were 100 h and 10 h respectively. Extensive further research was undertaken by Kashefipour et al. (2002) and Lin et al. (2003) where extensive field data of faecal coliform levels were used, together with artificial neural networks, to develop new formulations for the faecal coliform decay rate k .

3.4 Numerical model application

The hydro-environmental model was then set up for Cardiff Bay and the riverine inputs using a regular grid of 36×52 grid cells, of size 50 m, and with the downstream boundary being governed by the barrage sited across the mouth of the Bay. The 3-D model had 10 vertical layers, each of height 1.25 m. The model was run for 100 h and the time step was

1 s. Simulations were first undertaken to predict the movement of an arbitrary spillage of a conservative tracer with zero decay into the rivers Taff and Ely. The corresponding predictions were compared to the results obtained from the scaled physical model results, with good agreement being obtained between both sets of results (Harris et al., 2002). The model was then set up to study the impact of episodic inputs into the rivers and for a range of wind and riverine flow conditions. Some of these predictions were compared with the field data, with the corresponding comparisons for different boundary conditions enabling a comprehensive set of conclusions to be drawn to indicate river basin management strategies.

Finally, as part of this extensive research study, simulations were undertaken to investigate the impact of using the dynamically proposed varying decay rates for the faecal coliform levels of the receiving waters in the rivers and the bay. In particular, comparisons were undertaken for a range of variables and the results showed that the receiving water faecal coliform levels were highly dependent upon the key variables cited above. The hydro-environmental model was first run for hypothetical spillages into the rivers and for a constant decay rate (T_{90}), both for day-time and night-time, of 60 h. The model was then re-run for day-time and night-time decay rates cited above, i.e. ranging from 10 h to 100 h respectively and based on the representation given in Equation (9). The difference in the predictions was significant and indicated that, for this freshwater basin, night-time spillages during the autumn and winter months led to reduced faecal coliform levels in the rivers and Bay, in comparison with corresponding spillages occurring during the notional 12 h day-time period (see Figure 8). Further field measurements and model predictions were undertaken, with the die-off related to sunlight intensity, temperature and irradiance.

The corresponding test case results showed a further significant variation in the coliform levels of the receiving waters, and highlighted the need for further studies into establishing more precisely the relationship between the decay rate and a range of meteorological, hydrodynamic and bio-chemical processes. For further details of these studies see Harris et al. (2002).

More recently the studies relating to Cardiff Bay have been extended to include genetic programming simulations, with these hydroinformatics tools offering new decision support software tools for predicting water quality levels in the Bay. The approach involves using extensive data to establish complex functional relationships, specifically for faecal coliform levels across Cardiff Bay in this instance. This approach enables real-time predictions to be made of the governing variables once the programme has been trained. Detailed measurements were taken across Cardiff Bay at 17

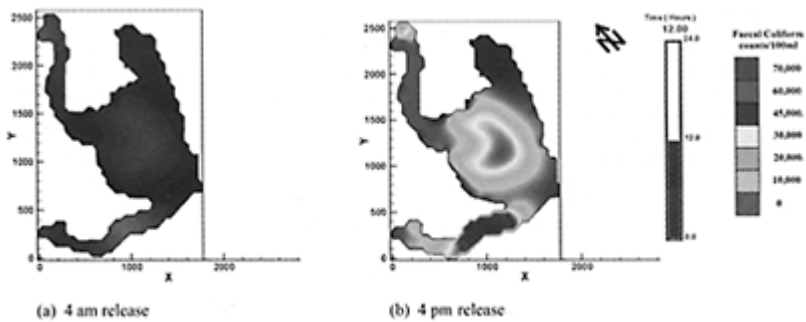


Figure 8. Faecal coliform distribution for arbitrary release into rivers Taff and Ely at: (a) 4 am and (b) 4 pm.

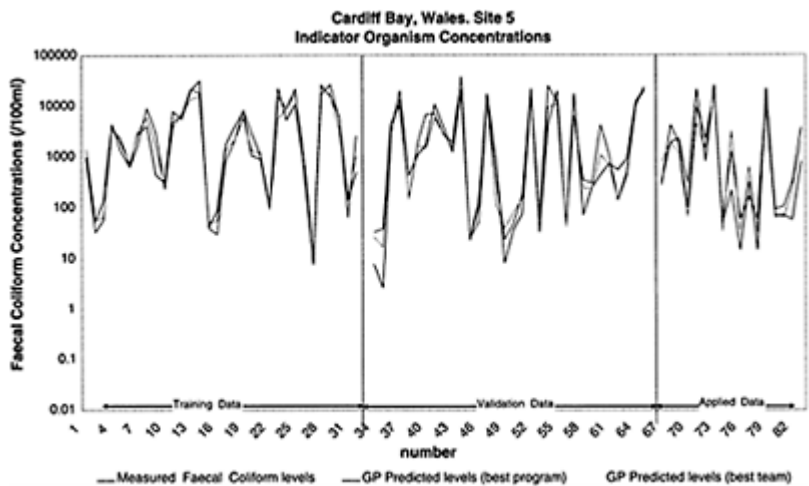


Figure 9. Comparison of measured and predicted faecal coliform levels using genetic programming.

sites and typical comparisons of measured versus predicted coliform level for one site are shown in Figure 9. Further details of this study are given in Harris (2003).

4 CONCLUSIONS

The paper discuss the challenges facing the City of Cardiff after the decline in the coal and iron and steel industries and the subsequent scheme implemented to regenerate the area to the south of the City. The main purpose of the scheme was to re-connect the City

of Cardiff with its waterfront and in fulfilling this objective a large tidal exclusion barrage was constructed across the mouth of Cardiff Bay—a coastal basin which used to experience the second highest rise and fall of tide in the world. The barrage has been highly successful in regenerating a poverty stricken area within South Wales and brief details are given herein of the tidal exclusion barrage, the fish pass, sluices and the navigation locks.

Details are then given of the application of an integrated modelling tool for predicting the receiving water faecal coliform levels in the Bay. This integrated package consisted of linking a CSO model (namely SWMM) with the Centre's 1-D and 3-D research models, named FASTER and TRIVAST respectively. In applying and developing the 3-D model particular attention was focussed on refining the treatment of bacterial decay and the model was extended to include decay rates that were highly dependent upon sunlight intensity. The model predictions were found to be highly dependent upon the value of the decay rate and good agreement was obtained between the numerical model predictions and field measured data. More recently, studies have been undertaken to develop a genetic programming based hydroinformatics tool aimed at providing a decision support tool—that is, almost instant—for predicting faecal coliform levels in the Bay for a range of different input and boundary conditions. This modelling approach has led to impressive agreement between measured and predicted coliform levels and offers considerable potential for the future in terms of managing the hydro-environmental response of such enclosed water bodies.

ACKNOWLEDGEMENTS

The research studies outlined in this paper were funded by the Natural Environment Research Council and the Engineering and Physical Sciences Research Council. The authors are also grateful to the following organizations for the provision of data: Cardiff Harbour Authority, Environment Agency Wales, and the Centre for Research into Environment and Health, of the University of Wales, Aberystwyth. The authors are also particularly indebted to their previous colleagues who were involved in this project, either directly or indirectly, including Prof. David Kay and Dr. Carl Stapleton (CREH, University of Wales, Aberystwyth), Dr. Emma Harris (Environment Agency Wales) and Dr. Seyed Kashefipour (Shiraz University, Iran).

REFERENCES

- Bellair, J.T., Parr-Smit, G.A. & Wallis, I.G. 1977. Significance of diurnal variations in faecal coliform die-off rates in the design of ocean outfalls, *Journal of Water Pollution Control Federation*, pp.2022–2030.
- Cahyono, M. 1993. Three-dimensional numerical modelling of sediment transport processes in non-stratified estuarine and coastal waters, *PhD thesis, University of Bradford, U.K.*, pp.287.
- Crompton, D. 2002. Cardiff Bay Barrage. *Water and Maritime Engineering, Proc. of Inst. Civil Engrs*, Vol.154, Issue2, pp.81–88.
- Gameson, A.L.H. & Saxon, J.R. 1967. Field studies on effect of daylight on mortality of coliform bacteria, *Water Research*, Vol.1, pp.279–295.

- Harris, E., Falconer, R.A., Kay, D. & Stapleton, C. 2002. Development of a modelling tool to quantify faecal indicator levels in Cardiff Bay, *Water and Maritime Engineering, Proc. of Inst. Civil Engrs.*, Vol.154, Issue 2, pp.129–135.
- Harris, E.L. 2003. Environmental hydroinformatics tools for recreational water quality modelling, *PhD thesis, University of Wales, Cardiff*, U.K., pp.208
- Hunter, P.D. & Gander, H.C.W. Cardiff Bay Barrage: planning and design, *Water and Maritime Engineering, Proc. of Inst. Civil Engrs.* Vol.154, Issue 2, pp.117–128.
- Kashefipour, S.M., Lin, B., Harris, E.L. & Falconer, R.A. 2002. Hydro-environmental modelling for bathing water compliance of an estuarine basin, *Water Research*, Vol.36, Issue 7, pp. 1854–1868.
- Leonard, B.P. 1991. The ULTIMATE conservative difference scheme applied to unsteady one-dimensional advection, *Computer Methods in Applied Mechanics and Engineering*, Vol.88, pp. 17–74.
- Lin, B. & Falconer, R.A. 1997. Three-dimensional layer integrated modelling of estuarine flows with flooding and drying, *Estuarine, Coastal and Shelf Science*, Vol.44, pp.737–751.
- Lin, B., Kashefipour, S.M. & Falconer, R.A. 2003. Predicting nearshore coliform bacteria using ANNs, *Water Science and Technology*, Vol.48, No.10, pp.225–232.
- Platt, N.J. 2002. Cardiff Bay Barrage: construction, *Water and Maritime Engineering, Proc. of Inst. Civil Engrs.*, Vol.154, Issue 2, pp.137–148.

River flow forecasting using artificial neural networks

M.Zakermoshfegh

PhD Student of Civil Engineering, Tarbiat Modarres University

M.Ghodsian

Associate Professor of Hydraulic Engineering, Tarbiat Modarres University

Gh.A. Montazer

Assistant Professor of Electrical Engineering, Tarbiat Modarres University

Hydraulics of Dams and River Structures—Yazdandoost & Attari (eds)

© 2004 Taylor & Francis Group, London, ISBN 90 5809 632 7

ABSTRACT: River flow forecasting is required to provide important information on a wide range of cases related to design and operation of river systems. Since there are a lot of parameters with uncertainties and non-linear relationships, the calibration of conceptual or physically-based models is often a difficult and time consuming procedure. So it is preferred to implement a heuristic black box model to perform a non-linear mapping between the input and output spaces without detailed consideration of the internal structure of the physical process.

The base of intelligent methods is to use the inner knowledge of data, extraction of native relationships between them and generalization in other locations. Artificial Neural Network (ANN) is one of the most popular methods of artificial intelligence that mimics the characteristics of the human brain and saves the information of data in the network weights during the training process.

In this study, the capability of ANNs for stream flow forecasting in the Sulaghan river at Kan hydrometric station was investigated. Two types of ANNs namely Multi Layer Perceptron (MLP) and Radial Basis Function (RBF) network were introduced and implemented. The results show that the discharge can be adequately forecasted by these kinds of ANNs.

1 INTRODUCTION

Estimation or forecasting the magnitude of hydrological variables is required in the case of water resources planning and management and river structures operation. Flood warning, drought forecasting and optimal operation of the reservoirs and power plants can be performed by appropriate river flow forecasting.

Many approaches have been used to hydrologic forecasting in the last few decades. These models are grouped into three categories (Babovic et.al., 2001).

1.1 *Lumped conceptual models*

This type of models approximates the general internal sub processes and physical mechanisms which govern the hydrologic cycle. The implementation and calibration of lumped conceptual models is encountered with some difficulties, requires significant amount of calibration data and depends on the expertise and experience with the model.

1.2 *Distributed physically based models*

The number of these models suitable for research is not so many. This kind of modeling systems needs a large amount of data. They utilize many parameters in their operation in a direct relation to topology, soil, vegetation and geology characteristics of catchments. In the other hand many of these parameters are not directly measured everywhere in the studied basin.

1.3 *Empirical black-box models*

This kind of models doesn't use any explicit well-defined representation of the physical process and governing equations of the phenomena. The accuracy of these models is highly depended on the quality of the observed data used to calibrate (to learn) these models. However, it has been shown that these models are useful operational tools and they are the only option in case where there are not enough meteorological data available.

In this regard, Artificial Neural Networks are non-linear, distributed, heuristic and adaptive learning models constructed from many simple processing elements, called "Neuron".

2 ARTIFICIAL NEURAL NETWORKS

Artificial Neural Network (ANN) is a mathematical tool, which tries to represent low-level intelligence in natural organisms (Gorzalczany, 2002) and it is a flexible structure, capable of making a non-linear mapping between input and output spaces.

Neural network processing is based on performance of many simple processing units called neuron, cell, node or PE. Each neuron in each layer is connected to all elements in the previous and the next layer with links, each has an associative weight. The general

ability of an ANN is to learn (Karayiannis & Venetsanopoulos, 1993) and to simulate the natural and complex phenomena.

2.1 Learning in ANNs

If we consider the $X=[x_1, x_2, \dots, x_n]$ as input vector and $W=[w_1, w_2, \dots, w_n]$ as network parameter (weight) vector and if the goal is approximating the multi variate function $f(x)$, the learning procedure is to find the best weight vector (W) to have the best approximation of the $f(x)$.

In this paper, two kinds of ANNs with different learning rules namely Multi Layer Perceptron (MLP) and Radial Basis Function (RBF) network are used.

2.2 Multi Layer Perceptron (MLP)

The MLP network (Sometimes is called Back Propagation (BP) network) is shown in Figure 1 is probably the most popular ANN in engineering problems in the case of non-linear mapping and is called "Universal Approximator" (Hecht-Nielson, 1987).

The learning process is performed using the well-known BP algorithm (Werbos, 1974; Rumelhart & McClelland, 1986). In this study, the standard BP algorithm based on the delta learning rule is used.

Two main processes are performed in a BP algorithm. A forward pass and a backward pass. In the forward pass an output pattern is presented to the network and its effect propagated through the network, layer by layer. For each neuron, the input value is calculated as follows:

$$net_i^n = \sum_{j=1}^m w_{ji}^n \cdot O_j^{n-1} \quad (1)$$

where net_i^n is the input value of i th neuron in n th layer; w_{ji}^n is the connection weight between j th neuron in n th layer and j th neuron in the $(n-1)$ th layer; O_j^{n-1} is the output of j th neuron in the $(n-1)$ th layer; m is the number of neurons in the $(n-1)$ th layer.

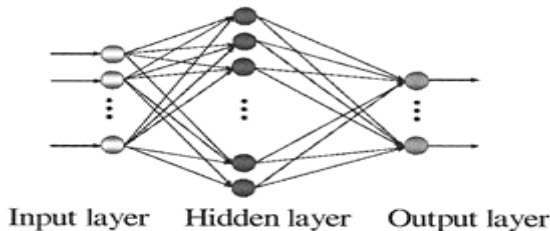


Figure 1. Multi Layer Perceptron neutral network.

In each neuron, the value calculated from Eq. (1) is transferred by an activation function. The common function for this purpose is the sigmoid function (Haykin, 1994), is given by:

$$Sig(net_j^n) = 1/(1 + Exp(-net_j^n)) \quad (2)$$

Hence the output of each neuron is computed and propagated through the next layer until the last layer. Finally, the computed output of the network is prepared to compare with the target output. In this regard, an appropriate objective function such as the Sum of Square Error (SSE) or Root Mean Square Error (RMSE) is calculated as follows:

$$SSE = \sum_{i=1}^{n_p} \sum_{j=1}^{n_o} (T_{pj} - O_{pj})^2 \quad (3)$$

$$RMSE = \sqrt{\frac{\sum_{i=1}^{n_p} \sum_{j=1}^{n_o} (T_{pj} - O_{pj})}{n_p \cdot n_o}} \quad (4)$$

where T_{pj} is the j th element of the target output related to the p th pattern; O_{pj} is the computed output of/th neuron related to the p th pattern; n_p is the number of patterns; n_o is the number of neurons in the output layer.

After calculating the objective function, the second step of the BP algorithm, i.e. the backward process is started by back propagation the network error to the previous layers. Using the gradient descent technique, the weights are adjusted to reduce the network error by performing the following equation (Rumelhart & McClelland, 1986):

$$\Delta w_{ji}^n(m+1) = \eta \cdot \frac{\partial(E)}{\partial w_{ji}^n} + \alpha \cdot \Delta w_{ji}^n(m) \quad (5)$$

where $\Delta w_{ji}^n(m+1)$ is the weight increment at the $(m+1)$ th iteration (Epoch); η is the learning rate (Rumelhart & McClelland, 1986; Haykin, 1994); α is the momentum term ($0 \leq \eta, \alpha \leq 1$).

This process is continued until the allowable network error occurred.

2.3 Radial Basis Function (RBF) neural network

A RBF network is a feed forward network consists of one hidden layer. The activation function of the hidden layer is often a Gaussian function and the output layer has often linear functions (Dibike et.al., 1999; Mason et.al., 1996). Learning of a RBF network is generally divided into two phases. The first one is an unsupervised (self-organizing) in which the hidden units parameters depend on the input distribution are adjusted. The second one is a supervised learning in which the weights between hidden and linear output layer are adjusted (Using gradient descent or linear regression techniques).

A RBF hidden neuron has one parameter associate with each input neuron. These parameters, w_{ij} are the centers of units. The output of each hidden neuron is a function of the distance between the input vector $X=[x_1, x_2, \dots, x_n]$ and radial center vector $W_j=[w_{1j}, w_{2j}, \dots, w_{nj}]$ and can be written as follows:

$$\delta = \sqrt{\sum_{i=1}^n (x_i - w_{ij})^2} \quad (6)$$

The hidden neuron output can be calculated in many ways. The most popular activation function for this purpose is the Gaussian one described as follows (Mason et.al, 1996):

$$f(\delta_j) = \text{Exp}(-\lambda \cdot \delta_j^2) \quad (7)$$

where λ is a constant. At last the output layer computes the output as follows:

$$Z_k = \frac{\sum_{j=1}^J b_{jk} y_j}{\sum_{j=1}^J y_j} \quad (8)$$

where b_{jk} is the weight coefficient between j th neuron between hidden layer and k th neuron of output layer and y_j is the output of the j th hidden neuron.

3 THECASESTUDYANDDATASET

The aim of this paper is to predict the mean daily discharge of the Sulaghan river at Kan hydrometric station, located few kilometers in the west of Tehran, Iran. In this regard the available dataset, i.e. the mean daily discharges from years 1984 up to 2001 have been collected and divided into two sets for model training and verification.

The training set is data from years 1994 up to 2001 and the rest of data is used to verify the model. In order to normalize dataset the following equation is used to transform data in to the range of [0.05, 0.95]:

$$x_n = 0.05 + 0.9 * \left(\frac{x - x_{\min}}{x_{\max} - x_{\min}} \right) \quad (9)$$

where x_n is the normalized value; x is the observed value; x_{\min} and x_{\max} are the minimum and the maximum of the observations, respectively.

4 MODELING ASSUMPTIONS

In the case of river flow forecasting without exogenous inputs (i.e. runoff at any day is just a function of runoff at the previous days.), it is very important to understand how many days can we go back to predict a specified discharge (Dibike et.al., 1999). In this regard, several models indicating different number of input discharges are evaluated. These models are:

$$M1: Q(t)=f[Q(t-1), Q(t-2), Q(t-3), Q(t-4)]$$

$$M2: Q(t)=f[Q(t-1), Q(t-2), Q(t-3)]$$

$$M3: Q(t)=f[Q(t-1), Q(t-2)]$$

$$M4: Q(t)=f[Q(t-1)]$$

where $Q(t)$ is the mean daily discharge at the t th day.

Many researchers have reported the importance of careful data preparation and the choice of effective input variables (Dawson & Wilby, 1998). So, the aforementioned four models (M1,..., M4) are evaluated using the two candidates ANNs, i.e. MLP and RBF neural networks.

5 APPLICATION OF ARTIFICIAL NEURAL NETWORKS

The training and verification datasets described in the previous sections are used to learn and test the MLP and RBF networks. Many different architectures (number of hidden layers for MLP, number of hidden neurons and activation functions) and number of optimal epochs are evaluated during the training and verification phases.

The model performance is evaluated using RMS error and correlation coefficient (R^2) between the observed and forecasted discharges.

The results are shown in Table 1. As shown in this table, when additional antecedent discharges were added to the input pattern, the performance of MLP network in the training period is improved, but in the verification period deteriorated.

In the other hand for the RBF network, removing the non-effective input parameters, improves the network performance in both training and verification periods.

Table 1. Performance evaluation of different models.

Model	MLP				RBF			
	Training		Verification		Training		Verification	
	R ²	RMSE	R ²	RMSE	R ²	RMSE	R ²	RMSE
M1	0.71	0.0205	0.77	0.0165	0.72	0.0203	0.71	0.0163
M2	0.69	0.0208	0.77	0.0165	0.74	0.0196	0.69	0.0159
M3	0.65	0.0217	0.78	0.0161	0.74	0.0196	0.65	0.0157
M4	0.67	0.0214	0.78	0.0160	0.72	0.0201	0.67	0.0157

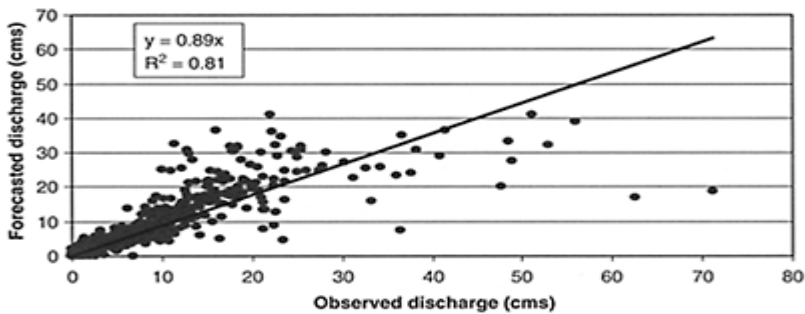


Figure 2. Forecasted discharge versus observed discharge in the verification period.

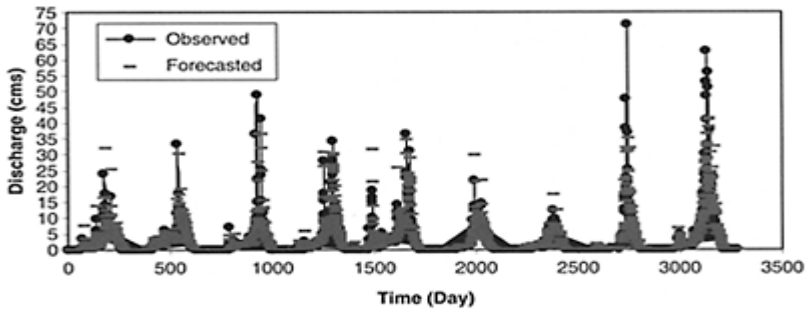


Figure 3. Observed and forecasted hydrographs in the verification period.

Corresponding to the Table 1, the M4 model is the proposed model for MLP network with two hidden units and sigmoid activation function (i.e. MLP 1-2-1). The M3 model is

the proposed one for the RBF network with twenty hidden neurons (i.e. 2-20-1, the best network).

The forecasted discharge by RBFN versus the observed discharge is plotted for the verification dataset in Figure 2. Figure 3, shows the observed and forecasted hydrographs by RBFN in the verification period.

6 CONCLUSION

ANN models applied to Sulaghan river flow forecasting show encouraging performance in the case of mean daily discharge forecasting. ANNs can provide useful tools in analyzing and solving a wide range of problems of water engineering.

- MLP network in the training period is not sensitive to non-effective input variables.
- Performance of the RBF network in both training and verification periods are highly depended on the number of the input variables. Removing the non-effective inputs can improve the RBF network performance.
- Comparing the MLP and RBF network architecture shows that the RBF network needs hidden neurons more than the MLP network, but it is trained faster than the MLP network.

REFERENCES

- Babovic, V. & Bojcow, V. 2001. *Runoff Modeling with Genetic Programming and Artificial Neural Networks*. D2K Technical Report D2K TR 0401-1.
- Dawson, C.W. & Wilby, R. 1998. An artificial neural network approach to rainfall-runoff modeling. *Hydrological ScL J*, Vol. 43 (1), 47–66.
- Dibike, Y.B., Solomatine, D.P. & Abbot, M.B. 1999. On the encapsulation of numerical-hydraulic models in artificial neural networks, *J. of hydraulic research*, Vol. 37(2), 147–161.
- Gorzalczany, M.B. 2002. *Computational Intelligence Systems and Applications*, Physica-Verlag Company, Heidelberg, Germany.
- Hecht-Nielsen, R. 1987. *Kolmogorov's Mapping Neural Network Existence Theorem*, 1st *IEEEICNN*, Vol. 3 San Diego, CA.
- Karayiannis, N.B. & Venetsanopoulos, A.N. 1993. *Artificial Neural Networks: Learning Algorithms, Performance Evaluation, And Applications*. Kluwer Academic Publishers, Boston.
- Mason, J.C., Price, R.K. & Tem' me. 1996. A neural network model of rainfall-runoff using radial basis functions. *J. of Hydraulic Research*, Vol. 34, 537–548.
- Rumelhart, D.E., McClelland, J.L. & the PDP research group. 1986. Parallel recognition in modern computers. *In processing: Explorations in the microstructure of cognition*. Vol. 1. Foundations, MIT Press/Bradford Books, Cambridge Mass.
- Werbos, P.J. 1974. *Beyond regression: New tools for prediction and analysis in behavior sciences*. PhD thesis, Harvard university, Cambridge, Mass.

Evaluation of the application of neural networks on real-time river flood prediction

M.T.Dastorani

*Assistant Professor, Faculty of Natural Resources Engineering,
University of Yazd, Iran*

Hydraulics of Dams and River Structures—Yazdandoost & Attari (eds)

© 2004 Taylor & Francis Group, London, ISBN 90 5809 632 7

ABSTRACT: This study aimed to model river flow in a multi-gauging station catchment and provide real-time prediction of peak flow downstream using artificial neural networks (ANN). Three types of ANN (Multi-Layer Perceptron (MLP), Recurrent, and Time Lag Recurrent) were adapted to evaluate the applicability of this technique. The study area covers the Upper Derwent River, a tributary of the River Trent in the UK. River flow was predicted at the subject site with lead times of 3, 6, 9 and 12 hours. Tests were completed using different lengths of input data to evaluate the effect of input data size in model outputs. The number of gauging sites to be used as data sources in the model was also evaluated. According to the results of this research it can be said that for real-time forecasting of flow in gauged catchments the type of neural network is an important factor and dynamic architectures, especially general recurrent networks, show a superior ability even for longer prediction horizons.

1 INTRODUCTION

The prediction of river flow is used in different aspects of water resources planning and management as well as flood damage protection or mitigation. Reliable prediction of flow discharge and its variability along rivers is an essential part of surface water planning projects. In addition, prediction of discharge at a particular point using upstream conditions helps in designing storage plans or control measures. Moreover, it is an important part of the projects such as flood warning systems and dam release operations. For most of these applications real-time prediction of river flow is usually required.

Improvements in river peak flow forecasting have resulted partly from the global increase in stream gauging stations and partly from accelerating advances in the technology of data collection as well as in computer-based data handling and telecommunication systems. The three main parameters in real-time flood forecasting are accuracy, reliability, and timeliness. In flood warning applications there is likely to be more emphasis on timing and the reproduction of distinctive shapes on the rising limb and crest segment of the hydrograph. It is therefore important to develop forecasting models, which are relatively simple, but quick and efficient to execute. The technique of artificial neural networks is widely used as an efficient tool in different areas of water related research activities. Some completed investigations in this area are: Bhattacharya

and Solomatine, 2000; Dawson and Wilby, 1998; Hsu, et al, 1995; Karunanithi, et al., 1994; Luk, et al, 1998; Minns and Hall, 1996; and Sezin, et al., 1999.

In this study it was decided to investigate the application of ANN to model river flow discharge variation between gauging stations and real-time prediction of flow in downstream points using upstream discharge. It would be a useful step to prevent damage by predicting flood flow in flood plains, where the risk of flooding is high, using the measured flow data from upstream gauging stations. The potential of artificial neural network models for simulating the hydrologic behaviour of catchments is presented in this research. The influence of the type of the neural network as well as the variation of input data in terms of record length and the number of sources (number of upstream sites used for data) on the prediction results have been the main elements to investigate in this research. Three different types of artificial neural networks (Multi-layer Perceptron, Recurrent, and Time Lag Recurrent) have been applied to evaluate the applicability of different types of the technique of ANN for this particular problem.

2 REAL-TIME FORECASTING PROCESS

Prediction of flow by the method presented in this research, is carried out for the next time step using the previous measured data. If $Q_{(t)}$ represents the discharge at subject site (Whatstandwell gauging station) at time t , and $q_{(t)}$ the discharge at an upstream gauging station at the same time (t), the prediction aim is:

$$Q_{(t+1)} = f(Q_{(t)}, Q_{(t-1)}, \dots, Q_{(t-n)} + q_{(t)}, q_{(t-1)}, \dots, q_{(t-n)} + e_{(t)})$$

where:

$f()$ is an unknown non-linear mapping function, $e_{(t)}$ is an unknown mapping error, n is the number of past inputs contributing to the prediction of flow at the next time-step.

$Q_{(t+1)}$ which is river flow at Whatstandwell for next time step ($t+1$), is predicted using upstream flow at time $t, t-1, \dots, t-n$. Due to use different upstream gauging sites as sources of input data as well as data at 30 minute intervals and four different prediction horizons in this research, predictions in first three tests are as follows:

$$\begin{aligned} \text{For 3 hours lead time, } Q_{(t)} = & f(Q_{(t-6)}, Q_{(t-7)}, \dots, Q_{(t-n)} + q_{(t-6)}(1), q_{(t-7)}(1), \dots, \\ & q_{(t-n)}(1) \\ & + q_{(t-6)}(2), q_{(t-7)}(2), \dots, q_{(t-n)}(2) \\ & + q_{(t-6)}(3), q_{(t-7)}(3), \dots, q_{(t-n)}(3) + e_{(t)}) \end{aligned}$$

$$\begin{aligned} \text{For 6 hours lead time, } Q_{(t)} = & f(Q_{(t-12)}, Q_{(t-13)}, \dots, Q_{(t-n)} + q_{(t-12)}(1), q_{(t-13)}(1), \dots, \\ & q_{(t-n)}(1) \\ & + q_{(t-12)}(2), q_{(t-13)}(2), \dots, q_{(t-n)}(2) \\ & + q_{(t-12)}(3), q_{(t-13)}(3), \dots, q_{(t-n)}(3) + e_{(t)}) \end{aligned}$$

and so on for 9 and 12 hours.

Variables $q_{(t)}(1)$, $q_{(t)}(2)$, and $q_{(t)}(3)$ are river flow at first, second and third upstream gauging stations at time t .

For the fourth test in which different numbers of upstream sites are used as data sources in different sub-tests, along with data at 1 hour intervals predictions will be as follows:

Sub-test 1 (only one upstream gauging site as data source):

For 3 hours lead time, $Q_{(t)} = f(q_{(t-3)}(1), q_{(t-4)}(1), \dots, q_{(t-n)}(1) + e_{(t)})$

For 6 hours lead time, $Q_{(t)} = f(q_{(t-6)}(1), q_{(t-7)}(1), \dots, q_{(t-n)}(1) + e_{(t)})$

and so on for 9 and 12 hours.

Sub-test 2 (two upstream gauging sites as data sources):

For 3 hours lead time, $Q_{(t)} = f(q_{(t-3)}(1), q_{(t-4)}(1), \dots, q_{(t-n)}(1) + q_{(t-3)}(2), q_{(t-4)}(2), \dots, q_{(t-n)}(2) + e_{(t)})$

For 6 hours lead time, $Q_{(t)} = f(q_{(t-6)}(1), q_{(t-7)}(1), \dots, q_{(t-n)}(1) + q_{(t-6)}(2), q_{(t-7)}(2), \dots, q_{(t-n)}(2) + e_{(t)})$

and so on for 9 and 12 hours.

Sub-test 3 (three upstream gauging sites as data sources):

For 3 hours lead time, $Q_{(t)} = f(q_{(t-3)}(1), q_{(t-4)}(1), \dots, q_{(t-n)}(1) + q_{(t-3)}(2), q_{(t-4)}(2), \dots, q_{(t-n)}(2) + q_{(t-3)}(3), q_{(t-4)}(3), \dots, q_{(t-n)}(3) + e_{(t)})$

For 6 hours lead time, $Q_{(t)} = f(q_{(t-6)}(1), q_{(t-7)}(1), \dots, q_{(t-n)}(1) + q_{(t-6)}(2), q_{(t-7)}(2), \dots, q_{(t-n)}(2) + q_{(t-6)}(3), q_{(t-7)}(3), \dots, q_{(t-n)}(3) + e_{(t)})$

and so on for 9 and 12 hours.

3 STUDY AREA AND DATA AVAILABILITY

The study area covers the upper Derwent River catchment located in the River Trent basin. The site for prediction is Whatstandwell gauging station. Three gauging stations called Matlock, Chatsworth and Mytham Bridge have been selected upstream with distances of about 10, 25 and 50 kilometres from the subject site respectively (Figure 1). Measured flow data for related gauging stations were collected from the Environment Agency. The original flow time series were measured with a 30 minute interval. For the first test, flow data at a 30 minute recording interval from January 1999 (1–31) was used as input. For the second and third tests a longer period of data was used, 6 months and 3 years respectively. For each experiment the data was split into three parts; training data (50%), cross-validation data (10%) to prevent model over-training, and testing data (40%). Table 1 gives information about the data used in different tests.



Figure 1. An index plan of the upper Derwent river catchment showing discharge measuring stations.

Table 1. Data has been used in training, testing and cross validation phases of each test.

Test	Length	Data set	% of data	No. of obs.
1	1 month	Training	50	734
		Cross val.	10	146
		Testing	40	588
		Total	100	1468
2	6 months	Training	50	4347
		Cross val.	10	869
		Testing	40	3477
		Total	100	8693
3	3 years	Training	50	26380
		Cross val.	10	8653
		Testing	40	17503
		Total	100	52536
4	1 month	Training	60	441

Cross val.	10	73
Testing	30	220
Total	100	734

4 PREPARATION OF DATA

As there are different distances between the subject site and each upstream gauging station, the travel time for flow will be different from one to the other. In this research, a correlation coefficient analysis procedure was used to determine the lag time between upstream gauging sites and the subject site. According to the results of this analysis the lag time was estimated at 5.5, 3.5 and 1.5 hours respectively for Mytham bridge, Chatsworth and Matlock to the subject site (Whatstandwell). According to the distances between the upstream stations and the subject site, the mean velocity of the water flow is determined about 2.52 m/s, 1.98 m/s and 1.85 m/s for the distances between the Mytham bridge and Whatstandwell, Chatsworth and Whatstandwell, and Matlock and Whatstandwell respectively.

5 ARTIFICIAL NEURAL NETWORKS

Neural networks must be trained with a set of typical input/output pairs of data called the training set. The final weight vector of a successfully trained neural network represents its knowledge about the problem. As different types of neural network deal with the problems in different ways, their ability varies depending on the nature of the problem in hand. Therefore, three types of ANN were used in this study. Multi-layer perceptron, which is a static architecture of neural networks as well as Recurrent and Time Lagged Recurrent neural networks, which are dynamic networks.

5.1 *Multi-layer perceptron neural network (MLP)*

In this network a connection is allowed from a node in layer i only to nodes in layer $i+1$, and not vice versa (Figure 2). An advantage of MLP in terms of mapping abilities is its capability of approximating arbitrary functions. This is an important point in the study of non-linear dynamics, and other function mapping problems. In this study different types of transfer and output functions for hidden and output layers as well as different numbers of hidden layers were used to find the best structure of MLP for this application. From these trials it was found that the tangent hyperbolic function was the most compatible one for the hidden layer. However, for the output layer the sigmoid function was the most suitable one. One hidden layer was most suited number to the model.

5.2 *Recurrent neural networks*

This type of network can be divided into fully and partially recurrent. Having a memory element distinguishes this network from the previous one (Figure 3). Although recurrent

networks are more powerful than feedforward networks, they are more difficult to train and their properties are not as well understood. The training of a recurrent network is much more sensitive to divergence. To construct the best architecture for this study, many structures were tested and the results were considered. The number of hidden layers, number of processing elements in hidden layers, type of transfer and output functions and type of learning rule and its parameters have been considered and evaluated. After using different types of transfer and output functions for hidden and output layers, it was realized that a tangent hyperbolic function was the

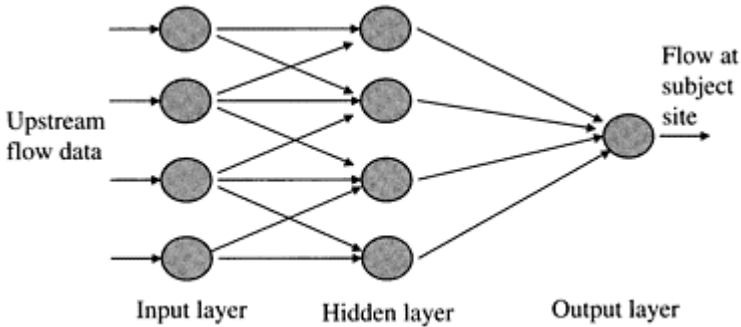


Figure 2. A typical 3 layer feedforward neural network.

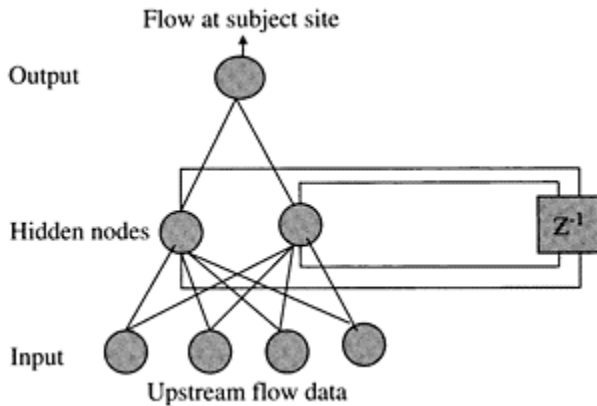


Figure 3. A typical recurrent neural network.

most suitable one for the hidden layer. However, for output layer the sigmoid function is a more compatible function. Between the dynamic processing elements of Gamma, Laguarre and Time delay, the Laguarre and Time delay gave better results. The number of hidden layers differed from one in tests with a shorter length of input data to two for a

longer length of input data. For the tests of this research, the partially recurrent network showed better adaption than fully recurrent one.

5.3 *Time lag recurrent neural networks*

This type of network contains locally recurrent layers with a single adaptable weight. As opposed to the Recurrent networks stability in Time Lag Recurrent networks is guaranteed. It usually suits temporal problems with short temporal dependency however it does not seem appropriate for more difficult temporal problems. For this type of neural network it was found that the tangent hyperbolic function and in few cases the sigmoid function was the best one for hidden layer. However, for output layer the sigmoid function suited better for all tests. Between the dynamic processing elements of Gamma, Laguarre and Time delay, the Gamma was found to be the most compatible. Networks with only one hidden layer presented the best performance.

6 PREDICTION OF FLOW

The amount and type of input data is always an important factor when using artificial neural networks. Therefore, in evaluating the performance of this technique for a particular application, using data with different characteristics as input would seem necessary. For flow data the length of the record period seems to be an important factor in terms of evaluation of the applicability of the models for real-time flow prediction. Another important variable to investigate is the number of input pattern to the neural network, which corresponds to the number of upstream gauging sites as data sources of data in present study. Therefore, the tests 1, 2 and 3 were carried out using three different lengths of data, while test 4 uses different upstream gauging sites as data sources.

6.1 *Prediction with a short data period*

In this test input data covers only one month (January 1999). After consideration of the flow at the gauging stations it was found that January 1999 is a good representative of the flow conditions in this catchment. During these months high and low flow discharges are seen and several flood waves occurred, which provides appropriate data for this test. Flow data with a 30-minute increment from upstream gauging stations and the subject site are entered to the model. Predicted hydrographs with different lead-times produced by recurrent network are seen in Figure 4 (it is not possible to show the results of all networks due to space limitation). The horizontal axis shows the time with 30 minutes intervals. Flow at any specific time step on this axis is predicted using flow at a previous time step, which one will depend on the lead-time.

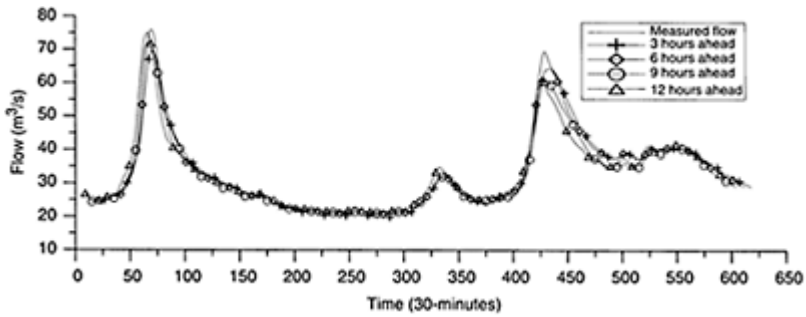


Figure 4. Hydrograph of the flow in Whatstandwell and the corresponding predicted hydrographs 3, 6, 9 and 12 hours ahead by Recurrent neural network with shorter length of input data (testing phase).

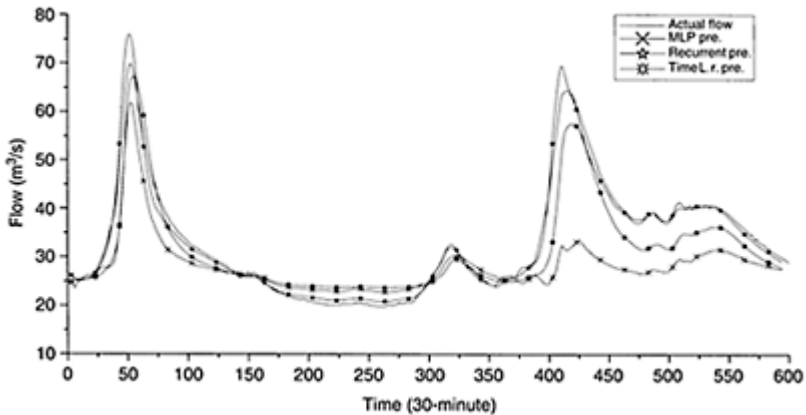


Figure 5. Actual hydrograph against the 3 hours ahead predicted hydrographs by different types of the neural networks and short length of input data (testing phase).

Figures 5 and 6 show the predicted hydrographs respectively 3 and 12 hours ahead produced by different networks. These figures facilitate the comparison of the outputs of different networks for the specific prediction horizon.

6.2 Prediction with a medium length of data

In this test the length of input data was increased to 6 months. Flow data measured with a 30-minute increment provided 8693 observations during the 6 months. Due to space limitation it is not possible to show the hydrographs but the results is discussed later.

6.3 Prediction with a long data period

In this test data with a longer period is used. River flow data for 3 years and with a 30-minute increment was prepared to train and test the models. This length of data record provided 52536 observations, which were divided into three sets for training, cross-validation and testing phases.

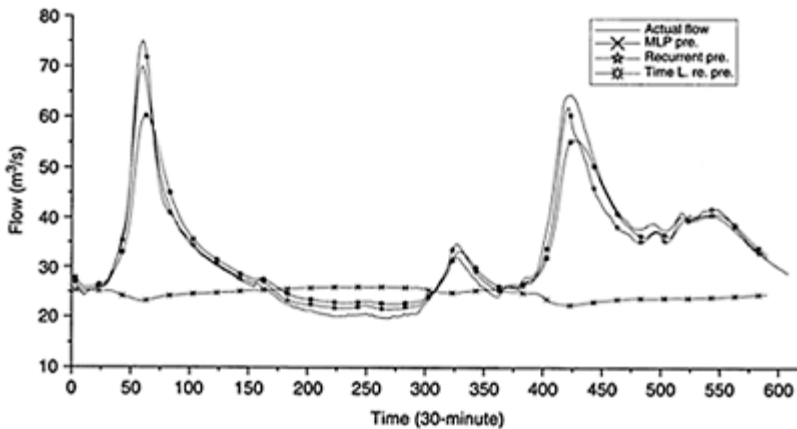


Figure 6. Actual hydrograph against the 12 hours ahead predicted hydrographs by different types of the neural networks and short length of input data (testing phase).

6.4 Prediction of flow using different numbers of upstream gauges

To evaluate the effects of the number of input patterns in the accuracy of the prediction results, three sub-tests were carried out by using input data from one, two and three upstream gauging sites respectively. In each sub-test all three types of neural network were employed to see the effects of different number of input patterns on the output of each type separately. These sub-tests are as follows:

- Sub-test 1 (using 1 upstream gauging station): In this sub-test river flow was predicted at Whatstandwell gauging station using previous flow data only from Chatsworth

gauging station. Predictions are carried out for 3 hours, 6 hours, 9 hours and 12 hours ahead.

- Sub-test 2 (using 2 upstream gauging station): In this sub-test the length of data used as input was the same as the previous test but the number of gauging stations used was increased. Networks were trained and tested using two input patterns and one output pattern. Similar to sub-test 1, flow has been predicted 3, 6, 9 and 12 hours ahead by three types of neural networks.
- Sub-test 3 (using 3 upstream gauging station): In this sub-test, the prediction of flow has been carried out at the subject site using data from three upstream gauging stations. There were three input patterns and one output pattern for each neurone. In terms of the number of upstream gauging stations and the length of data, this test is similar to test 1. However, there are two differences; the first one is the measured data interval, which is 1 hour in this test while it is 30 minutes in test 1. The second difference is the mode of training. In this test the network was trained using default mode but in test1 prediction mode was used to train the network. Lead-times were the same as in the previous sub-tests (3, 6, 9 and 12 hours).

6.5 Prediction using a naive method

In addition to three types of neural networks, prediction of flow at Whatstandwell was made with a simple naive method. In this method prediction of the future condition is made using only the historic time series of data at the subject site.

7 RESULTS AND DISCUSSION

Suitable statistical parameters of comparison were used to consider the accuracy of the output in different tests and sub-tests. To make a reliable comparison and judgment about the capabilities of

Table 2. The values of root mean square error (rmse) of the predicted flow with different type of the neural networks, input data length and lead-time in training and testing phases.

Test	Sub-test	Lead-time	Training phase			Testing phase		
			MLP	Rec.	T.L.R.	MLP	Rec.	T.L.R.
1	–	3hr	1.727	2.125	5.374	9.484	1.646	2.982
		6hr	3.480	3.012	4.604	11.485	1.818	3.006
		9hr	4.379	3.625	4.932	15.505	2.185	3.243
		12 hr	6.164	4.899	5.706	15.766	4.313	3.897
2	–	3hr	2.567	2.315	3.878	4.551	2.168	3.153
		6hr	3.842	3.267	5.290	6.772	2.185	3.344

3	–	9hr	4.418	4.234	3.690	7.472	3.159	3.388
		12 hr	6.562	5.207	4.769	11.230	3.182	4.298
		3hr	3.352	5.664	12.171	9.298	10.456	12.647
		6hr	6.237	6.990	14.976	14.958	10.783	13.084
4	1	9hr	8.689	9.813	18.329	21.367	11.539	18.736
		12 hr	10.727	11.637	21.504	24.342	11.734	19.930
		3hr	1.930	2.464	2.800	2.094	1.897	1.692
		6hr	1.939	3.217	3.669	3.325	1.923	1.937
	2	9hr	2.714	3.573	4.443	6.093	2.044	2.405
		12 hr	3.650	3.825	7.572	7.040	2.084	4.361
		3hr	1.434	3.325	2.472	1.984	2.696	2.097
		6hr	2.804	3.355	3.561	4.784	2.375	1.930
	3	9hr	3.791	3.803	4.010	6.029	2.164	1.841
		12 hr	4.865	3.929	4.489	6.162	2.157	1.807
		3hr	1.164	2.390	2.977	1.653	1.417	1.591
		6hr	2.555	2.357	3.215	5.267	1.656	1.593
		9hr	3.878	4.225	3.593	8.002	1.808	1.745
		12 hr	5.105	4.038	4.207	8.282	2.001	1.882

the different networks for real-time flow prediction RMSE (root mean square error) as well as R^2 (coefficient of efficiency) were used. Values of the root mean square error for the results of the tests 1, 2, 3 and 4 are shown in Table 2.

In tests 1, 2 and 3 all aspects were the same except the size of data used to train and test the models. Data were used from all three upstream gauging stations as well as the subject site. However, the nature of test 4 is different as the size of data for training and testing was the same in all three subtests but the number of input patterns was different i.e. a different number of upstream gauging sites were used as data sources in different sub-tests. In addition, no data from the subject site (Whatstandwell gauging station) was used in sub-tests of test 4. Another difference between the first three tests and test 4 is the mode of training. First three tests were trained using “Prediction Mode”, where data from the subject site is automatically used as input but all sub-tests of the test 4 were trained in a default way. The interval of the measured data used in test 4 was different from the first three tests. This was 30 minutes in tests 1, 2 and 3 and 1 hour in test 4. Because of these differences the results of networks will be discussed in the first three tests together, and then followed by sub-tests of the test 4.

The first thing that seems quite clear from the results of all tests is that MLP network does not perform well. In fact the results of this network are quite poor in the testing phases, and even the hydrograph for a 3 hours ahead prediction is not close to the actual hydrograph. Also the accuracy of the outputs decreases dramatically with the increase of

prediction horizon. The values of RMSE in Table 2 clearly indicate that the outputs are poor in the testing phase. However, for the training phase the results of this network seem quite close to the measured value. It seems that a form of over training has occurred during the training of this network despite employing a set of data as cross-validation. In general, the results of this network in test 2 are almost similar to those in test 1. Increasing the amount of input data has not helped the MLP. The only difference is with the predicted hydrograph 9 hours ahead, which shows improvement in test 2 comparison to the previous test, although it is still far from the actual hydrograph. In test 3 despite using a large number of data, there is no improvement in the results over first two tests. In this test the MLP has produced results that are considerably over estimated in contrast with its outputs in previous tests. The results of the MLP are still quite poor as in previous tests, and the main problem with MLP to produce appropriate results seems to be the lead-time. It gives good results when prediction is made with very short lead-time.

In contrast with the MLP, the results produced by the dynamic networks (recurrent and time lag recurrent) are quite close to the actual values, showing a very good performance in test 1. This is probably due to the memory unit in dynamic networks. This unit, which exists in dynamic networks such as Recurrent and Time Lag Recurrent, provides the network with a feedback and reminder of the previous iterations during the training. This helps the networks to be able to cope with a time series better than MLP, which is a static network and has no memory unit. The Recurrent network has presented the best results although the results of the Time Lag Recurrent network are also encouraging. Another important point about the outputs of the dynamic networks is the variation of the accuracy between different prediction horizons. Reduction of the prediction accuracy is quite gradual against the increase in prediction horizon. A final point to mention here is the variation of network performance in training and testing phases of these two types of networks. In some cases RMSE in the testing phase is even smaller than training phase, which shows superior ability of these networks to learn the process and establish a relationship between inputs and outputs and especially generalization to the new set of data. In test 2 the Recurrent network performed well except for the 12 hour horizon, which is slightly over estimated in some parts of the hydrograph. The main point about outputs of this network is the over estimation of the peak flows. As opposed to the Recurrent network, the Time Lag Recurrent network has produced results that are mostly underestimated. For the results of the Recurrent network and especially Time Lag Recurrent networks the effects of the prediction horizon on accuracy of the results is very small. In test 3 the dynamic networks have again produced quite good results but they do not seem as accurate as the outputs produced by these networks in previous tests. The accuracy of the predictions has even slightly declined for these despite using a large number of input data to train the models. In real-time prediction the time is very important, and fast prediction leads to more time for mitigating actions to be taken. Using a large number of data in test 3 required a long time for training to be completed.

The results produced in test 4 are slightly different from tests 1,2 and 3. The first important thing is the improvement of the results produced by MLP in all 3 sub-tests of this test in comparison to those of previous three tests. This is a result of the training mode. In tests 1, 2 and 3 the "prediction training mode" was used to train the models in which the data of the subject site is also automatically used as input but with delta time

step delay. In this mode of training manual preparation of the data to suit a specific lead-time is not needed. However, in test 4 this mode of training was not used and the training was carried out with normal mode in which the data of the subject site is not automatically used as input. To define the lead-times of predictions for the model input data were entered to the model with a delay equal to each lead-time, as no delta is used to do this in this mode.

In the testing phase of sub-test 1 although the outputs of MLP shows a considerable improvement from first three tests for short prediction horizons, but prediction accuracy decreases sharply when the lead-time increases. In sub-test 2 there is an improvement over sub-test 1 for all lead times given by MLP as well as the Time Lag Recurrent network. In addition, the rate of decrease in accuracy caused by the lead-time increase for these types of networks is smaller in sub-test 2 than sub-test 1. As the only change in the models used in sub-tests 1 and 2 is the number of input patterns (has been increased from one in sub-test 1 to two in sub-test 2), it can be said that the number of input patterns shows a clear influence on the results of MLP and Time Lag Recurrent networks. In sub-test 3 the output of the MLP for a 3 hour lead-time is quite close to the measured values but this closeness decreases considerably when the prediction lead-time increases to 6, 9 and 12 hours.

In Recurrent and Time Lag Recurrent neural networks the accuracy of the predictions decreases quite gradually when the lead-time of the predictions increases. The difference between the outputs of the Recurrent and Time Lag Recurrent networks is also considerable, and the results of the Recurrent network show accuracy much better than those of the Time Lag Recurrent network. In sub-test 2 as mentioned earlier the results of the Time Lag Recurrent network show an improvement over sub-test 1. However, there is no considerable difference between the outputs of the Recurrent network from sub-test 1 to sub-test 2. In sub-test 3 the outputs of the Recurrent and Time Lag Recurrent networks are also quite satisfactory even for 12 hours lead-time. However, the effect of additional gauging site on the results of this sub-test over sub-test 2 is negligible.

In real-time prediction, a decrease in the accuracy with increasing lead-time is usually assumed but the quality and quantity of this variation is important and case dependent. The maximum leadtime for satisfactory results is different from case to case and should be considered for any specific problem. Despite all three types of ANN presenting acceptable results for short prediction horizon, dynamic architectures (Recurrent and Time Lag Recurrent) have shown superior performance for this application even for 12 hours lead-time. Results produced by the naive method is almost comparable to those produced by MLP in accuracy but considerably poorer than the results of the dynamic networks.

8 CONCLUSIONS

Results obtained from this study show good performance of the ANN in predicting river flow using hydrological time series. All three types of ANN presented acceptable results for a short prediction horizon, but dynamic architectures (Recurrent and Time Lag Recurrent) have shown superior performance even for a 12 hour lead-time. MLP could not produce acceptable results for a prediction horizon longer than 3 hours. Using too

long a period of data, which produces a large number of exemplars does not give any improvement in the outputs. In addition, it makes the training time too long which is a disadvantage in the process of real-time prediction. The number of upstream gauging stations for input data does not show an important influence on the accuracy of prediction for Recurrent networks. However, for MLP and Time Lag Recurrent networks, using two upstream gauging stations produced results better than using one gauging station. In this test, in which data from the subject site was not entered to the model (training was carried out without using the prediction mode), the results produced by the MLP are considerably improved in comparison to the first three tests. It is concluded that appropriate prediction of flow with appropriate lead-time can be made using only flow data of the upstream gauging sites in headwater, steep catchments. In this regard appropriate selection of the neural network architecture has an important effect on quality of predictions.

REFERENCES

- Bhattacharya B. and D.P.Solomatine, *Application of artificial neural network in stage-discharge relationship*, Proc. 4th International Conference on Hydroinformatics, Iowa city, USA, July 2000.
- Dawson C.W. and R.Wilby, *An artificial neural network approach to rainfall-runoff modelling*, J. of Hydrological Sciences, 43 (1), February 1998.
- Dawson C.W. and R.Wilby, *A comparison of artificial neural network used for river flow forecasting*, J. of Hydrology and Earth System Sciences, 3 (4), pp. 529–540, 1998.
- Hsu K., H.V.Gupta, and S.Sorooshian, *Artificial neural network modeling of the rainfall-runoff process*, J. of Water resources research, Vol. 31, No. 10, pp. 2517–2530, October 1995.
- Karunanithi N., W.J.Grenney, D.Whitley, and K.Bovee, *Neural networks for flow prediction*, J. Computing in Civil Engineering, Volume 8, Number 2, 201–220, April 1994.
- Luk K.C., J.E.Ball, and A.Sharma, *Rainfall forecasting through artificial neural networks*, Hydroinformatics'98, Babovic and Larsen(eds), 1998, Balkema, Rotterdam, ISBN 9054109831.
- Minns A.W. and M.J.Hall, *Artificial neural networks as rainfall-runoff models*, J. of Hydrological Sciences, 41(3) June 1996.
- NeuroDimensions, *NeuroSolutions*, <http://www.nd.com/>, 2001.
- Sezin A.Tokar and P.A.Johnson, *Rainfall-runoff modeling using artificial neural networks*, J. Hydrologic Engineering, Vol. 4, No. 3, Jul 1999.

Prediction of salinity intrusion in Arvand River

B.Sherkati-Azin, A.Etemad-Shahidi & E.Jabbari

Dept. of Civil Eng., Iran Uni. Of Science and Technology, Tehran, Iran

Hydraulics of Dams and River Structures—Yazdandoost & Attari (eds)

© 2004 Taylor & Francis Group, London, ISBN 90 5809 632 7

ABSTRACT: Damming of rivers has impact on these natural waters and their environment. For example, integrity of tidal rivers depends on the balance between freshwater and oceanic seawater and reducing the freshwater input and disturbs this balance. Prolonged low-flow condition allows salinity intrusion in the upstream which deteriorates both the surface water quality and even the ground water quality. This study deals with the salt intrusion prediction in the Arvand estuary in the south west of Iran. The hydrological conditions in the Arvand are continuously changing. A steady reduction of the discharge of the rivers from which the Arvand River receives its water is caused by a consecutive development of irrigation and industrial schemes along the river courses, which demands construction of dams. A laterally averaged, two-dimensional hydrodynamics-water quality model called CE-QUAL-W2, was used for simulation of flow and salinity intrusion in this river. Recorded tidal levels of gauging stations in Abadan and Ghosbeh were used for calibrating the hydrodynamic module. The best fit of the recorded and computed water levels curves at Ghosbeh was obtained with a Manning friction factor of 0.02. After calibration of the model the maximum length of salt wedge intrusion was predicted both by numerical simulation and three empirical equations. It was found that most of the existing predictive models are limited to special conditions and are not valid for Arvand River. However, the method which was described by Savenije (1993) performs the best.

1 INTRODUCTION

The intrusion of salt water into estuaries is one of the greatest interests of engineers, increasingly called upon to modify the flow regime of natural estuaries for purposes of

improved navigation, land reclamation and flood control and to correct the conditions produced by the disposal of wastewaters. The main factors controlling the variation in salinity are the freshwater discharge, tidal variation, and bathymetry.

A number of systematic attempts have therefore been made with more or less success to correlate the intrusion of saline water with the tidal characteristics based on actual observation of the salinity conditions in real estuaries (e.g. Rigter 1973, Fischer 1972, Savenije 1993). From these studies the basis pattern of the interaction of tides, salinity and freshwater has become established qualitatively for the general case, while quantitative results are available through the one-dimensional theory and through experimental evidence for estuaries with simple geometric cross section and plan. Existing predictive models all have an empirical component and are either limited to special conditions. Rigter (1973) and Fischer (1972) proposed formulations on the base of laboratory experiments limited greatly in channels with constant cross-sections. Savenije (1993) described such a relationship for a steady-state salt intrusion model in alluvial estuaries. He considered the estuary shape in his formula.

This study also uses a two-dimensional hydrodynamic and water quality modeling. Although simulations with the numerical computer models are time consuming and need calibration but after calibration with field data they can be used for verifying the other predictive and empirical models. The performance of numerical model and empirical equations in prediction of salt intrusion are compared here.

2 DESCRIPTION OF MODEL

CE-QUAL-W2 version 3 is a two-dimensional water quality and hydrodynamic code developed US ACE waterways experiments station (Cole & Wells 2001). This model has been widely applied to stratified water systems such as lakes, reservoirs, and estuaries. It computes water levels, horizontal and vertical velocities, temperature and 21 other water quality parameters. Table 1 shows a summary of governing equations.

The algorithm and the vertical shear stress is:

$$\frac{\tau_{xz}}{\rho} = v_{turbulent} \frac{\partial U}{\partial z} = A_z \frac{\partial U}{\partial z} \quad (1)$$

In CE-QUAL-W2, the user can specify an algorithm to use for vertical eddy diffusivity. The algorithms are shown in Table 2.

Table 1. Governing equations for CE-QUAL-W2 with and without channel slope.

	Existing governing assuming no channel slope	Governing equation an arbitrary channel slope
x- momentum	$\frac{\partial UB}{\partial t} + \frac{\partial UUB}{\partial x} + \frac{\partial WUB}{\partial z}$ $= gB \sin \alpha + g \cos \alpha B \frac{\partial \eta}{\partial x} - \frac{g \cos \alpha B}{\rho} \int_{\eta}^z \frac{\partial \rho}{\partial x} dz$ $+ \frac{1}{\rho} \frac{\partial B \tau_{xx}}{\partial x} + \frac{1}{\rho} \frac{\partial B \tau_{xz}}{\partial z}$	$\frac{\partial UB}{\partial t} + \frac{\partial UUB}{\partial x} + \frac{\partial WUB}{\partial z}$ $= gB \frac{\partial \eta}{\partial x} - \frac{gB}{\rho} \int_{\eta}^z \frac{\partial \rho}{\partial x} dz$ $+ \frac{1}{\rho} \frac{\partial B \tau_{xx}}{\partial x} + \frac{1}{\rho} \frac{\partial B \tau_{xz}}{\partial z}$
z- momentum	$0 = g \cos \alpha - \frac{1}{\rho} \frac{\partial P}{\partial z}$	$0 = g - \frac{1}{\rho} \frac{\partial P}{\partial z}$
Free surface equation	$B_{\eta} \frac{\partial \eta}{\partial t} = \frac{\partial}{\partial x} \int_{\eta}^h UB dz - \int_{\eta}^h qB dz$	$B_{\eta} \frac{\partial \eta}{\partial t} = \frac{\partial}{\partial x} \int_{\eta}^h UB dz - \int_{\eta}^h qB dz$

Where U , W =horizontal and vertical velocity; B =channel width; P =pressure; g =acceleration due to gravity; τ_x , τ_z =lateral average shear stress in x and z directions; ρ =density; η =water surface; α =channel angle

Table 2. Vertical eddy viscosity, ν_t formulation in the model.

Ormulation	Formula	Reference
Nickuradse (NICK)	$\nu_t = l_m^2 \left \frac{\partial u}{\partial z} \right e^{-CRi}$ $l_m = H \left[0.14 - 0.08 \left(1 - \frac{z}{H} \right)^2 - 0.06 \left(1 - \frac{z}{H} \right)^4 \right]$	Rodi(1993)
Parabolic (PARAB)	$\nu_t = \kappa \kappa u_* z \left(1 - \frac{z}{H} \right) e^{-CRi}$	Engeland(1976)
W2(usedinVersion2)	$\nu_t = \kappa \left(\frac{l_m^2}{2} \right) \sqrt{\left[\left(\frac{\partial U}{\partial z} \right)^2 + \left(\frac{\tau_{wy} e^{-2kz}}{\rho \nu_t} \right)^2 \right] e^{(-CRi)}}$ $l_m = \Delta z_{max}$	Cole&Buchak(1995)
W2 with mixing length of Nickuradse (W2N)	$\nu_t = \kappa \left(\frac{l_m^2}{2} \right) \sqrt{\left[\left(\frac{\partial U}{\partial z} \right)^2 + \left(\frac{\tau_{wy} e^{-2kz}}{\rho \nu_t} \right)^2 \right] e^{(-CRi)}}$ $l_m = H \left[0.14 - 0.08 \left(1 - \frac{z}{H} \right)^2 - 0.06 \left(1 - \frac{z}{H} \right)^4 \right]$	Cole&Buchak(1995) Rodi(1993)
RNG (renormalization group)	$\nu_t = \nu \left[1 + \psi \left[3k \left(\frac{zu_*}{\nu_t} \right)^3 \left(1 - \frac{z}{H} \right)^3 - C_1 \right] \right]^{1/3} e^{-CRi}$	Simoes (1998)

Where l_m =mixing length, z =vertical coordinate, H =depth, u =horizontal velocity, Ri =Richardson number, C =constant (assumed 0.15), u_* =shear velocity, κ = Von Karman constant, τ_{wy} =cross-shear from wind, k =wave number. ρ =liquid density. Δz_{max} =maximum vertical grid spacing. $\psi = \max(0, x) = \nu$ molecular

viscosity, C_1 =empirical constant (assumed 100)

3 APPLICATION OF NUMERICAL MODEL TO ARVAND RIVER

The study area is shown in the Figure 1. For describing the geometry of the river at first, the distance between Abadan and Persian Gulf was divided to 43 segments with a length of about 1830 m. Then each segment was divided to the vertical layers with 1 m height. The maximum number of the layers was 25 along Arvand River.

A Manning coefficient was 0.02 was obtained in the calibration of hydrodynamics. The modelpredicted tidal levels are compared with the measured values in Figure 2.

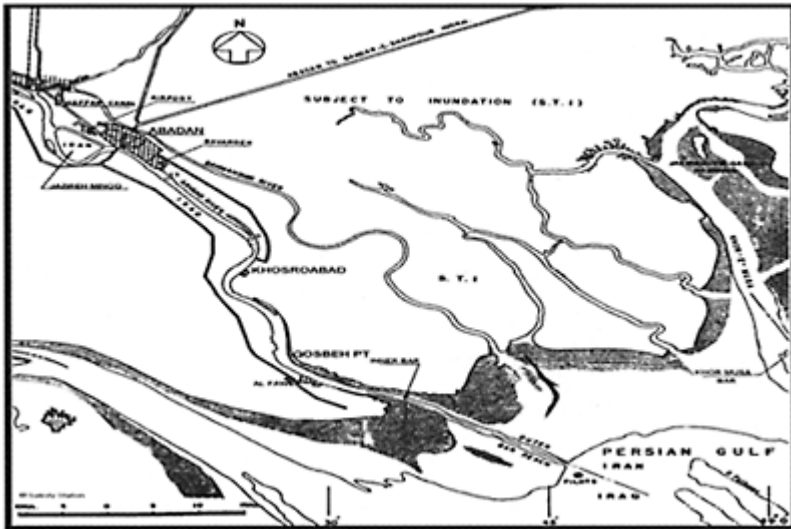


Figure 1. The area of study and the stations.

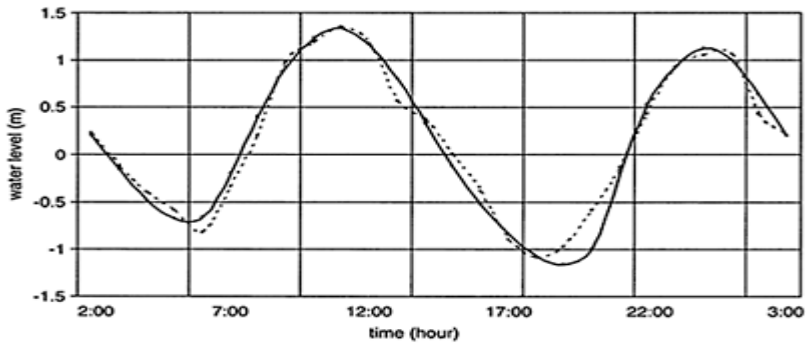


Figure 2. Comparison of recorded and predicted surface water levels in Ghosbeh (14 and 15 September 1974) (Recorded—Predicted).

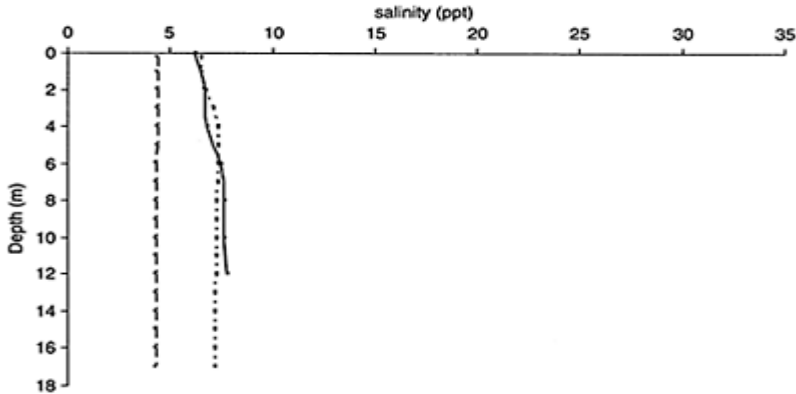


Figure 3. Comparison of recorded and predicted salinity profiles in Ghosbeh (—Recorded -----Predicted —. —. —. (W2N) predicted (Nick)).

In the simulation of salinity the upstream (Abadan) salinity was given 1.2 ppt and for the downstream (Persian Gulf) it was given 38ppt (Sweco, 1976). Initial conditions for all elements were chosen a constant vertical profile equals to 10ppt. The horizontal eddy viscosity and horizontal eddy diffusivity were assumed to be $10 \text{ m}^2\text{s}^{-1}$ suitable for estuaries (Chapra, 1998). The model was executed with two of the five existed vertical eddy diffusivity formulations. Figure 3 shows comparison between measured and simulated profiles of salinity in Ghosbeh. As seen the W2N formulation performs better than the other one. Then by using W2N formulation the intrusion length was obtained from the model at high tide. The numerical model showed that the maximum intrusion length is about 1.5 km.

4 EMPIRICAL MODELS

The most important output of predictive empirical models is the salinity intrusion length, the distance from the estuary mouth to the point where the salinity reaches the river salinity. Righer (1973), on the basis of flume data of Delft Hydraulic Laboratory and of the waterways experiment station (WES), proposed at the following empirical relation:

$$L = 1.5 \pi \frac{h_o}{f} (F_d^{-1} N^{-1} - 1.7) \quad (2)$$

where h_o =tidal average depth at the estuary mouth; f =Darcy-Weisbach's roughness; N =Canter Cremers' estuary number defined as the ratio of the freshwater entering the estuary during a tidal cycle to the flood volume of salt water entering the estuary over a tidal cycle, P_t . Hence:

$$N = \frac{Q_f^T}{P_t} = \frac{-Q_f^T}{A_o E_o} = \frac{\pi}{1.08} \frac{-Q_f}{A_o v_o} = \frac{\pi}{1.08} \frac{-u_o}{v_o} \quad (3)$$

where Q_f =fresh water discharge; u_o =fresh water velocity at the estuary mouth, which are negative since the positive x direction is taken upstream; A_o =cross-section area at the estuary mouth; T =tidal period.

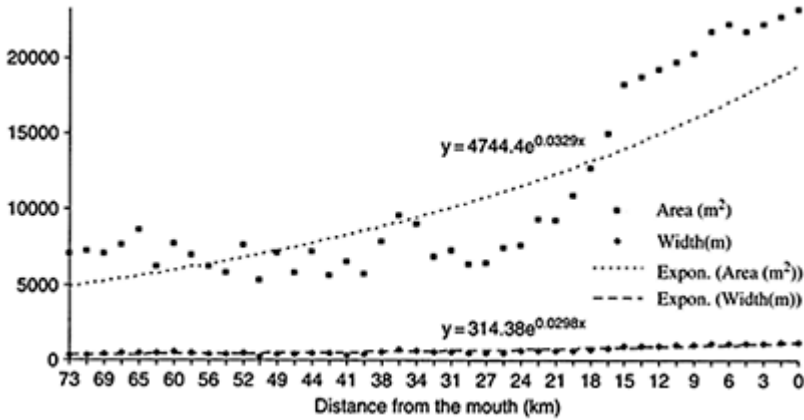


Figure 4. The exponential functions describing the cross-section area and width variations in Arvand River.

Savenije (1992) showed that the flume volume can be very well approximated by the product of A_o and the tidal excursion E_o at the estuary mouth and that $E_o = 1.08 v_o T / \pi$ where v_o is the tidal velocity amplitude at the estuary mouth which it can be calculated from the following formula (Ippen 1960):

$$v_o = H_o \sqrt{g/h} \quad (4)$$

where H_o =the tidal range at the estuary mouth; h =the depth of estuary mouth. In addition, the densimetric Froude number F_d in Eq. (1) is defined as:

$$F_d = \frac{\rho V_o^2}{\Delta \rho g h_o} = \frac{\rho}{\Delta \rho} F \quad (5)$$

where $F = v_o^2 / \sqrt{gh_o}$ and is the Froude number ρ =density of water; $\Delta\rho$ =the density difference over the intrusion length.

Fischer (1974) proposed the following formula:

$$L = 17.7 \frac{h_o}{f^{0.625}} F_d^{-0.75} N^{-0.25} \quad (6)$$

Savenije (1993) presented following formula:

$$L = a \ln \left(\frac{1}{\beta} + 1 \right) \quad (7)$$

where:

$$\beta = - \frac{K_a Q_f}{D_o A_o} = \frac{ka}{\alpha_o A_o} \quad (8)$$

where k =Van der Burg coefficient; a =convergence length; D_o =boundary condition for dispersion, k is defined as:

$$k = 0.16 \times 10^{-6} \frac{h_o^{0.69} \times g^{1.12} \times T^{2.26}}{H_o^{0.59} \times b^{1.1} \times B_o^{0.13}} \quad (9)$$

where b =width convergence length; B_o =width at the estuary mouth.

In this method, exponential functions (Eqs 10, 11) should be fitted to the cross-sectional area and estuary width. The curves are shown in Figure 4 for Arvand River.

$$A = A_o \exp \left(-\frac{x}{a} \right) \quad (10)$$

$$B = B_o \exp \left(-\frac{x}{b} \right) \quad (11)$$

5 APPLICATION OF EMPIRICAL MODELS IN THE ARVAND RIVER

Table 3 displays the different characteristics of the Arvand River which were used for calculating the intrusion length using empirical equations.

The intrusion lengths were computed using Table 3. The intrusion lengths computed with the Equations (1), (5) and (6) are shown in the Table 4. The intrusion length resulted from the numerical simulation is also mentioned in this table. The methods of Rigter (1993) and Fischer (1972) over predict the intrusion length.

6 SUMMARY AND CONCLUSIONS

In this work a laterally averaged 2-D hydrodynamics and water quality model called CE-QUAL-W2 was applied to Arvand River estuary in south east of Iran to study the salinity intrusion. The hydrodynamics of model was first calibrated by minimizing the difference between measured and simulated water levels. Then different vertical eddy diffusivity formulations were used for reproducing the measured salinity profiles by the model and it was found that W2N formula performs well.

Table 3. Characteristics of the Arvand River.

Characteristics	Definition	Amount
$B_o(m)$	width in the estuary mouth	15.09
$A_o(m^2)$	estuary mouth cross-section area	47.44
$a(km)$	cross sectional area's convergence length	30.39
$b(km)$	width convergence length	33.56
$h_o(m)$	tidal average depth	17
$T(sec)$	tidal period	90000
f	Darcy-Weisbach's Roughness	0.02
$Qf(m^3s^{-1})$	fresh water discharge	50
$u_o(ms^{-1})$	fresh water velocity at the estuary mouth	0.214
$v(ms^{-1})$	tidal velocity amplitude at the estuary mouth	0.8
$E_o(km)$	tidal excursion	23.8
F_d	densimetric Froude number	0.263
N	Canter Cremers' number	0.78
k	Van der Burg's coefficient	0.76

Table 4. Intrusion length computed by different methods.

Formulation	Intrusion length (km)
Rigter 1973	12.7
Fischer 1974	10.06
Savenije 1993	0.12
CE-QUAL-W2	1.5

Finally, several proposed empirical formulas were applied to the Arvand River and the predicted intrusion lengths were compared with that of the predicted by calibrated numerical model. It was noted that the Savenije (1993) formula performs the best while other methods over predict the length of salt intrusion. The first two methods are hampered by the assumption of constant cross-section. Savenije (1993) by inserting k in

his formula entered the effects of estuary shape. Therefore this method is suggested as a preliminary tool for salt intrusion prediction.

REFERENCES

- Chapra, S.C., Hamilton, D.P. & Patterson, J.C. 1998. Surface Water Quality Modeling. McGraw-Hill.
- Cole, T.M. & Wells, S.A. 2000. CE-QUAL-W2: A Two Dimensional, Laterally Averaged, Hydrodynamic and Water Quality Model, Version 3, User Manual. Prepared for U.S. Army Corps of Engineers Waterway Experiment Station.
- Cole, T.M. & Wells, S.A. 2001. CE-QUAL-W2: Appendix A, Hydrodynamics and Transport Equations. www.ce.pdx.edu/w2
- Cole, T.M. & Wells, S.A. 2001. CE-QUAL-W2: Appendix B, Water Quality Equations. www.ce.pdx.edu/w2
- Cole, T.M. & Wells, S.A. 2001. CE-QUAL-W2: Appendix C, input Data Description. www.ce.pdx.edu/w2
- Ippen, A. 1996. Estuary and coastline hydrodynamics. New York: McGraw-Hill.
- Savenije, H.G. 1993. Predictive model for salt intrusion in estuaries. *Journal of Hydrology*, 148, pp 203–218.
- Sweco. 1976. Abadan Island and Irrigation Project Report. *Khusestan Water and Power Authority, Mahab Ghods*.

Author index

Hydraulics of Dams and River Structures—Yazdandoost & Attari (eds)

© 2004 Taylor & Francis Group, London, ISBN 90 5809 632 7

Adduce, C. 319
Amador, A. 279
André, S. 189
Armanini, A. 385
Ataie-Ashtiani, B. 345
Ayyoubzadeh, S.A. 353

Bacchiega, J.D. 77
Bechteler, W. 335
Behrangi, A. 393
Berzi, D. 147
Bina, M. 197
Boillat, J.-L. 189
Bollaert, E.F.R. 117, 125, 173
Borghei, S.M. 327, 393

Cardoso, A.H. 311
Casado, J.M. 133, 139
Castro, C. 53, 69
Chanson, H. 3, 25, 287

Daemi, A.R. 327, 393
Dalri, C. 385
Dastorani, M.T. 431
Della Putta, F. 385
Dolz, J. 279
Drobir, H. 85

Etemad-Shahidi, A. 441

Fael, C.M.S. 311
Falconer, R.A. 413
Farhadi, L. 345
Farshi, D. 361
Fattor, C.A. 77, 133, 139
Fenton, J.D. 369
Firoozabadi, B. 377
Freer, R. 205

Fritz, H.M. 93

Ghodsian, M. 425

Gonzalez, C.A. 287

Gvelesiani, T.L. 109

Hager, W.H. 33, 93, 165, 305

Horr, A.M. 157

Huber, A. 109

Jabbari, E. 441

Keinberger, V. 85

Keller, U. 17

Knight, D.W. 401

Komaie, S. 335

Koutitas, Ch. 109

Kramer, K. 33

La Rocca, M. 319

Larcen, E. 147

Larcher, M. 385

Lin, B. 413

Lopardo, M.C. 133, 139

Lopardo, R.A. 133, 139

Loveless, J.H. 229, 237

Mambretti, S. 147

Manso, P.A. 117, 173

Marin, J. 61

Marcano, A. 53, 61, 69

Martinez, E. 69

Matcharadze, G.T. 109

Matos, J. 189

Mele, P. 319

Mendes, I. 69

Minor, H.-E. 17, 33, 165, 273, 361

Mohammadi, M. 401

Montazer, Gh.A. 425

Montilla, G. 53

Musavi-Jahromi, H. 157, 197

Najafi, A. 43

Navabi, A.H. 157

Nazari, A. 327

Negm, A.M. 181

Nuñez Gonzalez, F. 245

Oehy, C.D. 263

Okano, M. 255
Oliveto, G. 305
Orsi, E. 147

Pagliara, S. 165
Puertas, J. 279

Rampanelli, L. 385
Reyes, M. 61
Righetti, M. 385
Rojas-Sólorzano, L. 61
Rossi, A. 305

Sánchez Juny, M. 279
Sánchez-Tembleque, F. 279
Salmasi, F. 197
Scheuerlein, H. 245
Schleiss, A.J. 117, 173, 189, 263
Sherkati-Azin, B. 441
Sigg, H. 17
Siyam, A.M. 229

Tritthart, M. 245

Umeda, M. 255

Valentin, G. 273
Volkart, P.U. 17, 273

Wang, Z.Y. 213
Wu, B.S. 213

Yalin, M.S. 297
Yasi, M. 43
Yeoh, J.S. 229, 237
Yokomori, G. 255

Zahiri, A. 353
Zakermoshfegh, M. 425
Zerihun, Y.T. 369
Zweifel, A. 93